University of Oxford

Department of Chemistry

Alkaline-earth catalysts for biorenewable polymer synthesis

Rebecca Louise Jones

Balliol College

August 2023

This Thesis is submitted in partial fulfilment of the requirement for the degree of Doctor of Philosophy at the University of Oxford

For my family and friends

Preface

The work described in this Thesis was carried out in the Chemistry Research Laboratory at the University of Oxford between October 2019 and July 2023 under the supervision of Professor Dermot O'Hare. All work was performed by the author unless otherwise stated, and no part has been previously submitted for another degree at this or any other university.

Part of the work contained in this Thesis has been published in the following journal paper:

R. L. Jones, L. J. Morris, C. G. Collins Rice, Z. R. Turner and D. O'Hare, *Phys. Chem. Chem. Phys*., **2023**, *25*, 15463-15468.

And presented as *"Alkaline-earth complexes for biorenewable polymer synthesis"* at the following conferences:

SCI Early Career Materials Annual Conference, **July 2022** – London: *oral*.

29th International Conference on Organometallic Chemistry **July 2022** – Prague: *poster*.

44th International Conference on Coordination Chemistry **August 2022** – Rimini: *oral*.

Rebecca L. Jones

August 2023

Abstract

Alkaline-earth catalysts for biorenewable polymer synthesis

Rebecca L. Jones **D.Phil Thesis**

Balliol College **August 2023**

Plastics have become essential to 21st century human life; it is therefore unrealistic to reduce the usage of such single-life polymers enough to offset their hazardous environmental impacts. This has prompted research into the development of greener, non-fossil-fuel based alternatives. Polylactide (PLA) is one such material; it is a biorenewable, biocompatible, aliphatic polyester that is most efficiently produced via the ring-opening polymerisation (ROP) of lactide (LA). The use of alkaline-earth metals, particularly the heavier congeners, in catalysts for this process has been understudied even though they offer advantages like high activity, low toxicity, low cost and lack of colour. The aims of this Thesis were therefore: (i) to prepare new alkaline-earth-based bimetallic, *bis*(phenoxy-imine) systems, (ii) to test their performance as initiators in LA ROP and (iii) to evaluate the benefits of bimetallic complexes/cooperativity for this type of polymerisation.

The Thesis begins by offering a brief introduction to lactide as a biorenewable monomer in ring-opening polymerisation. The general ROP mechanisms are presented alongside a discussion of polymer characterisation techniques. An overview of previously reported catalysts for the ring-opening polymerisation of lactide is also described.

A series of alkaline-earth complexes based on the "NOON" motif ($H_2^{Dipp}L$; 2,7-(HC=NDipp)-1,8-OH-$C_{10}H_4$) were synthesised and fully characterised. These compounds were applied towards the ROP of *L*-, *D*-, *rac*- and *meso*-LA; a variety of polymerisation conditions (temperature, monomer stereochemistry and initiator concentration) were studied to determine the kinetics, mechanism and overall rate equation of the polymerisation. It was found that all of the prepared initiators were active however, they either suffered from low activity (k_{obs} = 0.0046–0.091 h^{-1} (Mg)) or poor polymerisation control ($1.23<M_w/M_n<1.73$ (Ca, Sr, Ba)).

Related alkaline-earth "NON" ($H^{R,Dipp}L$; 1-OH-2,6-(HC=NDipp)-4-R-C_6H_2 where R = H, Me, ^{t}Bu) systems were then prepared and fully characterised in attempts to improve polymerisation control and activity. The homo *vs*. heteroleptic nature of these complexes was found to differ between metals as a result of varying steric shielding and bonding lability. In most cases, these monometallic species showed improved polymerisation activity (k_p = 966 *vs*. 3.19 M^{-1} h^{-1} (Mg)) and control over their "NOON" counterparts. A variety of techniques were used to characterise the resultant polymers in order to deduce tacticity (P_r = 0.48-0.67), molecular weights and chain end groups.

The "NON" framework was then explored, via several synthetic routes, for the formation of cationic, bimetallic alkaline-earth complexes. The generation of protonated pro-ligands which could then be utilised for the insertion of multiple metals (Zn/Ca) by protonolysis was found to be a promising protocol.

Acknowledgements

Firstly, I would like to thank Professor Dermot O'Hare for giving me the opportunity to study within his research group, and for all his support and advice throughout my D.Phil. Secondly, I am grateful to SCG Chemicals Co., Ltd. (Thailand) for their financial support, which has not only permitted me to undertake this project, but has also facilitated travel to present my work at national and international conferences.

A huge thank you must also go to Zoë and Louis. Firstly, for proof reading the entirety of this Thesis, but more importantly for your constant guidance and advice over the past few years. The patient tuition that you have shown me is something that I will strive to give to others. I am also grateful to those who have taught me new techniques: Nick for solution and solid-state NMR and to Peace for PLA GPC/MALDI-TOF MS.

The rest of the O'Hare group also have my sincerest gratitude especially those in S2 and S3. Firstly, thank you to Katie for reminding me that there is life outside of the lab! Thank you to Justin and Alex for always trying to make me laugh and for hosting super fun BBQs. Thank you to Matt H., whose steadfast positivity and love for the 1975, never failed to bring a smile to my face. Thank you to Clem, for helping me cope with writing up as well as running crystals. And finally thank you to Gabi, for being my number one cheerleader and listening to all my rants about lactide!

A special thanks must also go to my family. To my parents – Janice and Glyn – for their unwavering support, to my brothers – Mark and Michael – for their competitiveness which has always pushed me to reach my potential, and to Gabriella and Siobhan for being the sisters I never had.

Finally, I want to thank my fiancé Sam. I would not be where I am today without your constant love, support and guidance. This Thesis, my magnum opus, is for you…

Nomenclature

Below is a summary of some of the commonly used terms throughout the Thesis.

Term	Definition
$\{^1H\}$	Proton decoupled
Å	Ångström, 10^{-10} m
av.	Average
b	Broad
BASH	Band selective decoupling experiment
BDI	β-diketiminato
BnOH	Benzyl alcohol, $C_6H_5CH_2OH$
COSY	2D correlation spectroscopy
d	Doublet
d	Deuterated
DCM	Dichloromethane
δ	Chemical shift
Δ%	Percentage disparity *vs*. $M_{n,(calcd)}$
Dipp	Diisopropyl-*aryl*
eq.	Equivalents
Et	Ethyl
$\Delta H^{\ddagger}$	Enthalpy of activation
$\Delta S^{\ddagger}$	Entropy of activation
FTIR	Fourier transform infrared
GPC	Gel permeation chromatography
HMBC/HSQC	Heteronuclear multiple bond correlation
HMDS	Bis(trimethylsilyl)amine

^{i}Pr	Isopropyl, $CHMe_2$
^{n}Pr	*n*-propyl, C_3H_7
IR	Infrared
k_{app}	Apparent rate constant
k_i	Initiation rate constant
k_{obs}	Observed rate constant
k_p	Propagation rate constant
k_{tr}	Transfer rate constant
KTFA	Potassium trifluoroacetate, $KO_2C_2F_3$
LA	Lactide
m	Multiplet
MALDI-TOF	Matrix-assisted laser desorption/ionisation time of flight
Me	Methyl, CH_3
M_n	Number average molecular weight
MS	Mass spectrometry
M_w	Weight average molecular weight
MWD or Đ	Molecular weight distribution, M_w/M_n
m/z	Mass to charge ratio
μ	Bridging
^{n}Bu	*n*-butyl, $CH_2CH_2CH_2CH_3$
NMR	Nuclear magnetic resonance
NOESY	Nuclear Overhauser Effect Spectroscopy
Ω	Solid angle
PDLA	Poly-*D*-lactide
Ph	Phenyl, C_6H_5
PLA	Polylactide
PLLA	Poly-*L*-lactide

P_m	Probability of forming a *meso* linkage
P_r	Probability of forming a *racemic* linkage
q	Quartet
ROP	Ring-opening polymerisation
ROCOP	Ring-opening, co-polymerisation
RT	Room temperature
s	Singlet
sr	Steridian
SSNMR	Solid-state nuclear magnetic resonance
t	Triplet
^{t}Bu	*tert*-butyl, CMe_3
THF/thf	Solvent/bound tetrahydrofuran, C_4H_8O
TOF	Turnover frequency

Compounds described in this Thesis

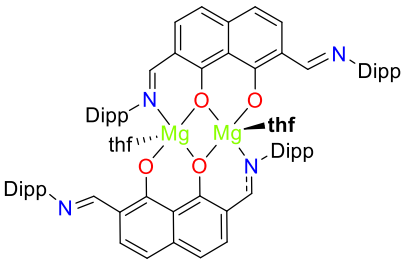

1

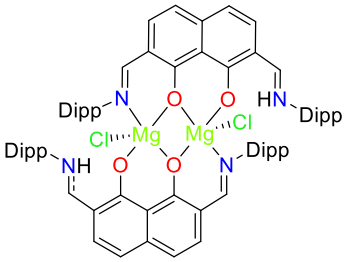

2

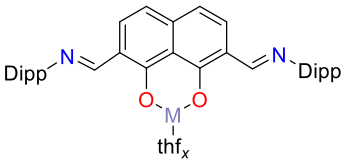

M = Ca (**3**) *x* = 2
Sr (**4**) *x* = 1
Ba (**5**) *x* = 1

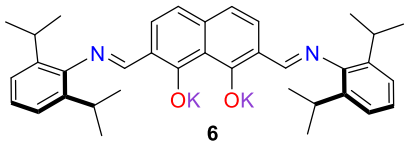

6

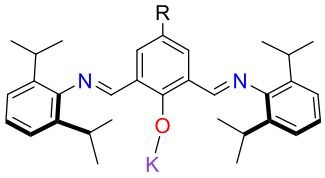

R = H (**7**)
Me (**8**)
^{t}Bu (**9**)

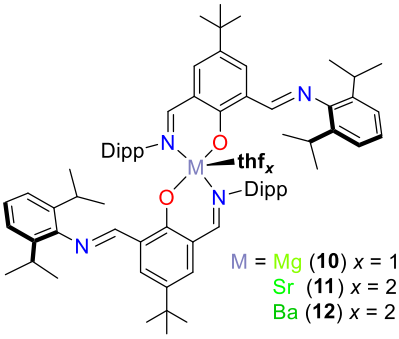

M = Mg (**10**) *x* = 1
Sr (**11**) *x* = 2
Ba (**12**) *x* = 2

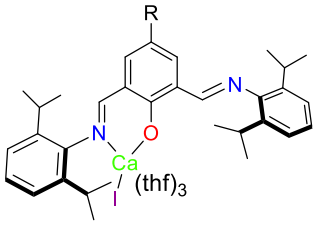

R = H (**13**)
Me (**14**)
^{t}Bu (**15**)

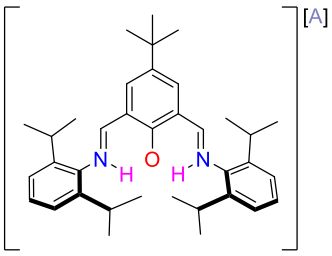

A = BF_4 (**16**)
$H_2N\{B(C_6F_5)_3\}_2$ (**18**)
$B(3,5\text{-}\{CF_3\}_2C_6H_3)_4$ (**20**)

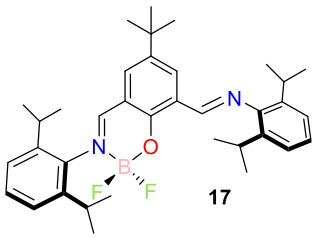

17

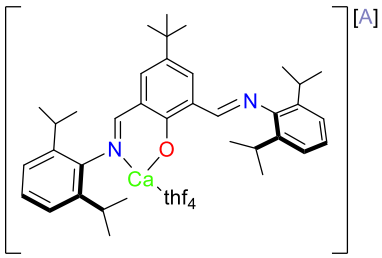

A = $H_2N\{B(C_6F_5)_3\}_2$ (**19**)
$B(3,5\text{-}\{CF_3\}_2C_6H_3)_4$ (**21**)

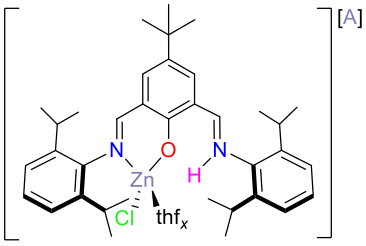

A = $H_2N\{B(C_6F_5)_3\}_2$, *x* = 1 (**22**)
$B(3,5\text{-}\{CF_3\}_2C_6H_3)_4$, *x* = 0 (**23**)

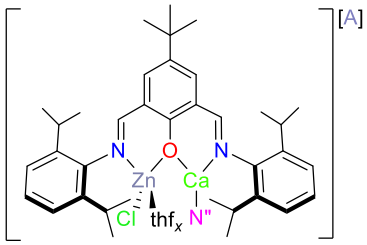

N" = $N(SiMe_3)_2$
A = $H_2N\{B(C_6F_5)_3\}_2$, *x* = 1 (**24**)
$B(3,5\text{-}\{CF_3\}_2C_6H_3)_4$, *x* = 0 (**25**)

Compound nomenclature

Number	Name	Number	Name
1	$[^{Dipp}LMg(thf)]_2$	**14**	$^{Me,Dipp}LCaI(thf)_3$
2	$[H^{Dipp}LMgCl]_2$	**15**	$^{t Bu,Dipp}LCaI(thf)_3$
3	^{Dipp}LCa	**16**	$[H_2{}^{t Bu,Dipp}L][BF_4]$
4	^{Dipp}LSr	**17**	$^{t Bu,Dipp}LBF_2$
5	^{Dipp}LBa	**18**	$[H_2{}^{t Bu,Dipp}L]$ $[H_2N\{B(C_6F_5)_3\}_2]$
6	$^{Dipp}LK_2$	**19**	$[^{t Bu,Dipp}LCa(thf)_4]$ $[H_2N\{B(C_6F_5)_3\}_2]$
7	^{Dipp}LK	**20**	$[H_2{}^{t Bu,Dipp}L]$ $[B(3,5\text{-}\{CF_3\}_2C_6H_3)_4]$
8	$^{Me,Dipp}LK$	**21**	$[^{t Bu,Dipp}LCa(thf)_4]$ $[B(3,5\text{-}\{CF_3\}_2C_6H_3)_4]$
9	$^{t Bu,Dipp}LK$	**22**	$[H^{t Bu,Dipp}LZnCl(thf)]$ $[H_2N\{B(C_6F_5)_3\}_2]$
10	$(^{t Bu,Dipp}L)_2Mg(thf)$	**23**	$[H^{t Bu,Dipp}LZnCl]$ $[B(3,5\text{-}\{CF_3\}_2C_6H_3)_4]$
11	$(^{t Bu,Dipp}L)_2Sr(thf)_2$	**24**	$[^{t Bu,Dipp}L\{ZnCl(thf)\}CaN(SiMe_3)_2]$ $[H_2N\{B(C_6F_5)_3\}_2]$
12	$(^{t Bu,Dipp}L)_2Ba(thf)_2$	**25**	$[^{t Bu,Dipp}L\{ZnCl\}CaN(SiMe_3)_2]$ $[B(3,5\text{-}\{CF_3\}_2C_6H_3)_4]$
13	$^{Dipp}LCaI(thf)_3$		

Table of Contents

Chapter 1

Introduction

1.1 Overview

This Chapter will introduce the concept and goals of a circular economy. General approaches in which scientists are working towards this goal will be described, with a focus taken on the ring-opening polymerisation (ROP) of the biorenewable feedstock: lactide (LA). Polymerisation mechanisms, kinetics, stereocontrol and initiators are also discussed alongside an overview of analytical techniques used for the characterisation of the resultant polymers.

1.2 The Circular Economy

Plastics are ubiquitous to the current human lifestyle; they have proven integral to most areas of society including agriculture, healthcare, electronics, energy, transport and building/construction.[1-4] As a result, the annual global production of plastics is rapidly increasing and is expected to exceed 500 million metric tons in the next 30 years.[5] The single-life nature of this commodity, coupled with poor after-use disposal mechanisms, has led to a distressing accumulation of these, mainly petrochemically-derived, polymers in either landfill sites or as pollutants in the environment.[2, 5] Gayer *et al*. estimate that of all the plastics produced between 1950–2015 (*ca*. 8300 million metric tonnes (Mt)), 79% were disposed of in landfills, 12% were incinerated and only 9% were recycled.[1] A more

recent, in-depth analysis of the current annual plastics economy discovered that the linear flow of these materials in fact only allows for 2% closed-loop recycling (**Figure 1.1a**).[6, 7] This high level of waste generation, estimated to be 24.5 million tonnes in 2020, leads to significant environmental challenges.[7] These include increasing greenhouse gas (GHG) emissions (on average the US plastics industry release 232 Mt of CO_2 annually)[8] and leakage of the used materials into the environment (2.41 Mt of plastic waste enters the oceans via rivers each year).[1, 2, 9] In addition to this waste generation, there are also increasing environmental concerns with the (sustainability of the) raw fossil fuel materials needed to produce the polymers.[4]

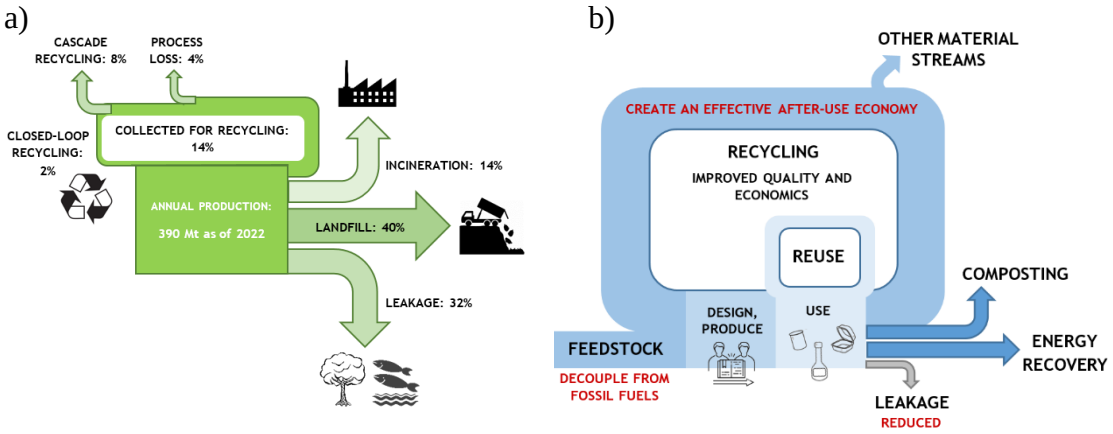

Figure 1.1 a) The current "linear-flow" of the plastics' economy and b) the desired "circular economy" (core aims highlighted in red); adapted from reports by Linder and co-workers.[6, 10]

Scientists, over the past few decades, have been developing alternative approaches to try and address these environmental issues as dramatically reducing the current usage of plastics seems unfeasible. One such method is to transform the current linear production of plastics into a circular economy.[11] This holistic approach aims to create a closed-loop, waste free chemical industry that is restorative and regenerative by design (**Figure 1.1b**). It also works towards keeping products, components and materials at their highest utility and value at all times.[11] The main aims of a circular plastics economy are therefore to improve the recyclability of the polymers, to reduce their leakage into the environment

and finally to decouple their formation from fossil fuel feedstocks.[6] Reports indicate that a doubling of the current system circularity (from 14 to 33%) would result in an 11 Mt reduction in CO_2 emissions as well as 4.7 Mt less plastic waste.[7]

Current research into this area of green "circular" chemistry can be divided into two approaches. The first is to improve the end of life options of plastics; this has involved the development of biodegradable materials[12, 13] and, more recently, completely recyclable/reusable polymers.[14-19] The second research avenue works towards replacing finite fossil fuel feedstocks with bio-derived, biodegradable, renewable alternatives. These are typically plant-based and contain high amounts of starch (i.e. corn and sugar beet) to allow fermentation into useful feedstock chemicals.[4, 20, 21] The most commonly studied bioplastics are polylactide (PLA), polycaprolactone (PCL), polyhydroxyalkonoates (PHA), polybutylene succinate (PBS) and polyglycolide (PGA).[2] Commercial examples of some of these sustainable polymers have already been developed (Ingeo-PLA[22] and Mirel-PHA[23]). However, they still only contribute less than one percent to the global, annual production of plastics.[10]

The formation of bio-based polymers also has associated economic and environmental issues; these include intensified crop farming competing with food production and potential accelerated deforestation (reduced natural CO_2 uptake).[22] However, due to the depleting nature of petroleum resources, efforts into researching them as viable alternatives should be continued.

1.3 Polylactide (PLA)

The bio-renewable plastic that forms the basis of this research is polylactide, also referred to as poly(lactic acid). It is a biodegradable, aliphatic polyester that can be derived from renewable resources (corn, beets) thus making it a sustainable alternative to polyolefins.[23]

It also has improved end of life options which include hydrolysis and subsequent enzyme-catalysed degradation into CO_2 and H_2O (**Scheme 1.1**).[20, 24] Recent life cycle analyses suggest that the formation of PLA results in reductions in both GHG emissions (~40%) and non-renewable energy usage (~25%) when compared to petrochemically derived plastics.[4, 25, 26]

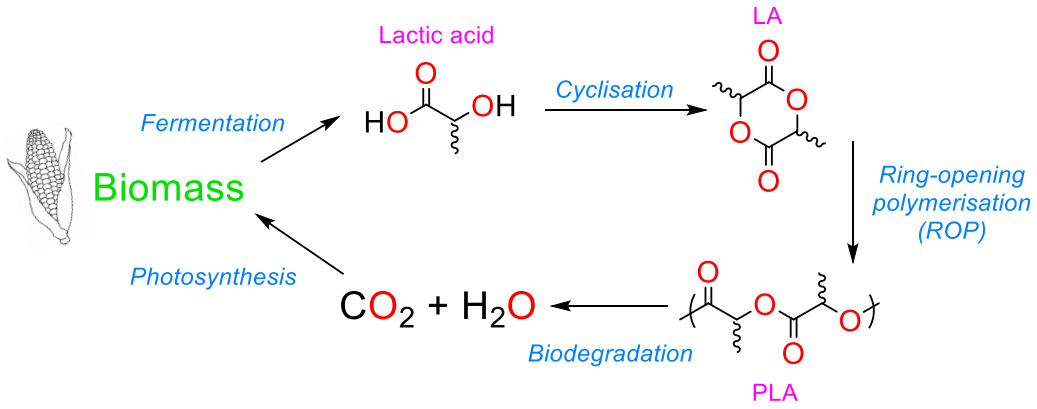

Scheme 1.1 The life cycle of polylactide (PLA).

It is one of the most widely studied "green polymers" due to its already proven versatile applications in packaging, films, pharmaceuticals and even biomedical engineering (it has been utilised in 3D printing techniques to fabricate tissue scaffolds).[24 27-29] As a result, it's global production capacity has almost doubled, and it now accounts for 20.7% of all bioplastics.[10] Market analysis reports suggest that this will only continue to increase with an estimated compound annual growth rate of 21.4% from 2023 to 2030.[28]

1.3.1 Synthesis of poly(lactide)

PLA was first discovered by Carothers *et al.* in 1932; the authors were able to isolate samples of low molecular weight PLA via the direct, reduced pressure condensation of lactic acid at 120 °C.[30] High molecular weight polymers were unattainable via this method due to the high concentration of water facilitating an equilibrium between lactic

acid and lactoyl oligomers. Azeotropic distillation in *m*-xylene was then employed to minimise the concentration of water, however, this still only produced relatively low molecular weight PLA (~30 000 $gmol^{-1}$).[31]

To date, the most successful route for the production of high molecular weight PLA is the ring-opening polymerisation (ROP) of lactide (LA; **Figure 1.2**). This method also facilitates enhanced control over other polymer macromolecular properties including polydispersity, stereoselectivity and nature of end-groups.[32]

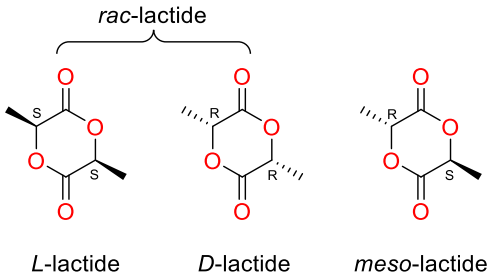

Figure 1.2 The three different isomers of the lactide (LA) monomer.

LA is the six-membered dimeric cyclic ester of lactic acid – a compound that can be chemically synthesised or, more conveniently, efficiently isolated during the bacterial fermentation of glucose.[33, 34] The polymerisation monomer contains two stereogenic carbon centres and thus is available as three stereoisomers: *L*-LA (*SS*-), *D*-LA (*RR*-) and *meso*-LA (*SR*-); the racemic 1:1 mixture of *L*-LA and *D*-LA is referred to as *rac*-LA (**Figure 1.2**).[35] It can be derived from lactic acid in one of three ways (**Scheme 1.2**).[32, 36] The first method, industrially commercialised by Cargill-Dow (Natureworks LLC) in 2001, involves the oligomerisation of lactic acid followed by depolymerisation (via intramolecular transesterification) of the low molecular weight polymers (1000–5000 $gmol^{-1}$).[24, 37-39] This process requires a catalyst, typically a tin(II) alkoxide or carboxylate, and high temperatures (> 200 ºC)/low pressures (1–80 mbar) in order to

distil pure *L*-LA from other contaminants (racemisation causes ~10% of reaction mixture to be *meso*-LA).[32, 37, 40, 41] A more direct route involves the vaporisation of lactic acid and subsequent transport, via an inert gas stream, over a plug-flow catalyst bed that is typically packed with group III, IV V or VIII oxides.[32, 36] It works at atmospheric pressure and thus is thought to be more economically viable than the two-step method.[32, 36] The final pathway was reported by Dusselier and co-workers in 2015. It employs microporous zeolite catalysts for the direct conversion of lactic acid to lactide.[32, 42] The enhanced selectivity properties of the initiator particles reduces racemisation thus allowing for the isolation of higher yields of pure *L*-LA (~79%).[42] The scale of this, and the gas phase method however, are still unable to compete with the industrially used oligomerisation-depolymerisation route.

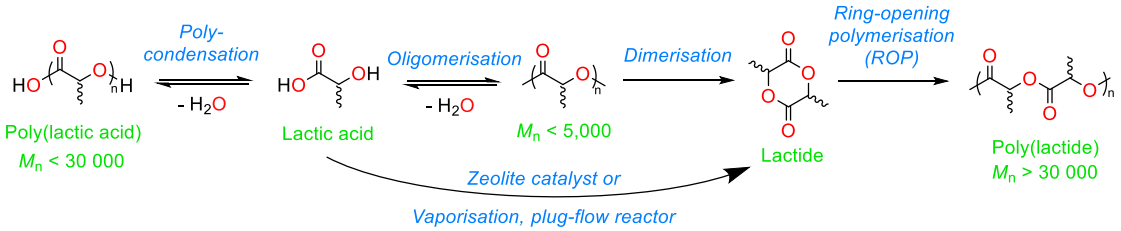

Scheme 1.2. The synthetic routes to polylactide (PLA).

1.4 The Ring-Opening Polymerisation (ROP) of Lactide (LA)

Unlike polycondensation, ROP is a form of chain-growth polymerisation; this offers advantages over the step-growth alternatives in terms of improved reaction and stereochemical control.[29] The relief of the monomer ring strain makes the polymerisation thermodynamically favourable at room temperature ($\Delta H = -22.9$ kJ mol^{-1} for 1.0 M dioxane solution of *L*-lactide).[43, 44]

Previously reported initiators for this process include (single-site) metal complexes (*vide infra* – **Section 1.6**), organic species[45-47] and even enzymes.[48-50]

1.4.1 Polymerisation mechanisms

The two most common mechanisms reported for the ROP of LA are the coordination-insertion (CI) and activated monomer (AM) pathways.[51, 52] The majority of neutral (single-site) metal-mediated polymerisations are thought to operate via CI whereas the AM route is more prevalent for cationic and organocatalytic systems.[45, 53]

1.4.1.1 Coordination-Insertion (CI)

The coordination-insertion mechanism is characteristically promoted by Lewis acidic metal complexes that contain labile, nucleophilic initiators (L_nM-R where typically R = alkyl, alkoxide, aryloxide; **Scheme 1.3**).[54, 55 56-58] It begins with monomer coordination, via a carbonyl oxygen, to the metal centre. Once activated, the lactide undergoes attack from the nearby nucleophilic initiating group. This facilitates acyl bond cleavage and subsequent ring-opening.[23] The resultant metal alkoxide is now the propagating species of the polymerisation and allows for efficient monomer insertion.[51, 52]

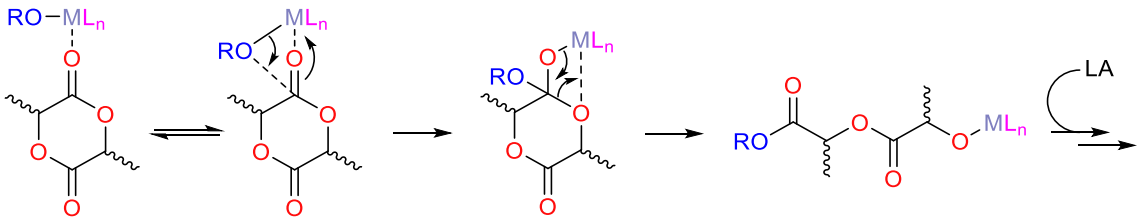

Scheme 1.3 The coordination-insertion mechanism for the ROP of LA catalysed by a metal alkoxide (L_nM-OR).[23, 51]

1.4.1.2 Activated Monomer (AM)

The activated monomer mechanism differs from that of coordination-insertion by the fact that the nucleophile is independent of the catalyst.[51]

1.4.1.2.1 Metal-mediated, AM ROP

In some cases where the polymerisation catalyst is a (single-site) metal complex, an activated monomer mechanism can be in effect. In these instances, the Lewis acidic metal centre activates the LA towards attack from an exogenous nucleophile (typically an alcohol; **Scheme 1.4**).[45, 53]

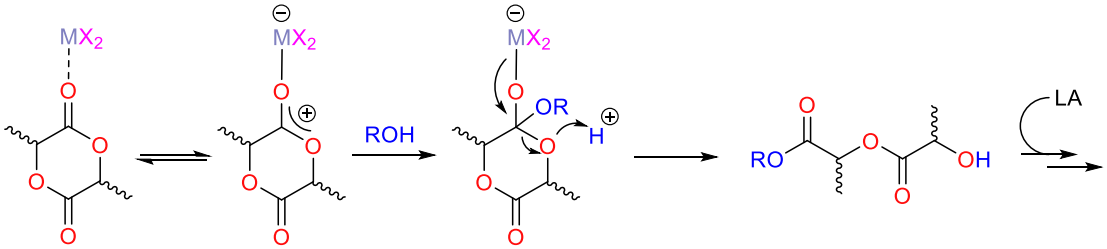

Scheme 1.4 The metal-mediated, activated monomer mechanism for the ROP of LA.

1.4.1.2.2 Cationic, AM ROP

The activated monomer mechanism for cationic ROP is very similar to that of the metal-mediated route. The only difference is that the typical activation of the LA monomer is achieved via its protonation (LA-H^+; **Scheme 1.5**) with a Brønsted acid.[59] $HCl{\cdot}OEt_2$ and HOTf are two examples of the acidic activators that have been previously employed in the cationic ROP of cyclic esters.[29, 46, 59-61]

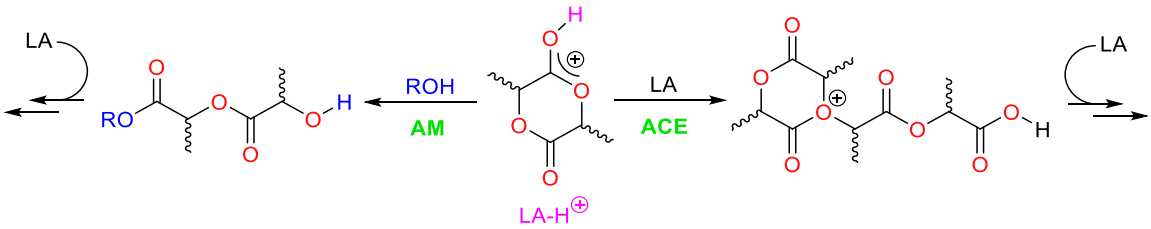

Scheme 1.5 The activated monomer (AM) and active chain end (ACE) mechanisms for the cationic ROP of LA.[59, 62]

An alternative, competing pathway referred to as the "active chain end" mechanism (ACE), can also occur during cationic ROP.[62] This is where the nucleophilic oxygen atom

of a neutral monomer attacks the α-carbon atom of a tertiary oxonium located at the end of a propagating polymer chain.[62] Compared to the AM route, ACE polymerisations often result in poorer control of molecular weights.[62] In addition, a common observation is the increased formation of cyclic polymers via intra-molecular chain transfer reactions (*vide infra* – **Section 1.4.2**).[62]

1.4.1.2.3 Organocatalytic, AM ROP

The activated monomer mechanism for the organocatalytic ROP of LA involves a transiently ring-opened alcohol (**Scheme 1.6**).[45-47, 52] The hydroxyl group of the final ring-opened adduct then initiates polymerisation propagation by interacting with another activated LA molecule.[59] Phosphines,[46, 63] pyridines,[64, 65] N-heterocyclic carbenes,[45, 66] and thiourea-amines,[67, 68] have all been reported as successful catalysts for this process.

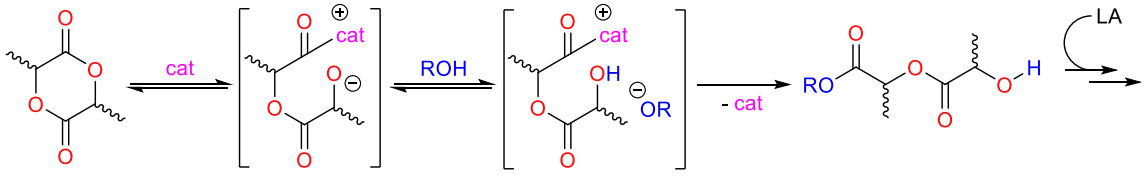

Scheme 1.6 The activated monomer mechanism for the organocatalytic ROP of LA.[46, 59]

Unfortunately, issues associated with low selectivity mean that this type of ROP is not used on the same experimental scale as metal-mediated polymerisations.

1.4.1.3 Other polymerisation mechanisms (i.e. anionic ROP)

The anionic mechanism for the ROP of LA is less widely studied. It typically involves ionic, nucleophilic catalysts such as alkali metal alkyls/alkoxides.[29, 59, 69-73] It is proposed to proceed via one of two initiation steps: monomer deprotonation (MD) or direct nucleophilic attack (NA; **Scheme 1.7**).[59] The active anionic chain ends, produced in both cases, are commonly observed to cause unwanted racemisation and/or transesterification

reactions. As a result, poor polymerisation control, as indicated by broad molecular weight distributions, is a characteristic feature of anionic ROP.[69]

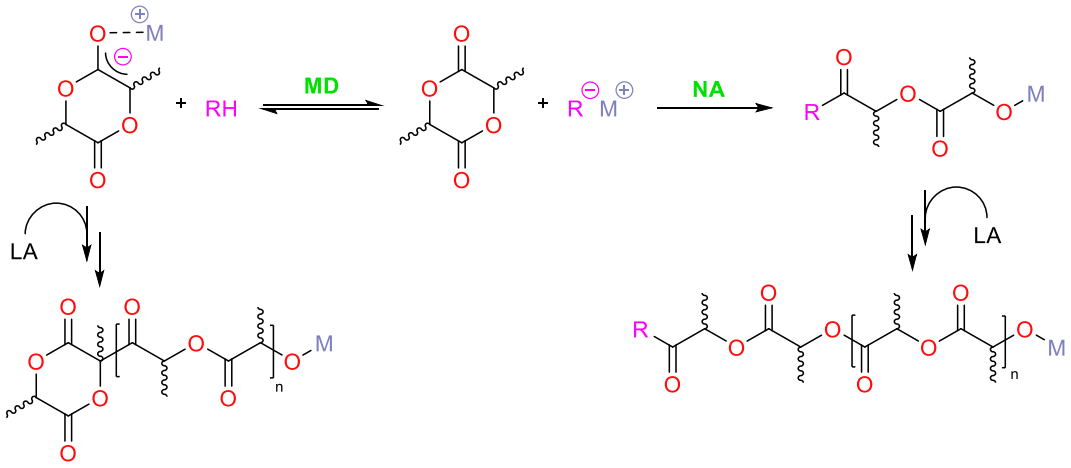

Scheme 1.7 The anionic mechanism for the ROP of LA is initiated by either monomer deprotonation (MD) or ring-opening nucleophilic attack (NA).[59]

1.4.2 Polymerisation control

During the ROP of LA, unwanted side reactions can compete with propagation thus reducing the polymerisation control. These transesterifications can occur both inter- and intra-molecularly resulting in the respective formation of different length or cyclic oligomers (**Figure 1.3**).[29, 59]

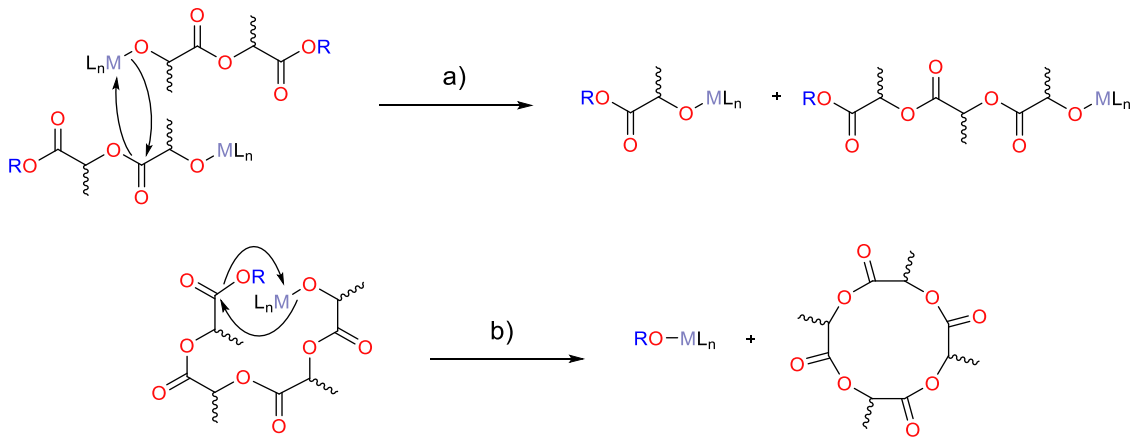

Figure 1.3 The a) inter- and b) intra-molecular transesterification reactions in the ROP of LA.[29]

The degree of transesterifications can be evaluated using Gel Permeation Chromatography (GPC) where there is the observation of broadened molecular weight distributions, and Matrix assisted, laser desorption time of flight mass spectrometry techniques (MALDI-TOF) which records lack of end groups for cyclic PLA/peak splitting of $\Delta m/z = 72$ as opposed to the expected $\Delta m/z = 144$; *vide infra*.[29, 74-78]

1.4.3 Polymerisation kinetics

The study of polymerisation kinetics is crucial to determine the reaction mechanism as well as the comparability of the initiator activity to others already reported. This comparison is usually based on the propagation rate constant, k_p, which is derived from the rate law of the polymerisation.[78] A typical rate law has the following form:

$$-\frac{d[LA]}{dt} = k_p[LA]^{\boldsymbol{x}}[\boldsymbol{cat}]^{\boldsymbol{y}} \qquad \textbf{Equation 1.1}$$

where: *x* and *y* represent the order with respect to monomer and catalyst concentration respectively.

Lactide polymerisations are typically first order with respect to the monomer concentration (i.e. "*x*" = 1; **Equation 1.1**)[78] however there have been reported cases of rare second[74, 79-85] and zero (rationalised by Michaelis-Menten kinetics controlling the rate determining step) order dependencies.[86-88] The order with respect to catalyst is determined by varying its concentration whilst holding that of LA constant. The observed rate constants, k_{obs}, for the different [LA]:[cat] ratios can then be used in plots of $-\ln(k_{obs})$ *vs*. $-\ln([cat]_0)$ and k_{obs} *vs*. $[cat]_0$ to calculate "*y*" and k_p respectively. The values of k_{obs} (sometimes referred to as k_{app}) are true for only a specific set of experimental conditions and thus they cannot form the basis of an accurate comparison unless the same reaction parameters are employed.

1.4.4 Living *vs.* immortal ROP

ROPs are generally "living" in nature; typical features of such polymerisations include a linear increase in polymer molecular weight with percentage conversion and narrow polydispersity indices (*Đ*; *vide infra* – **Section 1.5.1**).[78] For these to be achieved, the rate of initiation must greatly outweigh the rate of propagation ($k_i >> k_p$) thus ensuring that all catalyst molecules are able to start the polymerisation. In addition, the rate of chain termination/transfer reactions should be negligible.[43, 51]

An alternative type of polymerisation is referred to as "immortal ROP". It was originally coined by Inoue and co-workers in 1985 and involves the rapid and reversible transfer (k_{tr}) of propagating polymer chains and chain transfer agents (typically alcohols or amines; **Scheme 1.8**).[89, 90]

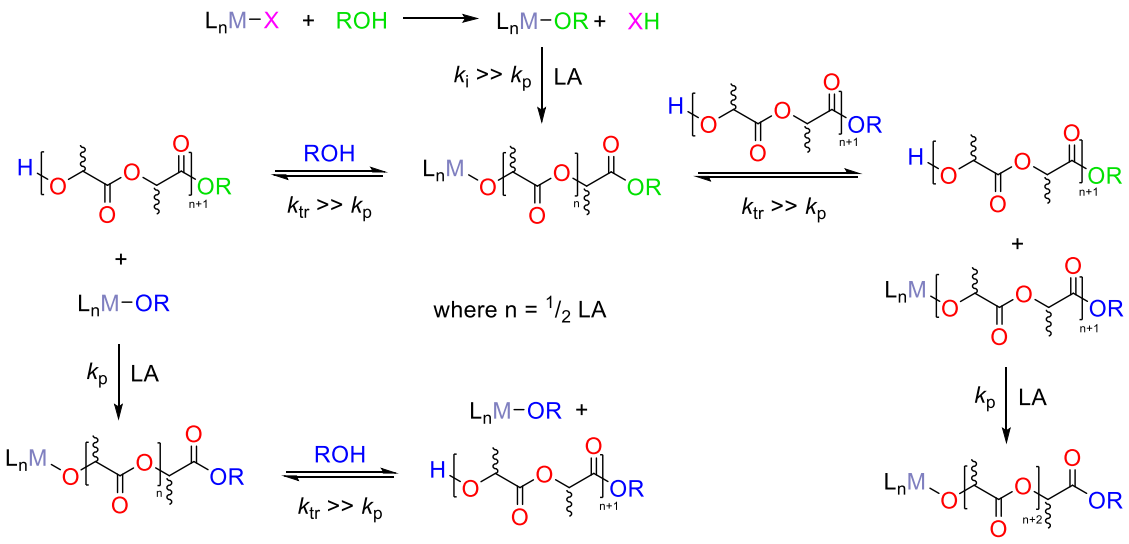

Scheme 1.8 The immortal ROP of LA by non-alkoxide species, L$_n$M–R (L = ligand, M = metal and X = initiator) in the presence of an alcohol (ROH).

In order to produce polymers of consistent molecular weights via this method, the rate of transfer must exceed that of propagation ($k_{tr} >> k_p$).[51, 91] Inoue's demonstration of this came via the use of a binary (tetraphenylporphinato)aluminium chloride/methanol system for the ROP of epoxide; the number of polymer chains was found to be consistent with

the sum of initiator and chain transfer equivalents.[89, 90] Since this report, various metals (group 2/12,[92-95] group 3/13,[96-99] group 14[100, 101]) and organocatalysts[102] have been used for immortal ROP.[91]

1.4.5 Stereocontrolled ROP

The stereoregularity, also termed "tacticity", of polylactides can be determined using $^{1}H\{^{1}H\}$ NMR spectroscopy (*vide infra* – **Section 1.5.3** and **Figure 1.4**). This property is a measure of the regularity of configurations of successive pseudochiral carbons in the polymer chain.[103] A *meso* or '*m*'-linkage refers to the joining of consecutive carbon centres with the same stereochemistry (-*RR*- and -*SS*-) whereas a *racemic* or '*r*'-linkage is the formation of a bond between carbon centres with opposing pseudochirality (-*RS*- and -*SR*-).

Tacticity is highly dependent on several factors; some of these include initiator chirality, polymerisation kinetics, extent of conversion (*vs*. side reactions) and monomer stereochemistry/composition.[104, 105] It is well known to affect the crystallinity of PLA (the higher the tacticity the more easily the polymer chains are able to pack together) thus influencing other macro-material properties including melting point (T_m), glass transition temperature (T_g), rigidity, and solubility.[106] As a result, a high degree of stereocontrol is desired.

In the absence of epimerisation, the enantiopure monomers (*L*-(*SS*)-LA or *D*-(*RR)*-LA) will ring-open to form isotactic (-[*SSSS*]$_n$- or –[*RRRR*]$_n$-) PLA – a semi crystalline polymer with a T_m = 173–178 °C (**Figure 1.4**).[107] An increase in this melt temperature (T_m = 230 °C) was observed by Ikda and co-workers upon co-crystallisation of PLLA and PDLA samples.[108, 109] It is proposed that this is due to increased chain interactions as a result of tighter packing.[110] The formation of stereoblock (-[*SSSS*]$_n$-[*RRRR*]$_n$-) PLA

from *rac*-LA, first discovered by Spassky *et al*. in 1996 through the use of a chiral Schiff base aluminium alkoxide initiator,[111] also results in enhanced polymer thermal properties (T_m = 179–210 °C).[112, 113]

The stereocontrolled ROP of *rac*-LA can produce heterotactic (-[*SSRR*]$_n$-) PLA – a typically amorphous polymer (T_g = < 45 °C) formed from the alternating enchainment of *L*- and *D*- monomers.[114] The same conformation of PLA can also be generated from *meso*-LA however this relies on a preference for *meso*-linkages. When the ROP of *meso*-LA favours *racemic*-linkages however, syndiotactic PLA – i.e. chains of alternating stereocentres is produced (-[*SRSR*]$_n$-; T_m = 149–153 °C).[115]

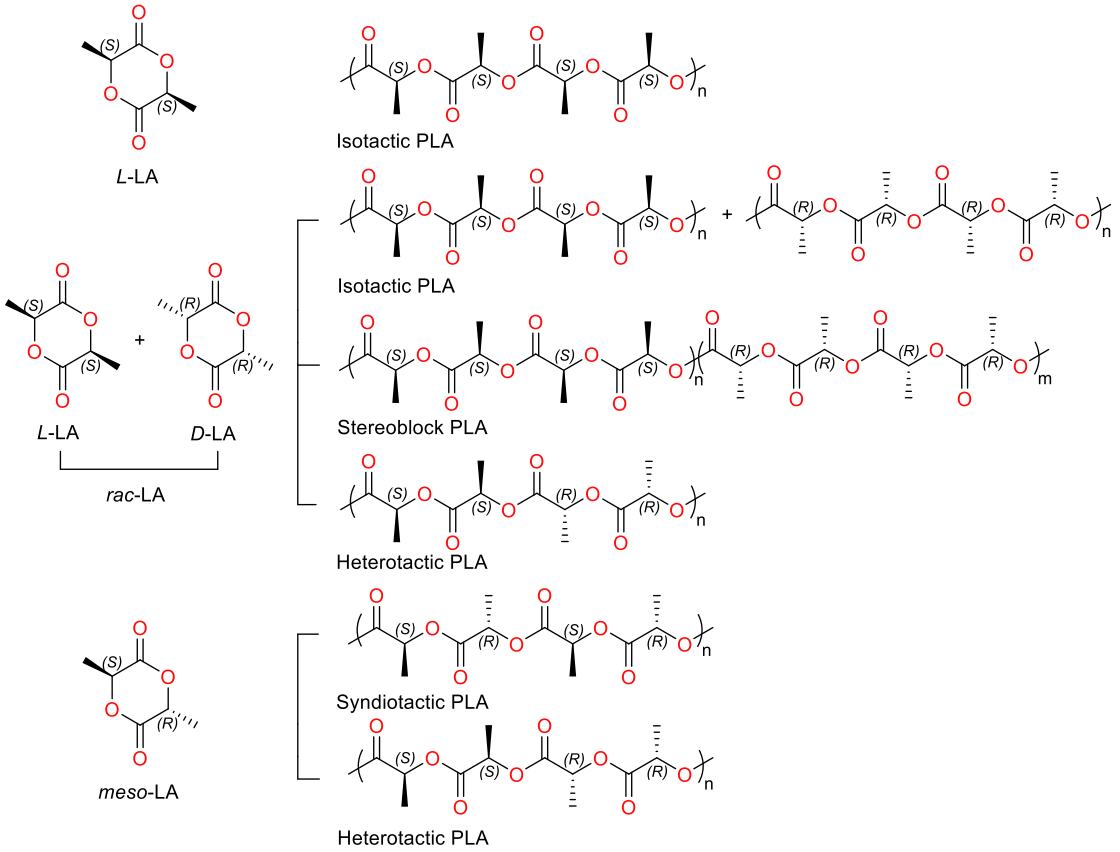

Figure 1.4 The possible arrangements of stereoregular PLA structures.[52]

Single-site catalysts can perform stereocontrolled ROP via two mechanisms.[52] The first is referred to as enantiomeric site control; this relies on the chirality of the polymerisation

initiator to determine the selectivity for a particular LA enantiomer.[107] The alternative pathway is known as chain-end control; this is where the last inserted monomer is responsible for controlling the stereochemistry of the next LA unit. It is common for this mechanism to result in the enchainment of opposing enantiomers in order to reduce the steric repulsions of the insertion-transition-state.[107] As a result, this form of control typically produces heterotactic and syndiotactic PLA from *rac*-LA and *meso*-LA respectively. If no stereocontrol is imparted via either mechanism, the polymer produced (from *rac*/*meso*-LA) has a random stereochemical sequence; this is referred to as atactic PLA which is commonly amorphous in nature (T_g = 44–55 °C).[114]

1.5 Polymer characterisation

1.5.1 Molecular weight definitions

The polydispersity of synthetic polymers means that their molecular weights cannot be defined by a single value.[116, 117] Instead they are reported as statistical averages (M_n, M_w) alongside a polydispersity index ($Đ = M_w/M_n$) that measures the broadness of the recorded distribution. A value of $Đ$ = 1.00 represents a sample where all polymer chains are of the same molecular weight; this can be highly desirable, especially in the case of LA ROP, as it indicates good reaction control. Slow initiation and unwanted side reactions however, have been noted as causes of deviations from this ideal value. In the context of LA ROP, narrow PDIs are considered to be <1.20 with intermediate ranging from 1.20–2.00.

The number average molecular weight (M_n), calculated via **Equation 1.2**, is the statistical measure of the average weight of all polymer chains in a given sample. The weight average molecular weight (M_w) is based on the number average molecular weight and so $M_w > M_n$ unless the polymer is monodispersed (**Equation 1.3**).

$$M_n = \frac{\sum N_i M_i}{\sum N_i} \quad \textbf{Equation 1.2} \qquad M_w = \frac{\sum W_i M_i}{\sum W_i} = \frac{\sum N_i M_i^2}{\sum N_i M_i} \quad \textbf{Equation 1.3}$$

where: N_i = number of chains; M_i = molecular weight of chain; W_i = $N_i M_i$ = total weight of chains

Characterisation techniques that enable the determination of M_n and M_w need to allow for the fractionation of the polymer sample. These typically include field flow fractionation, ultracentrifugation and Gel Permeation Chromatography (GPC).[118, 119]

1.5.2 Gel Permeation Chromatography (GPC)

Gel Permeation Chromatography, also known as Size Exclusion Chromatography (SEC), is a size-based separation technique.[117] The mobile phase, which is the polymer sample dissolved in a solvent such as chloroform or THF, is flushed through a column packed with cross-linked polystyrene/divinyl benzene beads of different pore sizes (3–20 μm). Large polymer molecules, which cannot enter these pores, are eluted first and thus have smaller retention times. The smaller chains however, can become entrapped in these hollow structures which therefore increases the length of time they spend in the column. The detection of the polymer samples in this Thesis were made by differentiating between the refractive index (RI) of the mobile phase *vs.* pure solvent.[120] The results were calibrated against a polystyrene standard and corrected for polylactide PLA using the appropriate Mark-Houwink factor of 0.58.[121] Confirmation of the cyclic nature of polymers is hard to confirm using only the RI detection method. Coupling this with light scattering or intrinsic viscosity measures enables the differentiation between polymer structures.[122]

1.5.3 Nuclear Magnetic Resonance (NMR) spectroscopy

NMR spectroscopy is a multi-functional analytical technique for polymer characterisation. It can be used to initially monitor the progress of the reaction and then to estimate polymer molecular weights (M_n), tacticity and end-groups.

Polymerisation kinetic analyses are examined through ^{1}H NMR spectroscopy; the percentage conversion of monomer to polymer is determined by comparing the integration of the C***H***Me resonances (around δ 5 ppm) of unreacted monomer and PLA.

Estimation of polymer end groups and M_n, by ^{1}H and ^{13}C{^{1}H} NMR spectroscopy, is limited on a resolution basis to PLA of low molecular weight.[123] The experimental molecular weight can be calculated via **Equation 1.4** which compares main chain (mc) and end group (eg) integrals – adjusting for the number of protons in each environment if needed – to determine the number of repeating units in the polymer.[124, 125]

$$\boldsymbol{M_n} = \left(M_{w,LA} \times n\right) + \left(M_{w,end\ group}\right) \qquad where\ n = \frac{\left({}^{I_{mc}}/_{N_{mc}}\right)}{\left({}^{I_{eg}}/_{N_{eg}}\right)} \qquad \textbf{Equation 1.4}$$

where: n = number of repeating units, I = intensity of polymer signal; N = number of associated protons.

The tacticity of the polylactide produced is investigated using ^{1}H{^{1}H} NMR spectroscopy.[126-128] In the ^{1}H{^{1}H} NMR spectra of *rac*/*meso*-derived PLA, several resonances corresponding to the *methine* protons (~ δ 5.20 ppm) are present due to varying polymer stereosequences (**Figure 1.5**). Deciphering the degree of tacticity of a PLA sample is conducted at the tetrad level because the chemical shifts of the polymer ^{1}H and ^{13}C nuclei are influenced by the stereoconfigurations of the CH groups of the three adjacent repeat units.[104] Hence the *methine* proton resonances are each assigned as one of the following tetrads: *mmm* (isotactic), *mmr/mrm/rmr* (heterotactic), or *rrm/rrr* (syndiotactic).[52, 103]

Assuming that the polymer obeys Bernoullian statistics (i.e. the probability of generating a specific sterochemical sequence *(m,r)* is independent of the stereochemical configuration of the chain already formed), the level of stereoregularity of the material is

computed using the relative areas underneath the appropriate resonances in the $^{1}H\{^{1}H\}$ NMR spectra and Bernoullian probabilities (**Table 1.1**).[103, 129] The probability of generating a *meso 'm'* linkage at the end of the growing polymer chain is denoted by the single parameter P_m (likewise P_r for a *racemic 'r'* sequence). Since the monomer addition can only generate either *m* or *r* linkages, $P_m + P_r = 1$; from this equation, all other probabilities are derived.[103] For the ROP of *rac*- or *meso*-lactide, a value of 0.50 for P_m or P_r suggests the polymer is atactic. $P_m = 1.00$ describes a perfectly isotactic or heterotactic polymer in terms of ROP of *rac*- and *meso*-lactide respectively. Conversely, a value of $P_r = 1.00$ represents a perfectly heterotactic or syndiotactic polymer in terms of ROP of *rac*- and *meso*- lactide respectively.[52]

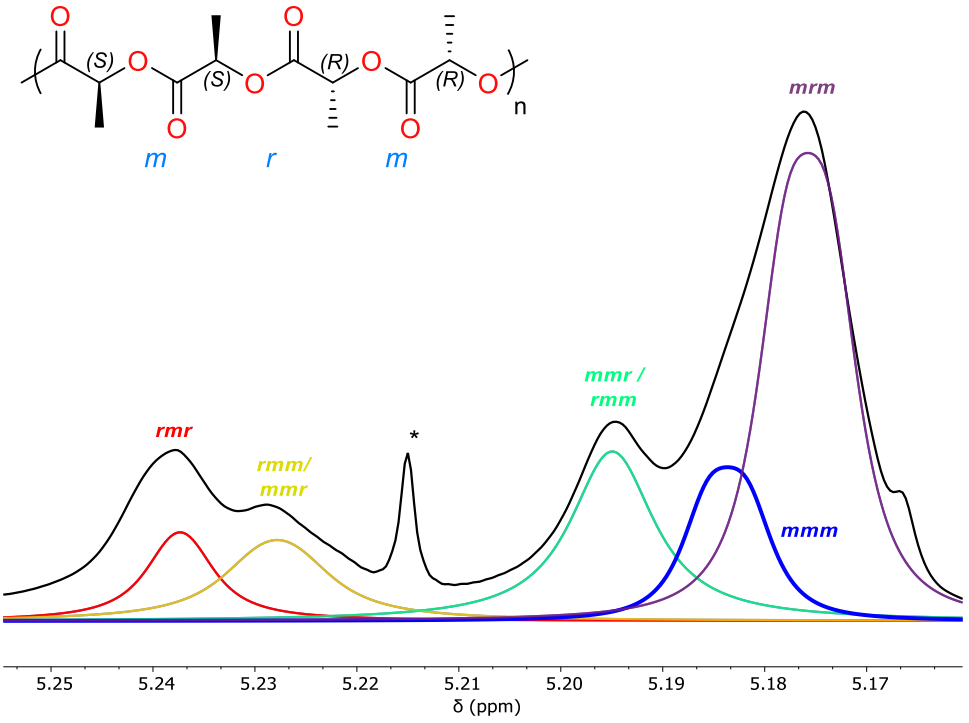

Figure 1.5 Example of a homonuclear decoupled $^{1}H\{^{1}H\}$ NMR spectrum of heterotactically enriched PLA (P_r = 0.74). * represents an artefact from the BASH (band selective decoupling) experiment set-up.

Table 1.1 The projections and Bernoullian probabilities of all possible polymer chain tetrads formed during the polymerisation of *rac*-lactide.[103, 129]

Tetrad	Projection	Bernoullian Probability	
		***rac*-LA**	***meso*-LA**
mmm	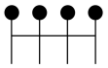	$P_m{}^2 + \frac{P_r P_m}{2}$	0
mmr	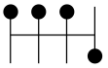	$\frac{P_r P_m}{2}$	0
mrm	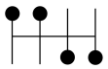	$\frac{P_r{}^2 + P_r P_m}{2}$	$\frac{P_m{}^2}{2}$
rmm	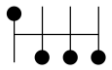	$\frac{P_r P_m}{2}$	0
mrr	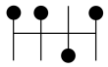	0	$\frac{P_r P_m}{2}$
rmr	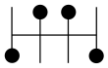	$\frac{P_r{}^2}{2}$	$\frac{P_m{}^2 + P_r P_m}{2}$
rrm	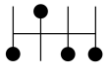	0	$\frac{P_r P_m}{2}$
rrr	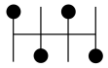	0	$P_r{}^2 + \frac{P_r P_m}{2}$
where $P_m + P_r = 1$			

1.5.4 Matrix Assisted Laser Desportion/Ionisation Time-of-Flight mass spectrometry (MALDI-ToF MS)

MALDI-TOF MS is a useful technique that enables the identification of a polymer's structural features (chain lengths, end groups etc.).[130] It is a soft ionisation method that employs short laser pulses to transform large molecules into minimalistic ion fragments.[131]

Polymer samples are combined with an absorbent matrix (typically dihydroxybenzoic acid (DHB) or 2-[(2E)-3-(4-tert-butylphenyl)-2-methylprop-2-enylidene]malononitrile (DCTB)) and, in some cases, a cationising agent prior to being dried for analysis.[132] Upon irradiation, this matrix absorbs the energy of the laser which subsequently results in the ionisation/desorption of the PLA sample.[133] The released positively charged ions are then accelerated (via a fixed applied voltage) through the flight tube to the detector. The recorded "time-of-flight" is directly related to the mass-to-charge ratio (*m*/*z*) of the ions (smaller the ion, faster the flight) thus allowing for the identification of polymeric sequences in the resultant mass spectra. A separation (Δ) of 144 *m*/*z* between the peaks corresponds to the addition of a LA monomer whilst a split (Δ) of 72 *m*/*z* indicates the occurrence of transesterification processes during polymerisation.[29, 74-78]

1.6 Initiators for the ROP of LA

1.6.1 Commonly used initiators

Initial studies of LA ROP catalysts focused mainly on tin(II) octanoate ($Sn(Oct)_2$),[57, 134-137] aluminium(III) isopropoxide (Al^iOPr_3),[56, 135, 138] and zinc(II) lactate ($Zn(Lact)_2$)[139-141] (**Figure 1.6**).[29, 59]

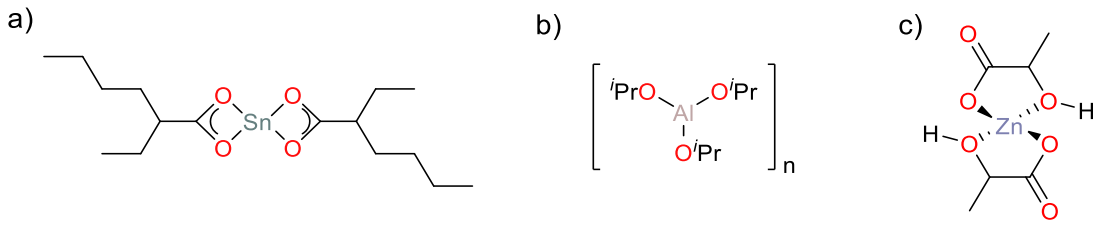

Figure 1.6 The chemical structure of three early studied LA ROP initiators: a) tin(II) octanoate, b) aluminium(III) isopropoxide and c) zinc(II) lactate.

$Sn(Oct)_2$ is the current catalyst used for the industrial bulk production of PLA (typical loadings between 0.02 and 0.002 mol %).[86] In the presence of an alcohol co-initiator (ROH), and at temperatures between 140–180 °C, the tin-based complex is able produce high molecular weight (100–1000 kg mol^{-1}) polyesters within a few hours.[134, 142] These polymers however, record broad molecular weight distributions ($M_w/M_n \geq 2.00$) due to a lack of polymerisation control;[134] this has been linked to the reversible formation of the active species ((Oct)Sn(OR)), via the *in situ* reaction between $Sn(Oct)_2$ and ROH (**Scheme 1.9**), resulting in unknown initiator concentrations.[136, 143, 144] Furthermore, $Sn(Oct)_2$ and octanoic acid (OctH) have both been documented to catalyse unwanted side reactions therefore exacerbating the decrease in polymerisation control.[143]

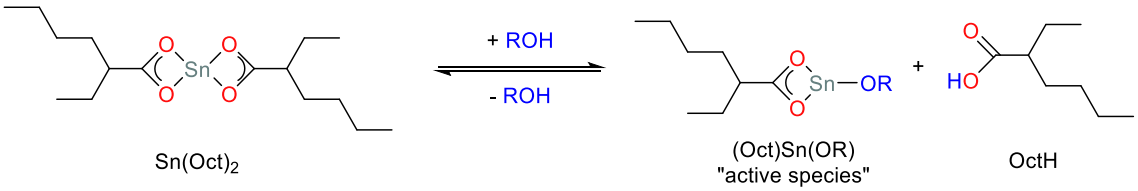

Scheme 1.9 The *in situ* formation of the active species of $Sn(Oct)_2$-catalysed LA ROP.[136, 143, 144]

In addition, although $Sn(Oct)_2$ has been approved by the U.S. Food and Drug Administration (FDA),[59, 144, 145] there are still concerns over the toxicity of tin(II) compounds. A recent study by Kricheldorf suggests that some Sn(II) species have comparable toxicity to readily available pharmaceuticals (LD_{50} – dose which kills 50% of the population (oral, rat) = 700 and 636 mg kg^{-1} for $SnCl_2$ and ibuprofen respectively). However, many polymers produced using this class of catalyst are still restricted from *in vivo* and biomedical applications.[146] This initiated the use of more biocompatible initiators such as $Zn(Lact)_2$ (where Lact = lactate); this catalyst however showed poorer activity for the ROP of LA: k_{obs} = 0.045 h^{-1} which is eight times slower than that of $Sn(Oct)_2$.[139]

Aluminium isopropoxide is also less active than $Sn(Oct)_2$ (converts 98% of 417 eq. LA in ~100 h)[55] and is found to suffer from induction periods.[55] This has been attributed to the aggregation of the alkoxide species in solution; an equilibrium between the trimer (Al_3) and tetramer (Al_4) is typically formed in which only Al_3 is highly active for ring-opening polymerisations.[138, 147]

In attempts to circumvent the above issues with these commonly used catalysts, the development of alternative single-site initiators: L_nMX (L_n = ancillary ligand(s), M = metal centre and X = initiating group) has been widely investigated. These have been largely based on aluminium, tin, transition or alkali metals.[27, 52, 59, 142] In contrast, the alkaline-earth metals, particularly the heavier congeners (Ca, Sr, Ba), have been understudied due to their propensity to redistribute in solution.[148-150] These group two metals however, offer advantages such as high activity, low toxicity, low cost and lack of colour. As a result, they were selected as the basis of this Thesis research. An overview of relevant, previously reported M^{2+} (alkaline-earth and related zinc) complexes for LA polymerisation will now be discussed.

1.6.2 Monometallic M^{2+} LA ROP initiators

The chemistry of the group 2 elements is defined by their highly stable +2 oxidation state; due to this, their reactivity is typically redox inert.[151] The nature of metal to ligand binding has a degree of covalency with magnesium but is typically dominated by non-directional ionic interactions with the heavier congeners as a result of the concurrent increase in electropositivity and polarisibility with ionic radius. The ionic nature of the bonding can result in very rapid reaction kinetics but it is also responsible for the inherent instability of well-defined heteroleptic alkaline-earth systems as it renders them susceptible to redistribution through Schlenk-type equilibria (**Scheme 1.10**).[151] In order to prevent such

equilibria, researchers have relied on bulky, hard, anionic, polydentate ligands to kinetically stabilise heteroleptic species. In some cases, additional pendant donors are also employed to afford high coordination numbers and stabilising chelate effects.[151] A range of such frameworks is discussed below.

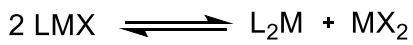

Scheme 1.10 The typical Schlenk-type redistribution associated with group 2 complexes (L = ligand, M = metal and X = reactive group).

1.6.2.1 *Tris*(pyrazolyl) borate and related complexes

Early examples of efficient M^{2+} LA ROP catalysts came in the form of *tris*(pyrazolyl)borate magnesium and zinc alkoxide systems (**Figure 1.7a**).[52, 152-155] Both initiators were able to efficiently polymerise the renewable monomer, with the magnesium derivative proving significantly more active than its zinc counterpart (k_{obs} = 2.34 *vs*. 0.0468 h^{-1}).[105] The authors attributed this to the increased electropositivity of the group two metal.[152, 153] Although slower, the zinc system proved to be more tolerant to air and moisture and therefore was taken forward and used in the preparation of polar-functionalised polylactides.[152] A few years later, a calcium analogue was shown to be even more reactive than the original two systems achieving > 90% conversion of 200 eq. in 1 minute as opposed to 1 h for magnesium and 6 days for zinc.[52, 153, 156] It was also found that this calcium derivative was highly selective for producing heterotactic polymers (P_r > 0.90) from *rac*-LA whereas both the magnesium and zinc species showed no enantiomeric preference.[52, 153, 156] The diastereocontrol (i.e. preference for either *rac*- or *meso*- monomers) was found to improve upon increasing the steric bulk of the ligand (i.e. switch from *tris*(pyrazolyl) to *tris*(indazolyl); **Figure 1.7b**).[152]

Mountford and co-workers have also reported a calcium catalyst featuring a similar *tris*(pyrazolyl) ancillary ligand (**Figure 1.7c**).[157] In this system, the BH_4 moiety acts as the initiating group converting over 90% of 200 eq. *rac*-LA at room temperature. This catalyst was also shown to be stereoselective, producing heterotactically-enriched PLA at all tested temperatures (P_r = 0.88–0.90 at –20 °C and 0.80 at room temperature).[157]

The early success with *tris*(pyrazolyl)borate ligands led others to investigate analogous tripodal frameworks with pyrazole donors. One such example came from Carpentier and co-workers who used a *bis*(pyrazolyl)amide backbone to stabilise magnesium systems (**Figure 1.7d**).[158] Treatment of this ligand with Mg(^{n}Bu)$_2$ resulted in the concomitant formation of inseparable heteroleptic and homoleptic species. Isolation of the pure homoleptic complex, was achieved via the addition of 0.5 eq. of magnesium reagent. The homoleptic complex proved an efficient LA ROP initiator, converting 97% of 200 eq. of *rac*-LA in 1 h at 20 °C.[158] The molecular weights of the resultant atactic polymers (M_w/M_n = 1.28–1.34) agreed with the assumption that both ligand amido groups initiated the polymerisation.[158]

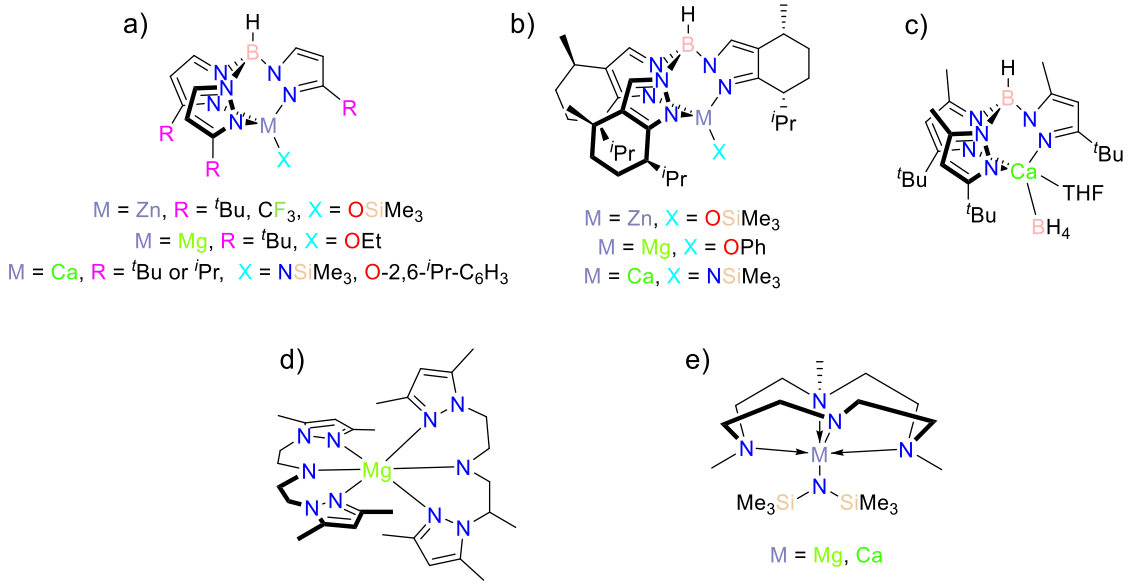

Figure 1.7. The *tris*(pyrazolyl) borate and related M^{2+} complexes reported for LA polymerisation.

Other analogous alkaline-earth systems – incorporating a macrocyclic NNNN-type ligand – were reported by Okuda *et al*. in 2011.[159] When employed in the ROP of *meso*-LA, both initiators achieved quantitative conversion of 100 eq. in 0.5 h at room temperature.[159] These high rates however resulted in transesterifications which broadened the molecular weight distributions of the isolated polymers (M_w/M_n = 1.51–1.82).[159] The observed rate constants for the *rac*- and *L*-LA polymerisations were much lower, suggesting that the formation of *meso* linkages was hindering the reaction; this aligns with the fact that, in all cases, the isolated PLA showed a modest preference for a syndiotactic microstructure ($0.58<P_r<0.64$).[159]

1.6.2.2 Schiff base and related amino-phenolate complexes

Schiff base, also referred to as phenoxy-imine or imino-phenolate ligands, have also been commonly used to isolate single site M^{2+} initiators for the ROP of LA. This is likely due to the ease of ligand preparation and ability to tune the steric and electronic profile of the system. A more in-depth discussion of this class of initiators is presented in **Chapter 5**, however a few general examples are listed below.

A family of heteroleptic Schiff base zinc systems, capable of lactide polymerisation, were reported by Chisholm in 2001 (**Figure 1.8a**).[27, 160] The rate of polymerisation using these catalysts was found to be highly dependent on the steric demands of the initiating group.[160] The bulkier, exogenous 2,6-*tert*-butylphenoxide ligand was found to impede the reaction, only achieving *ca*. 90% conversion after 72 h (cat. loading = 5 mol%).[27, 160] Neither catalyst showed any appreciable stereoselectivity as all collected polymeric material produced were determined to be atactic.[27, 160]

A series of similar, heteroleptic zinc amide systems, bearing related, yet tridentate, amino-phenolate ancillary ligands were subsequently published by Carpentier in 2008

(**Figure 1.8b**).[161] The authors report that the polymerisation kinetics and control were highly influenced by the nature of the *N*-donor fragment; in all cases the pyridyl systems were found to outperform their pyrazolyl counterparts (e.g. achieved quantitative conversion of 100 eq. *rac*-LA in 0.25 h *vs*. 24 h).[161] The poor control of these systems however, resulted in broad molecular weight distributions, which in some instances was as high as M_w/M_n = 3.6.[161]

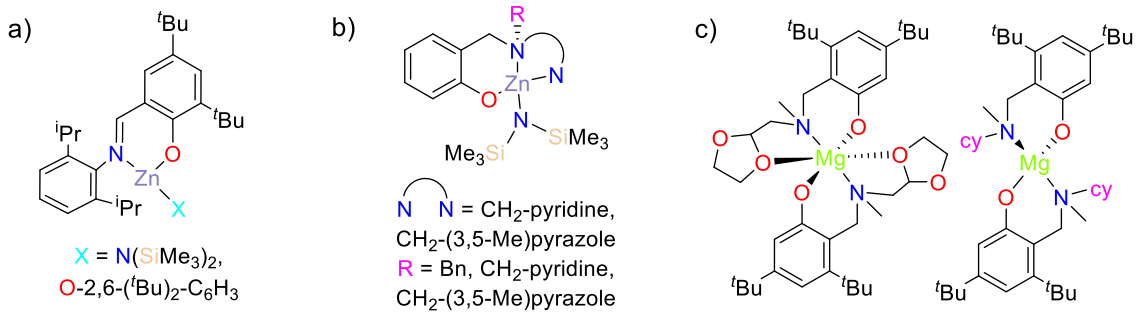

Figure 1.8 Examples of LA ROP M^{2+} systems prepared using Schiff base and related amino-phenolate ligands.

Tridentate amino-phenolate ligands have also been utilised for the isolation of homoleptic, *bis*(ligand) magnesium LA ROP catalysts (**Figure 1.8c**).[162] The donating nature of the oxolane amine substituent, as opposed to the non-coordinating cyclohexyl alternative, was found to moderately improve the activity of the catalyst (quantitative conversion of 200 eq. in 1.5 *vs.* 2 h respectively) without compromising on reaction control (M_w/M_n = 1.31 *vs*. 1.33).[162] Due to the lack of a conventional initiating group, the authors propose that the initial monomer insertion occurs into the Mg-$O_{phenoxide}$ bonds, thereby incorporating a ligand unit into the polyesters as a terminal group.[162]

1.6.2.3 β-diketiminate (BDI) complexes

β-diketiminate (BDI) ligands are also prevalent in many M^{2+} LA ROP systems. Research into the use of this ancillary framework was initially pioneered by Coates and co-workers in their development of zinc amide/alkoxide catalysts (**Figure 1.9a**).[163] The [{BDI-

Dipp}ZnO^{i}Pr] species was the first example of a group 12 catalyst capable of polymerising lactide (95% conversion of 200 eq in 0.33 h at room temperature or 2 h at 0 °C) with substantial stereocontrol (P_r = 0.90–0.94).[127, 164] This degree of control was diminished however, upon changing to less bulky flanking aryl groups (P_r = 0.76–0.79 for ethyl and *n*-propyl disubstituted aryl groups).[165] Variation of the initiating group was then tested; the overall trend in the polymerisation rate was found to follow: O^{i}Pr ~ lactate > amide > alkyl >> acetate.[165] Comparable conclusions were drawn for the ROP of LA using the mono-THF adducts ([{BDI-Dipp}ZnX(thf)]) reported by Chisholm in 2001.[166]

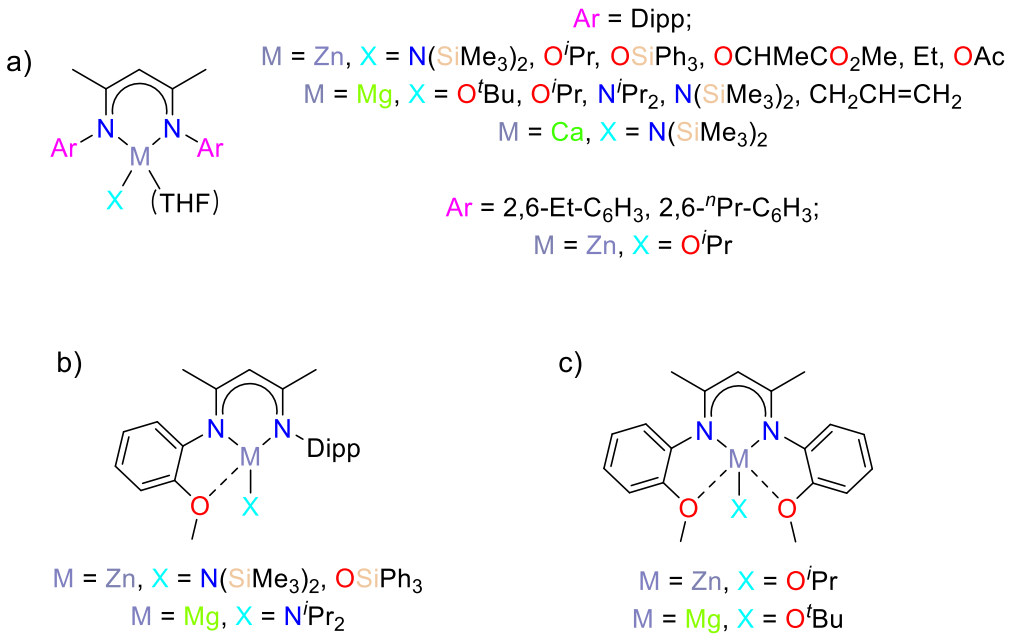

Figure 1.9. Magnesium, zinc and calcium complexes formed using first and second generation β-diketiminate (BDI) ligands.

Analogous magnesium and calcium amide BDI systems have since been reported ([{BDI-Dipp}MNSiMe$_3$]). Competition experiments, monitored by ^{1}H NMR spectroscopy, proposed that the reactivity of the M-N$_{amide}$ bond towards the polymerisation of *rac*-lactide follows the same trend as with the *tris*(pyrazolyl) alkoxide systems (Ca > Mg > Zn).[27] However, when utilising these complexes in preparative-scale polymerisations (i.e. 0.5 g *rac*-LA in 7.5 mL solvent with [*rac*-LA]$_0$:[**M**]$_0$ = 200), an inverse in calcium and

magnesium reactivity was observed (> 90% atactic PLA achieved in 2 h and > 90% heterotactic PLA achieved in 5 minutes for Ca and Mg respectively).[27, 153, 156] This was attributed to the fact that the BDI ligand does not provide adequate steric bulk to prevent aggregation or ligand scrambling of the larger calcium system.[27, 156] Further evidence of this is the lack of stereocontrol imparted in the calcium-catalysed ROP. This shows that larger ionic radii metal systems can be very catalytically active but require kinetic stabilisation with respect to Schlenk-type redistribution equilibria; this can be achieved by shielding the active site by a bulky ancillary ligand.[153, 156]

Second generation tri-(NNO) and tetra-(NNOO)-dentate BDI ligands have since been synthesised, by installing one or two ether appendages (**Figure 1.9b-c**).[167, 168] The NNO-zinc complexes proved to be more active than the first generation catalysts, achieving 81% conversion of 100 eq. of *rac*-LA in 8 minutes.[120] The reduced steric protection of the metal centre, however, resulted in poorer stereocontrol.[120] In contrast, the NNOO-magnesium systems suffered from hampered levels of activity yet improved stereoselectivity (P_r = 0.85).[168]

Similar M(II) BDI systems ([{BDI-R}ZnOAc]) have been utilised in other renewable polymer syntheses; in the case of the ring-opening co-polymerisation (ROCOP) of CO_2 and epoxides, Coates *et al*. discovered that these catalysts, under standard conditions (50 °C, 7 bar CO_2), were acting as loosely bound dimers (**Figure 1.10**).[169-172] Kinetic measurements confirmed this by indicating that the order with respect to zinc varied between 1.0–1.8, suggesting the presence of two active sites per catalyst molecule.[169-172]

Bimetallic cooperativity was proposed as the cause of the observed enhancement in activity, and this has since led to the rapid development of a range of bimetallic systems for the polymerisation of renewable monomers.

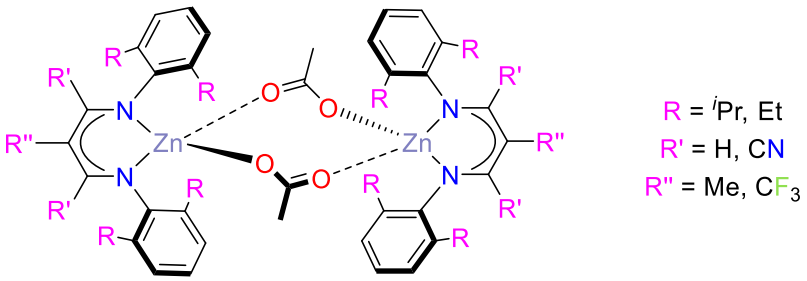

Figure 1.10 The active dimeric zinc BDI complex reported for the ROCOP of CO_2 and epoxides.[169-172]

1.6.3 Bimetallic M^{2+} LA ROP initiators

There are three different classes of such *bis*(metal) systems, these are: *dimeric* – contains two monomeric species typically bridged by heteroatoms (represented by "o" in **Figure 1.11**); *dinucleating* – a single framework capable of hosting two "cooperative" metal centres; and *tethered* – contains two independent metal centres bridged by ligand framework.[173]

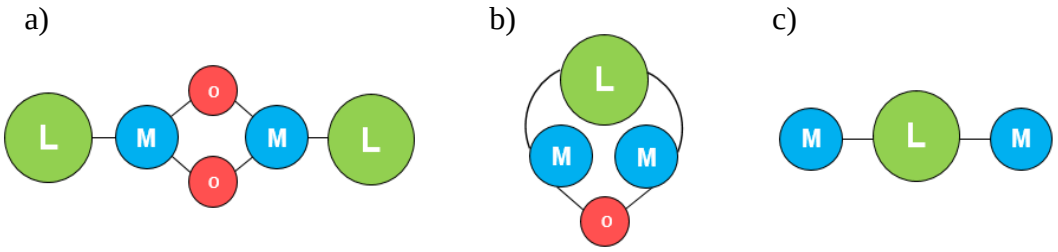

Figure 1.11 The three different classes of bimetallic catalysts: a) dimeric, b) dinucleating and c) tethered; adapted from the review published by Mehrkhodavandi and co-workers.[174]

It is hypothesised that bimetallic systems may mimic the active site of enzymes that perform similar reactions (e.g. hydrolysis).[175] In these natural systems, the metal centres are seen to work synergistically resulting in enhanced activity and selectivity. Other potential advantages of bimetallic polymerisation catalysts can include increased tolerance to polar functional groups, multi-centred directed covalent and non-covalent interactions, conformationally advantageous active-site-substrate proximities, improved monomer enchainment and potential for tandem catalysis.[174, 176]

1.6.3.1 Dimeric species

The majority of previously reported examples of bimetallic M^{2+} LA ROP catalysts lie within this category.

1.6.3.1.1 β-diketiminate (BDI) and related complexes

After observing the success of employing dimeric, bimetallic BDI species in the ROCOP of CO_2 and epoxides, Coates *et al.* employed the same initiators towards the ROP of LA.[27, 163, 165, 174] The dimeric [{BDI-Dipp}ZnO^iPr]$_2$ system proved efficient, converting 95% of 200 eq. of *rac*-LA in 0.33 h at room temperature (**Figure 1.12a**).[163] The system was also shown to be highly stereoselective generating heterotactic (P_r = 0.90; can be increased to 0.94 by cooling reaction to 0 °C) and syndiotactic (P_r = 0.76) PLA from *rac*-LA and *meso*-LA respectively.[163] The reaction kinetics and degree of polymer chain-end stereocontrol were highly influenced by the steric bulk of the ancillary BDI ligand; reducing this caused a decrease in the rate and stereoregularity of the collected PLA (comparable conversion of *rac*-LA achieved in 8 and 19 h for BDI-Et and BDI-^{n}Pr respectively with P_r = 0.79 and P_r = 0.76).[165] The order with respect to the [{BDI-Dipp}ZnO^iPr]$_2$ catalyst was determined to be 1.56 implying possible further aggregation of the dimeric species *in situ*.[55, 165] The analogous [{BDI-Dipp}MgO^iPr]$_2$ initiator was also developed and it proved more active than the zinc dimer, quantitatively converting 200 eq. of *rac*-LA in 2 minutes.[165] The higher polymerisation rate however, resulted in poorer control, yielding purely atactic PLA with moderate molecular weight distributions (M_w/M_n ~ 1.59).[165] The corresponding monometallic equivalent [{BDI-Dipp}MgO^iPr(thf)] was shown to impart some stereocontrol in THF alone; the authors attribute this to the possible formation of the corresponding dimer in solution.[177] Comparable dimeric M^{2+} BDI systems were further explored by Schaper and co-

workers.[178-181] The zinc variants [{BDI-C(R)HPh}ZnX] (where R = H, Me and X = Et, O^{i}Pr, NSiMe$_3$) were found to impart similar stereocontrol to those reported by Coates (P_r = 0.84),[178] though the magnesium and copper systems produced atactic PLA in all cases.[179-182]

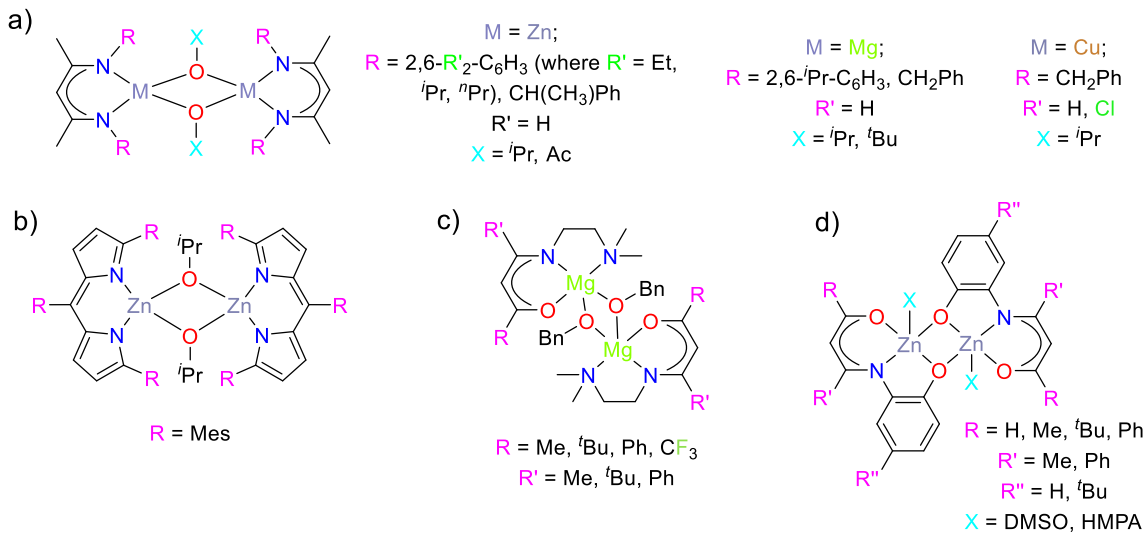

Figure 1.12 Dimeric BDI and related catalyst systems employed in the ROP of LA.

A comparable dimeric zinc *rac*-LA ROP initiator, stabilised by TMP (1,5,9-trimesityldipyrromethene) ligands was reported by Chisholm in 2016 (**Figure 1.12b**).[183] It was found to be more active and stereoselective in THF (k_{obs} = 1.12 h^{-1} with P_r = 0.95) relative to DCM (k_{obs} = 0.396 h^{-1} with P_r = 0.75); the authors propose this may in fact be due to the formation of active monomers in the coordinating solvent.[183]

A series of dimeric magnesium benzyl oxide catalysts, incorporating related N,N,O β-enaminoketonate ligands, were reported by Lin and co-workers in 2007 (**Figure 1.12c**).[184] This type of ancillary ligand is less widely studied due to the weaker steric protection they offer on one side of the compound. In order to overcome this, an additional pendant donor was incorporated into the ligand framework; this is a method that is frequently observed to enable the stabilisation of heteroleptic M^{2+} systems.[185-189] By varying the substituents on the ligand backbone, the authors were able to ascertain

how the steric and electronic effect of the ancillary ligand influenced the polymerisation activity. The addition of electron-withdrawing CF_3 groups at the ligand backbone increased the Lewis acidity of Mg, and thus the strength of the Mg-OBn bonds, resulting in diminished polymerisation activity (89% conversion of 200 eq. *L*-LA in 10 h *vs*. < 8 minutes for a methyl-only substituted system). In contrast, an increase in ligand bulk (Me → ^{t}Bu) enabled quantitative conversion of monomer in less than 2 minutes (much faster than other reported M^{2+} N,N,O *β*-ketiminate complexes);[190] this higher rate was rationalised by the increased steric hindrance enhancing the tendency for dissociation into the corresponding monomeric complexes which NMR spectroscopic studies suggest are the active species of the polymerisation. Similar zinc *β*-enaminoketonate systems, containing an additional alkoxide *vs*. amine donor, have since been reported (**Figure 1.12d**).[191, 192] In the presence of BnOH co-initiator, these catalysts were found to exhibit modest activity for the melt ROP of *rac*-LA and produce atactic PLA with broad molecular weight distributions (M_w/M_n = 1.64–1.84).

1.6.3.1.2 Schiff base and related amino-phenolate complexes

Other early examples of dimeric M^{2+} catalysts came from Tolman in 2003 (**Figure 1.13a**); they feature a tridentate, diamino-phenolate ancillary ligand with bridging μ-ethoxy moieties.[193] The systems were reported to be some of the most active zinc-based catalysts for the ROP of LA, converting up to 1500 eq. in under 20 minutes. The molecular weights of PLA produced were as high as 130 000 $gmol^{-1}$ with moderate distributions (M_w/M_n = 1.34–1.42). Although the initiators are dimeric in the solid state, further studies involving cross-over variable temperature (VT)/pulsed gradient spin−echo (PGSE) NMR measurements as well as laser desorption mass spectrometry (LDMS) suggest that they typically dissociate in solution; the authors therefore proposed that the actual active species of the polymerisation to be the monomeric, monometallic counterpart.

Chiral variants of Tolman's dimeric zinc amino-phenolates were subsequently published by Mehrkhodavandi and co-workers in 2009 (**Figure 1.13b**).[194-197] These racemic benzoxy-bridged species were reported to remain dinuclear in solution whilst converting >96% of 1000 eq. *rac*-LA in less than 10 minutes with excellent control over polymer molecular weights (M_w/M_n = 1.02–1.19). They were noted, in all cases, to outperform the mononuclear analogues which on average took 24 h to achieve comparable conversions.[194] Oxidation of the main ligand amine moiety led to an improvement in the stereoselective nature of these dimeric catalysts ($P_r \approx 0.56$ (amine); $P_r \approx 0.68$–0.85 (imine) which also proved active towards the ROP of β-butyrolactone.[196]

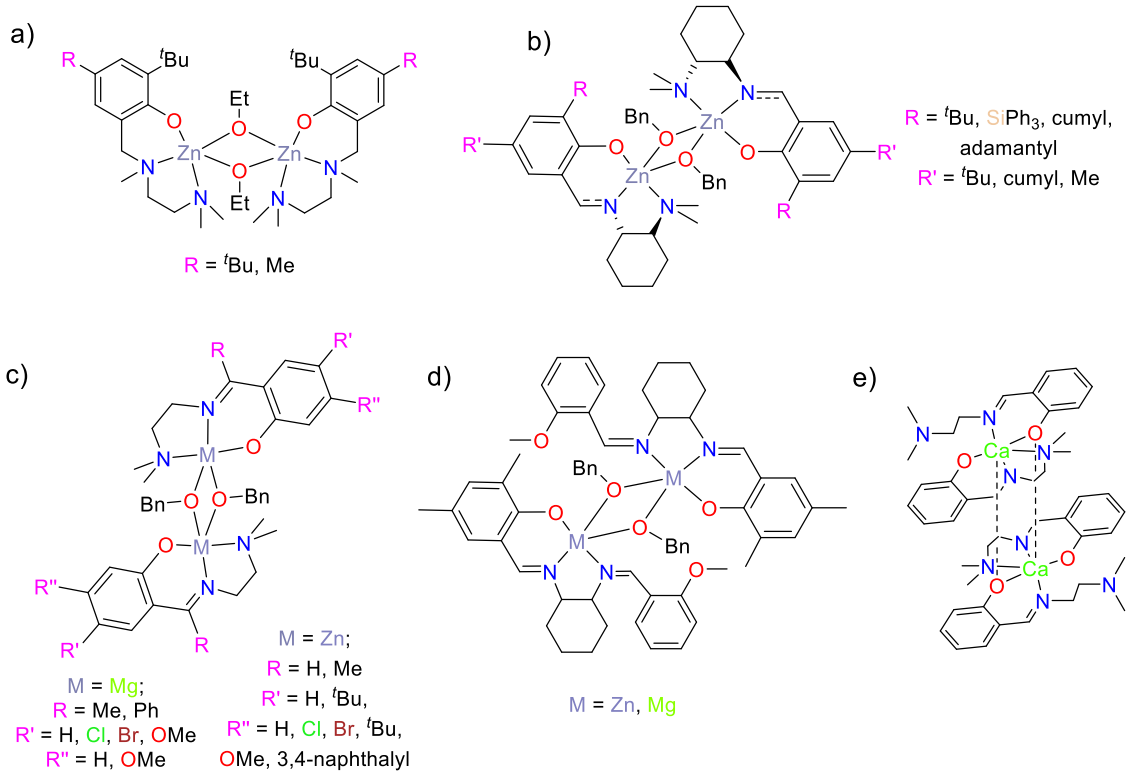

Figure 1.13 Dimeric, Schiff base and related amino-phenolate bimetallic catalysts reported for the ROP of LA.

A family of comparable dimeric, bimetallic, tridentate Schiff base magnesium and zinc systems [{ON-NMe_2}MOBn]$_2$ were published by Lin and co-workers in 2008 (ON-NMe_2 = 1-O-3-R-4-R'-6-CR''=N(C_2H_4)NMe_2; **Figure 1.13c**).[27, 79, 198 199, 200] The zinc

analogues were able to efficiently initiate the polymerization of *L*-LA, producing polymers with narrow distributions (M_w/M_n = 1.07–1.23) and molecular weights as high as 162 500 gmol^{-1}. The corresponding magnesium systems were also able to catalyse the ROP of LA and produce PLAs with narrow molecular weight distributions (M_w/M_n = 1.05–1.12).[199] As with the dimeric BDI systems reported by Lin, the addition of an electron-donating methoxy substituent increased the polymerisation activity (98% *vs* 65% conversion of 50 eq. *L*-LA in 3.5 h at 0 °C in DCM) whereas the introduction of electron-withdrawing halide substituents hampered the rate (~25% conversion of 50 eq. *L*-LA in 3.5 h at 0 °C in DCM).

Analogous tridentate, salen magnesium and zinc catalysts [{SalenMe}MOBn]$_2$ were also reported by Lin *et al*. (SalenMe = 1-O-2,4-Me-6-CH=N(C_6H_4)N=C(C_6H_4)-*o*-OMe; **Figure 1.13d**). Both complexes were efficient initiators for ring-opening polymerization of *L*-LA with conversions of 100 eq. reaching over 90% in 0.75 h (Mg; T = 25 °C) and 3.5 h (Zn; T = 60 °C).[79] In all cases, PLAs with narrow molecular weight distributions (M_w/M_n = 1.03–1.10) were produced, indicating a high degree of polymerisation control. In ROP of *rac*-LA, no stereocontrol is imparted by the Mg system (P_r = 0.57) whereas the zinc species generates heterotactically enriched polymer (P_r = 0.75). Kinetic analysis revealed an unusual second order dependence on monomer concentration for the Mg system (k_p = 28.53 M^{-2} minute^{-1}) but a typical first order relationship (k_p = 9.26 M^{-1} minute^{-1}) for the zinc variant. The authors attribute this to varying active species: a dimer for Mg but monomer, formed via ligand dissociation, for Zn.

An example of a dimeric, bimetallic, heavier alkaline-earth LA ROP catalyst was published by Lin *et al*. in 2007 (**Figure 1.13e**).[201] In the presence of BnOH co-initiator, the *bis*(calcium) system with an amine-tethered iminophenolate ligand was shown to be an efficient catalyst, with conversions reaching upwards of 96% (50<[LA]$_0$/[**Ca**]$_0$<125)

within 40–60 minutes at room temperature. In all cases, there was a relatively good agreement between experimental and calculated molecular weights (e.g. 5900 *vs.* 6200 $gmol^{-1}$) and narrow distributions (M_w/M_n = 1.11–1.26). The authors proposed that during the polymerisation the reversible association of THF solvent is replaced by monomer molecules. Subsequent dissociation of the hemilabile dimethylamino group allows the metal to interact with BnOH and facilitate the ring-opening.

1.6.3.1.3 Phenolate complexes

Examples of dimeric magnesium and zinc systems hosted by phenolate ligands were reported by Lin *et al*. in 2004 (**Figure 1.14a**).[92, 202] In dichloroethane, and with BnOH co-initiator, the magnesium catalysts were found to be active, converting 92–94% of 100 eq. of *L*-LA in 2 h at 80 °C. The molecular weight distributions of the PLLA produced were all narrow (M_w/M_n = 1.04–1.21) and a linear relationship between M_n and [*L*-LA]$_0$/[**M**]$_0$ was observed. End group analysis identified –OH/-OBn terminal moieties, implying that the aryloxide ligand was not responsible for initiation. The effect of ligand steric bulk was investigated using the zinc analogues; the authors report that increasing the steric bulk leads to higher activity.

Alternative dimeric magnesium alkoxide systems [(EDBP-S)Mg(μ-OBn)]$_2$ (where EDBP-S = 2,4-di-*tert*-butyl-6-(1-(3,5-di-*tert*-butyl-2-hydroxyphenyl)ethyl)phenyl benzenesulfonate; **Figure 1.14b**), also reported by Lin *et al*., were found to be highly efficient ROP catalysts achieving full conversion of 1000 eq. of *L*-LA within 4 minutes at 25 °C. The introduction of electron-withdrawing substituents (R) however, was found to significantly reduce this polymerisation activity.[203] Insufficient steric protection of the metal centres rendered the catalysts non-steroselective (P_r = 0.58–0.64). The resultant

polymer molecular weights (4300–84 800 gmol^{-1}) however, were some of the highest recorded for a magnesium initiator.[203]

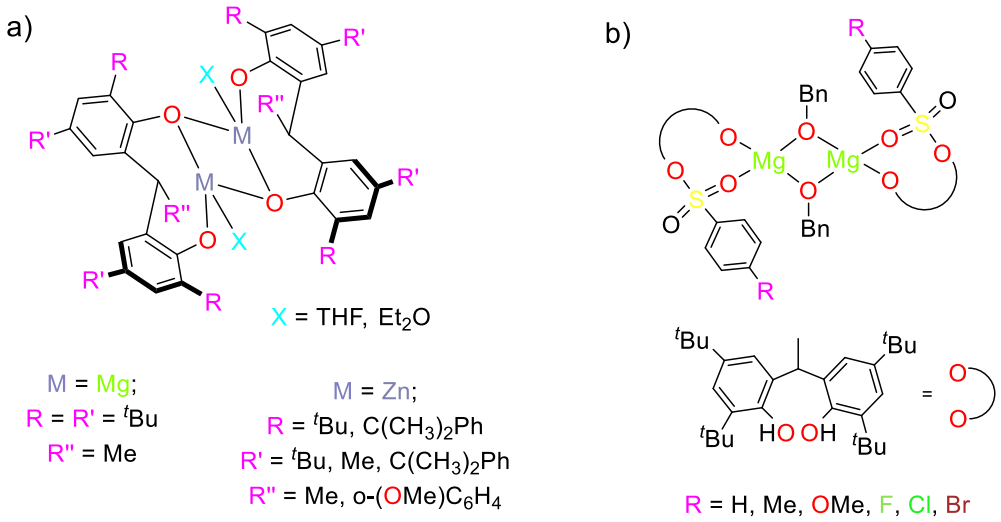

Figure 1.14 Dimeric LA ROP catalysts bearing phenolate ligands.

1.6.3.2 Dinucleating species

Several examples of dinucleating, bimetallic M^{2+} systems for the ROP of LA have been reported.

1.6.3.2.1 Schiff base and related amino-phenolate complexes

The first bimetallic, dinucleating initiator for the ROP of LA was reported by Tolman and co-workers in 2002 (**Figure 1.15a**).[23, 193, 204, 205] The *bis*(zinc) chloride alkoxide system achieved greater than 90% conversion to PLA within 0.5 h (k_p = 0.37 M^{-1} h^{-1}) but was found not to be stereoselective.[23] Its activity was six times less than a comparable, dimeric, zinc ethoxide Schiff base system (**Figure 1.13a**); the authors attributed this to the presence of the chloride ligands which decreased the Lewis acidity of zinc thus lowering the activity.[193] Further examination of this hypothesis suggested that the reaction kinetics did not directly correlate with the electronegativity of the halide (Br > Cl > I). Instead, a combination of halide electronegativity and nature of the ancillary ligand was found to effect the polymerisation activity. In terms of the ancillary ligand,

the slowest rate was observed when using the rigid, electron-rich imine framework, whereas the fastest rate resulted from the more flexible amine backbone.[205] Subsequently, *bis*(magnesium) and *bis*(cobalt) chloride amino-phenolate analogues have been produced and tested; they were shown to be less active (k_p = 0.0062 M^{-1} h^{-1} (Co), 0.0039 M^{-1} h^{-1} (Mg)) and rendered no improvements to the stereocontrol. The reduction in activity, with respect to the dizinc system, was rationalised by the crowded metal coordination spheres inducing a switch in rate determining step from insertion to coordination.[204]

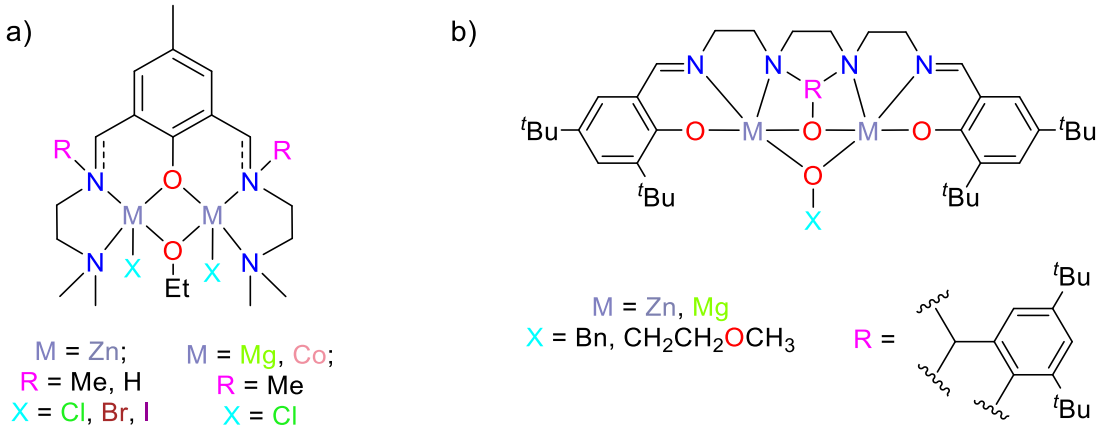

Figure 1.15 Bimetallic M^{2+} systems, supported by dinucleating Schiff base and related amino-phenolate ligands, for the ROP of LA.

In 2015, Wi and co-workers reported the use of an extended salen framework for the generation of dinucleating, bimetallic M^{2+} LA ROP initiators (**Figure 1.15b**).[206] At temperatures up to 80 °C, these catalysts were found to be inactive; the authors attributed this to the deactivation of the bridging benzyloxy moiety as a result of the strong binding effect of the M^{2+} ions. Subsequent activation was achieved, however, via either the addition of (up to 50 eq.) BnOH co-initiator or an increase in reaction temperature to 130 °C. In toluene at 80 °C with ratios of $[LA]_0$:[**M**]$_0$:$[BnOH]_0$ = 100:1:1, the magnesium and zinc catalysts (suggested to operate via an activated monomer route) achieve 90% and 15% conversion within 12 h respectively. The greater Lewis acidity of Mg^{2+} was rationalised as the cause of its enhanced activity compared to the zinc system. Upon

increasing the temperature to 130 °C, both complexes become active without the need for a co-initiator. In these conditions, the zinc complex is more active (66 *vs*. 19% conversion in 1 h). The authors propose this is due to a change in mechanism to a coordination-insertion pathway at high temperature; in this case, the increased strength of the magnesium-alkoxide bond (expected based on Hard-Soft-Acid-Base principle) reduces its corresponding activity.

1.6.3.2.2 Diphenylamine-based [2+2] iminemacrocycles

In 2016, Williams *et al.* reported the synthesis of dinucleating, diphenylamine-based, [2+2] iminemacrocyclic dizinc catalysts for the ROP of *rac*-LA (**Figure 1.16a**).[86, 174, 207]

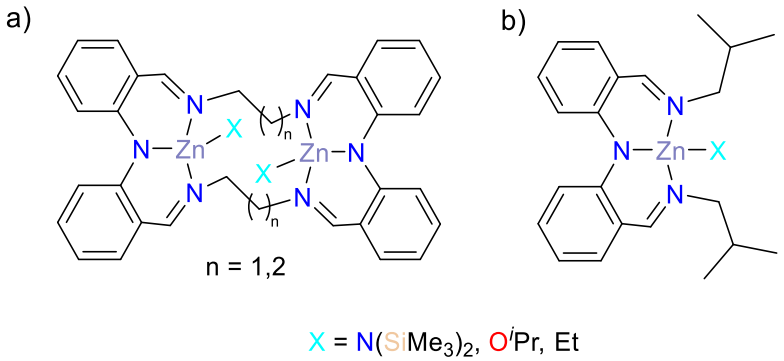

Figure 1.16 The a) bimetallic, and b) corresponding monometallic, dinucleating diphenylamine-based [2+2] iminemacrocyclic LA ROP catalysts synthesised by Williams *et al.* in 2016.

The *bis*(Zn-HMDS) systems quantitatively polymerised 1000 eq. within 1 minute at room temperature (TOF: 20 300–45 000 h^{-1}).[174] This is six hundred times faster than the [Zn-Et]$_2$ analogue and the activity per zinc site is up to three times greater than the monometallic variant, thus providing evidence for dinuclear cooperativity (**Figure 1.16b**). Under immortal conditions (addition of 10 eq. ^{i}PrOH co-initiator), this activity was improved even further with the recorded TOF now reaching 50 000–60 000 h^{-1} (three times higher than the fastest previously reported zinc LA ROP catalysts).[93] The dizinc amide catalysts were also shown to tolerate catalyst loadings as low at 0.002 mol%, making them of industrial relevance.

The analogous alkoxide compounds were found to be up to six hundred times less active than their amide counterparts (TOF: 30–13 000 h^{-1}). The authors propose this is due to the unique ligand conformations adopted in the different systems. For the amide species, the macrocycle adopts a folded structure in which the central carbon bridges form BDI-like chelates of the externally exposed active zinc sites; in contrast, the alkoxide catalysts adopt a more planar, less flexible conformation with involves bridging μ-^{i}OPr ligands (**Figure 1.17**).

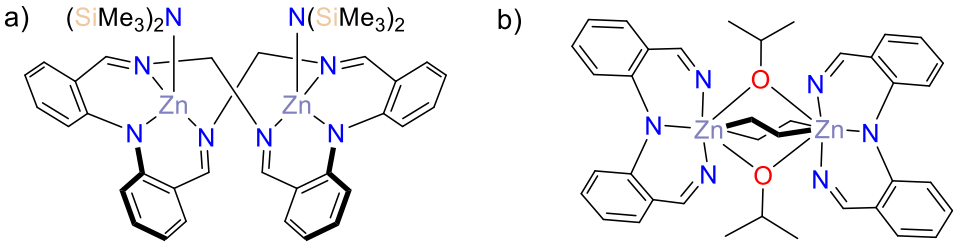

Figure 1.17 The different conformations adopted by the a) amide and b) aryloxide [2+2] iminemacrocyclic LA ROP catalysts.

1.6.3.2.3 *Bis*(pyrazole) alkane complexes

A series of cationic dizinc catalysts for the ROP of *rac*-LA were prepared by Comito and co-workers in 2022, via the Lewis acid abstraction of a methyl fragment from a *bis*(pyrazole) ligand (**Figure 1.18**).[208] These cationic initiators were moderately active (k_{obs} = 3.42 h^{-1}), only in the presence of BnOH co-initiator; this low efficiency was attributed to the reduced nucleophilicity of the zinc-bound ethyl groups upon cationisation. The unsubstituted ligand framework resulted in the fastest polymerisation rate, whilst replacing the $[B(\{3,5\text{-}CF_3\}_2C_6H_3)_4]^-$ anion with less weakly-coordinating anions (BF_4^-, TfO^-, Tf_2N^-, ClO_4^-, PF_6^-) retarded the catalysis entirely. The analogous mono-zinc systems were found to be more active (90% conversion of 100 eq. within 10 minutes at room temperature) yet less controlled (M_w/M_n = 1.19) possibly due to the aggregation of the zinc alkoxide species in solution.

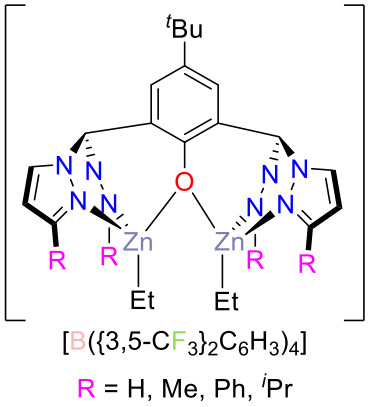

Figure 1.18 The bimetallic zinc complex supported by a dinucleating *bis*(pyrazole) alkane ancillary ligand for the ROP of LA.

1.6.3.3 Tethered species

This class of bimetallic has the smallest number of M^{2+} complexes; the details of some key examples relevant to this Thesis are described in **Chapter 2**, however some other representative species are described below.

In 2003, Westerhausen and co-workers reported the first examples of heteroleptic calcium LA ROP initiators; these were tethered, bimetallic systems comprised of chelating TMHD ligands (H-TMHD = 2,2,6,6-tetramethylheptane-3,5-dione; **Figure 1.19a**).[209, 210] Both β-diketonate systems proved active, converting over 90% of 150 eq. of *L*-LA within 30 minutes (amide) or 2 h (alkoxide). The amide catalyst produced polymers with uncontrolled molecular weights (M_w/M_n = 1.80–2.13) whereas the slower rate of the isolated alkoxide system, likely due to initiator aggregation in solution, resulted in better polymerisation control (M_w/M_n = 1.13–1.19). Addition of an alcohol co-initiator to the amide system resulted in both improved rates and molecular weight control ($M_{n,(calcd)}$: 2000 *vs.* $M_{n,(GPC)}$: 2200 $gmol^{-1}$).

Tethered, bimetallic magnesium heteroscorpionate complexes featuring apical Mg-alkyl bonds, have also been reported for the ROP of LA (**Figure 1.19b**).[211] When formed in THF, these *bis*(magnesium) catalysts were able to convert 94% of 100 eq. of *L*-LA in

7 minutes and 55% of 100 eq. of *rac*-LA in 2 h. In all cases, there were narrow polymer dispersities indices (M_w/M_n = 1.03–1.13) and good agreements between experimental and calculated molecular weights. End group analysis showed that initiation took place through the Mg-alkyl bonds, via the classic coordination-insertion mechanism. When synthesised in dioxane, two bimetallic units became bridged through a donating solvent molecule. These tetranuclear structures were less active than the bimetallic variants yet showed enhanced stereoselectivity (P_r = 0.75–0.78 *vs*. P_r = 0.68–0.71).

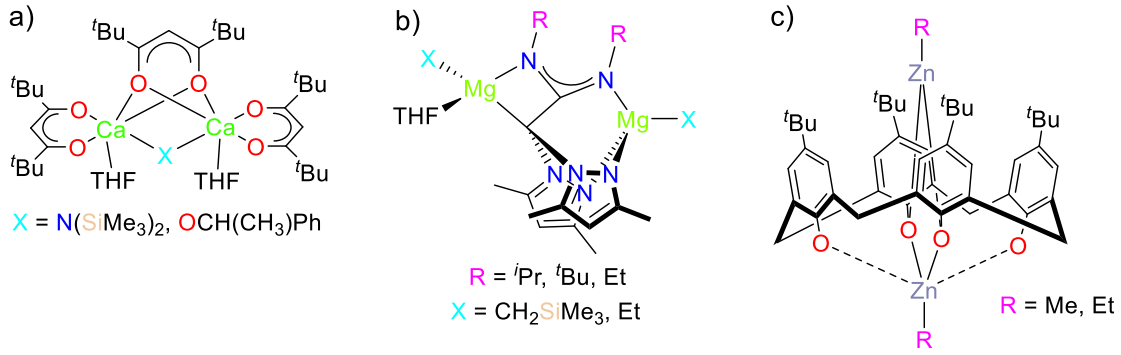

Figure 1.19 Examples of tethered, bimetallic M^{2+} catalysts reported for the ROP of LA.

Additional, early examples of tethered M^{2+} LA ROP initiators include calixarene zinc alkyl complexes (**Figure 1.19c**).[212, 213] These systems, reported by Vigalok *et al*. in 2005, proved only modestly active, converting 196 eq. of *L*-LA in 15 h at 60 °C. The authors attributed this to slow initiation as a result of the weak nucleophilicity of the zinc-methyl/ethyl groups; this was evidenced by the experimental molecular weights being up to four times higher than the predicted values. ^{1}H NMR diffusion experiments implied that the internal zinc moiety does not participate in the polymerisation and thus these systems should be considered as the first direct examples of single-site, bimetallic, catalytically active zinc systems.

1.6.3.4 Heterobimetallic, M^{2+} containing LA ROP initiators

It has been suggested that the use of heterobimetallic catalysts for RO(CO)Ps will have significant activity improvements over homobimetallic systems.[214] This is because the different metals can each be responsible for catalysing distinct reaction steps and therefore can be chosen/optimised for their specific roles.[214, 215]

The development of heterobimetallic, M^{2+} containing catalysts for the ROP of LA is a less well-developed area; relatively few examples exist, some of which are discussed below.

1.6.3.4.1 Phenolate complexes

Lin *et al*. synthesised one of the first families of heterobimetallic, M^{2+} containing systems for the ROP of *L*-LA (**Figure 1.20a**).[216] The complexes, supported by *bis*(phenolate) ligand frameworks, featured titanium(IV) in combination with either a zinc(II) or magnesium(II) centre. The dinuclear (IV)-(II) systems all proved to have superior activity to the mononuclear titanium analogues: 91% and 89% conversion of 100 eq. *L*-LA in 0.5 h and 3.5 h for Ti/Zn and Ti/Mg respectively (comparable rates to those reported for BDI catalysts).[165, 174, 216] The higher polymerisation rate observed for zinc was rationalised by its lower charge density resulting in a more labile Zn-O^{i}Pr initiating bond. It was found that activity could be increased further via the addition of Ti(IV)-stabilising electron donating groups to the ligand backbone.[216] Kinetic and molecular analysis of this system, via ^{1}H NMR studies, showed that the polymerisations were first order with respect to both monomer and catalyst and that only two of the alkoxide groups initiate the reaction.[216]

A similar set of hetero-dinuclear systems for the ROP of *rac*-LA was published by Thomas *et al.* in 2015 (**Figure 1.20b**).[217] In the presence of neopentyl alcohol, these

mixed metal complexes were found to be highly active and stereoselective. For example, the Li/Zn system was able to convert 62 eq. of *rac*-LA in 15 minutes at 20 °C with P_r = 0.88 whereas the Li/Mg species converted 88 eq. in the same time frame at –15 °C with P_r = 0.90.[217]

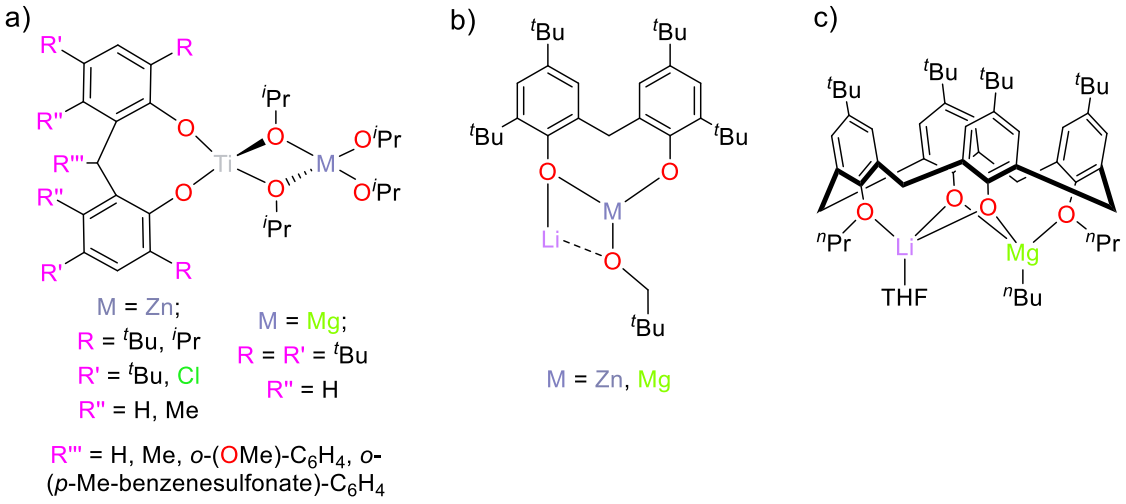

Figure 1.20 Examples of mixed valent, heterobimetallic phenolate systems for the ROP of LA.

A more recent example of a Li/Mg heterobimetallic ROP catalyst came from Redshaw in 2014 (**Figure 1.20c**).[218, 219] In DCM, and upon addition of 1 eq. of methanol, this species was capable of converting 55 eq. of *rac*-LA within 1 h at 20 °C (M_w/M_n = 1.22) whereas the mono-Mg counterpart required ~2 h to achieve the same conversion.[218] The experimental molecular weights of the PLA produced using the Li/Mg system were almost double the theoretical value (15 400 *vs.* 7960 $gmol^{-1}$); the authors attributed this to partial catalyst deactivation.[218] This is thought to be caused by the *in situ* formation of poorly initiating Mg-Cl moieties via the reaction of the magnesium butyl group with the chlorinated solvent.[218, 220, 221]

1.6.3.4.2 Schiff base and related amino-phenolate complexes

In 2017, Williams *et al.* utilised a macrocyclic amino-phenolate framework, which had previously been used for CO_2/epoxide ROCOP catalysts,[222-225] to isolate Ti(IV)/Zn(II) systems for the ROP of *rac*-LA (**Figure 1.21a**).[226] The mixed valency complexes were shown to be moderately active (whilst a *bis*-Ti(IV) complex was completely inactive) however they only exhibited a limited degree of stereoselectivity (P_r = 0.68).[174, 226]

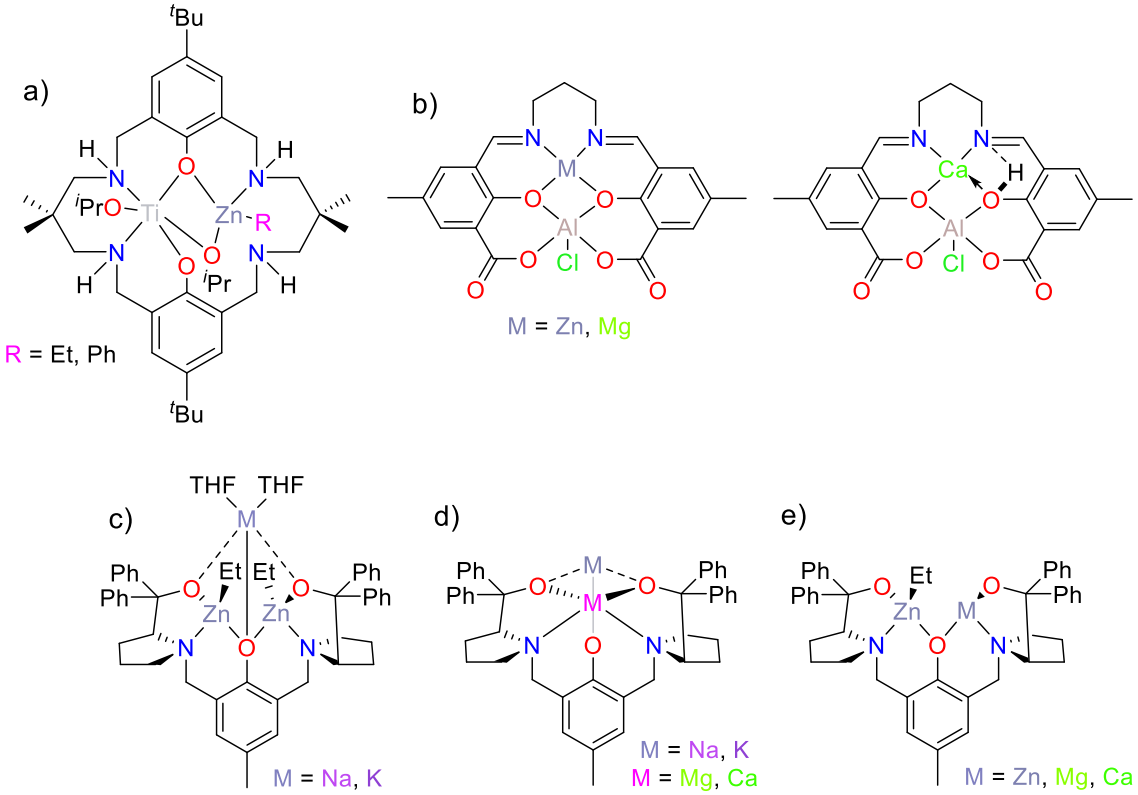

Figure 1.21 Heterobimetallic LA ROP initiators bearing Schiff base and related amino-phenolate ancillary ligands.

More recently, Garden and co-workers have reported salen Al(III)/M(II) (M = Zn, Mg, Ca) initiators for the ROP of *rac*-LA (**Figure 1.21b**).[219, 227] In the presence of propylene oxide co-initiator, the Al/Zn and Al/Mg systems were observed to outperform the mono-Al species by factors of two and eleven respectively (k_{obs} = 6.48 and 31.68 *vs*. 2.88 h^{-1}).[227] The results of molecular dynamics computational studies suggest that this enhanced

activity is caused by the relatively small intermetallic distances (Al-Zn: 3.04 Å; Al-Mg: 2.83 Å). This increases ligand strain and the rigidity of the aluminium's square pyramidal coordination geometry which results in improved monomer coordination.[227] M(II)-Cl-Al bridging interactions were also found to be present in solution as a result of the Lewis acidity of the M^{2+} ions. This weakens the Al-Cl bond strength (2.20 *vs*. 2.32 Å) which therefore enables faster initiation/insertion.[227] In contrast, the Al/Ca catalyst showed lower activity than the mono-Al counterpart (7% conversion in 15 minutes); this could be due to the fact that the catalyst retains a highly acidic phenolic proton which may quench the polymerisation (**Figure 1.21b**).[227]

The same group have also reported a series of hetero-bi-and-tri-metallic systems based on the Trost ProPhenol ligand (**Figure 1.21c**).[219, 228] The hetero-trimetallic systems were the first to be isolated after the catalytic testing of a similar homo-*bis*(zinc) complex proved promising.[229] The incorporation of Na/K resulted in the labilisation of the Zn-Et bonds thus initiating accelerated nucleophilic attack and LA ring-opening. The K/Zn_2 complex proved to be the fastest heterometallic LA ROP catalyst at that time, converting 60 eq. of *rac*-LA in just 20 seconds (k_{obs} = 61.2 h^{-1}).[228] This high level of activity relied on the addition of 2 eq. of BnOH co-initiator and produced PLA with moderate molecular weight distributions (M_w/M_n = 1.40). The use of the smaller alkali metal resulted in a five-fold decrease in polymerisation activity (k_{obs} = 11.52 h^{-1}); this highlighted the key role of the group 1 cations in coordinating/subsequently activating the monomer.[228]

Comparable hetero-bimetallic ProPhenol systems were subsequently isolated in 2022 (**Figure 1.21d**).[219, 230] In the presence of 1 eq. of BnOH co-initiator, these catalysts eclipsed the activity of the trimetallic variants by converting 83–98 eq. of *rac*-LA in 5 seconds (K/Ca and K/Mg respectively) or 85 eq. in 40 seconds (Na/Ca).[230] The more

active K-based complexes displayed reduced polymerisation control as opposed to the alternative Na-based species (M_w/M_n = 1.51–1.83 *vs*. 1.24).[230]

The only example of a completely divalent heterobimetallic system was published by Garden and co-workers in 2021 (**Figure 1.21e**).[219, 231] These systems were shown to be more active than their homometallic counterparts with an overall activity spectrum as follows: Ca/Zn > *bis*(Ca) > Mg/Zn ~ *bis*(Zn) > *bis*(Mg).[231] The greater availability of Lewis acidic coordination sites on the larger Ca^{2+} cation was used to rationalise its superior reactivity (converting 48 eq. of *rac*-LA in 5 s).[231]

1.7 Scope of Thesis

The primary aims of this Thesis are: (i) to synthesise and fully characterise new mono- and bimetallic alkaline-earth compounds, (ii) to test their catalytic capabilities in the ROP of LA and (iii) to evaluate the benefits of bimetallic complexes/cooperativity for this type of polymerisation.

Chapter 2 discusses the synthesis and characterisation of new alkaline-earth species bearing a *bis*(phenoxy-imine) – "NOON" – ancillary ligand. **Chapter 3** then presents the ability of these complexes to function as ROP catalysts; a range of conditions were explored in order to determine the overall polymerisation mechanisms and rate laws. **Chapter 4** details the synthesis and characterisation of monometallic group two compounds using an alternative "NON" class of ancillary ligand. **Chapter 5** then showcases the ability of these species to act as LA ROP catalysts. **Chapter 6** focuses on the exploration of the monoanionic "NON" framework for the formation of cationic, bimetallic initiators; the use of already isolated compounds as intermediates will be discussed alongside alternative methods involving novel *bis*(phenoxy-imine) diacids.

1.8 References

1. R. Geyer, J. R. Jambeck and K. L. Law, *Sci. Adv.*, 2017, **3**, e1700782.
2. *Nat. Commun.*, 2018, **9**, 2157.
3. J. Payne, P. McKeown and M. D. Jones, *Polym. Degrad. Stab.*, 2019, **165**, 170-181.
4. Y. Zhu, C. Romain and C. K. Williams, *Nature*, 2016, **540**, 354-362.
5. H. Sardon and A. P. Dove, *Science*, 2018, **360**, 380-381.
6. M. Linder, *Green Chem. Lett. Rev.*, 2017, **10**, 428-435.
7. SYSTEMIQ, *ReShaping Plastics: Pathways to a Circular, Climate Neutral Plastics System in Europe.*, **2022**.
8. J. Vallette, *The New Coal: Plastics & Climate Change*, Beyond Plastics at Bennington College, 2021.
9. L. C. M. Lebreton, J. van der Zwet, J.-W. Damsteeg, B. Slat, A. Andrady and J. Reisser, *Nat. Commun.*, 2017, **8**, 15611.
10. European-Bioplastics, https://docs.european-bioplastics.org/publications/EUBP_Facts_and_figures.pdf, (accessed 20/06/2023).
11. T. Keijer, V. Bakker and J. C. Slootweg, *Nat. Chem.*, 2019, **11**, 190-195.
12. K. L. Law and R. Narayan, *Nat. Rev. Mater.*, 2022, **7**, 104-116.
13. J.-G. Rosenboom, R. Langer and G. Traverso, *Nat. Rev. Mater.*, 2022, **7**, 117-137.
14. M. Hong and E. Y. X. Chen, *Nat. Chem.*, 2016, **8**, 42-49.
15. J. B. Zhu, E. M. Watson, J. Tang and E. Y. X. Chen, *Science*, 2018, **360**, 398-403.
16. Y. Wang, M. Li, J. Chen, Y. Tao and X. Wang, *Angew. Chem. Int. Ed.*, 2021, **60**, 22547-22553.
17. H.-Z. Fan, X. Yang, J.-H. Chen, Y.-M. Tu, Z. Cai and J.-B. Zhu, *Angew. Chem. Int. Ed.*, 2022, **61**, e202117639.
18. X. Zhou, Q. Liu, G. Xu, R. Yang, H. Sun and Q. Wang, *Chin. Chem. Lett.*, 2023, 108158.
19. Y. Xia, X. Yue, Y. Sun, C. Zhang and X. Zhang, *Angew. Chem. Int. Ed.*, 2023, **62**, e202219251.
20. A. J. Ragauskas, C. K. Williams, B. H. Davison, G. Britovsek, J. Cairney, C. A. Eckert, W. J. Frederick, J. P. Hallett, D. J. Leak, C. L. Liotta, J. R. Mielenz, R. Murphy, R. Templer and T. Tschaplinski, *Science*, 2006, **311**, 484-489.
21. G. E. Luckachan and C. K. S. Pillai, *J. Polym. Environ.*, 2011, **19**, 637-676.
22. R. Mülhaupt, *Macromol. Chem. Phys.*, 2013, **214**, 159-174.
23. C. K. Williams, N. R. Brooks, M. A. Hillmyer and W. B. Tolman, *Chem. Commun.*, 2002, 2132-2133.
24. R. E. Drumright, P. R. Gruber and D. E. Henton, *Adv. Mater.*, 2000, **12**, 1841-1846.
25. W. J. Groot and T. Borén, *Int J Life Cycle Assess*, 2010, **15**, 970-984.
26. M. F. Cosate de Andrade, P. M. S. Souza, O. Cavalett and A. R. Morales, *J. Polym. Environ.*, 2016, **24**, 372-384.
27. J. Wu, T.-L. Yu, C.-T. Chen and C.-C. Lin, *Coord. Chem. Rev.*, 2006, **250**, 602-626.

28. Grand-View-Research, https://www.grandviewresearch.com/industry-analysis/polylactic-acid-pla-market, (accessed 20/06/2023).
29. P. Dubois, O. Coulembier and J. M. Raquez, *Handbook of Ring-Opening Polymerization*, Wiley, 1st edn., 2009.
30. W. H. Carothers, G. L. Dorough and F. J. v. Natta, *J. Am. Chem. Soc.*, 1932, **54**, 761-772.
31. K. W. Kim and S. I. Woo, *Macromol. Chem. Phys.*, 2002, **203**, 2245-2250.
32. E. Balla, V. Daniilidis, G. Karlioti, T. Kalamas, M. Stefanidou, N. D. Bikiaris, A. Vlachopoulos, I. Koumentakou and D. N. Bikiaris, *Polymers*, 2021, **13**, 1822.
33. R. Auras, B. Harte and S. Selke, *Macromol. Biosci.*, 2004, **4**, 835-864.
34. K. L. Wasewar, A. A. Yawalkar, J. A. Moulijn and V. G. Pangarkar, *Ind. amp; Eng. Chem. Res.*, 2004, **43**, 5969-5982.
35. H. Du, A. H. Velders, P. J. Dijkstra, Z. Zhong, X. Chen and J. Feijen, *Macromolecules*, 2009, **42**, 1058-1066.
36. P. Van Wouwe, M. Dusselier, E. Vanleeuw and B. Sels, *ChemSusChem*, 2016, **9**, 907-921.
37. S. Mecking, *Angew. Chem. Int. Ed.*, 2004, **43**, 1078-1085.
38. R. Datta, S.-P. Tsai, P. Bonsignore, S.-H. Moon and J. R. Frank, *FEMS Microbiol. Rev.*, 1995, **16**, 221-231.
39. M. Dusselier, P. Van Wouwe, A. Dewaele, E. Makshina and B. F. Sels, *Energy Environ. Sci*, 2013, **6**, 1415-1442.
40. Y. Fan, H. Nishida, Y. Shirai and T. Endo, *Green Chem.*, 2003, **5**, 575-579.
41. T. Tsukegi, T. Motoyama, Y. Shirai, H. Nishida and T. Endo, *Polym. Degrad. Stab.*, 2007, **92**, 552-559.
42. M. Dusselier, P. Van Wouwe, A. Dewaele, P. A. Jacobs and B. F. Sels, *Science*, 2015, **349**, 78-80.
43. A. Duda and S. Penczek, in *Polymers from Renewable Resources*, American Chemical Society, 2001, vol. 764, ch. 13, pp. 160-198.
44. X. Zhang, M. Fevre, G. O. Jones and R. M. Waymouth, *Chem. Rev.*, 2018, **118**, 839-885.
45. E. F. Connor, G. W. Nyce, M. Myers, A. Möck and J. L. Hedrick, *J. Am. Chem. Soc.*, 2002, **124**, 914-915.
46. N. E. Kamber, W. Jeong, R. M. Waymouth, R. C. Pratt, B. G. G. Lohmeijer and J. L. Hedrick, *Chem. Rev.*, 2007, **107**, 5813-5840.
47. M. K. Kiesewetter, E. J. Shin, J. L. Hedrick and R. M. Waymouth, *Macromolecules*, 2010, **43**, 2093-2107.
48. J. Engel, A. Cordellier, L. Huang and S. Kara, *ChemCatChem*, 2019, **11**, 4983-4997.
49. H. Ö. Düşkünkorur, A. Bégué, E. Pollet, V. Phalip, Y. Güvenilir and L. Avérous, *J. Mol. Catal. B: Enzym.*, 2015, **115**, 20-28.
50. H. Zhao, G. A. Nathaniel and P. C. Merenini, *RSC Adv.*, 2017, **7**, 48639-48648.
51. J.-F. Carpentier and Y. Sarazin, in *Alkaline-Earth Metal Compounds: Oddities and Applications*, ed. S. Harder, Springer Berlin Heidelberg, Berlin, Heidelberg, 2013, pp. 141-189.
52. M. J. Stanford and A. P. Dove, *Chem. Soc. Rev.*, 2010, **39**, 486-494.

53. H. R. Kricheldorf, I. Kreiser-Saunders, C. Jürgens and D. Wolter, *Macromol. Symp.*, 1996, **103**, 85-102.

54. F. E. Kohn, J. G. Van Ommen and J. Feijen, *Eur. Polym. J.*, 1983, **19**, 1081-1088.

55. P. Dubois, C. Jacobs, R. Jerome and P. Teyssie, *Macromolecules*, 1991, **24**, 2266-2270.

56. H. R. Kricheldorf, M. Berl and N. Scharnagl, *Macromolecules*, 1988, **21**, 286-293.

57. A. Kowalski, A. Duda and S. Penczek, *Macromolecules*, 2000, **33**, 7359-7370.

58. E. L. Marshall, V. C. Gibson and H. S. Rzepa, *J. Am. Chem. Soc.*, 2005, **127**, 6048-6051.

59. O. Dechy-Cabaret, B. Martin-Vaca and D. Bourissou, *Chem. Rev.*, 2004, **104**, 6147-6176.

60. H. R. Kricheldorf and R. Dunsing, *Makromol. Chem.*, 1986, **187**, 1611-1625.

61. D. Bourissou, B. Martin-Vaca, A. Dumitrescu, M. Graullier and F. Lacombe, *Macromolecules*, 2005, **38**, 9993-9998.

62. M. Basko, *Pure Appl. Chem.*, 2012, **84**, 2081-2088.

63. M. Myers, E. F. Connor, T. Glauser, A. Möck, G. Nyce and J. L. Hedrick, *J. Polym. Sci., Part A: Polym. Chem.*, 2002, **40**, 844-851.

64. F. Nederberg, E. F. Connor, M. Möller, T. Glauser and J. L. Hedrick, *Angew. Chem. Int. Ed.*, 2001, **40**, 2712-2715.

65. C. Bonduelle, B. Martín-Vaca, F. P. Cossío and D. Bourissou, *Chem. Eur. J.*, 2008, **14**, 5304-5312.

66. A. P. Dove, H. Li, R. C. Pratt, B. G. G. Lohmeijer, D. A. Culkin, R. M. Waymouth and J. L. Hedrick, *Chem. Commun.*, 2006, 2881-2883.

67. R. C. Pratt, B. G. G. Lohmeijer, D. A. Long, P. N. P. Lundberg, A. P. Dove, H. Li, C. G. Wade, R. M. Waymouth and J. L. Hedrick, *Macromolecules*, 2006, **39**, 7863-7871.

68. A. P. Dove, R. C. Pratt, B. G. G. Lohmeijer, R. M. Waymouth and J. L. Hedrick, *J. Am. Chem. Soc.*, 2005, **127**, 13798-13799.

69. A. Bhaw-Luximon, D. Jhurry, N. Spassky, S. Pensec and J. Belleney, *Polymer*, 2001, **42**, 9651-9656.

70. H. R. Kricheldorf and I. Kreiser-Saunders, *Makromol. Chem.*, 1990, **191**, 1057-1066.

71. Z. Jedliński, W. Wałach, P. Kurcok and G. y. Adamus, *Makromol. Chem.*, 1991, **192**, 2051-2057.

72. H. R. Kricheldorf and S.-R. Lee, *Polymer*, 1995, **36**, 2995-3003.

73. J. Kasperczyk and M. Bero, *Polymer*, 2000, **41**, 391-395.

74. J. V. Lamb, J.-C. Buffet, J. E. Matley, C. M. R. Wright, Z. R. Turner and D. O'Hare, *Dalton Trans.*, 2019, **48**, 2510-2520.

75. Z. R. Turner, J. V. Lamb, T. P. Robinson, D. Mandal, J.-C. Buffet and D. O′Hare, *Dalton Trans.*, 2021, **50**, 4805-4818.

76. N. Diteepeng, J.-C. Buffet, Z. R. Turner and D. O'Hare, *Dalton Trans.*, 2019, **48**, 16099-16107.

77. N. Diteepeng, I. A. P. Wilson, J.-C. Buffet, Z. R. Turner and D. O'Hare, *Polym. Chem.*, 2020, **11**, 6308-6318.

78. R. H. Platel, L. M. Hodgson and C. K. Williams, *Polym. Rev.*, 2008, **48**, 11-63.

79. J.-C. Wu, B.-H. Huang, M.-L. Hsueh, S.-L. Lai and C.-C. Lin, *Polymer*, 2005, **46**, 9784-9792.

80. L. Clark, G. B. Deacon, C. M. Forsyth, P. C. Junk, P. Mountford, J. P. Townley and J. Wang, *Dalton Trans.*, 2013, **42**, 9294-9312.

81. P. I. Binda and E. E. Delbridge, *Dalton Trans.*, 2007, 4685-4692.

82. M. P. Blake, A. D. Schwarz and P. Mountford, *Organometallics*, 2011, **30**, 1202-1214.

83. T.-P.-A. Cao, A. Buchard, X. F. Le Goff, A. Auffrant and C. K. Williams, *Inorg. Chem.*, 2012, **51**, 2157-2169.

84. L. Clark, M. G. Cushion, H. E. Dyer, A. D. Schwarz, R. Duchateau and P. Mountford, *Chem. Commun.*, 2010, **46**, 273-275.

85. H.-Y. Chen, B.-H. Huang and C.-C. Lin, *Macromolecules*, 2005, **38**, 5400-5405.

86. A. Thevenon, C. Romain, M. S. Bennington, A. J. P. White, H. J. Davidson, S. Brooker and C. K. Williams, *Angew. Chem. Int. Ed.*, 2016, **55**, 8680-8685.

87. M. Normand, V. Dorcet, E. Kirillov and J.-F. Carpentier, *Organometallics*, 2013, **32**, 1694-1709.

88. K. Ding, M. O. Miranda, B. Moscato-Goodpaster, N. Ajellal, L. E. Breyfogle, E. D. Hermes, C. P. Schaller, S. E. Roe, C. J. Cramer, M. A. Hillmyer and W. B. Tolman, *Macromolecules*, 2012, **45**, 5387-5396.

89. S. Asano, T. Aida and S. Inoue, *J. Chem. Soc., Chem. Commun.*, 1985, 1148-1149.

90. S. Inoue, *J. Polym. Sci., Part A: Polym. Chem.*, 2000, **38**, 2861-2871.

91. N. Ajellal, J.-F. Carpentier, C. Guillaume, S. M. Guillaume, M. Helou, V. Poirier, Y. Sarazin and A. Trifonov, *Dalton Trans.*, 2010, **39**, 8363-8376.

92. M.-L. Shueh, Y.-S. Wang, B.-H. Huang, C.-Y. Kuo and C.-C. Lin, *Macromolecules*, 2004, **37**, 5155-5162.

93. V. Poirier, T. Roisnel, J.-F. Carpentier and Y. Sarazin, *Dalton Trans.*, 2009, 9820-9827.

94. V. Poirier, M. Duc, J.-F. Carpentier and Y. Sarazin, *ChemSusChem*, 2010, **3**, 579-590.

95. E. Grunova, T. Roisnel and J.-F. Carpentier, *Dalton Trans.*, 2009, 9010-9019.

96. C.-X. Cai, A. Amgoune, C. W. Lehmann and J.-F. Carpentier, *Chem. Commun.*, 2004, 330-331.

97. J. P. MacDonald, M. Sidera, S. P. Fletcher and M. P. Shaver, *Eur. Polym. J.*, 2016, **74**, 287-295.

98. P. Sumrit, P. Chuawong, T. Nanok, T. Duangthongyou and P. Hormnirun, *Dalton Trans.*, 2016, **45**, 9250-9266.

99. A. Amgoune, C. M. Thomas, T. Roisnel and J.-F. Carpentier, *Chem. Eur. J.*, 2006, **12**, 169-179.

100. V. Poirier, T. Roisnel, S. Sinbandhit, M. Bochmann, J.-F. Carpentier and Y. Sarazin, *Chem. Eur. J.*, 2012, **18**, 2998-3013.

101. L. Wang, V. Poirier, F. Ghiotto, M. Bochmann, R. D. Cannon, J.-F. Carpentier and Y. Sarazin, *Macromolecules*, 2014, **47**, 2574-2584.

102. M. Helou, O. Miserque, J.-M. Brusson, J.-F. Carpentier and S. M. Guillaume, *Chem. Eur. J.*, 2010, **16**, 13805-13813.

103. M. Chanda, *Introduction to Polymer Science and Chemistry: A Problem-Solving Approach*, CRC Press, 2nd edn., 2013.

104. K. A. M. Thakur, R. T. Kean, E. S. Hall, J. J. Kolstad and E. J. Munson, *Int. J. Polym. Anal. Charact.*, 1998, **4**, 379-391.

105. G. L. Baker, E. B. Vogel and M. R. Smith, *Polym. Rev.*, 2008, **48**, 64-84.

106. A. P. Dove, *Chem. Commun.*, 2008, 6446-6470.

107. S. M. Guillaume, E. Kirillov, Y. Sarazin and J.-F. Carpentier, *Chem. Eur. J.*, 2015, **21**, 7988-8003.

108. Y. Ikada, K. Jamshidi, H. Tsuji and S. H. Hyon, *Macromolecules*, 1987, **20**, 904-906.

109. S. Brochu, R. E. Prud'homme, I. Barakat and R. Jerome, *Macromolecules*, 1995, **28**, 5230-5239.

110. H. Tsuji and Y. Ikada, *Polymer*, 1999, **40**, 6699-6708.

111. N. Spassky, M. Wisniewski, C. Pluta and A. Le Borgne, *Macromol. Chem. Phys.*, 1996, **197**, 2627-2637.

112. S. Inkinen, M. Hakkarainen, A.-C. Albertsson and A. Södergård, *Biomacromolecules*, 2011, **12**, 523-532.

113. N. Nomura, R. Ishii, Y. Yamamoto and T. Kondo, *Chem. Eur. J.*, 2007, **13**, 4433-4451.

114. J. M. Becker, R. J. Pounder and A. P. Dove, *Macromol. Rapid Commun.*, 2010, **31**, 1923-1937.

115. T. M. Ovitt and G. W. Coates, *J. Am. Chem. Soc.*, 2002, **124**, 1316-1326.

116. D. J. Walton and J. P. Lorimer, *Polymers*, Oxford University Press, 2000.

117. H. G. B. Sadao Mori, *Size Exclusion Chromatography*, Springer, 1999.

118. J. C. Giddings, M. N. Myers, G.-C. Lin and M. Martin, *J. Chromatogr. A*, 1977, **142**, 23-38.

119. M. I. Malik and H. Pasch, *Prog. Polym. Sci.*, 2016, **63**, 42-85.

120. *Handbook of Size Exclusion Chromatography and Related Techniques*, Marcel Dekker Inc., Second edn., 2004.

121. J. R. Dorgan, J. Janzen, D. M. Knauss, S. B. Hait, B. R. Limoges and M. H. Hutchinson, *J. Polym. Sci., Part B: Polym. Phys.*, 2005, **43**, 3100-3111.

122. P. Piromjitpong, P. Ratanapanee, W. Thumrongpatanaraks, P. Kongsaeree and K. Phomphrai, *Dalton Trans.*, 2012, **41**, 12704-12710.

123. C. Rentero, J. Damián, A. Medel, M. Fernández-Millán, Y. Rusconi, G. Talarico, T. Cuenca, V. Sessini and M. E. G. Mosquera, *Polymers*, 2022, **14**, 2982.

124. J. U. Izunobi and C. L. Higginbotham, *J. Chem. Educ.*, 2011, **88**, 1098-1104.

125. J. M. Pérez, C. Ruiz and I. Fernández, *J. Chem. Educ.*, 2022, **99**, 1000-1007.

126. M. T. Zell, B. E. Padden, A. J. Paterick, K. A. M. Thakur, R. T. Kean, M. A. Hillmyer and E. J. Munson, *Macromolecules*, 2002, **35**, 7700-7707.

127. M. H. Chisholm, S. S. Iyer and M. E. Matison, *Chem. Commun.*, 1997, 1999-2000.

128. H. R. Kricheldorf, C. Boettcher and K.-U. Tönnes, *Polymer*, 1992, **33**, 2817-2824.

129. F. A. Bovey, *Polymer Conformation and Configuration*, Elsevier, 1st edn., 1969.

130. H. Räder and W. Schrepp, *Acta Polym.*, 1998, **49**, 272-293.

131. M. W. F. Nielen, *Mass Spectrom. Rev.*, 1999, **18**, 309-344.

132. C. Wesdemiotis, K. N. Williams-Pavlantos, A. R. Keating, A. S. McGee and C. Bochenek, *Mass Spectrom. Rev.*, 2023, 1-50.

133. A. P. Gies, in *Molecular Characterization of Polymers*, eds. M. I. Malik, J. Mays and M. R. Shah, Elsevier, 2021, pp. 305-368.

134. A. J. Nijenhuis, D. W. Grijpma and A. J. Pennings, *Macromolecules*, 1992, **25**, 6419-6424.

135. P. Degée, P. Dubois, R. Jérŏme, S. Jacobsen and H.-G. Fritz, *Macromolecular Symposia*, 1999, **144**, 289-302.

136. M. Ryner, K. Stridsberg, A.-C. Albertsson, H. von Schenck and M. Svensson, *Macromolecules*, 2001, **34**, 3877-3881.

137. G. Schwach, J. Coudane, R. Engel and M. Vert, *Polym. Bull.*, 1994, **32**, 617-623.

138. A. Kowalski, A. Duda and S. Penczek, *Macromolecules*, 1998, **31**, 2114-2122.

139. G. Schwach, J. Coudane, R. Engel and M. Vert, *Polym. Bull.*, 1996, **37**, 771-776.

140. G. Schwach, J. Coudane, R. Engel and M. Vert, *Polym. Int.*, 1998, **46**, 177-182.

141. X. Wu and S. Li, *Polym. Int.*, 2013, **62**, 1014-1021.

142. E. Fazekas, P. A. Lowy, M. Abdul Rahman, A. Lykkeberg, Y. Zhou, R. Chambenahalli and J. A. Garden, *Chem. Soc. Rev.*, 2022, **51**, 8793-8814.

143. M. Sriyai, T. Chaiwon, R. Molloy, P. Meepowpan and W. Punyodom, *RSC Adv.*, 2020, **10**, 43566-43578.

144. W. Rao, C. Cai, J. Tang, Y. Wei, C. Gao, L. Yu and J. Ding, *Chin. J. Chem.*, 2021, **39**, 1965-1974.

145. G. Li, M. Zhao, F. Xu, B. Yang, X. Li, X. Meng, L. Teng, F. Sun and Y. Li, *Molecules*, 2020, **25**, 5023.

146. H. R. Kricheldorf and S. M. Weidner, *Polym. Chem.*, 2022, **13**, 1618-1647.

147. A. Duda and S. Penczek, *Macromol. Rapid Commun.*, 1995, **16**, 67-76.

148. W. Schlenk and W. Schlenk jun., *Chem. Ber.*, 1929, **62**, 920-924.

149. A. G. Avent, M. R. Crimmin, M. S. Hill and P. B. Hitchcock, *Dalton Trans.*, 2005, 278-284.

150. M. Arrowsmith, M. S. Hill and G. Kociok-Köhn, *Organometallics*, 2011, **30**, 1291-1294.

151. M. S. Hill, D. J. Liptrot and C. Weetman, *Chem. Soc. Rev.*, 2016, **45**, 972-988.

152. M. H. Chisholm, N. W. Eilerts, J. C. Huffman, S. S. Iyer, M. Pacold and K. Phomphrai, *J. Am. Chem. Soc.*, 2000, **122**, 11845-11854.

153. M. H. Chisholm, J. Gallucci and K. Phomphrai, *Chem. Commun.*, 2003, 48-49.

154. R. Han and G. Parkin, *Organometallics*, 1991, **10**, 1010-1020.

155. R. Han and G. Parkin, *J. Am. Chem. Soc.*, 1992, **114**, 748-757.

156. M. H. Chisholm, J. C. Gallucci and K. Phomphrai, *Inorg. Chem.*, 2004, **43**, 6717-6725.

157. M. G. Cushion and P. Mountford, *Chem. Commun.*, 2011, **47**, 2276-2278.

158. B. Lian, C. M. Thomas, O. L. Casagrande, T. Roisnel and J.-F. Carpentier, *Polyhedron*, 2007, **26**, 3817-3824.

159. J.-C. Buffet, J. P. Davin, T. P. Spaniol and J. Okuda, *New J. Chem.*, 2011, **35**, 2253-2257.

160. M. H. Chisholm, J. C. Gallucci, H. Zhen and J. C. Huffman, *Inorg. Chem.*, 2001, **40**, 5051-5054.

161. Z. Zheng, G. Zhao, R. Fablet, M. Bouyahyi, C. M. Thomas, T. Roisnel, O. Casagrande Jr and J.-F. Carpentier, *New J. Chem.*, 2008, **32**, 2279-2291.

162. C. A. Wheaton, P. G. Hayes and B. J. Ireland, *Dalton Trans.*, 2009, 4832-4846.

163. M. Cheng, A. B. Attygalle, E. B. Lobkovsky and G. W. Coates, *J. Am. Chem. Soc.*, 1999, **121**, 11583-11584.

164. M. H. Chisholm, S. S. Iyer, D. G. McCollum, M. Pagel and U. Werner-Zwanziger, *Macromolecules*, 1999, **32**, 963-973.

165. B. M. Chamberlain, M. Cheng, D. R. Moore, T. M. Ovitt, E. B. Lobkovsky and G. W. Coates, *J. Am. Chem. Soc.*, 2001, **123**, 3229-3238.

166. M. H. Chisholm, J. C. Huffman and K. Phomphrai, *J. Chem. Soc., Dalton Trans.*, 2001, 222-224.

167. A. P. Dove, V. C. Gibson, E. L. Marshall, A. J. P. White and D. J. Williams, *Dalton Trans.*, 2004, 570-578.

168. M. H. Chisholm, J. C. Gallucci and K. Phomphrai, *Inorg. Chem.*, 2005, **44**, 8004-8010.

169. S. D. Allen, D. R. Moore, E. B. Lobkovsky and G. W. Coates, *J. Am. Chem. Soc.*, 2002, **124**, 14284-14285.

170. M. Cheng, E. B. Lobkovsky and G. W. Coates, *J. Am. Chem. Soc.*, 1998, **120**, 11018-11019.

171. D. R. Moore, M. Cheng, E. B. Lobkovsky and G. W. Coates, *J. Am. Chem. Soc.*, 2003, **125**, 11911-11924.

172. G. Trott, P. K. Saini and C. K. Williams, *Philos. Trans. R. Soc. A*, 2016, **374**, 20150085.

173. H.-C. Huang, B. Wang, Y.-P. Zhang and Y.-S. Li, *Polym. Chem.*, 2016, **7**, 5819-5827.

174. A. B. Kremer and P. Mehrkhodavandi, *Coord. Chem. Rev.*, 2019, **380**, 35-57.

175. W. N. Lipscomb and N. Sträter, *Chem. Rev.*, 1996, **96**, 2375-2434.

176. M. Delferro and T. J. Marks, *Chem. Rev.*, 2011, **111**, 2450-2485.

177. M. H. Chisholm, J. Gallucci and K. Phomphrai, *Inorg. Chem.*, 2002, **41**, 2785-2794.

178. F. Drouin, P. O. Oguadinma, T. J. J. Whitehorne, R. E. Prud'homme and F. Schaper, *Organometallics*, 2010, **29**, 2139-2147.

179. F. Drouin, T. J. J. Whitehorne and F. Schaper, *Dalton Trans.*, 2011, **40**, 1396-1400.

180. T. J. J. Whitehorne and F. Schaper, *Chem. Commun.*, 2012, **48**, 10334-10336.

181. T. J. J. Whitehorne and F. Schaper, *Inorg. Chem.*, 2013, **52**, 13612-13622.

182. T. J. J. Whitehorne and F. Schaper, *Can. J. Chem.*, 2014, **92**, 206-214.

183. V. Balasanthiran, M. H. Chisholm, K. Choojun, C. B. Durr and P. M. Wambua, *J. Organomet. Chem.*, 2016, **812**, 56-65.

184. H.-Y. Tang, H.-Y. Chen, J.-H. Huang and C.-C. Lin, *Macromolecules*, 2007, **40**, 8855-8860.

185. J. Hu, C. Kan, H. Wang and H. Ma, *Macromolecules*, 2018, **51**, 5304-5312.

186. W. Yi and H. Ma, *Inorg. Chem.*, 2013, **52**, 11821-11835.

187. D. J. Darensbourg, W. Choi, O. Karroonnirun and N. Bhuvanesh, *Macromolecules*, 2008, **41**, 3493-3502.

188. J. B. L. Gallaway, J. R. K. McRae, A. Decken and M. P. Shaver, *Can. J. Chem.*, 2012, **90**, 419-426.

189. Y. Sarazin, B. Liu, T. Roisnel, L. Maron and J.-F. Carpentier, *J. Am. Chem. Soc.*, 2011, **133**, 9069-9087.

190. W.-Y. Lee, H.-H. Hsieh, C.-C. Hsieh, H. M. Lee, G.-H. Lee, J.-H. Huang, T.-C. Wu and S.-H. Chuang, *J. Organomet. Chem.*, 2007, **692**, 1131-1137.

191. C. Di Iulio, M. Middleton, G. Kociok-Köhn, M. D. Jones and A. L. Johnson, *Eur. J. Inorg. Chem.*, 2013, 1541-1554.

192. N.-T. Crespo-Velasco, L.-G. Guerrero-Ram, M. Flores-Alamo and M.-Á. Muñoz-Hernández, *Main Group Chem.*, 2015, **14**, 141-157.

193. C. K. Williams, L. E. Breyfogle, S. K. Choi, W. Nam, V. G. Young, M. A. Hillmyer and W. B. Tolman, *J. Am. Chem. Soc.*, 2003, **125**, 11350-11359.

194. G. Labourdette, D. J. Lee, B. O. Patrick, M. B. Ezhova and P. Mehrkhodavandi, *Organometallics*, 2009, **28**, 1309-1319.

195. T. Ebrahimi, E. Mamleeva, I. Yu, S. G. Hatzikiriakos and P. Mehrkhodavandi, *Inorg. Chem.*, 2016, **55**, 9445-9453.

196. T. Ebrahimi, D. C. Aluthge, S. G. Hatzikiriakos and P. Mehrkhodavandi, *Macromolecules*, 2016, **49**, 8812-8824.

197. P. J. Dijkstra, H. Du and J. Feijen, *Polym. Chem.*, 2011, **2**, 520-527.

198. H.-Y. Chen, H.-Y. Tang and C.-C. Lin, *Macromolecules*, 2006, **39**, 3745-3752.

199. W.-C. Hung, Y. Huang and C.-C. Lin, *J. Polym. Sci., Part A: Polym. Chem.*, 2008, **46**, 6466-6476.

200. W.-C. Hung and C.-C. Lin, *Inorg. Chem.*, 2009, **48**, 728-734.

201. H.-Y. Chen, H.-Y. Tang and C.-C. Lin, *Polymer*, 2007, **48**, 2257-2262.

202. B.-H. Huang, C.-N. Lin, M.-L. Hsueh, T. Athar and C.-C. Lin, *Polymer*, 2006, **47**, 6622-6629.

203. J. Wu, Y.-Z. Chen, W.-C. Hung and C.-C. Lin, *Organometallics*, 2008, **27**, 4970-4978.

204. L. E. Breyfogle, C. K. Williams, J. V. G. Young, M. A. Hillmyer and W. B. Tolman, *Dalton Trans.*, 2006, 928-936.

205. P. D. Knight, A. J. P. White and C. K. Williams, *Inorg. Chem.*, 2008, **47**, 11711-11719.

206. Y. Sun, Y. Cui, J. Xiong, Z. Dai, N. Tang and J. Wu, *Dalton Trans.*, 2015, **44**, 16383-16391.

207. C. Romain, M. S. Bennington, A. J. P. White, C. K. Williams and S. Brooker, *Inorg. Chem.*, 2015, **54**, 11842-11851.

208. Z. Gu and R. J. Comito, *Organometallics*, 2022, **41**, 1911-1916.

209. Z. Zhong, S. Schneiderbauer, P. J. Dijkstra, M. Westerhausen and J. Feijen, *Polym. Bull.*, 2003, **51**, 175-182.

210. M. Westerhausen, S. Schneiderbauer, Alexander N. Kneifel, Y. Söltl, P. Mayer, H. Nöth, Z. Zhong, Pieter J. Dijkstra and J. Feijen, *Eur. J. Inorg. Chem.*, 2003, 3432-3439.

211. A. Garcés, L. F. Sánchez-Barba, J. Fernández-Baeza, A. Otero, M. Honrado, A. Lara-Sánchez and A. M. Rodríguez, *Inorg. Chem.*, 2013, **52**, 12691-12701.

212. E. Bukhaltsev, I. Goldberg and A. Vigalok, *Organometallics*, 2004, **23**, 4540-4543.

213. E. Bukhaltsev, L. Frish, Y. Cohen and A. Vigalok, *Org. Lett.*, 2005, **7**, 5123-5126.

214. P. K. Saini, C. Romain and C. K. Williams, *Chem. Commun.*, 2014, **50**, 4164-4167.

215. A. Buchard, F. Jutz, M. R. Kember, A. J. P. White, H. S. Rzepa and C. K. Williams, *Macromolecules*, 2012, **45**, 6781-6795.

216. H.-Y. Chen, M.-Y. Liu, A. K. Sutar and C.-C. Lin, *Inorg. Chem.*, 2010, **49**, 665-674.

217. J. Char, E. Brulé, P. C. Gros, M.-N. Rager, V. Guérineau and C. M. Thomas, *J. Organomet. Chem.*, 2015, **796**, 47-52.

218. M. J. Walton, S. J. Lancaster and C. Redshaw, *ChemCatChem*, 2014, **6**, 1892-1898.

219. W. Gruszka and J. A. Garden, *Nat. Commun.*, 2021, **12**, 3252.

220. M. H. Chisholm, K. Choojun, J. C. Gallucci and P. M. Wambua, *Chem. Sci.*, 2012, **3**, 3445-3457.

221. M. Hu, X. Song, F. Wang, W. Zhang, W. Ma and F. Han, *New J. Chem.*, 2022, **46**, 1175-1181.

222. J. A. Garden, P. K. Saini and C. K. Williams, *J. Am. Chem. Soc.*, 2015, **137**, 15078-15081.

223. A. C. Deacy, C. B. Durr, J. A. Garden, A. J. P. White and C. K. Williams, *Inorg. Chem.*, 2018, **57**, 15575-15583.

224. G. Trott, J. A. Garden and C. K. Williams, *Chem. Sci.*, 2019, **10**, 4618-4627.

225. A. C. Deacy, A. F. R. Kilpatrick, A. Regoutz and C. K. Williams, *Nat. Chem.*, 2020, **12**, 372-380.

226. J. A. Garden, A. J. P. White and C. K. Williams, *Dalton Trans.*, 2017, **46**, 2532-2541.

227. A. J. Gaston, Z. Greindl, C. A. Morrison and J. A. Garden, *Inorg. Chem.*, 2021, **60**, 2294-2303.

228. W. Gruszka, A. Lykkeberg, G. S. Nichol, M. P. Shaver, A. Buchard and J. A. Garden, *Chem. Sci.*, 2020, **11**, 11785-11790.

229. W. Gruszka, L. C. Walker, M. P. Shaver and J. A. Garden, *Macromolecules*, 2020, **53**, 4294-4302.

230. W. Gruszka and J. A. Garden, *Chem. Commun.*, 2022, **58**, 1609-1612.

231. W. Gruszka, H. Sha, A. Buchard and J. A. Garden, *Catal. Sci. Technol.*, 2022, **12**, 1070-1079.

Chapter 2

Synthesis and characterisation of alkaline-earth "NOON" complexes

2.1 Introduction

2.1.1 Overview

This chapter discusses the exploration of a 2,7-diimino-1,8-dihydroxynaphthalene ("NOON") ligand motif as a suitable backbone for bimetallic group two complexes. In total, the synthesis and characterisation of five new alkaline-earth compounds is presented; these include two bimetallic magnesium dimers as well as monometallic, monomeric heavier alkaline-earth (M = Ca, Sr, Ba) systems.

2.1.2 Literature reports involving the "NOON" system

The "NOON" ligand system, containing two phenoxy-imine groups (and therefore two potential [=N,O^-] binding pockets), was first published by Marks and co-workers in 2008. Their report details the synthesis and reactivity of a bimetallic di-zirconium olefin polymerisation catalyst (**Figure 2.1**).[1] The incorporation of a rigid backbone, to prevent the metal centres rotating away from each other, was proposed as a way of maximising metal-metal cooperativity and thus polymerisation activity.[2] The bimetallic catalyst

recorded improved co-monomer incorporation (7.3% *vs.* 4.1% for *1-octene*) as well as activities approximately eight-times higher than that of the mononuclear analogue (16 000 *vs*. 2100 $g_{PE}\ mol_{Zr}^{-1}\ h^{-1}\ atm^{-1}$).[1]

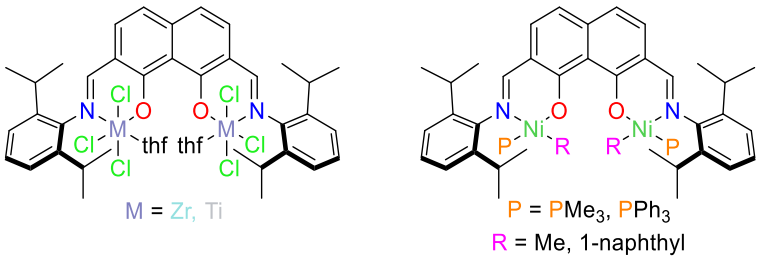

Figure 2.1 The previously reported bimetallic $^{Dipp}L(MX_n)_2$ catalysts incorporating the "NOON" ligand framework.

Since this report, similar di-titanium and di-nickel systems have been synthesised and tested (**Figure 2.1**).[2-4] The di-titanium species showed analogous reactivity to the highly effective di-zirconium complex, recording increased catalytic activity (5300 *vs.* 2500 $g_{PE}\ mol_{Ti}^{-1}\ h^{-1}\ atm^{-1}$) and co-monomer enchainment efficiency (e.g. 15.2% *vs*. 8.4% for *1-octene*).[2] The *bis*(nickel) systems also showed these improvements, as well as an increased selectivity for *methyl*-group branching (branch density, calculated by ^{1}H NMR spectroscopy, is approximately double that achieved by the mononuclear counterpart).[3, 4]

To date, there is no record of this "NOON" framework being used in conjunction with alkaline-earth metals. This, coupled with its already proven amenity to form cooperative, highly active, bimetallic polymerisation catalysts, led to it being chosen as the starting point for this Thesis research.

2.2 Pro-ligand synthesis

The pro-ligand, 2,7-di(2,6-diisopropylphenyl)-imino-1,8-dihydroxynaphthalene ($H_2^{Dipp}L$; 2,7-(HC=NDipp)-1,8-OH-$C_{10}H_4$), was prepared using an adaptation of the procedure reported by Marks and co-workers (**Scheme 2.1**).[2, 5]

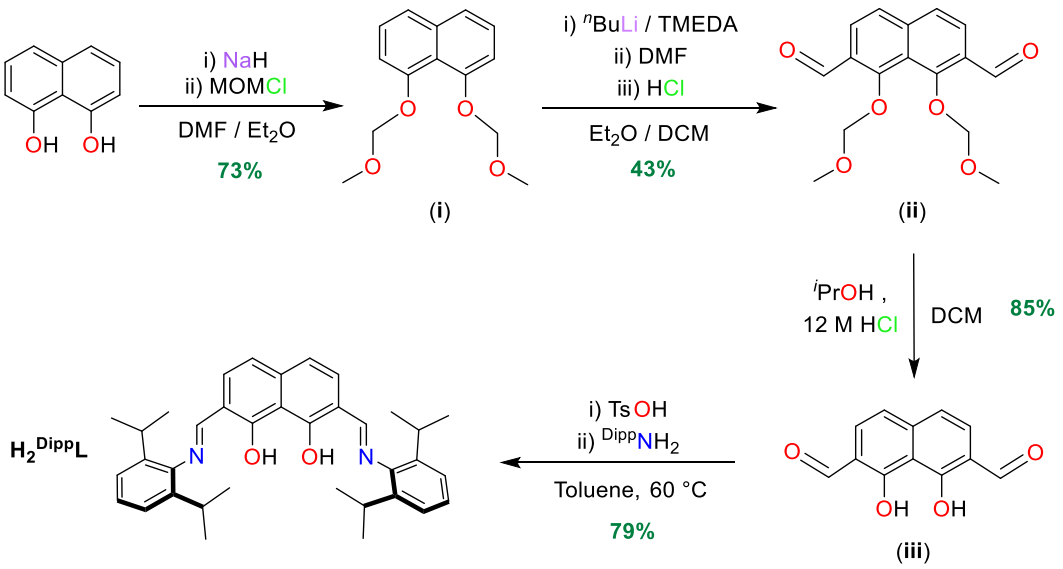

Scheme 2.1 Synthesis of $H_2^{Dipp}L$: 1,8-OH-2,7-{C(H)=N-2,6-^{i}Pr-C_6H_3}-$C_{10}H_6$.

The pro-ligand synthesis involved a four-step process which began with the protection of the alcohol functional groups of naphthalene-1,8-diol using chloromethyl methyl ether (MOMCl) (**i**). Lithiation of both *ortho*-positions of the aromatic rings was achieved with an *n*-butyl lithium (^{n}BuLi)/tetramethylethylenediamine (TMEDA) mixture before dimethylformamide (DMF) was added to initiate formation of the dialdehyde product (**ii**). Deprotection of the MOM groups was then achieved using a degassed solution of isopropanol and hydrochloric acid (**iii**). The final step of the synthesis involved a condensation reaction with 2,6-diisopropylaniline ($^{Dipp}NH_2$) which afforded $H_2^{Dipp}L$ as a bright orange powder in 79% isolated yield.

The overall yield of the four-step synthesis was almost doubled from 11% to 20% as a result of reaction optimisations. Unfortunately, no improvement to the yield of the second step was made. Attempts to use different protecting groups and to perform *in situ* sequential lithiations (i.e. combine steps one and two) proved unrewarding. This agrees with a report published by Glaser *et al*. in which they detail their investigation into potential modifications of this reaction.[6] After varying several parameters such as

equivalents of ^{n}BuLi, solvent, temperature and time, they concluded that the current protocol for the one-step *ortho*-lithiation/dialdehyde formation is still best practice.

However, the yield of the fourth and final step has been increased by 39%. This was the result of varying the catalytic acid (from formic to *p*-toluenesulfonic) and solvent (from dichloromethane to toluene) of the system. The starting materials were found to be only partially soluble in toluene; the use of a slurry and increased reaction temperature (facilitated by the higher boiling point solvent) proved to be key in improving the yield for this reaction.

2.2.1 NMR spectroscopic analysis

After isolation, the pro-ligand was analysed using NMR spectroscopy. The appearance of both O***H*** and N***H*** resonances in the ^{1}H NMR spectrum indicated its fluxional behaviour in solution (**Figure 2.2**). The dynamic process that occurs is the reversible (de)protonation of an imine nitrogen atom by the adjacent hydroxyl group (**Scheme 2.2**).[2]

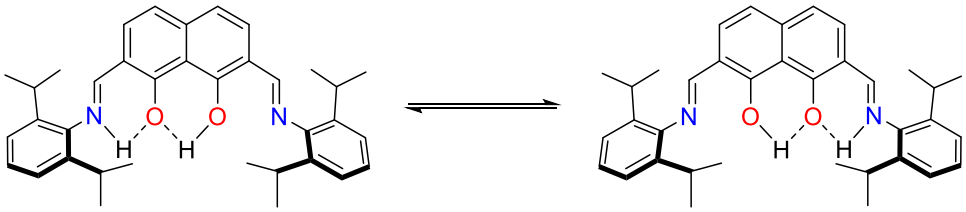

Scheme 2.2 Rapid reversible (de)protonation occurring in the pro-ligand in solution.

This tautomerism leads to a completely asymmetric species in solution; as a result, the ^{1}H NMR spectrum of $H_2^{Dipp}L$ contains 16 resonances; this agrees with previous literature reports (**Figure 2.2**).[2] The O***H*** and N***H*** resonances are located as a singlet and doublet at δ 14.75 and δ 13.51 ppm respectively. The corresponding singlet and doublet representing the ***H***C=N and ***H***C=NH protons are found at δ 8.80 and δ 7.72 ppm respectively. The other eight resonances in the aromatic region (δ 8.36–6.75 ppm)

correspond to the remaining C***H****-naphthyl* protons as well as those from the imine-*aryl* groups. The isopropyl *methine* and *methyl* protons are represented by the multiplets at δ 3.13 and δ 1.22 ppm respectively.

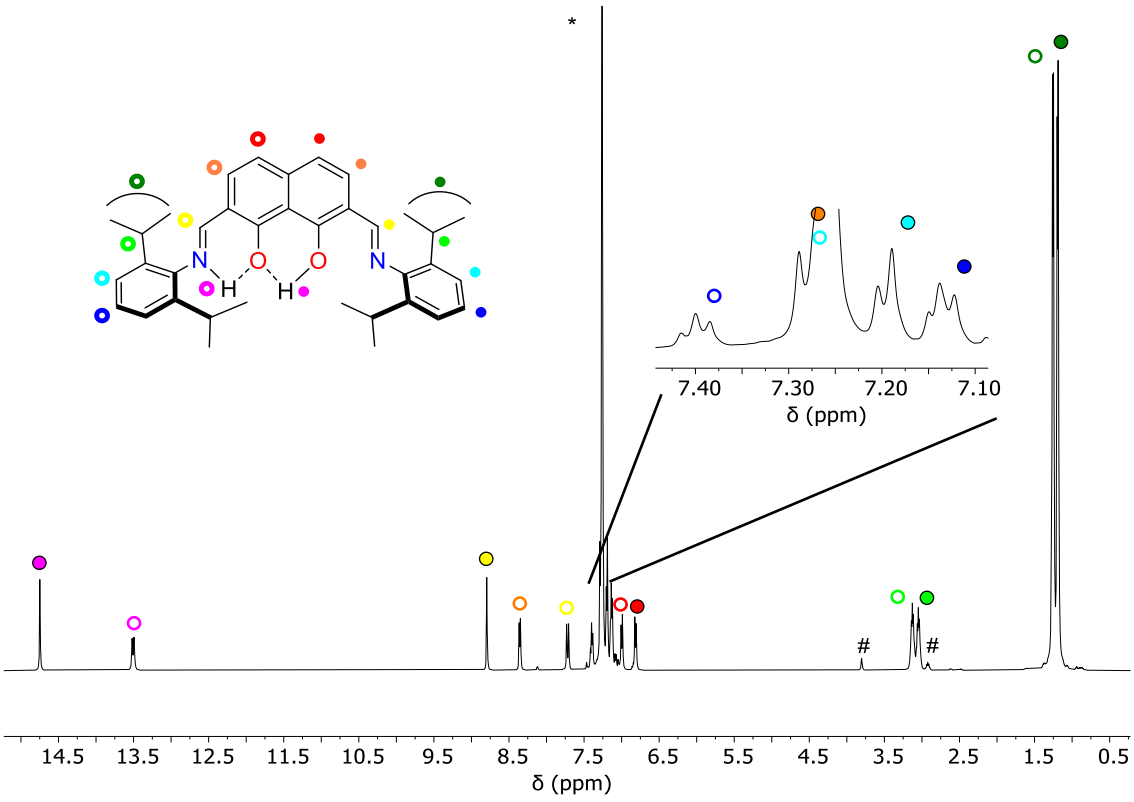

Figure 2.2 ^{1}H NMR spectrum (*chloroform-d_1, 500 MHz, 253 K) of $H_2{}^{Dipp}L$. # denotes residual $^{Dipp}NH_2$.

2.3 Dimeric, bimetallic magnesium complexes generated through protonolysis

Bimetallic magnesium complexes of the form $^{Dipp}L(MgN'')_2$ were initially targeted using protonolysis reactions. However, the equimolar reaction of $H_2{}^{Dipp}L$ with $[MgN''_2]_2$ (N'' = $N(SiMe_3)_2$) was unexpectedly found to be solvent dependent and instead afforded the bimetallic magnesium tetrahydrofuran adduct $[{}^{Dipp}LMg(thf)]_2$ (**1**) in THF and the magnesium chloride dimer $[H{}^{Dipp}LMgCl]_2$ (**2**) in chloroform (**Scheme 2.3**). The crude

reaction mixtures also contained 0.5 eq. of unreacted $[MgN"_2]_2$ alongside 4 eq. of the HN" amine protonolysis by-product. Repetition of the reactions in a 2:1 L:$[Mg]_2$ ratio afforded the same dimeric, bimetallic products. Large scale synthesis of complex **1** was found to consistently produce inseparable mixtures of **1** and unknown species. However, complex **2** could be isolated as an analytically pure solid in 40% yield.

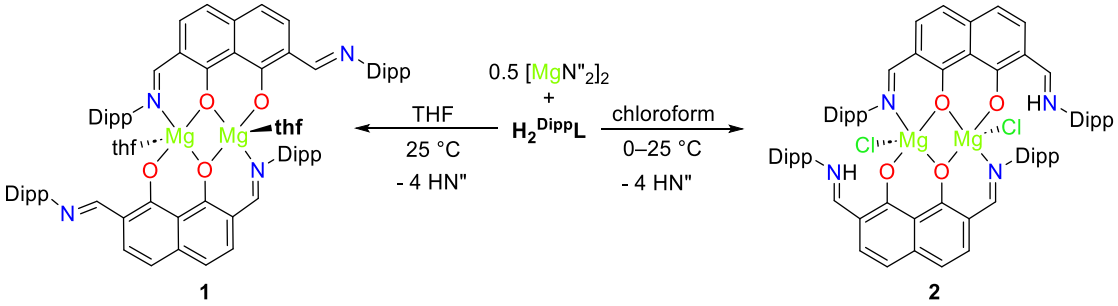

Scheme 2.3 Solvent dependent protonolysis reactions between $H_2{}^{Dipp}L$ and $[MgN"_2]_2$ affording $[{}^{Dipp}LMg(thf)]_2$ (**1**) and $[H^{Dipp}LMgCl]_2$ (**2**). Dipp = diisopropyl-*aryl*.

2.3.1 Proposed synthetic pathway

Varying the stoichiometric ratios of the reactions confirmed that only one metal centre interacted with each ligand framework. As a result, the first step of the synthesis is proposed to be the formation of a symmetric, monometallic intermediate which then readily dimerises to form the observed products (**Scheme 2.4a**). Coordination of magnesium in the central [O⁻,O⁻] binding pocket, as opposed to a [=N,O⁻] binding pocket, is supported by the highly oxophilic nature of the metal (Θ = 0.6)[7, 8] as well as results from similar reactions with the heavier group two congeners (**Section 2.4**). Furthermore, the second deprotonation being initiated by an intramolecular acid-base reaction (rendering the metal centre in the proposed [O⁻,O⁻] binding pocket) seems more feasible than the intermolecular alternative. The subsequent dimerisation most likely occurs to enable saturation of the metal’s coordination sphere (typical coordination

number of Mg^{2+} ions ~ 4-6).[8-14] As this could also be achieved through the binding of donating solvent (THF) molecules, an additional driving force for the dimerisation is likely to be the induction of chelating stabilisation.

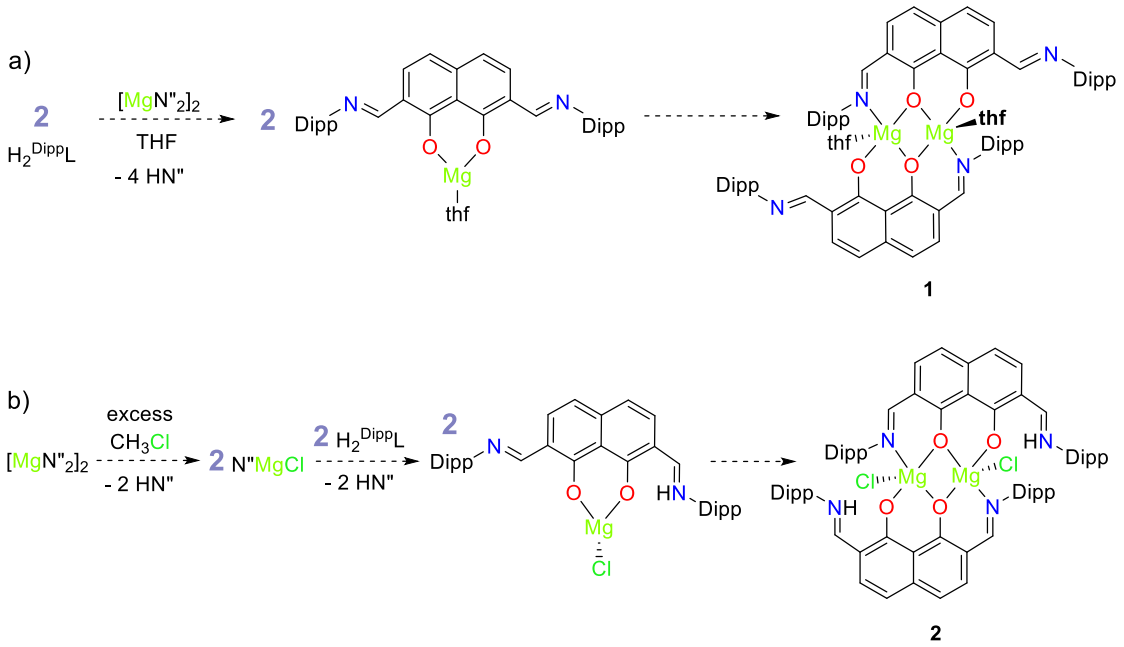

Scheme 2.4 Proposed synthetic pathways to a) [^{Dipp}LMg(thf)]$_2$ (**1**) and b) [H^{Dipp}LMgCl]$_2$ (**2**). Dipp = diisopropyl-*aryl*.

The chloride ligand present in complex **2** can only be derived from the solvent. For this to be the case, it is postulated that the magnesium reagent initially reacts with the chlorinated species prior to the addition of ligand. This was investigated by simply dissolving [MgN"$_2$]$_2$ in chloroform-d_1. The loss of the bridging-N(Si*Me*$_3$)$_2$ signal in the ^{1}H NMR spectrum, alongside the appearance of a new HN(Si*Me*$_3$)$_2$ resonance, suggests that the chlorinated solvent had broken up the starting dimer *in situ* (**Figure 2.3**).The result of this could likely be the formation of a new magnesium species – {N(SiMe$_3$)$_2$}NMgCl (N"MgCl) – which then subsequently reacts with the ligand. The incorporation of the anionic chloride ligand at the metal centre means that the monometallic intermediate formed in this case will be only partially deprotonated in order

to maintain charge balance (**Scheme 2.4b**). The residual N***H*** signals were not supressed (i.e. converted to N***D***) via the use of deuterated chloroform as the reaction media. This implies that that these protons likely originate from the $H_2^{Dipp}L$ reagent as opposed to being derived from the solvent. All of these observations align with the proposed synthetic pathway.

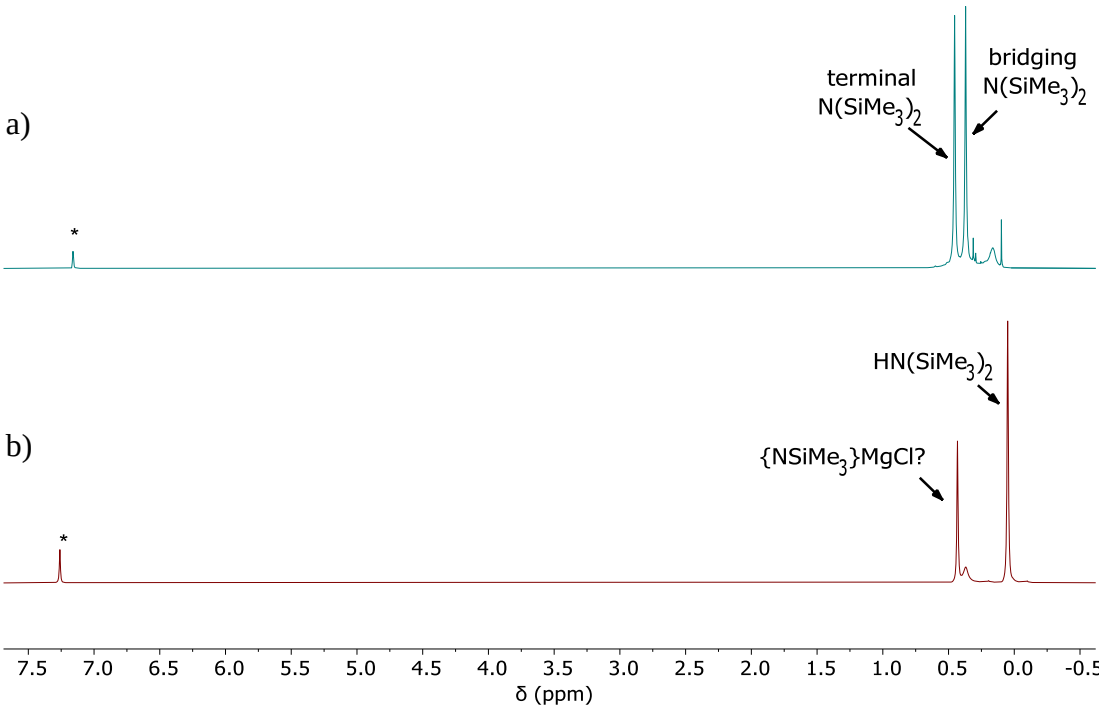

Figure 2.3 ^{1}H NMR spectra (400 MHz, 298 K) of $[Mg\{N(SiMe_3)_2\}_2]_2$ in a) *benzene-d_6 and b) *chloroform-d_1.

Chloroform, and related halocarbons, have been previously demonstrated to react with transition metal and low valent main group complexes via redox chemistry. For example, Figueroa and co-workers described the reaction of the 17e$^-$ monoradical $[Mn(CO)_3(CNAr^{Dipp})_2]$ (Ar^{Dipp} = 2,6-(2,6-^{i}Pr-C_6H_3)$_2$$C_6H_3$)with chloroform to yield a 1:1 mixture of $(Cl_2HC)Mn(CO)_3(CNAr^{Dipp})_2$ and the chloride complex $ClMn(CO)_3(CNAr^{Dipp})_2$.[15] The hydride complex [Mo(Tpms)H(CO)$_3$] (Tpms = $SO_3C(pz)_3$) was readily oxidised to the bridging oxo complex [{Mo(Tpms)OCl}$_2$](μ-O),

with new M-Cl bonds formed in the presence of O_2 and chloroform.[16] Andersen and co-workers studied the reaction of [1,2,4-^{t}Bu-C_5H_2]$_2$CeH with CH_3X (X = halide, OMe, NMe_2) which yielded the apparent products of a metathesis reaction ([1,2,4-^{t}Bu-C_5H_2]$_2$CeX and CH_4) but was shown to proceed through a two-step process involving α-CH activation.[17-19] In Ti(IV) complexes with redox non-innocent ligands, Wolczanski *et al.* report that LTi(thf) (L = [{−CH═N(1,2-C_6H_4)N(2,6-^{i}Pr-C_6H_3)}$_2$]) reacts with CH_3Cl (as well as other halocarbons) to afford a new titanium chloride species where the ligand backbone has been singly methylated; the mechanism of this formal oxidative addition was considered through radical chain processes as well as concerted processes.[20] And in main group chemistry, tetramesityldigermene ($Mes_2Ge=GeMes_2$) was shown to react with chloroform to afford $Mes_2(CHCl_2)Ge$-$Ge(Cl)Mes_2$ by Baines and co-workers.[21] Reactivity specifically with redox neutral alkaline-earth species however, has not yet been reported.

2.3.2 NMR spectroscopic analysis

The ^{1}H NMR spectrum of complex **1** indicates that the pro-ligand has been fully deprotonated via the absence of the high frequency O***H*** and N***H*** resonances present in the pro-ligand (**Figure 2.4**). With respect to the initially targeted heteroleptic product, ^{Dipp}L(MgN")$_2$, there is a descent in symmetry as a result of one magnesium-bound and one free imine group per [^{Dipp}L]$^{2-}$ fragment. This asymmetry is consistent with the solid-state structure, elucidated by single crystal X-ray diffraction analysis, and is retained upon dissolution of the crystals (*vide infra*). The chemical and magnetic inequivalence of the two halves of the ligand gives rise to unique proton environments in solution. For example, there are distinct singlets at δ 8.20 and δ 7.18 ppm for the magnesium-bound and free N=C***H*** protons respectively and four multiplets corresponding to the naphthalene

backbone protons. The inequivalent diisopropyl groups are each represented by a septet and mutually coupled ($^3J_{HH}$ = 6.9 Hz) doublet; this indicates that these aromatic groups are able to rapidly rotate on the NMR spectroscopic timescale at 298 K. COSY, HSQC and HMBC 2D NMR spectroscopic experiments were utilised to deduce the full assignment of the spectra.

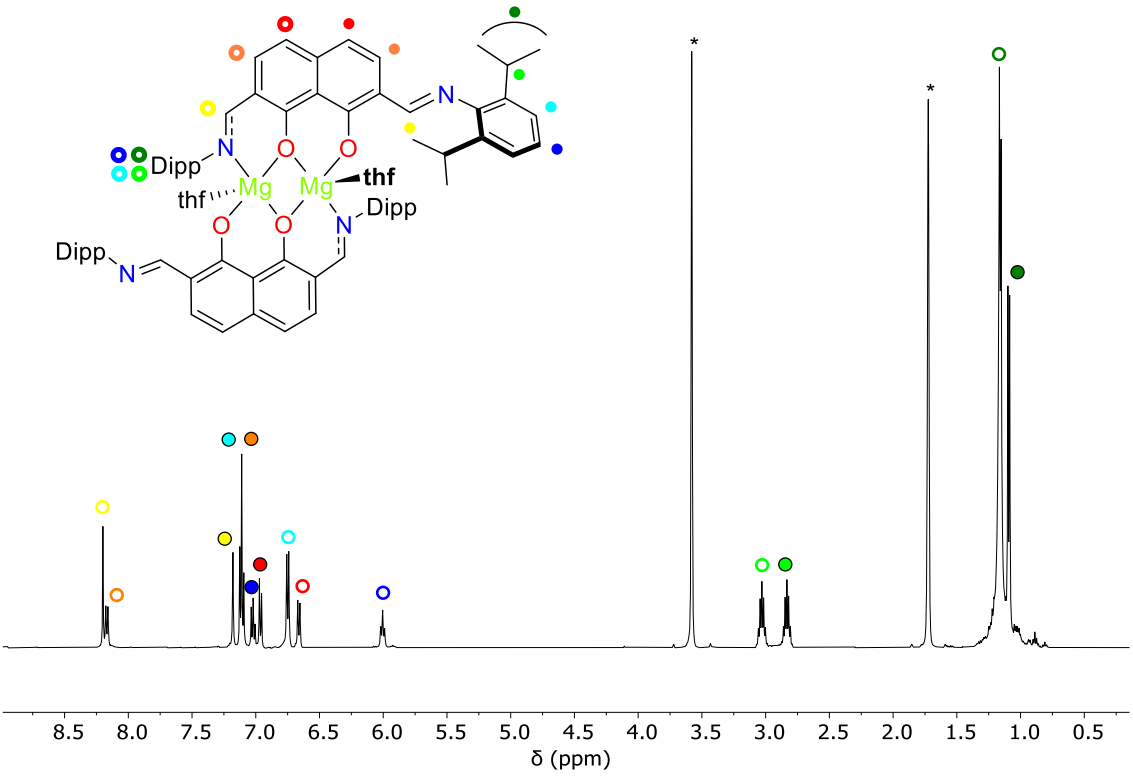

Figure 2.4 ^{1}H NMR spectrum (*THF-d_8, 400 MHz, 298 K) of [^{Dipp}LMg(thf)]$_2$ (**1**).

NMR spectroscopic analysis of complex **2** was performed on a crystalline sample in THF-d_8. Attempts to analyse subsequent crude powders in this solvent led to slow conversion of the product into complex **1** (via loss of HCl). As a result, all further analysis of this complex was performed in benzene-d_6 (see **Figures A.1-A.4** in **Appendix**). The ^{1}H NMR spectrum of a crystalline sample of complex **2** is diagnostic of a partially deprotonated *bis*(phenoxy-imine) ligand as it contains a high frequency doublet at δ 13.34 ppm corresponding to the residual N***H*** proton (**Figure 2.5**). The spectrum is

qualitatively similar to complex **1** as a result of the inherent asymmetry of the $[H^{Dipp}L]^-$ ligand.

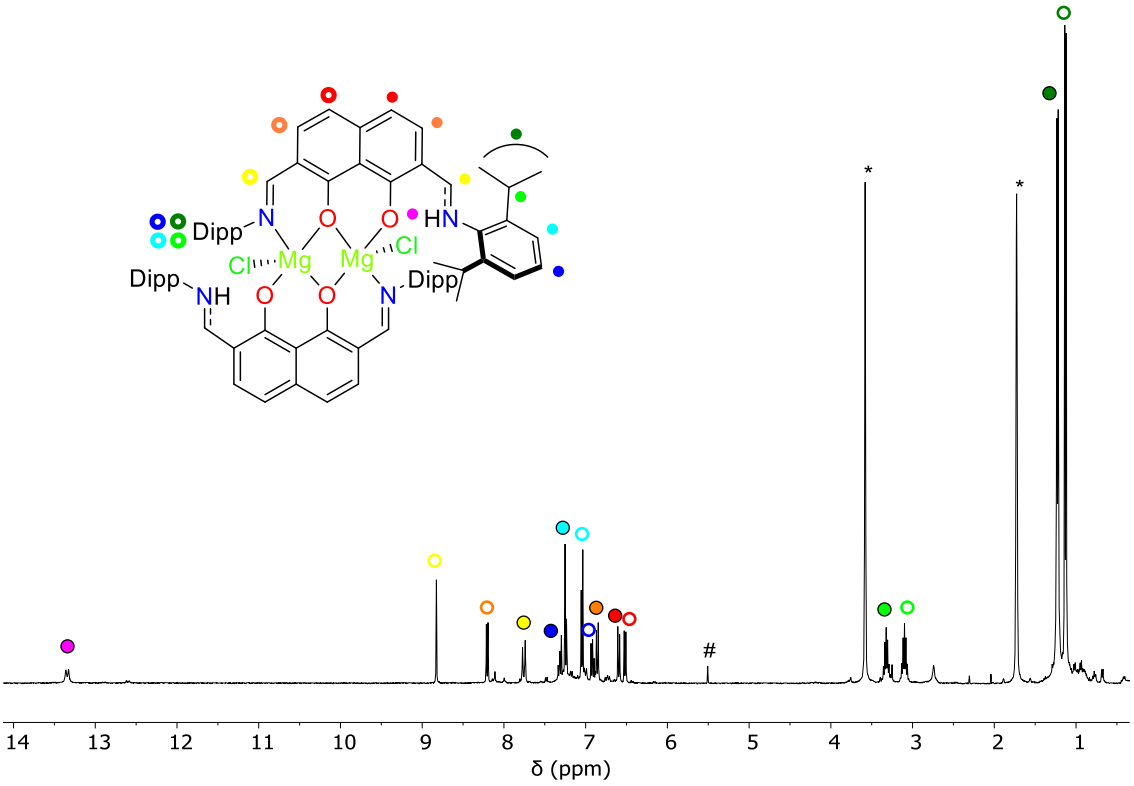

Figure 2.5 ^{1}H NMR spectrum (*THF-d_8, 400 MHz, 298 K) of $[H^{Dipp}LMgCl]_2$ (**2**). # denotes residual dichloromethane from crystallisation.

Cooling a sample of complex **2** to temperatures as low as 233 K revealed the dynamic behaviour of the freely rotating (solid green spot) diisopropyl groups in solution (**Figure 2.6**). The higher frequency doublet, assigned to the $CH(C\boldsymbol{H}_3)_2$ protons, splits into two separate doublets upon cooling. This suggests that the corresponding *methyl-* groups are now inequivalent as a result of their slowed rotation. These new environments however, coalesce at room temperature as previously discussed. Heating this compound to 333 K appeared to have no observable effect on the identity or nature of the sample, hence it can be described as thermally robust. In combination with solid-state structural data, this species was conclusively identified as $[H^{Dipp}LMgCl]_2$, where the chloride ligands are derived from the reaction solvent.

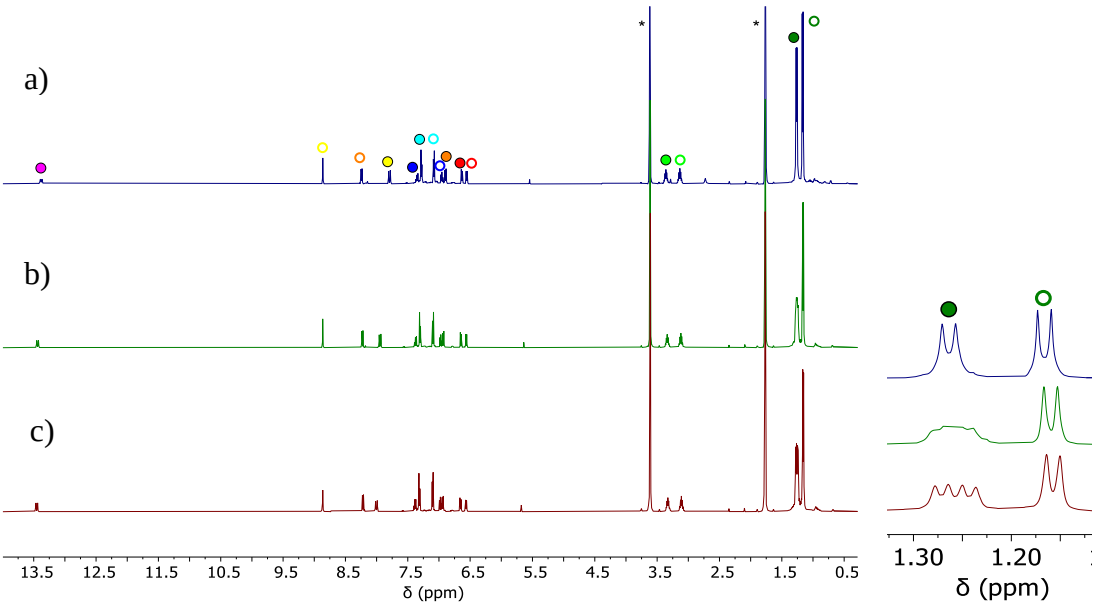

Figure 2.6 Variable temperature ^{1}H NMR spectra (*THF-d_8, 500 MHz) of $[H^{Dipp}LMgCl]_2$ (**2**) at a) 298 K, b) 253 K and c) 233 K.

To further assess the nuclearity of these species in solution, molecular weight determination, via diffusion-ordered spectroscopy (DOSY), was conducted. An internal standard $Si(SiMe_3)_4$ was added to a sample of complex **1** in THF-d_8 and this mixture was analysed at 298 K (**Figure A.5** in **Appendix**). The addition of the internal standard alleviated the need for direct viscosity measurements.[22] The experiment recorded a solute diffusion coefficient (D_{sol}) of 5.15 x10^{-10} m^2 s^{-1}, which after calibration of the observed internal standard D_{ref} to its literature value, gave a corrected D_{sol} of 5.97 x10^{-10} m^2 s^{-1}.[23] Substitution of this value in the Stokes-Einstein (**Equation 2.1**) and related equations (**Equation 2.2**) gave a proposed solute molecular weight of 1127 $gmol^{-1}$.[24, 25] This suggests that complex **1**, and most likely, complex **2** remain dimeric in solution. The disparity between the observed and true molecular weights (1127 *vs*. 1256 $gmol^{-1}$; Δ = 10.3%) is most likely the result of excluding shape correction factors from calculations by assuming the dimers were completely spherical.[23]

$$D_{sol} = \frac{k_B T}{6\pi\eta r_H}$$

Equation 2.1 The Stokes-Einstein equation.[22]

$$r_H = \sqrt[3]{\frac{3M_{sol}\bar{v}}{4\pi N_A}}$$

Equation 2.2 The relationship used to correlate the hydrodynamic radius ($\boldsymbol{r_H}$) of a ***spherical*** particle with its partial specific volume ($\boldsymbol{\bar{v}}$) and molecular weight ($\boldsymbol{M_{sol}}$).[22]

2.3.3 X-ray crystallographic analysis

Single crystals of complexes **1** and **2**, suitable for X-ray diffraction studies, were afforded; for **1**, from a room temperature saturated THF solution and for **2**, from layering a saturated dichloromethane solution with pentane and cooling to –30 °C. The solid-state molecular structures of **1** and **2** were solved in the monoclinic *I* 2/*a* and triclinic $P\bar{1}$ space groups respectively and are depicted in **Figure 2.7**. Selected bond lengths and angles are also presented in **Table 2.1**.

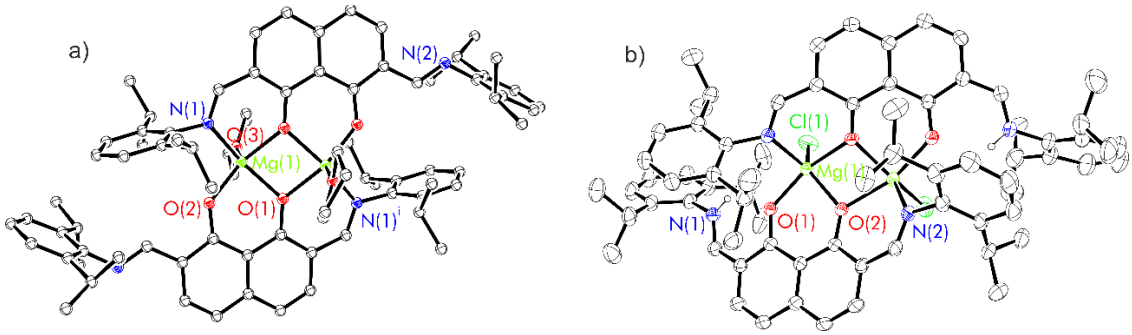

Figure 2.7 Thermal displacement ellipsoid drawings (30%) of a) [^{Dipp}LMg(thf)]$_2$ (**1**) and b) [H^{Dipp}LMgCl]$_2$ (**2**). All hydrogen atoms, except those bound to N atoms have been omitted for clarity. For complex **1**, the full molecule has been generated by applying the symmetry operation –x+1/2, –y+3/2, –z+3/2; the atoms generated by applying the symmetry operation are labelled with "i".

Table 2.1 Experimental metrical parameters (bond lengths (Å) and angles (°)) for $[^{Dipp}LMg(thf)]_2$ (**1**), $[H^{Dipp}LMgCl]_2$ (**2**) and related di-nickel complexes.[4, 26] Estimated standard deviations shown in brackets.

	$[^{Dipp}LMg(thf)]_2$ (**1**)[a]	$[H^{Dipp}LMgCl]_2$ (**2**)[b,d]	$[^{Dipp}LNi]_2$ [d,4]	$[^{Dipp}LNiO{=}PMe_3]_2$ [c,4]
M-N	2.1259(15)	2.110(3)	1.699(1)	2.014(4)
M-O	1.9056(13)	1.991(3)	1.969(3)	1.924(3)
M-O(b)	2.0040(12)/ 2.0258(12)	2.004(3)/ 2.058(3)	1.969(1)	2.000(4)/ 2.022(4)
M-X[a,b,c]	2.0310(16)	2.2936(18)	-	1.994(4)
M-M	3.0590(11)	3.0641(16)	2.992(9)	3.092(3)
O-M-N	94.63(6)	96.97(12)	103.7(5)	94.97(15)
N-M-O(b)	86.76(5)/ 154.05(6)	84.97(12)/ 120.46(13)	89.9(8)	90.88(15)/ 161.91(16)
O-M-O(b)	87.47(5)/ 156.05(7)	85.56(11)/ 160.53(13)	89.9(8)	88.42(14)/ 156.08(16)
O(b)-M-O(b)	81.23(5)	76.89(11)	95.3(5)	79.30(14)
τ_5[27]	0.033	0.66	0.17	0.10

M = metal; (b) = bridging; [a]X = O(thf); [b]X = Cl; [c]X = $OPMe_3$; [d]measurements based on M(1).

The asymmetric unit of the solid-state structure of **1** contains half of the centrosymmetric dimer. The geometry about the five coordinate magnesium centre is square-based pyramidal (τ_5 = 0.033),[27] with the dimeric structure resulting in a Mg_2O_2 diamond core with μ_2-O^{2-} ligating groups. Each metal centre is ligated by both oxide donors on one ligand, the imine N donor and one oxide from the second ligand all in the square planar base, with the thf coordinated in the apical position. The $[^{Dipp}L]^{2-}$ ligands are co-planar with the interplanar angle being defined by the naphthalene backbone: C3, C5, C7 = 0.0°. The individual ligand planes are separated by a distance of ~1.2 Å; this is facilitated by the *anti*-configuration of the coordinated thf molecules and by the free imine arms

twisting away from the metal core to relieve some of the steric strain in the system. The magnesium centres sit ~0.24 Å outside of the plane of the [O⁻,O⁻] binding pockets and, as expected, the bridging Mg-O(1) bond lengths are longer than the corresponding terminal Mg-O(2) bonds (2.0040(12)/2.0258(12) Å *vs.* 1.9056(13) Å respectively) in line with other related organometallic complexes (2.402(6)/2.009(6) *vs.* 2.072(6)[28]; 2.028(5) *vs.* 1.952(5)[29]; 2.03 *vs.* 1.93[30]).[31]

Related dinickel complexes [^{Dipp}LNi]$_2$ and [^{Dipp}LNi(O=PMe$_3$)]$_2$ were reported by Marks and co-workers (**Figure 2.8**); their solid-state structures featured the same metal coordination geometry and co-planar arrangement of [^{Dipp}L]$^{2-}$ ligands.[4, 26] In addition, in all cases the intramolecular M···M distances lie within the sum of the van der Waals radii (3.46 Å for Mg and 3.26 Å for Ni)[32]; this implies that direct interactions between the metal centres are feasible within these dimeric structures.[4]

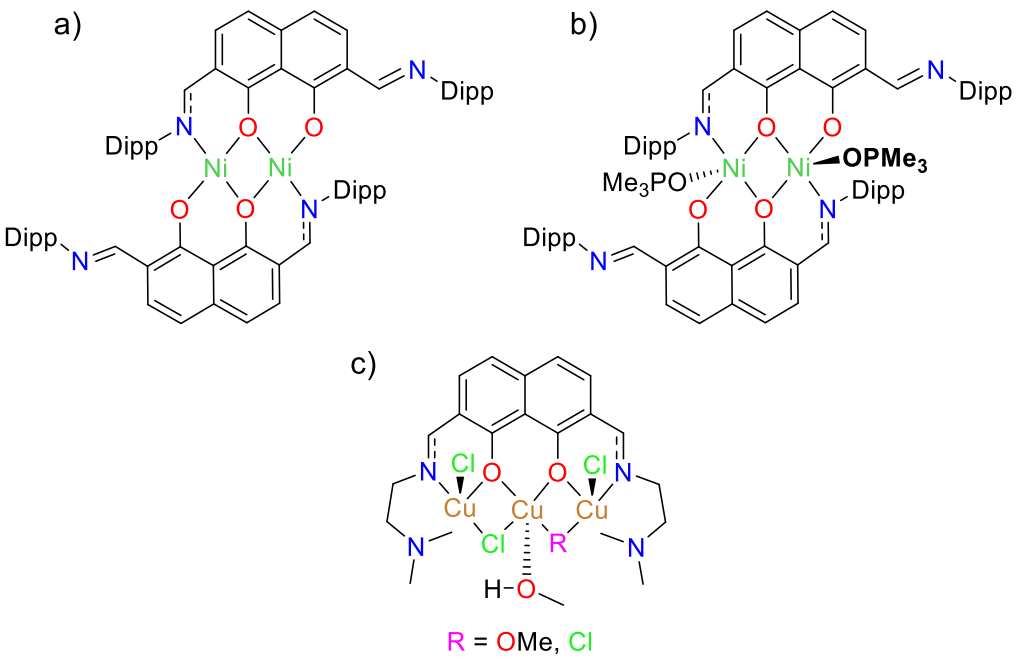

Figure 2.8 The related solid-state structures reported by Marks and Glaser; a) [^{Dipp}LNi]$_2$, b) [^{Dipp}LNi(O=PMe$_3$)]$_2$ and c) (^{NMe_2CH_2CH_2}L)Cu$_3$Cl$_3$R(MeOH) (R = OMe or Cl).[4, 33]

Metal coordination in the central [O^{-},O^{-}] binding pocket of an alternative 1,8-napthalenediol derived ligand, 2,7-(C=N$CH_2CH_2NMe_2$)-1,8-OH-$C_{10}H_4$ ($H_2{}^{NMe_2CH_2CH_2}L$) has also been observed (**Figure 2.8c**).[33] In 2007, Glaser *et al.* described the solid-state structures of two trinuclear Cu^{2+} complexes: ($^{NMe_2CH_2CH_2}L$)Cu_3Cl_3(OMe)(MeOH) and ($^{NMe_2CH_2CH_2}L$)Cu_3Cl_4(MeOH).[33] The incorporation of a coordinating amine arm into the backbone seems to prevent aggregation of the ligand frameworks thus enabling the isolation of monomeric, yet multimetallic species.

Similarly to **1**, the asymmetric unit of the crystal structure of complex **2** contains half of the centrosymmetric dimer. The structure contains an analogous Mg_2O_2 diamond core however, each magnesium centre now adopts a distorted trigonal bipyramidal (τ_5 = 0.66) coordination geometry.[27] The magnesium-oxygen bonds have an average length of 2.03 Å (Mg(1)-O(1) = 2.058(3) Å, Mg(1)-O(3) = 2.004(3) Å, Mg(2)-O(1) = 2.003(2) Å, Mg(2)-O(3) = 2.043(3) Å); this is comparable with the range of Mg-O bond lengths reported previously (1.880(3)–2.0233(8) Å).[14, 34] In contrast to **1**, the chloride ligands are in a *syn* configuration and each ligand is splayed with respect to the other (interplanar angle between planes defined by the naphthalene backbones = 73.6°) in order to minimise unfavourable interactions between the bulky imine aromatic groups. In addition, the structure clearly shows the single protonated imine group on each ligand; the N***H*** proton is aligned with the neighbouring oxygen atom in such a way that it could enable stabilising intramolecular hydrogen bonding. The associated C=N bond lengths (C(24)-N(2) = 1.314(5) Å and C(60)-N(4) = 1.305(6) Å) lie between the values of a single and double CN bond, as reported by Pyykkö in 2015, indicating the expected increase in delocalisation/decrease in bond order across the imine.[35] Furthermore, no loss in aromaticity was observed as the phenol CO bonds lie close to the expected value for such a single bond (1.309(4) *vs*.1.38 Å).[35]

2.3.4 Solid angle calculations

The atomic coordinates, produced from X-ray crystallographic analysis, were used in solid angle calculations. These were performed to quantify the steric shielding of the metal centres and thus the probability of an incoming monomer accessing them.[36] In these calculations a metal, which is located in the centre of a sphere of radius *r*, is viewed as a light source (**Figure 2.9**). The area (*A*) of the shadow that a given ligand casts upon the sphere is then related to the solid angle (*Ω*; **Equation 2.3**); an advantage of this approach is that the shadow area does not need to be spherical unlike Tolman cone angles.[37]

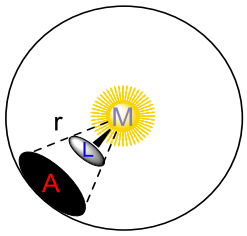

Figure 2.9 Graphical representation of the solid angle, *Ω*.

$$\Omega = \frac{A}{r^2}$$

Equation 2.3 Calculation of the solid angle (*Ω*).

Complete coverage of a metal centre would result in the maximum value of the solid angle: 4π Steradian (sr). The percentage coverage of the sphere (i.e. the *G*-parameter or *G*%) is therefore calculated using **Equation 2.4**. These *G*-parameter values are independent of ligand shape, size and symmetry. They can be calculated for individual ligands or the entire complex as a whole (accounting for spatial overlap) therefore providing an indication of how accessible a metal is towards incoming reagents. To allow for comparison of the same ligand in different complexes, the M-L distance is normalised to 2.28 Å ($G_{2.28}$). The results of this analysis for complexes **1** and **2** are presented in **Figures 2.10-2.11** and **Table 2.2**.

$$G\% = 100\frac{\Omega}{4\pi} = 100\frac{A}{4\pi r^2}$$

Equation 2.4 Calculation of the *G*-parameter (*G*%).

Table 2.2 Summary of ligand solid angles (Ω), the percentage of the sphere shielded by the ligand (*G*), the percent of the metal surface shielded by ligand atoms (*G*(M)) and the percentage of the metal surface "in contact" with ligated atoms (*S*(M)) for complexes **1** and **2**.

Complex	Ω($^{Dipp}L_1$) (sr)	Ω($^{Dipp}L_2$) (sr)	Ω(X) (sr)	*G*($^{Dipp}L_1$) (%)	*G*($^{Dipp}L_2$) (%)	*G*(X) (%)	$G_{2.28}$ ($^{Dipp}L_1$) (%)	$G_{2.28}$ ($^{Dipp}L_2$) (%)	$G_{2.28}$ (X) (%)	*G*(M) (%)	*S*(M) (%)
[a,c][^{Dipp}LMg(thf)]$_2$	5.28	4.60	2.20	41.98	36.61	17.47	32.70	26.76	14.48	78.25	71.41
[b,c][H^{Dipp}LMgCl]$_2$	5.27	5.09	1.77	41.95	40.51	14.05	33.10	31.32	14.39	74.40	69.75

[a] X = thf; [b] X = Cl; [c] calculations performed on both distinct metal centres and average values reported.

In both complexes, a greater steric effect is caused by the [=N,O$^-$] chelating ligand as opposed to the [O$^-$,O$^-$] bound one ($G_{2.28}$: 32.70% *vs*. 26.76% for **1** and 33.10% *vs*. 31.32% for **2**). This is most likely caused by the increased proximity of the metal centre to a diisopropyl-*aryl* group when located in the asymmetric pocket. The solid angle of the bound thf in **1** is considerably larger than that of the chloride ligand present in **2** (Ω: 2.20 sr *vs*. 1.77 sr); this is simply because the thf ligand lies closer to the metal centre (M-X: 2.0310(16) Å *vs*. 2.2936(18) Å; **Table 2.1**) and is therefore responsible for casting a larger shadow. When the exogenous ligands, however, are held equidistant from magnesium, they are seen to impart very similar steric shielding ($G_{2.28}$: 14.48% *vs*. 14.39%). The percent of metal surface shielded by ligand atoms is comparable in **1** and **2** despite the change in coordination geometry (*G*(M): 78.25% *vs*. 74.40%); the clear twist of the ligands in complex **2** may account for this.

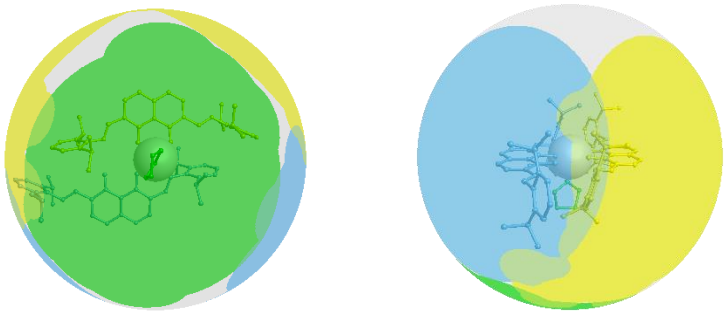

Figure 2.10 Visualisations of *G*(L) values in [^{Dipp}LMg(thf)]$_2$ (**1**), showing the percentage of the complex sphere shielded by each ligand. Blue = ^{Dipp}L$_1$, yellow = ^{Dipp}L$_2$, green = thf. Second metal centre removed for clarity.

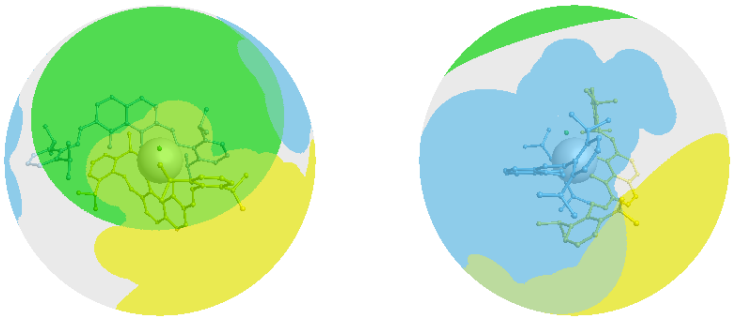

Figure 2.11 Visualisations of *G*(L) values in [H^{Dipp}LMgCl]$_2$ (**2**), showing the percentage of the complex sphere shielded by each ligand. Blue = ^{Dipp}L$_1$, yellow = ^{Dipp}L$_2$, green = Cl. Second metal centre removed for clarity.

2.4 Heavier alkaline-earth complexes generated through protonolysis

Treatment of H$_2$^{Dipp}L with 2 eq. of CaN"$_2$(thf)$_2$ in THF afforded a fully deprotonated, C_{2v} symmetric product (on the NMR timescale) containing the [^{Dipp}L]$^{2-}$ moiety. Also present in the crude mixture was 1 eq. of unreacted CaN"$_2$(thf)$_2$ and 2 eq. of the HN" amine protonolysis by-product. Repetition of the reaction in a 1:1 M:L ratio afforded 2 eq. of HN" alongside the same metal containing C_{2v} symmetric species in which the Ca centre

must be O,O-bound; the results of NMR spectroscopic and elemental analysis studies are consistent with the empirical formula ^{Dipp}LCa(thf)$_2$ (**3(thf)$_2$**) which can be isolated in 69% yield. Reactions with the Sr and Ba amide analogues were found to follow the same reactivity profile leading to the isolation of ^{Dipp}LSr(thf) (**4(thf)**) and ^{Dipp}LBa(thf) (**5(thf)**) respectively in 84% and 75% yields (**Scheme 2.5**).

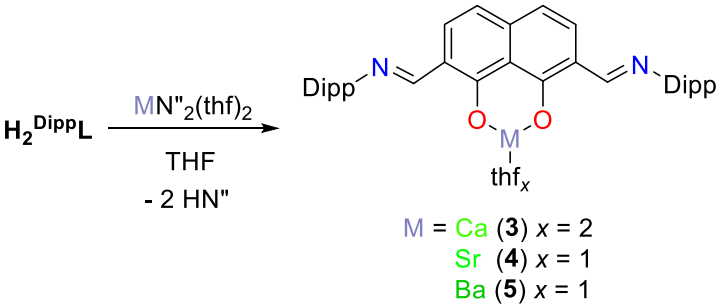

Scheme 2.5 Protonolysis reactions between $H_2{}^{Dipp}$L and MN"$_2$(thf)$_2$ affording ^{Dipp}LCa(thf)$_2$ (**3(thf)$_2$**) ^{Dipp}LSr(thf) (**4(thf)**) and ^{Dipp}LBa(thf) (**5(thf)**).

The oxophilic nature of the alkaline-earth cations (Θ = 0.6, 0.3, 0.5, and 0.7 for Mg, Ca, Sr and Ba respectively) drives their preferential binding in the central [O$^-$,O$^-$] pocket.[7] This oxophilic behaviour was therefore exploited, via the use of metal aryloxide reagents, in attempts to force [=N,O$^-$] binding and thus retain some functionality at the metal centre.[38-42] $H_2{}^{Dipp}$L was treated with two eq. of alkaline-earth aryloxide reagents M(O-2,6-^{t}Bu-4-Me-C$_6$H$_2$)$_2$(thf)$_2$ (M = Ca, Sr, Ba);[43] the crude reaction mixtures however, indicated the formation of the same C_{2v} symmetric species, alongside the unreacted eq. of starting metal aryloxide and 2 eq. of the released 2,6-di-*tert*-butyl-4-methyl phenol by-product (**Figure A.6** in **Appendix**).

2.4.1 NMR spectroscopic analysis

The ^{1}H NMR spectra of complexes **3-5(thf)$_x$**, each contain similar features (**Figure 2.12**). Using **3(thf)$_2$** as a representative example; there are two broad aromatic resonances at δ 8.58 and δ 7.84 ppm corresponding to the imine ***H***C=N and naphthalene 3,6-C$_{10}$***H***$_4$

protons, respectively. Multiplets in the range δ 7.03–6.72 ppm, integrating to a total of 8H, represent the diisopropyl-*aryl*-$C_6\boldsymbol{H}_3$ and *naphthyl*-4,5-$C_{10}\boldsymbol{H}_4$ protons. A septet at δ 3.05 ppm and mutually coupled doublet at δ 1.05 ppm ($^3J_{HH}$ = 6.9 Hz) define the isopropyl *methine* and *methyl* groups respectively.

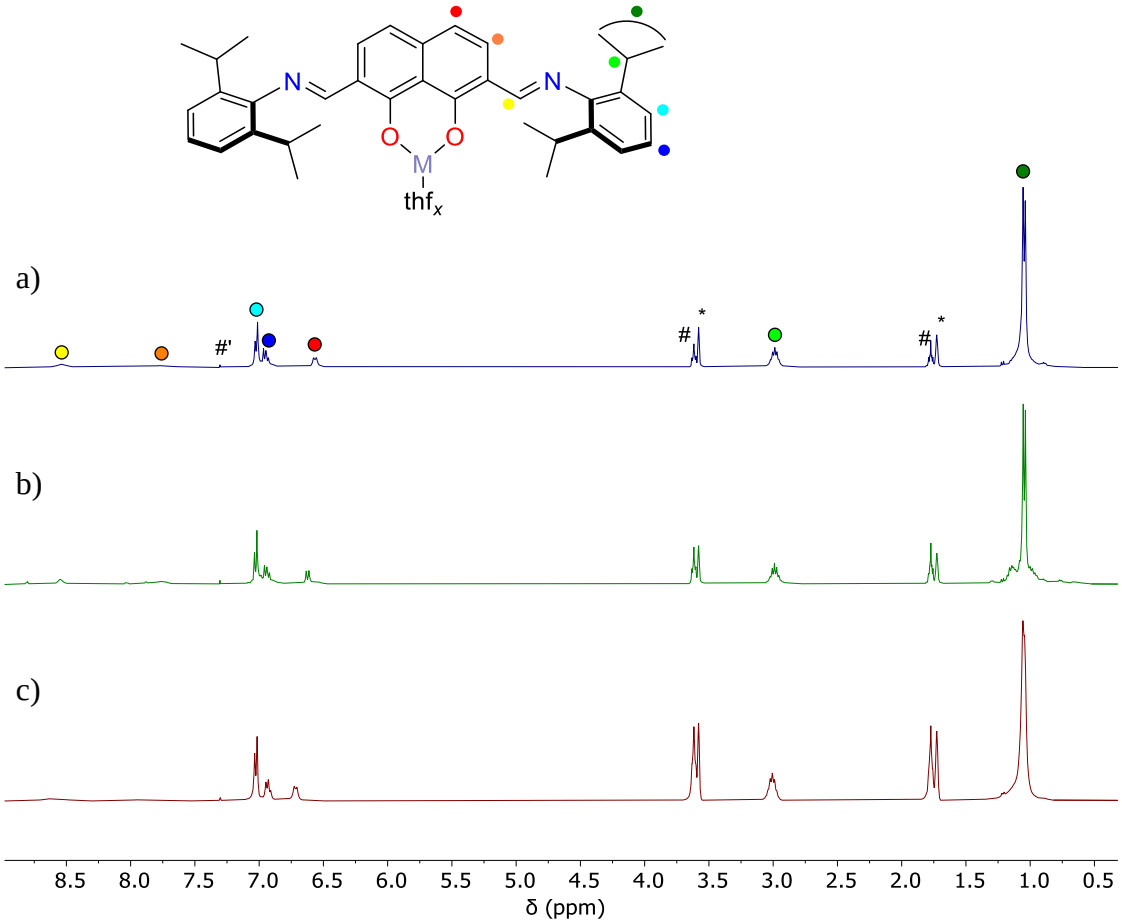

Figure 2.12 ^{1}H NMR spectra (*THF-d_8, 400 MHz, 298 K) of a) ^{Dipp}LCa(thf)$_2$ (**3(thf)$_2$**), b) ^{Dipp}LSr(thf) (**4(thf)**) and c) ^{Dipp}LBa(thf) (**5(thf)**). # and #' represent residual protio-THF and protio-benzene from reaction work-up respectively.

Variable temperature ^{1}H NMR spectroscopic studies were used to investigate the broadening of the aromatic signals. The results showed that cooling a sample of **5(thf)** caused the observed peaks to broaden further before splitting out into multiple resonances (**Figure 2.13**); this is characteristic of the slowing of a dynamic process in solution.

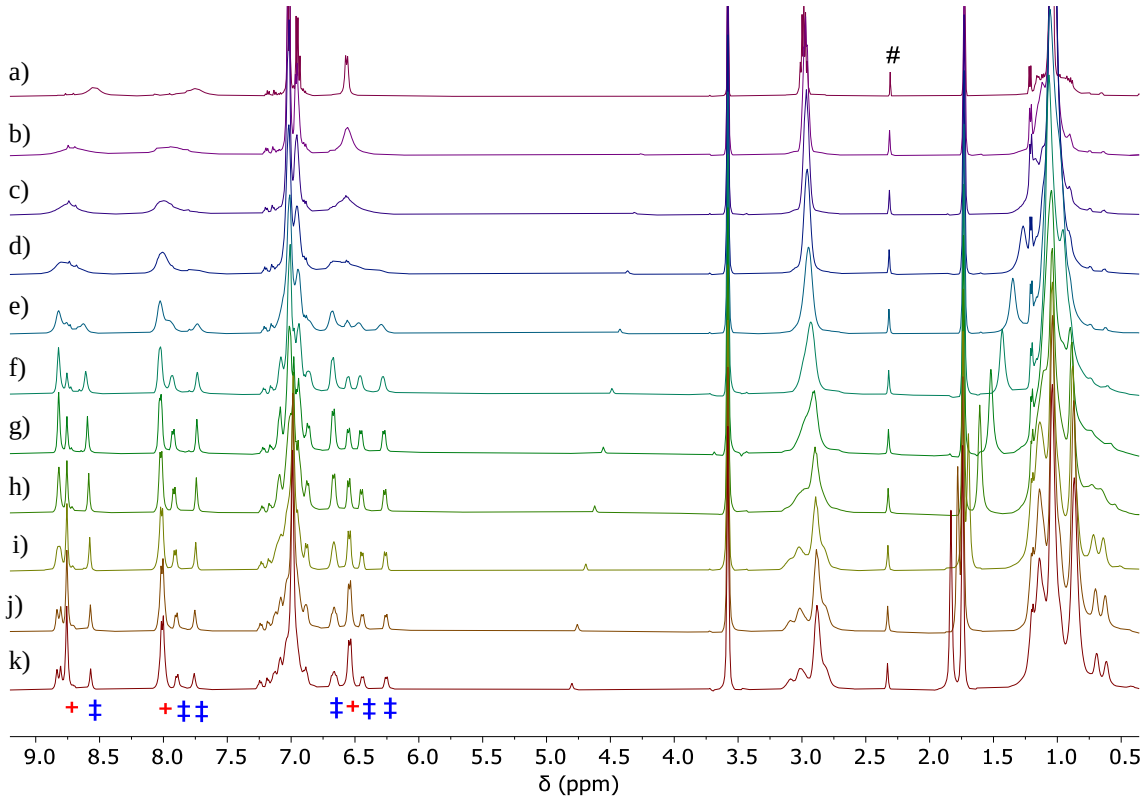

Figure 2.13 ^{1}H NMR spectra (*THF-d_8, 500 MHz) of ^{Dipp}LBa(thf) (**5(thf)**) at a) 298 K, b) 273 K, c) 263 K, d) 253 K, e) 243 K, f) 233 K, g) 223 K, h) 213 K, i) 203 K, j) 193 K and k) 183 K. + and ‡ correlate to complex **5(thf)** and an unknown species respectively whilst # represents acetone contamination of deuterated solvent.

At low temperatures, the resonances for **5(thf)** (**+**) are accompanied by signals corresponding to a second species. This unknown (**‡**) has twice the number of resonances (most clearly evidenced in the aromatic region) which indicates a descent in symmetry from the presumed monometallic compound **5(thf)**. Its signals are also comparable with those of complex **1**; this suggests that they represent the barium analogue of the dimeric Mg-thf system ([**5(thf)**]$_2$) in which one metal-bound and one free imine group per [^{Dipp}L]$^{2-}$ dimer fragment causes asymmetry.

The presence of both species simultaneously in solution indicates that an equilibrium must exist between them (**Scheme 2.6**). At low temperatures, the rate of monomer-dimer exchange is slowed below the NMR spectroscopic time scale, thus enabling the two

distinct compounds to be observed separately. In addition, this fluxional behaviour means that the room temperature spectrum, is likely to be a time averaged signal of these interchanging species (**X**/[**X**]$_2$). This explains why some of the observed resonances are broad and why no meaningful $^{13}C\{^1H\}$ NMR spectroscopic data could be acquired for these systems over a wide range of temperatures. Analogous observations were made when independently cooling samples of **3(thf)$_2$** and **4(thf)** (see **Figures A.7-A.8** in the **Appendix**). Unfortunately, no meaningful quantification of the dynamic behaviour of **3–5(thf)$_x$** can be made from the results of the variable temperature studies. This is due to the observed coalescence effect being the result of the proposed equilibrium as well as fluxional interactions similar to those described with complex **2** (i.e. rotation of Dipp groups).

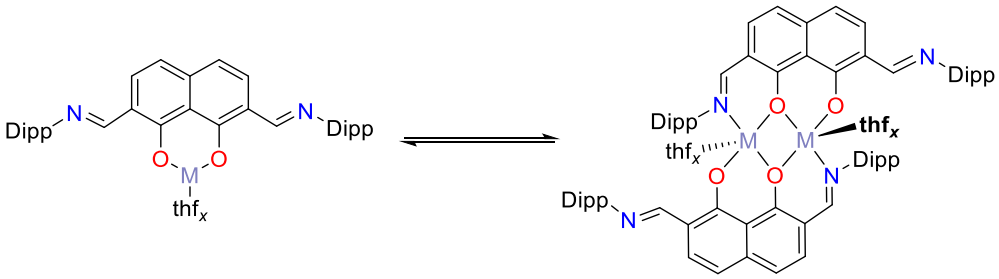

Scheme 2.6 The solution equilibrium present between the symmetric-monomeric (**3-5(thf)$_x$**) and asymmetric-dimeric [^{Dipp}LM(thf)$_x$]$_2$ (**[3-5(thf)$_x$]$_2$**) forms.

Attempts to trap the monomeric systems were made by addition of one equivalent of 18-crown-6 (18-c-6) to solutions of **3-5(thf)$_x$**. In the case of Ca, a mixture of starting materials and desired product, **3(18-c-6)** was always formed regardless of reaction time or temperature. Analysis of the ^1H, $^{13}C\{^1H\}$ and 2D NMR spectra of the resultant mixture however, enabled the identification and assignment of the signals associated with **3(18-c-6)** to be deduced (**Figures A.9-A.13** in **Appendix**).

For the Sr analogue, quantitative conversion to the crown-ether supported species **4(18-c-6)** was confirmed by ^{1}H NMR spectroscopy (**Figure 2.14**); this was easily identified via the sharpening of the two previously broad aromatic resonances present between δ 8.83–7.83 ppm and the addition of two broad resonances around δ 3.94 and δ 3.45 ppm, each integrating to 12H, which represent the protons of the crown ether. The fact that there are two resonances suggests that the ethereal ring is not labile and therefore its two faces are inequivalent. Stabilisation of the monometallic, monomeric species in this manner also allowed for the elucidation of the previously unobtainable ^{13}C{^{1}H} data (**Figure 2.15**). Comparable NMR spectroscopic data for the Ba-stabilised compound **5(18-c-6)** was obtained in a pyridine-d_5 solution, due to poor solubility in THF.

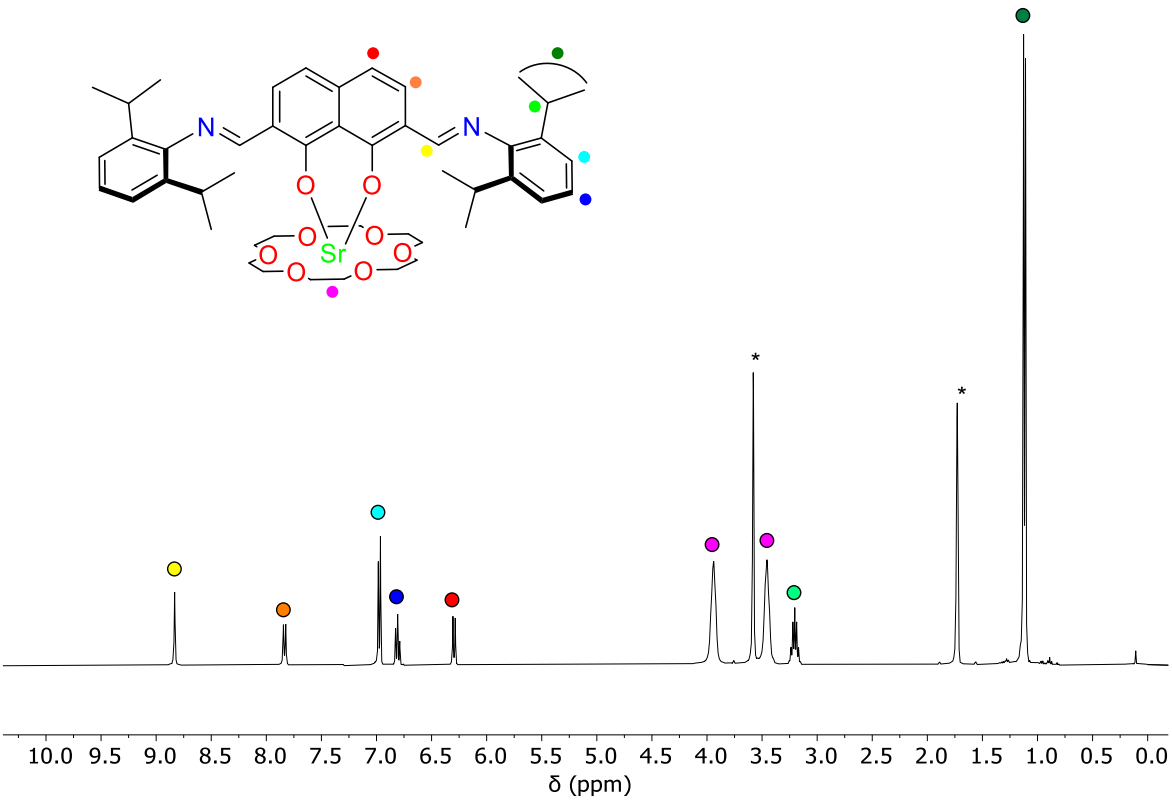

Figure 2.14 ^{1}H NMR spectrum (*THF-d_8, 400 MHz, 298 K) of ^{Dipp}LSr(18-c-6) (**4(18-c-6)**).

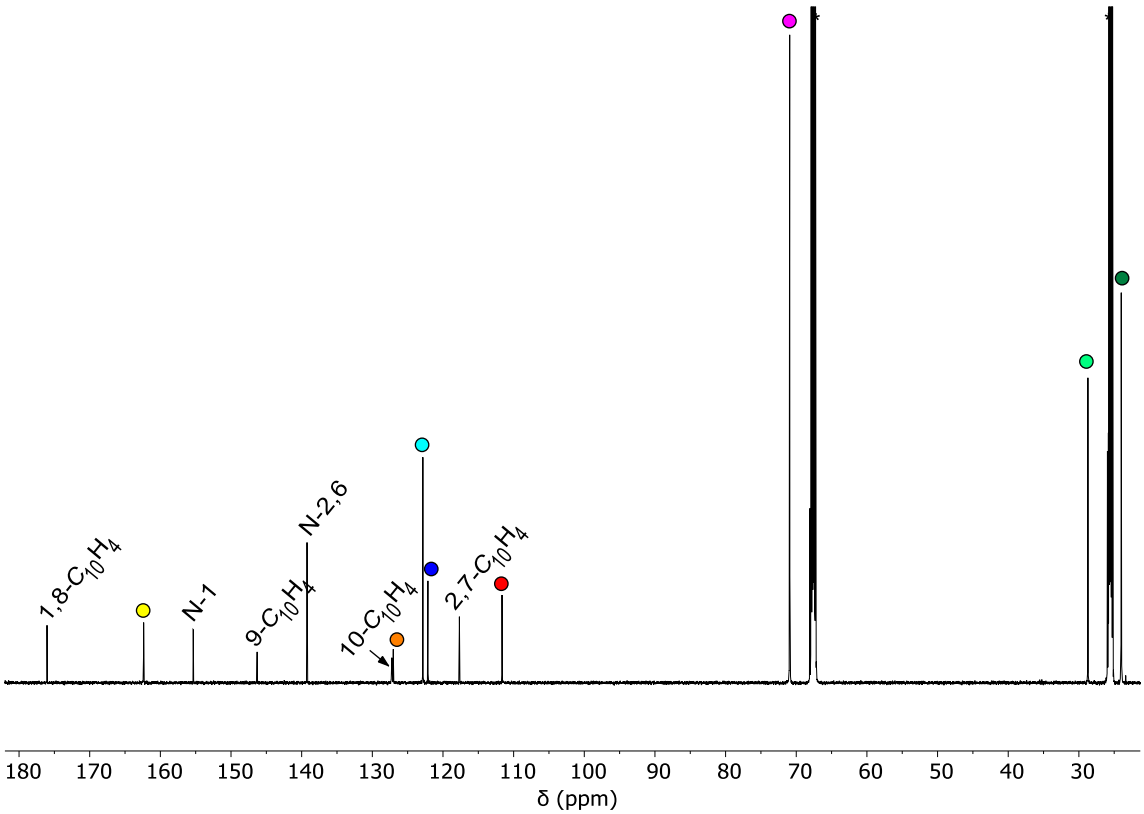

Figure 2.15 $^{13}C\{^{1}H\}$ NMR spectrum (*THF-d_8, 151 MHz, 298 K) of ^{Dipp}LSr(18-c-6) (**4(18-c-6)**).

2.4.2 X-ray crystallographic analysis

All efforts to crystallise solutions of **4(thf)**/[**4(thf)**]$_2$ and **5(thf)**/[**5(thf)**]$_2$ were unsuccessful. In contrast, slow evaporation of a saturated THF solution of **3(thf)$_2$**/[**3(thf)$_2$**]$_2$ allowed for the isolation of single crystals suitable for X-ray diffraction studies. The solid-state structure was identified as the dimeric complex [^{Dipp}LCa(thf)$_2$]$_2$ ([**3(thf)$_2$**]$_2$) and refined in the triclinic $P\bar{1}$ space group (**Figure 2.16** and **Table 2.3**). Crystallisation of this bimetallic species from the proposed time averaged mixture suggests that it is the thermodynamically favoured product of the equilibrium. Upon dissolution in THF-d_8, the crystals of [**3(thf)$_2$**]$_2$ rapidly equilibrate with **3(thf)$_2$** to give the previously observed pseudo-C_{2v} symmetric ^{1}H NMR spectrum (**Figure 2.12**); this is further evidence that these resonances correspond to a time-averaged signal.

Table 2.3 Experimental metrical parameters (bond lengths (Å) and angles (°)) for $[^{Dipp}LCa(thf)_2]_2$ ($[\mathbf{3(thf)_2}]_2$). Values are reported based on Ca(1).[4, 26] Estimated standard deviations shown in brackets.

Ca(1)-N(1')	2.437(3)
Ca(1)-O(1)	2.287(2)
Ca(1)-O(2)	2.201(2)
Ca(1)-O(3)	2.402(5)
Ca(1)-O(4)	2.384(13)
O(1)-C(1)	1.314(4)
O(2)-C(9)	1.280(4)
N(1')-C(11')	1.283(5)
Ca(1)-Ca(1')	3.5488(11)
O(1)-Ca(1)-N(1')	137.50(9)
O(1)-Ca(1)-O(2)	75.15(8)
O(2)-Ca(1)-N(1')	90.25(9)
O(2)-Ca(1)-O(1')	121.48(9)
O(1)-Ca(1)-O(1')	79.25(9)
Ca(1)-O(1)-Ca(1')	100.75(9)

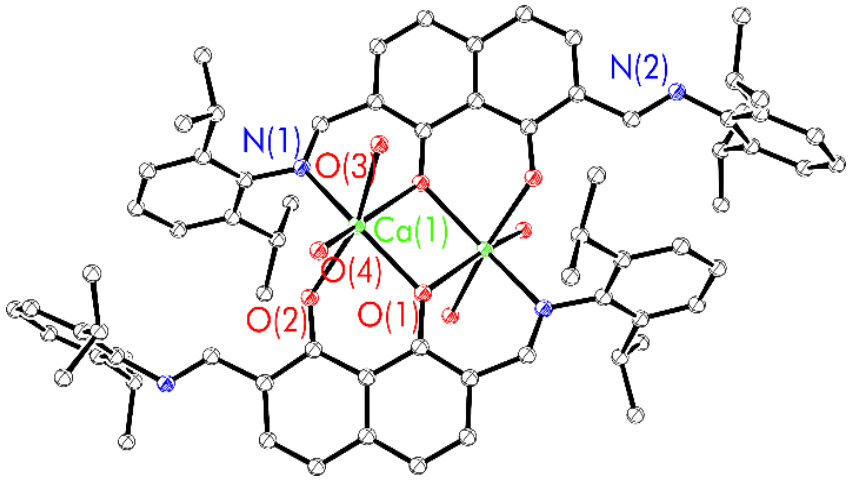

Figure 2.16 Thermal displacement ellipsoid drawings (30% probability) of $[^{Dipp}LCa(thf)_2]_2$ ($[\mathbf{3(thf)_2}]_2$). All hydrogen atoms have been omitted and the full thf molecules with O3 and O4 have been truncated. The full molecule has been generated by applying the symmetry operation ; –x+1, –y+1, –z+1.

The overall solid-state structure of [**3(thf)$_2$**]$_2$ is analogous to that of magnesium complex **1** with the asymmetric unit containing half of the centrosymmetric dimer. The structure contains a M_2O_2 diamond core in which each Ca centre is coordinated by both oxide donors on one ligand, the imine N donor and one oxide from the second ligand, and two thf molecules. This generates a 6-coordinate distorted octahedral geometry around the metal centres (with O(1), O(1)', O(2), and N(1) defining the equatorial plane and with O(3) and O(4) in the apical positions). The Ca-O bond lengths in the Ca_2O_2 core are 2.27 Å (*av.*) in comparison to 1.98 Å (*av.*) for Mg complex **1** reflecting the larger Ca^{2+} radius (Ca^{2+}(6-coordinate) = 1.00 Å, Mg^{2+}(5-coordinate) = 0.72 Å).[44] These distances are comparable with Ca-O bonds in related complexes (2.206(1)–2.875(17) Å).[45, 46] Similarly, the Ca-N_{imine} bond length of 2.437(3) Å falls within the range for Schiff base Ca complexes (2.4020(3)–2.5563(14) Å).[30, 47] Both thf molecules on one Ca centre are coordinated on the same side of the $[^{Dipp}L]^{2-}$ fragment, thus in an overall *anti*-configuration across the dimer. The naphthalene backbones are co-planar (interplanar angle defined by C3, C5 and C7 = 0.0°) and offset by ~2.6 Å. The Ca centre sits outside the plane of the [O^-,O^-] binding pocket by ~0.73 Å, resulting in the Ca_2O_2 diamond core being considerably more skewed across the $[^{Dipp}L]^{2-}$ ligands than in complex **1**. This is due to a combination of factors; the larger M^{2+} radius resulting in longer M-X bonds and the higher coordination number leading to greater offset of the $[^{Dipp}LCa]$ units (*cf.* Ca-Ca = 3.5488(2) Å and Mg-Mg = 3.0591(1) Å).

Single crystals of the crown-ether supported complexes, suitable for X-ray diffraction studies, were formed from saturated THF ([**3(18-c-6)**] and [**4(18-c-6)(thf)**]) or pyridine ([**5(18-c-6)(pyr)**]) solutions (**Figure 2.17**) and refined in monoclinic space groups (I2/a, P21/*c* and P21 for the Ca, Sr and Ba complexes respectively; **Table 2.4**).

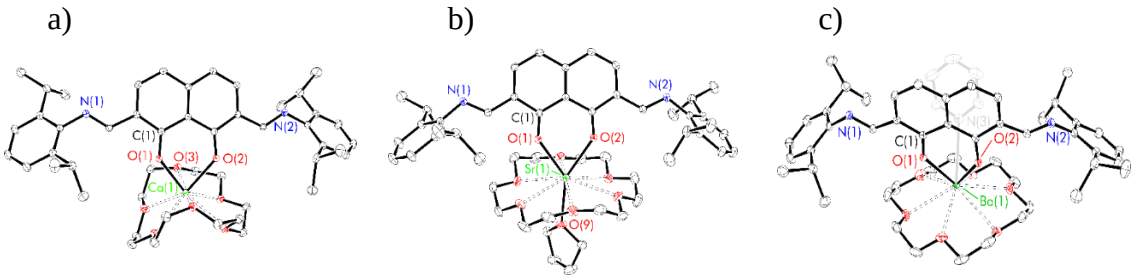

Figure 2.17 Thermal displacement ellipsoid drawings (30% probability) of a) ^{Dipp}LCa(18-c-6) [**3(18-c-6)**], b) ^{Dipp}LSr(18-c-6)(thf) [**4(18-c-6)(thf)**] and c) ^{Dipp}LBa(18-c-6)(pyr) [**5(18-c-6)(pyr)**]. All hydrogen atoms have been omitted for clarity.

The solid-state structure of **3(18-c-6)** reveals that the crown-ether adopts a folded conformation around the Ca centre (similar twisted D_{3d} conformations have been computed previously for Mg^{2+} species)[48]; this enables it to form a contracted cavity in which it is then able to stabilise the relatively small metal dication. However, the Ca-O(crown) bond lengths (2.56 Å *av.*) are larger than the optimised values (2.30-2.44 Å; based on the monohydrate and octahedrally coordinated hexahydrate compounds) indicating that the cavity is not of ideal size.[48] The inherent instability of this species, as a result of this cation-cavity size mismatch, rationalises why the reaction of **3(thf)$_2$** with 18-c-6 never reaches completion.

As the size of the alkaline-earth cation increases, the cation-cavity size disparity becomes less pronounced; this allows the chelating ligand to adopt a more stable "open" conformation in the Sr and Ba analogues. This agrees with previous reports that suggest the formation constants of 18-c-6-stabilised alkaline-earths follow the pattern: Ca < Sr < Ba.[49] In all cases, the M-O(crown) bonds align closely with the range of previously reported M^{2+} 18-c-6 stabilised species (Ca: 2.19-2.23 Å; Sr^{2+}: 2.64-2.75Å; Ba^{2+}: 2.74-2.85Å) and are longer than the corresponding M-O(ligand) bonds (**Table 2.4**).[50-52] This

is consistent with the fact that the crown oxygen atoms are neutral donors as opposed to the anionic phenoxide centres.

Table 2.4 Experimental metrical parameters (bond lengths (Å) and angles (°)) for ^{Dipp}LCa(18-c-6) [**3(18-c-6)**], ^{Dipp}LSr(18-c-6)(thf) [**4(18-c-6)(thf)**] and ^{Dipp}LBa(18-c-6)(pyr) [**5(18-c-6)(pyr)**]. Estimated standard deviations shown in brackets.

	^{Dipp}LCa(18-c-6) (**[3(18-c-6)]**)[a]	^{Dipp}LSr(18-c-6)(thf) (**[4(18-c-6)(thf)]**)[b]	^{Dipp}LBa(18-c-6)(pyr) (**[5(18-c-6)(pyr)]**)[c]
M-O(1)	2.2112(10)	2.3900(9)	2.505(2)
M-O(2)	2.2556(10)	2.3996(9)	2.538(2)
O(1)-C(1)	1.2909(17)	1.2832(15)	1.292(4)
[d]M(1)-O(18-c-6)	2.561	2.768	2.936
[b,c]M-X(solvent)	-	2.6711(10)	2.997(3)
O(1)-M-O(2)	77.28(4)	68.96(3)	66.06(8)
M-O(1)-C(1)	135.62(9)	141.54(8)	138.2(2)
M-O(2)-C(9)	133.80(9)	141.62(8)	139.8(2)

[a]Solid-state data not representative of bulk in solution; [b]Sr-O(thf); [c]Ba-N(pyr); [d]*av*. values.

2.4.3 Solid angle calculations

The atomic coordinates from X-ray crystallographic analysis were used in solid angle calculations; the results are presented in **Figures 2.18-2.21** and **Tables 2.5-2.6**.[36]

For [**3(thf)$_2$**]$_2$, analogous conclusions to the analysis of complex **1** can be drawn due to their similarity in structure. A greater steric effect is caused by the [=N,O$^-$] chelating ligand as a result of the increased proximity of a metal centre to a diisopropyl-*aryl* group ($G_{2.28}$: 32.10% *vs*. 27.10%; **Figure 2.18**). The two thf ligands impart minutely different shielding effects due to their slight difference in distance from the calcium centre (M-O(thf): 2.384(13) Å *vs*. 2.402(5) Å; **Table 2.3**). This variance however, does not change

upon normalisation of the M-O(thf) bond length ($G_{2.28}$: 14.23% *vs*. 15.72%) thus implying that bound thf 2 (green) is more parallel to the ligand backbone (and therefore covers more of the Ca centre) than bound thf 1 (yellow; **Figure 2.18**). This was confirmed by X-ray analysis which found that the dihedral angle (0° = *syn*-coplanar, 180° = *anti*-coplanar) between C(1)-O(1)-O(thf)-C(thf) is 71.7° for thf 1 and 124.9° for thf 2. The percent of the Ca surface that is shielded by the ligands in [**3(thf)$_2$**]$_2$ is lower than that of Mg in complex **1** (*G*(M): 67.36% *vs*. 78.25%); this is the result of the larger ionic radius of the Ca^{2+} cation.[44]

Figure 2.18 Visualisations of *G*(L) values in [^{Dipp}LCa(thf)$_2$]$_2$ ([**3(thf)$_2$**]$_2$), showing the percentage of the complex sphere shielded by each ligand. Blue = ^{Dipp}L$_1$, yellow = thf, green = thf, red = ^{Dipp}L$_2$. Second metal centre removed for clarity.

Table 2.5 Summary of ligand solid angles (Ω), the percentage of the sphere shielded by the ligand (*G*), the percent of the metal surface shielded by ligand atoms (*G*(M)) and the percentage of the metal surface "in contact" with ligated atoms (*S*(M)) for [^{Dipp}LCa(thf)$_2$]$_2$ (**[3(thf)$_2$]$_2$**).

Ω(^{Dipp}L$_1$) (sr)	Ω(^{Dipp}L$_2$) (sr)	Ω(X) (sr)	*G*(^{Dipp}L$_1$) (%)	*G*(^{Dipp}L$_2$) (%)	*G*(X) (%)	$G_{2.28}$ (^{Dipp}L$_1$) (%)	$G_{2.28}$ (^{Dipp}L$_2$) (%)	$G_{2.28}$ (X) (%)	*G*(M) (%)	*S*(M) (%)
4.48	4.00	[a]1.64	35.67	31.85	[a]13.06	32.10	27.10	[a]14.23	67.36	67.06
		[a]1.86			[a]14.77			[a]15.72		

[a] independent thf molecules.

For the well-defined, crown-ether supported monomeric systems, as expected, the solid angle and *G*-parameter associated with the ^{Dipp}L ligand decrease with increasing cation size (**Table 2.6**).

Table 2.6 Summary of ligand solid angles (Ω), the percentage of the sphere shielded by the ligand (*G*), the percent of the metal surface shielded by ligand atoms (*G*(M)) and the percentage of the metal surface "in contact" with ligated atoms (S(M)) for ^{Dipp}LCa(18-c-6) [**3(18-c-6)**], ^{Dipp}LSr(18-c-6)(thf) [**4(18-c-6)(thf)**] and ^{Dipp}LBa(18-c-6)(pyr) [**5(18-c-6)(pyr)**].

Complex	Ω(L) (sr)	Ω(18-c-6) (sr)	Ω(X) (sr)	*G*(L) (%)	*G*(18-c-6) (%)	*G*(X) (%)	$G_{2.28}$(L) (%)	$G_{2.28}$ (18-c-6) (%)	$G_{2.28}$ (X) (%)	*G*(M) (%)	*S*(M) (%)
^{Dipp}LCa (18-c-6)	3.73	7.55	-	29.68	60.11	-	25.12	-[c]	-	76.85	74.82
[a] ^{Dipp}LSr (18-c-6) (thf)	3.67	6.58	1.42	29.24	52.39	11.32	32.60	-[c]	14.51	75.32	70.77
[b] ^{Dipp}LBa (18-c-6) (pyr)	3.56	6.13	1.24	28.36	48.75	9.85	30.90	38.51	15.60	66.31	61.89

[a] X = thf; [b] X = pyridine. [c] No meaningful normalisation possible.

A similar reduction in percent metal coverage is observed for the crown-ether: Ca: 60.11% > Sr: 52.39% > Ba: 48.75%. The thf ligand in [**4(18-c-6)(thf)**] appears to have a larger shielding effect than the analogous pyridine ligand in [**5(18-c-6)(pyr)**] despite it being smaller in size (5 *vs*. 6 membered ring). This is because it resides closer to the metal centre, as confirmed by X-ray analysis (M-solvent: 2.6711(10) Å *vs*. 2.997(3) Å for Sr and Ba respectively; **Table 2.4**), and is therefore able to cast a larger shadow. However, when these exogenous ligands are held equidistant from the cations, the expected, opposite trend is observed ($G_{2.28}$: 14.51% *vs*. 15.60% for thf and pyr respectively). The planarity and orientation of the nitrogen-based donor, with respect to the metal centre, seems to contribute to its observed poorer shielding.

Figure 2.19 Visualisations of *G*(L) values in ^{Dipp}LCa(18-c-6) ([**3(18-c-6)**]), showing the percentage of the complex sphere shielded by each ligand. Blue = ^{Dipp}L, yellow = 18-c-6.

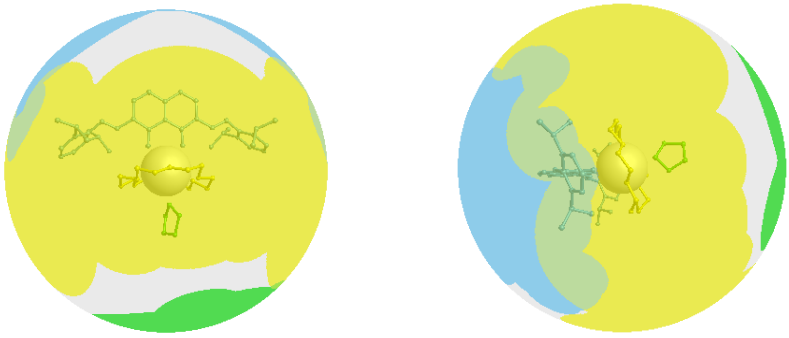

Figure 2.20 Visualisations of *G*(L) values in ^{Dipp}LSr(18-c-6)(thf) [**4(18-c-6)(thf)**], showing the percentage of the complex sphere shielded by each ligand. Blue = ^{Dipp}L, yellow = 18-c-6, green = thf.

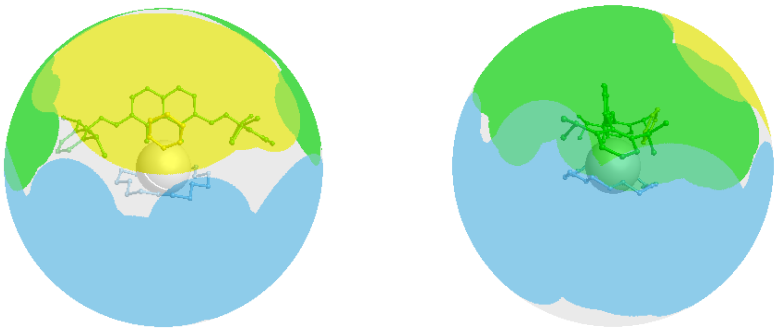

Figure 2.21 Visualisations of *G*(L) values in ^{Dipp}LBa(18-c-6)(pyr) [**5(18-c-6)(pyr)**], showing the percentage of the complex sphere shielded by each ligand. Green = ^{Dipp}L; blue = 18-c-6, yellow = pyridine.

2.5 Targeting bimetallic heavier alkaline-earth complexes through salt-metathesis

Following the observed protonolysis reactivity between $H_2{}^{Dipp}L$ and alkaline-earth metal amides and aryloxides, salt-metathesis reactions were explored as an alternative route to complexes of the form $^{Dipp}L(MX)_2$ (**Scheme 2.7**).

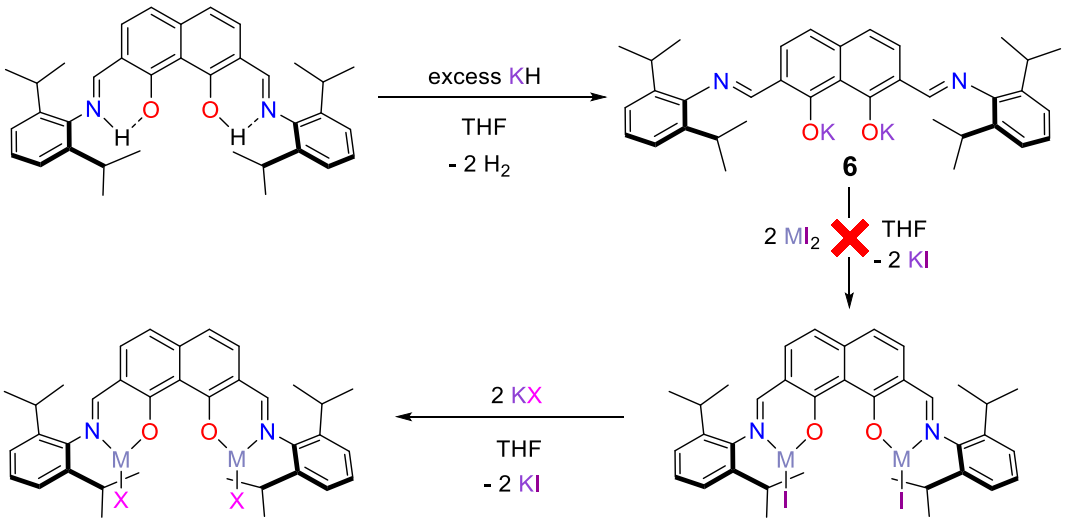

Scheme 2.7 Pathway to prepare bimetallic $^{Dipp}L(MX)_2$ complexes via double deprotonation of $H_2{}^{Dipp}L$ with KH and subsequent salt-metathesis reactions with alkaline-earth diiodides.

To this end, the dipotassium salt of the ligand was first prepared by treatment of $H_2{}^{Dipp}L$ with an excess of KH (2.5 equivalents) in THF. $^{Dipp}LK_2$ (**6**) was isolated cleanly as a pale orange powder, in a moderate yield of 41%, before being utilised in salt-metathesis reactions with various alkaline-earth diiodide materials, MI_2 (M = Ca, Sr and Ba). In all cases, these reactions yielded a mixture of inseparable products proposed to be $^{Dipp}LM(thf)_x$/$[^{Dipp}LM(thf)_x]_2$ (**3-5(thf)$_x$**/[**3-5(thf)$_x$**]$_2$) and $[H^{Dipp}LMI]_2$ (*vide infra*).

2.5.1 NMR spectroscopic analysis

The ^{1}H NMR spectrum of compound **6** contains the expected resonances for the C_{2v} symmetric product (**Figure 2.22**).

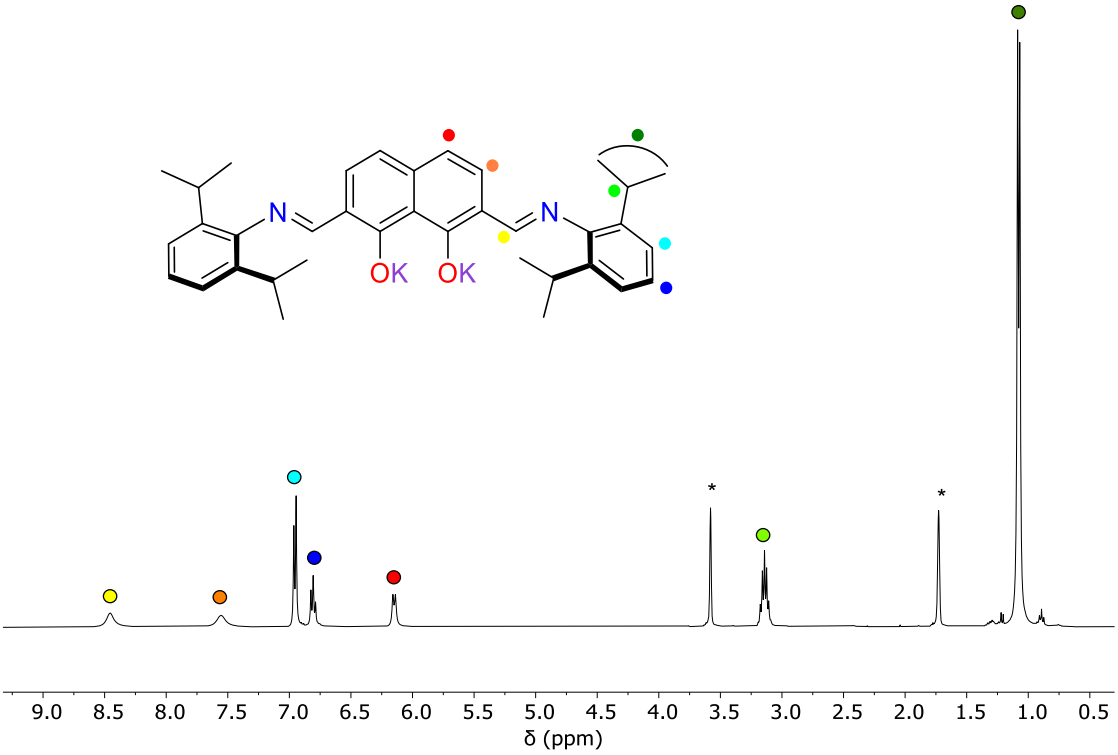

Figure 2.22 ^{1}H NMR spectrum (*THF-d_8, 400 MHz, 298 K) of ^{Dipp}LK$_2$ (**6**).

Like with complexes **1**, **3(thf)$_2$**, **4(thf)**, and **5(thf)**, complete deprotonation is clearly observed by the absence of the O***H*** and N***H*** protons characteristic of the pro-ligand. Two broad aromatic resonances at δ 8.45 and δ 7.56 ppm correspond to the imine ***H***C=N and naphthalene 3,6-C$_{10}$***H***$_4$ protons. The remaining aromatic resonances at δ 6.95–6.81 ppm and δ 6.15 ppm correspond to the diisopropyl-*aryl*-C$_6$***H***$_3$ and *naphthyl*-4,5-C$_{10}$***H***$_4$ protons respectively. The isopropyl *methine* and *methyl* protons are represented by the mutually coupling ($^{3}J_{HH}$ = 6.9 Hz) multiplets at δ 3.14 and δ 1.08 ppm.

After addition of alkaline-earth diiodides to THF solutions of **6**, evidence for the formation of mixtures of two compounds is most clearly observed in the *methine* region (i.e. δ 3–4 ppm) of the ^{1}H NMR spectra (**Figure 2.23**). This area contains singular septets (+) that align with the C_{2v} symmetric, time average signals for the heavier alkaline-earth systems (**3-5(thf)$_x$**/[**3-5(thf)$_x$**]$_2$). In addition, two other symmetric septets (‡) are present; this highlights the formation of a secondary asymmetric species.

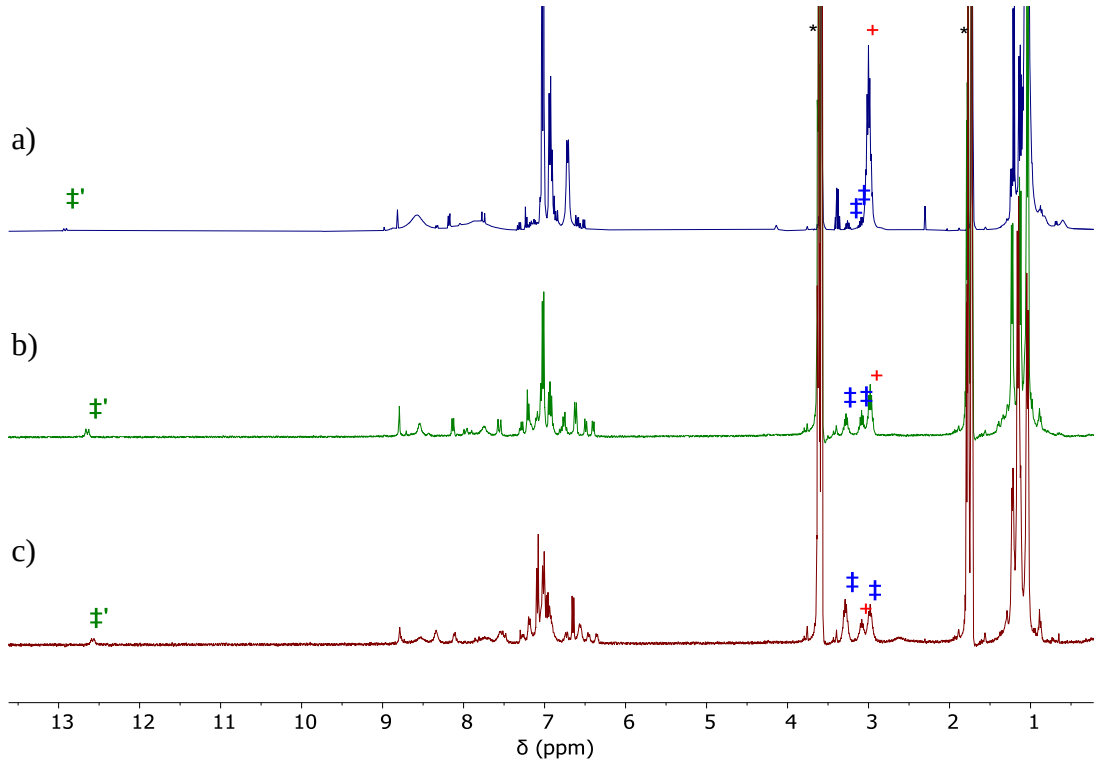

Figure 2.23 ^{1}H NMR spectra (*THF-d_8, 400 MHz, 298 K) of reaction mixtures after addition of MI_2 (a) M = Ca, b) M = Sr and c) M = Ba). + and ‡ represent [**3-5(thf)**$_x$]/[**3-5(thf)**$_x$]$_2$ and [H^{Dipp}LMI]$_2$ respectively. **‡'** indicates the residual N***H*** protons of the proposed asymmetric dimers.

The asymmetric compounds contain resonances comparable to those of complex **2**, most notably the residual N***H*** signal (‡') between δ 12-13 ppm. This therefore suggests that they are the heavier alkaline-earth, iodide containing, analogues of the partially deprotonated, magnesium halide dimer ([H^{Dipp}LMgI]$_2$; **Figure 2.24**). These results reiterate that this type of compound is a typical product of the reaction between H$_2^{Dipp}$L and alkaline-earth halide reagents. It is not formed cleanly in this case however, for several reasons. Firstly, the stoichiometry of the reaction was incorrect – M:L = 2:1 rather than 1:1. Secondly, full deprotonation of the pro-ligand had already occurred (in contrast to complex **2** where N"MgCl was used to singly deprotonate H$_2^{Dipp}$L); this therefore made the formation of the monomeric, monometallic product, via the elimination of both iodide ligands from a single metal centre, more feasible.

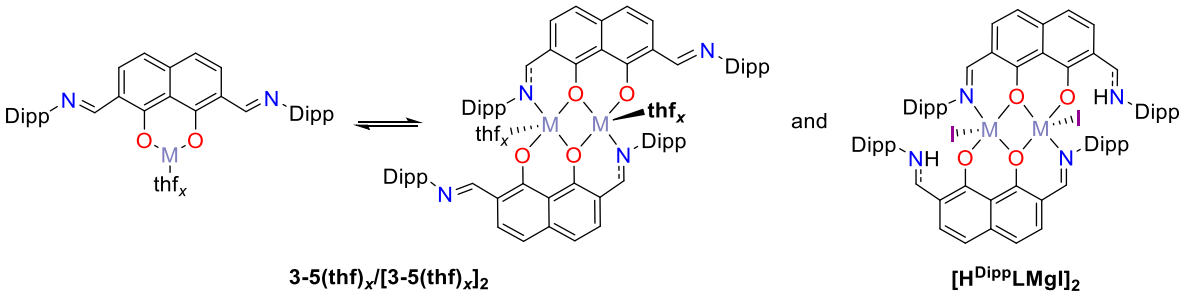

Figure 2.24 The proposed products of the reaction between $^{Dipp}LK_2$ (**6**) and alkaline-earth diiodides (M = Ca, Sr and Ba).

As the size of the metal increases, the proportion of the postulated dynamic/fixed dimeric products becomes more even (approx. **3-5(thf)$_x$**/[**3-5(thf)$_x$**]$_2$:**[H^{Dipp}LMgI]$_2$** ratios, calculated via integration of the *methine* region of ^{1}H NMR spectra are 95:5 (Ca), 70:30 (Sr) and 40:60 (Ba)). This aligns with the well-reported fact that larger metal centres are more able to prevent steric congestion, accommodate higher coordination numbers and thus more readily facilitate fixed, non-fluxional dimerisation.[53]

2.6 Conclusions

The *bis*(phenoxy-imine) pro-ligand, $H_2^{Dipp}L$ (2,7-di(2,6-diisopropylphenyl) imino-1,8-dihydroxynaphthalene), with two [=N,O$^-$] binding pockets, has not proven to be a suitable ligand scaffold for the preparation of bimetallic alkaline-earth complexes of the form $^{Dipp}L(MX)_2$. However, well-defined alkaline-earth metal complexes were isolated; the preferential binding of the oxophilic M^{2+} centres to the third [O$^-$,O$^-$] binding site resulted in the isolation of monomeric, or dimeric complexes where an imine N group additionally ligates to the metal centre.

Protonolysis reactions of $H_2^{Dipp}L$ with metal silylamides highlighted this behaviour in the absence of chlorinated solvents, forming; for M = Mg, [^{Dipp}LMg(thf)]$_2$ (**1**), and for M = Ca, Sr, Ba, $^{Dipp}LCa(thf)_2$ (**3(thf)$_2$**), ^{Dipp}LSr(thf) (**4(thf)**) and ^{Dipp}LBa(thf) (**5(thf)**)

respectively, which are in equilibrium with the corresponding dimeric forms $[(^{Dipp}L)M(thf)_x]_2$ (**X**/$[\mathbf{X}]_2$). For Mg, carrying out the reaction in chloroform led to chlorination of the metal centre and subsequent single deprotonation of the ligand framework to afford $[H^{Dipp}LMgCl]_2$ (**2**).

Salt metathesis reactions were explored as an alternative route and $^{Dipp}LK_2$ (**6**) was prepared in a straightforward manner. However, subsequent reactions with metal iodides did not afford $^{Dipp}L(MI)_2$ species but rather a mixture of $^{Dipp}LM(thf)_x \rightleftharpoons [^{Dipp}LM(thf)_x]_2$ and $[H^{Dipp}LMI]_2$.

The inability to devise a clean synthetic route to the desired bimetallic products initiated a shift away from the use of $H_2{}^{Dipp}L$ and similar ligands.[54, 55] Related scaffolds, that replace the problematic $[O^-,O^-]$ binding pocket with a C_3 bridge were subsequently pursued (**Chapter 4**).

2.7 References

1. M. R. Salata and T. J. Marks, *J. Am. Chem. Soc*, 2008, **130**, 12-13.
2. M. R. Salata and T. J. Marks, *Macromolecules*, 2009, **42**, 1920-1933.
3. B. A. Rodriguez, M. Delferro and T. J. Marks, *Organometallics*, 2008, **27**, 2166-2168.
4. B. A. Rodriguez, M. Delferro and T. J. Marks, *J. Am. Chem. Soc*, 2009, **131**, 5902-5919.
5. C.-Y. Peng, J.-Y. Shen, Y.-T. Chen, P.-J. Wu, W.-Y. Hung, W.-P. Hu and P.-T. Chou, *J. Am. Chem. Soc*, 2015, **137**, 14349-14357.
6. T. Glaser and L. Liratzis, *Synlett*, 2004, 735-737.
7. K. P. Kepp, *Inorg. Chem.*, 2016, **55**, 9461-9470.
8. N. Walker, M. P. Dobson, R. R. Wright, P. E. Barran, J. N. Murrell and A. J. Stace, *J. Am. Chem. Soc*, 2000, **122**, 11138-11145.
9. D. Rutkowska-Zbik, M. Witko and L. Fiedor, *J. Mol. Model.*, 2013, **19**, 4661-4667.
10. Y. Yang, H. Wang and H. Ma, *Polyhedron*, 2016, **117**, 569-578.
11. W.-C. Hung and C.-C. Lin, *Inorg. Chem.*, 2009, **48**, 728-734.
12. S. Song, H. Ma and Y. Yang, *Dalton Trans.*, 2013, **42**, 14200-14211.
13. V. McKee, O. C. Choon and G. A. Rodley, *Inorg. Chem.*, 1984, **23**, 4242-4248.
14. C. C. Roberts and J. M. Fritsch, *Polyhedron*, 2010, **29**, 1271-1278.

15. D. W. Agnew, C. E. Moore, A. L. Rheingold and J. S. Figueroa, *Angew. Chem. Int. Ed.*, 2015, **54**, 12673-12677.

16. C. Dinoi, M. F. C. Guedes da Silva, E. C. B. A. Alegria, P. Smoleński, L. M. D. R. S. Martins, R. Poli and A. J. L. Pombeiro, *Eur. J. Inorg. Chem.*, 2010, **2010**, 2415-2424.

17. E. L. Werkema, E. Messines, L. Perrin, L. Maron, O. Eisenstein and R. A. Andersen, *J. Am. Chem. Soc*, 2005, **127**, 7781-7795.

18. E. L. Werkema, R. A. Andersen, A. Yahia, L. Maron and O. Eisenstein, *Organometallics*, 2009, **28**, 3173-3185.

19. E. L. Werkema, R. A. Andersen, L. Maron and O. Eisenstein, *Dalton Trans.*, 2010, **39**, 6648-6660.

20. S. P. Heins, B. Zhang, S. N. MacMillan, T. R. Cundari and P. T. Wolczanski, *Organometallics*, 2019, **38**, 1502-1515.

21. M. S. Samuel, M. C. Jennings and K. M. Baines, *Organometallics*, 2001, **20**, 590-592.

22. T. D. W. Claridge, in *High-Resolution NMR Techniques in Organic Chemistry (Third Edition)*, ed. T. D. W. Claridge, Elsevier, Boston, 2016, pp. 381-419.

23. A. Macchioni, G. Ciancaleoni, C. Zuccaccia and D. Zuccaccia, *Chem. Soc. Rev.*, 2008, **37**, 479-489.

24. R. Evans, Z. Deng, A. K. Rogerson, A. S. McLachlan, J. J. Richards, M. Nilsson and G. A. Morris, *Angew. Chem. Int. Ed.*, 2013, **52**, 3199-3202.

25. R. Evans, G. Dal Poggetto, M. Nilsson and G. A. Morris, *Anal. Chem.*, 2018, **90**, 3987-3994.

26. M. P. Weberski Jr., C. Chen, M. Delferro and T. J. Marks, *Eur. J. Chem*, 2012, **18**, 10715-10732.

27. A. W. Addison, T. N. Rao, J. Reedijk, J. van Rijn and G. C. Verschoor, *J. Chem. Soc., Dalton Trans.*, 1984, 1349-1356.

28. M. T. Caudle and J. W. Kampf, *Inorg. Chem.*, 1999, **38**, 5474-5475.

29. F. Corazza, C. Floriani, A. Chiesi-Villa, C. Guastini and S. Ciurli, *J. Chem. Soc., Dalton Trans.*, 1988, 2341-2345.

30. T. J. Boyle, J. M. Sears, J. A. Greathouse, D. Perales, R. Cramer, O. Staples, A. L. Rheingold, E. N. Coker, T. M. Roper and R. A. Kemp, *Inorg. Chem.*, 2018, **57**, 2402-2415.

31. J. Wu, Y.-Z. Chen, W.-C. Hung and C.-C. Lin, *Organometallics*, 2008, **27**, 4970-4978.

32. A. Bondi, *J. Phys. Chem.*, 1964, **68**, 441-451.

33. T. Glaser, I. Liratzis, R. Fröhlich and T. Weyhermüller, *Chem. Commun.*, 2007, 356-358.

34. M. Ma, X. Shen, W. Wang, J. Li, W. Yao and L. Zhu, *Eur. J. Inorg. Chem.*, 2016, **2016**, 5057-5062.

35. P. Pyykkö, *J. Phys. Chem. A*, 2015, **119**, 2326-2337.

36. I. A. Guzei and M. Wendt, *Dalton Trans.*, 2006, 3991-3999.

37. C. A. Tolman, *Chem. Rev.*, 1977, **77**, 313-348.

38. F. Coleman, D. Dux and A. Erxleben, *Z. Anorg. Allg. Chem.*, 2013, **639**, 1584-1589.

39. J. I. Bullock, M. F. C. Ladd, D. C. Povey and H. A. Tajmirriahi, *Acta. Crystallogr. B. Struct. Sci. Cryst. Eng. Mater.*, 1979, **35**, 2013-2020.

40. F. C. J. M. Van Veggel, S. Harkema, M. Bos, W. Verboom, C. J. Van Staveren, G. J. Gerritsma and D. N. Reinhoudt, *Inorg. Chem.*, 1989, **28**, 1133-1148.

41. S. Hayami, S. Nomiyama, S. Hirose, Y. Yano, S. Osaki and Y. Maeda, *J. Radioanal. Nucl. Chem.*, 1999, **239**, 273-277.

42. L. Carbonaro, M. Isola, P. La Pegna, L. Senatore and F. Marchetti, *Inorg. Chem.*, 1999, **38**, 5519-5525.

43. K. F. Tesh, T. P. Hanusa, J. C. Huffman and C. J. Huffman, *Inorg. Chem.*, 1992, **31**, 5572-5579.

44. R. D. Shannon and C. T. Prewitt, *Acta. Crystallogr. B. Struct. Sci. Cryst. Eng. Mater.*, 1969, **B 25**, 925-946.

45. A. Causero, G. Ballmann, J. Pahl, C. Färber, J. Intemann and S. Harder, *Dalton Trans.*, 2017, **46**, 1822-1831.

46. Y.-Y. Yang, Z.-Q. Huang, X.-M. Chen and S. Weng Ng, *Z. Anorg. Allg. Chem.*, 2003, **629**, 1901-1903.

47. M. Westerhausen, S. Schneiderbauer, Alexander N. Kneifel, Y. Söltl, P. Mayer, H. Nöth, Z. Zhong, Pieter J. Dijkstra and J. Feijen, *Eur. J. Inorg. Chem.*, 2003, 3432-3439.

48. E. D. Glendening and D. Feller, *J. Am. Chem. Soc*, 1996, **118**, 6052-6059.

49. K. Ozutsumi, K. Kohyama, K. Ohtsu and T. Kawashima, *J. Chem. Soc., Dalton Trans.*, 1995, 3081-3085.

50. J. Steinbauer, A. Spannenberg and T. Werner, *Green Chem.*, 2017, **19**, 3769-3779.

51. S. M. Härling, S. Krieck, H. Görls and M. Westerhausen, *Inorg. Chem.*, 2017, **56**, 9255-9263.

52. T. S. Pochekutova, V. K. Khamylov, G. K. Fukin, B. I. Petrov, A. S. Shavyrin, A. V. Arapova, N. M. Lazarev, V. I. Faerman, T. I. Kulikova, E. V. Baranov and N. M. Khamaletdinova, *Polyhedron*, 2020, **177**, 114263.

53. K. M. Fromm and E. D. Gueneau, *Polyhedron*, 2004, **23**, 1479-1504.

54. H.-C. Huang, B. Wang, Y.-P. Zhang and Y.-S. Li, *Polym. Chem.*, 2016, **7**, 5819-5827.

55. M. R. Radlauer, A. K. Buckley, L. M. Henling and T. Agapie, *J. Am. Chem. Soc*, 2013, **135**, 3784-3787.

Chapter 3

Lactide polymerisation studies with alkaline-earth "NOON" complexes

3.1 Introduction

3.1.1 Overview

The exploration of complexes **2**, **3(thf)$_2$**, **4(thf)** and **5(thf)**, as single-site catalysts for the ring-opening polymerisation of *L*-, *D*-, *rac*- and *meso*-lactide, is presented (**Figure 3.1**). A variety of conditions (temperature, monomer stereochemistry, initiator concentration) and analytical techniques (NMR spectroscopy, mass spectrometry, gel permeation chromatography) have been utilised to study the kinetics of polymerisation and resultant polymer structure.

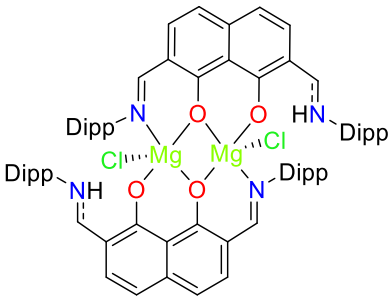

2

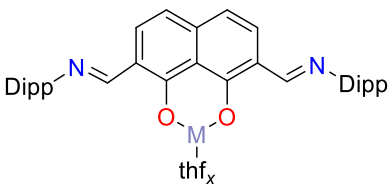

M = Ca (**3**) *x* = 2
Sr (**4**) *x* = 1
Ba (**5**) *x* = 1

Figure 3.1 The initiators tested in this Chapter.

3.1.2 Literature reports of related alkaline-earth ROP catalysts

In the context of lactide polymerisation, there have been numerous reports of well-defined bimetallic M^{2+} systems with N/O-donating ligands; the majority are zinc or magnesium-based and incorporate highly active amide/alkoxide initiating groups.[1-3] Investigations of analogous heavier *bis*(group 2) systems are much less common due to their propensity to redistribute in solution.[4] There are however, some examples monometallic Ca, Sr and Ba LA ROP catalysts; the coordination sphere of these complexes is typically filled with donating solvent molecules as opposed to dedicated initiating groups.[5-7] This precludes polymerisation activity via the typical coordination-insertion and (in the absence of a co-initiator) activated monomer pathways. Selected examples relevant to this study, are discussed in the following sections (**3.1.2.1**–**3.1.2.3**).

3.1.2.1 Dimeric, bimetallic Mg systems

A family of heteroleptic, tethered-bimetallic magnesium complexes was reported by Harder and co-workers in 2008 (**Figure 3.2a**).[1] These initiators were all capable of polymerising *rac*-LA; their activity was found to be dependent on the nature of the bridging unit and solvent used for polymerisation.[1] The *para*-phenylene-bridged catalysts performed better than the corresponding *meta*-bridged species (*para*-79% *vs*. *meta*-56% conversion of 50 eq. in 5 h) suggesting that intermetallic distance is a contributing factor to their activity. In apolar solvents, the *pyridyl*-bridged initiator was the most active; the authors report that this may be due to intramolecular coordination of the bridging nitrogen at the metal centre.[1] This is unlikely to happen in a coordinating solvent like THF thus explaining the complex's poor activity in this polar solvent. In all cases, the molecular weights of the resultant atactic poly(lactide) were higher than expected. This, combined with the relatively broad molecular weight distributions (M_w/M_n = 1.42–1.97), implies

that the polymerisations proceeded with only moderate control (likely caused by slow initiation and/or transesterification side reactions).[1]

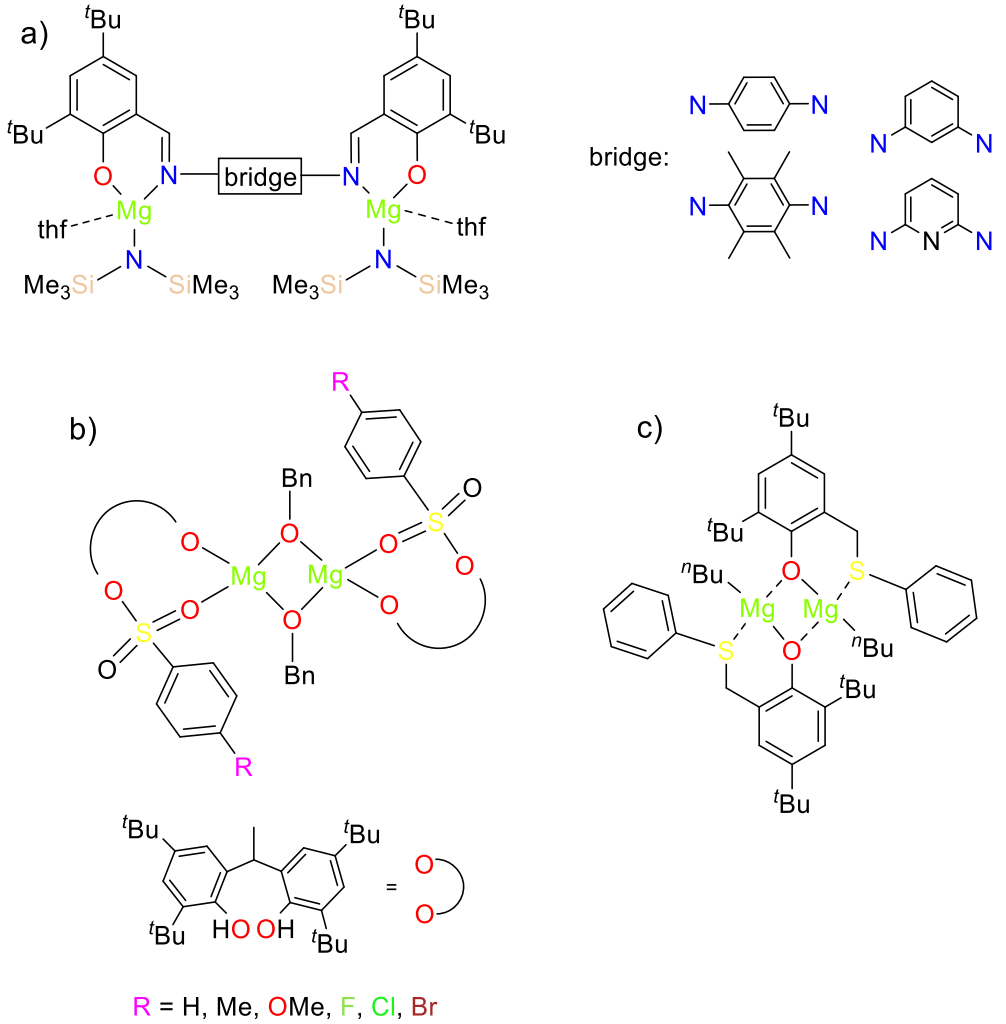

Figure 3.2 Bimetallic magnesium initiators previously reported for the ring-opening polymerisation of lactide.[1-3]

Dimeric magnesium alkoxide systems, reported by Lin *et al.*, were found to be highly efficient ROP catalysts achieving full conversion of 1000 eq. of *L*-lactide within 4 minutes at 25 °C (**Figure 3.2b**).[2] The molecular weights of the resultant polymers (4300–84 800 $gmol^{-1}$) were some of the highest recorded for a magnesium catalyst; the slight discrepancy between the observed and predicted values was attributed to poor solubility of the monomer in aromatic solvents and possible back biting side reactions

($1.08<M_w/M_n<1.20$).[2] The addition of electron-withdrawing substituents on the phenyl ring (R) was found to significantly reduce the isolated yield of polymer (F: 31% < Cl: 77% < Br: 96%).[2] In addition, the insufficient steric bulk of the ligand resulted in poor selectivity and formation of atactic PLA with slight heterotactic enrichment from *rac*-lactide ($P_r = 0.58–0.64$).[2]

Phenoxy-thioether zinc and magnesium complexes have also been reported as initiators for the ring-opening polymerisation of lactide (**Figure 3.2c**).[3] The magnesium dimers exhibited higher activity (converting 100 eq. of *rac*-LA in 5 h at room temperature) due to the greater ionic character of the Mg^{2+} centre (results in higher binding constants).[3] An induction period of 4 minutes was observed for these polymerisations. The authors attributed this to ligand rearrangement and dissociation of the dimer into active monomeric species.[3] Experiments determined that the kinetic order with respect to Mg was 1.47; this non-integer value supports the theory of a possible solution (de)aggregation equilibrium.[3]

3.1.2.2 Heavier alkaline-earth bimetallics

Bimetallic calcium and strontium 2,4-di-*tert*-butyl phenolates (DBP) have been studied, by Mountford *et al*., as initiators for the ring-opening polymerisation of lactide.[4] The tethered calcium system (**Figure 3.3a**) was capable of converting 89% of 100 eq. of *rac*-LA in 150 minutes.[4] During the same time, 86% conversion was achieved with the dinuclear strontium catalyst (**Figure 3.3b**).[4]

The recorded molecular weights seemed consistent with one poly(lactide) chain per terminal Ae-DBP unit (4 for Ca: $M_{n,(GPC)}$: 4050 *vs*. $M_{n,(calcd)}$: 3200 $gmol^{-1}$; 1 for Sr: $M_{n,(GPC)}$: 13 200 *vs*. $M_{n,(calcd)}$: 12 400 $gmol^{-1}$).[4] However, the proposed DBP end group could not be identified in either ^1H NMR or MALDI-TOF spectra suggesting that the

polymerisation was producing cyclic polymers.[4] This implies that transesterification and back-biting reactions were prevalent during the reaction. The poor control of the polymerisation was highlighted by the observation of broad and in the case of strontium, bimodal, molecular weight distributions (M_w/M_n = 1.5–2.6).[4] The bimodal nature of the strontium GPC trace may indicate the presence of multiple active species in solution (such as the different environments of the two metal centres within the dinuclear structure), or formation of different polymeric structures (i.e. a mixture of linear and cyclic PLA as a result of transesterification).

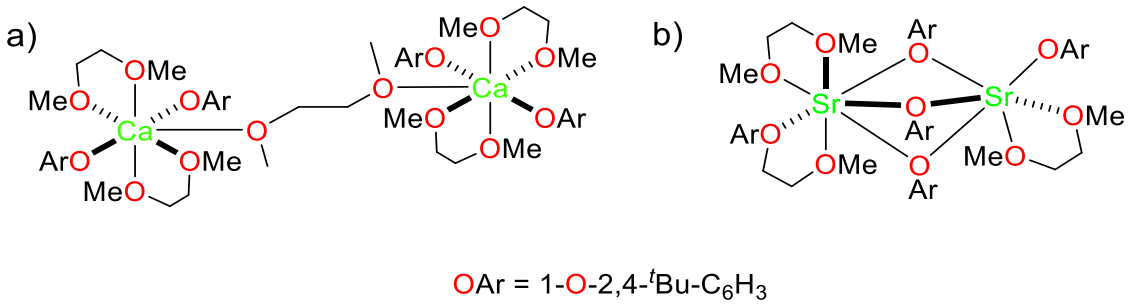

Figure 3.3 The bimetallic calcium and strontium phenolates, reported by Mountford *et al.*, for the ring-opening polymerisation of lactide.[4]

3.1.2.3 Monometallic, heavier alkaline-earth systems

A series of group two iminopyrrolyl compounds, with no dedicated initiating groups, have been reported as efficient catalysts for the ring-opening polymerisation of the cyclic ester ε-caprolactone (**Figure 3.4a**).[5, 6] The calcium analogue showed comparable activity to that of the magnesium variants.[6] In contrast, the strontium and barium systems showed improved reactivity (600 eq. were converted within 5–10 minutes at 25 °C) without comprising polymerisation control (M_w/M_n < 1.59).[6] The authors report that this due to the larger ionic radii of the Sr^{2+} and Ba^{2+} cations increasing the availability of space for initiator-monomer interactions.[6, 7]

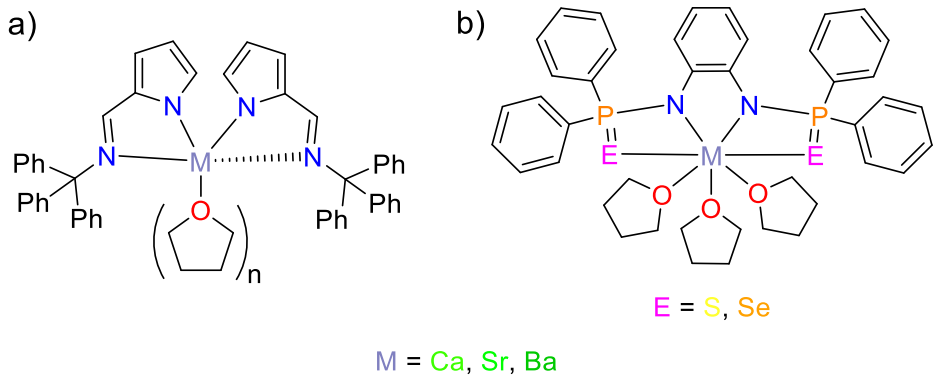

Figure 3.4 Previously reported monomeric, heavier alkaline-earth initiators for the ring-opening polymerisation of lactide.[5-7]

A similar trend in polymerisation activity (Ca: 0.137 < Sr: 0.149 < Ba: 0.839 M^{-1} h^{-1}; E=S; M_w/M_n < 1.6) was observed in related chalcogen containing systems (**Figure 3.4b**).[7] The rate of polymerisation was also found to correlate with the donor atoms of the ligand (S < Se; for Ba: 0.839 (S) *vs.* 0.906 (Se) M^{-1} h^{-1}).[7] The larger size of the selenium atoms causes them to reside further from the metal centre; this increased the lability of the Ae-chalcogen bond enabling more efficient lactide initiation.[7]

3.2 General considerations for lactide polymerisation studies

Lactide (LA) polymerisations were performed in J. Young's tap NMR tubes with an initial monomer concentration ($[LA]_0$) of 0.5 M. The reactions were halted by submerging the NMR tubes in an ice bath and conversion to polylactide (PLA) was monitored by ^{1}H NMR spectroscopy. Benzene-d_6 was chosen as the polymerisation solvent due to poor solubility of the initiators in chloroform-d_1 and inability to monitor reaction kinetics in THF-d_8 (due to overlapping monomer and polymer signals). Upon completion, the reaction mixture was decanted and the resultant polymer was precipitated by addition of pentane.

Control polymerisations using only $H_2^{Dipp}L$ (with and without a benzyl alcohol co-initiator) as the catalyst were also conducted; no activity was observed after 24 h, even at the highest temperature studied. As a result, it can be concluded that any observed polymerisation activity is due solely to the alkaline-earth complexes (and co-catalyst if present).

3.3 Testing the catalytic capabilities of $[H^{Dipp}LMgCl]_2$ (2)

3.3.1 Introduction of co-initiator

Polymerisation of *L*-LA employing solely complex **2** proved to be extremely slow achieving only 77% conversion of 50 eq. *L*-LA in 336 h at 80 °C (**Figure 3.5a** and **Table 3.1**). This low activity is not surprising as chloride ligands are typically poor initiating groups due to the high strength of metal-halide bonds.[8] As a result, alkoxide and amide ligands are more commonly employed as initiating groups with high activity (**Figure 3.2**).[1-4] To this end, 2 eq. of benzyl alcohol ($C_6H_5CH_2OH$, BnOH) were added to the catalyst solution. It is postulated that, in agreement with literature, this results in the formation of a more active benzyloxide complex ($[LMg\text{-}OBn]_2$) *in situ* via exchange of the chloride ligands with the co-initiator.[9-11]

Table 3.1 ROP of *L*-LA using **2** and BnOH with $[L\text{-LA}]_0$:$[\mathbf{Mg}]_0$(:$[BnOH]_0$) = 50:1(:1) at 80 °C.[a]

BnOH	Time (h)	Conv. (%)[b]	k_{obs} (h^{-1})[c]	R^{2c}	M_n (GPC)[d]	M_n (calcd)[e]	M_w/M_n
No	336	77	0.0046 ± 0.0001	0.995	9156	5630	1.55
Yes	58	78	0.032 ± 0.001	0.993	6615	6546	1.14

[a]Conditions: $[L\text{-LA}]_0$:$[\mathbf{Mg}]_0$(:$[BnOH]_0$) = 50:1(:1), $[L\text{-LA}]_0$ = 0.5 M in 0.6 mL benzene-d_6 at 80 °C. [b]Average reported; measured by ^{1}H NMR spectroscopic analyses. [c]First-order rate constant (k_{obs}) and R^2 were obtained from average plots of $\ln([L\text{-LA}]_0/[L\text{-LA}]_t)$ *vs.* time. [d]Determined by GPC in THF against PS standards using the appropriate Mark-Houwink corrections.[12] [e]Calculated M_n for PLA synthesised = (conv.(%) × $[L\text{-LA}]_0/[\mathbf{Mg}]_0$) × 144.13 + ($M_w$ of end groups).

The introduction of BnOH resulted in a ~7-fold increase in the rate of polymerisation (k_{obs}: 0.0046 h^{-1} *vs.* 0.032 h^{-1}); this agrees well with reported literature that suggests the ROP of LA is facile and well-controlled in the presence of exogenous alcohols.[8-10, 13, 14] In both cases, linear plots of ln([*L*-LA]$_0$/[*L*-LA]$_t$) *vs.* time (from which the experimental rate constants, k_{obs}, were derived) were observed; this indicates a first-order dependency on monomer concentration (**Figure 3.5b**).

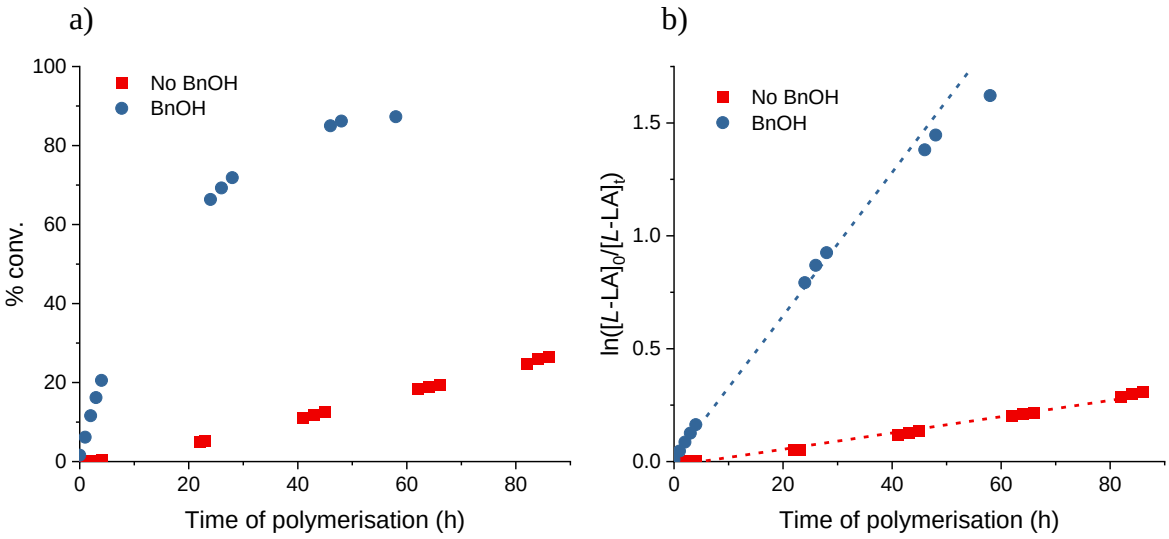

Figure 3.5 a) Plots of percentage conversion *vs.* time. b) Plots of ln([*L*-LA]$_0$/[*L*-LA]$_t$) *vs.* time. Red squares: No BnOH (k_{obs} = 0.0046 h^{-1}. R^2 = 0.995); blue circles: BnOH (k_{obs} = 0.032 h^{-1}. R^2 = 0.993). Conditions: [*L*-LA]$_0$:[**Mg**]$_0$(:[BnOH]$_0$) = 50:1(:1), [*L*-LA]$_0$ = 0.5 M in 0.6 mL benzene-d_6 at 80 °C.

As expected, the experimental rates of this MgCl/BnOH binary system are still much slower than those of previously reported dinuclear magnesium systems with pre-formed, highly active initiating groups. For example, the tethered-bimetallic magnesium amides, published by Harder *et al.*, were able to convert between 36–72% of 50 eq. of *rac*-LA in 5 h at 80 ºC.[1] Furthermore, in the presence of isopropanol, phenoxy-thioether *bis*(magnesium) systems were shown to quantitatively convert 100 eq. of *rac*-LA in 5 h at room temperature.[3] In the cases of dinuclear catalysts with preformed alkoxides, the observed rates are even higher: 92% conversion of 50 eq. *L*-LA in 1.67 h at 30 ºC and

quantitative conversion of 1000 eq. of *L*-LA within 4 minutes at 25 ºC for [(NNO)Mg(μ-OCH_2Ph)]$_2$[15] and [(EDBP)Mg(μ-OCH_2Ph)]$_2$[2] respectively (NNO = (4Z)-4-{[X](phenyl)methylene}-3-methyl-1-phenyl-1H-pyrazol-5(4H)-one where X = 2-(dimethylamino)ethylamino or (pyridin-2-yl)methylamino; EDBP = 2,2′-ethylidene *bis*(4,6-di-*tert*-butylphenol)). These comparisons therefore suggest that conversion of **2** into a pre-formed [LMg-OR]$_2$ species would likely increase the rate.

GPC analysis of the polymers produced revealed unimodal molecular weight distributions with narrow to intermediate polydispersity indices (*Đ* = M_w/M_n; **Figure A.14** and **Table 3.1**). The experimental molecular weights (M_n (GPC)) of the poly-*L*-lactide produced using **2** lie within the range reported, at this $[LA]_0/[cat]_0$ ratio, for comparable dimeric magnesium systems (3600–19 900 $gmol^{-1}$).[1, 3, 15, 16] In the presence of benzyl alcohol, there is a good agreement between the experimental and calculated molecular weights (6615 *vs*. 6546 $gmol^{-1}$) which implies that the catalyst is behaving as a single-site initiator (i.e. has one growing polymer chain per metal centre). The theoretical values ($M_{n,(calcd)}$) were computed using **Equation 3.1**, assuming this single-site behaviour, and with the proposed polymer end groups consisting of a proton and chloride or alkoxide group for the respective cases without or with co-initiator.[9, 10, 14, 17]

$$M_n^{calcd} = \left(M_{\mathrm{LA}} \times \frac{[\mathrm{LA}]_0}{[\mathbf{Mg}]_0} \times \frac{\mathrm{conversion}}{100}\right) + M_{\mathrm{end\ group}} \qquad \textbf{Equation 3.1}$$

When no co-initiator was employed, the experimental molecular weights were found to be higher than the calculated values (Δ% *vs*. $M_{n,(calcd)}$ = 39; **Table 3.1**). This implies that only a proportion of the metal centres were active during the polymerisation. The poorer control of the reaction without the co-initiator was confirmed by the larger recorded polydispersity index (M_w/M_n = 1.55 *vs*. 1.14). The increased control upon addition of BnOH led to it being employed in all subsequent experiments.

3.3.2 Variable temperature studies

The effect of temperature on the rate of polymerisation was then probed (**Figure 3.6** and **Table 3.2**). Polymerisations were run between 60 and 80 °C with two eq. of benzyl alcohol co-initiator, [*L*-LA]$_0$/[**Mg**]$_0$ = 50 and [*L*-LA]$_0$ = 0.5 M.

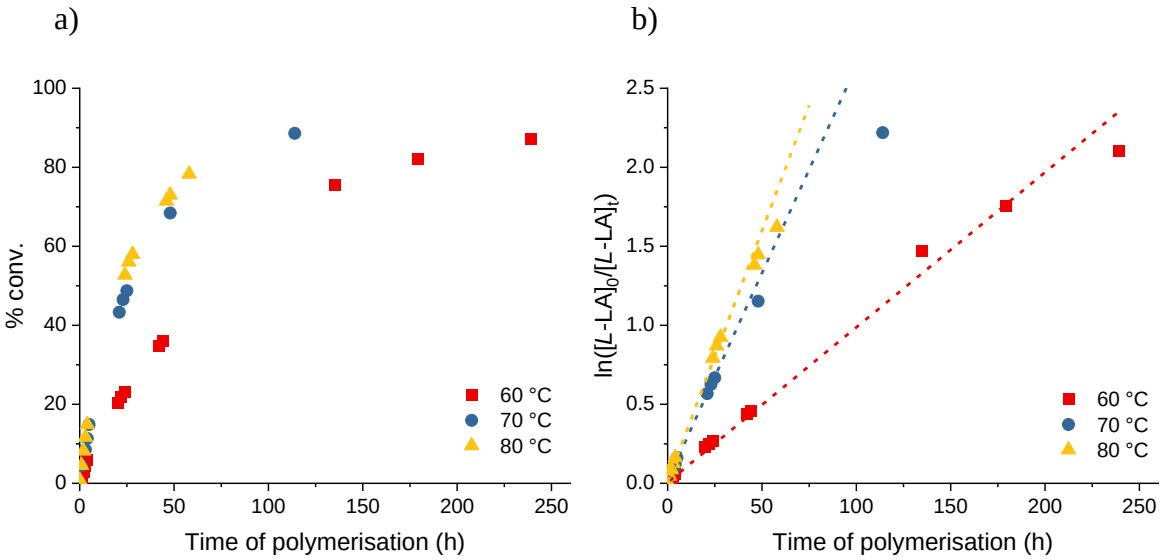

Figure 3.6 a) Plots of percentage conversion *vs.* time. b) Plots of ln([*L*-LA]$_0$/[*L*-LA]$_t$) *vs.* time using **2**/BnOH. Red squares: 60 °C (k_{obs} = 0.0098 h^{-1}. R^2 = 0.986); blue circles: 70 °C (k_{obs} = 0.026 h^{-1}. R^2 = 0.999); yellow up triangles: 80 °C (k_{obs} = 0.032 h^{-1}. R^2 = 0.993). Conditions: [*L*-LA]$_0$:[**Mg**]$_0$:[BnOH]$_0$ = 50:1:1, [*L*-LA]$_0$ = 0.5 M in 0.6 mL benzene-d_6 at stated temperature.

As expected, an increase in temperature resulted in an increase in the observed rate (**60 °C**: k_{obs} = 0.0098 h^{-1} < **70 °C**: k_{obs} = 0.026 h^{-1} < **80 °C**: k_{obs} = 0.032 h^{-1}). Similar temperature effects are commonly reported for this type of polymerisation.[8-10, 14, 16-19] The experimental rates are significantly lower than those of dinuclear magnesium systems with pre-formed alkoxide initiating groups (k_{app} = ~238 h^{-1})[2] but are more comparable to that of an analogous magnesium chloride system reported by Hu and co-workers in 2022 ([(ONN)MgCl] where ONN = 1-O-2,4-Br-6-CH$_2$N(Dipp-C$_6$H$_3$)CH$_2$(pyr); **Figure 3.7**).[8]

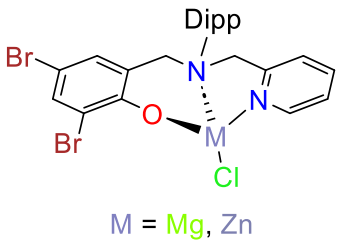

Figure 3.7 Comparable M^{2+} halide systems reported for the ROP of LA; diisopropyl-*aryl* abbreviated to Dipp for clarity.[8]

The authors report that this catalyst operates with two distinct stages of polymerisation. The second stage appeared much slower than the first (0.23–0.34 h^{-1} *vs*. 1.12–2.31 h^{-1} for $[LA]_0$:[**Mg**]$_0$ of 100–200 with 1 eq. BnOH in toluene at 130 °C); this was attributed to the aggregation of the initiator *in situ*. The aggregation number, determined via the reciprocal of the gradient of a plot of ln[k_{obs}] *vs*. ln[**Mg**], was found to be two.[8] The proposed formation of a $[LMgCl]_2$ dimer therefore makes the values reported for this second stage directly comparable to those of **2**; the order of magnitude difference between them (0.032 *vs*. 0.34 h^{-1}) could be the result of the different reaction temperatures and/or the increased steric bulk of **2** hindering monomer access to the Lewis acidic metal centre.

Table 3.2 ROP of *L*-LA using **2**/BnOH with [*L*-LA]$_0$:[**Mg**]$_0$:[BnOH]$_0$ = 50:1:1 at the stated temperature.[a]

Temp. (°C)	Time (h)	Conv. (%)[b]	k_{obs} (h^{-1})[c]	R^{2c}	M_n (GPC)[d]	M_n (calcd)[e]	M_w/M_n
60	239	87	0.0098 ± 0.004	0.986	7282	6104	1.09
70	114	89	0.026 ± 0.002	0.999	5717	6742	1.14
80	58	78	0.032 ± 0.001	0.993	6615	6546	1.14

[a]Conditions: [*L*-LA]$_0$:[**Mg**]$_0$:[BnOH]$_0$ = 50:1:1, [*L*-LA]$_0$ = 0.5 M in 0.6 mL benzene-d_6 at stated temperature. [b]Average reported; measured by ^{1}H NMR spectroscopic analyses. [c]First-order rate constant (k_{obs}) and R^2 were obtained from average plots of ln([*L*-LA]$_0$/[*L*-LA]$_t$) *vs*. time. [d]Determined by GPC in THF against PS standards using the appropriate Mark-Houwink corrections.[12] [e]Calculated M_n for PLA synthesised = (conv.(%) × [*L*-LA]$_0$/[**Mg**]$_0$) × 144.13 + (M_w of end groups).

In all cases unimodal GPC traces were recorded (**Figure 3.8**). At 60 ºC, the experimental molecular weight is higher than the calculated value implying only a portion of metal centres were active during the polymerisation (**Table 3.2**). The opposite trend was observed at 70 ºC; this suggests the occurrence of unwanted transesterification/chain termination reactions is now the dominant cause of the disparity in the values.[9, 20]

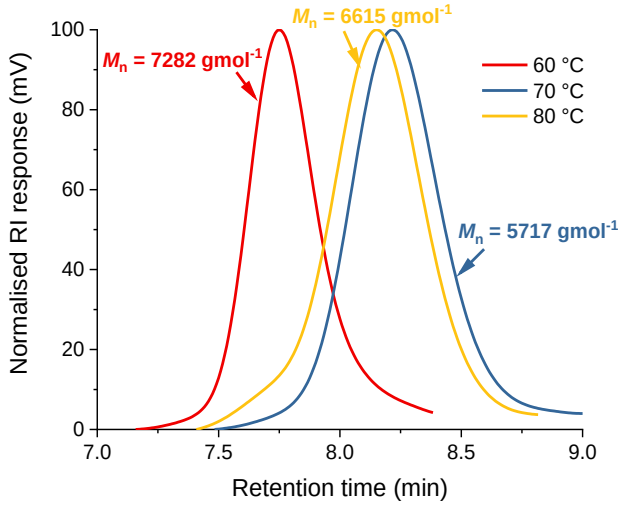

Figure 3.8 GPC traces of PLAs synthesised from the ROP of *L*-LA using **2**/BnOH. Red: 60 °C, M_n = 7282 gmol^{-1}, M_w/M_n = 1.09; blue: 70 °C, M_n = 5717 gmol^{-1}, M_w/M_n = 1.14; yellow: 80 °C, M_n = 6615 gmol^{-1}, M_w/M_n = 1.14. Conditions: [*L*-LA]$_0$:[**Mg**]$_0$:[BnOH]$_0$ = 50:1:1, [*L*-LA]$_0$ = 0.5 M in 0.6 mL benzene-d_6 at stated temperature.

From these results, and the construction of an Eyring plot (**Figure 3.9**), the thermodynamic activation parameters of the ring-opening polymerisation ($\Delta H^{\ddagger}$, $\Delta S^{\ddagger}$ and $\Delta G^{\ddagger}$) were determined to be 55 kJ mol^{-1}, –117 J K^{-1} mol^{-1} and 94–96 kJ mol^{-1}. The negative value for entropy implies the formation of a more ordered transition state upon monomer binding; this is a typical indication that the polymerisation is proceeding through a coordination insertion mechanism.[17, 19, 21] The nucleophilic attack on the adjacent carbonyl that follows is the cause of the moderate positive change in enthalpy.[14, 18, 19] The value for the Gibbs free energy of activation (96 kJ mol^{-1}) is higher than that

reported for lactide polymerisations catalysed using the industrial standard: stannous(II) 2-ethylhexanoate ($SnOct_2$; $\Delta G^{\ddagger}$ = 70.9 ± 1.5 kJ mol^{-1}).[22] The extra energy required when using the [H^{Dipp}LMgCl]$_2$ and BnOH system may be the direct result of the dimer's steric bulk hindering monomer access to the active sites (solid angle calculations suggest that ~75% of the metal centres are shielded by ligand atoms; **Chapter 2**). Similar activation parameters however, have been recorded for a chiral alkoxy-bridged dimeric indium catalyst ($\Delta H^{\ddagger}$ = 49 ± 2 kJ mol^{-1} and $\Delta S^{\ddagger}$= –140 ± 12 J K^{-1} mol^{-1})[18] as well as group 4 permethylindenyl chloride complexes when used in conjunction with benzyl alcohol co-initiator (62 < $\Delta H^{\ddagger}$ < 96 kJ mol^{-1} and –40 < $\Delta S^{\ddagger}$ < –155 J K^{-1} mol^{-1}).[9] The reliability of this data could have been improved if a fourth temperature had been tested.

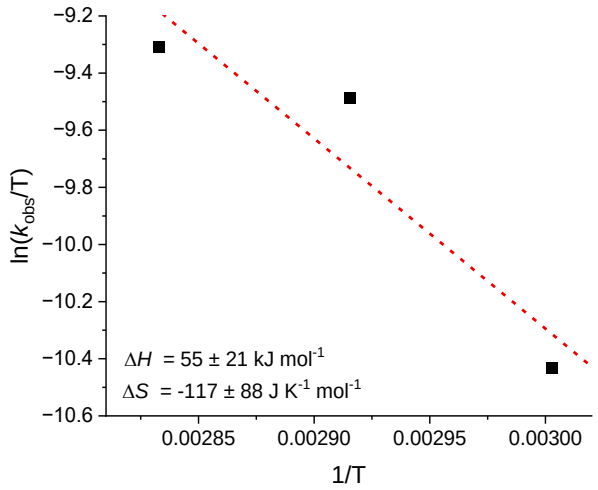

Figure 3.9 Eyring plot of ln(k_{obs}/T) *vs.* 1/T. Slope = −6654 ± 2491, Intercept = 9.7 ± 7.3. R^2 = 0.878. $\Delta H^{\ddagger}$ = 55 ± 21 kJ mol^{-1}, $\Delta S^{\ddagger}$ = −117 ± 88 J K^{-1} mol^{-1} for ROP of *L*-LA using **2**/BnOH.

3.3.3 Varying monomer stereochemistry

The effect of monomer stereochemistry was investigated by carrying out polymerisations using *rac*-, *L*-, *D*-, and *meso*-lactide at 60 °C with two eq. of benzyl alcohol co-initiator, [LA]$_0$/[**Mg**]$_0$ = 50 and [LA]$_0$ = 0.5 M. The results, presented in **Figure 3.10** and **Table 3.3**, were found to follow the trend: *rac*- < *L*- ≈ *D*- < *meso*-.

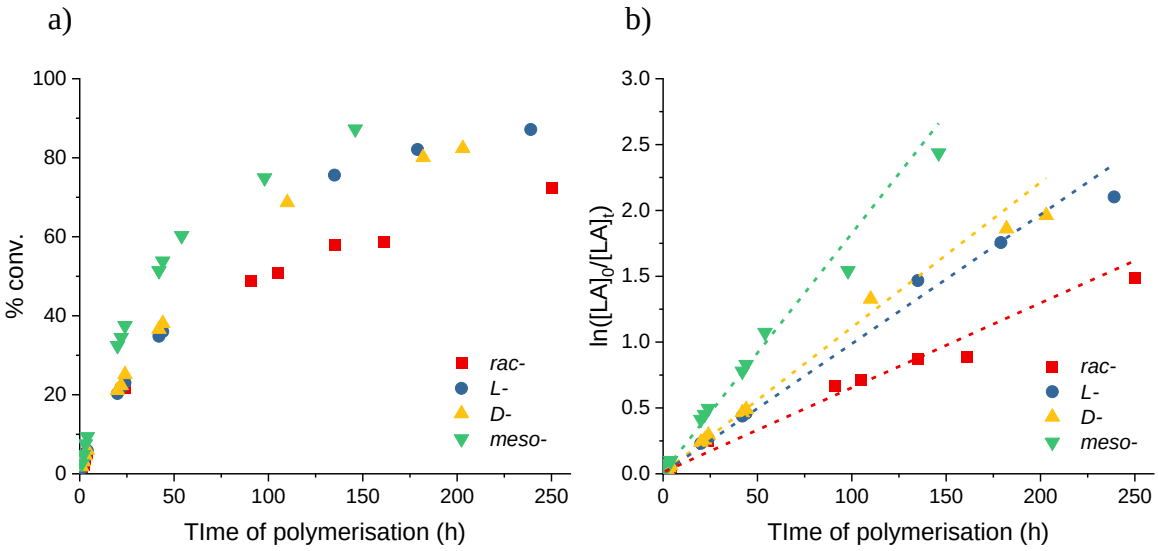

Figure 3.10 a) Plots of percentage conversion *vs.* time. b) Plots of $\ln([LA]_0/[LA]_t)$ *vs.* time using **2**/BnOH. Red squares: *rac*-LA (k_{obs} = 0.0064 h^{-1}. R^2 = 0.987); blue circles: *L*-LA (k_{obs} = 0.0098 h^{-1}. R^2 = 0.986); yellow up triangles: *D*-LA (k_{obs} = 0.0011 h^{-1}. R^2 = 0.991); green down triangles: *meso*-LA (k_{obs} = 0.018 h^{-1}. R^2 = 0.985). Conditions: $[LA]_0$:[**Mg**]$_0$:$[BnOH]_0$ = 50:1:1, $[LA]_0$ = 0.5 M in 0.6 mL benzene-d_6 at 60 °C.

The *meso*-LA polymerisation was shown to be the fastest (k_{obs} = 0.018 h^{-1}) achieving, on average, 87% conversion of 50 eq. in 146 h. This is due to the ground state of the strained *meso*-monomer lying higher in energy than its *L*- or *D*- counterparts, thus reducing the activation barrier of the polymerisation.[23, 24] Similar observations were recorded by Okuda *et al*. when conducting LA polymerisations with group 4-OSSO-tetradentate *bis*(phenolate) based catalysts (k_{obs} = 0.016 and 0.003 h^{-1} for *meso*- and *L*-lactide respectively at 100 °C with $[LA]_0$:$[M]_0$ = 100).[25] The polymerisations involving **2** and the *L*- and *D*- monomers were seen to progress at very similar rates (*L*-: 0.0098 h^{-1} and *D*-: 0.011 h^{-1}; k_L/k_D = 0.89 ≈ 1); this implies that the ligand environment shows no preference for either enantiomer. A similar k_L/k_D ratio was observed by Darensbourg and co-workers when employing a family of amino-acid based zinc catalysts in polymerising 50 eq. of LA at room temperature (k_L/k_D = 1.03–1.16 ≈ 1).[26] However, the recorded rate constants for these Zn(II) catalysts were between one and two orders of magnitude higher

(k_{obs} = 0.06–3.13 h^{-1}) than for the complex **2** and BnOH system.[26] The slower rate observed for the *rac*- monomer (achieving only 72% conversion of 50 eq. in 250 h) suggests that the formation of racemic linkages within the polymer chain hinders the propagation of the polymerisation.

In all cases, the polymeric materials produced had narrow, unimodal molecular weight distributions (**Table 3.3** and **Figure A.15**).

Table 3.3 ROP of LA using **2**/BnOH with $[LA]_0$:[**Mg**]$_0$:$[BnOH]_0$ = 50:1:1 at 60 °C.[a]

LA	Time (h)	Conv. (%)[b]	k_{obs} (h^{-1})[c]	R^{2c}	M_n (GPC)[d]	M_n (calcd)[e]	M_w/M_n
rac-	250	72	0.0064 ± 0.003	0.987	4295	6481	1.15
L-	239	87	0.0098 ± 0.004	0.986	7282	6104	1.09
D-	203	82	0.011 ± 0.003	0.991	7017	5910	1.09
meso-	146	87	0.018 ± 0.007	0.985	5693	5989	1.20

[a]Conditions: $[LA]_0$:[**Mg**]$_0$:$[BnOH]_0$ = 50:1:1, $[LA]_0$ = 0.5 M in 0.6 mL benzene-d_6 at 60 °C. [b]Average reported; measured by ^{1}H NMR spectroscopic analyses. [c]First-order rate constant (k_{obs}) and R^2 were obtained from average plots of $\ln([LA]_0/[LA]_t)$ *vs.* time. [d]Determined by GPC in THF against PS standards using the appropriate Mark-Houwink corrections.[12] [e]Calculated M_n for PLA synthesised = (conv.(%) × $[LA]_0$/[**Mg**]$_0$) × 144.13 + (M_w of end groups).

3.3.3.1 Polymer microstructure analysis

Homonuclear decoupled ^{1}H{^{1}H} NMR spectra of the polymeric products were used to determine their microstructure. The values of P_m and P_r (probability of forming *meso*- and *racemic*- linkages respectively) were calculated by evaluation of the observed tetrads with the probabilty analysis reported by Coudane and co-workers.[27]

The results showed that atactic PLA (P_r = 0.53) is formed from *rac*-LA; this suggests that the initiator does not impart a high level of stereocontrol. Contrastingly, when *meso*-LA is polymerised, the resultant polymeric material is heterotactic enriched (P_m = 0.70). This indicates that the polymerisations, catalysed by **2** and BnOH, are chain-end controlled

and that the stereocentre of the last monomer unit of the propagating chain favours *meso*-enchainment.[16, 28] This agrees with the proposal that the formation of racemic linkages was the rate limiting factor of the *rac*-LA polymerisations.

The polymerisation of *L*-LA proceeded without epimerisation (random inversion of stereochemistry at a single chiral centre)[29] to produce purely isotactic PLA (P_m = 1.00); this was confirmed by a single resonance in the *methine* region of the $^1H\{^1H\}$ NMR spectrum (**Figure 3.11**).[9, 10, 14, 17, 30] Identical results were obtained when *D*-LA was employed as the monomer.

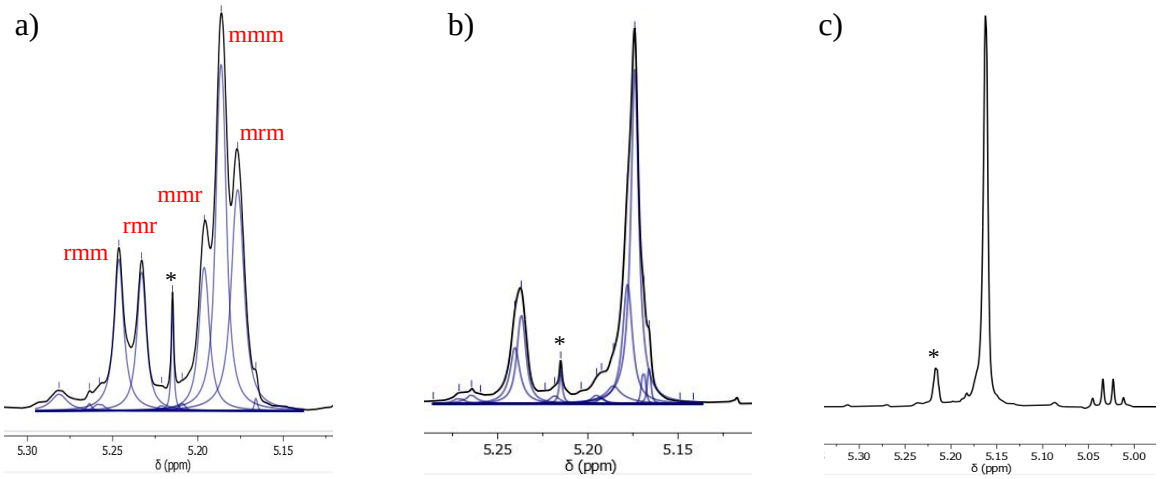

Figure 3.11 $^1H\{^1H\}$ NMR spectra of the methine protons in the PLA produced from: a) *rac*-LA (P_r = 0.53); b) *meso*-LA (P_m = 0.70) and c) *L*-/*D*-LA (P_m = 1.00). Conditions: $[LA]_0$:$[\mathbf{Mg}]_0$:[BnOH] = 50:1:1, $[LA]_0$ = 0.5 M in 0.6 mL benzene-d_6 at 60 °C. * denotes an artefact from NMR "BASH" experiment set-up.

3.3.4 Initiator concentration dependency

In order to determine the kinetic order dependence on catalyst concentration, polymerisations of *L*-LA with **2** and BnOH were carried out at 80 °C using various monomer to catalyst ratios. The concentration of *L*-LA was held constant at 0.5 M while that of the catalyst was varied to provide the ratio of $[L\text{-LA}]_0$:$[\mathbf{Mg}]_0$ = 10, 50, 200 and 500. In all cases, linear plots of $\ln([L\text{-LA}]_0/[L\text{-LA}]_t)$ *vs.* time were observed which

confirms a first-order dependence on monomer concentration (**Figure 3.12** and **Table 3.4**).

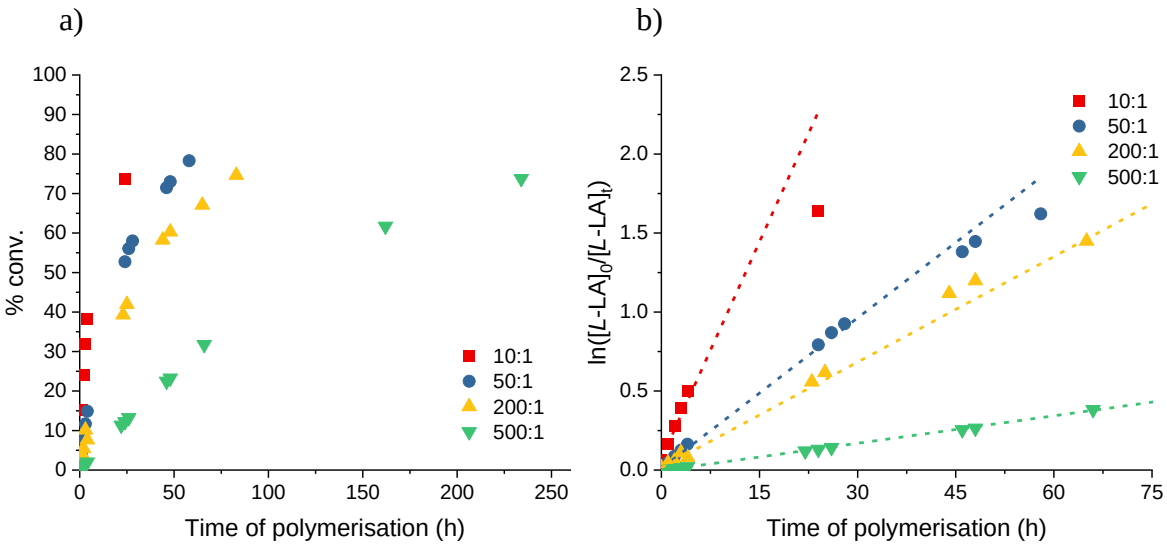

Figure 3.12 a) Plots of percentage conversion *vs.* time. b) Plots of ln([*L*-LA]$_0$/[*L*-LA]$_t$) *vs.* time using **2**/BnOH. Red squares: 10:1 (k_{obs} = 0.091 h^{-1}. R^2 = 0.950); blue circles: 50:1 (k_{obs} = 0.032 h^{-1}. R^2 = 0.993); yellow up triangles: 200:1 (k_{obs} = 0.022 h^{-1}. R^2 = 0.971) and green down triangles: 500:1 (k_{obs} = 0.0058 h^{-1}. R^2 = 0.999). Conditions: [*L*-LA]$_0$:[**Mg**]$_0$ as stated, [*L*-LA]$_0$ = 0.5 M in 0.6 mL benzene-d_6 at 80 °C.

The observed rate constants, k_{obs}, were found to increase in parallel with initiator concentration (k_{obs} = **500:1**: 0.0058 < **200:1**: 0.022 < **50:1**: 0.032 < **10:1**: 0.091 h^{-1}); this is due to the increased number of active sites associated with greater [**Mg**]$_0$ content.[31, 32] The opposite trend was observed with respect to experimental polymer molecular weights; the recorded M_n values increased with decreasing catalyst concentration as a result of the increased probability of propagation ($M_{n,(GPC)}$ = 1079, 6615, 12 631 and 22 791 gmol^{-1} for [*L*-LA]$_0$/[**Mg**]$_0$ ratios of 10:1, 50:1, 200:1 and 500:1 respectively). Similar results were also reported for dinuclear phenoxy-thioether ($M_{n,(GPC)}$ ranged from 2900–10 300 gmol^{-1} for ratios between 20–100:1; **Figure 3.2c**) and dimeric benzylalkoxide magnesium catalysts ($M_{n,(GPC)}$ ranged from 4300–84 800 gmol^{-1} for

ratios between 25–1000:1; **Figure 3.2b**).[2, 3, 15] In all cases involving **2** however, the experimental molecular weights were found to be lower than the theoretical values, indicating the occurrence of inter- and intra- molecular transesterification (**Table 3.4**). The disparity between the values grows with increasing [*L*-LA]$_0$/[**Mg**]$_0$ ratio as the longer reaction time provides more opportunities for the side reactions to occur.

Table 3.4 ROP of *L*-LA using **2**/BnOH with various ratios of [*L*-LA]$_0$:[**Mg**]$_0$.[a]

[LA]$_0$:[**Mg**]$_0$	Time (h)	Conv. (%)[b]	k_{obs} (h^{-1})[c]	R^{2c}	M_n (GPC)[d]	M_n (calcd)[e]	M_w/M_n
10:1	24	74	0.091 ± 0.001	0.950	1079	1445	1.29
50:1	58	78	0.032 ± 0.001	0.993	6615	6546	1.14
200:1	83	75	0.022 ± 0.001	0.971	12 631	21 889	1.32
500:1	234	73	0.0058 ± 0.003	0.999	22 791	53 256	1.29

[a]Conditions: [*L*-LA]$_0$:[**Mg**]$_0$ as stated; [*L*-LA]$_0$ = 0.5 M in 0.6 mL benzene-d_6 at 80 °C. [b]Average reported; measured by ^{1}H NMR spectroscopic analyses. [c]First-order rate constant (k_{obs}) and R^2 were obtained from average plots of ln([*L*-LA]$_0$/[*L*-LA]$_t$) *vs.* time. [d]Determined by GPC in THF against PS standards using the appropriate Mark-Houwink corrections.[12] [e]Calculated M_n for PLA synthesised = (conv.(%) × [*L*-LA]$_0$/[**Mg**]$_0$) × 144.13 + (M_w of end groups).

A plot of −ln(k_{obs}) *vs.* −ln[**Mg**]$_0$ was then generated to determine the order with respect to catalyst (**Figure 3.13a**); this gave a linear relationship with a gradient of 0.64 ± 0.13. This value and its associated error imply a first-order dependency on catalyst concentration. The non-integer value of the gradient may result from incomplete conversion to the active *bis*(alkoxide) species *in situ*. Assuming that the concentration of the initiator remains constant throughout the reaction, the following rate law can be derived for the ROP of lactide catalysed by **2** and BnOH:

$$-\frac{d[\mathrm{LA}]}{dt} = k_p[\mathrm{LA}][\mathbf{Mg}] \qquad \text{where} \qquad k_{obs} = k_p[\mathbf{Mg}] \qquad \textbf{Equation 3.2}$$

Comparable dimeric magnesium systems were also found to exhibit the same rate equation.[3, 15] This overall rate law, along with the computed thermodynamic parameters

of the reaction, is consistent with the typical coordination-insertion mechanism.[33] An activated monomer pathway for this system however, cannot be completely ruled out as dependence on co-initiator concentration was not investigated.

The propagation rate constant (k_p), present in the proposed rate law, was calculated via a plot of k_{obs} *vs.* [**Mg**]$_0$, to be 3.19 ± 0.39 M^{-1} h^{-1} (**Figure 3.13b**). This value is much lower than that reported for a *bis*(magnesium) system, with pre-formed alkoxide initiating groups, that follows the same rate equation (k_p = 416 M^{-1} h^{-1} for [(NNO)Mg(μ-OCH_2Ph)]$_2$).[15] It is however, comparable to the value of k_p computed for the second stage of LA polymerisations using the aggregating [(ONN)MgCl]$_x$ species reported by Hu and co-workers (k_p = 4.32 M^{-1} h^{-1}).[8]

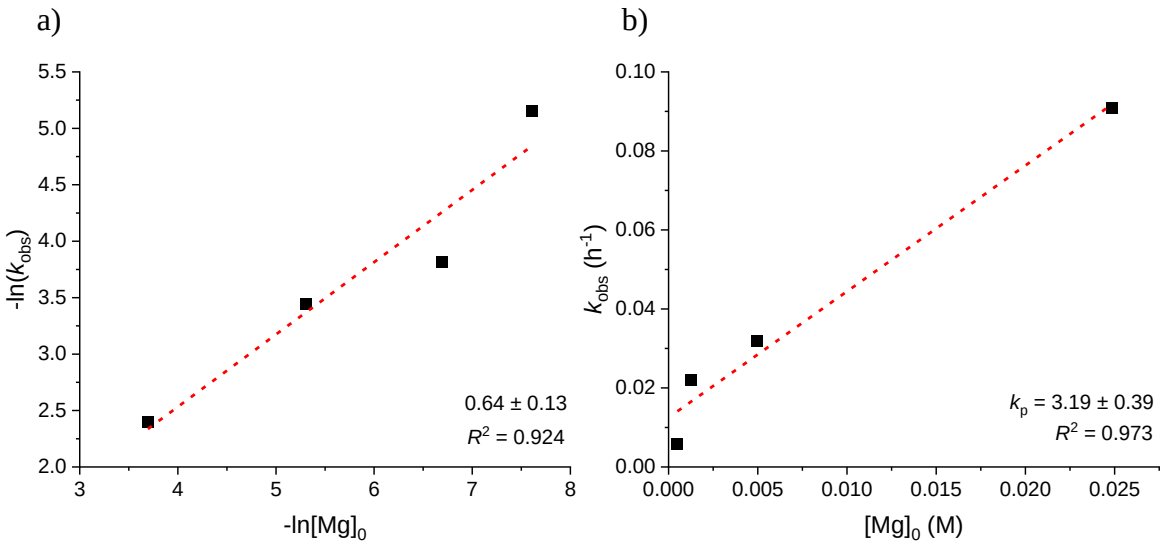

Figure 3.13 a) Plot of –ln(k_{obs}) *vs.* –ln[**Mg**]$_0$ for ROP of *L*-LA using **2**/BnOH shows that the order of reaction with respect to [**Mg**]$_0$ is equal to 0.64 ± 0.13; R^2 = 0.924. b) Plot of k_{obs} *vs.* [**Mg**]$_0$ for ROP of *L*-LA using **2** with BnOH shows k_p = 3.19 ± 0.39 M^{-1} h^{-1}; R^2 = 0.973.

3.3.5 Polymer end group analysis

Matrix-assisted, laser desorption/ionisation time of flight (MALDI-TOF) mass spectrometry was used to determine the end groups of the polymers produced using the [H^{Dipp}LMgCl]$_2$ and BnOH catalytic system; a representative example is shown in **Figure**

3.14. The mass spectrum is consistent with PLA containing the expected –OCH_2Ph and –OH end groups.

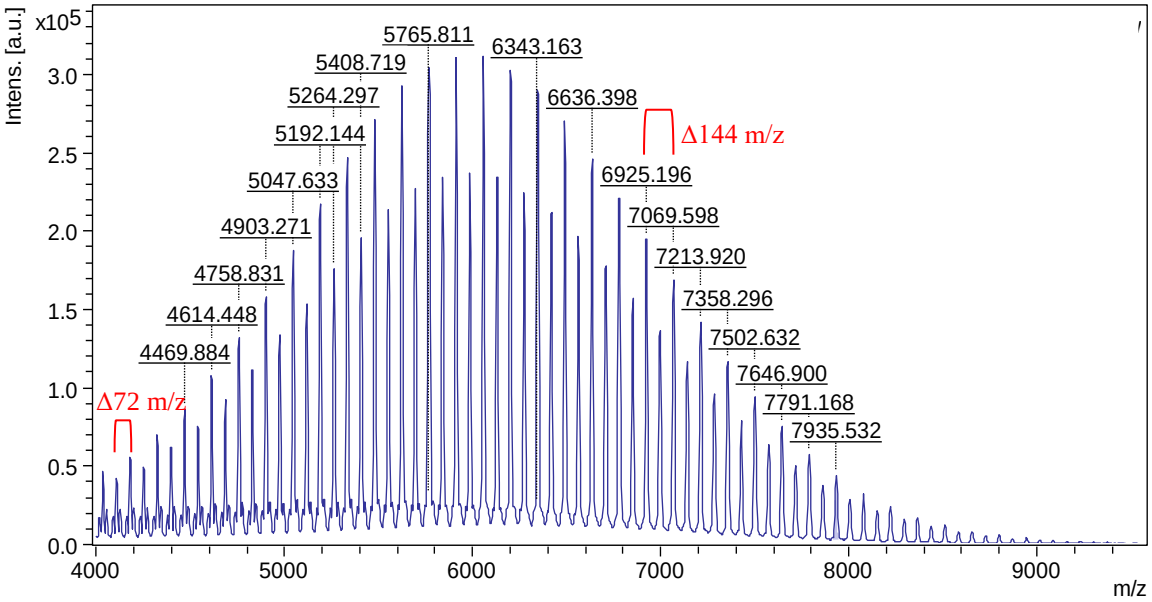

Figure 3.14 MALDI-TOF mass (m/z) spectrum of PLA produced using **2**/BnOH. Conditions: [*D*-LA]$_0$:[**Mg**]$_0$:[BnOH]$_0$ = 50:1:1, [*D*-LA]$_0$ = 0.5 M, 0.6 mL benzene-d_6, 60 °C. M_w/M_n = 1.09.

For example, the peak centred at 5047.6 gmol^{-1} is attributed to –OCH_2Ph/–OH terminated PLA, comprising of 34 units of LA with K^+ [144.13(34) + 108.14 + 39.1]. The benzyl alcohol end group was also detected in the ^1H and $^{13}C\{^1H\}$ NMR spectra (examples shown in **Figure 3.15** and **Figure A.17**); a multiplet at δ 4.36 ppm corresponds to the –OC***H***(CH_3)OH proton and the aromatic signals of the –OCH***Ph***$_2$ group appear at δ 7.29–7.38 ppm.

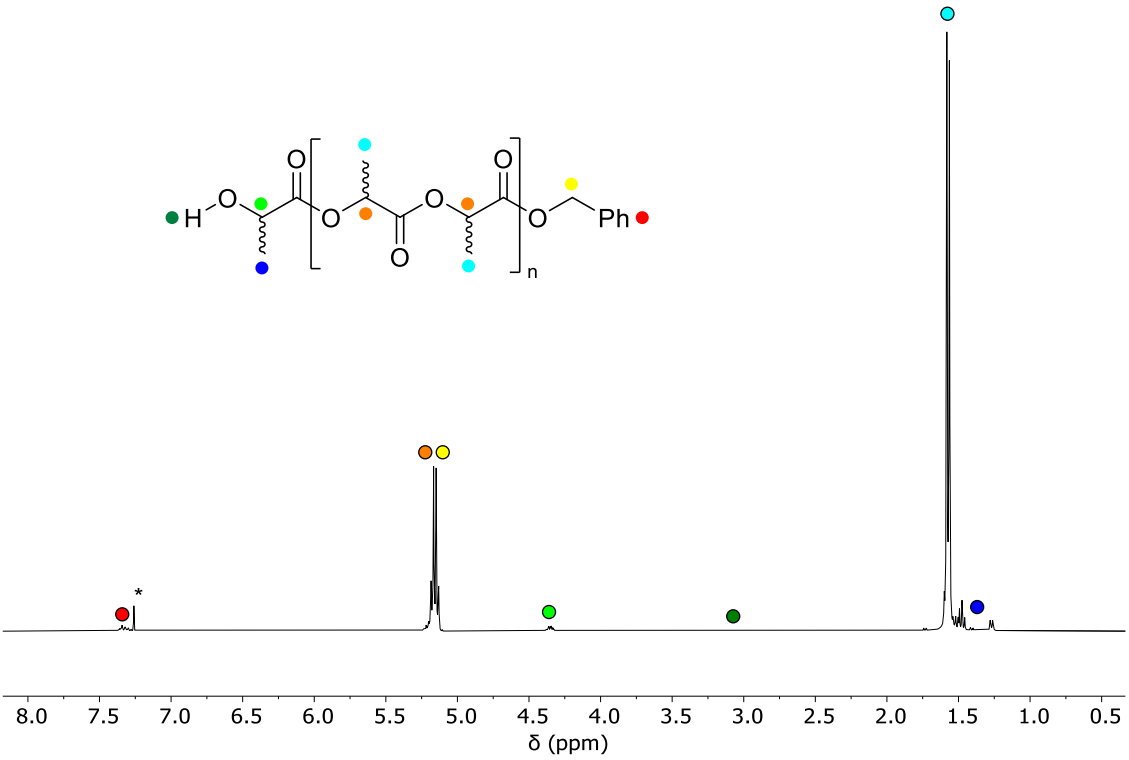

Figure 3.15 ^{1}H NMR spectrum (*chloroform-d_1, 400 MHz, 298 K) of PLA produced using **2**/BnOH. Polymerisation conditions: [*L*-LA]$_0$:[**Mg**]$_0$:[BnOH]$_0$ = 50:1:1, [*L*-LA]$_0$ = 0.5 M, 0.6 mL benzene-d_6, 60 °C. M_w/M_n = 1.09.

In the mass spectrum, the peaks are separated by 72 *m*/*z*; this is typically indicative of transesterification reactions.[9, 10, 14, 17, 21] However, in this case the peaks that differ by 72 *m*/*z* form two distinct envelopes (one of high and one of low intensity). This implies that two different types of polymer samples were being consistently produced during the reaction. A 2004 report by Kricheldorf and co-workers, describing the use of bismuth(III) acetate as a LA ROP initiator, suggests that the different species formed are polymers containing odd- and even- numbered chains (consider LA to be a repeating unit of 72 *m*/*z* rather than 144 *m*/*z*).[34] The close proximity of two active catalytic metal centres is thought to be the cause of this process as it facilitates an intramolecular reaction between the last activated lactide unit of one polymer and the chain end of the other (**Scheme 3.1**).[34] This proposed intramolecular reaction is directly applicable to the [H^{Dipp}LMgCl]$_2$ and BnOH

system as a result of the initiator being bimetallic with a relatively small intermetallic distance of 3.06 Å (compared to other literature compounds containing a similar Mg_2O_2 diamond core: 2.862(2)–3.779 Å).[2, 35, 36]

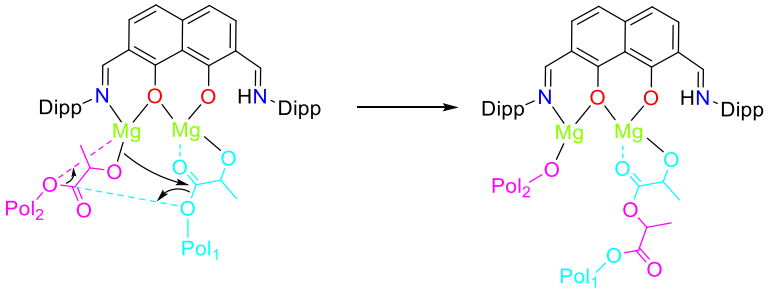

Scheme 3.1 The intramolecular reaction that is thought to occur during **2**/BnOH catalysed polymerisations causing the formation of both odd- and even- numbered polymer chains.[34] The second "NOON" and chloride ligands have been omitted for clarity in addition to the diisopropyl-*aryl* groups being abbreviated to "Dipp".

3.4 Preliminary lactide polymerisation studies using ^{Dipp}LM(thf)$_x$ (M = Ca (3), Sr (4), Ba (5))

As discussed in **Chapter 2** (**Section 2.4**), the speciation of complexes **3(thf)**$_2$, **4(thf)** and **5(thf)** is not well-defined. These complexes are dimeric in the solid-state ([**3(thf)**$_2$/**4(thf)**/**5(thf)**]$_2$), but exist as an equilibrium mixture of monomer and dimer in solution. In order to collect consistently comparable results therefore, the stoichiometries in the following polymerisation studies were calculated with respect to the molecular weight of the monomeric, monometallic alkaline-earth systems. As a result, and for simplicity, the initiators will be referred to as **3** (Ca), **4** (Sr) and **5** (Ba) throughout.

Initial testing of complexes **3**, **4** and **5** as initiators in the ring-opening polymerisation of lactide showed that all three systems were capable of polymerising 500 eq. of *L*-LA at ambient temperatures (**Figure 3.16** and **Table 3.5**).

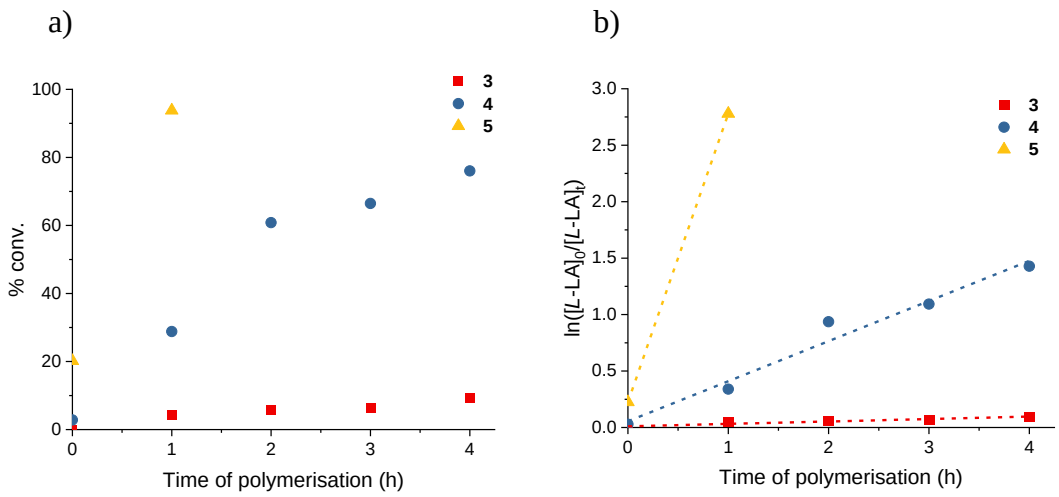

Figure 3.16 a) Plots of percentage conversion *vs.* time. b) Plots of ln([*L*-LA]$_0$/[*L*-LA]$_t$) *vs.* time. Red squares: cat = **3** (k_{obs} = 0.018 h^{-1}. R^2 = 0.999); blue circles: cat = **4** (k_{obs} = 0.29 h^{-1}. R^2 = 0.970); yellow up triangles: cat = **5** (no k_{obs} or R^2 could be recorded). Conditions: [*L*-LA]$_0$:[**M**]$_0$= 500:1, [*L*-LA]$_0$ = 0.5 M in 0.6 mL benzene-d_6 at 40 °C.

Table 3.5 ROP of *L*-LA using **3-5** with [*L*-LA]$_0$:[**M**]$_0$ = 500:1 in benzene-d_6 at 40 °C.[a]

M	Time (h)	Conv. (%)[b]	k_{obs} (h^{-1} or M^{-1} h^{-1})[c]	R^{2c}	M_n (GPC)[e]	M_n (calcd)[f]	M_w/M_n
Ca (3(thf)$_2$)	118	88	0.018 ± 0.02[c]	0.999	55 276	60 705	1.59
Sr (4(thf))	5	66	0.36 ± 0.001[c] 1.57 ± 0.2[d]	0.970 0.971	34 403	54 784	1.69
Ba (5(thf))	1	94	-	-	40 556	67 590	1.55

[a]Conditions: [*L*-LA]$_0$:[**M**]$_0$ = 500:1, [*L*-LA]$_0$ = 0.5 M in 0.6 mL benzene-d_6 at 40 °C. [b]Measured by ^{1}H NMR spectroscopic analyses. [c]First-order rate constant (k_{obs}; h^{-1}) and R^2 were obtained from plots of ln([*L*-LA]$_0$/[*L*-LA]$_t$) *vs.* time. [d]Second-order rate constant (k_{obs}; M^{-1} h^{-1}) and R^2 were obtained from plots of 1/[*L*-LA]$_t$ *vs.* time. [e]Determined by GPC in THF against PS standards using the appropriate Mark-Houwink corrections.[12] [f]Calculated M_n for PLA synthesised = (conv.(%) × [*L*-LA]$_0$/[**M**]$_0$) × 144.13 + (M_w of end groups).

The activity of the catalysts followed the trend: Ba > Sr > Ca with 94%, 29% and 4% conversion after 1 h for **5**, **4** and **3** respectively. Similar patterns have been widely reported and are rationalised by the larger cations being less sterically congested and

having more labile bonding – both of which result in lower kinetic barriers towards monomer coordination/insertion.[6, 7, 37, 38] The reaction catalysed by **5** was rapid thus preventing the accurate acquisition of kinetic data (even at higher $[L\text{-LA}]_0/[\mathbf{Ba}]_0$ ratios). In contrast, plots of $\ln([L\text{-LA}]_0/[L\text{-LA}]_t)$ *vs.* time for the Ca (**3**) and Sr (**4**) initiated polymerisations, enabled experimental rate constants to be determined (**Figure 3.17b**). For **3**, the first-order rate constant was computed to be 0.018 h^{-1}; this value aligns with others reported for heavier alkaline-earth *bis*(diphenylphosphinothioic/selenoic) amine catalysts (k_{obs} range from 0.15–0.43 h^{-1} for Ca; 0.15–1.21 h^{-1} for Sr and 0.906–1.54 h^{-1} for Ba for $[LA]_0/[\mathbf{M}]_0 = 200$; **Figure 3.4**).[7, 38] The kinetic data for the analogous strontium system had a much poorer correlation with the first-order linear fit (R^2 = 0.970). This suggested that the polymerisation may be second-order with respect to monomer concentration and thus the true rate constant is 1.57 $M^{-1}\,h^{-1}$ under these conditions. The second-order nature of the Sr-catalysed polymerisations was confirmed, via plots of $1/[LA]_t$ *vs.* time, in further experiments (*vide infra*; **Section 3.4.1**).

The polymerisations using **3**, **4** and **5** all proceeded with moderate control; this was reflected in broad molecular weight distributions (**Figure A.18**) indicated by intermediate polydispersity indices (M_w/M_n = 1.55–1.69; **Table 3.5**). These values are comparable to those reported for other heavier alkaline-earth, monometallic initiators: M_w/M_n = 1.01–1.57.[7, 38] The experimental molecular weights however, are slightly lower than the previously documented range for the polymerisation of 500 eq. using Ca, Sr and Ba systems (67 000–74 100 $gmol^{-1}$).[7, 38] There is a relatively good agreement between the experimental and calculated molecular weights (based on the monometallic initiating unit propagating a single chain) in the case of **3** (55 276 *vs.* 60 705 $gmol^{-1}$). However, as the size of the cation increases, the agreement between these values becomes poorer (Δ% *vs.* $M_{n,(calcd)}$ = 37 for **4** and Δ% = 40 for **5**); this is most likely due to the larger ions being

able to host multiple propagating chains, each with a length that is a fraction of the calculated value. In fact, chain count calculations (**Equation 3.3**) confirm, that on average, more than one polymer chain was growing per monometallic initiator in both the strontium (**4**, *av*. 1.59) and barium (**5**, *av*. 1.67) systems. The non-integer averages reflect the nature of the poor speciation of the active species i.e. the polymerisation solution is likely to be a simultaneous mixture of multiple chains per monometallic initiator (cat = **4**/**5**) and single/multiple chains per metal centre of the dimeric form of the catalyst (cat = [**4**/**5**]$_2$). For simplicity, the results of the chain count calculations (i.e. two chains per monometallic initiator) were assumed for all subsequent theoretical molecular weight calculations for the **4** and **5** systems.

$$\mu mol_{pol} \div \mu mol_{Ca} = \frac{chains}{metal} \qquad \textbf{Equation 3.3}$$

3.4.1 Introduction of co-initiator

Addition of 1 eq. of benzyl alcohol as co-initiator was tested for the calcium (**3**) and strontium (**4**) systems. As the catalysts in these reactions contain no pre-formed initiating group(s), it is likely that the exogenous alcohol is responsible for the rapid nucleophilic ring-opening of the metal-activated LA. This activated monomer pathway (see **Chapter 1**, **Section 1.4.1.2.1**) was confirmed by the presence of –OCH$_2$Ph/-OH end groups in the ^{1}H and ^{13}C{^{1}H} NMR spectra of the isolated PLA (**Figures A.19-20**).

Kinetic studies revealed that the dependency on monomer concentration varied with respect to which alkaline-earth metal was employed. In the case of the binary calcium-based system (**3**/BnOH), linear plots of ln([*L*-LA]$_0$/[*L*-LA]$_t$) *vs*. time indicated a first-order dependence on [*L*-LA] (k_{obs} = 0.14 h^{-1} ~ 8-fold increase *vs*. no co-initiator; **Figure 3.17a**). Analogous plots for the strontium system (**4**) revealed non-linear relationships implying that the order with respect to monomer concentration exceeds one (**Figure**

A.22b). A rare, yet not unprecedented, second-order dependency was however confirmed via linear plots of $1/[L\text{-LA}]_t$ *vs.* time (**Figure 3.17b**).[4, 9, 39-44] This suggests that two monomers are required per active site for the reaction to proceed.[40] Such a monomer-triggering polymerisation mechanism has been postulated by Ystenes and involves a monomer-insertion transition state which can only be by-passed if a second monomer molecule enters the coordination sphere.[45]

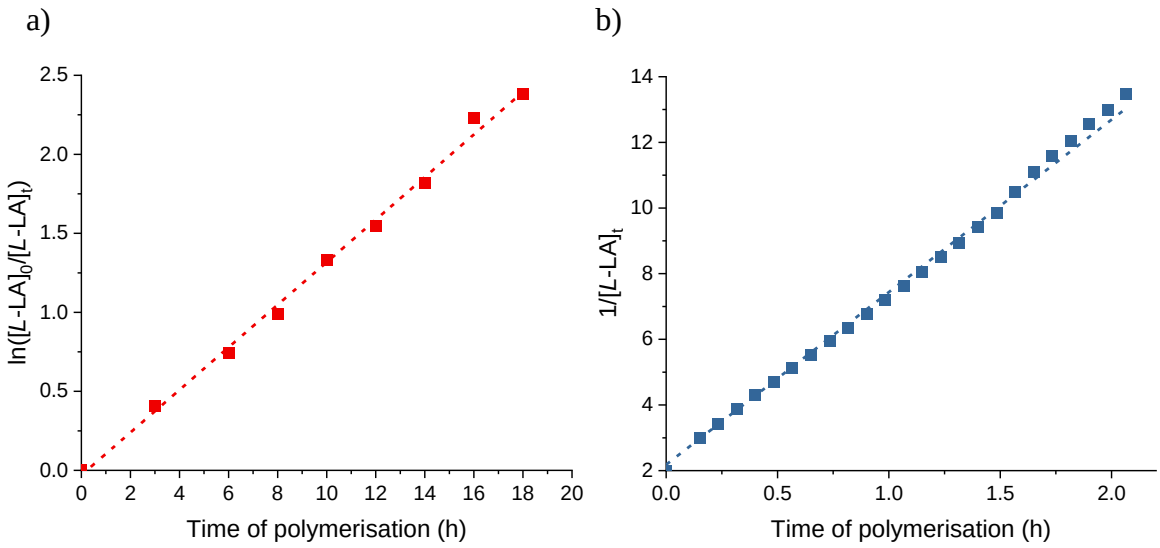

Figure 3.17 a) Plot of $\ln([L\text{-LA}]_0/[L\text{-LA}]_t)$ vs. time for *L*-LA polymerisation using cat = **3**/BnOH (k_{obs} = 0.14 h^{-1}. R^2 = 0.992). b) Plot of $1/[L\text{-LA}]_t$ *vs.* time for *L*-LA polymerisation using cat = **4**/BnOH (k_{obs} = 5.30 M^{-1} h^{-1}. R^2 = 0.999). Conditions: $[L\text{-LA}]_0$:[**M**]$_0$:$[BnOH]_0$= 500:1:1, $[L\text{-LA}]_0$ = 0.5 M in 0.6 mL benzene-d_6 at 40 °C.

In the presence of BnOH, the second-order rate constant is ~3-fold faster than in the absence of co-initiator (k_{obs} = 5.30 *vs.* 1.57 M^{-1} h^{-1}; **Table 3.6**). The same second-order dependency on monomer concentration and comparable experimental rate constant (k_{obs} = 6.6 M^{-1} h^{-1}) were observed for [(SalenMe)Mg(μ-OCH_2Ph)]$_2$ at 25 °C with $[LA]_0$/[**Mg**]$_0$ = 42 (SalenMe; 1-O-2,4-Me-6-CH=N(C_6H_4)N=C(C_6H_4)-*o*-OMe).[39] A much higher second-order rate constant was recorded however for a trimetallic β-diketiminato (BDI) zinc alkoxide species ([(BDI-OMe)Zn(μ-OCH_2Ph)]$_2$

Zn(μ-OCH$_2$Ph)$_2$ – k_{obs} = 118.8 M^{-1} h^{-1} at 25 °C with [LA]$_0$/[**Zn**]$_0$ = 200 (BDI-OMe = N-1,3-Me-C$_3$H-N).[44]

Table 3.6 ROP of *L*-LA using **3-4**/BnOH with [*L*-LA]$_0$:[**M**]$_0$:[BnOH]$_0$ = 500:1:1 in benzene-d_6 at 40 °C.[a]

M	Time (h)	Conv. (%)[b]	k_{obs} (h^{-1} or M^{-1} h^{-1})	R^{2c}	M_n (GPC)[e]	M_n (calcd)[f]	M_w/M_n
Ca (3(thf)$_2$)	18	91	0.14 ± 0.003[c]	0.992	20 722	52 809	1.23
Sr (4(thf))	2	85	0.78 ± 0.04[c] 5.30 ± 0.03[d]	0.933 0.999[d]	31 197	30 736[g]	1.38

[a]Conditions: [*L*-LA]$_0$:[**M**]$_0$:[BnOH]$_0$ = 500:1:1, [*L*-LA]$_0$ = 0.5 M in 0.6 mL benzene-d_6 at 40 °C. [b]Average reported; measured by ^{1}H NMR spectroscopic analyses. [c]First-order rate constant (k_{obs}: h^{-1}) and R^2 were obtained from average plots of ln([*L*-LA]$_0$/[*L*-LA]$_t$) *vs.* time. [d]Second-order rate constant (k_{obs}: M^{-1} h^{-1}) and R^2 were obtained from average plots of 1/[*L*-LA]$_t$ *vs.* time. [e]Determined by GPC in THF against PS standards using the appropriate Mark-Houwink corrections.[12] [f]Calculated M_n for PLA synthesised = (conv.(%) × [*L*-LA]$_0$/[**M**]$_0$) × 144.13 + (M_w of end groups). [g]Calculated assuming that two polymer chains propagate per metal centre.

When using initiator **4** with BnOH, there is a good agreement between experimental and theoretical molecular weights assuming that two polymer chains grow per monometallic initiator (31 197 *vs.* 30 736 gmol^{-1}; **Figure 3.18** and **Table 3.6**). Conversely, when catalyst **3** was employed with BnOH, a large disparity in experimental and theoretical molecular weights was recorded (20 772 *vs*. 52 809 gmol^{-1}), assuming that the smaller metal centre still hosts only a single polymer chain. The reduction in experimental molecular weight may be due to free benzyl alcohol acting as a chain transfer agent.[9, 14] However, since this behaviour was not observed for **4**/BnOH, it is alternatively postulated that the addition of co-initiator to **3** results in a change in mechanistic regime to allow two polymer chains to grow per monometallic unit (i.e. it now behaves more similarly to **4**). If this is the case, the experimental and computed values are more comparable: 20 722 *vs*. 32 790 gmol^{-1}.

The unusual second-order kinetics observed with **4** prompted further investigation. Subsequent polymerisations were carried out in the absence of co-initiator, in order to investigate the mechanism of the polymerisations catalysed solely by **4**.

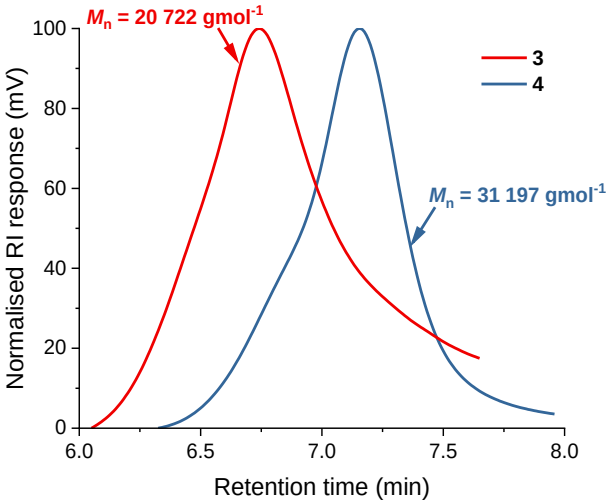

Figure 3.18 GPC traces of PLAs synthesised from the ROP of *L*-LA. Red: cat = **3**/BnOH, M_n = 20 772 gmol^{-1}, M_w/M_n = 1.23; blue: cat = **4**/BnOH, M_n = 31 197 gmol^{-1}, M_w/M_n = 1.38. Conditions: [*L*-LA]$_0$:[**M**]$_0$:[BnOH]$_0$ = 500:1:1, [LA]$_0$ = 0.5 M in 0.6 mL benzene-d_6 at 40 °C.

3.4.2 Further studies with ^{Dipp}LSr(thf)/[^{Dipp}LSr(thf)]$_2$ (4)

3.4.2.1 Variable temperature studies

The effect of temperature on the rate of polymerisation using **4** was probed (**Figure 3.19** and **Table 3.7**). Polymerisations were run between 40 and 70 °C with no co-initiator, [*L*-LA]$_0$/[**Sr**]$_0$ = 500 and [*L*-LA]$_0$ = 0.5 M and in all cases, linear plots of 1/[*L*-LA]$_t$ were observed. Unusually, no distinct increase in the reaction rate was observed between 40 and 60 °C (i.e. the experimental second-order rate constants are all within error; **Table 3.7**). A spike in the rate, however, was observed when going from 60 to 70 °C (0.91 *vs.* 2.2 M^{-1} h^{-1}); this implies that only at this highest temperature did the system have sufficient energy to easily overcome the activation barriers of the polymerisation.

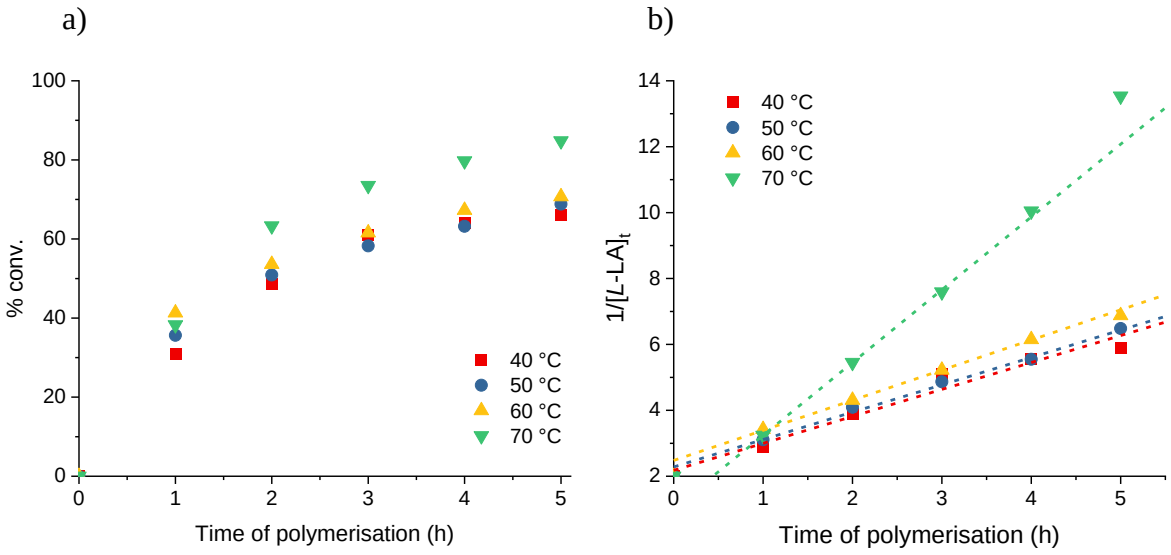

Figure 3.19 a) Plots of percentage conversion *vs.* time. b) Plots of $1/[L\text{-LA}]_t$ *vs.* time for *L*-LA polymerisation using **4**. Red squares: 40 °C (k_{obs} = 0.82 M^{-1} h^{-1}. R^2 = 0.963); blue circles: 50 °C (k_{obs} = 0.83 M^{-1} h^{-1}. R^2 = 0.993); yellow up triangles: 60 °C (k_{obs} = 0.91 M^{-1} h^{-1}. R^2 = 0.992); green down triangles: 70 °C (k_{obs} = 2.20 M^{-1} h^{-1}. R^2 = 0.999). Conditions: $[L\text{-LA}]_0$:[**Sr**]$_0$= 500:1, $[L\text{-LA}]_0$ = 0.5 M in 0.6 mL benzene-d_6 at stated temperature.

Table 3.7 ROP of *L*-LA using **4** with $[L\text{-LA}]_0$:[**Sr**]$_0$ = 500:1 in benzene-d_6 at stated temperature.[a]

Temp. (°C)	Time (h)	Conv. (%)[b]	k_{obs} (M^{-1} h^{-1})[c]	R^2[c]	M_n (GPC)[d] **1**[e]	M_n (GPC)[d] **2**[f]	M_n (calcd)[g]	M_w/M_n **1**[e]	M_w/M_n **2**[f]	*H*:*L*[h]
40	5	66	0.82 ± 0.08	0.963	23 766	2401	27 392	1.52	1.39	85:15
50	5	75	0.83 ± 0.03	0.993	29 961	2001	26 405	1.68	1.61	60:40
60	5	71	0.91 ± 0.04	0.992	26 468	1888	24 560	1.59	1.67	58:42
70	5	85	2.20 ± 0.01	0.999	31 845	1945	31 478	1.56	1.70	56:44

[a]Conditions: $[L\text{-LA}]_0$:[**Sr**]$_0$ = 500:1, $[L\text{-LA}]_0$ = 0.5 M in 0.6 mL benzene-d_6 at stated temperature. [b]Average reported; measured by ^{1}H NMR spectroscopic analyses. [c]Second-order rate constant (k_{obs}) and R^2 were obtained from average plots of $1/[L\text{-LA}]_t$ *vs.* time. [d]Determined by GPC in THF against PS standards using the appropriate Mark-Houwink corrections.[12] [e]Data corresponding to the higher molecular weight fraction. [f]Data corresponding to the lower molecular weight fraction. [g]Calculated M_n for PLA synthesised (assuming two polymer chains propagate per metal centre) = [(conv.(%) × $[L\text{-LA}]_0$/[**Sr**]$_0$) × 144.13]/2. [h]Average higher:lower (H:L) molecular weight fraction ratio determined from area of peaks in average GPC trace.

The nature of the rate determining step, which is responsible for the polymerisation activation barriers, depends on the mechanism of the reaction. As this catalyst system contains no direct initiating group(s) or co-initiator, the conventional coordination-insertion or activated monomer mechanisms can be disregarded. It is therefore proposed that the polymerisation propagates via an anionic mechanism which is initiated by deprotonation of the monomer by the aryloxyimine ligand (**Scheme 3.2**). This is supported by MALDI-TOF mass spectrometric and ^{1}H NMR spectroscopic end group analysis (**Section 3.4.2.4**). Similar anionic mechanisms are typical for simple alkali metal initiators (^{n}BuLi, ROK (R = Me, ^{t}Bu, $C_6H_5C(O)O$),[46-51] but it has also been shown for the magnesium catalyst $^{n}Bu_2Mg$.[50, 51]

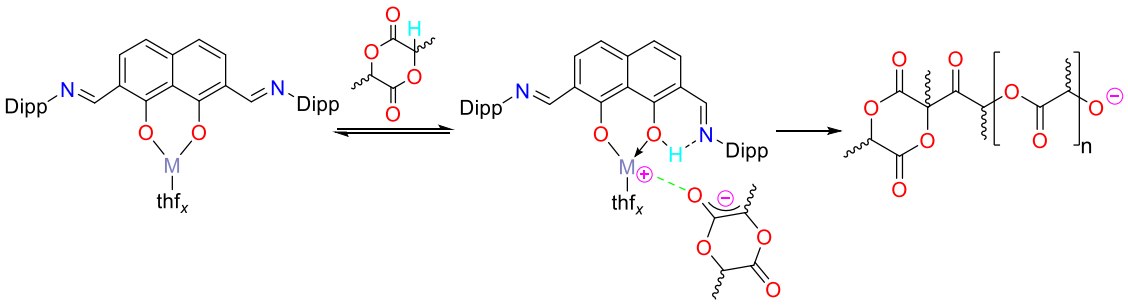

Scheme 3.2 The proposed anionic mechanism for the ring-opening polymerisation of lactide catalysed by complexes **3**–**5**.

In this mechanism, the ligand scaffold deprotonates the monomer ($R^{-}M^{+}$ + LA-H → RH + $M^{+}LA^{-}$). In the case of catalyst **4**, residual $H_2^{Dipp}L$ was detected in the ^{1}H NMR spectra of the polymerisation mixtures (**Figure 3.20**). It was considered that these pro-ligand signals were an indication of catalyst decomposition, however, they were observed not to increase over the course of the polymerisation and were therefore interpreted as evidence in support of the postulated anionic mechanism.

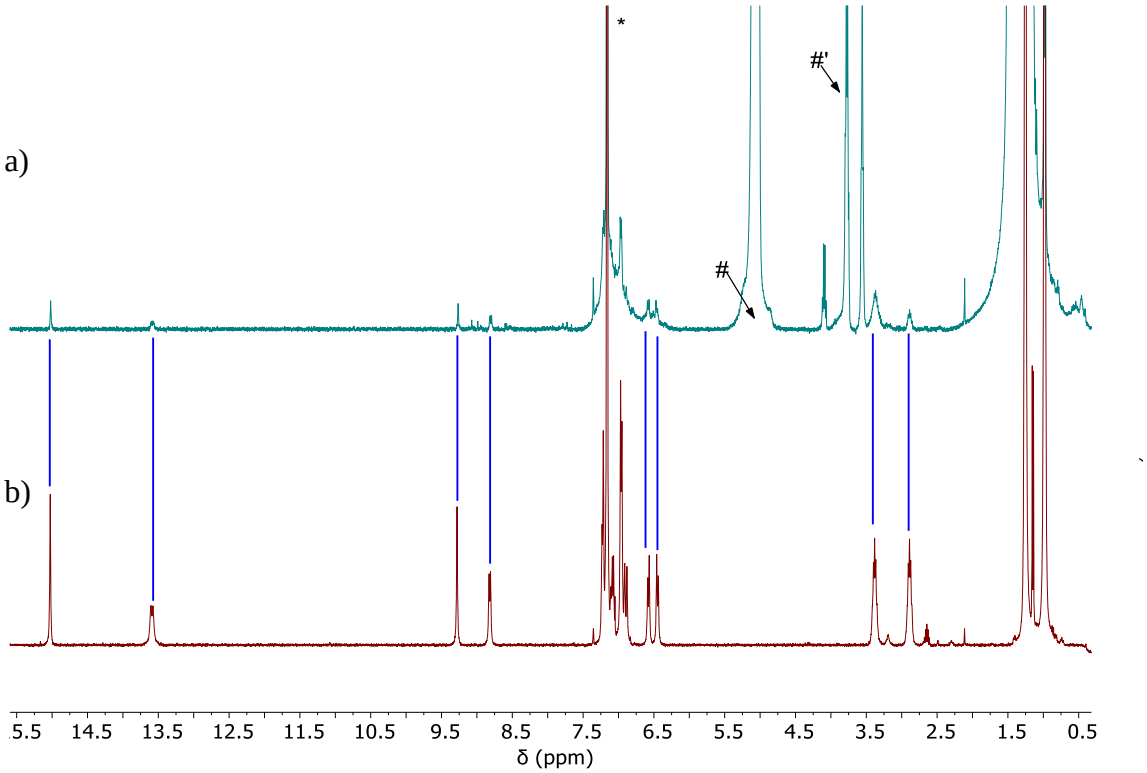

Figure 3.20 ^{1}H NMR spectra (*benzene-d_6, 400 MHz, 298 K) of a) an example polymerisation mixture and b) $H_2^{Dipp}L$. The presence of pro-ligand is highlighted by the blue dashed lines. # and #’ represent PLA and LA respectively.

At all temperatures, the GPC traces of the PLA produced using complex **4** were bimodal; similar observations were made by Schubert and co-workers when employing strontium *iso*-propoxide as a catalyst.[52] This bimodality may result from different initiating species in solution (i.e. **4**/[**4**]$_2$) or, as suggested by Chisholm *et al*., the formation of different polymer structures.[19] In their study of lactide polymerisation using an amido tin (Ph_3SnNMe_2) catalyst, the authors propose that the two GPC curves correspond to linear and cyclic PLA respectively.[19] This was rationalised by the fact that polymeric rings elute later than their straight chained analogues as a result of their smaller hydrodynamic volume.[53] The formation of such different polymeric structures is highly plausible for **4**, given that the proposed anionic ROP mechanism typically suffers from frequent transesterification and back-biting reactions as a result of the propagating anionic polymer chain ends.[46-51]

Unfortunately, the GPC data obtained is unable to confirm the presence of cyclic polylactide as the instrument used did not contain the required light scattering/intrinsic viscosity measures. End group analysis (**Section 3.4.2.4**) however, does provide evidence to support the different polymer structure theory but, as the catalyst is not well-defined in solution (**4**/[**4**]$_2$), the presence of different initiating species, or combination of the two factors, cannot be ruled out as the cause of the bimodality. As a result, the different GPC curves will be referred to as the higher/lower molecular weight fractions throughout (**1** and **2** respectively in the figures depicting GPC traces and results tables).

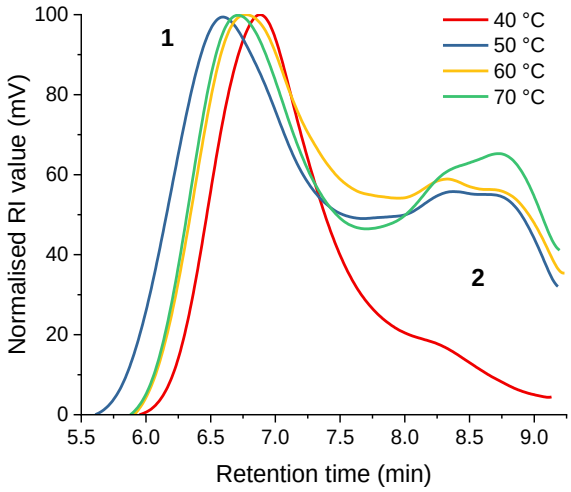

Figure 3.21 Bimodal GPC traces of PLAs synthesised from the ROP of *L*-LA using **4**. Red: 40 °C, M_n = 23 766 (**1**), 2401 (**2**) gmol^{-1}, M_w/M_n = 1.52 (**1**), 1.39 (**2**); blue: 50 °C, M_n = 29 961 (**1**), 2001 (**2**) gmol^{-1}, M_w/M_n = 1.68 (**1**), 1.61 (**2**); yellow: 60 °C, M_n = 26 468 (**1**), 1888 (**2**) gmol^{-1}, M_w/M_n = 1.59 (**1**), 1.67 (**2**); green: 70 °C, M_n = 31 845 (**1**), 1945 (**2**) gmol^{-1}, M_w/M_n = 1.56 (**1**), 1.70 (**2**). Conditions: [*L*-LA]$_0$:[**Sr**]$_0$ = 500:1, [*L*-LA]$_0$ = 0.5 M in 0.6 mL benzene-d_6 at stated temperature.

The proportion of lower molecular weight products increases with temperature, as assessed by comparison of GPC peak areas (**Figure 3.21**). This implies poorer polymerisation control at higher temperatures, possibly leading to unwanted back-biting reactions. This is reflected in the increased polydispersity (M_w/M_n) indices for peak **2**

with temperature: 1.39, 1.59, 1.67 and 1.70 for 40, 50, 60 and 70 ºC respectively (**Table 3.7**). Additionally, the molecular weights of the heavier fraction are larger than the theoretical values (e.g. at 70 ºC – $M_{n,(GPC)}$: 31 845 *vs.* $M_{n,(calcd)}$: 31 478 gmol^{-1}) which assume 100% of monomers are incorporated into two propagating chains per metal centre. This suggests that not all metal centres are active during polymerisation.

3.4.2.2 Varying monomer stereochemistry

The effect of monomer stereochemistry on the reaction kinetics was investigated by carrying out polymerisations with *rac*-, *L*-, *D*-, and *meso*-lactide at 70 °C with no co-initiator, $[LA]_0/[\mathbf{Sr}]_0$ = 500 and $[LA]_0$ = 0.5 M. The results, presented in **Figures 3.22-3.23** and **Table 3.8**, were found to follow the same trend as the complex **2**/BnOH system: *rac*- < *L*- ≈ *D*- < *meso*-.

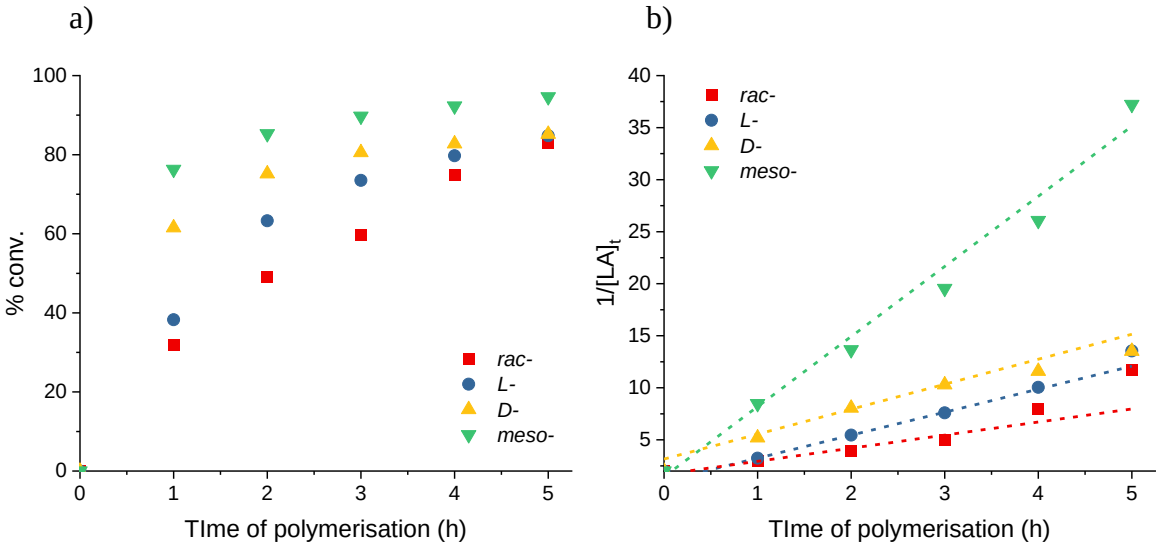

Figure 3.22 a) Plots of percentage conversion *vs.* time. b) Plots of $1/[LA]_t$ *vs.* time for LA polymerisation using **4**. Red squares: *rac*-LA (k_{obs} = 1.30 M^{-1} h^{-1}. R^2 = 0.961); blue circles: *L*-LA (k_{obs} = 2.20 M^{-1} h^{-1}. R^2 = 0.999); yellow up triangles: *D*-LA (k_{obs} = 2.40 M^{-1} h^{-1}. R^2 = 0.982); green down triangles: *meso*-LA (k_{obs} = 6.70 M^{-1} h^{-1}. R^2 = 0.987). Conditions: $[LA]_0$:$[\mathbf{Sr}]_0$= 500:1, $[LA]_0$ = 0.5 M in 0.6 mL benzene-d_6 at 70 °C.

The *meso*-LA polymerisation was shown to be the fastest (k_{obs} = 6.70 M^{-1} h^{-1}) achieving,

on average, 95% conversion of 500 eq. in 5 h (**Table 3.8**); this can be attributed to the inherent ring strain of the monomer acting as a driving force during the reaction.[23, 24] The $H_2^{Dipp}L$ ligand environment again showed no preference for the insertion of either enantiomer, with almost identical rates for *L*- and *D*- monomers (*L*-: 2.20 M^{-1} h^{-1} and *D*-: 2.40 M^{-1} h^{-1}; $k_L/k_D = 0.92 \approx 1$). The slowest second-order rate constant was recorded for the *rac*- monomer: k_{obs} = 1.30 M^{-1} h^{-1}. In all cases however, the experimental rate constants were of the same order of magnitude as related alkaline-earth complexes with the same second-order dependence on monomer concentration: [(SalenMe)Mg(μ-OCH_2Ph)]$_2$ (k_{obs} = 6.85 M^{-1} h^{-1} for [*L*-LA]:[**Mg**] = 42, in chloroform-d_1 at 20 ºC) and [Sr_2(DBP)(μ-DBP)$_3$(DME)$_3$] (k_{obs} = 2.28 M^{-1} h^{-1} for [*rac*-LA]:[**Sr**]:[BnOH] = 400:1:2.5 in THF at room temperature).[54] In contrast to these two examples, catalyst **4** did not require the use of a co-initiator/pre-formed alkoxide initiating group to achieve relatively high polymerisation rates.

Table 3.8 ROP of LA using **4** with [LA]$_0$:[**Sr**]$_0$ = 500:1 in benzene-d_6 at 70 °C.[a]

LA	Time (h)	Conv. (%)[b]	k_{obs} (M^{-1} h^{-1})[c]	R^{2c}	M_n (GPC)[d] **1**[e]	M_n (GPC)[d] **2**[f]	M_n (calcd)[g]	M_w/M_n **1**[e]	M_w/M_n **2**[f]	*H:L*[h]
rac-	5	83	1.30 ± 0.2	0.961	20 871	1625	30 177	1.59	1.54	44:56
L-	5	85	2.20 ± 0.01	0.999	31 845	1945	31 478	1.52	1.70	56:44
D-	5	85	2.40 ± 0.2	0.982	26 969	1863	30 487	1.63	1.56	58:42
meso-	5	95	6.70 ± 0.4	0.987	19 294	1252	34 231	1.46	1.73	33:67

[a]Conditions: [LA]$_0$:[**Sr**]$_0$ = 500:1, [LA]$_0$ = 0.5 M in 0.6 mL benzene-d_6 at 70 °C. [b]Average reported; measured by ^{1}H NMR spectroscopic analyses. [c]Second-order rate constant (k_{obs}) and R^2 were obtained from average plots of 1/[LA]$_t$ *vs.* time. [d]Determined by GPC in THF against PS standards using the appropriate Mark-Houwink corrections.[12] [e]Data corresponding to the higher molecular weight fraction. [f]Data corresponding to the lower molecular weight fraction. [g]Calculated M_n for PLA synthesised (assuming two polymer chains propagate per metal centre) = [(conv.(%) × [LA]$_0$/[**Sr**]$_0$) × 144.13]/2. [h]Average higher:lower (H:L) molecular weight fraction ratio determined from area of peaks in average GPC trace.

Mixtures of higher and lower molecular weight fractions of PLA were formed with all the different isomers as highlighted by the observed bimodal GPC traces (**Figure 3.23a**). The proportion of lower molecular weight products formed during the reaction was higher for *rac*- and *meso*- *vs*. *L*- and *D*- (*av*. 62% *vs*. 43%); this implies that the formation of *racemic* (-*RS*- or –*SR*-) linkages in the polymer chain facilitated increased transesterification behaviour.

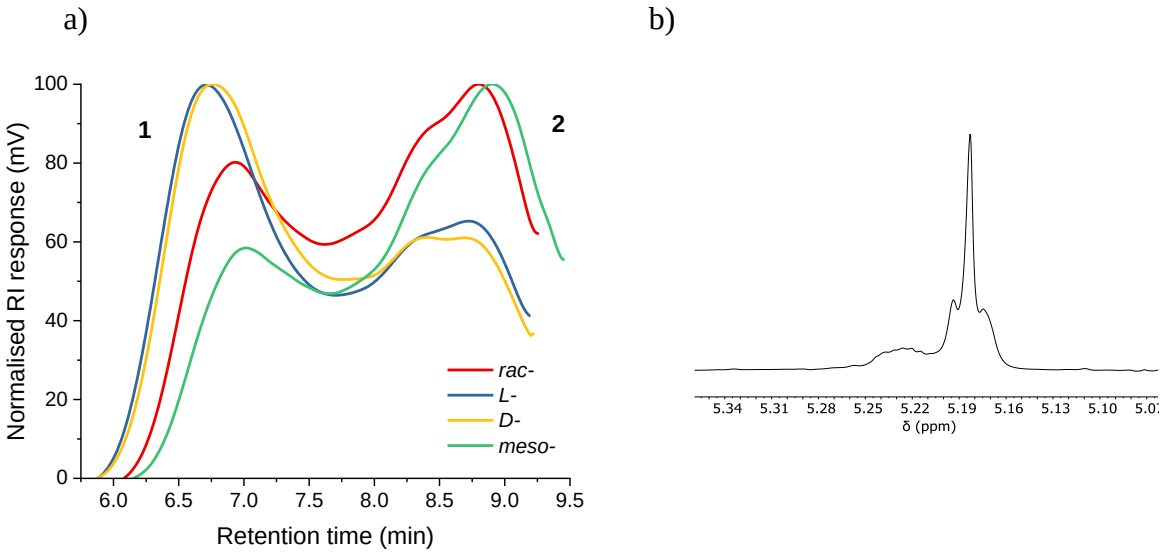

Figure 3.23 a) Bimodal GPC traces of PLAs synthesised from the ROP of LA using **4**. Red: *rac*-LA, M_n = 20 871 (**1**), 1625 (**2**) gmol^{-1}, M_w/M_n = 1.59 (**1**), 1.54 (**2**); blue: *L*-LA, M_n = 31 845 (**1**), 1945 (**2**) gmol^{-1}, M_w/M_n = 1.52 (**1**), 1.70 (**2**); yellow: *D*-LA, M_n = 26 969 (**1**), 1863 (**2**) gmol^{-1}, M_w/M_n = 1.63 (**1**), 1.56 (**2**); green: *meso*-LA, M_n = 19 294 (**1**), 1252 (**2**) gmol^{-1}, M_w/M_n = 1.46 (**1**), 1.73 (**2**). Conditions: $[LA]_0$:$[\mathbf{Sr}]_0$ = 500:1, $[LA]_0$ = 0.5 M in 0.6 mL benzene-d_6 at 70 °C. b) $^1H\{^1H\}$ NMR spectrum (chloroform-d_1, 500 MHz, 298 K) of the methine protons in the PLA produced from the **4** system and *L*/*D*-lactide. Conditions: $[LA]_0$:$[\mathbf{Sr}]_0$ = 500:1, $[LA]_0$ = 0.5 M in 0.6 mL benzene-d_6 at 70 °C.

Homonuclear decoupled $^1H\{^1H\}$ NMR spectra of the polymeric products were used to determine their microstructure (**Figure 3.23b** and **Figure A.23**). The results showed that atactic PLA (P_r = 0.48) is formed from *rac*-LA. The lack of stereocontrol in complex **4** is most likely due to insufficient (directed) shielding of the metal centre. When *meso*-LA is polymerised, the resultant PLA is syndiotactic enriched (P_r = 0.74). In contrast to the

complex **2**/BnOH system, this indicates that the polymerisations catalysed by **4** favour *racemic* enchainment.[16] PLA with comparable –*SRSR*- microstructures has previously been synthesised by Coates and co-workers using a chiral, BINAP-based aluminium calalyst.[55, 56] Epimerisation, most likely caused by the increased favourability of *racemic* linkages, was detected in the polymerisations of *L*- and *D*-lactide. This lack of reaction control was confirmed by the observation of multiple resonances in the *methine* region of the polymer $^{1}H\{^{1}H\}$ NMR spectra (**Figure 3.23b**), and is known to affect the physical properties (i.e. lower the melting point) of the resultant PLA.[57, 58]

3.4.2.3 Initiator concentration dependency

In order to determine the kinetic order dependence on catalyst concentration, polymerisations of *L*-LA with **4** were carried out at 70 °C using various monomer to catalyst ratios. The concentration of *L*-LA was held constant at 0.5 M while that of the catalyst was varied to provide the ratio of $[L\text{-LA}]_0$:$[\mathbf{Sr}]_0$ = 500, 750 and 1000. In all cases, linear plots of $1/[L\text{-LA}]_t$ *vs*. time were observed, reflecting the second-order dependence on monomer concentration (**Figure 3.24**). The observed second-order rate constants were found to increase with initiator concentration (k_{obs} = **1000:1**: 1.10 < **750:1**: 1.90 < **500:1**: 2.20 $M^{-1}\,h^{-1}$). Like with complex **2**, this is due to the higher catalyst concentration having a greater number of active sites present during the polymerisation.[31, 32]

At all ratios, the molecular weight of the heavier fraction is consistent (31 845–32 806 $gmol^{-1}$; Δ% = 3; **Table 3.9**) suggesting that the number of chain transfer events increases with the $[L\text{-LA}]_0/[\mathbf{Sr}]_0$ ratio. This is most likely due to the longer reaction times resulting in more opportunities for these side reactions to occur, and is highlighted by the increasing of the higher molecular weight polydispersity indices (M_w/M_n = 1.52, 1.60, 1.73 for **500:1**, **750:1** and **1000:1** respectively; **Figure A.24**). In contrast, the results show

that higher catalyst concentrations, and subsequent higher reaction rates, favour (possible) back-biting transesterifications; this is reflected in the higher proportion of lower molecular weight PLA being produced at smaller [*L*-LA]$_0$/[**Sr**]$_0$ ratios (**500:1** = 56:44; **750:1** = 63:37; **1000:1** = 67:33).

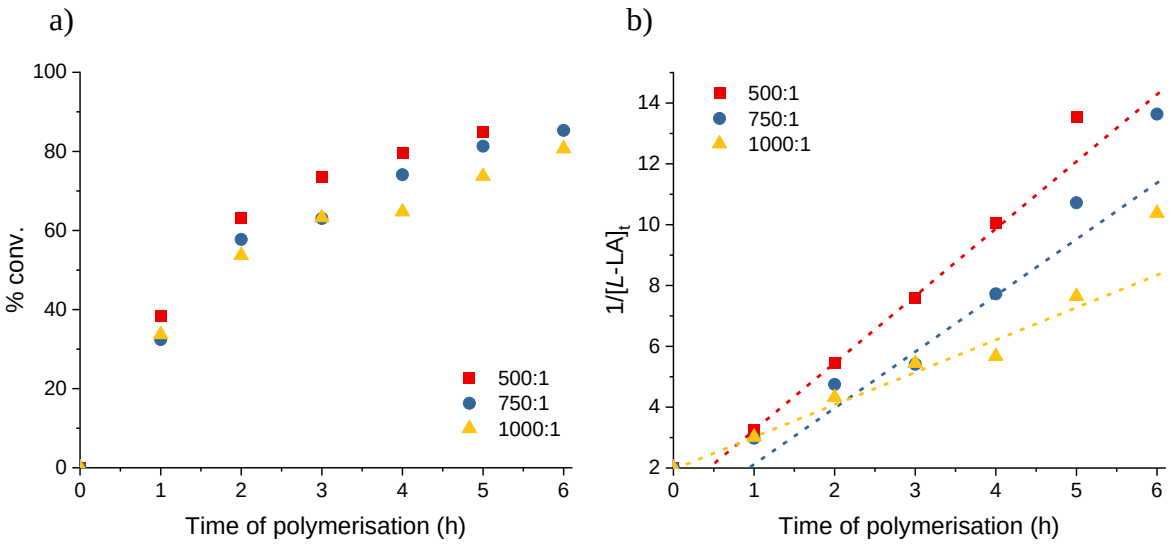

Figure 3.24 a) Plots of percentage conversion *vs.* time. b) Plots of 1/[*L*-LA]$_t$ *vs.* time for *L*-LA polymerisation using **4**. Red squares: 500:1 (k_{obs} = 2.20 M^{-1} h^{-1}. R^2 = 0.999); blue circles: 750:1 (k_{obs} = 1.90 M^{-1} h^{-1}. R^2 = 0.948); yellow up triangles: 1000:1 (k_{obs} = 1.10 M^{-1} h^{-1}. R^2 = 0.970). Conditions: [*L*-LA]$_0$:[**Sr**]$_0$= 500:1, [*L*-LA]$_0$ = 0.5 M in 0.6 mL benzene-d_6 at 70 °C.

Table 3.9 ROP of *L*-LA using **4** with [*L*-LA]$_0$:[**Sr**]$_0$ as stated in benzene-d_6 at 70 °C.[a]

[LA]$_0$: [**Sr**]$_0$	Time (h)	Conv. (%)[b]	k_{obs} (M^{-1} h^{-1})[c]	R^2[c]	M_n (GPC)[d] **1**[e]	M_n (GPC)[d] **2**[f]	M_n (calcd)[g]	M_w/M_n **1**[e]	M_w/M_n **2**[f]	*H*:*L*[h]
500:1	5	85	2.20 ± 0.01	0.999	31 845	1945	31 478	1.52	1.70	56:44
750:1	6	85	1.90 ± 0.3	0.948	32 806	1902	45 790	1.60	1.65	63:37
1000:1	6	81	1.10 ± 0.08	0.970	32 782	1828	58 913	1.73	1.53	67:33

[a]Conditions: [*L*-LA]$_0$:[**Sr**]$_0$ as stated, [*L*-LA]$_0$ = 0.5 M in 0.6 mL benzene-d_6 at 70 °C. [b]Average reported; measured by ^{1}H NMR spectroscopic analyses. [c]Second-order rate constant (k_{obs}) and R^2 were obtained from average plots of 1/[*L*-LA]$_t$ *vs.* time. [d]Determined by GPC in THF against PS standards using the appropriate Mark-Houwink corrections.[12] [e]Data corresponding to the higher molecular weight fraction. [f]Data corresponding to the lower molecular weight fraction. [g]Calculated M_n for PLA synthesised (assuming two polymer chains propagate per metal centre) = [(conv.(%) × [*L*-LA]$_0$/[**Sr**]$_0$) × 144.13]/2. [h]Average higher:lower (H:L) molecular weight fraction ratio determined from area of peaks in average GPC trace.

A linear plot of $-\ln(k_{obs})$ *vs.* $-\ln[\mathbf{Sr}]_0$ determined the order with respect to catalyst to be 0.96 ± 0.4 (**Figure 3.25a**). This value and its associated error, imply a first-order dependency on catalyst concentration. Assuming this remains constant throughout the polymerisation, the following rate law can be derived for the ROP of LA catalysed by **4**:

$$-\frac{d[\mathrm{LA}]}{dt} = k_p[\mathrm{LA}]^2[\mathbf{Sr}] \qquad \textbf{Equation 3.4}$$

The propagation rate constant (k_p), was calculated via a plot of k_{obs} *vs.* $[\mathbf{Sr}]_0$, to be 2025 ± 970 M^{-1} h^{-1} (**Figure 3.25b**). This is comparable to that of a magnesium benzyloxide complex, $[(SalenMe)Mg(\mu\text{-}OCH_2Ph)]_2$, that follows the same rate equation (k_p = 1711 M^{-2} h^{-1}).[39] It is, however, much lower than the values reported for bimetallic calcium and strontium phenolates in the presence of a $BnNH_2$ co-initiator (k_p = 276 × 10^7 $M^{-4.5}$ h^{-1} and 156 × 10^7 $M^{-4.5}$ h^{-1} respectively).[4]

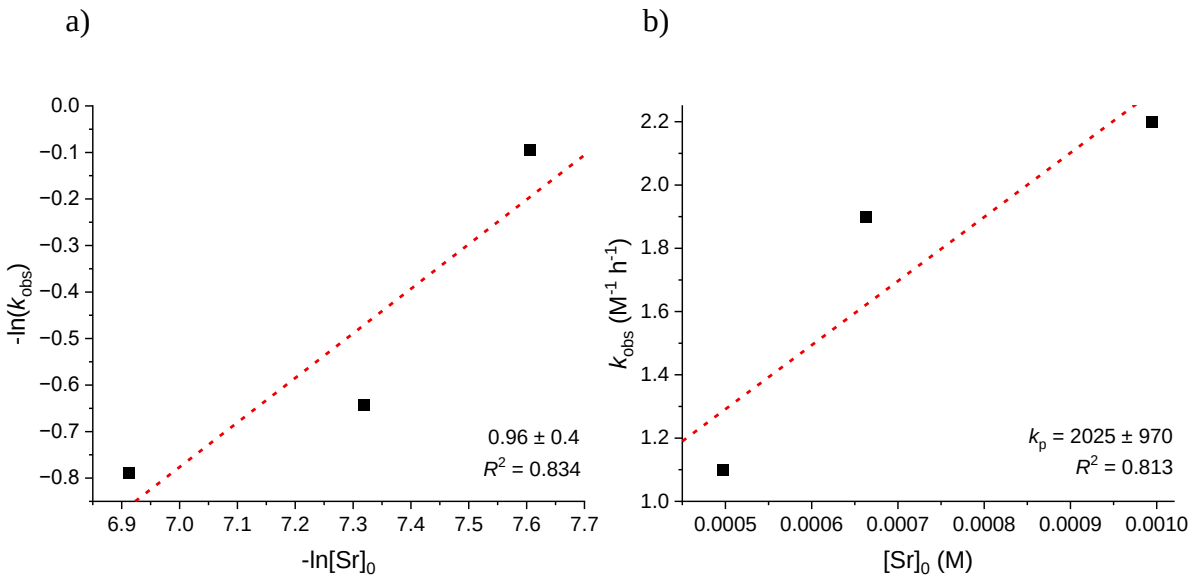

Figure 3.25 a) Plot of $-\ln(k_{obs})$ *vs.* $-\ln[\mathbf{Sr}]_0$ for ROP of *L*-LA using **4** shows that the order of reaction with respect to $[\mathbf{Sr}]_0$ is equal to 0.96 ± 0.4; R^2 = 0.834. b) Plot of k_{obs} *vs.* $[\mathbf{Sr}]_0$ for ROP of *L*-LA using **4** shows k_p = 2025 ± 970 $M^{-1}h^{-1}$; R^2 = 0.813.

3.4.2.4 Polymer end group analysis

As the proposed mechanism would result in linear chains terminated with a proton and monomer in enolate form (**Scheme 3.2**), their molecular weight would be identical to that of a cyclic polymeric ring.[59] As a result, MALDI-TOF mass spectrometry cannot be used to determine if different polymer structures are present. It does confirm, however, a polymeric sequence of multiples of 144.13 *m/z* (**Figure 3.26**); for example, the peak centred at 5950.4 gmol^{-1} is attributed to the linear –$C_6H_7O_4$/–OH terminated and cyclic PLA, comprising of 41 units of LA with K^+ [144.13(41) + 39.1]. The 72 *m/z* separation between the peaks indicates the occurrence of transesterification reactions; this is consistent with the high polydispersity indices as well as possible cyclic polymer formation.[9, 10, 14, 17, 21]

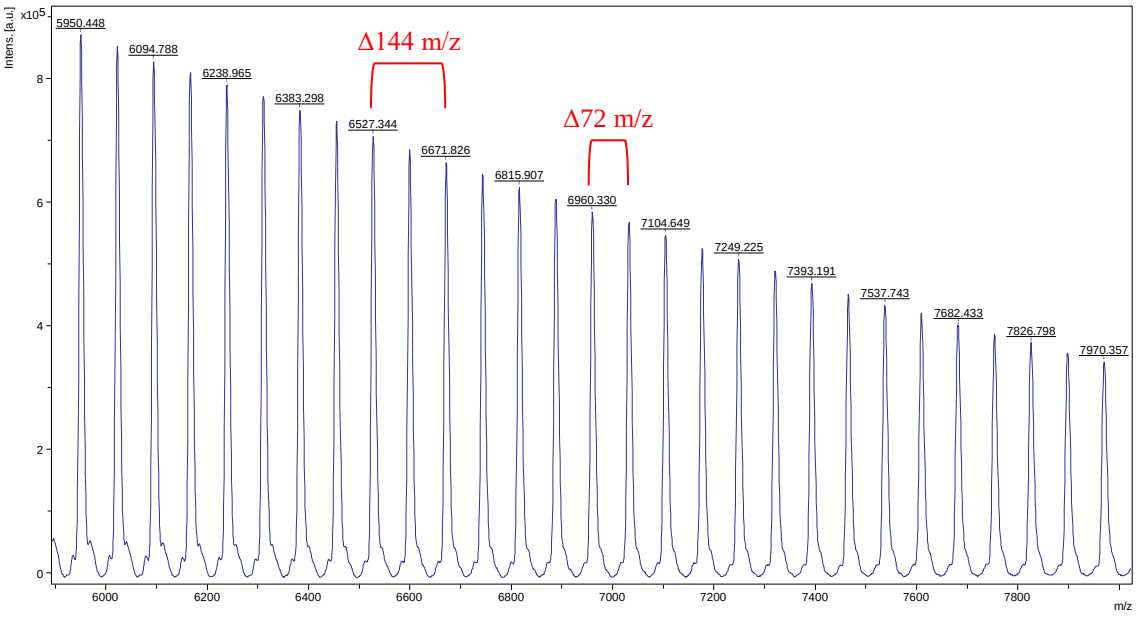

Figure 3.26 Expanded MALDI-TOF mass (*m/z*) spectrum of PLA produced using the **4** system. Conditions: [*L*-LA]$_0$:[**Sr**]$_0$ = 50:1, [*L*-LA]$_0$ = 0.5 M, 0.6 mL benzene-d_6, 40 °C.

In all cases, the ^{1}H NMR spectra of the resultant polymers revealed broad signals (**Figure 3.27**). It is postulated that this is the result of the overlapping of resonances associated with different repeating structures (i.e. linear and cyclic). The terminal proton/enolate

monomer of the linear chains are represented by a broad singlet at δ 3.55 ppm and multiplets at δ 4.37 and δ 1.47 ppm respectively.[59] The carbon signals of the same enolate end-group appear as shoulders to those of the main polymer chain (**Figure A.25**).

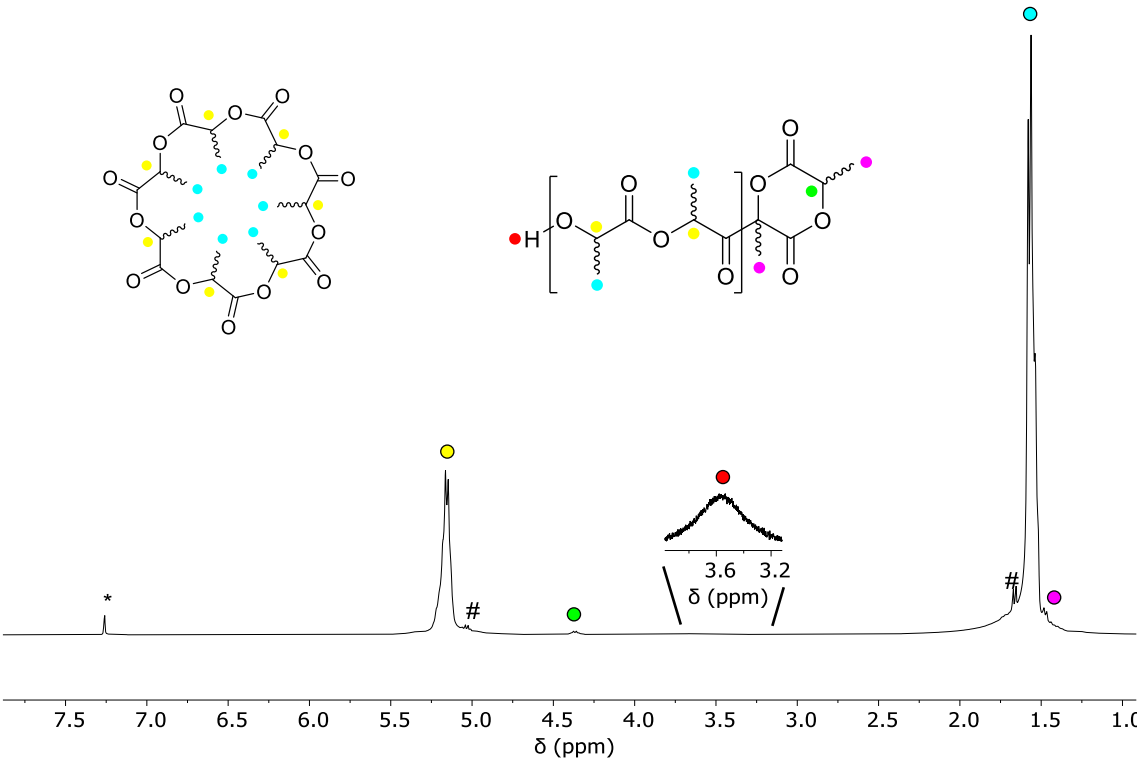

Figure 3.27 ^{1}H NMR spectrum (*chloroform-d_1, 400 MHz, 298 K) of PLA produced using the **4** system. Conditions: [*L*-LA]$_0$:[**Sr**]$_0$ = 500:1, [*L*-LA]$_0$ = 0.5 M, 0.6 mL benzene-d_6, 40 °C. M_w/M_n = 1.52, 1.39. # represents residual monomer.

3.5 Conclusions

Complex **2** was found to be active towards the ROP of LA. In the presence of benzyl alcohol co-initiator, the observed rate was found increase ~7-fold (k_{obs}: 0.0046 h^{-1} *vs.* 0.032 h^{-1}). Although comparable to an analogous [{ONN}MgCl]$_2$/BnOH system, these observed rates are much slower than other dimeric magnesium species with pre-formed amide/alkoxide initiating groups.

The trend in the rates of the different isomers (*rac*- < *L*- ≈ *D*- < *meso*-) suggested that a chain-end control mechanism was dominating the stereochemistry of the PLA. This was confirmed via microstructure analysis of resultant polymers, which found that complex **2** produced isotactic PLA for the ROP of *L*- and *D*- lactide (P_m = 1.00), atactic PLA from the ROP of *rac*-lactide (P_r = 0.53) and heterotactic-enriched PLA for the ROP of *meso*- (P_m = 0.70). Polymer end-group analysis, conducted via MALDI-TOF mass spectrometry, detected the expected –OCH_2Ph/–OH terminal groups as well as indicated the presence of transesterification processes.

All polymerisations with benzyl alcohol were shown to have narrow molecular weight distributions (M_n/M_w <1.32), indicating good polymerisation control. The molecular weights of the polymers produced were in relatively good agreement with the theoretical numbers for one chain per metal centre. The slight lowering of the experimental values can be attributed to excess/unreacted benzyl alcohol acting as a chain transfer agent.

In all cases, a first-order dependency on monomer concentration was displayed via linear plots of $\ln([LA]_0/[LA]_t)$. Initiator concentration studies revealed a similar first-order dependency on catalyst concentration; the overall polymerisation equation therefore can be described by **Equation 3.2** in which k_p was calculated to be 3.19 ± 0.39 M^{-1} h^{-1}.

$$-\frac{d[\mathrm{LA}]}{dt} = k_p[\mathrm{LA}][\mathbf{Mg}] \qquad \textbf{Equation 3.2}$$

The moderate value of enthalpy of activation (55 kJ mol^{-1}) and negative value of entropy of activation (–117 J K^{-1} mol^{-1}), computed from the variable temperature studies, are indicative of the typical coordination-insertion mechanism. An activated monomer pathway for this system however, cannot be completely ruled out as dependence on co-initiator concentration was not fully investigated.

Complexes **3–5** all proved active initiators for the ROP of LA converting over 500 eq. at ambient temperatures. The dependency on monomer concentration was found to vary depending on the alkaline-earth metal used. Calcium (**3**) exhibited first-order dependency with respect to monomer in all cases; the proposed number of metal chains propagating per monomeric initiator molecule however, depended on whether a co-initiator was added. Under all conditions, the strontium system (**4**) displayed second-order monomer dependency, via linear plots of $1/[LA]_t$, with two chains growing per monometallic initiator (confirmed by chain count calculations). Although kinetics for the barium complex **5** were too rapid for quantitative analysis, the propagation of more than one polymer chain per metal centre is also likely in this case.

Addition of benzyl alcohol as a co-initiator resulted in a ~8-fold and ~3-fold increase in the observed rate for **3** ($0.0018\ h^{-1}$ *vs.* $0.14\ h^{-1}$) and **4** ($1.57\ M^{-1}\ h^{-1}$ *vs.* $5.3\ M^{-1}\ h^{-1}$) respectively. In these systems, presence of the expected $–OCH_2Ph$/–OH end groups, formed via the activated monomer pathway, were confirmed by ^1H and $^{13}C\{^1H\}$ NMR spectra of the isolated polymers.

Further investigations with complex **4** suggested that without addition of co-initiator, the ROP proceeded via an anionic mechanism in which the initiating step is monomer deprotonation. In all cases, this anionic pathway resulted in poor polymerisation control. This was highlighted by broad, bimodal molecular weight distributions ($1.23 < M_w/M_n < 1.73$) and 72 m/z split of the peaks in the MALDI-TOF mass spectra of the isolated polymers.

The separate peaks in the GPC traces indicated the presence of different initiating species and/or the formation of a mixture of linear and cyclic PLA.[19] It is proposed that the broad signals present in the polymer ^1H and $^{13}C\{^1H\}$ NMR spectra confirm the formation of the

different polymeric structures. It remains inconclusive however, as to whether this is the sole cause of the GPC bimodality because the ill-defined nature of the catalyst (**4**/[**4**]$_2$) in solution may also result in a variety of simultaneous initiating species. The formation of lower molecular weight cyclic polylactide, was found to be favoured by higher reaction temperatures, lower [*L*-LA]$_0$/[**Sr**]$_0$ ratios and the formation of *racemic*-linkages within the polymer chain. Under any of the tested conditions however, the exclusive formation of either the higher or lower molecular weight species was not observed.

Variation of initiator concentration revealed a first-order dependency on catalyst concentration; the overall rate law for the ROP using system **4** is therefore described by **Equation 3.4** in which k_p was calculated to be 2025 ± 970 M^{-1} h^{-1}.

$$-\frac{d[\mathrm{LA}]}{dt} = k_p[\mathrm{LA}]^2[\mathbf{Sr}] \qquad \textbf{Equation 3.4}$$

Since these "NOON" initiators generally exhibit either low activity (**2**) or poor control (**3-5** – likely caused by poor speciation), an alternative "NON" ligand framework was targeted; the synthesis and polymerisation testing of which is presented in **Chapter 4** and **Chapter 5** respectively.

3.6 References

1. S. Range, D. F.-J. Piesik and S. Harder, *Eur. J. Inorg. Chem.*, 2008, 3442-3451.
2. J. Wu, Y.-Z. Chen, W.-C. Hung and C.-C. Lin, *Organometallics*, 2008, **27**, 4970-4978.
3. A. Pilone, M. Lamberti, M. Mazzeo, S. Milione and C. Pellecchia, *Dalton Trans.*, 2013, **42**, 13036-13047.
4. L. Clark, G. B. Deacon, C. M. Forsyth, P. C. Junk, P. Mountford, J. P. Townley and J. Wang, *Dalton Trans.*, 2013, **42**, 9294-9312.
5. J. Bhattacharjee, A. Sarkar and T. K. Panda, *Chem. Rec.*, 2021, **21**, 1898-1911.
6. R. K. Kottalanka, A. Harinath, S. Rej and T. K. Panda, *Dalton Trans.*, 2015, **44**, 19865-19879.
7. J. Bhattacharjee, A. Harinath, H. P. Nayek, A. Sarkar and T. K. Panda, *Chem. Eur. J.*, 2017, **23**, 9319-9331.

8. M. Hu, X. Song, F. Wang, W. Zhang, W. Ma and F. Han, *New J. Chem.*, 2022, **46**, 1175-1181.
9. J. V. Lamb, J.-C. Buffet, J. E. Matley, C. M. R. Wright, Z. R. Turner and D. O'Hare, *Dalton Trans.*, 2019, **48**, 2510-2520.
10. N. Diteepeng, I. A. P. Wilson, J.-C. Buffet, Z. R. Turner and D. O'Hare, *Polym. Chem.*, 2020, **11**, 6308-6318.
11. M.-W. Hsiao and C.-C. Lin, *Dalton Trans.*, 2013, **42**, 2041-2051.
12. J. R. Dorgan, J. Janzen, D. M. Knauss, S. B. Hait, B. R. Limoges and M. H. Hutchinson, *J. Polym. Sci., Part B: Polym. Phys.*, 2005, **43**, 3100-3111.
13. X. Tang, M. Hong, L. Falivene, L. Caporaso, L. Cavallo and E. Y. X. Chen, *J. Am. Chem. Soc.*, 2016, **138**, 14326-14337.
14. N. Diteepeng, J.-C. Buffet, Z. R. Turner and D. O'Hare, *Dalton Trans.*, 2019, **48**, 16099-16107.
15. Y. Huang, W.-C. Hung, M.-Y. Liao, T.-E. Tsai, Y.-L. Peng and C.-C. Lin, *J. Polym. Sci., Part A: Polym. Chem.*, 2009, **47**, 2318-2329.
16. B. M. Chamberlain, M. Cheng, D. R. Moore, T. M. Ovitt, E. B. Lobkovsky and G. W. Coates, *J. Am. Chem. Soc.*, 2001, **123**, 3229-3238.
17. Z. R. Turner, J. V. Lamb, T. P. Robinson, D. Mandal, J.-C. Buffet and D. O′Hare, *Dalton Trans.*, 2021, **50**, 4805-4818.
18. A. F. Douglas, B. O. Patrick and P. Mehrkhodavandi, *Angew. Chem. Int. Ed.*, 2008, **47**, 2290-2293.
19. M. H. Chisholm and E. E. Delbridge, *New J. Chem.*, 2003, **27**, 1167-1176.
20. M. Save, M. Schappacher and A. Soum, *Macromol. Chem. Phys.*, 2002, **203**, 889-899.
21. P. Dubois, O. Coulembier and J. M. Raquez, *Handbook of Ring-Opening Polymerization*, Wiley, 1st edn., 2009.
22. D. R. Witzke, R. Narayan and J. J. Kolstad, *Macromolecules*, 1997, **30**, 7075-7085.
23. J.-C. Buffet and J. Okuda, *Polym. Chem.*, 2011, **2**, 2758-2763.
24. M. H. Chisholm, N. W. Eilerts, J. C. Huffman, S. S. Iyer, M. Pacold and K. Phomphrai, *J. Am. Chem. Soc.*, 2000, **122**, 11845-11854.
25. J.-C. Buffet, A. N. Martin, M. Kol and J. Okuda, *Polym. Chem.*, 2011, **2**, 2378-2384.
26. D. J. Darensbourg and O. Karroonnirun, *Inorg. Chem.*, 2010, **49**, 2360-2371.
27. J. Coudane, C. Ustariz-Peyret, G. Schwach and M. Vert, *J. Polym. Sci., Part A: Polym. Chem.*, 1997, **35**, 1651-1658.
28. I. A. Shuklov, H. Jiao, J. Schulze, W. Tietz, K. Kühlein and A. Börner, *Tetrahedron Lett.*, 2011, **52**, 1027-1030.
29. J.-B. Zhu and E. Y. X. Chen, *J. Am. Chem. Soc.*, 2015, **137**, 12506-12509.
30. R. C. Pratt, B. G. G. Lohmeijer, D. A. Long, P. N. P. Lundberg, A. P. Dove, H. Li, C. G. Wade, R. M. Waymouth and J. L. Hedrick, *Macromolecules*, 2006, **39**, 7863-7871.
31. Z. R. Turner, J.-C. Buffet and D. O'Hare, *Organometallics*, 2014, **33**, 3891-3903.
32. R. Dattatray Karande, V. K. Abitha, A. Vasudeo Rane and R. K. Mishra, *J. Mater. Sci. Eng. Adv. Tech.*, 2015, **12**, 1-37.

33. Y. Cui, W. Gu, Y. Wang, B. Zhao, Y. Yao and Q. Shen, *Catal. Sci. Technol.*, 2015, **5**, 3302-3312.
34. H. R. Kricheldorf, H. Hachmann-Thiessen and G. Schwarz, *Biomacromolecules*, 2004, **5**, 492-496.
35. M. T. Caudle and J. W. Kampf, *Inorg. Chem.*, 1999, **38**, 5474-5475.
36. F. Corazza, C. Floriani, A. Chiesi-Villa, C. Guastini and S. Ciurli, *J. Chem. Soc., Dalton Trans.*, 1988, 2341-2345.
37. R. K. Kottalanka, A. Harinath and T. K. Panda, *RSC Adv.*, 2015, **5**, 37755-37767.
38. A. Harinath, J. Bhattacharjee, A. Sarkar, H. P. Nayek and T. K. Panda, *Inorg. Chem.*, 2018, **57**, 2503-2516.
39. J.-C. Wu, B.-H. Huang, M.-L. Hsueh, S.-L. Lai and C.-C. Lin, *Polymer*, 2005, **46**, 9784-9792.
40. P. I. Binda and E. E. Delbridge, *Dalton Trans.*, 2007, 4685-4692.
41. M. P. Blake, A. D. Schwarz and P. Mountford, *Organometallics*, 2011, **30**, 1202-1214.
42. T.-P.-A. Cao, A. Buchard, X. F. Le Goff, A. Auffrant and C. K. Williams, *Inorg. Chem.*, 2012, **51**, 2157-2169.
43. L. Clark, M. G. Cushion, H. E. Dyer, A. D. Schwarz, R. Duchateau and P. Mountford, *Chem. Commun.*, 2010, **46**, 273-275.
44. H.-Y. Chen, B.-H. Huang and C.-C. Lin, *Macromolecules*, 2005, **38**, 5400-5405.
45. M. Ystenes, *J. Catal.*, 1991, **129**, 383-401.
46. O. Dechy-Cabaret, B. Martin-Vaca and D. Bourissou, *Chem. Rev.*, 2004, **104**, 6147-6176.
47. A. Bhaw-Luximon, D. Jhurry, N. Spassky, S. Pensec and J. Belleney, *Polymer*, 2001, **42**, 9651-9656.
48. H. R. Kricheldorf and I. Kreiser-Saunders, *Makromol. Chem.*, 1990, **191**, 1057-1066.
49. Z. Jedliński, W. Wałach, P. Kurcok and G. y. Adamus, *Makromol. Chem.*, 1991, **192**, 2051-2057.
50. H. R. Kricheldorf and S.-R. Lee, *Polymer*, 1995, **36**, 2995-3003.
51. J. Kasperczyk and M. Bero, *Polymer*, 2000, **41**, 391-395.
52. D. Bandelli, C. Weber and U. S. Schubert, *Macromol. Rapid Commun.*, 2019, **40**, 1900306.
53. P. Wongmahasirikun, P. Prom-on, P. Sangtrirutnugul, P. Kongsaeree and K. Phomphrai, *Dalton Trans.*, 2015, **44**, 12357-12364.
54. J. C. Wu, B. H. Huang, M. L. Hsueh, S. L. Lai and C. C. Lin, *Polymer*, 2005, **46**, 9784-9792.
55. T. M. Ovitt and G. W. Coates, *J. Am. Chem. Soc.*, 1999, **121**, 4072-4073.
56. M. C. D'Alterio, C. De Rosa and G. Talarico, *Chem. Commun.*, 2021, **57**, 1611-1614.
57. N. Nomura, J. Hasegawa and R. Ishii, *Macromolecules*, 2009, **42**, 4907-4909.
58. C. Goonesinghe, H.-J. Jung, H. Roshandel, C. Diaz, H. A. Baalbaki, K. Nyamayaro, M. Ezhova, K. Hosseini and P. Mehrkhodavandi, *ACS Catal.*, 2022, **12**, 7677-7686.
59. C. Rentero, J. Damián, A. Medel, M. Fernández-Millán, Y. Rusconi, G. Talarico, T. Cuenca, V. Sessini and M. E. G. Mosquera, *Polymers*, 2022, **14**, 2982.

Chapter 4

Synthesis and characterisation of monometallic alkaline-earth "NON" complexes

4.1 Introduction

4.1.1 Overview

The problematic nature of competitive binding pockets in $H_2^{Dipp}L$ led to a change in the type of ligand investigated in this project. The new frameworks are a class of 2,7-diiminophenol ("NON") compound that contain only two possible [=N,O$^-$] binding sites. They were chosen specifically due to their reported utilisation in heterobimetallic ethylene polymerisation initiators as well as rare-earth complexes for C-H activation and CO_2/epoxide ROCOP catalysis.[1, 2] The monoanionic nature of these motifs however, now renders the target bimetallic alkaline-earth systems as cationic.

This chapter discusses the synthesis and characterisation of six new monometallic alkaline-earth compounds: three homoleptic complexes (M = Mg, Sr and Ba) and three heteroleptic complexes (M = Ca) alongside their intermediate potassium salts. Attempts to utilise these systems as intermediates in the synthesis of bimetallic alkaline-earth cations are discussed in **Chapter 6**.

4.1.2 Literature reports involving the "NON" system

Previous coordination studies of *bis*(imino)phenoxide ligands involve a wide array of metals; these include aluminium,[3] nickel,[4-7] cobalt,[7, 8] gallium,[9] indium,[9] scandium,[2] yttrium,[2] titanium,[10, 11] zirconium,[10-12] hafnium,[10, 11] copper,[13] iron,[14] zinc,[15] magnesium[16] and calcium (**Figure 4.1**).[17]

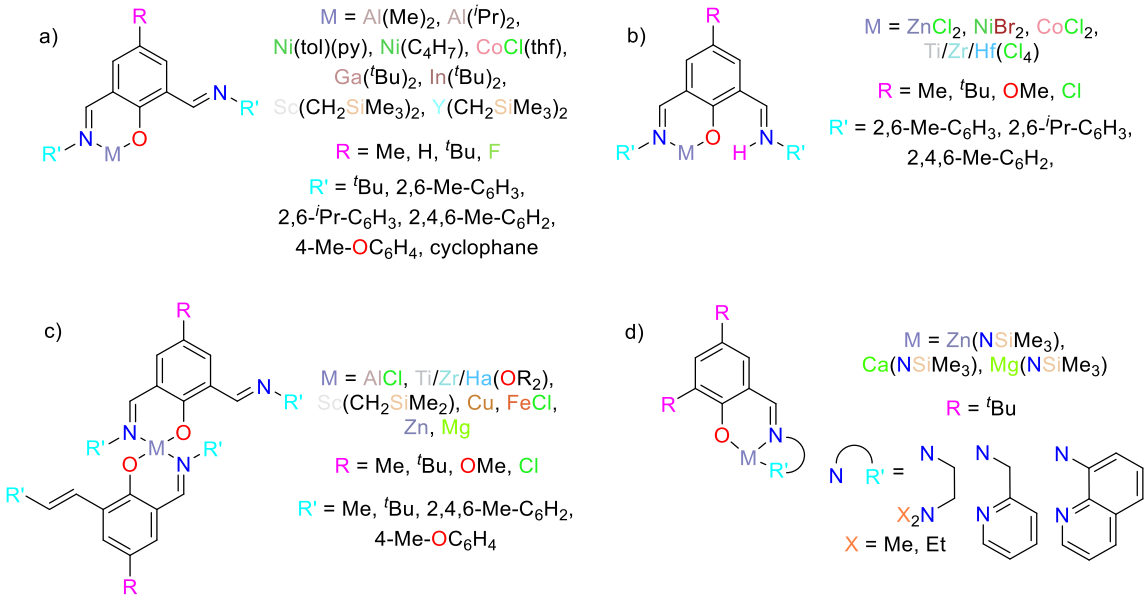

Figure 4.1 Previously reported metal complexes involving *bis*(imino)phenoxide "NON" and related ligands.

Heteroleptic "NON" complexes have most commonly been isolated through either, salt-metathesis of alkali metal "NON" complexes with a metal halide, or protonolysis reactions of the pro-ligand with metal-alkyl reagents (**Figure 4.1a**). [2-6, 8, 9] The majority

of these compounds have then been tested as polymerisation catalysts.[2, 4-6, 8, 9] The nickel olefin polymerisation system (Ni(tol)(py), R = Me, R′ = cyclophane), reported by Mecking and co-workers found enhanced thermal stability via the introduction of a cyclophane ring into the ligand backbone.[4] In addition, this also suppressed chain transfer and branch formation, thus allowing for the isolation of higher molecular weight polyethylene (1.5 kg mol^{-1} *vs.* 1.1 kg mol^{-1}).[4] The gallium and indium ($M(^tBu)_2$) complexes were tested as initiators for the solvent free, ring-opening polymerisation of lactide (**Figure 4.1a**). The authors report that the superior reactivity and control imparted by the gallium system (converts 200 eq. *rac*-LA in 9 minutes (M_w/M_n = 1.02-1.06) *vs*. 16 minutes (M_w/M_n = 1.08-1.15)) is a direct result of the increased Lewis acidity of the metal centre.[9]

Where the ligand was reacted with metal chloride reagents, the end products remained fully protonated with dative binding of the metal species in one of the [=N,O^-] pockets (**Figure 4.1b**). The permanence of the protonated imine arm in these structures was confirmed by unsuccessful neutralisation with Et_3N.[10] The cobalt and nickel species were found to be active for ethylene oligmerisation (Co: $<1.0\times10^3$ g mol^{-1} h^{-1} atm^{-1}; Ni: 2.1×10^5 g mol^{-1} h^{-1} atm^{-1}) with the steric bulk in the *ortho*-aryl position directly influencing the recorded activity (*ortho*-isopropyl: 1.2×10^5 g mol^{-1} h^{-1} atm^{-1}; *ortho*-methyl: 1.9×10^5 g mol^{-1} h^{-1} atm^{-1}).[7] Unusually, the group four systems all appeared as zwitterionic compounds capable of catalysing the ring-opening of numerous cyclic esters; the observed activity was found to follow the trend: Ti > Zr > Hf.[10]

Homoleptic *bis*(ligand) compounds are also reported for the group four metals (**Figure 4.1c**); these are typically formed, regardless of reaction stoichiometry, when group four metal aryl/alkyloxide reagents are employed.[11, 12] Similar species have also been

documented with aluminium,[3] scandium,[2] and zinc[17]; the use of copper resulted in isolation of tetranuclear clusters which proved to be virtually inactive for ring-opening polymerisation.[13] Poor polymerisation activity was also observed for the homoleptic iron complexes as a result of inefficient catalyst initiation, where the propylene oxide co-initiator struggled to insert into strong Fe-Cl bond.[14] In contrast, the corresponding magnesium complex was found to be the first example of a monomeric Mg species capable of catalysing the ring-opening co-polymerisation of CO_2 and styrene oxide (TON: 890-970 and TOF: 37-40 h^{-1}).[16]

As eluded to in the previous paragraphs, there is a tendency to form homoleptic complexes with this "NON" framework. In terms of alkaline-earth systems, this is exacerbated by their typically observed redistribution behaviour. The isolation of a few related heteroleptic M^{2+} phenoxy-imine species has been achieved however, via the use of additional pendant donor arms (**Figure 4.1d**). All of the {ON-R"}MNSiMe$_3$ (M = Zn, Mg and Ca) initiators, reported by Shaver *et al*., were capable of polymerising *rac*-lactide with the zinc analogue shown to be the fastest converting 100 eq. in under 30 minutes at 70 ºC.[17]

4.2 Pro-ligand syntheses ($H^{R,Dipp}L$)

The synthesis of the *para*-unsubstituted phenoxy-imine pro-ligand ($H^{Dipp}L$; 1-OH-2,6-(HC=NDipp)-C_6H_3) was achieved in a four-step process with an overall yield of 11% (**Scheme 4.1**).[18-20]

The initial step utilised pyridine and acetyl chloride to protect the alcohol functional group of 2,6-dimethyl phenol. The double bromination of the methyl substituents was then initially attempted at 90 °C using infra-red-activated N-bromosuccinimide (NBS).[21]

However, this technique resulted in uncontrollable bromination of both the methyl groups and phenol ring.[21] The desired level of bromination was achieved using an alternative method that employed much milder conditions (anhydrous aluminium trichloride catalyst, room temperature).[19] Initial reactions using 0.25 mol% of catalyst were monitored by ^{1}H NMR spectroscopy and were found to achieve approximately 90% conversion to the desired (4-Br) product in twelve days**.** Optimisation of the reaction conditions (increasing catalyst loading to 1 mol% and utilising a slight excess of 4.3 equiv. NBS) resulted in the reduction of reaction time to four days. Subsequent, simultaneous acetyl deprotection and dialdehyde formation was achieved by refluxing the brominated system in a basic solution of potassium hydroxide.[20] The final step involved a *p*-toluenesulfonic acid-catalysed condensation reaction with 2,6-diisopropylaniline ($^{Dipp}NH_2$); this afforded H^{Dipp}L as a pale yellow powder in 58% yield.

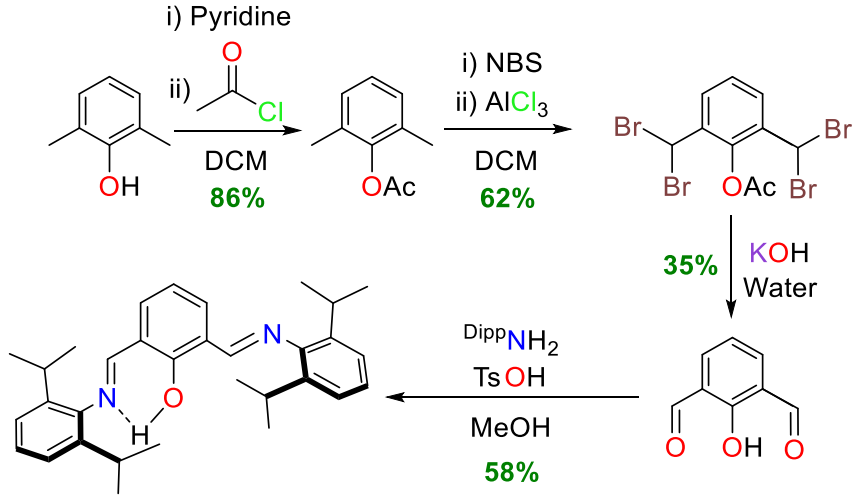

Scheme 4.1 Four-step synthesis of H^{Dipp}L.[18-20]

The 4-methyl (H^{Me,Dipp}L; 1-OH-2,6-(HC=NDipp)-4-Me-C_6H_2) and 4-*tert*-butyl (H$^{t\text{Bu,Dipp}}$L; 1-OH-2,6-(HC=NDipp)-4-^{t}Bu-C_6H_2) variants of the "NON" ligands were prepared in a different manner using a two-step process (**Scheme 4.2**).[22, 23] Diformylation

from the corresponding *para*-substituted phenols was achieved *via* a one-step, one pot reaction that utilised hexamethylenetetramine (HMTA) as the source of the formyl carbons (for mechanism see **Scheme A.1** in **Appendix**).[22-24] This process is only applicable to *para*-substituted phenols as the electron-donating nature of the alcohol renders the 4-position susceptible to electrophilic attack unless it is protected. Using this method, 4-methyl-2,6-diformyl phenol and 4-*tert*-butyl-2,6-diformyl phenol were isolated as yellow solids in 72% and 99% yield respectively. The second step of the synthesis was the same *p*-toluenesulfonic-catalysed condensation reaction employed when generating $H^{Dipp}L$. This afforded the desired ligands, $H^{Me,Dipp}L$ and $H^{tBu,Dipp}L$, as bright yellow powders in 48% and 89% isolated yield respectively. As the *tert*-butyl-analogue proved to be the highest yielding pro-ligand, it formed the basis of the majority of complexation studies.

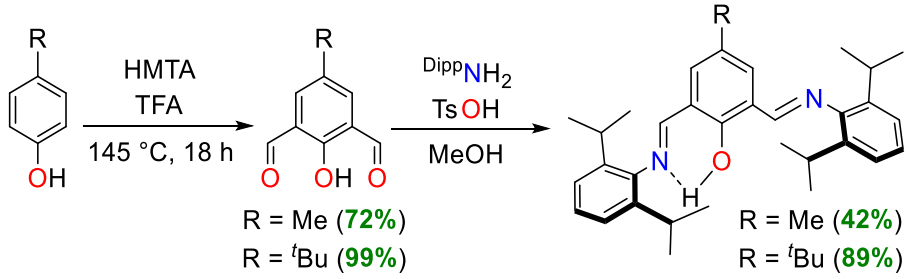

Scheme 4.2. Two-step synthesis of $H^{R,Dipp}L$ (R = Me or ^{t}Bu).[22, 23]

4.2.1 NMR spectroscopic analysis

In all three compounds, a fluxional interaction of the O***H*** proton with one of the imine nitrogen atoms, causes asymmetry within the ligand core. This is evidenced in the ^{1}H NMR spectra which exhibit broadened signals at 298 K and twice the number of environments expected for a C_{2v} symmetric $[L]^{-}$ framework when recorded at 223 K (**Figure 4.2**).

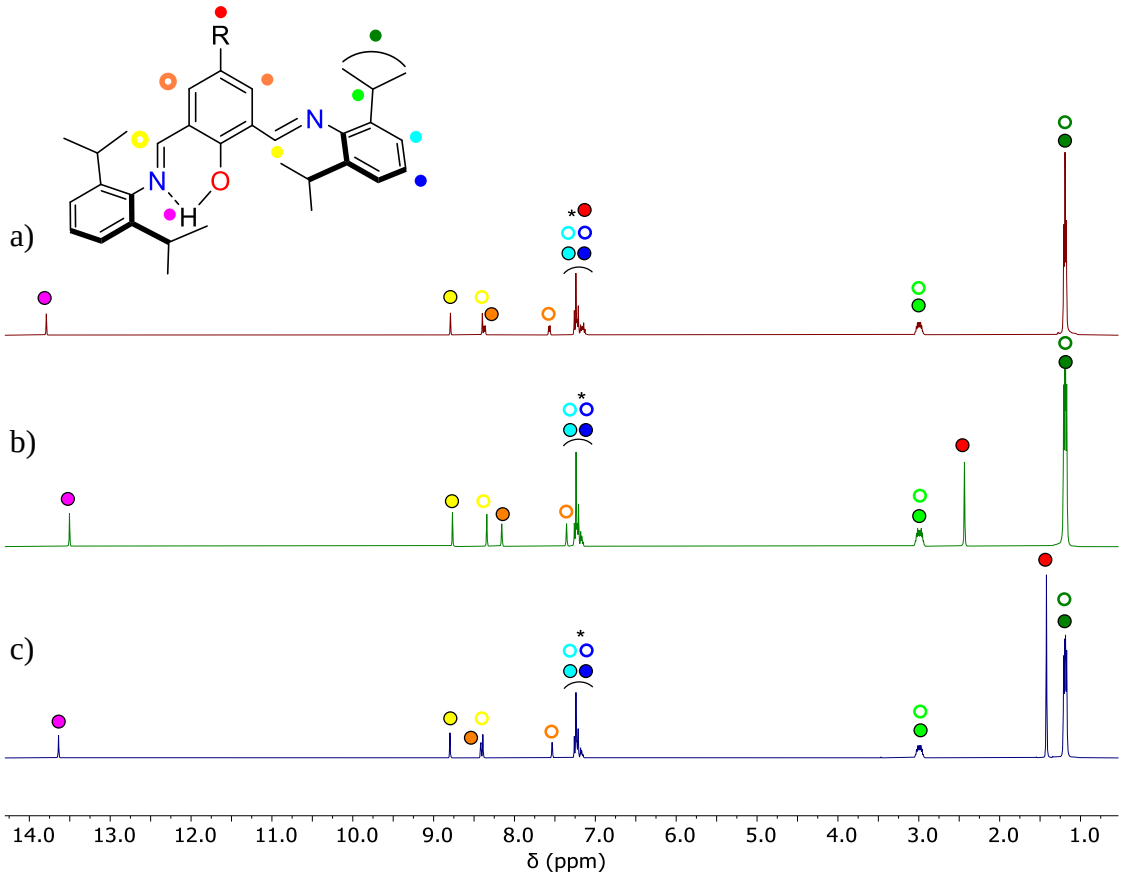

Figure 4.2 ^{1}H NMR spectra (*chloroform-d_1, 500 MHz, 223 K) of a) $H^{Dipp}L$, b) $H^{Me,Dipp}L$ and c) $H^{tBu,Dipp}L$.

Using $H^{Dipp}L$ as a representative example; the singlets corresponding to the ***H***C=N and ***H***C=N(H) protons can be found at δ 8.79 and δ 8.40 ppm respectively whereas the protons of the central aromatic ring are represented by the doublets at lower frequency at δ 8.37 and δ 7.57 ppm. The remaining resonances in the aromatic region (δ 7.28–7.11 ppm) correspond to the remaining phenolic proton and the C***H*** protons from the imine-*aryl* group. The isopropyl *methine* and *methyl* protons are represented by the multiplets at δ 3.00 and δ 1.16 ppm respectively. The NMR spectra for the $H^{R,Dipp}L$ pro-ligands differ only in that they also contain singlets found at δ 2.43 and δ 1.42 ppm which corresponding to the methyl- and *tert*-butyl- protons respectively.

Full assignment of the asymmetric spectra was made possible by NOESY NMR experiments performed at 223 K (**Figure 4.3**).[25] Through-space interactions were detected between the imine and central aromatic ring protons on the side of the pro-ligand where the imine nitrogen interacts with the O***H***. Rotation of the *"free"* imine (to alleviate some of the system's steric strain) positions the corresponding protons on the opposite side of the molecule too far apart to interact.

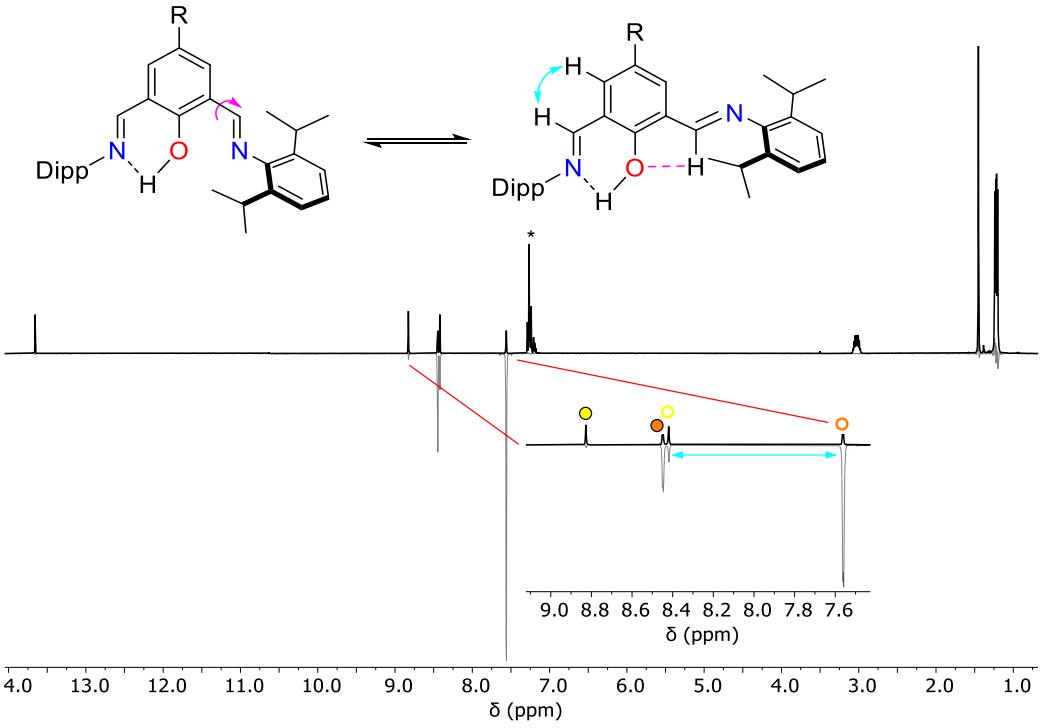

Figure 4.3 NOESY NMR spectrum (*chloroform-d_1, 500 MHz, 223 K) of H$^{t\text{Bu,Dipp}}$L. The plot highlights the through space interactions between the imine and central aromatic ring protons of the N···*H*O bound side of the pro-ligand (blue arrows).

4.3 Targeting alkaline-earth "NON" complexes through salt-metathesis

A typical method of complexing "NON" pro-ligands is to utilise them in salt-metathesis reactions.[1, 4-6, 26] As a result, and because of the unsuccessful protonolysis reactivity with

the original "NOON" ligand, this reaction pathway was tested for the synthesis of group two "NON" species. An overall summary of the observed reactivity is shown in **Scheme 4.3**.

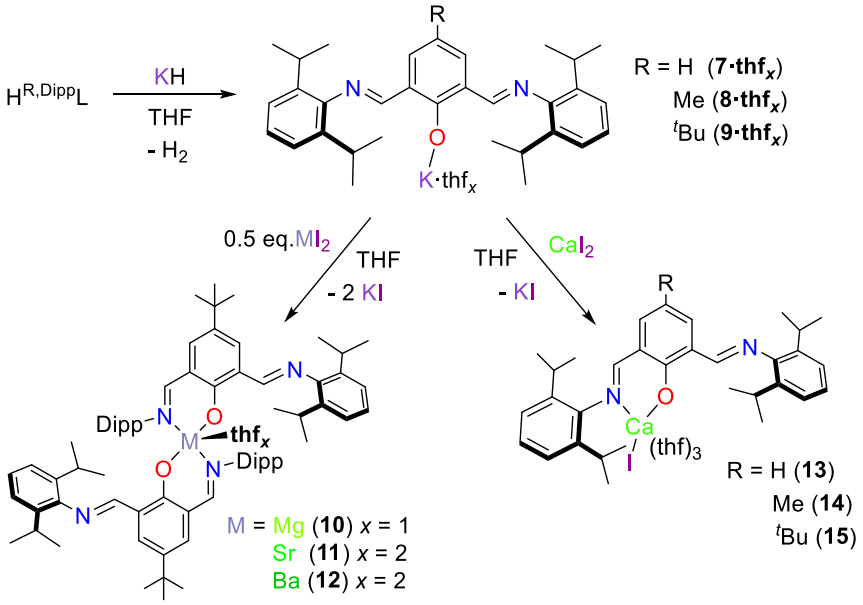

Scheme 4.3. Salt-metathesis route from (^{R,Dipp}L)K·thf$_x$ (R = H (**7·thf$_x$**), Me (**8·thf$_x$**), ^{t}Bu (**9·thf$_x$**)) to ($^{t Bu,Dipp}$L)$_2$M(thf)$_x$ (M = Mg (**10**), Sr (**11**), Ba (**12**)) and ^{R,Dipp}LCaI(thf)$_3$ (R = H (**13**), Me (**14**) or ^{t}Bu (**15**)).

4.3.1 Synthesis of potassium phenoxide salts

The pro-ligands H^{R,Dipp}L were first deprotonated with an excess of KH to form ^{R,Dipp}LK·thf$_x$ (R = H (**7·thf$_x$**), Me (**8·thf$_x$**), ^{t}Bu (**9·thf$_x$**)) in 71%, 91% and 75% yield respectively. In all cases, the crude product was obtained as an oily solid. Trituration with pentane gave free flowing yellow powders which were always isolated bearing residual solvent (thf$_x$).

4.3.1.1 NMR spectroscopic analysis

The ^{1}H NMR spectra of complexes **7-9·thf$_x$** are consistent with C_{2v} molecular symmetry (**Figure 4.4**).

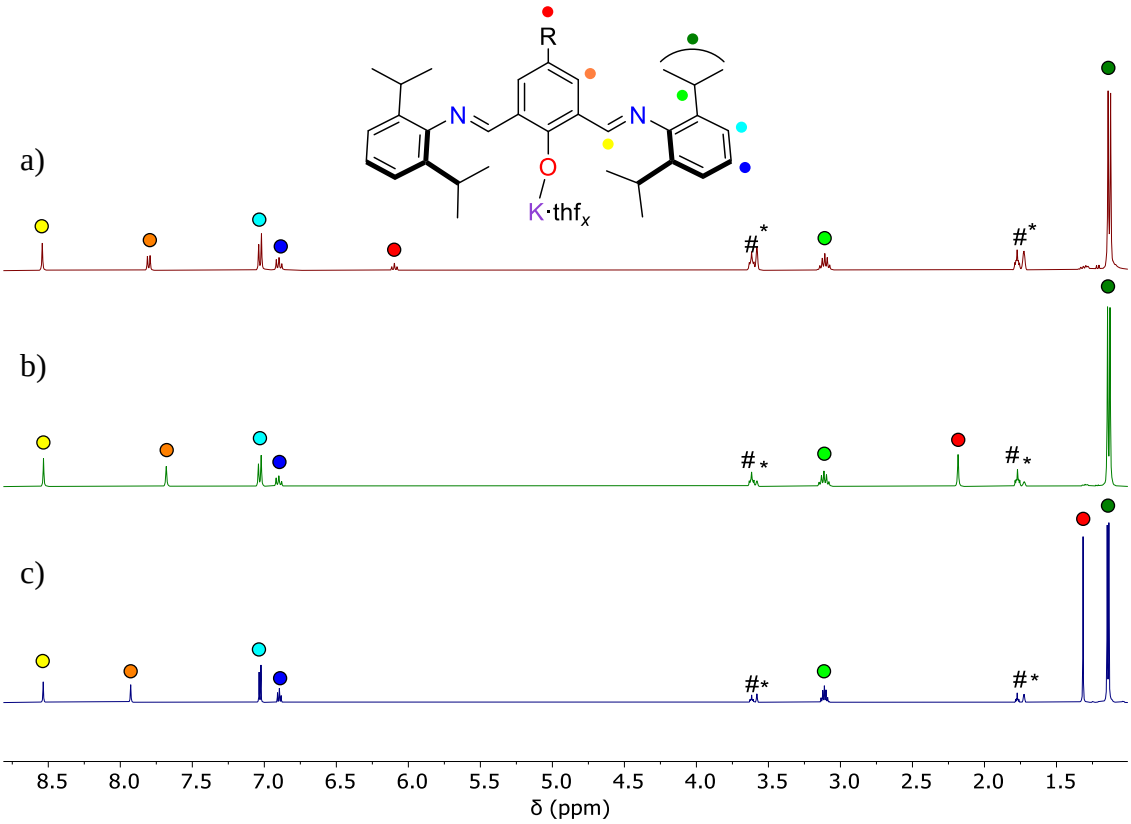

Figure 4.4 ^{1}H NMR spectra (*THF-d_8, 600 MHz, 298 K) of a) ^{Dipp}LK.thf$_{1.4}$ (**7·thf$_{1.4}$**), b) ^{Me,Dipp}LK.thf$_{0.7}$ (**8·thf$_{0.7}$**) and c) $^{t Bu,Dipp}$LK.thf$_{0.6}$ (**9·thf$_{0.6}$**). # represents residual protio THF.

Using **9·thf$_x$** as a representative example: two singlets at δ 8.53 and δ 7.93 ppm correspond to the ***H***C=N and 3-C$_6$***H***$_2$ protons respectively. Mutually coupled doublet and triplet signals at δ 7.03 and δ 6.90 ppm ($^3J_{HH}$ = 6.9 Hz) represent the C$_6$***H***$_3$ diisopropyl-*aryl* protons while the isopropyl *methine* and *methyl* protons are depicted by the multiplets at δ 3.11 and δ 1.14 ppm respectively. Finally, a singlet at δ 1.32 ppm corresponds to the nine *tert*-butyl protons.

The NMR spectra for the analogous potassium salts differ only in that they contain alternative resonances for the *para*-substituent; in **7·thf$_x$** this a doublet at δ 6.10 ppm that corresponds to the *para*-substituted proton whereas in **8·thf$_x$**, there is a singlet at δ 2.18 ppm to represent the methyl group.

4.3.1.2 X-ray crystallographic analysis

Single crystals of **[7(18-c-6)]*n***, **[8(18-c-6)]*n***, and **[9(18-c-6)(thf)]**, were grown from saturated THF solutions at room temperature in the presence of 1 eq. of 18-crown-6, and refined in the monoclinic $P2_1/n$ space group (**Figure 4.5**). All attempts to grow single crystals of the crown-free complexes were unsuccessful.

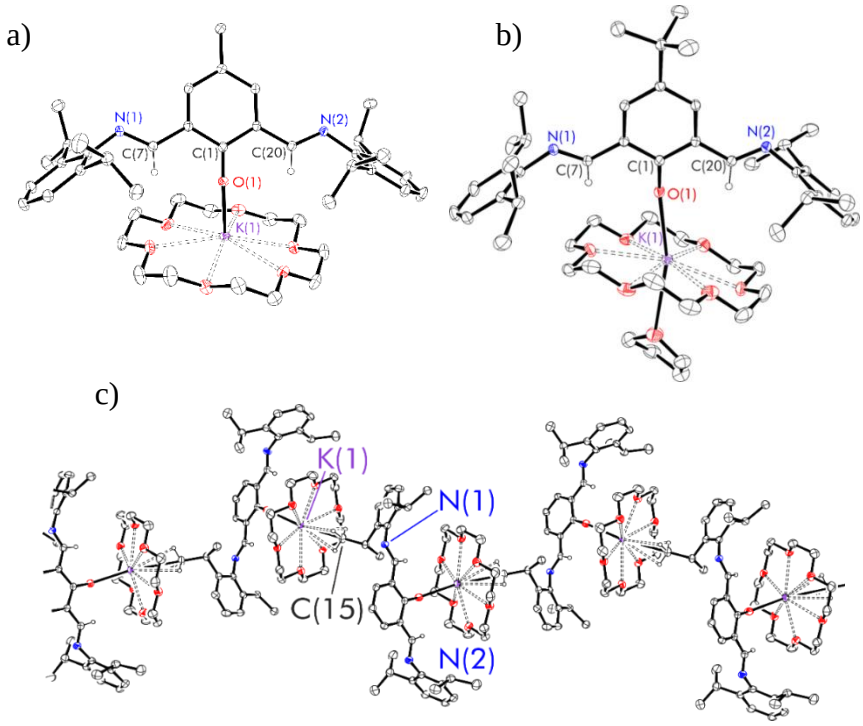

Figure 4.5. Thermal displacement ellipsoid drawings (30%) of asymmetric units of a) [^{Me,Dipp}LK(18-c-6)]$_n$ **[8(18-c-6)]*n*** and b) ^{tBu,Dipp}LK(18-c-6)(thf) [**9(18-c-6)(thf)**]. All hydrogen atoms, except those bound to C(7) and C(20) have been omitted for clarity. c) The extended structure of complex [^{Dipp}LK(18-c-6)]$_n$ **[7(18-c-6)]*n***, is represented showing the hydrogen atoms bound to C(15) which demonstrate a binding interaction with the potassium centre; symmetry equivalent atomic positions have been generated by the symmetry operators –x+3/2, y+1/2, –z+1/2 and –x+3/2, y–1/2, –z+1/2.

In all cases, the salts have 8-coordinate potassium centres bound to both the central oxygen of the phenoxy-imine ligand and the crown ether. The imine arms of the ligand

are rotated away from the metal to reduce unfavourable steric interactions. In the solid-state, the potassium salts of the less sterically bulky ligands pack together to form 1D polymers (R = H (**[7(18-c-6)]*n***), Me (**[8(18-c-6)]*n***)). These propagate through non-covalent interactions between the potassium and isopropyl methyl groups. In contrast, the coordination sphere of potassium when R = ^{t}Bu is completed by a thf-ligand resulting in a simple molecular structure (**[9(18-c-6)(thf)]**).

The metrical parameters clearly differentiate these coordination preferences (**Table 4.1**); for example, the K-$O_{phenoxide}$ bond lengths are similar for the ligands with smaller *para*-substituents (R = H and Me) but largest for the R = ^{t}Bu derivative (K-O bond lengths: 2.509(4) Å (**[7(18-c-6)]*n***), 2.5041(11) Å (**[8(18-c-6)]*n***), 2.5786(15) (**[9(18-c-6)(thf)]**) Å). This value agrees with the literature value for a single K-O bond (2.59 Å) as reported by Pyykkö in 2015.[27] The same trend is also observed for the C_{ipso}-O-K bond angles (147.4(3)° (**[7(18-c-6)]*n***), 145.76(10)° (**[8(18-c-6)]*n***) and 165.15(15)° (**[9(18-c-6)(thf)]**)).[27] The similar $O_{phenoxide}$-K-C and $O_{phenoxide}$-K-O_{thf} bond angles of 168.12° (**[7(18-c-6)]*n***), 168.9° (**[8(18-c-6)]*n***) and 164.94(6)° (**[9(18-c-6)(thf)]**) reflect the steric constraints of the crown ether ligating the potassium ion.

Often, potassium complexes with 18-crown-6 feature charge separated ions with a $[K(18\text{-}c\text{-}6)(thf)_2]^+$ moiety.[28-30] The inherent stabilisation of the extended structures in **[7(18-c-6)]*n***, and **[8(18-c-6)]*n*** however, arise from rare non-covalent interactions between the diisopropyl-*methyl* groups and the potassium centre.[31-33] It is more common for potassium cations to interact with diisopropyl-*aryl* groups *via* π-facial interactions,[34-36] but it is appears that systems with the [^{Me,Dipp}L] and [^{Dipp}L] ligands cannot align correctly in space to facilitate such an interaction. In addition, the coordinatively demanding crown-ether may also disfavour poly-hapto *aryl* interactions.

Table 4.1 Experimental metrical parameters (bond lengths (Å) and angles (°)) of ^{Dipp}LK(18-c-6) **[7(18-c-6)]$_n$**, ^{Me,Dipp}LK(18-c-6) **[8(18-c-6)]$_n$**, and $^{t Bu,Dipp}$LK(18-c-6)(thf) **[9(18-c-6)(thf)]**. Estimated standard deviations shown in brackets.

	^{Dipp}LK(18-c-6) (**[7(18-c-6)]$_n$**)	^{Me,Dipp}LK(18-c-6) (**[8(18-c-6)]$_n$**)	$^{t Bu,Dipp}$LK(18-c-6)(thf) (**[9(18-c-6)(thf)]**)
K-O(1)	2.509(4)	2.5041(11)	2.5786(15)
O(1)-C(1)	1.273(6)	1.2735(17)	1.274(2)
M-O(thf)	-	-	2.895(2)
C(1)-O(1)-K	147.4(3)	145.76(10)	165.15(15)
[a]O(1)-K-X	168.12	168.9	164.94(6)

[a]X = C (polymeric chain) for **[7(18-c-6)]$_n$** and **[8(18-c-6)]$_n$** and X = O(thf) for **[9(18-c-6)(thf)]**.

4.3.1.3 Solid angle calculations

The atomic coordinates, obtained from X-ray crystallographic analysis, were used in solid angle calculations; the results are presented in **Figures 4.6-4.8** and **Table 4.2**.

Table 4.2 Summary of ligand solid angles (Ω), the percentage of the sphere shielded by the ligand (G), the percent of the metal surface shielded by ligand atoms (G(M)) and the percentage of the metal surface "in contact" with ligated atoms (S(M)) for the potassium salts: ^{Dipp}LK(18-c-6) [**7(18-c-6)**], ^{Me,Dipp}LK(18-c-6) [**8(18-c-6)**] and $^{t Bu,Dipp}$LK(thf) [**9(18-c-6)(thf)**].

Complex	**Ω(^{Dipp}L) (sr)**	**Ω(18-c-6) (sr)**	**Ω(thf) (sr)**	**G(^{Dipp}L) (%)**	**G(18-c-6) (%)**	**G(thf) (%)**	**$G_{2.28}$ (^{Dipp}L) (%)**	**$G_{2.28}$ (18-c-6) (%)**	**$G_{2.28}$ (thf) (%)**	**G(M) (%)**	**S(M) (%)**
^{Dipp}LK	3.48	6.53	-	27.67	51.99	-	36.55	-[a]	-	58.90	47.39
^{Me,Dipp}LK	3.49	6.57	-	27.76	52.31	-	36.33	-[a]	-	59.13	47.53
$^{t Bu,Dipp}$LK(thf)	3.53	6.73	1.37	28.08	53.54	10.91	30.80	-[a]	15.46	66.60	54.34

[a] No meaningful normalisation possible.

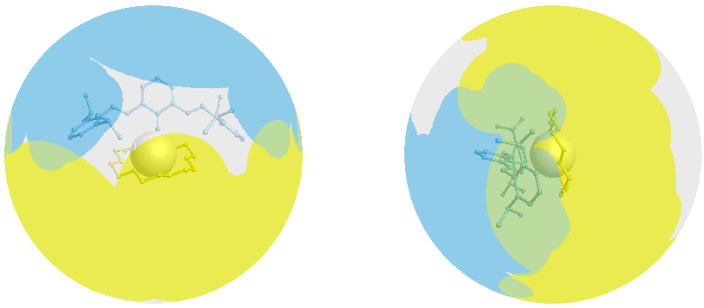

Figure 4.6 Visualisations of *G*(L) values in ^{Dipp}LK [**7(18-c-6)**], showing the percentage of the complex sphere shielded by each ligand. Blue = ^{Dipp}L, yellow = 18-c-6.

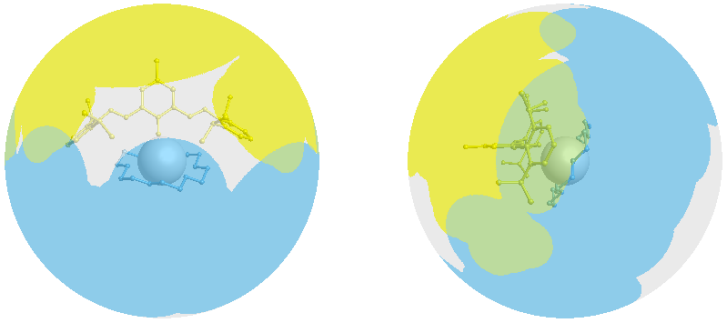

Figure 4.7 Visualisations of *G*(L) values in ^{Me,Dipp}LK [**8(18-c-6)**], showing the percentage of the complex sphere shielded by each ligand. Blue = 18-c-6, yellow = ^{Me,Dipp}L.

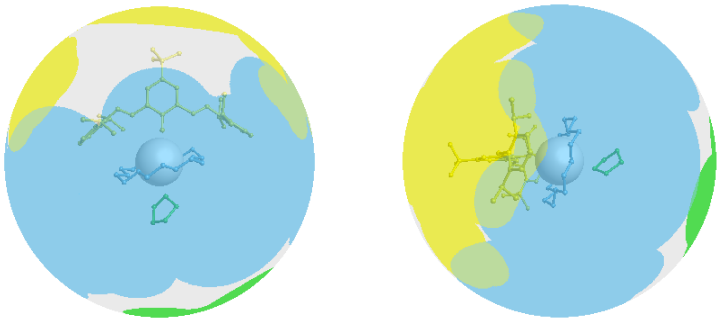

Figure 4.8 Visualisations of *G*(L) values in $^{t Bu,Dipp}$LK(18-c-6)(thf) [**9(18-c-6)(thf)**], showing the percentage of the complex sphere shielded by each ligand. Blue = 18-c-6, yellow = $^{t Bu,Dipp}$L, green = thf.

Compounds [**7(18-c-6)]** and [**8(18-c-6)]** show almost identical shielding parameters; this is to be expected considering the only change in structure occurs on the opposite side of the ligand to the metal centre. In contrast, potassium salt **[9(18-c-6)(thf)]** exhibits slightly different shielding values due to the presence of the thf molecule in its solid-state coordination sphere (*G*(M): 58.90% for **[7(18-c-6)]**, 59.13% for **[8(18-c-6)]** and 66.60% for **[9(18-c-6)(thf)] –** an average increase of ~7%). The "NON" ligand framework has the weakest shielding effect in **[9(18-c-6)(thf)]**; this is the result of the metal centre being situated the farthest from the phenoxide centre (**Table 4.1**; K-O(1) bond lengths: 2.509(4) Å (**[7(18-c-6)]**), 2.5041(11) Å (**[8(18-c-6)]**), 2.5786(15) (**[9(18-c-6)(thf)]**) Å). The shielding imparted in the polymeric structures of **[7(18-c-6)]*n***, and **[8(18-c-6)]*n*** could not be calculated using the Solid Angle programme due to the sequential monomers not lying within the bonding limits of the application.

4.3.2 Synthesis of *bis*(ligand), homoleptic alkaline-earth (M = Mg, Sr, Ba) initiators

After successful isolation of $^{t\text{Bu,Dipp}}$LK·thf$_x$ (**9·thf$_x$**), it was employed in various salt-metathesis reactions with alkaline-earth diiodides; the desired products were monometallic, heteroleptic complexes which may act as intermediates in the synthesis of cationic bimetallics.

An equimolar reaction of **9·thf$_x$** and MI_2 (M = Mg, Ba) in THF afforded 0.5 eq. of the *bis*(ligand) complex ($^{t\text{Bu,Dipp}}$L)$_2$M(thf)$_x$ (M = Mg [x = 1; **10**], Ba [x = 2; **12**]), KI and 0.5 eq. MI_2 at room temperature. The presence of unreacted alkaline-earth species was detected by further precipitation of KI upon addition of extra equivalents of potassium salt. Variation of reaction conditions such as temperature, solution concentration and method

of addition all resulted in the isolation of the same species as indicated by ^{1}H NMR spectroscopy. Rational synthesis of these complexes was achieved by reaction of **9·thf$_x$** and MI_2 in a 2:1 ratio, resulting in the isolation of free-flowing yellow powders in 81% (**10**) and 58% (**12**) yield (**Scheme 4.4**).

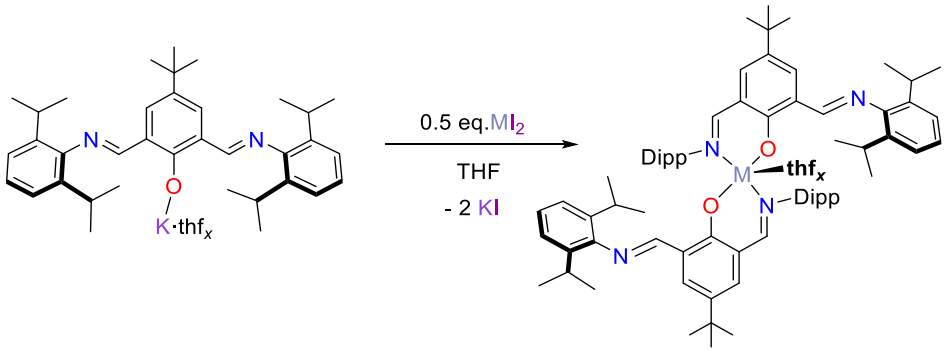

Scheme 4.4 Synthesis of ($^{t\text{Bu,Dipp}}$L)$_2$M(thf)$_x$ (M = Mg [x = 1; **10**], Sr [x = 2; **11**] and Ba [x = 2; **12**]) via the salt-metathesis reaction between $^{t\text{Bu,Dipp}}$LK.thf$_x$ (**9·thf$_x$**) and MI_2.

The analogous equimolar salt-metathesis reaction between **9·thf$_x$** and SrI_2 in THF resulted in the formation of a mixture of homoleptic and heteroleptic species (**Figure 4.9**). These proved to be inseparable due to similar solubility profiles, but full conversion to the homoleptic *bis*(ligand) strontium species ($^{t\text{Bu,Dipp}}$L)$_2$Sr(thf)$_2$ could be achieved in using a 2:1 stoichiometric ratio (**11**; **Scheme 4.4**). Like the magnesium and barium variants, complex **11** was isolated as a free-flowing yellow powder in 59% yield.

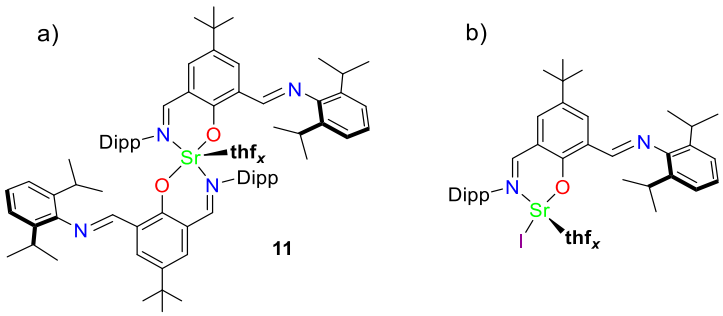

Figure 4.9 The a) homoleptic (**11**) and b) proposed heteroleptic species formed from the 1:1 reaction between **9·thf$_x$** and SrI_2.

4.3.2.1 NMR spectroscopic analysis

The ^{1}H NMR spectrum of ($^{t\text{Bu,Dipp}}$L)$_2$Mg(thf) (**10**) has 14 signals, indicating fixed asymmetry within a single ligand unit caused by the (un)bound imine arms (**Figure 4.10**).

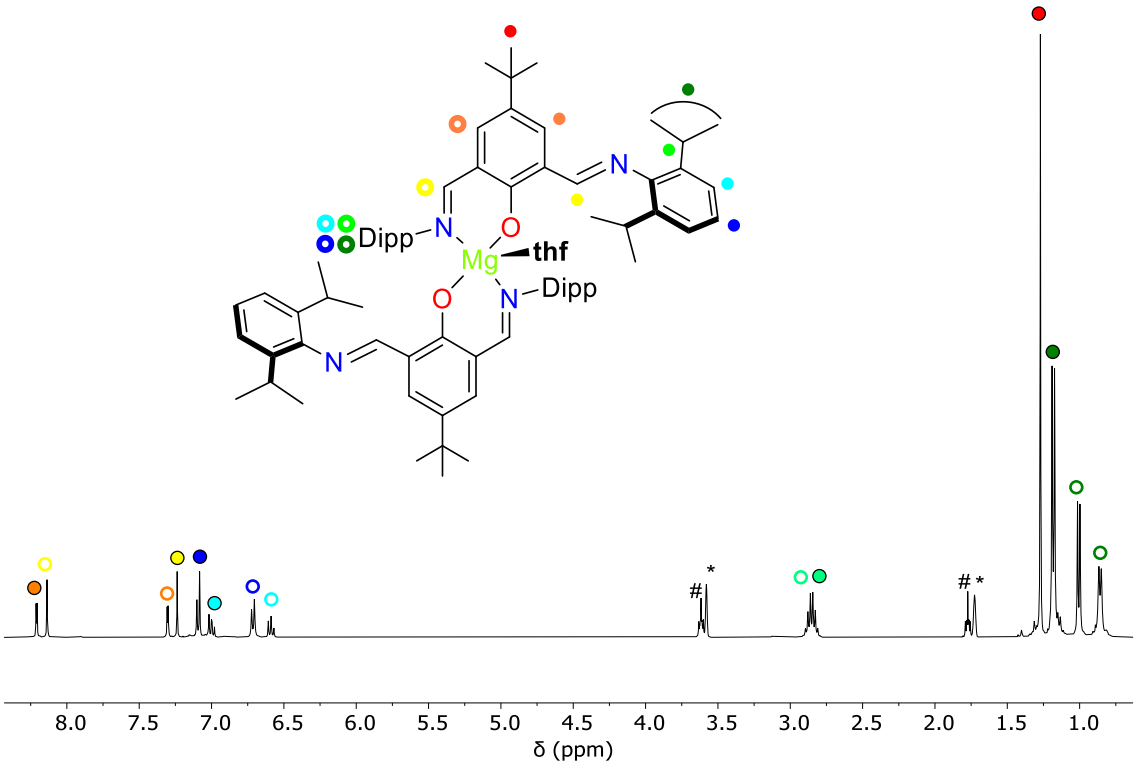

Figure 4.10 ^{1}H NMR spectrum (*THF-d_8, 600 MHz, 298 K) of ($^{t\text{Bu,Dipp}}$L)$_2$Mg(thf) (**10**). # represents the bound-thf.

The two protons of the central aromatic ring, located at δ 8.21 and δ 7.30 ppm, appear as doublets with coupling constants ($^{4}J_{HH}$) of 2.9 Hz. The sharp singlets that represent the imine (***H***C=N) protons of the "bound" and "free" arms are found at δ 8.14 ppm and δ 7.24 ppm respectively. The final four aromatic resonances correspond to the imine-*aryl* C***H*** protons; the "free" imine arm twists away from the metal centre and therefore its corresponding pair of signals appear more deshielded. At δ 2.85 ppm there are two overlapping septets which represent the *methine* protons of the diisopropyl groups. The

mutually coupling doublets ($^3J_{HH}$ = 6.9 Hz) for the diisopropyl *methyl* protons are located as three separate resonances between δ 1.20 and δ 0.80 ppm. The first at δ 1.18 ppm, integrates to 24H, and represents the *methyl* groups of the freely rotating, unbound imine arm. The restricted rotation of the magnesium-bound diisopropyl group causes its *methyl* protons to appear as the remaining two doublets which each integrate to 12H. The final resonance at δ 1.27 ppm corresponds to the *tert*-butyl protons; the presence of only one singlet for this group indicates that the two ligand fragments are related by a C_2 rotational axis.

The ^{1}H NMR spectra of complexes **11** and **12** contain half as many resonances as that of compound **10** (**Figure 4.11**); this implies that the fixed asymmetry found within the magnesium system is not apparent in the heavier analogues on the NMR timescale. Instead, the larger Sr and Ba metal centres allow for fluxional behaviour in solution which causes the observed peak broadening and *pseudo* C_{2v} symmetry. This dynamic behaviour may involve ligand exchange between metal centres, or the exchange of the metal centre within the different binding pockets of a single ligand unit.

In both systems, the two signals corresponding to the imine ***H***C=N and 3,5-C_6***H***$_2$ protons in the central phenyl ring, located between δ 9.00 and δ 7.50 ppm, are broadened into the baseline at 298 K. A mutually coupling doublet and triplet ($^3J_{HH}$ = 7.7 (**11**), 7.6 (**12**) Hz) represent the imine-*aryl* C***H*** protons while the *methine* protons of the isopropyl groups correlate to the septet close to δ 3.00 ppm. The mutually coupling isopropyl *methyl* groups are highlighted by: a broad, unresolved multiplet (δ 0.96 ppm) for the Sr species and a sharp doublet (δ 1.02 ppm; $^3J_{HH}$ = 6.9 Hz) for the Ba compound. This indicates free-rotation of of these groups in solution for barium, but partial restriction of the

rotation as a result of increased steric congestion around the smaller strontium metal centre. The final singlet, around δ 1.25 ppm, corresponds to the nine *tert*-butyl protons.

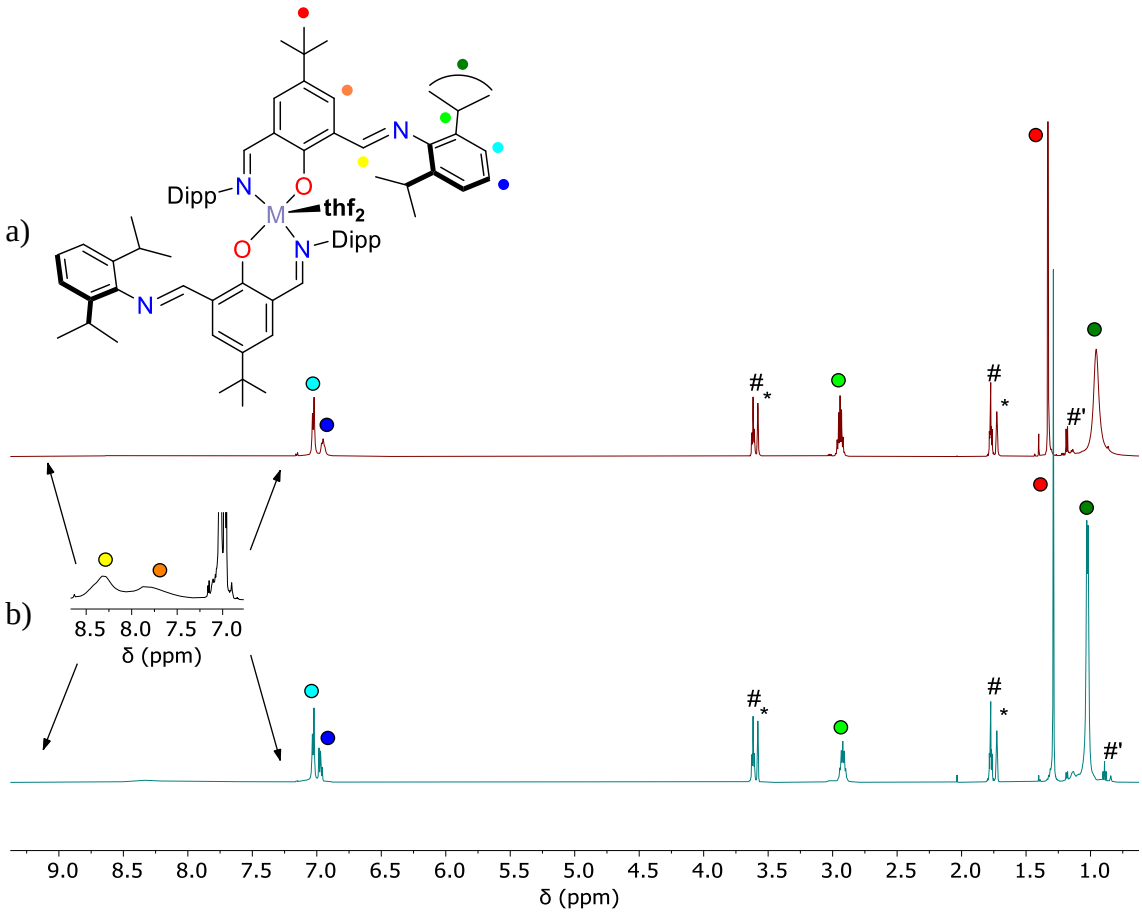

Figure 4.11 ^{1}H NMR spectra (*THF-d_8, 600 MHz, 298 K) of a) ($^{t\text{Bu,Dipp}}$L)$_2$Sr(thf)$_2$ (**11**) and b) ($^{t\text{Bu,Dipp}}$L)$_2$Ba(thf)$_2$ (**12**). # and #' represent bound-thf and residual pentane from reaction work up.

The fluxional behaviour of the ligands and *pseudo* C_{2v} symmetry of these complexes was investigated by cooling THF-d_8 solutions of **11** and **12** in the NMR spectrometer; the results of these variable temperature experiments can be seen in **Figure 4.12** and **Figure A.26**. When the samples were cooled to at least 253 K, each of the resonances split into two as a result of the asymmetric binding mode of the ligand. Coalescence was observed upon warming the sample. Heating the compound to temperatures up to 323 K appeared to have no observable effect on the identity or quality of the samples. The observed

coalescence temperature (298 K) and peak to peak separation of the imine (378 (**11**), 341 (**12**) Hz) and central aromatic ring (494 (**11**), 485 (**12**) Hz) protons were used in the equations reported by Duncalf *et al*. (**Equations 4.1-4.2**) to estimate average activation barriers ($\Delta G^{\ddagger}$) and rates of ligand exchange/binding pocket fluctuation of the metal centres.[37] These values were computed to be 56 kJ mol^{-1} and 685 s^{-1} for the strontium complex and 57 kJ mol^{-1} and 649 s^{-1} for the barium species.

$$\Delta G^{\ddagger} = RT_c(23 + \ln(\frac{T_c}{\Delta\nu})) \qquad k = \frac{\pi\Delta\nu}{2} \qquad \textbf{Equations 4.1-4.2}$$

where T_c is coalescence temperature and $\Delta\nu$ is peak separation in Hz

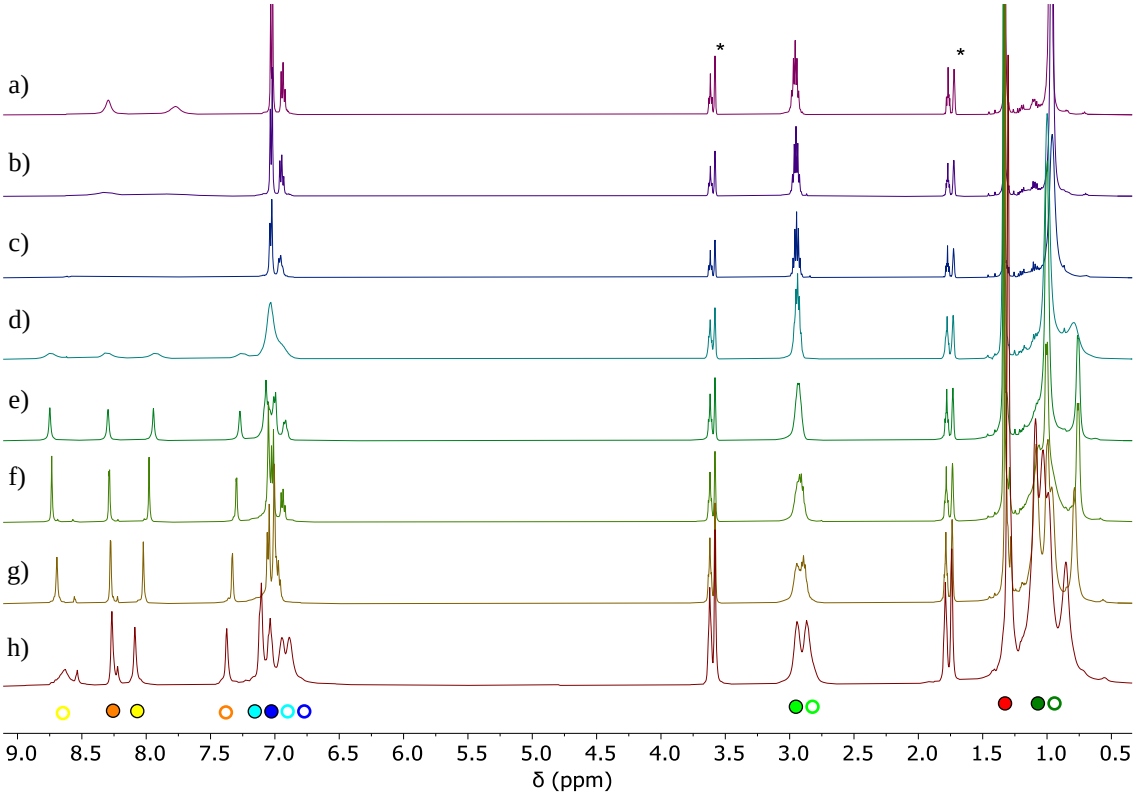

Figure 4.12 VT ^{1}H NMR spectra (*THF-d_8, 500 MHz, 298 K) of ($^{t\text{Bu,Dipp}}$L)$_2$Sr(thf)$_2$ (**11**) at a) 323 K, b) 313 K, c) 298 K, d) 273 K, e) 253 K, f) 233 K, g) 213 K and h) 193 K.

4.3.2.2 X-ray crystallographic analysis

Verification of the structures of complexes **10-12** in the solid-state was achieved by X-ray diffraction analysis on single crystals, grown at room temperature from saturated THF/pentane, hexamethyldisiloxane (HMDSO), and pentane solutions, respectively (**Figures 4.13-4.14** and **Tables 4.3-4.4**).

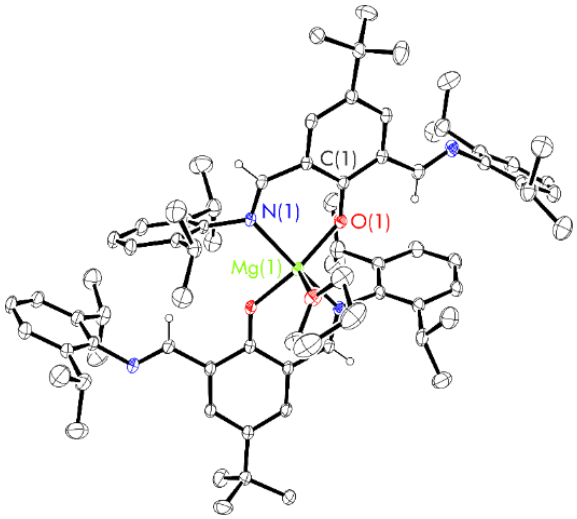

Figure 4.13 Thermal displacement ellipsoid drawings (30% probability) of ($^{t\text{Bu,Dipp}}$L)$_2$Mg(thf) (**10**). All hydrogen atoms, except those bound to C(7) and C(24) have been omitted for clarity.

The magnesium centre in complex **10** is in a 5-coordinate square pyramidal coordination environment, as indicated by τ_5 = 0.03, where τ_5 = 0 corresponds to an idealised square pyramid and τ_5 = 1.00 corresponds to an idealised trigonal bypyramid.[38] The phenoxy-imine ligands occupy the basal plane with a coordinated thf ligand in the apical position (Mg(1) lies 0.341 Å above the N_2O_2 plane). Only one of the ligands is crystallographically unique, thus confirming that the individual ligand units are related by a C_2 rotational axis. The ligands, each containing one imine N atom bound to the magnesium centre and one free imine arm, are orientated *anti* with respect to each other to further minimise steric congestion. The bound and free C=N imine distances are similar (1.279(4) and

1.266(4) Å respectively; **Table 4.3**). The Mg-$O_{phenoxide}$ (1.952(2) Å) and Mg-N_{imine} (2.177(2) Å) bond lengths are within the range of previously reported phenoxy-imine magnesium complexes (Mg-$O_{phenoxide}$: 1.899(2)–2.0028(13) Å; Mg-N_{imine}: 2.105(2)–2.3533(15) Å).[16, 39, 40]

Table 4.3 Comparison of experimental metrical parameters (bond lengths (Å) and angles (°)) between ($^{t^{Bu,Dipp}}$L)$_2$Mg(thf) (**10**) and similar reported compounds.[16, 39] Estimated standard deviations shown in brackets.

	($^{t^{Bu,Dipp}}$L)$_2$Mg(thf) (**10**)	(^{2}L)$_2$Mg(thf)[39]	(^{MeO,Dipp}L)$_2$Mg(thf)[16]
Space group	$P4_12_12$	$P2_1/n$	$P2_1/c$
Mg-O(1)	1.952(2)	1.9432(15)	1.940(3)
Mg-N(1)	2.177(2)	2.1522(17)	2.151(4)
Mg-O(thf)	2.036(4)	2.0433(17)	2.035(4)
O(1)-Mg-N(1)	85.59(9)	86.52(6)	87.31(14)
O(1)-Mg-O(2)	159.98(16)	176.08(7)	178.0(15)
N(1)-Mg-N(2)	161.88(16)	133.88(7)	122.4(15)
τ_5 [a]	0.03	0.70	0.93

[a] $\tau_5 = 1$ for trigonal bipyramidal; $\tau_5 = 0$ for square-based pyramidal.[38]

Related solid state structures of *bis*(imine)phenoxide Mg complexes (^{R,Dipp}L)$_2$Mg(L) (R = Me, L = dioxane; R = OMe or Cl, L = thf) have been reported by Chakraborty and co-workers and were prepared by the reaction of H^{R,Dipp}L and Et_2Mg in a 2:1 ratio.[16, 41] While the ligands show the same asymmetric coordination, resulting in 5-coordinate geometries, the Mg centre in each case is in a distorted trigonal bipyramidal coordination environment (τ_5 = 0.90, R = Me; 0.93, R = OMe; 0.85, R = Cl).[38] Related structures with bidentate

phenoxy-imine ligands are four, five or six coordinate dependent on the steric encumbrance of the ligand framework and choice of solvent for reaction and recrystallisation.[38, 39, 41]

The solid-state structures of compounds **11** and **12** are the only examples of heavier alkaline-earth homoleptic "NON" complexes; previous reports of analogous systems use calcium[42], zinc[43], nickel[26] and copper[13]. In both structures, the metal centres adopt distorted octahedral geometries (**Figure 4.14**). The six coordination sites are filled by two imine and two phenoxide donors of the "NON" frameworks as well as two thf molecules.

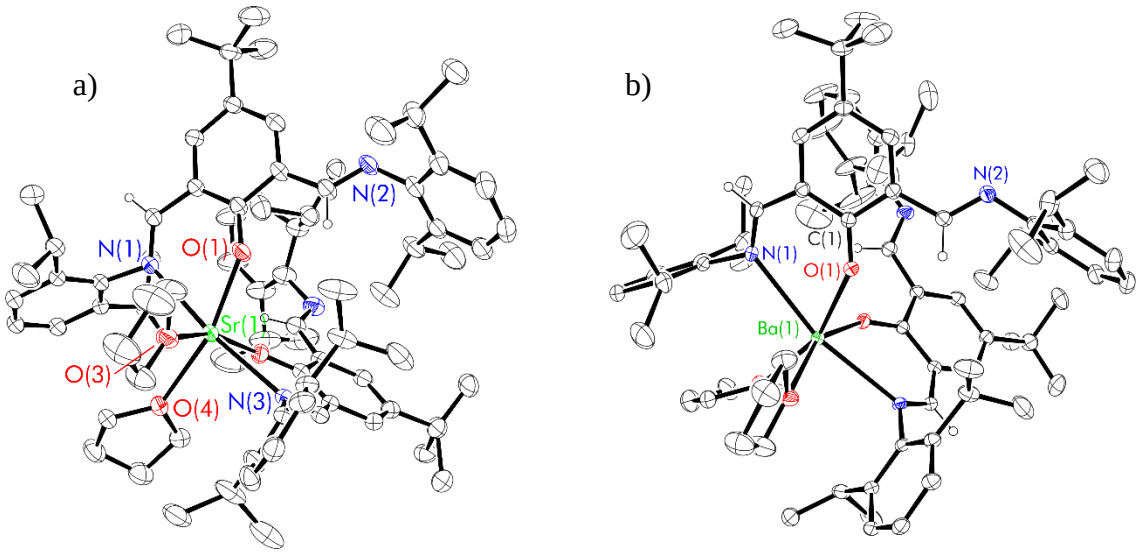

Figure 4.14 Thermal displacement ellipsoid drawings (30% probability) of a) $(^{t\text{Bu,Dipp}}\text{L})_2\text{Sr(thf)}_2$ (**11**) b) and $(^{t\text{Bu,Dipp}}\text{L})_2\text{Ba(thf)}_2$ (**12**). All hydrogen atoms, except those bound to C(7) and C(24) have been omitted for clarity.

In contrast to **10**, the two ligand units are not co-planar. Instead, each ligand is splayed with respect to the other (interplanar angle between planes defined by the central aromatic rings of the "NON" ligands = 70.4° (**11**), 69.9° (**12**)); this is most likely to enable the binding of an additional thf molecule to the larger metal ions, as well as minimise unfavourable interactions between the bulky imine aromatic groups. The bound and free

C=N imine distances are similar in both structures (1.279(3) Å and 1.273(3) Å for **11** 1.284(2) Å and 1.276(3) Å for **12** respectively). The average M-$O_{phenoxide}$ (Sr: 2.339 Å, Ba: 2.486 Å) and M-N_{imine} (Sr: 2.692 Å, Ba: 2.848 Å) bond lengths are comparable to previously reported strontium and barium complexes bearing similar donors atoms (Sr-O: 2.498-2.730 Å; Sr-N: 2.510(2)–2.78 Å; Ba-O: 2.59-2.756 Å; Ba-N: 2.623(3)-2.712(2) Å)[44-50] and follow the trend: **10** < **11** < **12** (**Table 4.4**). This reflects the increasing size of the ionic radii: Mg^{2+}(5-coordinate) = 0.72 Å, Sr^{2+}(6-coordinate) = 1.16 Å, Ba^{2+}(6-coordinate) = 1.36 Å.[51]

Table 4.4 Experimental metrical parameters (bond lengths (Å) and angles (°)) of ($^{t\text{Bu,Dipp}}$L)$_2$Sr(thf)$_2$ (**11**) and ($^{t\text{Bu,Dipp}}$L)$_2$Ba(thf)$_2$ (**12**). Estimated standard deviations shown in brackets.

	($^{t\text{Bu,Dipp}}$L)$_2$Sr(thf)$_2$ (**11**)	($^{t\text{Bu,Dipp}}$L)$_2$Ba(thf)$_2$ (**12**)
Space group	$P2_1/c$	$P2_1/c$
M-N	2.699(3)/ 2.684(8)	2.8458(18)/ 2.8499(17)
M-O	2.326(2)/ 2.351(2)	2.4766(16)/ 2.8499(17)
M-O(thf)	2.563(2)/ 2.571(2)	2.7621(16)/ 2.7818(17)
O(1)-M-N(1)	70.23(8)	64.99(5)
O(1)-M-O(2)	100.61(8)	101.94(5)
N(1)-M-N(3)	173.8(2)	166.79(5)

4.3.2.3 Solid angle calculations

The atomic coordinates of the homoleptic *bis*(ligand) alkaline-earth complexes **10**-**12**, produced from X-ray crystallographic analysis, were used in solid angle calculations. The results are presented in **Figures 4.15-4.17** and **Table 4.5**.

As expected, the solid angle and *G*-parameters associated with the $^{t\text{Bu,Dipp}}$L ligands decrease with increasing cation size (*G*(M): 77.02% (**10**), 64.83% (**11**), 53.48% (**12**)). Within each complex however, the values for the individual "NON" frameworks are very similar; this suggests that in all cases the shielding is uniform with neither ligand unit dominating the coverage. A similar reduction in percent metal coverage is observed for the bound thf molecule(s): **10**: 17.25% > **11**: 11.69% (*av*.) > **12**: 10.81% (*av*.). These results imply that the metal centre is the most accessible in the Ba system and thus the general trend of polymerisation activity should follow Mg < Sr < Ba.

Table 4.5 Summary of ligand solid angles (*Ω*), the percentage of the sphere shielded by the ligand (*G*), the percent of the metal surface shielded by ligand atoms (*G*(M)) and the percentage of the metal surface "in contact" with ligated atoms (*S*(M)) for the isolated bis-ligated, homoleptic complexes: ($^{t\text{Bu,Dipp}}$L)$_2$Mg(thf) (**10**), ($^{t\text{Bu,Dipp}}$L)$_2$Sr(thf)$_2$ (**11**) and ($^{t\text{Bu,Dipp}}$L)$_2$Ba(thf)$_2$ (**12**).

Complex	*Ω*($^{\text{Dipp}}$L) (sr)	*Ω*($^{\text{Dipp}}$L$_2$) (sr)	*Ω*(thf) (sr)	*G*($^{\text{Dipp}}$L) (%)	*G*($^{\text{Dipp}}$L$_2$) (%)	*G*(thf) (%)	$G_{2.28}$ ($^{\text{Dipp}}$L) (%)	$G_{2.28}$ ($^{\text{Dipp}}$L$_2$) (%)	$G_{2.28}$ (thf) (%)	*G*(M) (%)	*S*(M) (%)
($^{t\text{Bu,Dipp}}$L)$_2$Mg(thf)	5.21	5.21	2.17	41.44	41.45	17.25	32.68	32.71	14.33	77.02	70.79
($^{t\text{Bu,Dipp}}$L)$_2$Sr(thf)$_2$	4.45	4.41	[a]1.45	35.43	35.03	[a]11.55	36.13	34.76	[a]20.93	64.83	56.74
			[a]1.48			[a]11.83			[a]20.80		
($^{t\text{Bu,Dipp}}$L)$_2$Ba(thf)$_2$	4.28	4.32	[a]1.33	34.04	34.35	[a]10.56	33.80	35.64	[a]14.28	53.48	49.71
			[a]1.39			[a]11.05			[a]19.05		

[a] independent thf molecules.

When the exogenous ligands are normalised to be 2.28 Å away from the metal centres, the "NON" frameworks are seen to cast similar shadows across all three complexes (*av.*

32.70% in **10**, 34.45% in **11** and 34.72% in **12**). The shielding of **10** appears to be reduced at this distance as a result of the ligands being forced further away from the metal centre than in the solid-state structure (**Table 4.3**). In contrast, the thf molecules in complexes **11** and **12** are brought much closer to the metal centre hence the observed increase in their supposed shielding effects (*G vs.* $G_{2.28}$: 11.69% *vs.* 20.87% (**11**) and 10.81% *vs.* 16.67% (**12**)).

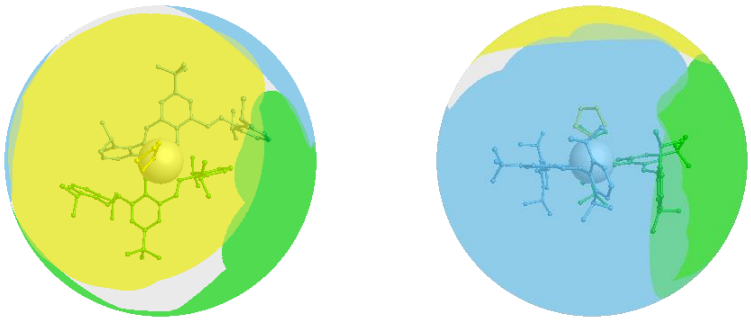

Figure 4.15 Visualisations of *G*(L) values in ($^{t\text{Bu,Dipp}}$LMg)$_2$(thf) (**10**), showing the percentage of the complex sphere shielded by each ligand. Blue = $^{t\text{Bu,Dipp}}$L, green = $^{t\text{Bu,Dipp}}$L$_2$, yellow = thf.

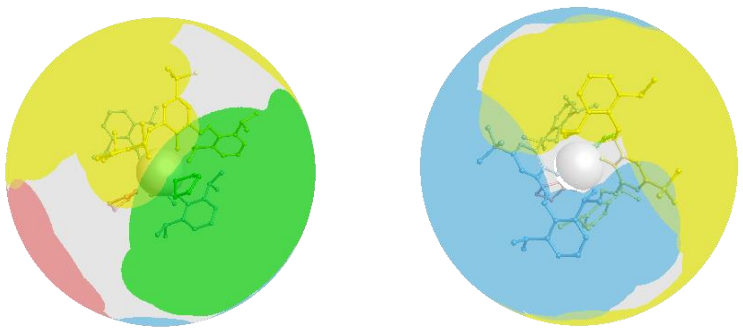

Figure 4.16 Visualisations of *G*(L) values in ($^{t\text{Bu,Dipp}}$LSr)$_2$(thf)$_2$ (**11**), showing the percentage of the complex sphere shielded by each ligand. Blue = $^{t\text{Bu,Dipp}}$L, yellow = $^{t\text{Bu,Dipp}}$L$_2$, green = thf, red = thf.

Figure 4.17 Visualisations of *G*(L) values in ($^{t\text{Bu,Dipp}}$LBa)$_2$(thf)$_2$ (**12**), showing the percentage of the complex sphere shielded by each ligand. Blue = $^{t\text{Bu,Dipp}}$L, yellow = $^{t\text{Bu,Dipp}}$L$_2$, green = thf, red = thf.

4.3.3 Alternative attempts to synthesise a heteroleptic $^{t\text{Bu,Dipp}}$LMgI(thf)$_3$ initiator

As the salt metathesis reaction between $^{t\text{Bu,Dipp}}$LK.thf$_x$ (**9·thf$_x$**) and MgI$_2$ resulted in ligand redistribution, an alternative, protonolysis pathway to the desired heteroleptic MgI complex was investigated. To this end, the pro-ligand was treated with *methyl*-magnesium iodide (**Scheme 4.5**).

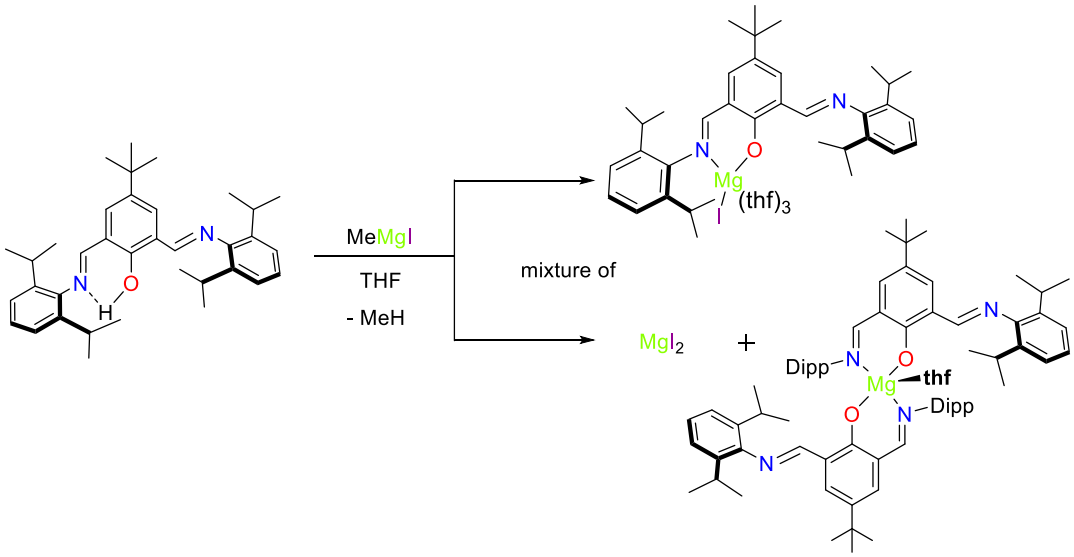

Scheme 4.5 The mixture of products formed via the protonolysis reaction between H$^{t\text{Bu,Dipp}}$L and MeMgI.

Initial reaction conditions, based on literature protocols, involved dropwise addition of ligand to Grignard at –78 °C.[52] Analysis of the crude mixture by ^{1}H NMR spectroscopy revealed that multiple species were present (**Figure 4.18**): the *bis*(ligand) homoleptic magnesium complex (**10**), residual pro-ligand (indicated by O***H*** signal at δ 13.5 ppm) and an unknown compound. This species was tentatively assigned as the desired heteroleptic complex as it has similar spectroscopic features to **13-15** (*vide infra*).

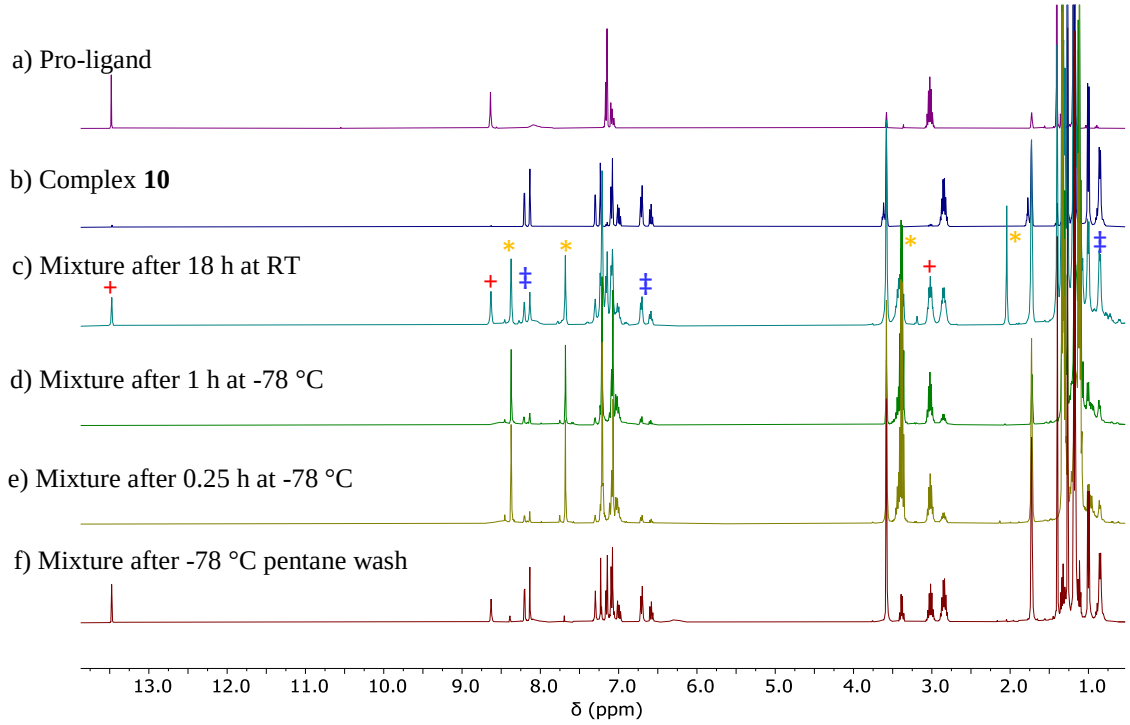

Figure 4.18 ^{1}H NMR spectra (*THF-d_8, 400 MHz, 298 K) of a) H$^{t\text{Bu,Dipp}}$L (+), b) ($^{t\text{Bu,Dipp}}$L)$_2$Mg(thf) (**10**, ‡), c) reaction mixture after 18 h at room temperature, d) reaction mixture after 1 h at –78 °C, e) reaction mixture after 15 mins at –78 °C and f) reaction mixture after attempted work-up with pentane. * represents the unknown species.

Variation of reaction conditions (concentration, rate of addition, time and temperature) to disfavour ligand redistribution, were then conducted. Cooling the mixture and reducing the reaction time inhibited the presence of residual pro-ligand and reduced the percentage

contamination of complex **10** (originally 50%, now 24%). The similar solubility profiles of the unknown and ($^{t\text{Bu,Dipp}}$L)$_2$Mg(thf) however, meant that any attempt to remove the contaminant/extract the desired product proved unfruitful. In most cases, the amount of **10** increased upon washing, suggesting rapid Schlenk-type redistribution to the homoleptic compound and (presumably) MgI_2 as the thermodynamic sink of this reaction profile.

4.3.4 Synthesis of heteroleptic calcium (R = H, Me, ^{t}Bu) initiators

The analogous salt-metathesis reaction of an equimolar mixture of CaI_2 and $^{\text{Dipp}}$LK.thf$_x$ (**9·thf$_x$**) in THF resulted in immediate precipitation of the expected insoluble potassium iodide by-product. After stirring for 30 minutes at room temperature, the reaction mixture was filtered, dried, and triturated with pentane. This allowed for the isolation of the heteroleptic initiator: $^{\text{Dipp}}$LCaI(thf)$_3$ (**13**) as a free-flowing yellow powder in 42% yield (**Scheme 4.6**). Following this method, the corresponding *para*-methyl and *para-tert*-butyl calcium-iodide complexes were prepared and fully characterised ($^{\text{Me,Dipp}}$LCaI(thf)$_3$ (**14**) = 82%; $^{t\text{Bu,Dipp}}$LCaI(thf)$_3$ (**15**) = 75%).

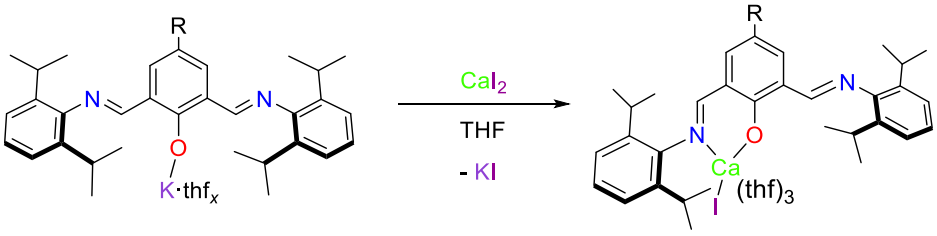

Scheme 4.6 Formation of the heteroleptic calcium-iodide "NON" complexes (R = H (**13**), Me (**14**), ^{t}Bu (**15**)) via the salt metathesis reaction between the corresponding potassium salts (**7-9·thf$_x$**) and CaI_2.

Initial evidence for the formation of the heteroleptic (*vs.* homoleptic) species came from visual observations. Dissolution of the yellow powders in benzene gave clear,

homogeneous solutions suggesting that no residual CaI_2 was present in the samples (its poorly solubility in aromatic solvents would result in precipitation).[53] This therefore implied that the reagents must have reacted in a 1:1 fashion.

4.3.4.1 NMR spectroscopic analysis

The ^{1}H NMR spectra of complexes **13-15** are similar to those of **11** and **12** (**Figure 4.19**). They each contain seven resonances which implies that the compounds have *pseudo*-C_{2v} symmetry in solution. Like the Sr and Ba systems, this is caused by fluxional behaviour; in the case of **13-15**, it is proposed that this is the exchange of the calcium centre between the two [=N,O$^-$] binding pockets of a single ligand unit. There is a possibility of ligand exchange between metal centres but since previous results with the other alkaline-earth metals suggest such redistribution favours the formation of homoleptic species, this seems less likely. Further evidence to support this is that solutions of **13-15** are stable for days in solution without showing signs of redistribution to the homoleptic analogues.

Using **15** as a representative example: the resonances corresponding to the imine ***H***C=N and 3,5-C_6***H***$_2$ protons of the central phenyl ring (δ 8.46 and δ 7.87 ppm, respectively) are broadened due to dynamic interactions with the freely rotating imine arm(s). The remaining aromatic resonances represent the imine-*aryl* group C***H*** protons. The mutually coupled septet at δ 3.01 ppm and doublet at δ 1.17 ppm ($^3J_{HH}$ = 6.9 Hz) correspond to the isopropyl *methine* and *methyl* protons respectively. A singlet at δ 1.32 ppm, correlates to the *tert*-butyl protons and integrates to 9H. The ^{1}H NMR spectra of complexes **13** and **14** are analogous to that of complex **15**; the only difference is the resonance associated with the *para*-substituent.

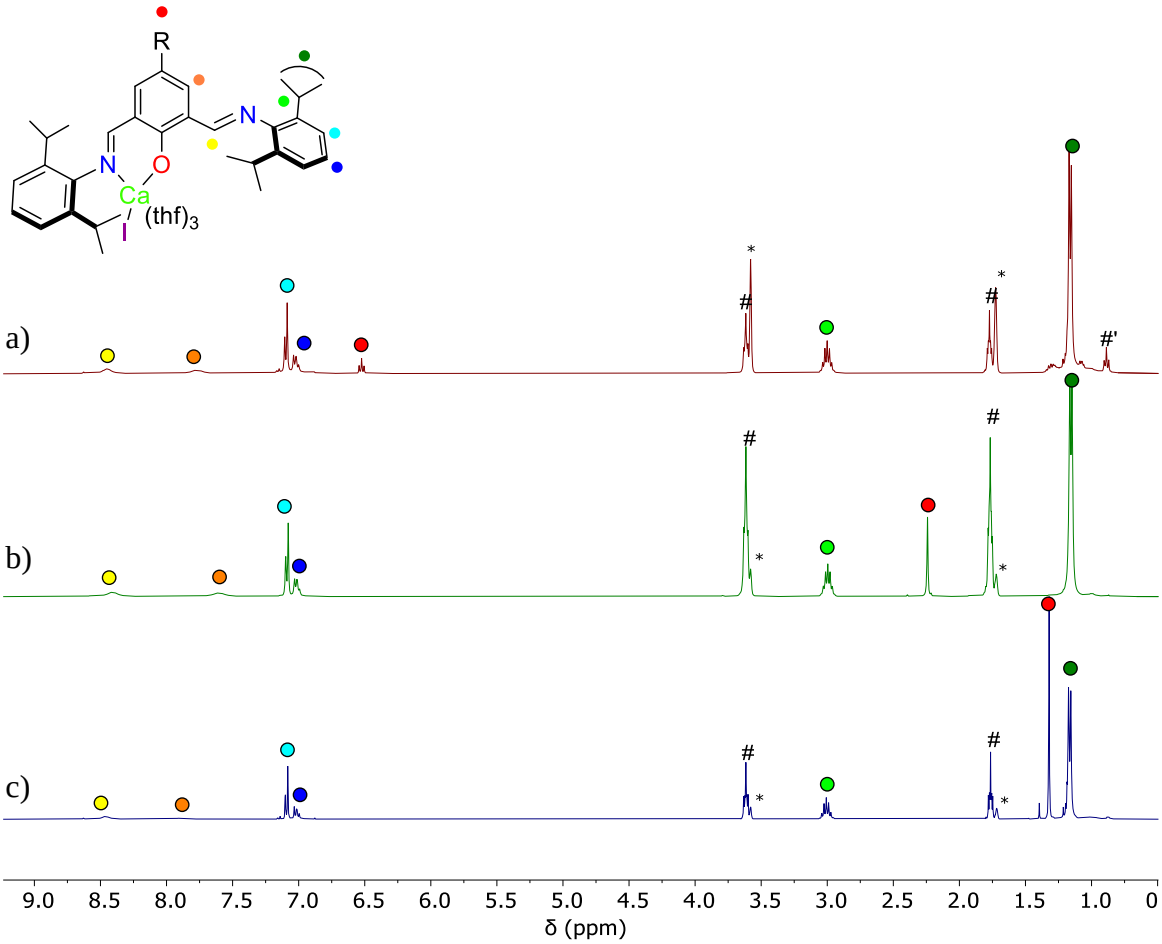

Figure 4.19 ^{1}H NMR spectra (*THF-d_8, 400 MHz, 298 K) of a) ^{Dipp}LCaI(thf)$_3$ (**13**), b) ^{Me,Dipp}LCaI(thf)$_3$ (**14**) and c) ^{tBu,Dipp}LCaI(thf)$_3$ (**15**). # and #' represent bound-thf and residual pentane from work-up.

The fluxional behaviour of the metal centre and *pseudo*-C_{2v} symmetry of these complexes was investigated by cooling down a sample of ^{Me,Dipp}LCaI(thf)$_3$ (**14**). When the sample was cooled to 233 K, the asymmetric binding mode of the "NON" ligand became distinguishable. This was evidenced by the doubling of the number of resonances observed compared to the room temperature spectrum (**Figure 4.20**). Warming the solution up resulted in coalescence of the resonances. Heating the compound to temperatures up to 323 K appeared to have no observable effect on the identity or quality of the sample. The observed coalescence temperature (273 K) and peak to peak

separation of the imine (324 Hz) and central aromatic ring (378 Hz) protons were used in **Equations 4.1-4.2** to estimate average activation barrier ($\Delta G^{\ddagger}$) and rate of binding pocket fluctuation of the calcium centre.[37] These values were computed to be 52 kJ mol^{-1} and 552 s^{-1}. The activation barrier for the dynamics in these heteroleptic systems is *ca.* 5 kJ mol^{-1} lower than that of the homoleptic analogues. This aligns with the suggestion that the nature of the fluxional behaviour is different between the mono- and *bis*(ligand) systems (i.e. ligand exchange *vs*. binding pocket fluctuation).

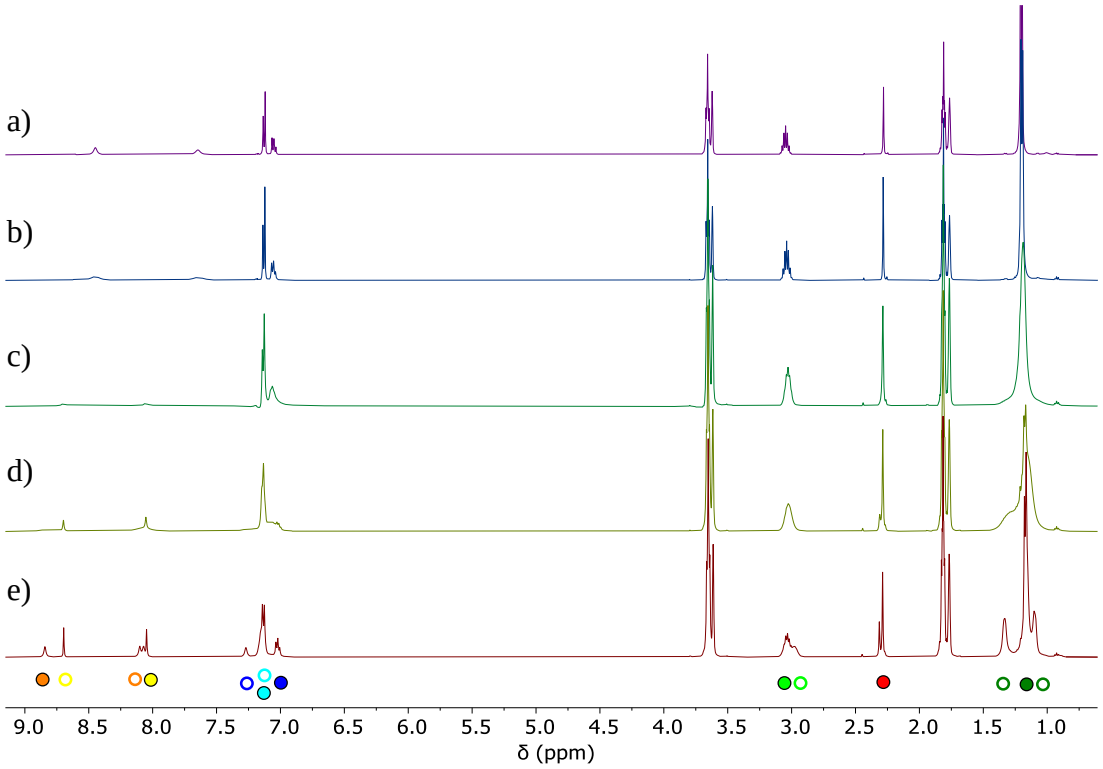

Figure 4.20 ^{1}H NMR spectra (*THF-d_8, 500 MHz) of ^{Me,Dipp}LCaI(thf)$_3$ (**14**) at a) 323 K, b) 298 K, c) 273 K, d) 253 K and e) 233 K. Hollow circles represent Ca-bound side of molecule.

4.3.4.2 X-ray crystallographic analysis

Single crystals of **15**, suitable for X-ray crystallographic analysis, were grown from a saturated THF solution at room temperature. The solid-state structure, refined in the monoclinic $P2_1/c$ space group, verified the heteroleptic nature of the compound (**Figure**

4.21 and **Table 4.6**). The coordination sphere of calcium is seen to require stabilisation by three bound thf molecules; this results in a six-coordinate, octahedral geometry around the metal centre. Currently, there is only a single related example of a crystallographically characterised heteroleptic calcium complex bound by a phenoxy-imine framework with pendant donors ({ON-NMe_2}$CaNSiMe_3$(thf)).[54] This, and other related compounds: $CaI_2(thf)_4$ and {NON}$Y(CH_2SiMe_3)_2(thf)_2$, exhibit comparable coordination geometries to that of **15** (**Table 4.6**).[2, 55]

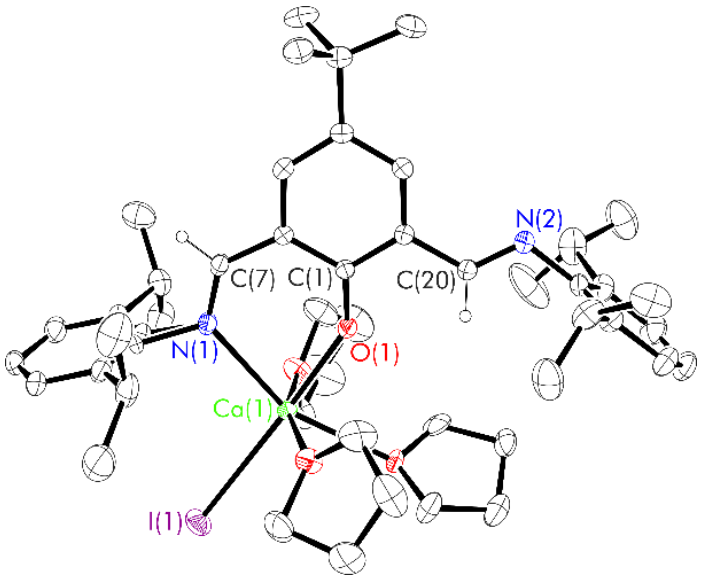

Figure 4.21 Thermal displacement ellipsoid drawings (30% probability) of $^{t\text{Bu,Dipp}}$LCaI$(thf)_3$ (**15**). All hydrogen atoms apart from those on C7 and C20 have been omitted for clarity.

The Ca-$O_{phenoxide}$ (2.1952(19) Å) and Ca-N_{imine} (2.506(2) Å) bond lengths are comparable to {ON-NMe_2}$CaNSiMe_3$(thf)[54] as well as the few examples of dimeric or homoleptic phenoxy-imine calcium complexes (Ca-O: 2.223(2)–2.391(4) Å; Ca-N: 2.479(2)–2.752(5) Å) and the Ca-O/Ca-N single bond lengths predicted by Pyykkö (Ca-O: 2.34 Å; Ca-N: 2.42 Å).[27, 42, 56, 57] The Ca-O bond is shorter than its Ca-N equivalent as a result of the smaller electronegative atom as well as increased electron density transfer to the metal

centre. This is to be expected as the oxygen atom is the formal site of negative charge within the ligand framework, acting as an X-type donor. Similar to both [**9(18-c-6)(thf)]** and{NON}Y(CH_2SiMe_3)$_2$(thf)$_2$, the unbound imine arm is twisted away from the ligand core to relieve steric strain.[2] The calcium-iodide bond (3.0848(5) Å) is similar in length to that of $CaI_2(thf)_4$[55] and falls within the broad range for terminal Ca-I bond lengths (2.9605(18)–3.619(5) Å).[58, 59] The relatively long bond length reflects the large covalent radius of the halogen (1.33 Å) and alkaline-earth atoms (1.00 Å) in addition to the high coordination number.[27, 51] In **15**, the iodide atom is positioned away from the bulky ligand substituents, and without any intermolecular close contacts. The ease of access to this initiating group makes this complex an ideal candidate for polymerisation catalysis.

Table 4.6 Comparison of experimental metrical parameters (bond lengths (Å) and angles (°)) between $^{t\text{Bu,Dipp}}$LCaI(thf)$_3$ (**15**) and similar reported compounds.[2, 55] Estimated standard deviations shown in brackets.

	$^{t\text{Bu,Dipp}}$LCaI(thf)$_3$ (**15**)	{ON-NMe$_2$} CaNSiMe$_3$(thf)[54]	$CaI_2(thf)_4$[55]	{NON} Y(CH_2SiMe_3)$_2$(thf)$_2$[2]
[a]M-O(1)	2.1952(19)	2.1914(16)	2.34(1)	2.1994(15)
[a]M-N(1)	2.506(2)	2.474(2)	-	2.5159(18)
[a]M-O(thf)	2.28(3)/ 2.505(9)/ 2.379(2)	2.3494(18)	2.34(1)	2.3779(18)/ 2.4637(17)
[a]M-R	3.0848(5)	2.3512(19)	3.106(2)	2.423(2)
[a]O(1)-M-R	175.28(6)	112.16(7)	-	86.17(7)

[a]M = metal; R = initiating group.

4.3.4.3 Solid angle calculations

The atomic coordinates of **15**, produced from X-ray crystallographic analysis, were used in solid angle calculations. The results are presented in **Figure 4.22** and **Table 4.7**. The analysis suggests that the individual bound-thf ligands impart similar shielding on the metal centre (*av.* 13.29%). The iodide anion creates less of a shadow due to the fact that it resides much further from calcium in the solid-state structure (3.0848(5) Å *vs.* 2.3768 Å; **Table 4.6**). When the metal-ligand distances are normalised however, the opposite trend is observed (23.76% *vs.* 14.91% *av.*); this implies that the radius of the anion exceeds that of a neutral THF molecule.

Table 4.7 Summary of ligand solid angles (Ω), the percentage of the sphere shielded by the ligand (G), the percent of the metal surface shielded by ligand atoms (G(M)) and the percentage of the metal surface "in contact" with ligated atoms (S(M)) for the isolated heteroleptic calcium iodide complex: $^{t\text{Bu,Dipp}}$LCaI(thf)$_3$ (**15**).

Complex	Ω($^{\text{Dipp}}$L) (sr)	Ω(I) (sr)	Ω(thf) (sr)	G($^{\text{Dipp}}$L) (%)	G(X) (%)	G(thf) (%)	$G_{2.28}$ ($^{\text{Dipp}}$L) (%)	$G_{2.28}$ (X) (%)	$G_{2.28}$ (thf) (%)	G(M) (%)	S(M) (%)
$^{t\text{Bu,Dipp}}$LCaI(thf)$_3$	4.53	1.42	[a]1.67	36.08	11.28	[a]13.26	32.69	23.76	14.92	63.34	61.13
			[a]1.66			[a]13.18			14.89		
			[a]1.69			[a]13.42			14.93		

[a] independent thf molecules.

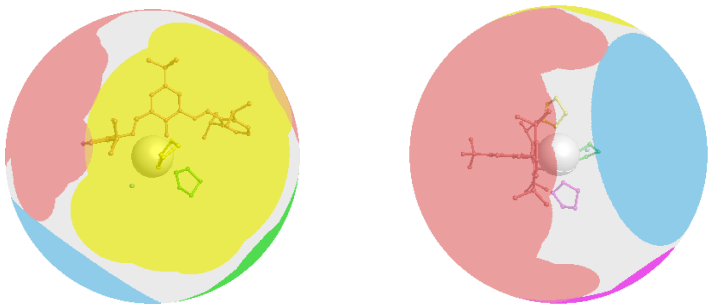

Figure 4.22 Visualisations of *G*(L) values in $^{t\text{Bu,Dipp}}$LCaI(thf)$_3$ (**15**), showing the percentage of the complex sphere shielded by each ligand. Blue = I, green = thf, yellow = thf, pink = thf, red = $^{t\text{Bu,Dipp}}$L.

The shielding parameter of the *tert*-butyl ligand framework in complex **15** is very similar to the average value reported for the homoleptic compounds **10**-**12** (32.69% *vs*. 34.29% *av*.). This shows that regardless of the nature of the complex (homo- *vs*. heteroleptic), the individual frameworks are only capable of shadowing a certain proportion of the metal centre. The percentage of metal surface “in contact” with the ligands is comparable to that of complex **12** (63.34% *vs*. 64.83%); this indicates that the calcium centre does not need a second “NON” framework to achieve sufficient steric protection. Instead, the supplementary kinetic stabilisation can be afforded by multiple, smaller exogenous ligands. Their combined shielding however, would not afford the same protection of the larger Sr^{2+} and Ba^{2+} cations (6-coordinate: Ca^{2+} = 1.00 Å; Sr^{2+} = 1.16 Å and Ba^{2+} = 1.36 Å);[51] this may help to explain why Schlenk-type redistribution to homoleptic species was observed for the heavier, more labile analogues. This size-based rationale, however, would dictate that the heteroleptic magnesium system would also be stable, and this is not the case. An additional stabilising factor, which explains the difference in reactivity between Mg and Ca, must therefore also be in effect. This could be derived from the

strength of the M-I bond which would be much lower for the magnesium system as a result of the Hard-Soft-Acid-Base theory (hence its observed redistribution).

4.4 Conclusions

The preparation of potassium salts of "NON" phenoxy-imine ligands, $H^{R,Dipp}L$; 1-OH-2,6-(HC=NDipp)-4-R-C_6H_2 (R = H, Me and ^{t}Bu), and subsequent synthesis of mononuclear alkaline-earth metal complexes, has been explored.

The potassium salts (**7-9·thf$_x$**) showed interesting structural properties as crown ether-coordination derivatives in the solid-state; for the smaller ligands (R = H and Me), 1D coordination polymers were formed as a result of through-space interactions between the diisopropyl-*methyl* groups and potassium centres.

Regardless of reaction conditions, ligand redistribution occurred during the salt-metathesis reactions with Mg, Sr and Ba diiodide materials to afford the monometallic, homoleptic *bis*(ligand) systems: $(^{t\text{Bu,Dipp}}L)_2M(thf)_x$ (M = Mg (**10**), Sr (**11**), Ba (**12**)). Curiously, no redistribution occurred when using calcium, thus allowing for the isolation of three well-defined heteroleptic complexes: $^{R,Dipp}LCaI(thf)_3$ (R = H (**13**), Me (**14**), ^{t}Bu (**15**)). Attempts to synthesise an analogous heteroleptic magnesium system via protonolysis of a Grignard reagent, proved unsuccessful.

The catalytic capability of compounds **10**-**15** to act as initiators in the ring-opening polymerisation of lactide is presented in **Chapter 5**, whilst exploration of the heteroleptic complexes as intermediates in the synthesis of cationic, bimetallic alkaline-earth systems is described in **Chapter 6**.

4.5 References

1. H.-C. Chiu, A. Koley, P. L. Dunn, R. J. Hue and I. A. Tonks, *Dalton Trans.*, 2017, **46**, 5513-5517.
2. L. Qu, T. Roisnel, M. Cordier, D. Yuan, Y. Yao, B. Zhao and E. Kirillov, *Inorg. Chem.*, 2020, **59**, 16976-16987.
3. V. C. Gibson, D. Nienhuis, C. Redshaw, A. J. P. White and D. J. Williams, *Dalton Trans.*, 2004, 1761-1765.
4. E. Schiebel, M. Voccia, L. Falivene, I. Göttker-Schnetmann, L. Caporaso and S. Mecking, *Angew. Chem. Int. Ed.*, 2021, **60**, 18472-18477.
5. S. J. Na, D. J. Joe, S. S, W.-S. Han, S. O. Kang and B. Y. Lee, *J. Organomet. Chem.*, 2006, **691**, 611-620.
6. D. Chandran, C. Bae, I. Ahn, C.-S. Ha and I. Kim, *J. Organomet. Chem.*, 2009, **694**, 1254-1258.
7. L. Wang, W.-H. Sun, L. Han, Z. Li, Y. Hu, C. He and C. Yan, *J. Organomet. Chem.*, 2002, **650**, 59-64.
8. X.-M. Chen, L.-C. Huang and W. Gao, *Dalton Trans.*, 2021, **50**, 5218-5225.
9. S. Ghosh, R. R. Gowda, R. Jagan and D. Chakraborty, *Dalton Trans.*, 2015, **44**, 10410-10422.
10. D. Chakraborty, E. R. Chokkapu, M. Mandal, R. R. Gowda and V. Ramkumar, *ChemistrySelect*, 2016, **1**, 5218-5229.
11. T. Kumar Saha, B. Rajashekhar and D. Chakraborty, *RSC Adv.*, 2012, **2**, 307-318.
12. T. K. Saha, B. Rajashekhar, R. R. Gowda, V. Ramkumar and D. Chakraborty, *Dalton Trans.*, 2010, **39**, 5091-5093.
13. X. Wang, K.-Q. Zhao, M. R. J. Elsegood, T. J. Prior, X. Liu, L. Wu, S. Sanz, E. K. Brechin and C. Redshaw, *RSC Adv.*, 2015, **5**, 57414-57424.
14. E. Fazekas, G. S. Nichol, J. A. Garden and M. P. Shaver, *ACS Omega*, 2018, **3**, 16945-16953.
15. Q. Hu, S. Jie, P. Braunstein and B.-G. Li, *J. Organomet. Chem.*, 2019, **882**, 1-9.
16. S. Ghosh, D. Chakraborty and V. Ramkumar, *J. Polym. Sci., Part A: Polym. Chem.*, 2015, **53**, 1474-1491.
17. J. B. L. Gallaway, J. R. K. McRae, A. Decken and M. P. Shaver, *Can. J. Chem.*, 2012, **90**, 419-426.
18. X. Wang, T. Zhao, B. Yang, Z. Li, J. Cui, Y. Dai, Q. Qiu, H. Qiang, W. Huang and H. Qian, *Biorg. Med. Chem.*, 2015, **23**, 132-140.
19. Y. Zhang, K. Shibatomi and H. Yamamoto, *Synlett*, 2005, 2837-2842.
20. M. T. Rispens, O. J. Gelling, A. M. de Vries, A. Meetsma, F. van Bolhuis and B. L. Feringa, *Tetrahedron*, 1996, **52**, 3521-3546.
21. C. Zondervan, E. K. van den Beuken, H. Kooijman, A. L. Spek and B. L. Feringa, *Tetrahedron Lett.*, 1997, **38**, 3111-3114.
22. L. F. Lindoy, G. V. Meehan and N. Svenstrup, *Synthesis*, 1998, 1029-1032.

23. P. D. Knight, A. J. P. White and C. K. Williams, *Inorg. Chem.*, 2008, **47**, 11711-11719.
24. J. March, *Advanced Organic Chemistry: Reactions, Mechanisms, and Structure*, Wiley, New York, 3rd edn., 1985.
25. R. A. Bell and J. K. Saunders, *Can. J. Chem.*, 1970, **48**, 1114-1122.
26. K. Ohno, K. Arima, S. Tanaka, T. Yamagata, H. Tsurugi and K. Mashima, *Organometallics*, 2009, **28**, 3256-3263.
27. P. Pyykkö, *J. Phys. Chem. A*, 2015, **119**, 2326-2337.
28. C. G. Werncke and I. Müller, *Chem. Commun.*, 2020, **56**, 2268-2271.
29. E. Kounalis, M. Lutz and D. L. J. Broere, *Organometallics*, 2020, **39**, 585-592.
30. Y. Ohki, K. Ishihara, M. Yaoi, M. Tada, W. M. C. Sameera and R. E. Cramer, *Chem. Commun.*, 2020, **56**, 8035-8038.
31. G. C. Forbes, A. R. Kennedy, R. E. Mulvey, B. A. Roberts and R. B. Rowlings, *Organometallics*, 2002, **21**, 5115-5121.
32. V. Y. Lee, T. Yokoyama, K. Takanashi and A. Sekiguchi, *Chem. Eur. J.*, 2009, **15**, 8401-8404.
33. J. Knizek and H. Nöth, *J. Organomet. Chem.*, 2000, **614-615**, 168-187.
34. R. J. Schwamm, M. P. Coles and C. M. Fitchett, *Organometallics*, 2015, **34**, 2500-2507.
35. P. Yang, X.-J. Yang, J. Yu, Y. Liu, C. Zhang, Y.-H. Deng and B. Wu, *Dalton Trans.*, 2009, 5773-5779.
36. R. J. Schwamm, M. D. Anker, M. Lein and M. P. Coles, *Angew. Chem. Int. Ed.*, 2019, **58**, 1489-1493.
37. D. J. Duncalf, P. B. Hitchcock and G. A. Lawless, *J. Organomet. Chem.*, 1996, **506**, 347-349.
38. A. W. Addison, T. N. Rao, J. Reedijk, J. van Rijn and G. C. Verschoor, *J. Chem. Soc., Dalton Trans.*, 1984, 1349-1356.
39. G. T. Quinque, A. G. Oliver and J. A. Rood, *Eur. J. Inorg. Chem.*, 2011, **2011**, 3321-3326.
40. W. Cao, X.-J. Zheng, J.-P. Sun, W.-T. Wong, D.-C. Fang, J.-X. Zhang and L.-P. Jin, *Inorg. Chem.*, 2014, **53**, 3012-3021.
41. J. A. Rood, A. M. Landis, D. R. Forster, T. Goldkamp and A. G. Oliver, *Acta Crystallogr. C*, 2016, **72**, 990-996.
42. M.-W. Hsiao, G.-S. Wu, B.-H. Huang and C.-C. Lin, *Inorg. Chem. Commun.*, 2013, **36**, 90-95.
43. M. Fuchs, S. Schmitz, P. M. Schäfer, T. Secker, A. Metz, A. N. Ksiazkiewicz, A. Pich, P. Kögerler, K. Y. Monakhov and S. Herres-Pawlis, *Eur. Polym. J.*, 2020, **122**, 109302.
44. D. E. Fenton, D. H. Cook, I. W. Nowell and P. E. Walker, *J. Chem. Soc., Chem. Commun.*, 1978, 279-280.
45. B.-G. P. Kyu-Hwan Yeon, Lee, Kang Mun, Do, Youngkyu, & Taek-Mo Jeong, *Bull. Korean Chem. Soc*, 2012, **33**, 2059-2062.
46. S. Harder, *Organometallics*, 2002, **21**, 3782-3787.
47. D. H. Cook and D. E. Fenton, *J. Chem. Soc., Dalton Trans.*, 1979, 810-813.

48. L. Carbonaro, M. Isola, P. La Pegna, L. Senatore and F. Marchetti, *Inorg. Chem.*, 1999, **38**, 5519-5525.

49. M. Hamelin, *Acta Crystallogr. B*, 1976, **32**, 364-370.

50. B. Liu, T. Roisnel, J.-F. Carpentier and Y. Sarazin, *Angew. Chem. Int. Ed.*, 2012, **51**, 4943-4946.

51. R. D. Shannon and C. T. Prewitt, *Acta. Crystallogr. B. Struct. Sci. Cryst. Eng. Mater.*, 1969, **B 25**, 925-946.

52. M. Ma, X. Shen, W. Wang, J. Li, W. Yao and L. Zhu, *Eur. J. Inorg. Chem.*, 2016, **2016**, 5057-5062.

53. A. M. Johns, S. C. Chmely and T. P. Hanusa, *Inorg. Chem.*, 2009, **48**, 1380-1384.

54. D. J. Darensbourg, W. Choi, O. Karroonnirun and N. Bhuvanesh, *Macromolecules*, 2008, **41**, 3493-3502.

55. K. F. Tesh, D. J. Burkey and T. P. Hanusa, *J. Am. Chem. Soc.*, 1994, **116**, 2409-2417.

56. H.-Y. Chen, H.-Y. Tang and C.-C. Lin, *Polymer*, 2007, **48**, 2257-2262.

57. Y. Sarazin, R. H. Howard, D. L. Hughes, S. M. Humphrey and M. Bochmann, *Dalton Trans.*, 2006, 340-350.

58. M. J. C. Dawkins, A. N. Simonov and C. Jones, *Dalton Trans.*, 2020, **49**, 6627-6634.

59. F. Gschwind, O. Sereda and K. M. Fromm, *Inorg. Chem.*, 2009, **48**, 10535-10547.

Chapter 5

Lactide polymerisation studies with alkaline-earth "NON" complexes

5.1 Introduction

5.1.1 Overview

The exploration of complexes **10–15** (**Figure 5.1**), in behaving as single-site catalysts for the ring-opening polymerisation of *L*-, *D*-, *rac*- and *meso*-lactide, is presented. This is the first time that phenoxy-imine strontium and barium systems have been tested for this application.

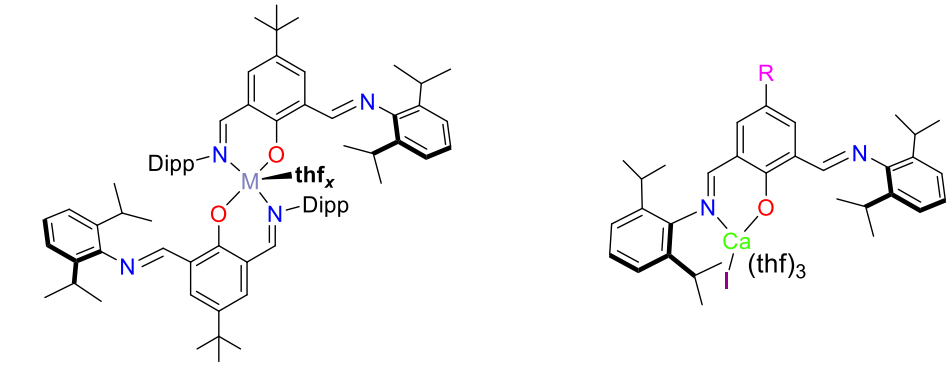

M = Mg (*x* = 1; **10**), Sr (*x* = 2; **11**), Ba (*x* = 2; **12**)

R = H (**13**), Me (**14**), ^{t}Bu (**15**)

Figure 5.1 The initiators tested in this Chapter.

A variety of conditions (temperature, monomer stereochemistry, initiator concentration) and analytical techniques (NMR spectroscopy, mass spectrometry, gel permeation chromatography) have been utilised to study the kinetics of polymerisation and resultant polymer structure.

5.1.2 Literature reports of monometallic, alkaline-earth ROP initiators

In the context of lactide polymerisation, there have been numerous reports of highly active phenoxy-imine group 2 initiators.[1-12] The majority of the studies have focused on magnesium (and zinc)[1, 2, 6, 7, 11] with the role of the heavier alkaline-earths being less explored.[3-5, 7-12] In fact, there are no examples of strontium or barium phenoxy-imine ROP catalysts to date, even though they offer the potential for fast kinetics due to their increased bonding lability.

Most reported group 2 Schiff base catalytic systems are, unsurprisingly, homoleptic in nature.[1-5] Having no preformed initiating group means that homoleptic complexes typically react via the activated monomer pathway, and thus have a dependence on co-initiator concentration.[2, 4] The formation of heteroleptic complexes based on this ligand system is more rare, but has been successfully achieved by increasing the steric bulk of the ligand and/or including additional pendant donor arms.[6, 7, 9-12] In the presence of a co-initiator, these systems have typically shown excellent behaviour in the immortal ROP of LA.[11, 12] Selected examples, that are relevant to this study, are discussed in the following sections (**5.1.2.1** and **5.1.2.2**).

5.1.2.1 Homoleptic systems

In 2015, Chakraborty *et al.* published a large family of homoleptic *mono*- and *bis*-phenoxy-imine systems (**Figure 5.2a**).[1] They all proved to be highly efficient initiators

for the melt ROP of LA, with the monoimine species outperforming their *bis*(imine) counterparts in all cases (e.g. quantitative conversion of 200 eq. *L*-LA in 25 and 50 minutes for the isopropyl substituted *mono*- and *bis*-imine catalysts respectively).[1] Direct variation of the imine substituent was found to have no observable effect on the rate thus implying that the increased steric bulk of the second imine "arm", shielding the metal centre from incoming monomers, was the sole cause of the difference in activity. Good polymerisation control was evidenced by the agreeable molecular weight comparisons and narrow molecular weight distributions (M_w/M_w = 1.12–1.27).[1] Analysis of the resultant polymers identified the pro-ligand as a polymer terminal end group; this is the result of the polymerisation being initiated by either the Mg-N or Mg-O bonds.[1]

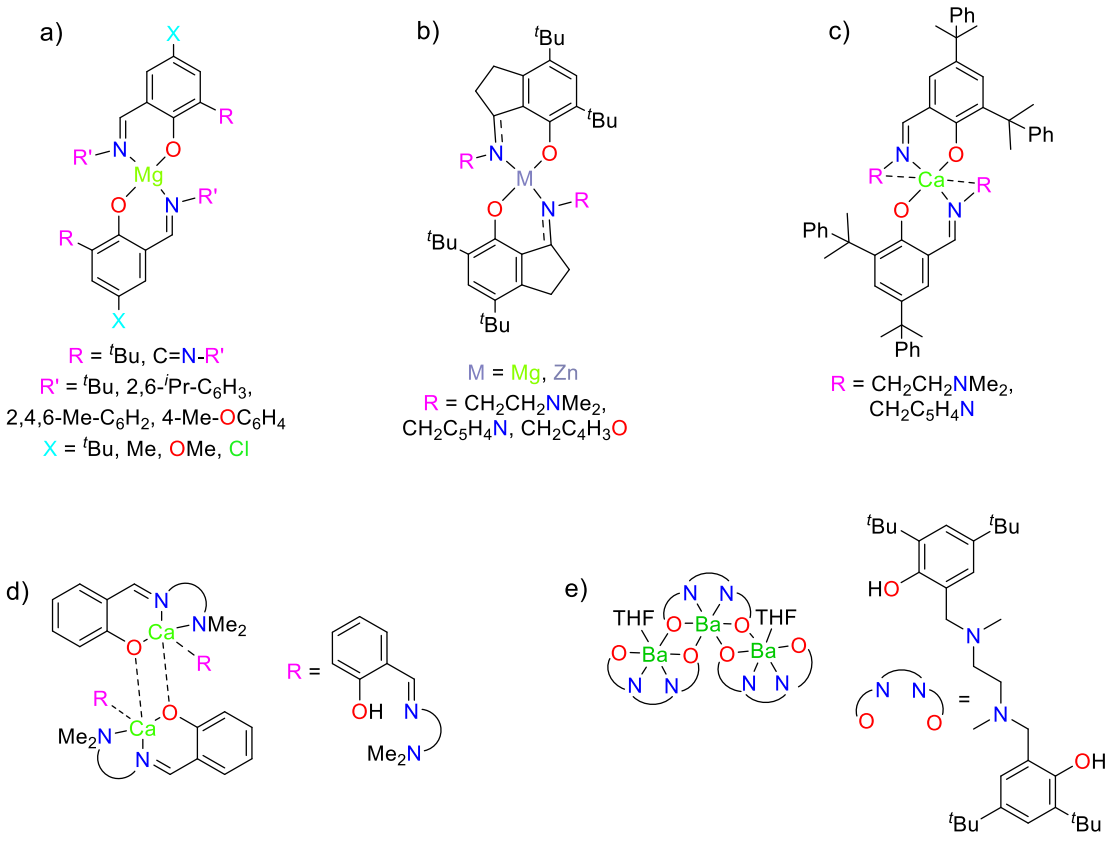

Figure 5.2 Previously reported homoleptic M^{2+} phenoxy-imine (and related) systems.[1-5]

A collection of similar homoleptic, monometallic phenoxy-imine M^{2+} catalysts have since been reported by Phomphrai and co-workers (**Figure 5.2b**).[2] In the presence of benzyl alcohol (BnOH), the catalysts were found to operate *via* the activated monomer mechanism. An increase in BnOH concentration did not significantly improve the rate, however, it decreased the molecular weight of the resultant polymers due to chain-transfer interactions (1 eq.: 49 100 $gmol^{-1}$; 2 eq.: 23 900 $gmol^{-1}$; 5 eq.: 9 900 $gmol^{-1}$).[2] Reduction of the ligand-imine functional groups to amines resulted in a dramatic increase in the polymerisation rate (for Zn^{2+}: 67% conversion in 5 days *vs*. 96% conversion in 1 minute); this may be attributed to the increased flexibility of the reduced framework. The *bis*(amine) magnesium analogue was found to be less active (95% conversion in 30 minutes) as a result of the metal's increased Lewis acidity causing binding competition between the amine side arm and incoming monomers.[2]

A similar hindrance of the polymerisation rate, as a result of strong pendant donors, was also observed in the case of the homoleptic Schiff base calcium catalysts reported by Lin and co-workers (**Figure 5.2c**).[3] The authors propose that the use of a pendant pyridine (*vs*. dimethyl amine) resulted in a slower reaction due to its greater affinity for the metal centre.[3] In the absence of BnOH, the activity of these Schiff base systems is rather low, achieving only 31% conversion of 100 eq. *L*-LA in 2 h.[3] Conversely, when the co-initiator is present, excellent activity in the ROP of LA (reaction time reduced to as low as 5 minutes) is observed, resulting in polymers with comparable experimental and theoretical molecular weights and narrow-intermediate molecular weight distributions (M_w/M_w = 1.14–1.35).[3]

An analogous tridentate, homoleptic, calcium Schiff base species was described by the same group in 2007 (**Figure 5.2d**).[4] One major difference is that this system exists as a

dimer in solution, supported by two exogenous ligand frameworks. This clustering of calcium centres has negligible effects on the polymerisation rate (>96% conversion achieved in 0.6–1 h at room temperature with $[LA]_0/[\mathbf{Ca}]_0$ ranging from 50–125:1) yet results in improved reaction control (M_w/M_w = 1.11–1.26).[4] Moreover, this system also recorded a first-order dependency with respect to both monomer and co-initiator concentrations, which suggests polymerisation proceeded via the activated monomer pathway.[4]

There are no published reports of heavier alkaline-earth (Sr, Ba) homoleptic phenoxy-imine initiators for the ROP of LA. One comparable trimetallic, homoleptic barium amine *bis*(phenolate) system, however, has been reported (**Figure 5.2e**). This complex catalyses 60% conversion of 900 eq. of *L*-LA at 130 ºC in 3.5 h with a moderate degree of control (M_w/M_w = 1.57). Higher conversion levels were limited by the increased viscosity of the melt mixture.[5]

5.1.2.2 Heteroleptic systems

In 2018, Ma and co-workers reported rare examples of stereoselective heteroleptic magnesium phenoxy-imine initiators (**Figure 5.3a**).[6] In the presence of an alcohol co-initiator, the *racemic* mixture of magnesium complexes could convert 94% of 500 eq. of *rac*-LA in 15 minutes.[6] Enantiomorphic site control, most likely caused by the chirality of the ligand framework, was evidenced by the disparity in the observed rates of the individual *L*- (2.46 ± 0.06 h^{-1}) and *D*- (8.64 ± 0.24 h^{-1}) monomers.[6] This enabled the formation of tapered stereoblock, semi-crystalline (T_m = 164 ºC) polymers, with molecular weights as high as M_n = 461 000 $gmol^{-1}$, from *rac*-LA.[6]

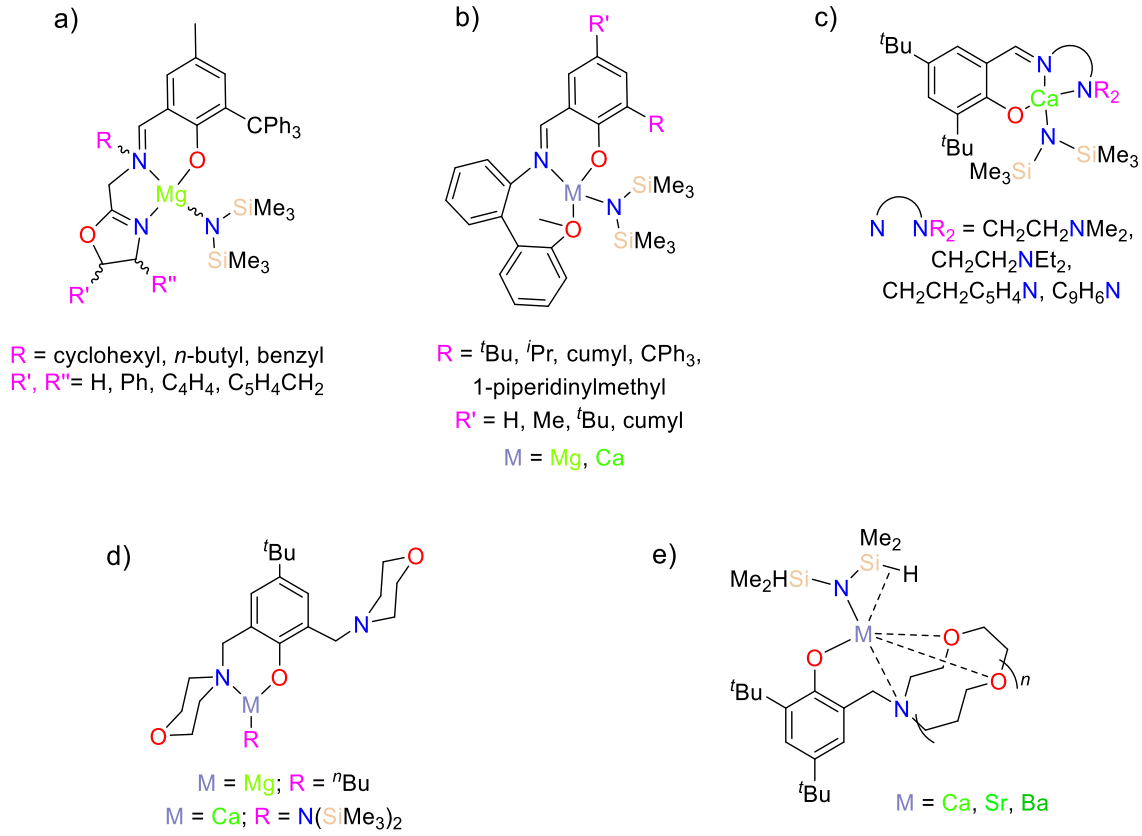

Figure 5.3 Previously reported heteroleptic alkaline-earth phenoxy-imine (and related) systems.[6-12]

A family of comparable tridentate, heteroleptic, M^{2+} systems were reported by Ma *et al.* in 2013 (**Figure 5.3b**).[7] The authors report that the polymerisation activity of the magnesium catalysts increased in parallel with the steric bulk of the *ortho*-substituent on the phenolate ring (R = CPh_3; k_{obs} = 6.60 h^{-1} > cumyl; k_{obs} = 0.735 h^{-1} > ^{t}Bu; k_{obs} = 0.66 h^{-1} > ^{i}Pr; k_{obs} = 0.258 h^{-1}).[7] This was rationalised by the increased shielding of the metal centre providing protection against ligand scrambling and/or initiator aggregation/subsequent deactivation in solution.[7] This same hypothesis was used to explain why the analogous calcium systems were not as effective catalysts (converting 89% in 25 minutes *vs*. 92% in 20 minutes for Mg). In all cases, polymerisation proceeded with only moderate control (M_w/M_w = 1.12–1.75) as a result of slow initiation by the only slightly nucleophilic silylamido group.[7]

Analogous tridentate, calcium Schiff base complexes have been reported by Darensbourg *et. al.* for the ROP of cyclic esters including *rac*-LA (**Figure 5.3c**).[8-10] Solution studies revealed a first-order dependence on both monomer and catalyst concentration, suggesting that polymerisation were occurred via the typical coordination-insertion mechanism.[8-10] The electronics of the pendant donor were found to effect the rate of polymerisation; the calcium system with the most electron donating imine arm (R = $CH_2CH_2NMe_2$) was found to be approximately twice as active as those containing electron-withdrawing (R = C_9H_6N) substituents (TOF: 1125 *vs*. 502; units of *L*-LA consumed/(mol of Ca·h)).[8-10] The stereoselectivity of these systems was also found to be temperature dependent: P_r = 0.73 and 0.52 for PLA produced at –33 and 25 °C respectively.[8-10]

In 2009, Sarazin and co-workers published the first stable, hetereoleptic magnesium and calcium systems capable of catalysing large-scale immortal ROPs of *L*-LA (**Figure 5.3d**).[11] Incorporating a *bis*(morpholinomethyl)phenoxy ligand, the magnesium variant was able to polymerise up to 5000 eq. of *L*-LA in the presence of up to 100 eq. of ^{i}PrOH co-initiator.[11] In all cases, narrow polydispersity indices were recorded (M_w/M_n = 1.10–1.20), indicating that the rate constant for chain transfer between growing polymer chains and "resting" alcohols exceeded that of routine chain propagation ($k_{tr} >> k_p$).[11] Furthermore, the calcium analogue was shown to be more active than its magnesium counterpart.[11]

No reports of strontium or barium heteroleptic phenoxy-imine based catalysts have been made. There are, however, studies of related heavier alkaline-earth *bis*(dimethylsilyl)amide systems in the ROP of LA (**Figure 5.3e**).[12] In the presence of 25 eq. of ^{i}PrOH co-initiator, the strontium analogue converted 87% of 1000 eq. of *L*-LA

within 10 minutes at 30 ºC.[12] Good agreement between theoretical and experimental molecular weights ($M_{n,(calcd)}$ = 5000 and $M_{n,(GPC)}$ = 6900 gmol^{-1}) and the recorded narrow molecular weight distributions (M_w/M_n = 1.23) are consistent with controlled coordination-insertion polymerisations that exhibit immortal behaviour (fast, reversible chain transfer).[12]

5.2 General considerations for lactide polymerisation studies

Lactide polymerisations were performed in J. Young's tap NMR tubes with an initial monomer concentration ($[LA]_0$) of 0.5 M. The reactions were halted by submerging the NMR tubes in an ice bath and conversion to polylactide (PLA) was monitored by ^{1}H NMR spectroscopy. Upon completion, the reaction mixture was decanted and the resultant polymer was precipitated by addition of pentane.

Control polymerisations using only $H^{R,Dipp}L$ as the catalyst (with and without BnOH co-initiator) were also conducted; no activity was observed after 24 h, even at the highest temperature studied. As a result, it can be concluded that any observed polymerisation activity is due solely to the complexes themselves (and co-catalyst if present).

5.3 Using the homoleptic initiators

The capability of homoleptic complexes **10**-**12** to act as initiators in the ROP of LA has been investigated. The effect of co-initiator addition, temperature, monomer stereochemistry and (co-)initiator concentration has been probed.

5.3.1 Introduction of co-initiator

Polymerisation of 50 eq. *L*-LA, using catalyst **10**, in chloroform-d_1 at 60 ºC proved to be extremely slow, achieving 81% conversion only after 16 h (**Figure 5.4a**). The polymerisation also suffered from a 3.5 h initiation period which suggests that the first insertion of a lactide monomer is the rate limiting step (i.e. $k_{LA_1} << k_{LA_2} < k_{prop}$).[13, 14] Similar observations have been reported by Turner and co-workers in their investigation of bismuth pincer LA catalysts.[13] A more in-depth study of initiation periods was carried out by Chen *et al*. with regard to their aluminium ketamine complexes.[14] The authors report that steric, electronic and chelating factors all influenced the initiation period (ranged from 0-35 minutes) of cyclic ester polymerisations.[14] In the case of **10**, the observed initiation period may be due to the catalyst having no dedicated initiating group. This feature of the initiator also resulted in the polymerisations producing exclusively cyclic PLA as highlighted via end-group analysis (**Section 5.3.6**).

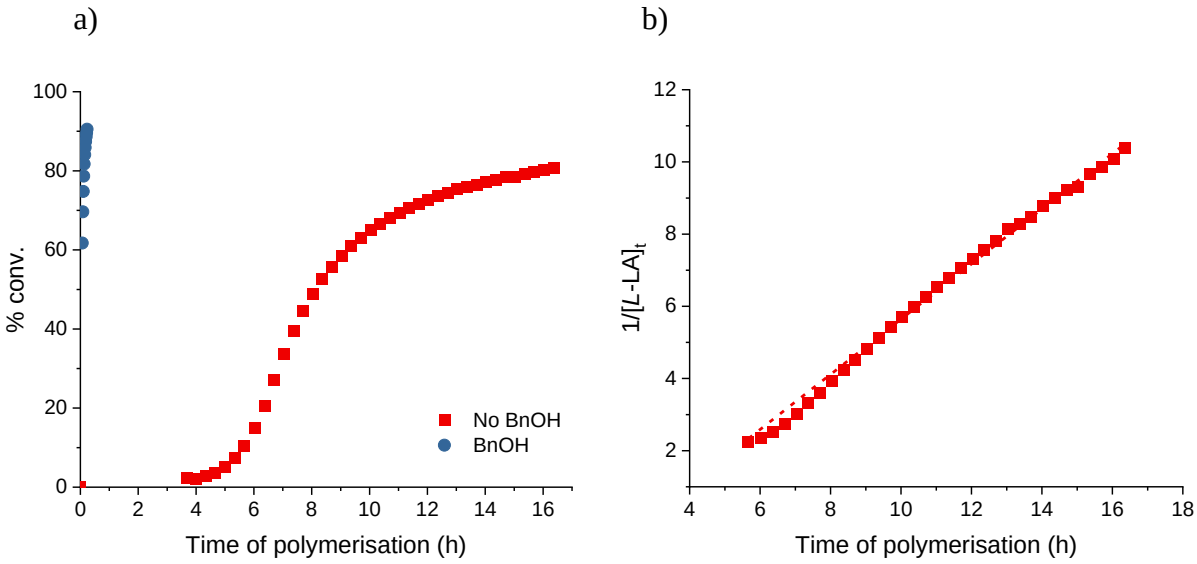

Figure 5.4 a) Plots of percentage conversion *vs.* time. Red squares: no BnOH; blue circles: BnOH. b) Plot of $1/[L\text{-LA}]_t$ *vs.* time for *L*-LA polymerisation with no BnOH co-initiator (k_{obs} = 0.76 M^{-1} h^{-1}. R^2 = 0.999). Conditions: $[L\text{-LA}]_0$:[**Mg**]$_0$(:$[BnOH]_0$) = 50:1(:1), $[L\text{-LA}]_0$ = 0.5 M in 0.6 mL chloroform-d_1 at 60 °C.

Other catalysts with no preformed initiating group have previously been reported and are thought to operate via the activated monomer mechanism in the presence of a co-initiator.[15, 16] Addition of benzyl alcohol as a co-initiator was therefore tested; as expected, a (twelve-fold) increase in the rate of polymerisation was observed resulting in 91% conversion in 0.2 h (**Table 5.1**). In the presence of BnOH, the experimental rate constant (k_{obs} = 9.37 h^{-1}) is comparable to those reported by Chakraborty and co-workers in their investigation of LA polymerisations catalysed by analogous homoleptic *bis*(phenoxy-imine) magnesium systems (k_{obs} = 4.02–9.08 h^{-1} for [LA]/[**Mg**] = 200:1).[1]

Table 5.1 ROP of *L*-LA using **10** with [*L*-LA]$_0$:[**Mg**]$_0$(:[BnOH]$_0$) = 50:1(:1) in chloroform-d_1 at 60 °C.[a]

BnOH	Time (h)	Conv. (%)[b]	k_{obs} (h^{-1} or M^{-1} h^{-1})	R^{2c}	M_n (GPC)[e]	M_n (calcd)[f]	M_w/M_n
No	16.4	81	0.76 ± 0.003[c]	0.999	35 941	5926	1.53
Yes	0.2	91	9.37 ± 0.4[d]	0.987	4141	6936	1.31

[a]Conditions: [*L*-LA]$_0$:[**Mg**]$_0$(:[BnOH]$_0$) = 50:1(:1), [*L*-LA]$_0$ = 0.5 M in 0.6 mL chloroform-d_1 at 60 °C. [b]Average reported; measured by ^{1}H NMR spectroscopic analyses. [c]Second order rate constant (k_{obs}: M^{-1} h^{-1}) and R^2 were obtained from average plots of 1/[*L*-LA]$_t$ *vs.* time. [d]First order rate constant (k_{obs}: h^{-1}) and R^2 were obtained from average plots of ln([*L*-LA]$_0$/[*L*-LA]$_t$) *vs.* time. [e]Determined by GPC in THF against PS standards using the appropriate Mark-Houwink corrections.[17] [f]Calculated M_n for PLA synthesised = (conv.(%) × [*L*-LA]$_0$/[**Mg**]$_0$) × 144.13 + (M_w of end groups).

Kinetic studies revealed that the dependency on monomer concentration varied with and without use of the co-initiator. In the absence of BnOH, an unusual second-order dependency on *L*-LA concentration was observed, as indicated by the linear plots of 1/[*L*-LA]$_t$ *vs*. time (**Figure 5.4b**; non-linear first-order plot is shown in **Figure A.27**).[18-25] Like with the catalyst **4**/[**4**]$_2$ system, this implies a Ystenes-like mechanism is taking place in

which two monomers are required per active site for the reaction to proceed.[26] In contrast, when BnOH is added, plots of $\ln([L\text{-LA}]_0/[L\text{-LA}]_t)$ *vs.* time reveal linear relationships indicating first-order dependence with respect to monomer concentration (**Figure 5.5a**); this aligns with the proposed rate law of an activated monomer mechanism.[15]

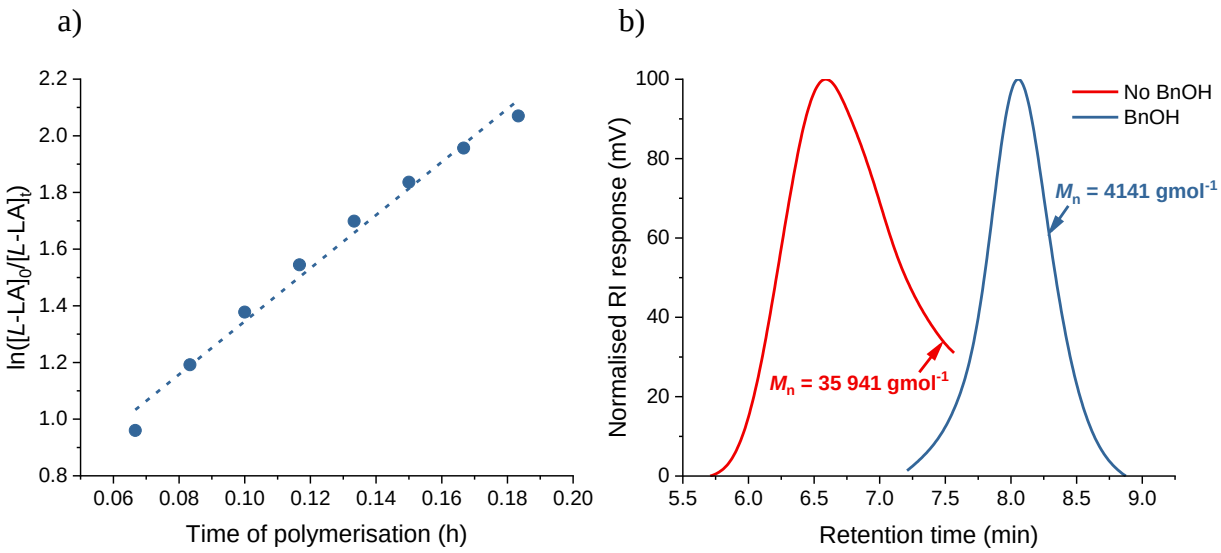

Figure 5.5 a) Plot of $\ln([L\text{-LA}]_0/[L\text{-LA}]_t)$ *vs.* time for *L*-LA polymerisation using **10**/BnOH (k_{obs} = 9.37 h^{-1}. R^2 = 0.987). b) GPC traces of PLAs synthesised from the ROP of *L*-LA using **10** with and without BnOH. Red: no BnOH, M_n = 35 941 $gmol^{-1}$, M_w/M_n = 1.53; blue: BnOH, M_n = 4141 $gmol^{-1}$, M_w/M_n = 1.31). Conditions: $[L\text{-LA}]_0$:[**Mg**]$_0$(:$[BnOH]_0$) = 50:1(:1), $[L\text{-LA}]_0$ = 0.5 M in 0.6 mL chloroform-d_1 at 60 °C.

With and without the co-initiator, the polymerisations proceed with only moderate control as indicated by the intermediate molecular weight distributions (M_w/M_n = 1.31–1.53; **Figure 5.5b**); this lack of control resulted in disparity between the calculated and experimental molecular weights (**Table 5.1**). When the co-initiator is not used, the experimental molecular weights recorded are six-times larger than the calculated values (35 941 *vs.* 5926 $gmol^{-1}$); this implies that not all the metal centres were active during the polymerisation. This lower concentration of active sites, coupled with the requirement

for two lactide monomer to bind simultaneously, helps to explain why the polymerisation rate is so slow in the absence of a co-initiator. Contrastingly, there is a relatively good agreement between the experimental and calculated molecular weights when the co-initiator is added (4141 *vs*. 6936 $gmol^{-1}$). This implies that benzyl alcohol activates more metal centres thus leading to the initiator behaving more like a single-site system. The slight difference in values can be accounted for by the occurrence of transesterification side reactions (noted by the peak splitting of 72 *m*/*z* in the mass spectrum of the resultant polymer; *vide infra*: **Figure 5.16**). The experimental molecular weights (M_n (GPC)) of the poly-*L*-lactide produced using **10** and BnOH lie close to the range reported for comparable magnesium Schiff base systems (7400–18 370 $gmol^{-1}$ for $[LA]_0/[\mathbf{Mg}]_0$ = 100:1).[1, 2]

The polymerisation of 50 eq. *L*-LA was also carried out using the heavier alkaline-earth homoleptic systems: **11** and **12**. In chloroform-d_1 and without BnOH, the polymerisations reached completion before the first NMR spectroscopic measurement could be taken. As a result, and in order to collect accurate kinetic data, the polymerisations were conducted in benzene-d_6; the results are presented in **Figures 5.6-5.7** and **Table 5.2**.

Without benzyl alcohol, neither catalyst showed an initiation period; this, coupled with the fact that the barium-catalysed polymerisation proceeded faster than its strontium analogue (**Figure 5.6a**), suggests a lower barrier to monomer insertion for metals with a larger ionic radius. A similar trend in alkaline-earth reactivity (Mg < Ca < Sr < Ba) has previously been observed in chalcogen-containing group two polymerisation initiators.[27]

Like with catalyst **10**, the barium system **12** was found to have a second-order dependence on *L*-LA concentration as evidenced by linear plots of $1/[L\text{-LA}]_t$ (**Figure 5.6b**; non-linear

first-order plot is shown in **Figure A.28**). The experimental rate constant for the **12** system was an order of magnitude higher than that of **10** (k_{obs} = 19.53 *vs.* 0.76 M^{-1} h^{-1}), even when recorded in a less polar solvent which limits monomer solubility. This rapid monomer conversion aligns with the report of a comparable trimetallic, *bis*(phenolate) barium system (**Figure 5.2e**) that was capable of achieving 60% conversion of 900 eq. in 3.5 h.[5]

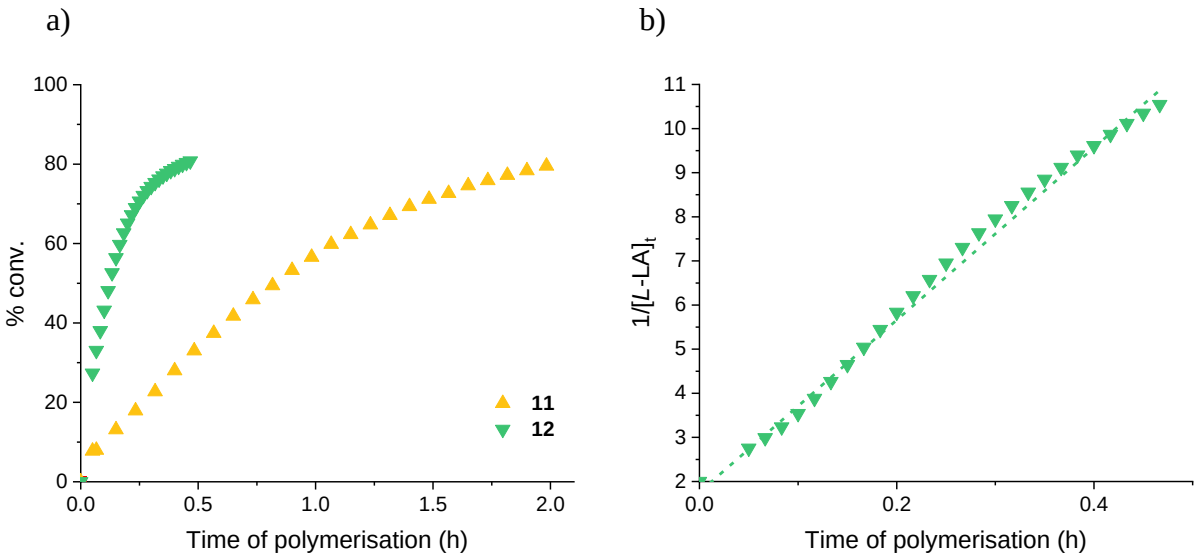

Figure 5.6 a) Plots of percentage conversion *vs.* time. Yellow up triangles: cat = **11**; green down triangles: cat = **12**. b) Plot of 1/[*L*-LA]$_t$ *vs.* time for *L*-LA polymerisation with **12** (k_{obs} = 19.53 h^{-1}. R^2 = 0.993). Conditions: [*L*-LA]$_0$:[**M**]$_0$ = 50:1, [*L*-LA]$_0$ = 0.5 M in 0.6 mL benzene-d_6 at 60 °C.

In contrast, a first order dependence on monomer concentration was recorded for the strontium system, **11** (**Figure 5.7**); this helps to explain why its rate of polymerisation is much slower than that of the barium catalyst. The first-order experimental rate constant for **11** (k_{obs} = 0.84 h^{-1}) is similar to that of a *tert*-butyl substituted, phenoxy-imine magnesium initiator incorporating a biphenyl-based pendant arm (0.66 h^{-1}; **Figure 5.3b**).[7]

Table 5.2 ROP of *L*-LA using **11** and **12** with $[L\text{-LA}]_0:[\mathbf{M}]_0 = 50:1$ in benzene-d_6 at 60 °C.[a]

Catalyst	Time (h)	Conv. (%)[b]	k_{obs} (h^{-1} or M^{-1} h^{-1})	R^{2c}	M_n (GPC)[e]	M_n (calcd)[f]	M_w/M_n
11	2.0	80	0.84 ± 0.008[c]	0.998	34 698	5816	1.56
12	0.5	81	19.53 ± 0.3[d]	0.993	47 200	6415	1.51

[a]Conditions: $[L\text{-LA}]_0:[\mathbf{M}]_0 = 50:1$, $[L\text{-LA}]_0 = 0.5$ M in 0.6 mL benzene-d_6 at 60 °C. [b]Average reported; measured by ^{1}H NMR spectroscopic analyses. [c]First order rate constant (k_{obs}: h^{-1}) and R^2 were obtained from average plots of $\ln([L\text{-LA}]_0/[L\text{-LA}]_t)$ *vs.* time. [d]Second order rate constant (k_{obs}: M^{-1} h^{-1}) and R^2 were obtained from average plots of $1/[L\text{-LA}]_t$ *vs.* time [e]Determined by GPC in THF against PS standards using the appropriate Mark-Houwink corrections.[17] [f]Calculated M_n for PLA synthesised = (conv.(%) × $[L\text{-LA}]_0/[\mathbf{M}]_0$) × 144.13.

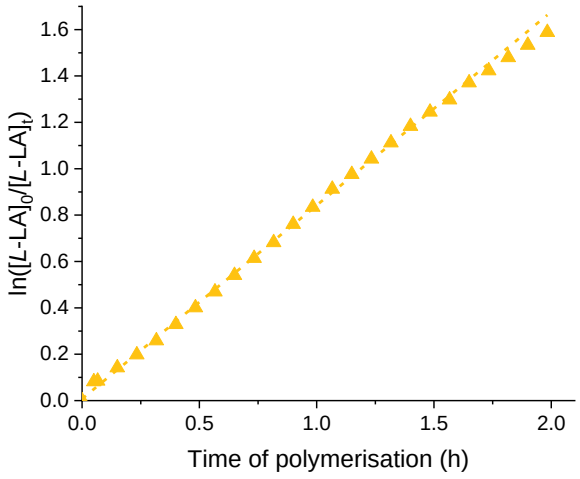

Figure 5.7 Plot of $\ln([L\text{-LA}]_0/[L\text{-LA}]_t)$ *vs.* time for *L*-LA polymerisation using **11** ($k_{obs} = 0.84$ h^{-1}. $R^2 = 0.998$). Conditions: $[L\text{-LA}]_0:[\mathbf{Sr}]_0 = 50:1$, $[L\text{-LA}]_0 = 0.5$ M in 0.6 mL benzene-d_6 at 60 °C.

GPC analysis of the resultant polymers showed that, like with catalyst **10**, the experimental molecular weights are much higher than the theoretical values (**Table 5.2**). Percentage active catalyst calculations confirm that this is due to dormant metal centres, as on average, only 15% of the homoleptic initiators were found to be active in the

absence of BnOH (**10**: 16%, **11**: 17% and **12**: 12%).[28] In addition to inactive metal centres, the moderate reaction control (M_w/M_n = 1.51 (**11**), 1.56 (**12**)) is also caused by the occurrence of transesterification reactions. These were confirmed *via* MALDI-TOF MS analysis; exemplar mass spectra can be found in **Figures A.29-30**.

Upon addition of benzyl alcohol, the strontium and barium catalysts were found to decompose into pro-ligand. As a result, co-catalytic polymerisations involving the binary **11**/BnOH and **12**/BnOH systems could not be investigated. The lower stability of these complexes may result from their larger ionic radii making them more susceptible to aggregation and/or filling of their coordination sphere with alcohol. To supress such redistributions, and therefore harness their potential catalytic capabilities, synthetic approaches involving bulkier, multidentate ancillary ligands are required.

Due to the poor stability of the strontium and barium homoleptic complexes in the presence of BnOH, a full polymerisation study was only conducted with the binary **10**/BnOH system. However, as the polymerisation of 50 eq. *L*-LA with this co-catalytic system was so rapid, all subsequent polymerisations employed 500 eq. of monomer as standard in order to collect high quality kinetic data.

5.3.2 Variable temperature studies

The temperature dependence on the rate of polymerisation using **10** and BnOH system was investigated. Polymerisations were run between 30 and 50 °C with one eq. of benzyl alcohol co-initiator, $[L\text{-LA}]_0/[\mathbf{Mg}]_0$ = 500 and $[L\text{-LA}]_0$ = 0.5 M. As expected, an increase in polymerisation temperature, from 30 to 50 °C, resulted in an increase in the observed rate (**30 °C**: k_{obs} = 1.88 h^{-1} < **40 °C**: k_{obs} = 2.21 h^{-1} < **45 °C**: k_{obs} = 2.70 h^{-1} < **50 °C**: k_{obs} = 3.18 h^{-1}; **Figure 5.8** and **Table 5.3**). Complex **10** shows better activity for LA

polymerisation, with higher monomer loadings, compared to other Schiff base magnesium catalysts in the literature (k_{obs} = 0.096–9.08 h^{-1} for 25–200:1 ratios).[1, 7]

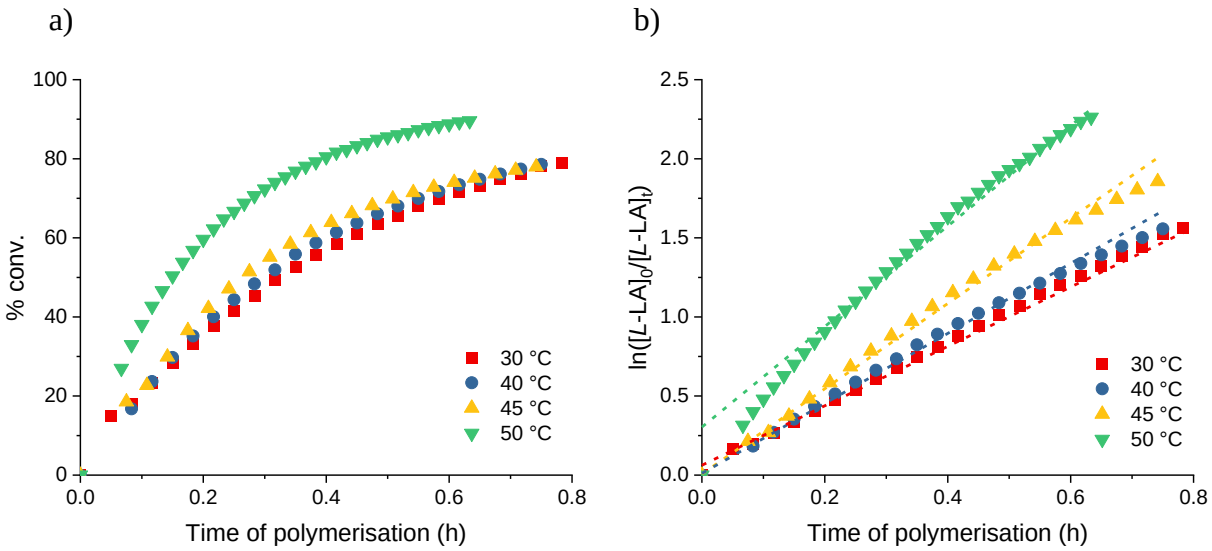

Figure 5.8 a) Plots of percentage conversion *vs*. time. b) Plots of ln([*L*-LA]$_0$/[*L*-LA]$_t$) *vs*. time for *L*-LA polymerisation with **10**/BnOH. Red squares: 30 °C (k_{obs} = 1.88 h^{-1}. R^2 = 0.999); blue circles: 40 °C (k_{obs} = 2.21 h^{-1}. R^2 = 0.996); yellow up triangles: 45 °C (k_{obs} = 2.70 h^{-1}. R^2 = 0.995); green down triangles: 50 °C (k_{obs} = 3.18 h^{-1}. R^2 = 0.992). Conditions: [*L*-LA]$_0$:[**Mg**]$_0$:[BnOH]$_0$ = 500:1:1, [*L*-LA]$_0$ = 0.5 M in 0.6 mL chloroform-d_1 at stated temperature.

Narrow molecular weight distributions were recorded for the PLA produced at the different temperatures tested (M_w/M_n = 1.11–1.17; **Figure 5.9a**); this suggests that the polymerisations proceed with relatively high levels of control in all cases. Comparable polydispersity indices have previously been reported for a variety of magnesium-based phenoxy-imine catalysts (M_w/M_n = 1.03–1.75).[1, 2, 7] The experimental molecular weights, however, were always found to be lower than the calculated values (Δ% = 56-80; **Table 5.3**). This may result from excess/unreacted co-initiator acting as a chain transfer agent throughout the polymerisation or from multiple propagating polymer chains growing per

metal centre. Simultaneous chain binding in this system is likely, considering that the order with respect to monomer concentration exceeds one in the absence of co-initiator.

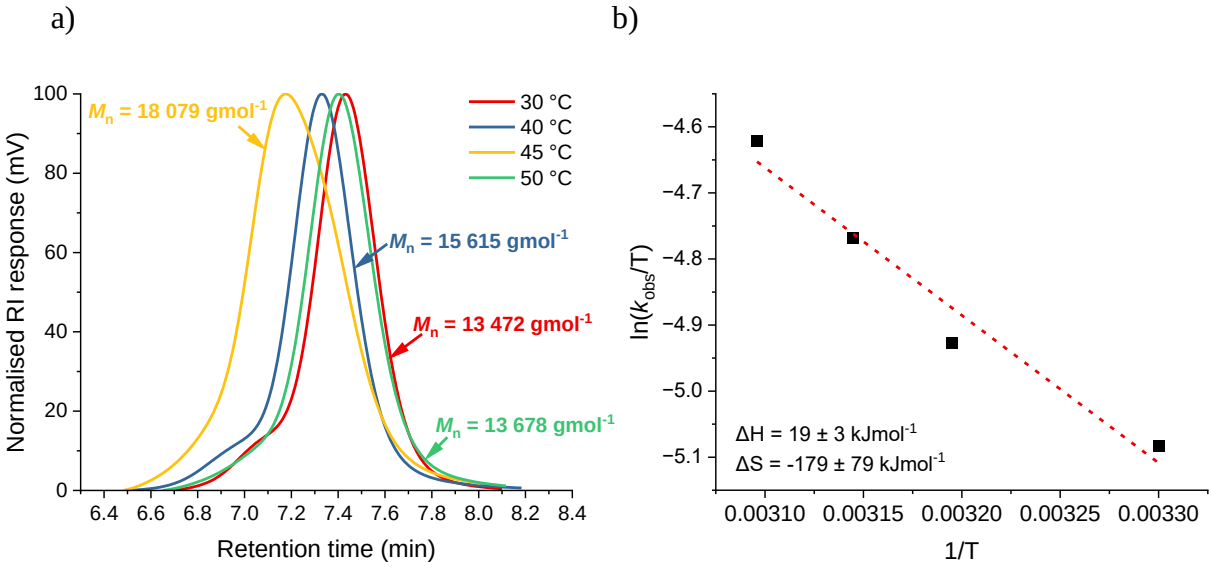

Figure 5.9 a) GPC traces of PLAs synthesised from the ROP of *L*-LA using **10**/BnOH. Red: 30 °C, M_n = 13 472 gmol^{-1}, M_w/M_n = 1.11; blue: 40 °C, M_n = 15 615 gmol^{-1}, M_w/M_n = 1.13; yellow: 45 °C, M_n = 18 079 gmol^{-1}, M_w/M_n = 1.17; green: 50 °C, M_n = 13 678 gmol^{-1}, M_w/M_n = 1.12. b) Eyring plot of ln(k_{obs}/T) *vs.* 1/T. Slope = −2235 ± 315, Intercept = 2.3 ± 1.0. R^2 = 0.962. $\Delta H^{\ddagger}$ = 19 ± 3 kJ mol^{-1}, $\Delta S^{\ddagger}$ = −179 ± 79 J K^{-1} mol^{-1}. Conditions: [*L*-LA]$_0$:[**Mg**]$_0$:[BnOH]$_0$ = 500:1:1, [*L*-LA]$_0$ = 0.5 M in 0.6 mL chloroform-d_1 at stated temperature.

Construction of an Eyring plot allowed the thermodynamic parameters of polymerisation catalysed by **10** and BnOH to be probed. The enthalpy ($\Delta H^{\ddagger}$) and entropy ($\Delta S^{\ddagger}$) of activation were determined, via the gradient and intercept values, to be 19 kJ mol^{-1} and –179 J K^{-1} mol^{-1} respectively (**Figure 5.9b**). This leads to Gibbs free energy ($\Delta G^{\ddagger}$) values of 73–78 kJ mol^{-1} for the temperature range tested. The modest positive enthalpy value aligns with the proposed mechanistic pathway for this catalytic system as prior activation of the lactide monomer should enable more facile nucleophilic attack. In addition, the large negative entropic factor implies that a more ordered transition state is

formed upon monomer binding. The values determined for the Gibbs free energy of activation are comparable to that reported for lactide polymerisation catalysed by the industrial standard: stannous(II) 2-ethylhexanoate ($SnOct_2$; $\Delta G^{\ddagger}$ = 70.9 ± 1.5 kJ mol^{-1}).[29] They are also much lower than those computed for group 3, 4 and 13 permethylindenyl complexes ($\Delta G^{\ddagger}$ = 85–120 kJ mol^{-1}), highlighting the increased favourability for the polymerisation to be catalysed by complex **10**.[18, 30]

Table 5.3 ROP of *L*-LA using **10**/BnOH with [*L*-LA]$_0$:[**Mg**]$_0$:[BnOH]$_0$ = 500:1 in chloroform-d_1 at stated temperature.[a]

Temp. (°C)	Time (h)	Conv. (%)[b]	k_{obs} (h^{-1})[c]	R^{2c}	M_n (GPC)[d]	M_n (calcd)[e]	M_w/M_n
30	1.3	91	1.88 ± 0.007	0.999	13 472	65 377	1.11
40	0.8	79	2.21 ± 0.03	0.996	15 615	57 501	1.13
45	0.7	78	2.70 ± 0.04	0.995	18 079	40 753	1.17
50	0.6	90	3.18 ± 0.05	0.992	13 678	66 776	1.12

[a]Conditions: [*L*-LA]$_0$:[**Mg**]$_0$:[BnOH]$_0$ = 500:1:1, [*L*-LA]$_0$ = 0.5 M in 0.6 mL chloroform-d_1 at stated temperature. [b]Average reported; measured by ^{1}H NMR spectroscopic analyses. [c]First order rate constant (k_{obs}) and R^2 were obtained from average plots of ln([*L*-LA]$_0$/[*L*-LA]$_t$) *vs.* time. [d]Determined by GPC in THF against PS standards using the appropriate Mark-Houwink corrections.[17] [e]Calculated M_n for PLA synthesised = (conv.(%) × [*L*-LA]$_0$/[**Mg**]$_0$) × 144.13 + (M_w of end groups).

5.3.3 Varying monomer stereochemistry

The effect of monomer stereochemistry was investigated by carrying out polymerisations using *rac*-, *L*, *D*, and *meso*-lactide at 40 °C with one eq. of benzyl alcohol co-initiator, [LA]$_0$/[**Mg**]$_0$ = 500 and [LA]$_0$ = 0.5 M. The results, which are presented in **Figure 5.10** and **Table 5.4** were found to follow the same trend as the magnesium "NOON" complex, **2**: *rac*- < *L*- ≈ *D*- < *meso*-.

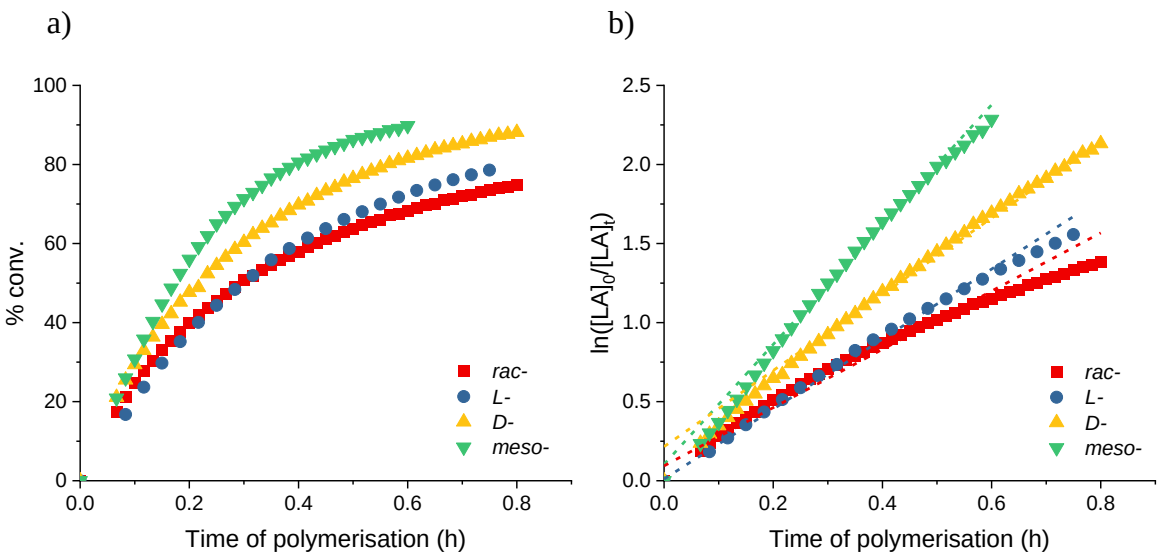

Figure 5.10 a) Plots of percentage conversion *vs.* time. b) Plots of $\ln([LA]_0/[LA]_t)$ *vs.* time for LA polymerisation with **10**/BnOH. Red squares: *rac*-LA (k_{obs} = 1.84 h^{-1}. R^2 = 0.983); blue circles: *L*-LA (k_{obs} = 2.21 h^{-1}. R^2 = 0.996); yellow up triangles: *D*-LA (k_{obs} = 2.41 h^{-1}. R^2 = 0.999); green down triangles: *meso*-LA (k_{obs} = 3.79 h^{-1}. R^2 = 0.996). Conditions: $[LA]_0$:[**Mg**]$_0$:$[BnOH]_0$ = 500:1, $[LA]_0$ = 0.5 M in 0.6 mL chloroform-d_1 at 40 °C.

The polymerisation of *meso*-lactide was found to be the fastest (k_{obs} = 3.79 h^{-1}); this is likely due to the inherent ring strain of the monomer acting as a driving force during the reaction.[31-33] On the other hand, the polymerisation of *rac*-LA was found to be the slowest (k_{obs} = 1.84 h^{-1}) thus implying a preference for the formation of polymeric *meso*-linkages. A similar trend was observed when conducting polymerisations with the magnesium "NOON" dimer (**2**). The dominating stereocontrol mechanism is likely to be chain-end control as the reactions involving the *L*- and *D*- monomers were seen to progress at very similar rates, suggesting that catalyst framework shows no preference for either isomer (k_L/k_D = 0.92 ≈ 1). Similar k_L/k_D ratios were observed by Darensbourg and co-workers in their investigations of amino-acid based zinc catalysts (k_L/k_D = 1.03–1.16 ≈ 1; $[LA]_0/[\mathbf{Zn}]_0$ = 49).[34] In contrast, Ma *et al*. report a k_L/k_D of ~0.28 for their chiral

oxazolinyl heteroleptic magnesium catalysts (k_{obs} = 0.041 and 0.144 h^{-1} for *L*- and *D*-LA respectively).[6]

Table 5.4 ROP of LA using **10**/BnOH with $[LA]_0$:[**Mg**]$_0$:$[BnOH]_0$ = 500:1 in chloroform-d_1 at 40 °C.[a]

LA	Time (h)	Conv. (%)[b]	k_{obs} (h^{-1})[c]	R^{2c}	M_n (GPC)[d]	M_n (calcd)[e]	M_w/M_n
rac-	0.8	75	1.84 ± 0.04	0.983	8234	57 155	1.75
L-	0.8	79	2.21 ± 0.03	0.996	15 615	57 501	1.13
D-	0.8	88	2.41 ± 0.01	0.999	13 969	67 395	1.12
meso-	0.6	90	3.79 ± 0.04	0.996	5795	68 419	1.72

[a]Conditions: $[LA]_0$:[**Mg**]$_0$:$[BnOH]_0$ = 500:1:1, $[LA]_0$ = 0.5 M in 0.6 mL chloroform-d_1 at 40 °C. [b]Average reported; measured by ^{1}H NMR spectroscopic analyses. [c]First order rate constant (k_{obs}) and R^2 were obtained from average plots of $\ln([LA]_0/[LA]_t)$ *vs.* time. [d]Determined by GPC in THF against PS standards using the appropriate Mark-Houwink corrections.[17] [e]Calculated M_n for PLA synthesised = (conv.(%) × $[LA]_0$/[**Mg**]$_0$) × 144.13 + (M_w of end groups).

GPC analysis showed narrow and intermediate molecular weight distributions for the polymers formed from *L*/*D*-LA (M_w/M_n = 1.12–1.13) and *rac*/*meso*-LA (M_w/M_n = 1.72–1.75; **Figure A.31**) respectively. This implies that the reaction control becomes poorer as a result of the formation of *racemic* polymer linkages. The lessened polymerisation control with the *rac*-/*meso*-LA also agrees with the greater disparity between experimental and theoretical molecular weight values for these monomers (*rac*: 8234 *vs.* 57 155 $gmol^{-1}$; *meso*: 5795 *vs.* 68 419 $gmol^{-1}$; **Table 5.4**). In all cases, there is a clear discrepancy between calculated and experimental molecular weight values; this is the result of transesterification (identified via the mass spectrum of the PLA) as well as multiple polymer chains potentially propagating from a single metal centre.

5.3.3.1 Microstructure analysis

The microstructure of the isolated polylactide was analysed by $^{1}H\{^{1}H\}$ NMR spectroscopy (**Figure 5.11**); atactic PLA was formed when either *rac*-LA (P_r = 0.48) or *meso*-LA (P_r = 0.54) was used. This implies a lack of enantiomorphic-site and chain-end stereocontrol mechanisms. The low degree of stereocontrol imparted by complex **10** may be due to its planar configuration enabling the metal centre to be equally accessible from both faces. Increasing the steric bulk in one half of the metal's coordination sphere or introducing chirality into the ligand framework may help to improve the level of stereoregularity imparted on the polymeric products.

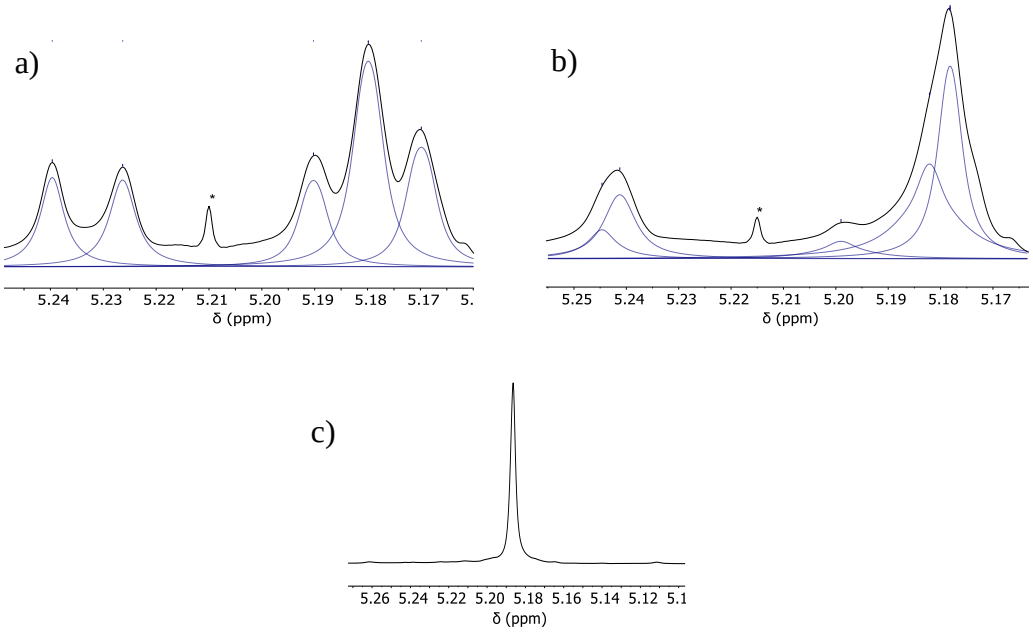

Figure 5.11 $^{1}H\{^{1}H\}$ NMR spectra (chloroform-d_1, 500 MHz, 298 K) of the *methine* protons in the PLA produced from a) *rac*-LA (P_r = 0.48), b) *meso*-LA (P_r = 0.54) and c) *L*-/*D*-LA (P_m = 1.00). * represents an artefact from BASH processing. Conditions: $[LA]_0$:[**Mg**]$_0$:$[BnOH]_0$ = 500:1, $[LA]_0$ = 0.5 M in 0.6 mL chloroform-d_1 at 40 °C.

In the case of *L*- and *D*-LA, a single resonance was observed in the *methine* region of the homonuclear decoupled NMR spectra. This confirms the formation of isotactic PLA (P_m

= 1.00) and absence of epimerisation (random inversion of stereochemistry at a single chiral centre).

5.3.4 Initiator concentration dependency

In order to determine the kinetic order in catalyst concentration, the polymerisation of *L*-LA with **10** and BnOH was carried out at 40 °C using various molar ratios of monomer to catalyst. The concentration of *L*-LA was held constant at 0.5 M, while that of the catalyst was varied to provide the ratio of $[L\text{-LA}]_0$:$[\mathbf{Mg}]_0$ = 50, 250, 500, 750 (**Figure 5.12** and **Table 5.5**).

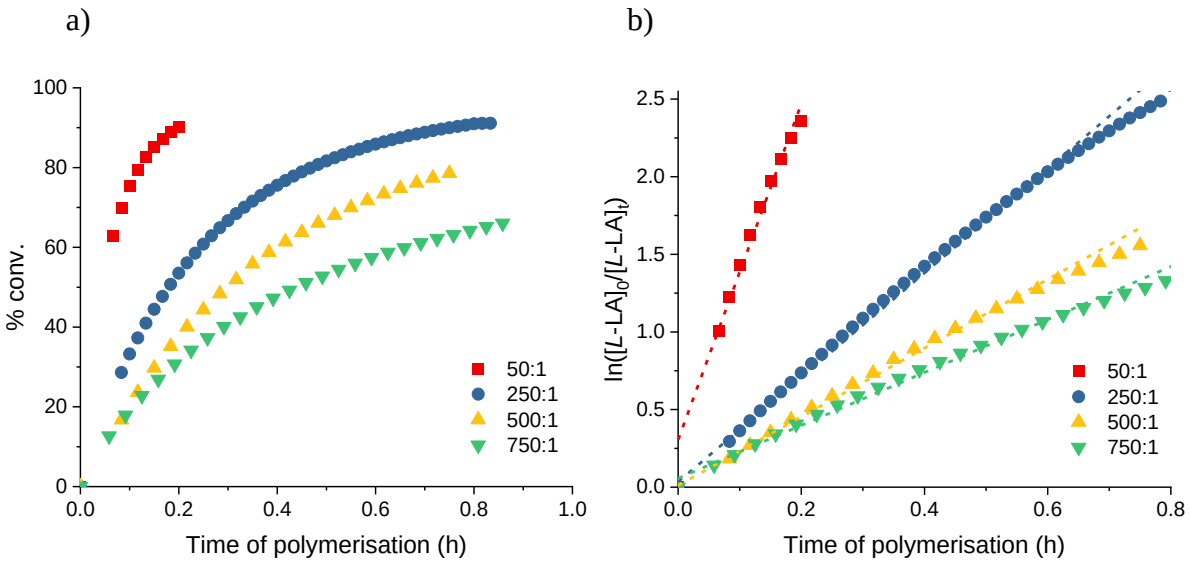

Figure 5.12 a) Plots of percentage conversion *vs.* time. b) Plots of $\ln([L\text{-LA}]_0/[L\text{-LA}]_t)$ *vs.* time for *L*-LA polymerisation with **10**/BnOH. Red squares: 50:1 (k_{obs} = 10.82 h^{-1}. R^2 = 0.987); blue circles: 250:1 (k_{obs} = 3.37 h^{-1}. R^2 = 0.996); yellow up triangles: 500:1 (k_{obs} = 2.21 h^{-1}. R^2 = 0.996); green down triangles: 750:1 (k_{obs} = 1.70 h^{-1}. R^2 = 0.995). Conditions: $[L\text{-LA}]_0$:$[\mathbf{Mg}]_0$ as stated, $[L\text{-LA}]_0$ = 0.5 M in 0.6 mL chloroform-d_1 at 40 °C.

In all cases, a first-order dependence on monomer concentration was observed; this was evidenced by the linear plots of $\ln([L\text{-LA}]_0/[L\text{-LA}]_t)$ *vs.* time (**Figure 5.12**). The non-zero

intercept for the 50:1 run is most likely due to the reaction occurring too fast to collect accurate initial kinetic data. A reduction in initiator (and therefore active site) concentration resulted in a decrease in the observed rate (k_{obs} = **750:1**: 1.70 < **500:1**: 2.21 < **250:1**: 3.37 < **50:1**: 10.82 h^{-1}).

Table 5.5 ROP of *L*-LA using **10**/BnOH with [*L*-LA]$_0$:[**Mg**]$_0$ as stated in chloroform-d_1 at 40 °C.[a]

[*L*-LA]$_0$: [**Mg**]$_0$	Time (h)	Conv. (%)[b]	k_{obs} (h^{-1})[c]	R^{2c}	M_n (GPC)[d]	M_n (calcd)[e]	M_w/M_n
50:1	0.2	91	10.82 ± 0.4	0.987	4373	6974	1.51
250:1	0.8	91	3.37 ± 0.03	0.996	11 043	30 008	1.14
500:1	0.8	79	2.21 ± 0.03	0.996	15 615	57 501	1.13
750:1	0.9	66	1.70 ± 0.03	0.995	29 311	69 636	1.13

[a]Conditions: [*L*-LA]$_0$:[**Mg**]$_0$ as stated, [*L*-LA]$_0$ = 0.5 M in 0.6 mL chloroform-d_1 at 40 °C. [b]Average reported; measured by ^{1}H NMR spectroscopic analyses. [c]First order rate constant (k_{obs}) and R^2 were obtained from average plots of ln([*L*-LA]$_0$/[*L*-LA]$_t$) *vs.* time. [d]Determined by GPC in THF against PS standards using the appropriate Mark-Houwink corrections.[17] [e]Calculated M_n for PLA synthesised = (conv.(%) × [*L*-LA]$_0$/[**Mg**]$_0$) × 144.13 + (M_w of end groups).

A plot of −ln(k_{obs}) *vs.* −ln[**Mg**]$_0$ was generated to determine the order with respect to catalyst **10** (**Figure 5.13**); this gave a linear relationship with a gradient of 0.68 ± 0.02. This slope and its associated error imply a first-order dependency on catalyst concentration. The non-integer value may reflect possible aggregation of initiating species in solution.[35-37] The propagation rate constant of the polymerisation (k_p) was calculated via a plot of k_{obs} *vs.* [**Mg**]$_0$, to be 966 ± 26 M^{-1} h^{-1}. This is an order of magnitude smaller than the value reported for a comparable homoleptic calcium species incorporating a tridentate N,N,O-phenoxyimine ligand system (k_p = 7020 M^{-1} h^{-1}). This

calcium catalyst however was found to dimerise in solution. The bimetallic nature of the active species may contribute to its superior reactivity alongside other factors such as the different metal, ligand and/or conditions.[4]

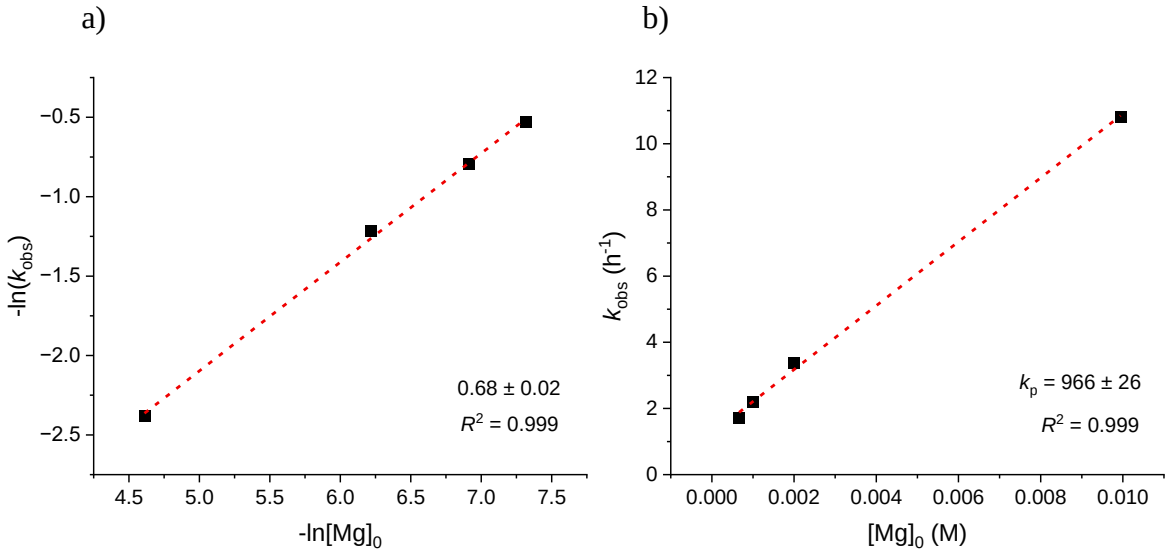

Figure 5.13 a) Plot of $-\ln(k_{obs})$ *vs.* $-\ln[\mathbf{Mg}]_0$ for ROP of *L*-LA using **10**/BnOH shows that the order of reaction with respect to $[\mathbf{Mg}]_0$ is equal to 0.68 ± 0.02; R^2 = 0.999. b) Plot of k_{obs} *vs.* $[Mg]_0$ for ROP of *L*-LA using **10**/BnOH shows k_p = 966 ± 26 M^{-1} h^{-1}; R^2 = 0.999.

GPC analysis of the polymers produced depicts narrow molecular weight distributions at all catalyst concentrations (**Figure A.32**). As the $[L\text{-LA}]_0$:$[\mathbf{Mg}]_0$ ratio increases, the rate of polymerisation decreases, thus resulting in improved polymerisation control (M_w/M_n = 1.51, 1.14, 1.13 and 1.13 for $[L\text{-LA}]_0/[\mathbf{Mg}]_0$ ratios of 50:1, 250:1, 500:1 and 750:1 respectively; **Table 5.5**). The experimental M_n values also increased with decreasing catalyst concentration as a result of the greater probability of reaction propagation ($M_{n,(GPC)}$ = 4373, 11 043, 15 615 and 29 311 $gmol^{-1}$ for $[L\text{-LA}]_0/[\mathbf{Mg}]_0$ ratios of **50:1**, **250:1**, **500:1** and **750:1** respectively). Analogous observations were made by Chakraborty *et al*. in their study of homoleptic *bis*(phenoxy-imine) catalysts for the ROP of LA.[1] In all cases, however, the experimental molecular weights were found to be lower

than the calculated values; this highlights the occurrence of transesterification reactions as well as the possibility of multiple chains propagating per metal centre.

5.3.5 Co-initiator concentration dependency

As catalyst **10** contains no pre-formed initiating group, it is likely that the polymerisations with BnOH proceed via an activated monomer pathway with an evident rate dependence on co-initiator concentration (i.e. $[BnOH]_0$ is present in the overall rate law).[38] To determine whether this is the case, polymerisations of *L*-LA with **10** were carried out at 40 °C in chloroform-d_1 using various $[\mathbf{Mg}]_0$:$[BnOH]_0$ ratios. In all cases, a first-order dependence on monomer concentration was observed as evidenced by the linear plots of $\ln([L\text{-LA}]_0/[L\text{-LA}]_t)$ *vs*. time (**Figure 5.14b**).

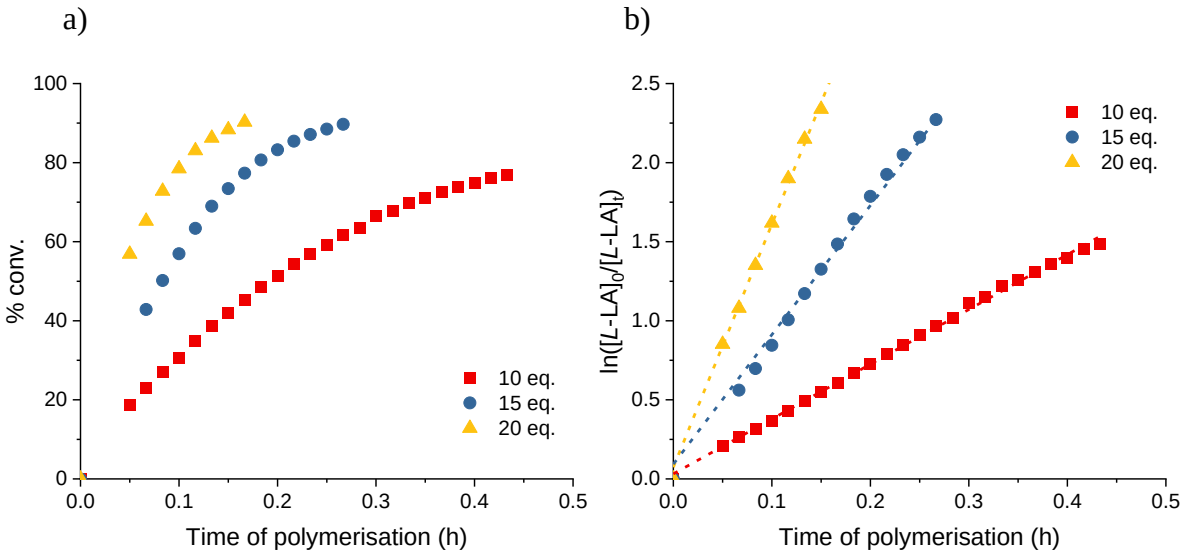

Figure 5.14 a) Plots of percentage conversion *vs.* time. b) Plots of $\ln([L\text{-LA}]_0/[L\text{-LA}]_t)$ *vs.* time for *L*-LA polymerisation with **10**/BnOH. Red squares: 10 eq. BnOH (k_{obs} = 3.42 h^{-1}. R^2 = 0.999); blue circles: 15 eq. BnOH (k_{obs} = 8.18 h^{-1}. R^2 = 0.994); yellow up triangles: 20 eq. BnOH (k_{obs} = 15.37 h^{-1}. R^2 = 0.998). Conditions: $[\mathbf{Mg}]_0$:$[BnOH]_0$ as stated, $[L\text{-LA}]_0$ = 0.5 M in 0.6 mL chloroform-d_1 at 40 °C.

A non-linear increase in the experimental rate constants was observed, however, as the doubling of the co-initiator eq. resulted in a 4.5-fold increase in k_{obs} (3.42 h^{-1} for 10 eq. *vs.* 15.37 h^{-1} for 20 eq.). A plot of $-\ln(k_{obs})$ *vs.* $-\ln[BnOH]_0$ revealed a linear relationship (R^2 = 0.999) with a gradient of 2.17 ± 0.01 indicating a second-order dependency on $[BnOH]_0$ (**Figure 5.15a**). The second-order nature of this dependency is rare but not unprecedented.[39] It suggests that two molecules of co-initiator are required for reaction propagation; this helps to explains the observed non-linear trend in experimental rate constants.

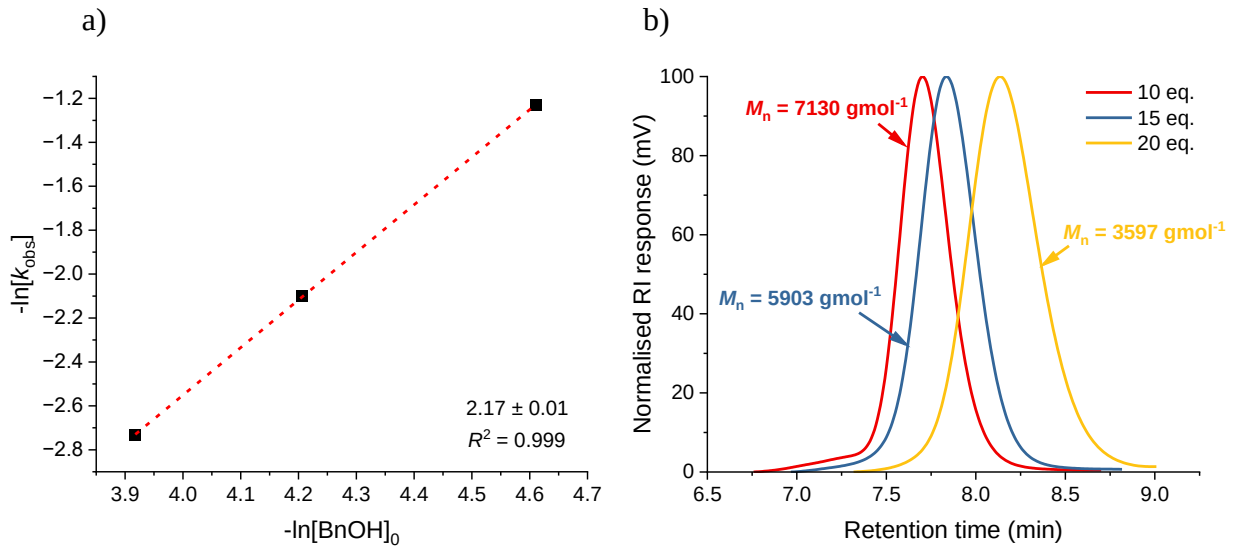

Figure 5.15 a) Plot of $-\ln(k_{obs})$ *vs.* $-\ln[BnOH]_0$ for ROP of *L*-LA using **10**/BnOH shows that the order of reaction with respect to $[BnOH]_0$ is equal to 2.17 ± 0.01; R^2 = 0.999. b) GPC traces of PLAs synthesised from the ROP of *L*-LA using **10**/BnOH. Red: 10 eq. BnOH, M_n = 7930 $gmol^{-1}$, M_w/M_n = 1.13; blue: 15 eq. BnOH, M_n = 5903 $gmol^{-1}$, M_w/M_n = 1.18; yellow: 20 eq. BnOH, M_n = 3597 $gmol^{-1}$, M_w/M_n = 1.15. Conditions: $[\mathbf{Mg}]_0$:$[BnOH]_0$ as stated, $[L\text{-LA}]_0$ = 0.5 M in 0.6 mL chloroform-d_1 at 40 °C.

Assuming a constant concentration of the (co-)initiator remains throughout the reaction, the following rate law can be derived for the ROP of lactide catalysed by **10** and BnOH:

$$\frac{d[\mathrm{LA}]}{dt} = k_p[\mathrm{LA}][\mathbf{Mg}][\mathrm{BnOH}]^2 \qquad \text{where} \qquad k_{obs} = k_p[\mathbf{Mg}] \qquad \textbf{Equation 5.1}$$

At all co-initiator concentrations, polymerisation proceeded with good control, as evidenced by the recorded narrow molecular weight distributions (M_w/M_n = 1.13–1.18; **Figure 5.15b** and **Table 5.6**). The experimental molecular weights are consistent with the calculated value that assumes the number of propagating chains is equal to the sum of the catalyst and initiator eq. (values depicted in brackets in **Table 5.6**). This immortal behaviour, which implies that the rate of transfer (k_{tr}) is far greater than the rate of propagation (k_p), has been previously reported for a wide range of similar M^{2+} systems.[2, 11, 12, 40]

Table 5.6 ROP of *L*-LA using **10**/BnOH with $[\mathbf{Mg}]_0$:$[\mathrm{BnOH}]_0$ as stated in chloroform-d_1 at 40 °C.[a]

$[\mathbf{Mg}]_0$: $[\mathrm{BnOH}]_0$	Time (h)	Conv. (%)[b]	k_{obs} (h^{-1})[c]	R^{2c}	M_n (GPC)[d]	M_n (calcd)[e]	M_w/M_n
10:1	0.4	77	3.42 ± 0.02	0.999	7930	64 008 (5819)	1.13
15:1	0.3	90	8.18 ± 0.18	0.994	5903	69 463 (4341)	1.18
20:1	0.2	90	15.37 ± 0.24	0.998	3597	70 400 (3352)	1.15

[a]Conditions: $[\mathbf{Mg}]_0$:$[\mathrm{BnOH}]_0$ as stated, $[L\text{-LA}]_0$ = 0.5 M in 0.6 mL chloroform-d_1 at 40 °C. [b]Average reported; measured by ^{1}H NMR spectroscopic analyses. [c]First order rate constant (k_{obs}) and R^2 were obtained from average plots of $\ln([L\text{-LA}]_0/[L\text{-LA}]_t)$ *vs.* time. [d]Determined by GPC in THF against PS standards using the appropriate Mark-Houwink corrections.[17] [e]Calculated M_n for PLA synthesised = (conv.(%) × $[L\text{-LA}]_0/[\mathbf{Mg}]_0$) × 144.13 + ($M_w$ of end groups); value in brackets is the calculated M_n if all BnOH acts as a chain transfer agent.

5.3.6 Polymer end group analysis

Matrix-assisted laser desorption/ionisation time of flight (MALDI-TOF) mass spectrometry and NMR spectroscopy were used to determine the end groups of the polymers produced using the **10** and BnOH catalytic system; representative spectra are presented in **Figures 5.16-5.18**.

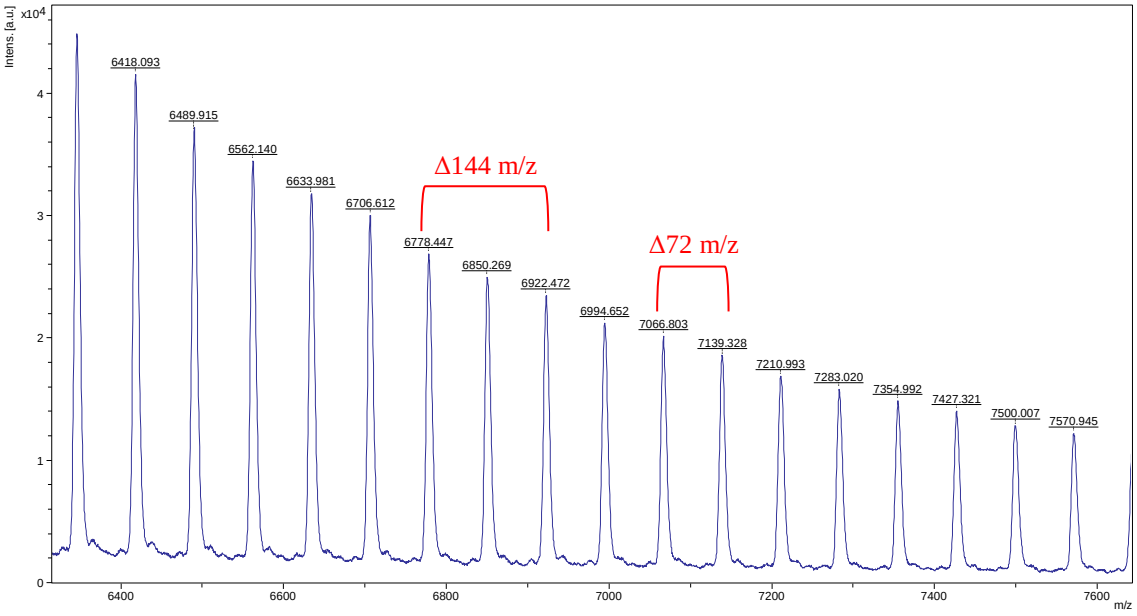

Figure 5.16 MALDI-TOF mass (*m*/*z*) spectrum of PLA produced using **10**/BnOH. Conditions: $[L\text{-LA}]_0$:[**Mg**]$_0$:$[\text{BnOH}]_0$ = 50:1:1, $[L\text{-LA}]_0$ = 0.5 M, 0.6 mL chloroform-d_1, 60 °C. M_w/M_n = 1.31.

The mass spectrum is consistent with PLA containing the expected $–OCH_2Ph$ and –OH end groups. For example, the peak centred at 6634.0 gmol^{-1} is attributed to $–OCH_2Ph$/–OH terminated PLA, comprising of 45 units of LA with K^+ [144.13(45) + 108.14 + 39.1]. The 72 *m*/*z* split between the peaks confirms the occurrence of transesterification reactions during the polymerisation.[18, 30, 41-43] The benzyl alcohol end group was also detected in the ^{1}H and $^{13}C\{^1H\}$ NMR spectra; a multiplet at δ 4.35 ppm corresponds to the $–C\boldsymbol{H}(CH_3)OH$ proton and the aromatic signals of the $–OCH_2\boldsymbol{Ph}$ group appear at δ 7.28–7.40 ppm.

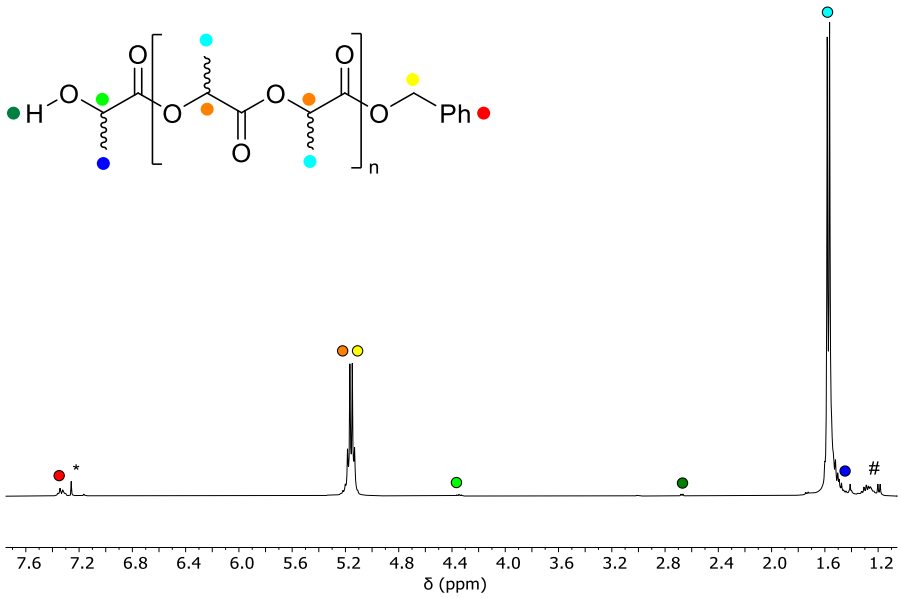

Figure 5.17 ^{1}H NMR spectrum (*chloroform-d_1, 400 MHz, 298 K) of PLA produced using the **10**/BnOH system. # represents residual protio pentane from work-up. Conditions: [*L*-LA]$_0$:[**Mg**]$_0$:[BnOH]$_0$ = 50:1:1, [*L*-LA]$_0$ = 0.5 M, 0.6 mL chloroform-d_1, 60 °C. M_w/M_n = 1.79.

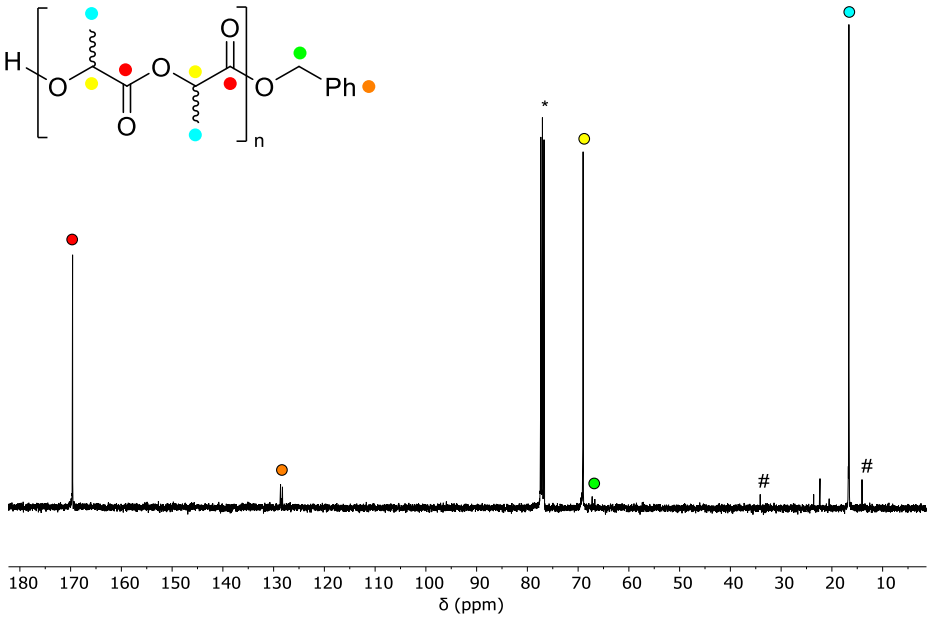

Figure 5.18 ^{13}C{^{1}H} NMR spectrum (*chloroform-d_1, 101 MHz, 298 K) of PLA produced using the **10**/BnOH system**.** # represents residual protio pentane from work-up. Conditions: [*L*-LA]$_0$:[**Mg**]$_0$:[BnOH]$_0$ = 50:1:1, [*L*-LA]$_0$ = 0.5 M, 0.6 mL chloroform-d_1, 60 °C. M_w/M_n = 1.79.

In the cases where **10** was used without BnOH, the MALDI-TOF mass spectra indicated the absence of polymer end groups (**Figure 5.19**). It is therefore likely that the polymers formed in these conditions are cyclic in nature.[44-46] For example, the peak centred at 5561.9 $gmol^{-1}$ is attributed to cyclic PLA, comprising of 39 units of LA with K^+ [144.13(39) + 39.1]. Similar observations were made when **11** or **12** were employed as the catalyst; the exemplar mass spectra for these systems can be found in **Figures A.29-30**.

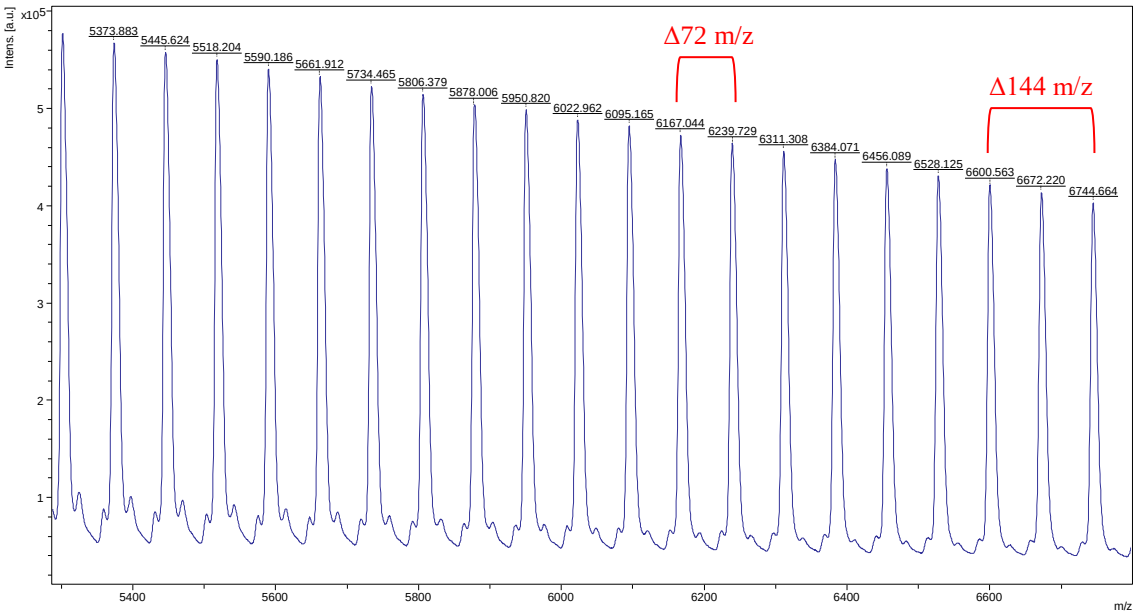

Figure 5.19 MALDI-TOF mass (m/z) spectrum of PLA produced using **10**. Conditions: [*L*-LA]$_0$:[**Mg**]$_0$ = 50:1, [*L*-LA]$_0$ = 0.5 M, 0.6 mL chloroform-d_1, 60 °C. M_w/M_n = 1.51.

5.4 Using the heteroleptic initiators

The capability of heteroleptic calcium complexes **13–15** to act as initiators in the ring-opening polymerisation of lactide has also been investigated. The effect of co-initiator addition, solvent, monomer stereochemistry, temperature and catalyst/co-initiator concentration have been probed.

As the activity of the different catalysts were similar, only the results of the full study with **15** are presented below. Analogous data from the ROPs with **13** and **14** are referenced where appropriate. Complete experimental results for the *H*- and *Me*-substituted catalysts can be found in the **Chapter 5** section of the **Appendix**.

5.4.1 Introduction of co-initiator

The ROP of *L*-LA employing **15** as the catalyst proved to be slow, achieving only 78% conversion in 25 h (**Figure 5.20**). Consistent with polymerisation data using complex **2**, this is most likely the result of the poorly initiating halide group.[47] To improve the rate of polymerisation, benzyl alcohol was added as a co-initiator; it was proposed that this would generate a more reactive Ca-OBn initiator *in situ*. As anticipated, this resulted in a (twelve-fold) increase in the observed rate (0.70 *vs*. 0.06 h^{-1}; **Table 5.7**).

Table 5.7 ROP of *L*-LA using **15** and BnOH with [*L*-LA]$_0$:[**Ca**]$_0$(:[BnOH]$_0$) = 50:1(:1) at 60 °C.[a]

BnOH	Time (h)	Conv. (%)[b]	k_{obs} (h^{-1})[c]	R^{2c}	M_n (GPC)[d]	M_n (calcd)[e]	M_w/M_n
No	25.0	78	0.06 ± 0.003	0.990	22 636	5648	1.72
Yes	4.0	93	0.70 ± 0.03	0.993	3895	7050	2.08

[a]Conditions: [*L*-LA]$_0$:[**Ca**]$_0$(:[BnOH]$_0$) = 50:1(:1), [*L*-LA]$_0$ = 0.5 M in 0.6 mL benzene-d_6 at 60 °C. [b]Average reported; measured by ^{1}H NMR spectroscopic analyses. [c]First order rate constant (k_{obs}) and R^2 were obtained from average plots of ln([*L*-LA]$_0$/[*L*-LA]$_t$) *vs.* time. [d]Determined by GPC in THF against PS standards using the appropriate Mark-Houwink corrections.[17] [e]Calculated M_n for PLA synthesised = (conv.(%) × [*L*-LA]$_0$/[**Ca**]$_0$) × 144.13 + (M_w of end groups).

This agrees with previous reports that show the ROP of LA is facile and well-controlled in the presence of alcohols.[18, 30, 42, 47, 48] A similar improvement in the rate of polymerisation upon addition of 1 eq. BnOH was reported by Lin *et al*. in their study of

Schiff base N,N,O-tridentate calcium systems (31% conversion in 120 minutes *vs*. 99% conversion in 30 minutes).[3]

With and without the co-initiator, linear plots of $\ln([L\text{-LA}]_0/[L\text{-LA}]_t)$ *vs.* time were observed, implying that the polymerisations are first-order with respect to LA (**Figure 5.20b**).

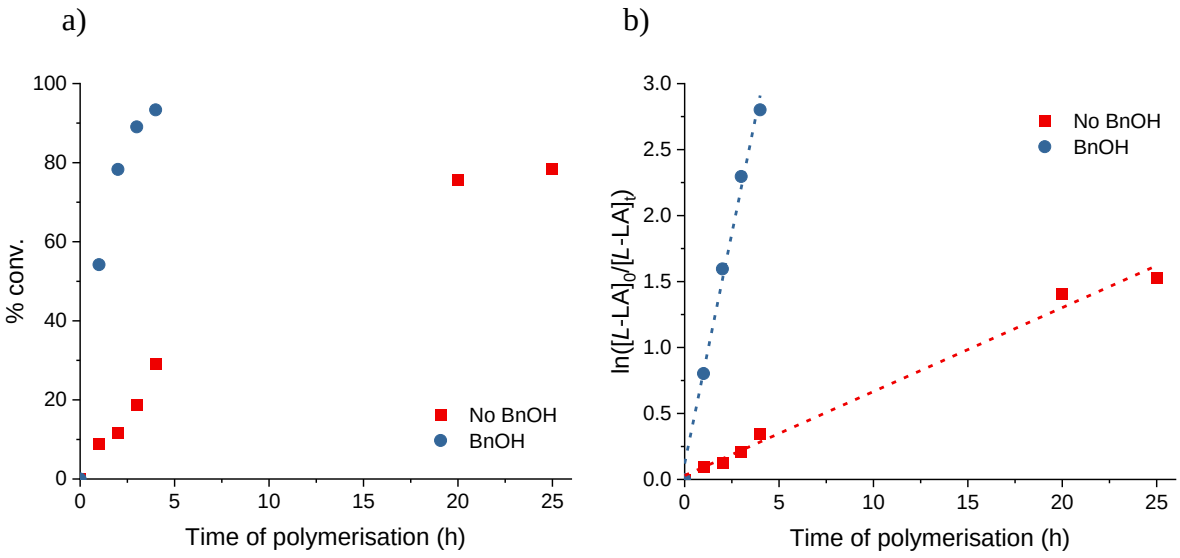

Figure 5.20 a) Plots of percentage conversion *vs.* time. b) Plots of $\ln([L\text{-LA}]_0/[L\text{-LA}]_t)$ *vs.* time for *L*-LA polymerisation with **15** with and without BnOH. Red squares: no BnOH (k_{obs} = 0.06 h^{-1}. R^2 = 0.990; blue circles: BnOH (k_{obs} = 0.70 h^{-1}. R^2 = 0.993). Conditions: $[L\text{-LA}]_0$:[**Ca**]$_0$(:$[BnOH]_0$) = 50:1(:1), $[L\text{-LA}]_0$ = 0.5 M in 0.6 mL benzene-d_6 at 60 °C.

Both polymerisations were found to proceed with only moderate control as indicated by broad polydispersity values (M_w/M_n = 1.72–2.08; **Table 5.7**). This suggests that transesterification, and possibly dormant catalysts, were present during the reaction. The latter seems to be the case in the absence of co-initiator as the experimental molecular weight is much larger than the theoretical value (22 636 *vs*. 5648 $gmol^{-1}$; Δ% = 75). Contrastingly, there is a relatively good agreement between the experimental and calculated molecular weights when the co-initiator was added. This implies that benzyl

alcohol activates more metal centres, leading to more single-site-like behaviour. As a result, BnOH was added for all subsequent polymerisations. The molecular weight of the PLA recorded in the presence of BnOH lies within the range reported for similar Ca^{2+}/BnOH systems (2600–110 600 $gmol^{-1}$ for $[LA]_0/[\mathbf{Ca}]_0$ = 50–250:1).[3, 4, 7-9, 11, 12]

5.4.2 Solvent variation

Due to the observed lack of polymerisation control in benzene-d_6 (M_w/M_n = 2.08), the effect of solvent properties on the reaction kinetics was investigated. To do this, polymerisations in benzene-d_6, chloroform-d_1 and THF-d_8 were conducted simultaneously and monitored every hour for 4 hours (**Figure 5.21**).

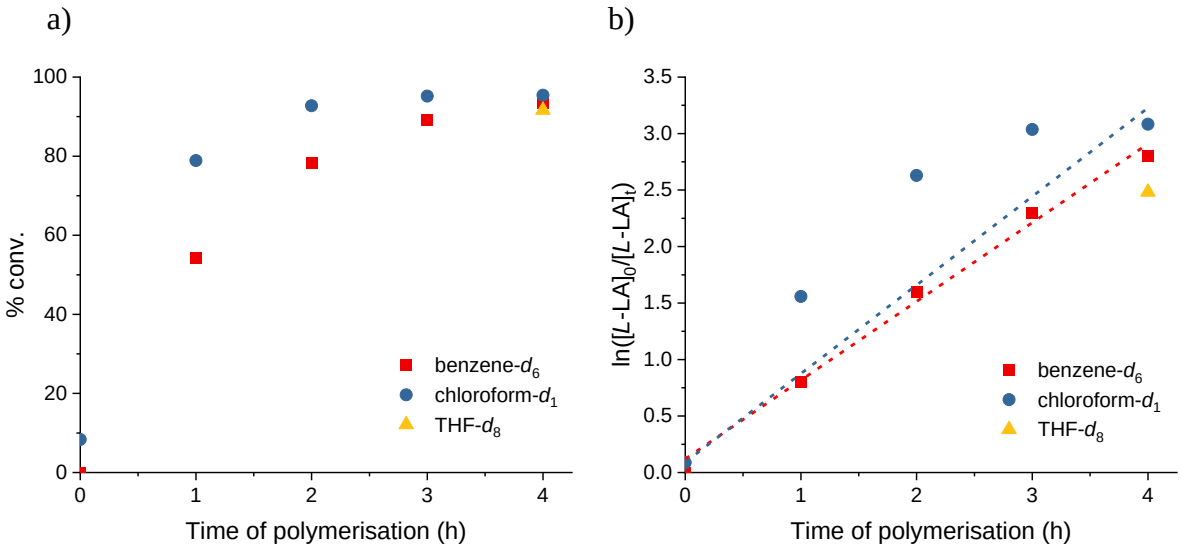

Figure 5.21 a) Plots of percentage conversion *vs*. time. b) Plots of $\ln([L\text{-LA}]_0/[L\text{-LA}]_t)$ *vs*. time for *L*-LA polymerisation with **15**/BnOH. Red squares: benzene-d_6 (k_{obs} = 0.70 h^{-1}. R^2 = 0.993); blue circles: chloroform-d_1 (k_{obs} = 0.78 h^{-1}. R^2 = 0.984); yellow up triangles: THF-d_8 (unable to monitor conversion via ^{1}H NMR due to overlapping monomer/polymer peaks). Conditions: $[L\text{-LA}]_0$:$[\mathbf{Ca}]_0$:$[BnOH]_0$ = 50:1:1, $[L\text{-LA}]_0$ = 0.5 M in 0.6 mL stated solvent at 60 °C.

In the case of THF-d_8, only a final percentage conversion could be reported, as overlapping monomer/polymer NMR spectroscopic signals prevented the calculation of

k_{obs} and R^2 values. The ROP was seen to occur the fastest, and most controlled, when run in chloroform-d_1 (k_{obs} = 0.78 h^{-1} *vs.* 0.70 h^{-1} for benzene-d_6; **Table 5.8**); this is most likely due to improved monomer solubility. As a result, all future polymerisation testing was conducted entirely in chloroform-d_1.

The poor R^2 value (0.984) recorded for the chloroform-d_1 run in the solvent screening test, was the result of the reaction happening too fast to accurately monitor it with hourly aliquots. Thus, an alternative method, in which the NMR scale polymerisations were monitored every five minutes, was subsequently employed.

Table 5.8 ROP of *L*-LA using **15**/BnOH with [*L*-LA]$_0$:[**Ca**]$_0$:[BnOH]$_0$ = 50:1:1 at 60 °C. [a]

Solvent	Time (h)	Conv. (%)[b]	k_{obs} (h^{-1})[c]	R^{2c}	M_n (GPC)[d]	M_n (calcd)[e]	M_w/M_n
benzene-d_6	4.0	93	0.70 ± 0.03	0.993	3895	7050	2.08
chloroform-d_1	4.0	95	0.78 ± 0.06	0.984	4527	6978	1.92
THF-d_8	4.0	92	-	-	3409	6713	1.99

[a]Conditions: [*L*-LA]$_0$:[**Ca**]$_0$:[BnOH]$_0$ = 50:1:1, [*L*-LA]$_0$ = 0.5 M in 0.6 mL of stated solvent at 60 °C. [b]Average reported; measured by ^{1}H NMR spectroscopic analyses. [c]First order rate constant (k_{obs}) and R^2 were obtained from average plots of ln([*L*-LA]$_0$/[*L*-LA]$_t$) *vs.* time. [d]Determined by GPC in THF against PS standards using the appropriate Mark-Houwink corrections.[17] [e]Calculated M_n for PLA synthesised = (conv.(%) × [*L*-LA]$_0$/[**Ca**]$_0$) × 144.13 + (M_w of end groups).

5.4.3 Variable temperature studies

The temperature dependence on the rate of polymerisation using the **15** and BnOH system was investigated. Polymerisations were carried out between 45 and 60 °C, with one eq. of benzyl alcohol co-initiator, [*L*-LA]$_0$/[**Ca**]$_0$ = 50 and [*L*-LA]$_0$ = 0.5 M.

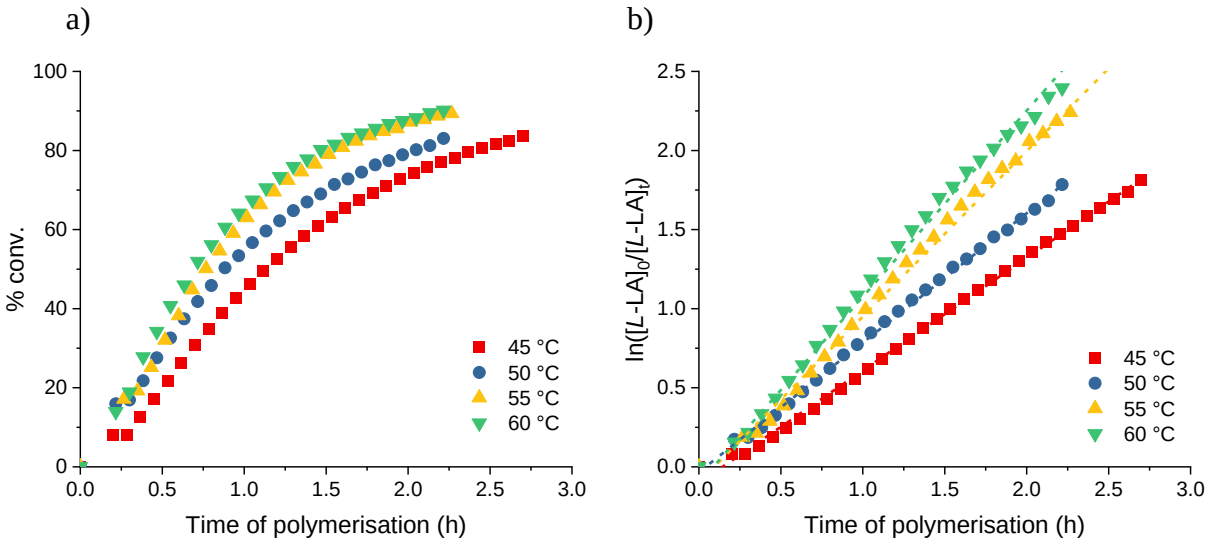

Figure 5.22 a) Plots of percentage conversion *vs.* time. b) Plots of ln([*L*-LA]$_0$/[*L*-LA]$_t$) *vs.* time for *L*-LA polymerisation with **15**/BnOH. Red squares: 45 °C (k_{obs} = 0.71 h^{-1}. R^2 = 0.998); blue circles: 50 °C (k_{obs} = 0.82 h^{-1}. R^2 = 0.997); yellow up triangles: 55 °C (k_{obs} = 1.05 h^{-1}. R^2 = 0.997); green down triangles: 60 °C (k_{obs} = 1.18 h^{-1}. R^2 = 0.997). Conditions: [*L*-LA]$_0$:[**Ca**]$_0$:[BnOH]$_0$ = 50:1:1, [*L*-LA]$_0$ = 0.5 M in 0.6 mL chloroform-d_1 at stated temperature.

As expected, an increase in polymerisation temperature, from 45 to 60 °C, resulted in an increase in the observed rate (**45 °C**: k_{obs} = 0.71 h^{-1} < **50 °C**: k_{obs} = 0.82 h^{-1} < **55 °C**: k_{obs} = 1.05 h^{-1} < **60 °C**: k_{obs} = 1.18 h^{-1}; **Figure 5.22** and **Table 5.9**). The experimental rate constants are comparable to those reported by Darensbourg *et al*. in their investigation of heteroleptic tridentate N,N,O phenoxy-imine calcium catalysts (k_{obs} = 0.0955 (**25 °C**), 0.4731 (**41 °C**) and 0.8083 h^{-1} (**51 °C**)).[9]

GPC analysis of the polymers produced, indicates that as the temperature increases, the polymerisation control decreases (i.e. the molecular weight distribution becomes broader: M_w/M_n = 1.26, 1.40, 1.79 and 2.33 for **45**, **50**, **55** and **60** °C respectively; **Figure 5.23a**). This correlates with the increase in observed polymerisation rate and thus the presumed increased rate of corresponding transesterification/chain termination reactions. The

presence of such side reactions was confirmed by the disparity between the observed and calculated molecular weights (Δ% *av*. = 20) and polymer end group analysis (**Section 5.4.7**).[18, 49]

Table 5.9 ROP of *L*-LA using **15**/BnOH with [*L*-LA]$_0$:[**Ca**]$_0$:[BnOH]$_0$ = 50:1:1 at stated temperature.[a]

Temp. (°C)	Time (h)	Conv. (%)[b]	k_{obs} (h^{-1})[c]	R^{2c}	M_n (GPC)[d]	M_n (calcd)[e]	M_w/M_n
45	2.7	84	0.71 ± 0.006	0.998	4053	5224	1.26
50	2.2	83	0.82 ± 0.009	0.997	5486	6267	1.40
55	2.3	89	1.05 ± 0.01	0.997	6700	4010	1.79
60	2.2	90	1.18 ± 0.01	0.997	5703	6206	2.33

[a]Conditions: [*L*-LA]$_0$:[**Ca**]$_0$:[BnOH]$_0$ = 50:1:1, [*L*-LA]$_0$ = 0.5 M in 0.6 mL chloroform-d_1 at stated temperature. [b]Average reported; measured by ^{1}H NMR spectroscopic analyses. [c]First order rate constant (k_{obs}) and R^2 were obtained from average plots of ln([*L*-LA]$_0$/[*L*-LA]$_t$) *vs.* time. [d]Determined by GPC in THF against PS standards using the appropriate Mark-Houwink corrections.[17] [e]Calculated M_n for PLA synthesised = (conv.(%) × [*L*-LA]$_0$/[**Ca**]$_0$) × 144.13 + (M_w of end groups).

The results of the variable temperature tests were then used to probe the thermodynamic parameters of the catalysis. The enthalpy ($\Delta H^{\ddagger}$) and entropy ($\Delta S^{\ddagger}$) of activation for the **15** and BnOH system were computed, *via* an Eyring plot (**Figure 5.23b**), to be 28 kJ mol^{-1} and –160 J K^{-1} mol^{-1} respectively. This leads to Gibbs free energy ($\Delta G^{\ddagger}$) values of 79-81 kJ mol^{-1} for the temperature range tested. The analogous results, and plots, for the **13**/**14** and BnOH systems are also presented in **Figure 5.23b**. The computed values for the enthalpy, entropy and Gibbs free energy were found to be 65 kJ mol^{-1}, –50 J K^{-1} mol^{-1} and 81-82 kJ mol^{-1} for **13** and 66 kJ mol^{-1}, –44 J K^{-1} mol^{-1} and 80-81 kJ mol^{-1} for **14**.

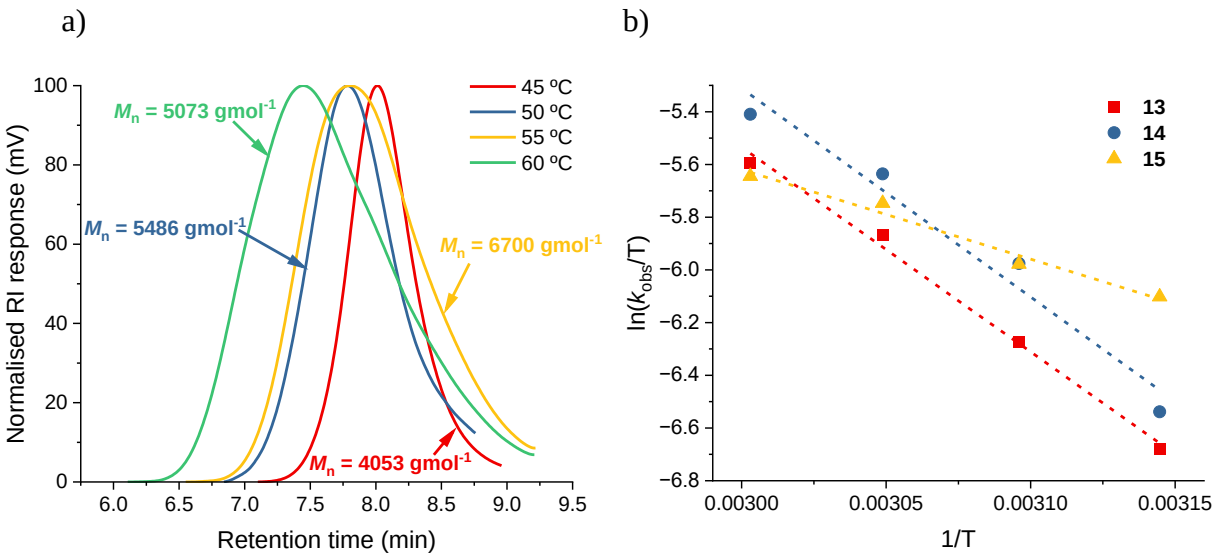

Figure 5.23 a) GPC traces of PLAs synthesised from the ROP of *L*-LA using **15**/BnOH. Red: 45 ºC, M_n = 4053 gmol^{-1}, M_w/M_n = 1.26; blue: 50 ºC, M_n = 5486 gmol^{-1}, M_w/M_n = 1.40; yellow: 55 ºC, M_n = 6700 gmol^{-1}, M_w/M_n = 1.79; green: 60 ºC, M_n = 5073 gmol^{-1}, M_w/M_n = 2.33. b) Eyring plots of ln(k_{obs}/T) *vs.* 1/T for catalysts **13**-**15**/BnOH. Red sqaures: cat = **13**, slope = −7664 ± 424, Intercept = 17.8 ± 1.3. R^2 = 0.994. $\Delta H^{\ddagger}$ = 65 ± 4 kJ mol^{-1}, $\Delta S^{\ddagger}$ = −50 ± 4 J K^{-1} mol^{-1}; blue circles: cat = **14**, slope = −7916 ± 1060, Intercept = 18.4 ± 3.3. R^2 = 0.965. $\Delta H^{\ddagger}$ = 66 ± 9 kJ mol^{-1}, $\Delta S^{\ddagger}$ = −44 ± 8 J K^{-1} mol^{-1}; yellow up triangles: cat = **15**, slope = −3995 ± 355, Intercept = 4.6 ± 1.1. R^2 = 0.979. $\Delta H^{\ddagger}$ = 28 ± 3 kJ mol^{-1}, $\Delta S^{\ddagger}$ = −160 ± 38 J K^{-1} mol^{-1}. Conditions: [LA]$_0$:[**Ca**]$_0$:[BnOH]$_0$ = 50:1:1, [LA]$_0$ = 0.5 M in 0.6 mL chloroform-d_1 at stated temperature.

In all cases, the negative value for entropy is indicative of a more ordered transition state upon monomer binding.[43] The nucleophilic attack that follows is the cause of the positive change in enthalpy.[42, 50, 51] The values determined for the Gibbs free energy of activation are comparable to that reported by Darensbourg and co-workers for lactide polymerisations catalysed by a similar yet tridentate heteroleptic calcium Schiff base complex ($\Delta G^{\ddagger}$ = 86.1 kJ mol^{-1} at 25 ºC).[9] It is also similar to the value determined for the industrial standard stannous(II) 2-ethylhexanoate ($SnOct_2$; $\Delta G^{\ddagger}$ = 70.9 ± 1.5 kJ mol^{-1}).[29] The modest enthalpy value for the *tert*-butyl substituted system (**15**) suggests that its

polymerisation activity is the most thermodynamically favoured at lower temperatures; this agrees with the experimental rate constants which show **15** to be the most active at 45 ºC: k_{obs} = 0.40, 0.46 and 0.71 h^{-1} for **13**, **14** and **15** respectively. This trend in polymerisation activity at lower temperatures (^{t}Bu > Me > H) reflects the electron donating capabilities of the *para*-substituents, and has been observed before.[52, 53] This implies that the electronics of the system (i.e. donation of electron density into the central benzene ring) is the dominating factor in determining the catalyst's activity at low temperatures. To further explore this hypothesis, more extreme variations in electron donating/withdrawing substituents should be incorporated into the ligand framework and tested; these may include *nitro* (–NO_2) and amine (–NH_2) groups.

The rate of polymerisation with **15** stagnates, and is overtaken by both **13** and **14**, at higher polymerisation temperatures (k_{obs} = 1.24, 1.49 and 1.18 h^{-1} for **13**, **14** and **15** at 60 ºC respectively). This may suggest that, although remote from the metal centre, the steric factor of the *para*-substituent also plays a role in determining the catalyst's performance (i.e. the larger the substituent, the greater hindrance towards incoming monomers). No direct comparable study of the influence of the steric encumbrance of the *para*-position have been demonstrated; attempts were made by Lin *et al*. in their investigation of tridentate N,N,O-Schiff base zinc complexes however, the rapid activity of all the initiators meant that the individual rates were indistinguishable.[54] Similar observations have been widely observed however, upon variation of the *ortho*-position steric bulk; this is most likely due to this position lying closer to the active metal centre.[52, 53, 55-57]

At 60 ºC, the methyl substituted catalyst is the most active; this may be due to this system having the best balance of electronic and steric factors.

5.4.4 Varying monomer stereochemistry

The effect of monomer stereochemistry was investigated by carrying out polymerisations using *rac*-, *L*, *D*, and *meso*-lactide at 60 °C with one eq. of benzyl alcohol co-initiator, $[LA]_0/[\mathbf{Ca}]_0 = 50$ and $[LA]_0 = 0.5$ M. The results, presented in **Figures 5.24-5.27** and **Table 5.10**, were found to follow the trend: *L*- ≈ *D*- < *rac*- < *meso*-.

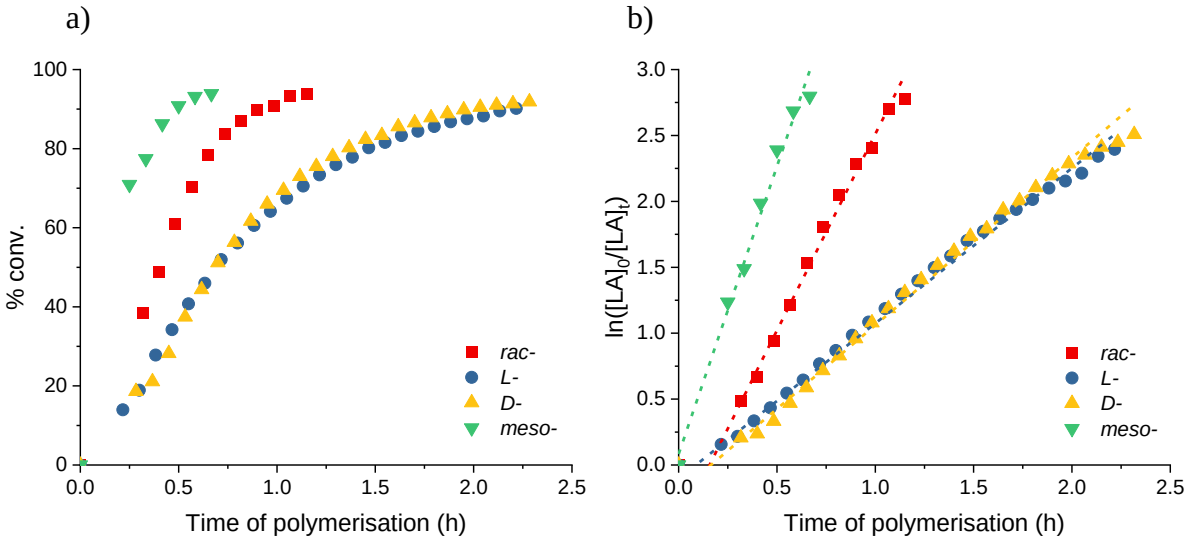

Figure 5.24 a) Plots of percentage conversion *vs.* time. b) Plots of $\ln([LA]_0/[LA]_t)$ *vs.* time for LA polymerisation with **15**/BnOH. Red squares: *rac*-LA (k_{obs} = 2.98 h^{-1}. R^2 = 0.997); blue circles: *L*-LA (k_{obs} = 1.18 h^{-1}. R^2 = 0.997); yellow up triangles: *D*-LA (k_{obs} = 1.27 h^{-1}. R^2 = 0.997); green down triangles: *meso*-LA (k_{obs} = 4.36 h^{-1}. R^2 = 0.987). Conditions: $[LA]_0$:$[\mathbf{Ca}]_0$:$[BnOH]_0$ = 50:1:1, $[LA]_0$ = 0.5 M in 0.6 mL chloroform-d_1 at 60 °C.

The polymerisation of *meso*-lactide was shown to be the fastest, achieving 94% conversion in 0.7 h (k_{obs} = 4.36 h^{-1}). This can be attributed to the higher energy ground state of this monomer acting as a driving force during the reaction.[31-33] The reactions involving the *L*- and *D*- monomers were seen to progress at very similar rates, suggesting that the $H^{tBu,Dipp}L$ ligand framework shows no preference for either enantiomer (k_L/k_D = 0.93 ≈ 1). Feijen and co-workers report contrasting results when employing an

aluminium-isopropoxide catalyst hosted in a comparable salen ligand; the authors found a k_L/k_D of ~14 implying a preference for the *L*-isomer (for $[LA]_0/[\mathbf{Al}]_0 = 62$, $k_{obs} = 0.038$ and 0.003 h^{-1} for *L*- and *D*-LA respectively).[58]

Table 5.10 ROP of LA using **15**/BnOH with $[LA]_0:[\mathbf{Ca}]_0:[BnOH]_0 = 50:1:1$ at 60 °C.[a]

LA	Time (h)	Conv. (%)[b]	k_{obs} (h^{-1})[c]	R^{2c}	M_n (GPC)[d]	M_n (calcd)[e]	M_w/M_n
rac-	1.2	94	2.98 ± 0.05	0.997	2129	6875	1.62
L-	2.2	90	1.18 ± 0.01	0.997	5703	6206	2.33
D-	2.3	92	1.27 ± 0.01	0.997	3885	6740	1.93
meso-	0.7	94	4.36 ± 0.2	0.987	2820	7045	1.74

[a]Conditions: $[LA]_0:[\mathbf{Ca}]_0:[BnOH]_0 = 50:1:1$, $[LA]_0 = 0.5$ M in 0.6 mL chloroform-d_1 at 60 °C. [b]Average reported; measured by ^{1}H NMR spectroscopic analyses. [c]First order rate constant (k_{obs}) and R^2 were obtained from average plots of $\ln([LA]_0/[LA]_t)$ *vs.* time. [d]Determined by GPC in THF against PS standards using the appropriate Mark-Houwink corrections.[17] [e]Calculated M_n for PLA synthesised = (conv.(%) × $[LA]_0/[\mathbf{Ca}]_0$) × 144.13 + (M_w of end groups).

The increased rate of reaction for *rac*-LA *vs*. *L*-/*D*-LA (2.98 *vs*. 1.18/1.27 h^{-1}) suggests that the formation of heterotactic (-*RS*- or -*SR*-) linkages is more favourable during the polymerisation; this was confirmed through microstructure analysis of the polymers produced (see **Section 5.4.4.1**). Due to the absence of chirality in the initiator, it is likely that this selectivity is imparted *via* a chain-end control mechanism. Similar observations have previously been made by Turner and co-workers in their report investigating the catalytic capability of bismuth pyridine dipyrrolide complexes pincer complexes.[13]

In all cases, the resultant polymers recorded intermediate molecular weight distributions (M_w/M_n = 1.62–2.33; **Figure 5.25**). The lower molecular weights observed for the *meso*- and *rac*-derived polymer products are consistent with an increased degree of side

reactions facilitated by the higher reaction rates. However, the polydispersity indices of the *L*- and *D*- based polymers are broader; this is most likely the result of the longer reaction times allowing for more opportunities for chain transfers to take place.

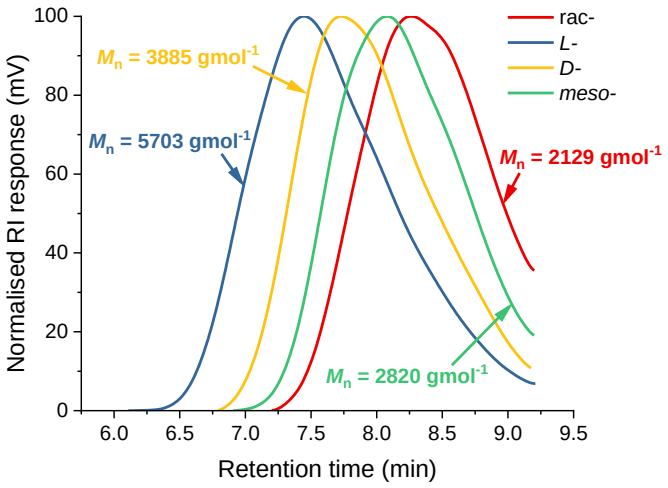

Figure 5.25 GPC traces of PLAs synthesised from the ROP of LA using **15**/BnOH. Red: *rac*-LA, M_n = 2129 gmol^{-1}, M_w/M_n = 1.62; blue: *L*-LA, M_n = 5703 gmol^{-1}, M_w/M_n = 2.33; yellow: *D*-LA, M_n = 3885 gmol^{-1}, M_w/M_n = 1.93; green: *meso*-LA, M_n = 2820 gmol^{-1}, M_w/M_n = 1.74. Conditions: $[LA]_0$:[**Ca**]$_0$:$[BnOH]_0$ = 50:1:1, $[LA]_0$ = 0.5 M in 0.6 mL chloroform-d_1 at 60 °C.

5.4.4.1 Polymer microstructure analysis

The tacticity of the PLA produced using catalysts **13**–**15**, was analysed by $^1H\{^1H\}$ NMR spectroscopy (**Figure 5.26**). In all cases, heterotactic-enriched PLA (P_r = 0.55–0.62) was formed from *rac*-lactide thus confirming the preference for racemic linkages within the polymer chain. Further evidence of this was the formation of syndiotactic-enriched polylactide (P_r = 0.51–0.67) when *meso*-LA was employed as the monomer. In both cases, the already identified transesterification reactions play a role in reducing the stereoregularity of the resulting polymers. The probabilities of forming heterotactic linkages may be improved by increasing the steric bulk in the metal's coordination sphere

or by introducing chirality into the initiator’s framework. In the case of *L*- and *D*-LA, isotactic polylactide was produced. This, and the lack of epimerisation, were confirmed by the presence of a single resonance in the *methine* region of the homonuclear decoupled NMR spectra.

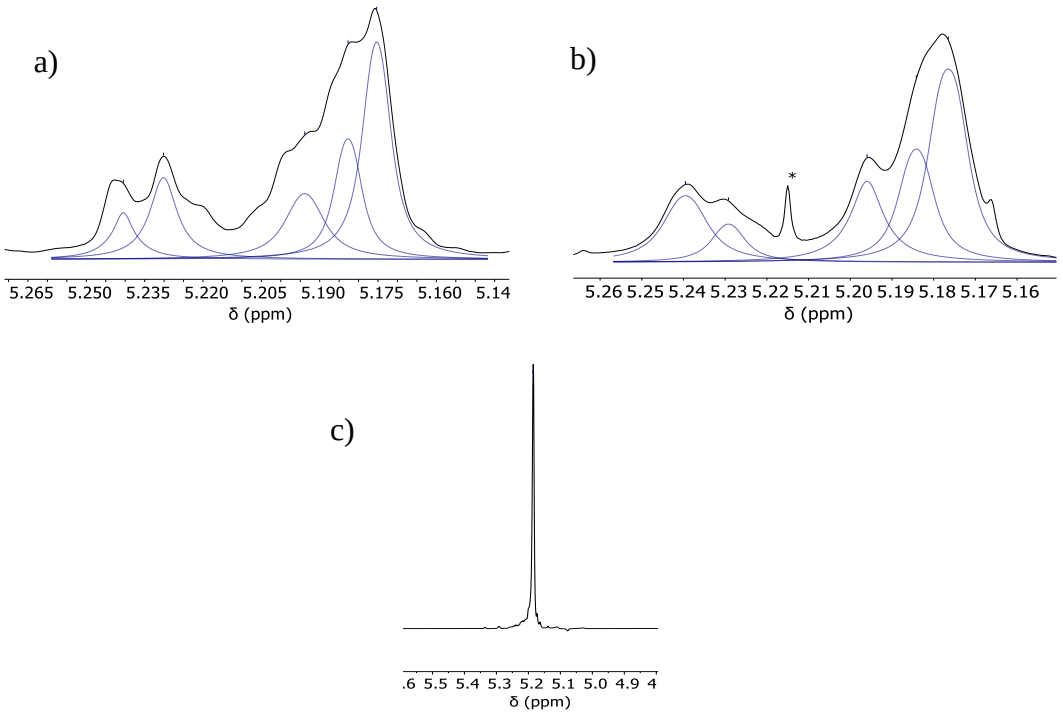

Figure 5.26 $^{1}H\{^{1}H\}$ NMR spectra (chloroform-d_1, 500 MHz, 298 K) of the *methine* protons in the PLA produced from the **15**/BnOH system and a) *rac*-lactide (P_m = 0.62), b) *meso*-lactide (P_r = 0.67) and c) *L*/*D*-lactide (P_m = 1.00). Conditions: $[LA]_0$:[**Ca**]$_0$:$[BnOH]_0$ = 50:1:1, $[LA]_0$ = 0.5 M in 0.6 mL chloroform-d_1 at 60 °C. * denotes an artefact from NMR “BASH” experiment set-up.

5.4.5 Initiator concentration dependency

In order to determine the kinetic order dependence on catalyst concentration, the polymerisation of *L*-LA with **15** and BnOH was carried out at 60 °C using various monomer to catalyst ratios. The concentration of *L*-LA was held constant at 0.5 M while that of the catalyst was varied to provide the ratio of [*L*-LA]$_0$:[**Ca**]$_0$ = 50, 100, 200, 500.

In all cases, a first-order dependence on monomer concentration was observed; this is evidenced by the linear plots of $\ln([L\text{-LA}]_0/[L\text{-LA}]_t)$ *vs.* time (**Figure 5.27**).

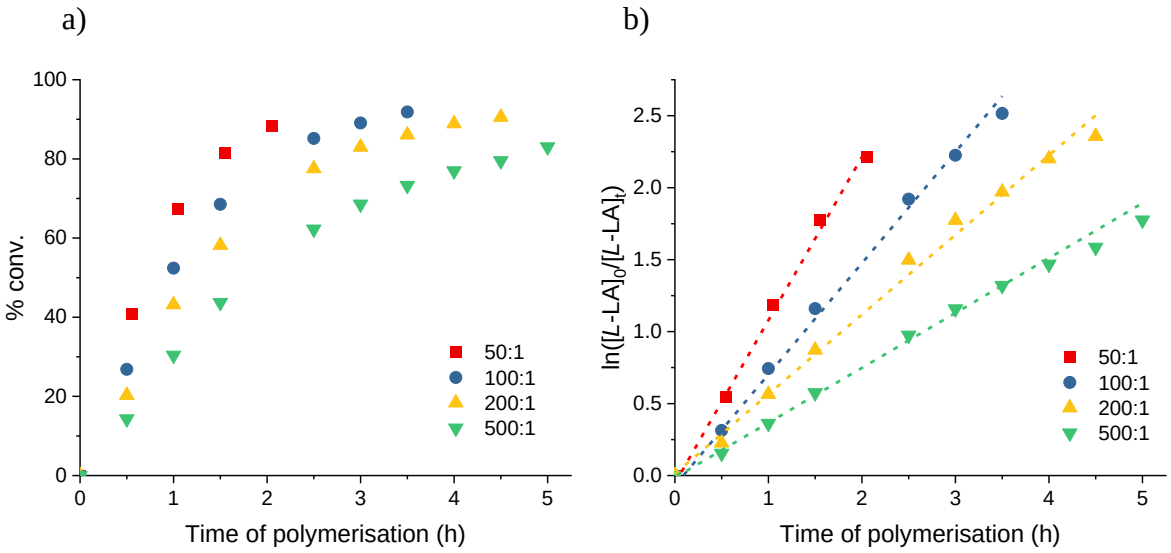

Figure 5.27 a) Plots of percentage conversion *vs.* time. b) Plots of $\ln([L\text{-LA}]_0/[L\text{-LA}]_t)$ *vs.* time for *L*-LA polymerisation with **15**/BnOH. Red squares: 50:1 (k_{obs} = 1.18 h^{-1}. R^2 = 0.997); blue circles: 100:1 (k_{obs} = 0.77 h^{-1}. R^2 = 0.996); yellow up triangles: 200:1 (k_{obs} = 0.55 h^{-1}. R^2 = 0.995); green down triangles: 500:1 (k_{obs} = 0.38 h^{-1}. R^2 = 0.999). Conditions: $[L\text{-LA}]_0$:$[\mathbf{Ca}]_0$ as stated, $[L\text{-LA}]_0$ = 0.5 M in 0.6 mL chloroform-d_1 at 60 °C.

As expected, the observed rate constants were found to decrease with increasing [*L*-LA]:[**Ca**] ratio (k_{obs} = **500:1**: 0.38 < **200:1**: 0.55 < **50:1**: 0.77 < **10:1**: 1.18 h^{-1}); this is due to the coinciding decrease in concentration of catalyst active sites. In contrast, the experimental molecular weights were found to increase in parallel with the [*L*-LA]:[**Ca**] ratio ($M_{n,(GPC)}$ = 5073, 11 612, 20 533 and 31 065 $gmol^{-1}$ for **50:1**, **100:1**, **200:1** and **500:1** ratios respectively). Similar observations have commonly been made for other M^{2+} phenoxy-imine based catalysts.[1, 3, 4, 9]

GPC analysis of the polymers produced depicts intermediate polydispersity indices (M_w/M_n = 1.57–2.33; **Figure A.55**). These molecular weight distributions become

narrower as the [*L*-LA]:[**Ca**] ratio increases due to the slower reaction rates affording better polymerisation control. In all cases however, the experimental molecular weights were found to be lower than the theoretical values; this indicates the occurrence of transesterifications (**Table 5.11**). The disparity between the values grows with increasing $[L\text{-LA}]_0/[\mathbf{Ca}]_0$ ratio as the longer reaction time provides more opportunities for the side reactions to take place.

Table 5.11 ROP of *L*-LA using **15**/BnOH with $[L\text{-LA}]_0:[\mathbf{Ca}]_0$ as stated at 60 °C.[a]

$[L\text{-LA}]_0$: $[\mathbf{Ca}]_0$	Time (h)	Conv. (%)[b]	k_{obs} (h^{-1})[c]	R^{2c}	M_n (GPC)[d]	M_n (calcd)[e]	M_w/M_n
50:1	2.2	90	1.18 ± 0.01	0.997	5703	6206	2.33
100:1	3.5	92	0.77 ± 0.02	0.996	11 612	13 495	1.73
200:1	4.5	91	0.55 ± 0.02	0.995	20 533	26 259	1.59
500:1	5.0	83	0.38 ± 0.005	0.999	31 065	59 519	1.57

[a]Conditions: $[L\text{-LA}]_0:[\mathbf{Ca}]_0$: as stated, $[L\text{-LA}]_0$ = 0.5 M in 0.6 mL chloroform-d_1 at 60 °C. [b]Average reported; measured by ^{1}H NMR spectroscopic analyses. [c]First order rate constant (k_{obs}) and R^2 were obtained from average plots of $\ln([L\text{-LA}]_0/[L\text{-LA}]_t)$ *vs.* time. [d]Determined by GPC in THF against PS standards using the appropriate Mark-Houwink corrections.[17] [e]Calculated M_n for PLA synthesised = (conv.(%) × $[L\text{-LA}]_0/[\mathbf{Ca}]_0$) × 144.13 + ($M_w$ of end groups).

Plots of $-\ln(k_{obs})$ *vs.* $-\ln[\mathbf{Ca}]_0$ were generated to determine the order with respect to catalyst for complexes **13**–**15** (**Figure 5.28**). In all cases, linear relationships were observed; this, and the gradient values of 0.49–0.84 are an indication of a first-order dependence on initiator concentration. Non-integer values have previously been reported for comparable N,N,O-ketiminate magnesium complexes (1.75)[37] as well as a dimeric $[\{BDI\}ZnO^iPr]_2$ system (1.56), and were proposed to result from catalyst aggregation in solution.[36] Similar non-integer values have also been reported by Turner and co-workers

in their investigation of group 4 permethylpentalene aryl/alkoxide LA ROP initiators (0.58–0.62).[41]

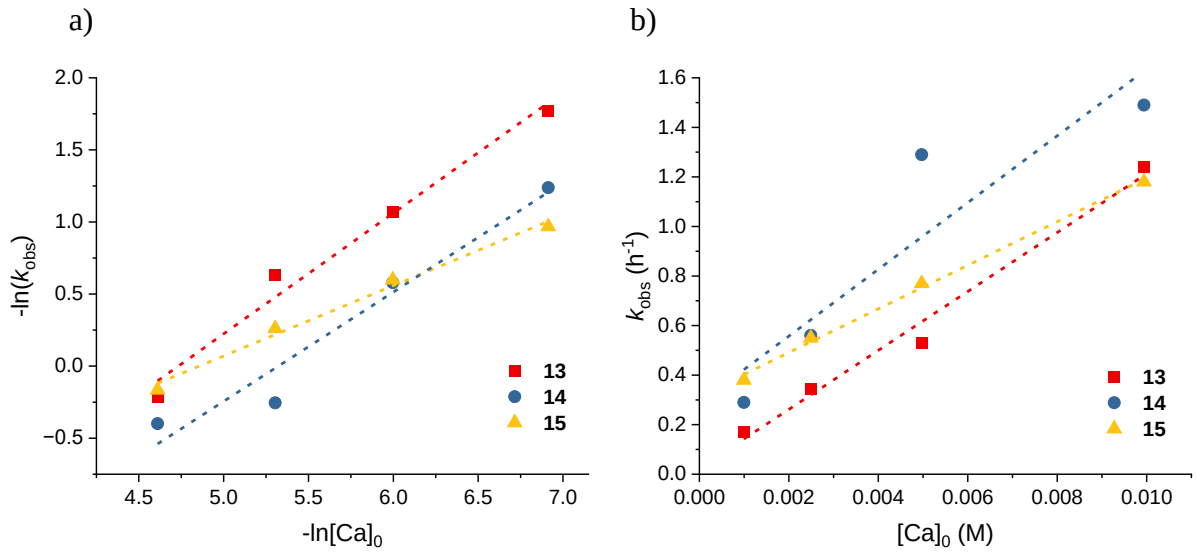

Figure 5.28 a) Plots of $-\ln(k_{obs})$ *vs.* $-\ln[\mathbf{Ca}]_0$ for ROP of *L*-LA using catalysts **13-15**/BnOH. Red squares: cat = **13**, shows that the order of reaction with respect to $[\mathbf{Ca}]_0$ is equal to 0.84 ± 0.08; R^2 = 0.961; blue circles: cat = **14**, shows that the order of reaction with respect to $[\mathbf{Ca}]_0$ is equal to 0.76 ± 0.12; R^2 = 0.952; yellow up triangles: cat = **15**, shows that the order of reaction with respect to $[\mathbf{Ca}]_0$ is equal to 0.49 ± 0.04; R^2 = 0.990. b) Plots of k_{obs} *vs.* $[\mathbf{Ca}]_0$ for ROP of *L*-LA using catalysts **13-15**/BnOH. Red squares: cat = **13**, shows k_p = 119 ± 10 M^{-1} h^{-1}; R^2 = 0.986; blue circles: cat = **14**, shows k_p = 135 ± 40 M^{-1} h^{-1}; R^2 = 0.847; yellow up triangles: cat = **15**, shows k_p = 88 ± 4 M^{-1} h^{-1}; R^2 = 0.997.

Assuming constant initiator concentration throughout the reaction, the following rate law can be derived for the ROP of LA catalysed by **13-15** and BnOH:

$$-\frac{d[\mathrm{LA}]}{dt} = k_p[\mathrm{LA}][\mathbf{Ca}] \qquad \text{where} \qquad k_{obs} = k_p[\mathbf{Ca}] \qquad \textbf{Equation 5.2}$$

Comparable heteroleptic phenoxy-imine calcium systems have been reported to follow the same rate equation.[9] The propagation rate constant (k_p), present in this rate law, was calculated via plots of k_{obs} *vs.* $[\mathbf{Ca}]_0$, to be 119 ± 10 M^{-1} h^{-1}, 135 ± 40 M^{-1} h^{-1} and 88 ±

4 M^{-1} h^{-1} for **13**, **14** and **15** respectively. This range of propagation rate constants is much higher than the reported k_p value (19.9 M^{-1} h^{-1}) for the comparable heteroleptic (tridentate) calcium Schiff base catalysts published by Darensbourg and co-workers.[9]

5.4.6 Co-initiator concentration dependency and mechanistic discussion

Throughout this study it has been assumed that the LA polymerisations, conducted by **15** and BnOH, followed the common coordination-insertion mechanism.[59, 60] For this pathway to occur, the co-initiator would need to react with the catalyst in order to form the active alkoxide species (Ca-OBn) *in situ*. ^{1}H NMR spectroscopic studies suggest however, that this does not happen when benzyl alcohol is added to a solution of **15**; the analysis instead shows that the two reagents remain unreacted after several days, both at room and elevated temperatures such as 333 K (i.e. the highest temperature that polymerisations were conducted at; **Figure 5.29a-d**). Addition of 1 eq. of *L*-LA to the **15**/BnOH mixture triggers the simultaneous consumption of the co-initiator's acidic proton (‡) alongside the formation of a new phenolic resonance around δ 13.48 ppm (+; **Figure 5.29d**). This O***H*** signal does not grow over time, even when further eq. of monomer are added, thus suggesting that it does not represent complex degradation into pro-ligand. This was confirmed via a shift in the observed resonances from those of free pro-ligand, and coincides with the differentiated polymerisation rates for the complexes of varying electronics/steric bulk. Instead, these observations imply that the active catalytic species contains a protonated phenoxide species (**Scheme 5.1**); similar results were described in 2015 by Kozak *et. al.* as part of their proposed "ligand assisted, activated monomer" mechanism.[61] In this mechanism, the exogenous nucleophile (BnOH) is activated via hydrogen bonding interactions with a ligand-phenolate oxygen.

This results in protonation of the ligand framework and facilitates the subsequent activation of the lactide monomer.[61, 62]

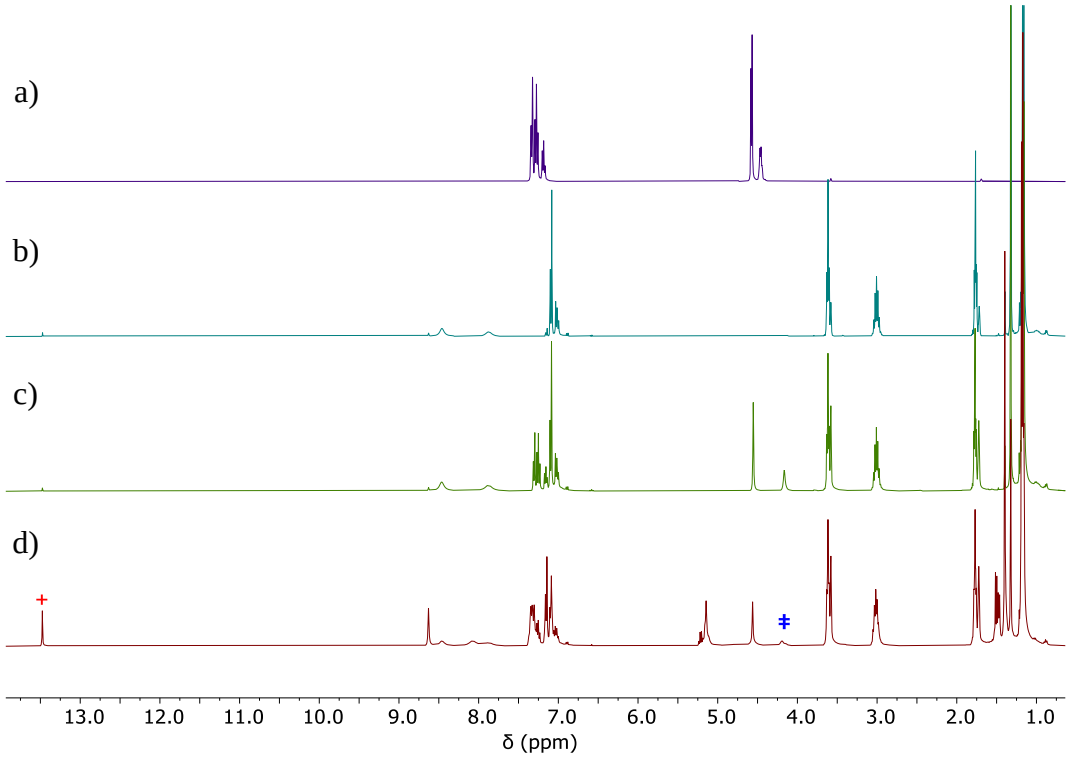

Figure 5.29 ^{1}H NMR spectra (*THF-d_8, 500 MHz, 298 K) of a) BnOH, b) complex **15**, c) mixture of **15** and BnOH and d) the **15** and BnOH mixture after addition of 1 eq. of *L*-LA.

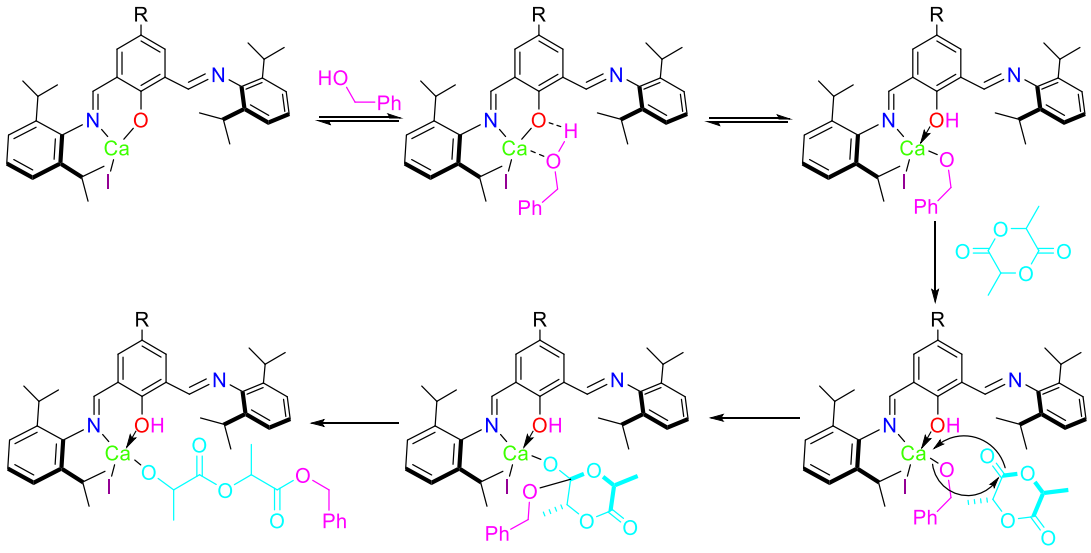

Scheme 5.1 The proposed "ligand assisted, activated-monomer" mechanism for the polymerisation of lactide using the **13–15** and benzyl-alcohol system.[61]

The possibility of the **15**/BnOH-catalysed LA polymerisations proceeding via this mechanism was investigated by studying the dependence on $[BnOH]_0$. In order to do this, polymerisations of *L*-LA with **15** were carried out at 60 °C in chloroform-d_1 using various $[\mathbf{Ca}]_0$:$[BnOH]_0$ ratios. It is proposed that the inclusion of the co-initiator in the overall rate law would imply a classical activated monomer pathway (i.e. BnOH is involved in the rate-determining step) whereas in the proposed mechanism, the rate-determining step would be insertion of the monomer into the preformed Ca-OBn bond (in a manner similar to that of a coordination-insertion pathway) thus rendering only catalyst and monomer present in the rate law.

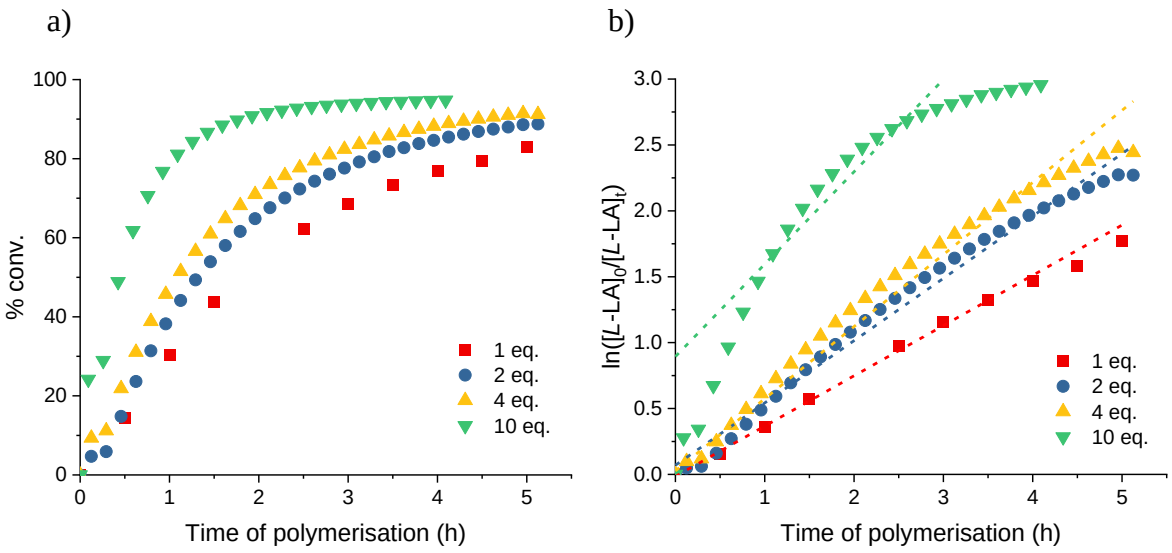

Figure 5.30 a) Plots of percentage conversion *vs.* time. b) Plots of $\ln([L\text{-LA}]_0/[L\text{-LA}]_t)$ *vs.* time for *L*-LA polymerisation with **15**/BnOH. Red squares: 1 eq. BnOH (k_{obs} = 0.38 h^{-1}. R^2 = 0.999); blue circles: 2 eq. BnOH (k_{obs} = 0.47 h^{-1}. R^2 = 0.992); yellow up triangles: 4 eq. BnOH (k_{obs} = 0.55 h^{-1}. R^2 = 0.984); green down triangles: 10 eq. BnOH (k_{obs} = 0.70 h^{-1}. R^2 = 0.794). Conditions: $[\mathbf{Ca}]_0$:$[BnOH]_0$ as stated, $[L\text{-LA}]_0$ = 0.5 M in 0.6 mL chloroform-d_1 at 60 °C.

The results of the co-initiator dependency tests showed that, in most cases, a first-order dependence on monomer concentration was observed, as evidenced by the linear plots of

ln([*L*-LA]$_0$/[*L*-LA]$_t$) *vs*. time; **Figure 5.30**. However, when 10 eq. of BnOH were employed, a deviation from this regime was detected. This, alongside the non-linear increase in the observed rate with increasing [BnOH]$_0$ (**Table 5.12**), implies that there is only a fractional dependence on co-initiator concentration. This was confirmed *via* a plot of −ln(k_{obs}) *vs.* −ln[BnOH]$_0$ which depicted that the order with respect to BnOH is 0.26 ± 0.01 (**Figure 5.31a**). From these results, it can be inferred that an excess of benzyl alcohol does not have a significant impact on the rate of polymerisation and therefore BnOH is not included in the overall polymerisation rate law (i.e. **Equation 5.2** is correct). It is therefore likely that the polymerisations catalysed by the **13-15**/BnOH binary systems proceed via the "ligand assisted, activated-monomer" mechanism.

Table 5.12 ROP of *L*-LA using **15** and various eq. of BnOH in chloroform-d_1 at 60 °C.[a]

[**Ca**]$_0$: [BnOH]$_0$	Time (h)	Conv. (%)[b]	k_{obs} (h^{-1})[c]	R^{2c}	M_n (GPC)[d]	M_n (calcd)[e]	M_w/M_n
1:1	5.0	83	0.38 ± 0.005	0.999	31 065	59 519 (29 760)	1.57
2:1	5.1	89	0.47 ± 0.01	0.992	15 236	60 895 (20 298)	1.64
4:1	5.1	91	0.55 ± 0.01	0.984	11 686	64 873 (12 975)	1.52
10:1	4.1	95	0.70 ± 0.05	0.794	4762	68 635 (6240)	1.73

[a]Conditions: [**Ca**]$_0$:[BnOH]$_0$ as stated, [*L*-LA]$_0$ = 0.5 M in 0.6 mL chloroform-d_1 at 60 °C. [b]Average reported; measured by ^{1}H NMR spectroscopic analyses. [c]First order rate constant (k_{obs}) and R^2 were obtained from average plots of ln([*L*-LA]$_0$/[*L*-LA]$_t$) *vs.* time. [d]Determined by GPC in THF against PS standards using the appropriate Mark-Houwink corrections.[17] [e]Calculated M_n for PLA synthesised = (conv.(%) × [*L*-LA]$_0$/[**Ca**]$_0$) × 144.13 + (M_w of end groups); value in brackets is the calculated M_n if all BnOH acts as a chain transfer agent.

GPC analysis of the PLLA produced revealed unimodal molecular weight distributions in all cases (**Figure 5.31b**). The observed reduction in experimental molecular weights is consistent with the number of polymer chains being equal to the sum of the catalyst and co-initiator eq. (values in brackets in **Table 5.12**); this is a typical characteristic of immortal polymerisation behaviour which has been widely reported before.[2, 11, 12, 40] Under such conditions, polymers of comparable molecular weights are produced when the rate of transfer vastly exceeds that of propagation (k_{tr} >> k_p).[15, 16] This doesn't seem to be the case with the **13**–**15**/BnOH systems, as the recorded polydispersity values are intermediate in nature (M_w/M_n = 1.52–1.73).

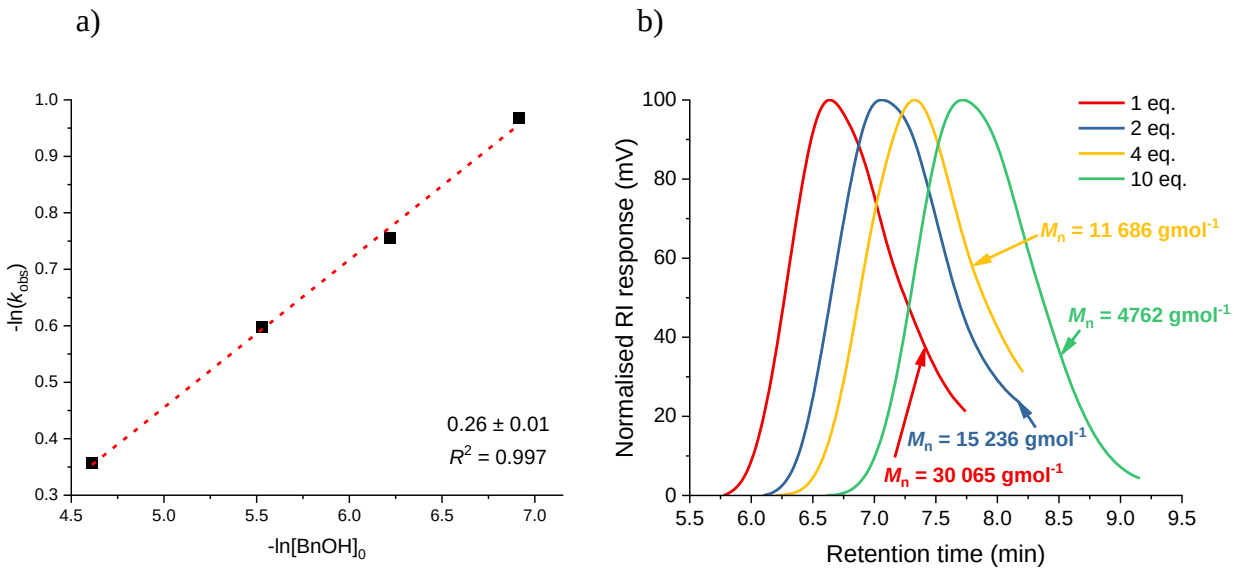

Figure 5.31 a) Plot of $-\ln(k_{obs})$ *vs.* $-\ln[BnOH]_0$ for ROP of *L*-LA using **15**/BnOH shows that the order of reaction with respect to $[BnOH]_0$ is equal to 0.26 ± 0.01; R^2 = 0.997. Conditions: $[\mathbf{Ca}]_0$:$[BnOH]_0$ as stated, $[L\text{-LA}]_0$ = 0.5 M in 0.6 mL chloroform-d_1 at 60 °C. b) GPC traces of PLAs synthesised from the ROP of *L*-LA using **15**/BnOH. Red: 1 eq. BnOH, M_n = 31 065 gmol^{-1}, M_w/M_n = 1.57; blue: 2 eq. BnOH, M_n = 15 236 gmol^{-1}, M_w/M_n = 1.64; yellow: 4 eq. BnOH, M_n = 11 686 gmol^{-1}, M_w/M_n = 1.52; green: 10 eq. BnOH, M_n = 4762 gmol^{-1}, M_w/M_n = 1.73.

5.4.7 Polymer end group analysis

Matrix-assisted laser desorption/ionisation time of flight (MALDI-TOF) mass spectrometry was used to determine the end groups of the polymers produced using the **15**/BnOH catalytic system; a representative example is shown in **Figure 5.32**.

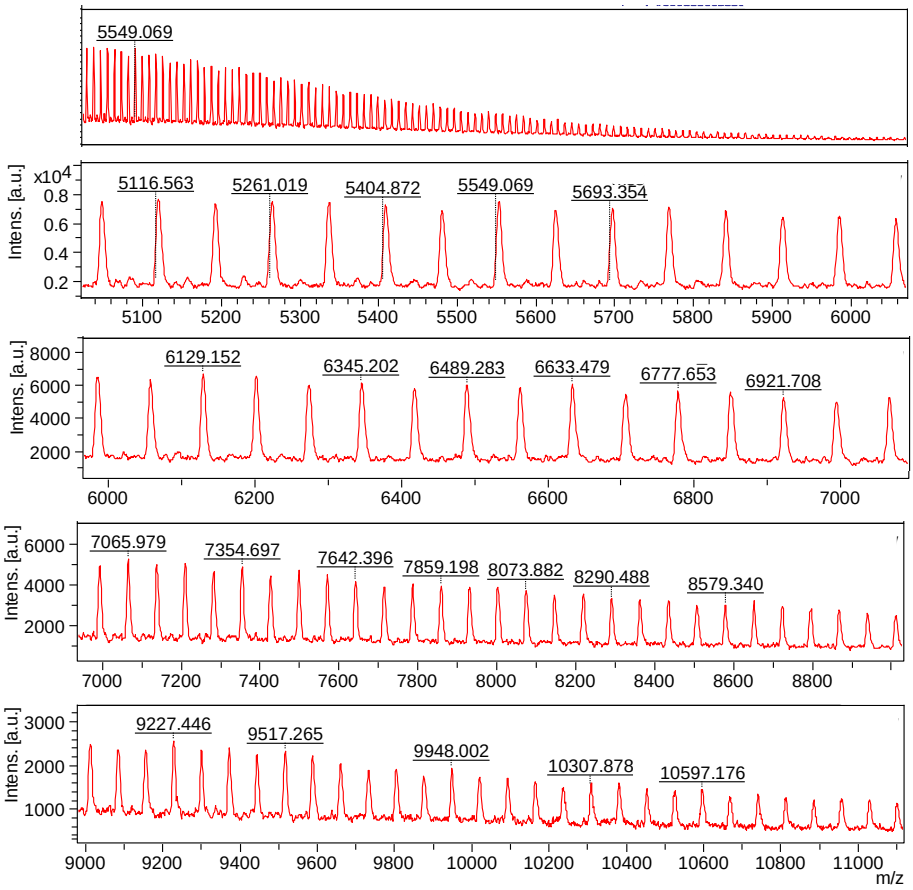

Figure 5.32 MALDI-TOF mass (*m/z*) spectrum of PLA produced using **15**/BnOH. Polymerisation conditions: [*L*-LA]$_0$:[**Ca**]$_0$:[BnOH] = 50:1:1, [*L*-LA]$_0$ = 0.5 M, 0.6 mL chloroform-d_1, 60 °C. M_w/M_n = 2.33.

The mass spectrum is consistent with PLA containing the expected –OCH_2Ph and –OH end groups. For example, the peak centred at 6777.7 gmol^{-1} is attributed to –OCH_2Ph/–OH terminated PLA, comprising of 46 units of LA with K^+ [144.13(46) + 108.14 + 39.1].

The 72 *m*/*z* split between the peaks indicates the occurrence of transesterification reactions.[18, 30, 41-43]

The benzyl alcohol end group was also detected in the ^{1}H and ^{13}C{^{1}H} NMR spectra (examples shown in **Figure 5.33** and **Figure A.56**); a quartet ($^{3}J_{HH}$ = 6.9 Hz) at δ 4.36 ppm corresponds to the –C***H***(CH$_3$)OH proton and the aromatic signals of the –OCH$_2$***Ph*** group appear at δ 7.28–7.40 ppm. Similar observations were made for the polymers produced using the **13**/**14** and BnOH catalytic systems; the representative characterising spectra can be found in the **Chapter 5** section of the **Appendix**.

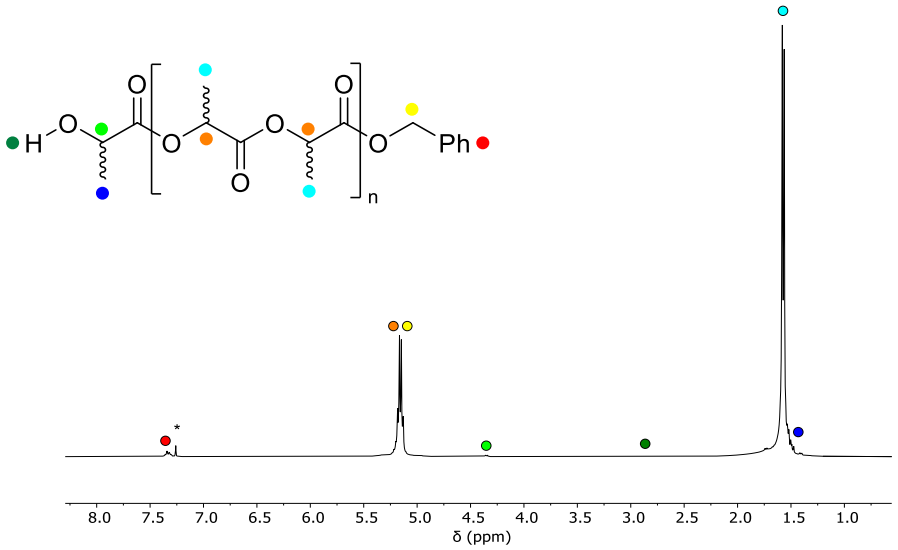

Figure 5.33 ^{1}H NMR spectrum (*chloroform-d_1, 400 MHz, 298 K) of PLA produced using the **15**/BnOH system. Polymerisation conditions: [*L*-LA]$_0$:[**Ca**]$_0$:[BnOH]$_0$ = 50:1:1, [*L*-LA]$_0$ = 0.5 M, 0.6 mL chloroform-d_1, 60 °C. M_w/M_n = 2.33.

5.5 Conclusions

All of the isolated monometallic “NON” complexes (**10**-**15**) were found to be active for polymerisation, with complexes **11** and **12** being the first recorded examples of phenoxy-imine strontium/barium LA ROP initiators.

In the absence of a co-initiator, an initiation period of 3.5 h was observed for the homoleptic magnesium catalyst (**10**). Complex **10** and its barium analogue **12**, both displayed a second-order dependence on monomer concentration (k_{obs} = 9.57 and 19.53 M^{-1} h^{-1} for **10** and **12** respectively), whereas the strontium species **11** recorded a typical first-order dependency (k_{obs} = 0.84 h^{-1}). Addition of BnOH resulted in the decomposition of the heavier alkaline-earth systems.

All polymerisations catalysed by **10**/BnOH displayed linear plots of ln($[LA]_0/[LA]_t$), thus implying a first-order dependency on $[LA]_0$. An increase in polymerisation rate, with higher monomer loadings, was observed compared to other Schiff base magnesium catalysts in the literature (k_{obs} = 0.096–9.08 h^{-1} for 25–200:1 ratios).[1, 7] The trend in the rates of the different isomers (*rac*- < *L*- ≈ *D*- < *meso*-) highlighted a preference for the formation of polymeric *meso*-linkages, however, **10** was unable to impart much of this desired stereoregularity into the polymeric chains as atactic PLA was produced in the case of both *rac*- (P_r = 0.48) and *meso*-LA (P_r = 0.54).

(Co)-initiator concentration studies revealed a first and second-order dependency on **10** and BnOH concentrations respectively. The overall rate law for the ROPs of LA catalysed by **10**/BnOH is therefore be described by **Equation 5.1** in which the propagation rate constant was computed to be 966 ± 26 M^{-1} h^{-1}. This, along with the modest enthalpy (19 kJ mol^{-1}) and negative entropy (–179 J K^{-1} mol^{-1}) of activation, is consistent with an activated monomer polymerisation mechanism for this catalytic system.

$$\frac{d[\mathrm{LA}]}{dt} = k_p[\mathrm{LA}][\mathbf{Mg}][\mathrm{BnOH}]^2 \qquad \textbf{Equation 5.1}$$

All polymerisations with **10** and benzyl alcohol proceeded with good control, as indicated by the recorded narrow-intermediate molecular weight distributions (1.11<

M_n/M_w <1.75). The experimental molecular weights, however, were always found to be lower than the calculated values; this may result from excess/unreacted co-initiator acting as a chain transfer agent throughout the polymerisation or from multiple propagating polymer chains growing per metal centre.

All three heteroleptic calcium initiators (**13**–**15**) also proved active towards the ROP of LA. In the presence of BnOH, the observed rate was seen to dramatically increase, e.g. ~12 fold difference for **15** (0.70 *vs*. 0.06 h^{-1}). The experimental rate constants are comparable to those reported by Darensbourg *et al*. in their investigation of heteroleptic tridentate N,N,O phenoxy-imine calcium catalysts (k_{obs} = 0.0955–0.8083 h^{-1}).[9]

Variation of the *para*-substituent proved to have little effect on the microstructure of the resultant PLA as heterotactic- and syndiotactically-enriched polymers were formed in all cases from *rac*- (P_r = 0.55–0.62) and *meso*-LA respectively (P_r = 0.51–0.67).

The results of variable temperature studies showed that the thermodynamic parameters of the heteroleptic-catalysed polymerisations lay in the ranges: 28 < $\Delta H^{\ddagger}$ < 66 kJ mol^{-1}, –44 < $\Delta S^{\ddagger}$ < –160 J K^{-1} mol^{-1} and 79 < $\Delta G^{\ddagger}$ < 82 kJ mol^{-1}. Catalyst **15** was found to be fastest of the three complexes at low temperature, but the slowest at higher temperatures; this implies that a delicate balance of sterics and electronics is needed to achieve optimal activity.

For all heteroleptic initiators, the polymerisations displayed a first-order dependency on $[LA]_0$, as evidenced by linear plots of $\ln([LA]_0/[LA]_t)$. Initiator concentration studies also revealed a first order dependency and thus the overall rate law for the ROPs of LA catalysed by **13**–**15**/BnOH is therefore be described by **Equation 5.2**. The propagation rate constant was found to lie within the range 88–135 M^{-1} h^{-1}.

$$\frac{d[\mathrm{LA}]}{dt} = k_p[\mathrm{LA}][\mathbf{Ca}] \qquad \textbf{Equation 5.2}$$

Variation of co-initiator concentration revealed only a fractional dependence on BnOH; this agrees with the other experimental observations, which suggest the heteroleptic catalysts work via an unusual "ligand-assisted, activated monomer" mechanism.

5.6 References

1. S. Ghosh, D. Chakraborty and V. Ramkumar, *J. Polym. Sci., Part A: Polym. Chem.*, 2015, **53**, 1474-1491.
2. T. Pongpanit, T. Saeteaw, P. Chumsaeng, P. Chasing and K. Phomphrai, *Inorg. Chem.*, 2021, **60**, 17114-17122.
3. M.-W. Hsiao, G.-S. Wu, B.-H. Huang and C.-C. Lin, *Inorg. Chem. Commun.*, 2013, **36**, 90-95.
4. H.-Y. Chen, H.-Y. Tang and C.-C. Lin, *Polymer*, 2007, **48**, 2257-2262.
5. M. G. Davidson, C. T. O'Hara, M. D. Jones, C. G. Keir, M. F. Mahon and G. Kociok-Köhn, *Inorg. Chem.*, 2007, **46**, 7686-7688.
6. J. Hu, C. Kan, H. Wang and H. Ma, *Macromolecules*, 2018, **51**, 5304-5312.
7. W. Yi and H. Ma, *Inorg. Chem.*, 2013, **52**, 11821-11835.
8. D. J. Darensbourg, W. Choi and C. P. Richers, *Macromolecules*, 2007, **40**, 3521-3523.
9. D. J. Darensbourg, W. Choi, O. Karroonnirun and N. Bhuvanesh, *Macromolecules*, 2008, **41**, 3493-3502.
10. J. B. L. Gallaway, J. R. K. McRae, A. Decken and M. P. Shaver, *Can. J. Chem.*, 2012, **90**, 419-426.
11. V. Poirier, T. Roisnel, J.-F. Carpentier and Y. Sarazin, *Dalton Trans.*, 2009, 9820-9827.
12. Y. Sarazin, D. Roşca, V. Poirier, T. Roisnel, A. Silvestru, L. Maron and J.-F. Carpentier, *Organometallics*, 2010, **29**, 6569-6577.
13. Z. R. Turner, J. T. Wilmore, N. H. Rees and J.-C. Buffet, *Dalton Trans.*, 2022, **51**, 3060-3074.
14. H.-C. Tseng, M. Y. Chiang, W.-Y. Lu, Y.-J. Chen, C.-J. Lian, Y.-H. Chen, H.-Y. Tsai, Y.-C. Lai and H.-Y. Chen, *Dalton Trans*, 2015, **44**, 11763-11773.
15. N. Ajellal, J.-F. Carpentier, C. Guillaume, S. M. Guillaume, M. Helou, V. Poirier, Y. Sarazin and A. Trifonov, *Dalton Trans.*, 2010, **39**, 8363-8376.
16. J.-F. Carpentier and Y. Sarazin, in *Alkaline-Earth Metal Compounds: Oddities and Applications*, ed. S. Harder, Springer Berlin Heidelberg, Berlin, Heidelberg, 2013, pp. 141-189.
17. J. R. Dorgan, J. Janzen, D. M. Knauss, S. B. Hait, B. R. Limoges and M. H. Hutchinson, *J. Polym. Sci., Part B: Polym. Phys.*, 2005, **43**, 3100-3111.

18. J. V. Lamb, J.-C. Buffet, J. E. Matley, C. M. R. Wright, Z. R. Turner and D. O'Hare, *Dalton Trans.*, 2019, **48**, 2510-2520.

19. J.-C. Wu, B.-H. Huang, M.-L. Hsueh, S.-L. Lai and C.-C. Lin, *Polymer*, 2005, **46**, 9784-9792.

20. L. Clark, G. B. Deacon, C. M. Forsyth, P. C. Junk, P. Mountford, J. P. Townley and J. Wang, *Dalton Trans.*, 2013, **42**, 9294-9312.

21. P. I. Binda and E. E. Delbridge, *Dalton Trans.*, 2007, 4685-4692.

22. M. P. Blake, A. D. Schwarz and P. Mountford, *Organometallics*, 2011, **30**, 1202-1214.

23. T.-P.-A. Cao, A. Buchard, X. F. Le Goff, A. Auffrant and C. K. Williams, *Inorg. Chem.*, 2012, **51**, 2157-2169.

24. L. Clark, M. G. Cushion, H. E. Dyer, A. D. Schwarz, R. Duchateau and P. Mountford, *Chem. Commun.*, 2010, **46**, 273-275.

25. H.-Y. Chen, B.-H. Huang and C.-C. Lin, *Macromolecules*, 2005, **38**, 5400-5405.

26. M. Ystenes, *J. Catal.*, 1991, **129**, 383-401.

27. J. Bhattacharjee, A. Harinath, H. P. Nayek, A. Sarkar and T. K. Panda, *Chem. Eur. J.*, 2017, **23**, 9319-9331.

28. A. Thevenon, C. Romain, M. S. Bennington, A. J. P. White, H. J. Davidson, S. Brooker and C. K. Williams, *Angew. Chem. Int. Ed.*, 2016, **55**, 8680-8685.

29. D. R. Witzke, R. Narayan and J. J. Kolstad, *Macromolecules*, 1997, **30**, 7075-7085.

30. N. Diteepeng, I. A. P. Wilson, J.-C. Buffet, Z. R. Turner and D. O'Hare, *Polym. Chem.*, 2020, **11**, 6308-6318.

31. J.-C. Buffet and J. Okuda, *Polym. Chem.*, 2011, **2**, 2758-2763.

32. M. H. Chisholm, N. W. Eilerts, J. C. Huffman, S. S. Iyer, M. Pacold and K. Phomphrai, *J. Am. Chem. Soc.*, 2000, **122**, 11845-11854.

33. I. A. Shuklov, H. Jiao, J. Schulze, W. Tietz, K. Kühlein and A. Börner, *Tetrahedron Lett.*, 2011, **52**, 1027-1030.

34. D. J. Darensbourg and O. Karroonnirun, *Inorg. Chem.*, 2010, **49**, 2360-2371.

35. A. Pilone, M. Lamberti, M. Mazzeo, S. Milione and C. Pellecchia, *Dalton Trans.*, 2013, **42**, 13036-13047.

36. B. M. Chamberlain, M. Cheng, D. R. Moore, T. M. Ovitt, E. B. Lobkovsky and G. W. Coates, *J. Am. Chem. Soc.*, 2001, **123**, 3229-3238.

37. H.-J. Chuang, H.-L. Chen, J.-L. Ye, Z.-Y. Chen, P.-L. Huang, T.-T. Liao, T.-E. Tsai and C.-C. Lin, *J. Polym. Sci., Part A: Polym. Chem.*, 2013, **51**, 696-707.

38. Y. Cui, W. Gu, Y. Wang, B. Zhao, Y. Yao and Q. Shen, *Catal. Sci. Technol.*, 2015, **5**, 3302-3312.

39. M.-W. Hsiao and C.-C. Lin, *Dalton Trans.*, 2013, **42**, 2041-2051.

40. N. Liu, J. Zhang, J. Wen, X. You and D. Fang, *Polym. Chem.*, 2022, **13**, 1978-1985.

41. Z. R. Turner, J. V. Lamb, T. P. Robinson, D. Mandal, J.-C. Buffet and D. O'Hare, *Dalton Trans.*, 2021, **50**, 4805-4818.

42. N. Diteepeng, J.-C. Buffet, Z. R. Turner and D. O'Hare, *Dalton Trans.*, 2019, **48**, 16099-16107.

43. P. Dubois, O. Coulembier and J. M. Raquez, *Handbook of Ring-Opening Polymerization*, Wiley, 1st edn., 2009.

44. F. Bonnet, F. Stoffelbach, G. Fontaine and S. Bourbigot, *RSC Adv.*, 2015, **5**, 31303-31310.

45. G. Montaudo, M. S. Montaudo, C. Puglisi, F. Samperi, N. Spassky, A. LeBorgne and M. Wisniewski, *Macromolecules*, 1996, **29**, 6461-6465.

46. C. Goonesinghe, H.-J. Jung, H. Roshandel, C. Diaz, H. A. Baalbaki, K. Nyamayaro, M. Ezhova, K. Hosseini and P. Mehrkhodavandi, *ACS Catal.*, 2022, **12**, 7677-7686.

47. M. Hu, X. Song, F. Wang, W. Zhang, W. Ma and F. Han, *New J. Chem.*, 2022, **46**, 1175-1181.

48. X. Tang, M. Hong, L. Falivene, L. Caporaso, L. Cavallo and E. Y. X. Chen, *J. Am. Chem. Soc.*, 2016, **138**, 14326-14337.

49. M. Save, M. Schappacher and A. Soum, *Macromol. Chem. Phys.*, 2002, **203**, 889-899.

50. M. H. Chisholm and E. E. Delbridge, *New J. Chem.*, 2003, **27**, 1167-1176.

51. A. F. Douglas, B. O. Patrick and P. Mehrkhodavandi, *Angew. Chem. Int. Ed.*, 2008, **47**, 2290-2293.

52. C. C. Roberts, B. R. Barnett, D. B. Green and J. M. Fritsch, *Organometallics*, 2012, **31**, 4133-4141.

53. N. M. Rezayee, K. A. Gerling, A. L. Rheingold and J. M. Fritsch, *Dalton Trans.*, 2013, **42**, 5573-5586.

54. W.-C. Hung, Y. Huang and C.-C. Lin, *J. Polym. Sci., Part A: Polym. Chem.*, 2008, **46**, 6466-6476.

55. H.-Y. Chen, H.-Y. Tang and C.-C. Lin, *Macromolecules*, 2006, **39**, 3745-3752.

56. X.-F. Yu, C. Zhang and Z.-X. Wang, *Organometallics*, 2013, **32**, 3262-3268.

57. S. Tabthong, T. Nanok, P. Kongsaeree, S. Prabpai and P. Hormnirun, *Dalton Trans.*, 2014, **43**, 1348-1359.

58. Z. Zhong, P. J. Dijkstra and J. Feijen, *J. Am. Chem. Soc.*, 2003, **125**, 11291-11298.

59. W. Rao, C. Cai, J. Tang, Y. Wei, C. Gao, L. Yu and J. Ding, *Chin. J. Chem.*, 2021, **39**, 1965-1974.

60. S. Penczek, M. Cypryk, A. Duda, P. Kubisa and S. Słomkowski, *Prog. Polym. Sci.*, 2007, **32**, 247-282.

61. K. Devaine-Pressing, J. H. Lehr, M. E. Pratt, L. N. Dawe, A. A. Sarjeant and C. M. Kozak, *Dalton Trans.*, 2015, **44**, 12365-12375.

62. S.-C. Roşca, D.-A. Roşca, V. Dorcet, C. M. Kozak, F. M. Kerton, J.-F. Carpentier and Y. Sarazin, *Dalton Trans.*, 2013, **42**, 9361-9375.

Chapter 6

Exploration of the "NON" scaffold for the synthesis of cationic, bimetallic complexes

6.1 Introduction

6.1.1 Overview

This chapter discusses the attempts to synthesise cationic, bimetallic, alkaline-earth "NON" initiators for the ROP of LA. It is proposed that these multimetallic systems may enhance polymerisation selectivity and activity by providing multiple, cooperative catalytic sites for monomer activation/subsequent nucleophilic attack.

The area of cationic, bimetallic group 2 "NON" research is particularly understudied. Most previous reports of bimetallic *bis*(phenoxy-imine) systems involve transition metals (**Section 6.1.2.1**) and no reports of cationic alkaline-earth ROP initiators incorporate the use of the "NON" ligand framework (**Section 6.1.2.2**).

Several synthetic routes to the targeted cationic "NON" bimetallic complexes were tested. These involved treatment of the already isolated heteroleptic calcium iodide complex (**15**) with neutral and cationic alkaline-earth reagents, as well as generating additionally protonated pro-ligands to use for the insertion of multiple metals by protonolysis.

6.1.2 Previous relevant literature reports

6.1.2.1 Bimetallic complexes featuring the *bis*(phenoxy-imine) "NON" framework

The first example of a dinucleating bimetallic aluminium "NON" system was published by Redshaw *et al*. in 2004 (**Figure 6.1a**).[1] The authors report that the formation of the *bis*(aluminium) species, via treatment of the pro-ligand with 2 eq. of $AlMe_3$, was facilitated by an intramolecular methyl transfer and thus subsequent reduction of one of the ligand imine groups.[1]

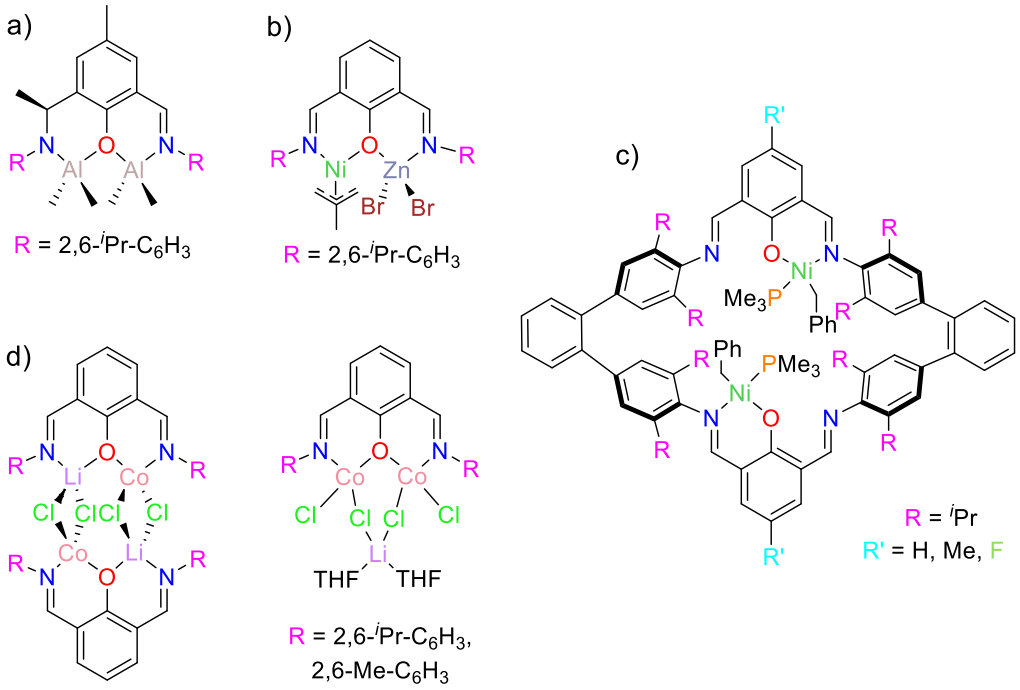

Figure 6.1 Previous reports of bimetallic systems incorporating the *bis*(phenoxy-imine) "NON" framework.[1-4]

A similar ligand system was used by Tonks and co-workers in their isolation of a dinucleating heterobimetallic (Ni/Zn) "NON" ethylene polymerisation catalyst (**Figure 6.1b**).[2] This datively-bound active species results in the formation of lower molecular weight polyethylene than monometallic counterparts. DFT calculations suggested that

this was due to β-H elimination reactions being more facile in the bridging bimetallic conformation.[2]

Other examples of nickel-containing bimetallic "NON" systems came from Lee and co-workers in 2006 (**Figure 6.1c**).[3] The study involved the use of a macrocyclic tetraiminodiphenol pro-ligand to form tethered *bis*(nickel) olefin polymerisation initiators. These species were only moderately active (360–620 kg_{PE} mol_{Ni}^{-1} h^{-1}) for ethylene polymerisation however, due to poor thermal stability and solubility in hydrocarbon media.[3]

Examples of dimeric, bimetallic (Co/Li) "NON" systems have been reported by Gao and co-workers (**Figure 6.1d**).[4] The heterobimetallic compounds were synthesised via lithiation of ^{Ar}[NCN]Br followed by subsequent exposure to dioxygen and 1 eq. of $CoCl_2$. Variation of reaction stoichiometry (i.e. use of 2 eq. of $CoCl_2$) also enabled the isolation of analogous dinucleating *bis*(cobalt)-lithiate complexes.[4] All of these dicobalt systems showed only moderate activity for isoprene polymerisation (~97% conversion in 2 h at room temperature), yet good *cis*-1,4 regioselectivity (~77%). In all cases, the dinuclear complexes outperformed the monometallic variants; the authors propose that this is due to synergistic effects of the two cobalt metal centres.[4]

6.1.2.2 Cationic initiators for the ring-opening polymerisation of lactide

Over the past 15 years, Hayes *et al*. have been investigating the use of *mono*- and *bis*(phosphinimine) pincer ligands for the generation of cationic M^{2+} ROP initiators (**Figure 6.2a**).[5-11] The *mono*-$ZnEt^{+}$ species proved active converting 90% of 100 eq. of *L*-LA after 6 h at 100 ºC.[5, 6] Poor polymerisation control however, was identified via bimodal molecular weight distributions.[6] Substitution of the ethyl initiating group for

lactate improved the reaction control (M_w/M_n = 1.81–1.98) and allowed for the formation of higher molecular weight polymers (M_n = 17 000–36 000 gmol^{-1}).[7]

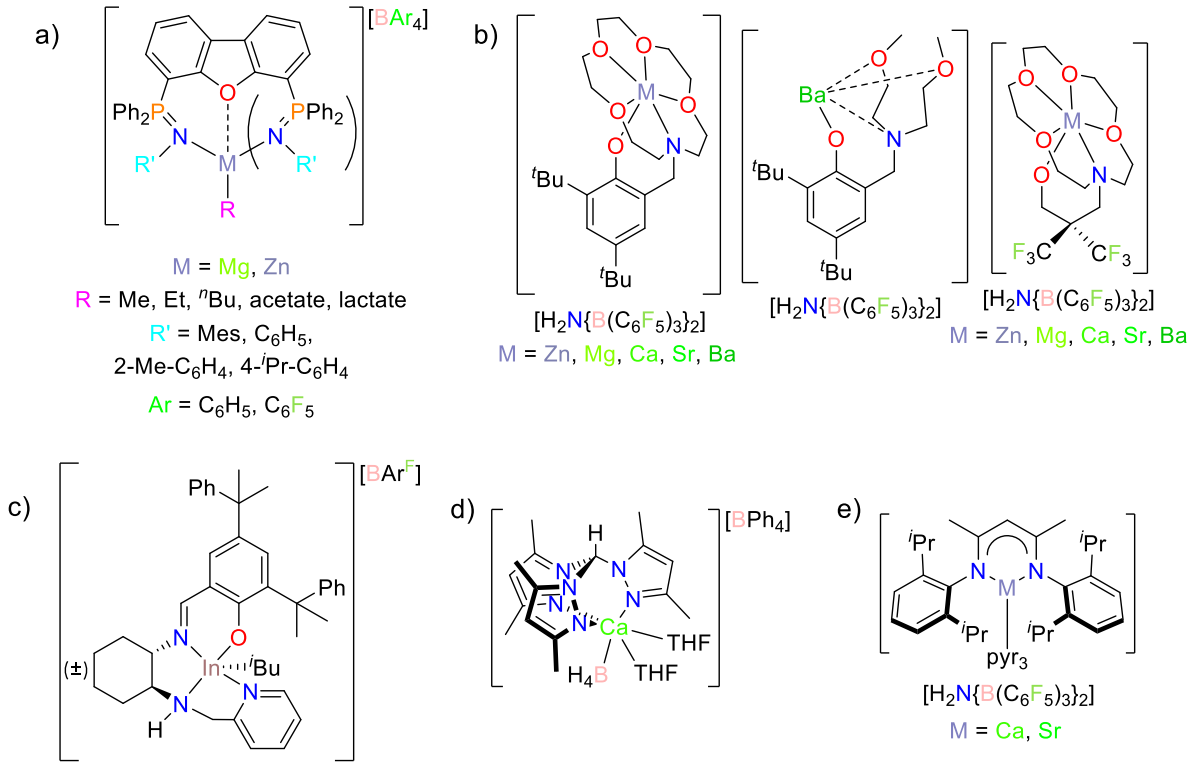

Figure 6.2 Previous reports of cationic initiators for the ring-opening polymerisation of lactide.[5-19]

The *bis*-Mg^{n}Bu$^+$, *bis*-ZnMe$^+$ and *bis*-Zn(acetate)$^+$ systems all proved to be inactive towards the ROP of LA (**Figure 6.2a**).[5, 8-10] A reduction in steric bulk of the *ortho*-N-*aryl* position, coupled with the introduction of lactate as the initiating group, resulted in subsequent activation of the catalysts.[8] The rates of polymerisation with the active Zn initiators were reported to be: 1.31 h^{-1} (R' = 2-Me-C$_6$H$_4$), 3.11 h^{-1} (R' = 4-^{i}Pr-C$_6$H$_4$) and 1.84 h^{-1} (R' = C$_6$H$_5$); the reduction in activity between the *para*-isopropyl and unsubstituted analogues was attributed to the decreased electron donating capabilities of the ligand.[5, 8]

Carpentier *et al*. have completed an analogous study on cationic, solvent-free M^{2+} (M = Zn, Mg, Ca, Sr and Ba) phenolate-based systems (**Figure 6.2b *left***).[12-15] The first series of initiators, incorporating a pendant crown ether functionality to stabilise the metal centres, were found to follow the immortal *L*-LA polymerisation activity trend: Zn < Mg < Ca < Sr < Ba.[12] The calcium system however, displayed the best control resulting in narrow polydispersity indices (M_w/M_n = 1.05–1.08) and good agreements between experimental and theoretical molecular weights (13 000 *vs*. 12 900 $gmol^{-1}$).[12] Variation of the pendant stabilisation moiety to a *bis*(2-methoxyethyl)amino group enabled only the isolation of the solvent-free barium analogue (**Figure 6.2b *centre***).[13] This catalyst, in the presence of an alcohol co-initiator, was able to achieve quantitative conversion of 1000 eq. of *L*-LA within 15 minutes at 30 ºC. This high rate of polymerisation however (TOF > 3800 $mol_{L\text{-}LA}\ mol_{Ba}^{-1}\ h^{-1}$), resulted in poor control (M_w/M_n = 1.85) which could only be marginally improved by modification of experimental variables.[13] Substitution of the phenolate moiety for an alkoxide functionality, containing electron-withdrawing CF_3 groups, was then tested (**Figure 6.2b *right***). These systems were less catalytically active as a result of secondary metal-fluorine interactions making monomer coordination less kinetically favourable.[14, 15]

A cationic indium catalyst has also been reported, by Mehrkhodavandi and co-workers, for the ROP of LA (**Figure 6.2c**).[16] This air-stable catalyst is capable of selectively producing cyclic-PLA with molecular weights up to 416 000 $gmol^{-1}$ (M_w/M_n ~ 1.3).[16] The cyclic nature of the polymer produced was confirmed by MALDI-TOF mass spectrometry, NMR spectroscopy and intrinsic viscosity measurements ($[\eta]_{cyclic}/[\eta]_{linear}$ = 0.70 due to the smaller hydrodynamic radius of the non-linear polymers).[16]

Mountford *et al*. have reported the use of a cationic calcium borohydride complex for the ROP of *rac*-LA (**Figure 6.2d**).[17] This system is capable of converting up to 250 eq. within

2 h at ambient temperatures.[17] The resultant polymers were atactic, with relatively good agreements between experimental and theoretic molecular weights (43 200 *vs.* 32 800 $gmol^{-1}$) and narrow polydispersity values (M_w/M_n = 1.2–1.4).[17]

Similar, cationic, alkaline-earth β-diketiminate (BDI) systems have since been reported by Sarazin and co-workers (**Figure 6.2e**).[18] In the presence of 10 eq. of BnOH co-initiator, the calcium system was able to convert 66% of 1000 eq. *L*-LA in 3 h.[18] The analogous strontium system however, achieved quantitative conversion in just 90 minutes; the higher activity of this system was attributed to its increased electrophilicity and greater accessibility of the metal centre.[18] The TOF of the strontium system (4920 $mol_{L\text{-}LA}\ mol_{Sr}^{-1}\ h^{-1}$) also outclasses the related cationic catalysts previously discussed in this section.[18]

In most of these reported cases, the cationic ROP of LA suffers from low activities and poor reaction control (likely caused by the activated chain ends present in the mechanism). As a result, there is still a need to develop highly efficient, well-defined, positively charged ROP initiators. If the mechanism by which they work can be controlled, cationic species offer advantages over their neutral counterparts. By analogy with group 4 and rare earth olefin polymerisation catalysts,[14] the enhanced Lewis acidity of positively charged initiators should improve monomer binding. In addition, they should also show improved capabilities in immortal ROP conditions as the greater electrophilicity will increase the rate of initiation with exogenous chain transfer agents.

6.2 Initial attempts to form cationic, bimetallic "NON" systems

Initial attempts focused on utilising the previously isolated heteroleptic calcium iodide complex (**15**) as an intermediate in the formation of the desired "NON" bimetallics (**Scheme 6.1**).

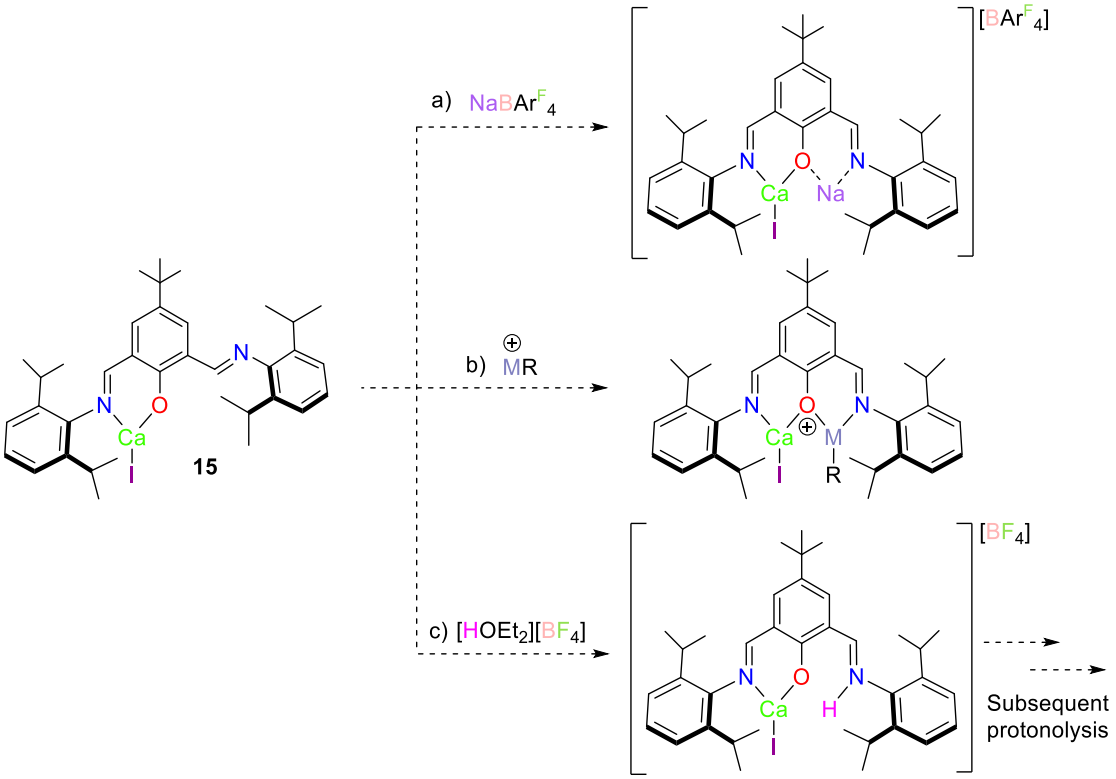

Scheme 6.1 The proposed routes to cationic, bimetallic "NON" systems derived from complex **15** (the bound-thf molecules of **15** have been removed for clarity).

6.2.1 Treatment of $^{t\text{Bu,Dipp}}$LCaI(thf)$_3$ (15) with NaBAr$^F_4$

The first proposed synthetic pathway to a "NON" bimetallic involved treatment of complex **15** with Na[BAr$^F_4$] (Ar^F = 3,5-{CF$_3$}$_2$C$_6$H$_3$) (**Scheme 6.1a**). This group one reagent was specifically chosen as the stability of the weakly coordinating anion towards strong electrophiles makes it an ideal candidate to enable the isolation of low-coordinate cationic species.[20, 21]

Unfortunately, ^{1}H NMR analysis indicated that no reactivity occurred, even after several days at 298 K (**Figure 6.3**). In addition, no change to the reaction mixture was detected after an increase in reaction temperature to 333 K. Hence, this reaction pathway to "NON" bimetallics was deemed unsuitable and alternatives were sought.

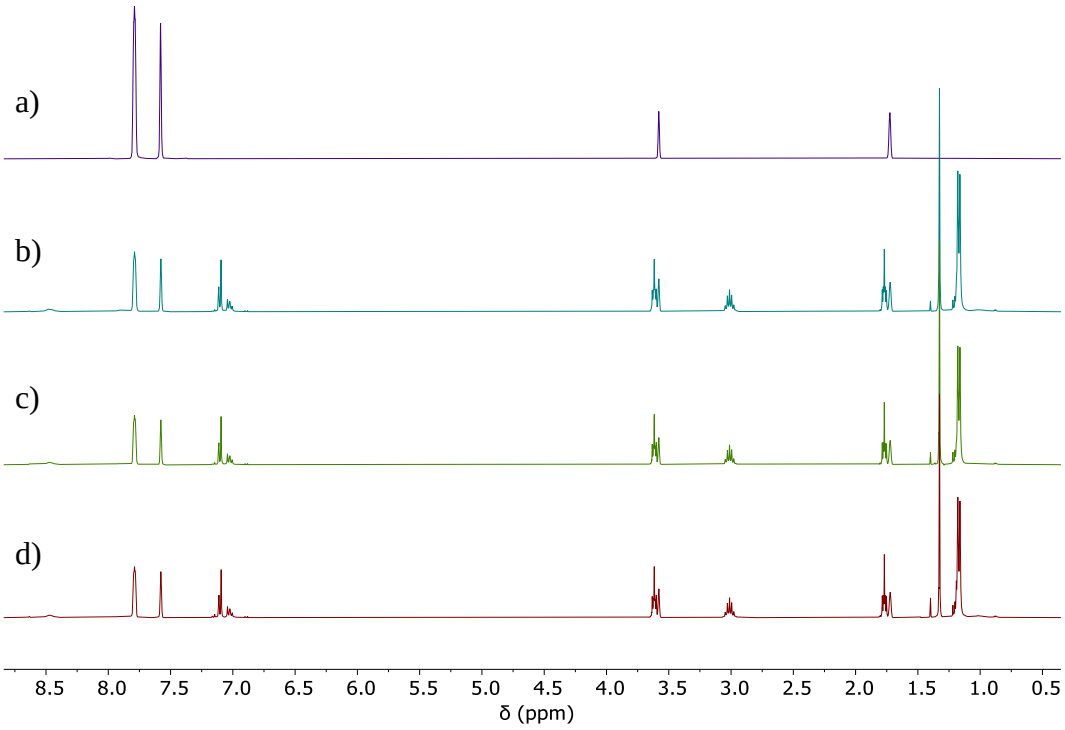

Figure 6.3 ^{1}H NMR spectra (*THF-d_8, 500 MHz, 298 K) of a) $NaBAr^{F}_{4}$, b) the initial mixture of $NaBAr^{F}_{4}$ and **15**, c) the mixture of $NaBAr^{F}_{4}$ and **15** after 72 h at 298 K and d) the mixture of $NaBAr^{F}_{4}$ and **15** after 24 h at 333 K.

6.2.2 Treatment of ^{tBu,Dipp}LCaI(thf)$_3$ (15) with cationic alkaline-earth reagents

Treatment of compound **15** with cationic alkaline-earth species was proposed as an alternative route to "NON" bimetallics (**Scheme 6.1b**). Such positively charged M^{2+} reagents were previously isolated by Bochmann and co-workers in 2004.[19]

Addition of 1 eq. of acid ($[H(OEt_2)_2][H_2N\{B(C_6F_5)_3\}_2]$) to THF-$d_8$ solutions of group two (M = Mg, Ca) dialkyl, diamide or diaryloxide reagents led to the clean, quantitative (confirmed by ^{1}H NMR spectroscopy), *in situ* formation of the corresponding alkaline-earth cations ($[MR][H_2N\{B(C_6F_5)_3\}_2]$; **Scheme 6.2**). Addition of complex **15** to these solutions however, resulted in mixtures of inseparable species.

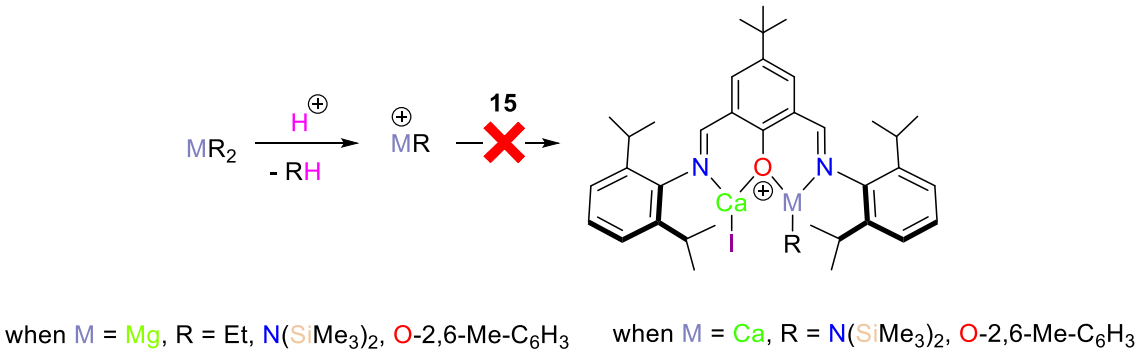

Scheme 6.2 The proposed synthesis of "NON" bimetallics via treatment of **15** with cationic alkaline-earth reagents (the bound-thf molecules in **15** have been removed for clarity).

^{1}H NMR analysis suggested that the addition of **15** to the *in situ* formed calcium-based cations resulted in an intractable mixture of products. Small amounts of pro-ligand could however be identified, thus suggesting that undesirable partial hydrolysis had occurred. In all reactions involving the magnesium cations, the homoleptic *bis*(ligand) system (**10**) was found to be the major product (*av*. 78%). Due to previous unsuccessful efforts in removing this species from a mixture, this synthetic pathway was no longer pursued.

6.2.3 Treatment of $^{t\text{Bu,Dipp}}$LCaI(thf)$_3$ (15) with [HOEt$_2$][BF$_4$]

A third method for the synthesis of "NON" bimetallics from **15** involved protonation of the second [=N,O^{-}] binding pocket and subsequent protonolysis reaction (**Scheme 6.1c**). Precedent for the plausibility of this pathway came from work published by Mecking *et al*. in 2021.[22] In their investigation of Schiff base nickel polymerisation catalysts (incorporating a cyclophane moiety), the authors were able to protonate the secondary binding pocket using an ethereal solution of HBF$_4$.

To this end, initial NMR scale protonation reactions were conducted using ethereal HBF$_4$ in THF-d_8. The ^{1}H NMR spectrum of the crude mixture exhibited a shift in the signals from those associated with the starting complex (**Figure 6.4**). In addition, the presence of a broad singlet close to δ 15 ppm highlighted the presence of a O***H***/N***H*** proton

(indicated by "+" in **Figure 6.4**). Dissolution and subsequent crystallisation of a sample in benzene, however, revealed the identity of the product to be [H_2^{tBu,Dipp}L][I] (**Figure 6.5**). This charge separated ion pair contains a cationic, doubly protonated, pro-ligand and iodide anion; it is likely formed, alongside $Ca(BF_4)_2$, via anion exchange (**Scheme 6.3**). The rational synthesis and complete characterisation of analogous diacids is discussed in **Section 6.3**.

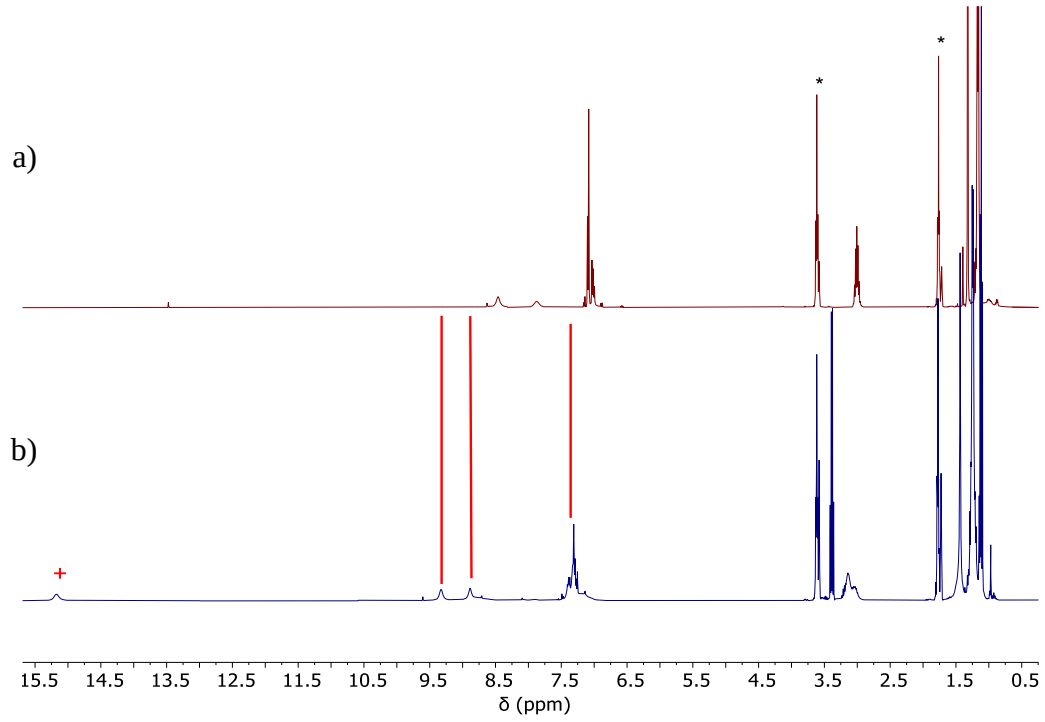

Figure 6.4 ^{1}H NMR spectra (*THF-d_8, 500 MHz, 298 K) of a) ^{tBu,Dipp}LCaI(thf)$_3$ (**15**) and b) **15** after treatment with [$HOEt_2$][BF_4]. + represents the acidic proton present in the reaction mixture.

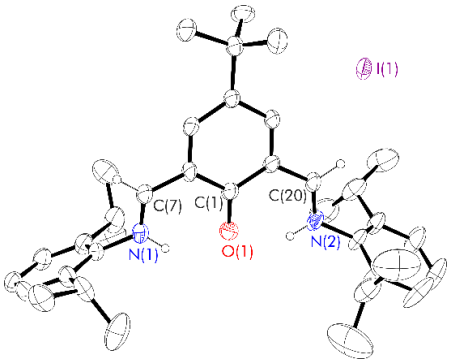

Figure 6.5 Thermal displacement ellipsoid drawing (30% probability) of [H_2^{tBu,Dipp}L][I]. All hydrogen atoms apart from those on N1, N2, C7 and C20 have been omitted for clarity.

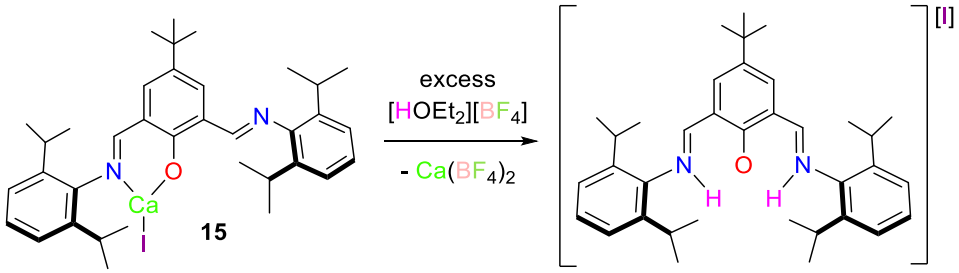

Scheme 6.3 The formation of $[H_2{}^{tBu,Dipp}L][I]$ via the protonation of **15** with ethereal HBF_4.

6.3 Synthesis and reactivity of protonated pro-ligands: $[H_2{}^{tBu,Dipp}L][X]$

6.3.1 Protonation of $H{}^{tBu,Dipp}L$ with $[HOEt_2][BF_4]$

The possibility of pro-ligand protonation (**Section 6.2.3**) opened up a new potential synthetic pathway to bimetallic "NON" species. This involved treatment of the intermediate organocation with 2 eq. of alkaline-earth reagent (**Scheme 6.4**).

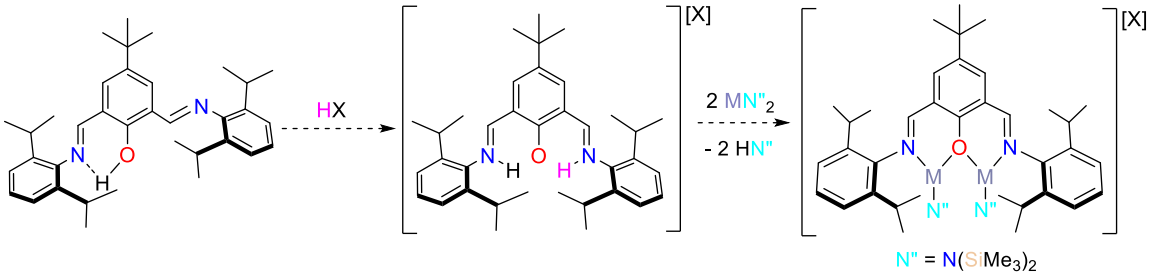

Scheme 6.4 The proposed synthetic route to bimetallic "NON" systems via a protonated pro-ligand intermediate. For clarity, "$N(SiMe_3)_2$" has been abbreviated to "N"".

Clean and efficient protonation of the pro-ligand was achieved via treatment with ethereal HBF_4. After trituration of the crude oily solid with pentane, $[H_2{}^{tBu,Dipp}L][BF_4]\cdot thf_4$ (**16·thf$_4$**) was afforded in 81% yield, as an air-sensitive orange powder. ·

6.3.1.1 NMR and IR spectroscopic analysis

The ^1H NMR spectrum of **16·thf$_x$** contains the expected resonances of a C_{2v} symmetric product on the NMR spectroscopic timescale (**Figure 6.6**). A highly deshielded doublet

at δ 15 ppm, with a coupling constant ($^3J_{HH}$) of 13.5 Hz, represents the two acidic protons. The remaining four aromatic resonances (δ 7.3–9.1 ppm) correspond to the imine, central aromatic ring and N-*aryl* C***H*** protons. The isopropyl *methine*- and *methyl*- protons are represented by the multiplets at δ 3.4 and δ 1.3 ppm respectively. The final resonance, which corresponds to the remaining nine *tert*-butyl protons, is a singlet at δ 1.4 ppm. These spectral features align with those reported by Dutta and co-workers in their spectroscopic investigation of comparable macrocyclic tetraiminodiphenol perchlorate salts.[23]

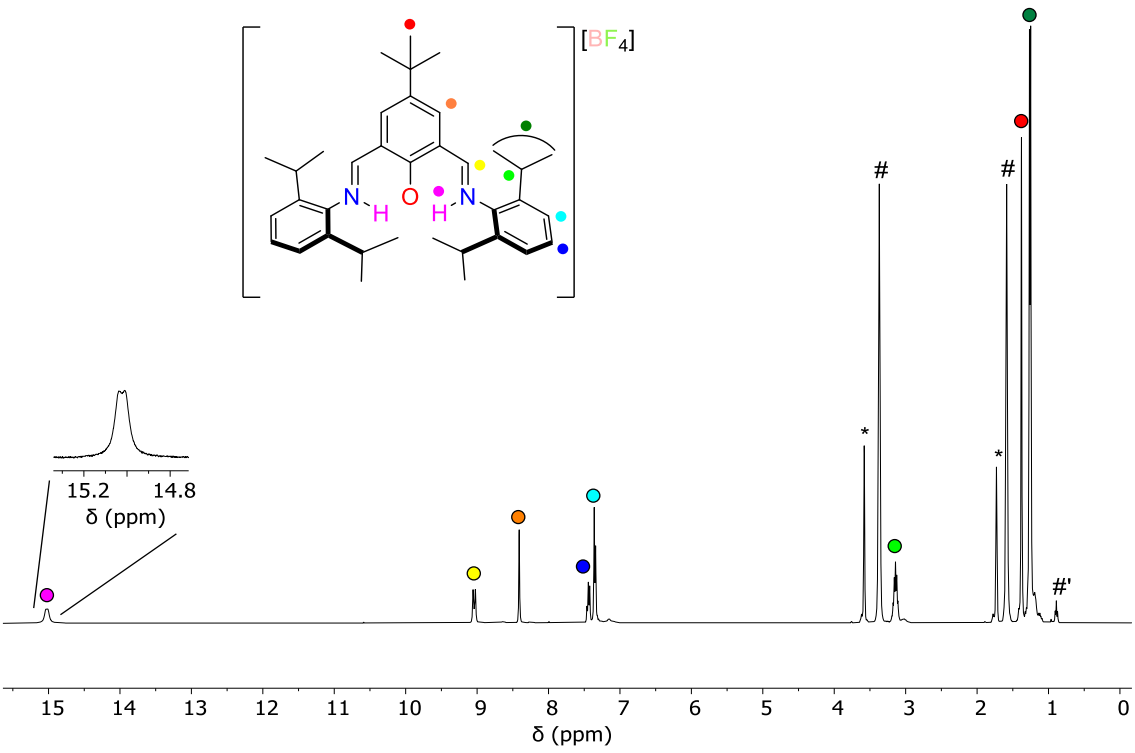

Figure 6.6 ^{1}H NMR spectrum (*THF-d_8, 400 MHz, 298 K) of [$H_2{}^{t\text{Bu,Dipp}}$L][BF_4] (**16·thf**$_x$). # and #' represent residual protio THF and pentane from reaction work up.

Variable temperature ^{1}H NMR studies revealed retention of the observed C_{2v} symmetry at temperatures as low as 223 K (**Figure A.57**). This indicates that the highly deshielded signal is not the coalescent of distinct N***H***, O***H*** resonances and thus the acidic protons must be chemically equivalent. It also implies that the fluxional interactions between

hydroxyl and imine groups, as seen in the unsymmetrical low temperature ^{1}H NMR spectrum of the H$^{t\text{Bu,Dipp}}$L (**Chapter 4**, **Section 4.2.1**), are not occurring. For these two statements to be true, either both imine arms are fixed in space away from the oxygen or there is no O***H*** present in the system.

Infrared spectroscopic analysis of **16·thf$_x$** supports the second theory as no absorbances were detected in the standard hydroxyl stretching region (3200–3700 cm^{-1}; **Figure 6.7**).[24] N***H*** stretching modes were recorded however, implying that the protonated pro-ligand takes a *bis*(iminium) form in solution. The observed N***H*** signal (3060 cm^{-1}) appeared red-shifted which previous literature reports suggest is due to the formation of N***H***···O hydrogen bonds.[23, 25-34]

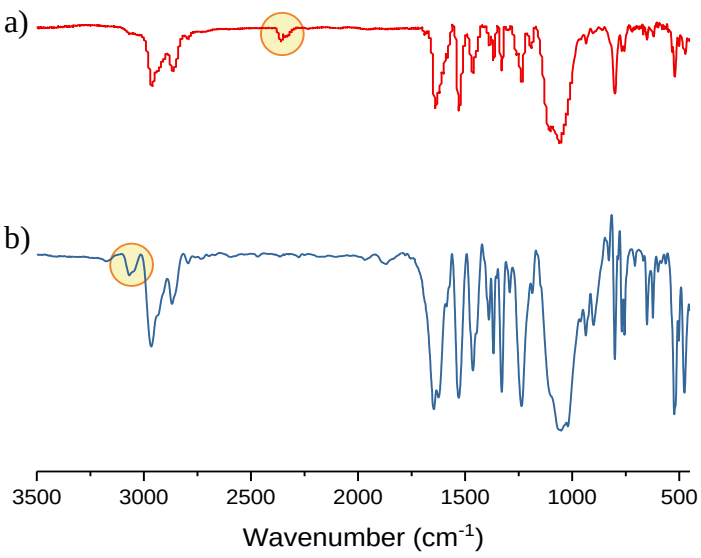

Figure 6.7 IR spectra of a) [D$_2$$^{t\text{Bu,Dipp}}$L][BF$_4$] and b) its protio analogue: [H$_2$$^{t\text{Bu,Dipp}}$L][BF$_4$] (**16·thf$_x$**). The corresponding N***D*** and N***H*** signals are highlighted.

Partial deuteration of compound **16·thf$_x$** further confirmed the assignment of the proposed N***H*** signals. After stirring a sample in either methanol-d_1 or ethanol-d_1, the initially observed absorption was suppressed and a new peak, corresponding to N***D*** stretching modes, appeared ~2360 cm^{-1}. This value coincides with other reported N***D***

signals and the predicted vibrational frequency when using the harmonic oscillator approximation (2400 cm^{-1}).[35-38]

Complete N***H*** deuteration was also verified by ^{1}H NMR spectroscopy (**Figure A.58**); in the spectrum of the deuterated species, the highly deshielded acidic proton signal is supressed. It's mutually coupling doublet, close to δ 9.00 ppm, corresponding to the imine ***H***C=N protons, is also converted into a broad singlet. The linewidth of this peak exceeds the anticipated $^{3}J_{HD}$ coupling and therefore the expected 1:1:1 triplet remained unresolved.

6.3.1.2 X-ray crystallographic analysis

Single crystals of **16**, suitable for an X-ray diffraction study, were grown from a room temperature saturated benzene solution and solved in the monoclinic space group, $P2_1$. In the solid-state, the compound exists as charge-separated ion pairs. The asymmetric unit contained two crystallographically independent, yet essentially-identical cations, alongside their corresponding anions and four solvent molecules. The following discussion relates solely to the O1-containing cationic fragment (the experimental metrical parameters of the alternate cation can be found in **Table A.7**).

The X-ray crystallographic analysis of **16** depicts that in the solid-state, the cation adopts a C_{2v} symmetric "closed-conformation" in which both imine groups are co-planar with the central π-ring and orientated towards the oxygen centre (**Figure 6.8**). This agrees with the solution ^{1}H NMR data and previous literature reports of similar monomeric *bis*(iminium) systems.[30, 39-41] It contrasts however, to the solid-state structure of the original *bis*(imino)phenol pro-ligand, as well as those of other ligands/metal complexes incorporating the "NON" framework. In these cases, one imine-*aryl* arm tends to rotate away from the oxygen centre to relieve steric strain and facilitate imine-C***H***···O hydrogen

bonds.[2, 22, 42-44] The adoption of this particular arrangement of atoms in space therefore suggests that the typical steric constraint of the system is outweighed by alternative stabilising features.

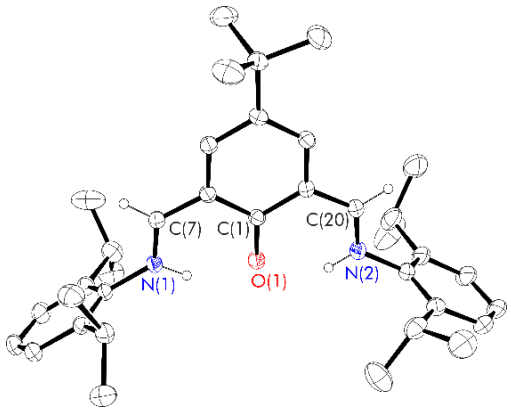

Figure 6.8 Thermal displacement ellipsoid drawings (30% probability) of $[H_2{}^{t\text{Bu,Dipp}}L][BF_4]$ (**16**); cation only displayed. All hydrogen atoms apart from those on N1, N2, C7 and C20 have been omitted for clarity. Only one of two independent molecules in the asymmetric unit is shown for clarity.

Table 6.1 Experimental metrical parameters (bond lengths (Å)) for $H^{t\text{Bu,Dipp}}L$ and $[H_2{}^{t\text{Bu,Dipp}}L][BF_4]$ (**16**). Estimated standard deviations shown in brackets.

	$\mathbf{H^{tBu,Dipp}L}^{a}$	**16**
C(1)-O(1)	1.3477(18)	1.284(3)
C(1)-C(2)	1.408(2)	1.434(3)
C(1)-C(6)	1.398(2)	1.435(3)
C(2)-C(7)	1.457(2)	1.424(3)
C(6)-C(20)	1.470(2)	1.429(3)
N(1)-C(7)	1.269(2)	1.295(4)
N(2)-C(20)	1.266(2)	1.298(3)
N(1)-H(1)	-	0.86(5)
N(2)-H(2)	-	0.95(4)

[a]X-ray crystal structure of conjugate base reported by Sun and co-workers.[44]

One such force is the increased delocalisation of oxygen electron density into the central π-ring and pendent iminiums. This was confirmed by analysis of the experimental metrical parameters of the solid-state structure (**Table 6.1**). Pro-ligand protonation was seen to lead to a reduction in the C(1)-O(1) bond length (1.37 *vs*. 1.28 Å for the neutral and cationic species respectively); this reflects an increase in bond order (Pyykkö reported the value of a C=O double bond to be 1.24 Å)[45], and thus an increase in electron density transfer between the two atoms.[34] An analogous shortening is also observed for the C-C_{imine} bonds (1.47 *vs*. 1.42 Å). In contrast, a slight elongation of the imine C=N bonds is observed (1.27 *vs*. 1.29 Å); this agrees with previous literature reports of similar cations, and highlights the reduction of electron density on the nitrogen atoms.[30, 32, 39, 41] This increased delocalisation implies that the "closed-*bis*(iminium)-conformation" is able to access a greater number of *phenoxide-like*, resonance forms (**Figure 6.9**). These are unachievable in the presence of a hydroxyl group thus reaffirming that, in both solution and solid-state, the cations only contain acidic N***H*** protons. This conclusion was further supported by the fact that the acidic protons were located on the nitrogen atoms and freely refined in the X-ray crystal structure.

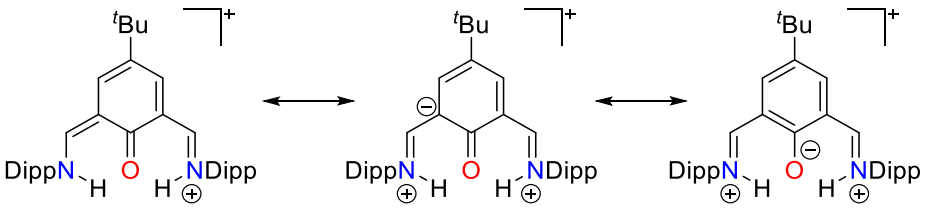

Figure 6.9 The accessible resonance forms of the *bis*(iminium) phenoxide cation of **16**.

Additional stabilisation of this unusual tautomer may also result from the presence of the electrostatic $N^{+}\boldsymbol{H}\cdots O$ hydrogen bonds suggested by IR analysis.[23, 30-34] These interactions, which due to the lack of a phenoxy group must take a symmetric form ($N^{+}\boldsymbol{H}\cdots O^{-}\cdots \boldsymbol{H}N^{+}$), are potentially evidenced by the N***H***···O distance (*av*. 1.84 Å) being

considerably longer than the N***H*** bond lengths (*av*. 0.91 Å) yet shorter than the sum of the van der Waals radii (2.72 Å).[43, 46, 47]

6.3.1.3 Density functional theory (DFT) calculations

To further understand the inherent structure and stabilisation of the protonated pro-ligand (**16**), density functional theory (DFT) calculations were conducted. The optimised geometry of the cation was in good agreement with the experimental crystal structure in terms of symmetry and bond parameters (e.g. computed N***H*** distances of 1.03 Å were consistent with the assigned *bis*(iminium) phenoxide tautomer).

The calculated molecular orbital maps of the cation of **16** can be seen in **Figure 6.10**; the HOMO was found span the entire π-system with a significant contribution also coming from the oxygen centre. This supports the theory that the "closed" arrangement of atoms in space is able to facilitate a high degree of electron transfer. In contrast, the HOMO of the original pro-ligand is localised on a ^{Dipp}NC unit, with negligible involvement of the oxygen atom.

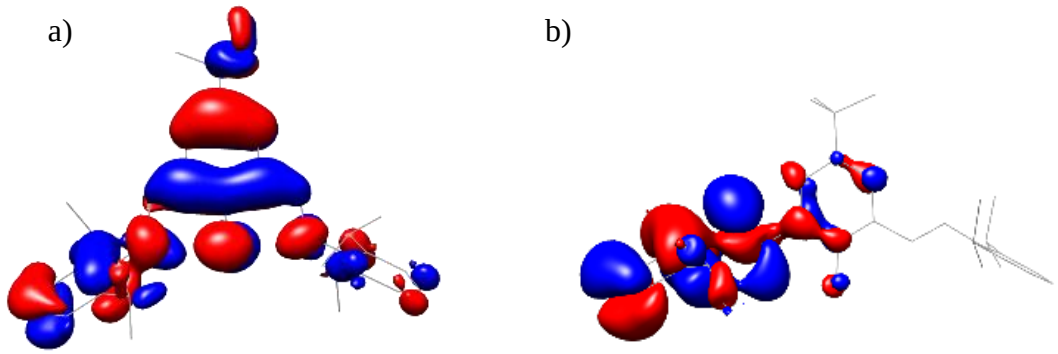

Figure 6.10 DFT-computed (B3LYP) molecular orbitals: a) HOMO and b) LUMO of the cation of the protonated pro-ligand (**16**) - $[H_2{}^{tBu,Dipp}L]^+$.

Upon protonation, the enhanced resonance causes the delocalised electrons to become more evenly distributed across the conjugated system. This is evidenced by the computed

delocalisation indices (δ(A,B); **Figure 6.11**).[48] The values of δ(C,O) and δ(C,N) are observed to increase and decrease by (*av*.) 0.24; these changes directly reflect the proposed resonance forms (**Figure 6.9**) of the *bis*(iminium) tautomer.

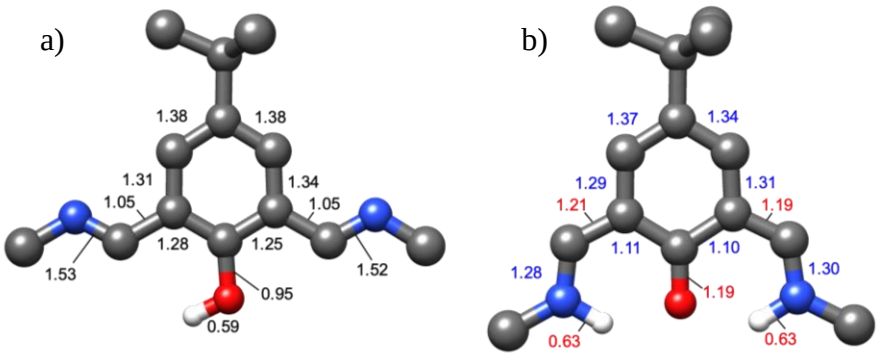

Figure 6.11 Computed delocalisation indices – δ(A,B) – for a) $H^{tBu,Dipp}L$ and b) the cation of compound **16**; red values increase upon formation of **16**, whereas blue values decrease.

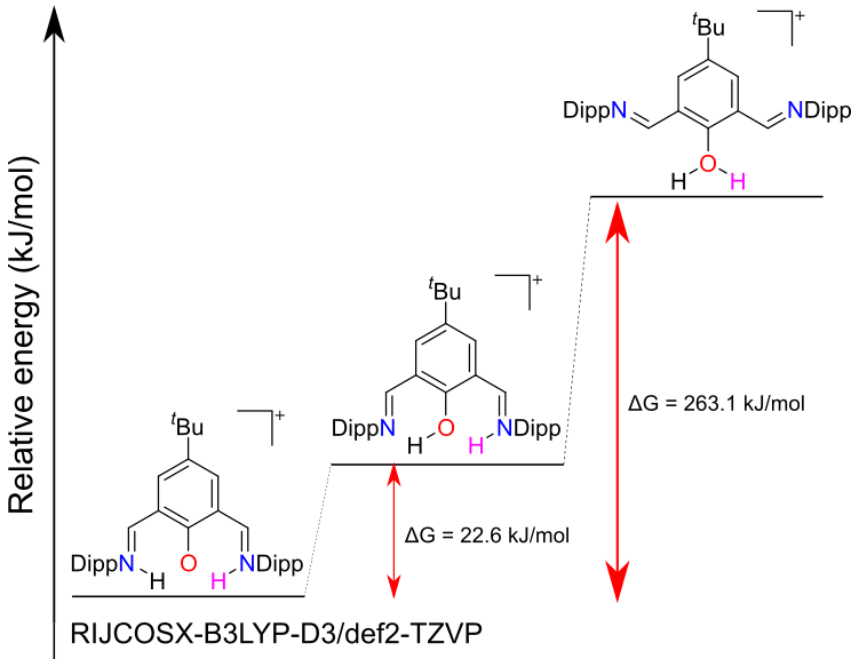

Figure 6.12 DFT-calculated potential energy diagram displaying the energy difference between the possible cationic tautomers: $[HN<O>NH]^+$, $[N<OH>NH]^+$ and $[N<OH_2>N]^+$.

Confirmation that the *bis*(iminium) tautomer ([HN<O>NH]$^+$) was the true thermodynamic sink was sought by optimising the geometries of the alternative cations in which one ([HN<OH>N]$^+$), or both ([N<OH_2>N]$^+$), acidic protons were localised on the oxygen atom. These alternative tautomers converged at energy (ΔG) minima 22.6 kJ mol^{-1} and 263.1 kJ mol^{-1} higher relative to the observed structure implying that it is unfavourable for even a single acidic proton to be located on the oxygen atom (**Figure 6.12**; see **Appendix** for further details). This agrees with the experimental observations that never detected the presence of a hydroxyl group (both in solution or solid-state).

Direct evidence for the proposed N$^+$***H***···O$^-$ hydrogen bonds was found via topological analysis; this indicated the presence of (3,–1) bonding critical points (BCPs) between both the N,H and H,O atoms (**Figure 6.13**). At the N,H BCPs, high electron density (0.325/0.326 a.u.) coincides with negative Laplacian values ($\nabla^2\rho$(**r**): –0.186/–0.189 a.u.; **Figure A.59**) indicating concentration of charge/regions of covalent bonding at these points.[49] In contrast, the O,H BCPs have low electron density (0.0367/0.0368 a.u.) and positive Laplacian values (0.120/0.121 a.u.). This means these bonding critical points occur in regions of charge depletion and so do not represent covalent interactions between atoms but instead weaker intramolecular electrostatic attractions i.e. hydrogen bonds.[49-51] These results corroborate the proposed notion that the oxygen atom interacts with the acidic protons in a purely electrostatic fashion. The energy associated with these hydrogen bonds was then estimated using the methods reported by Lu *et al.* (see **Appendix** for further details).[52] In the *bis*(iminium) tautomer, the average contribution of each charged N$^+$***H***···O$^-$ interaction was –55.6 kJ mol^{-1} therefore resulting in a total hydrogen bonding stabilisation energy of –111.2 kJ mol^{-1}. In comparison, the stabilisation imparted on the [N<OH>NH]$^+$ tautomer, from the neutral N···***H***O and charged N$^+$***H***···O$^-$ hydrogen bonds, was calculated to be –112.2 kJ mol^{-1} (1.0 kJ mol^{-1}

more than in the thermodynamically favoured system). This suggests that the extra stabilisation of the [HN<O>NH]$^+$ system must result from the increased resonance. For this to be the case, the number of delocalised electrons in that system must exceed that of the alternative conformer. This was quantified by comparing the sum of the delocalisation indices of the possible isomers to that of H$^{t\text{Bu,Dipp}}$L as a reference (see **Table A.10**). The following trend was observed: [HN<O>NH]$^+$ (+0.16) > [N<OH>NH]$^+$ (+0.11) > [N<OH$_2$>N]$^+$ (+0.08). These results map those of the geometry optimisations and indicate that the greatest impact of resonance is found in the [HN<O>NH]$^+$ system.

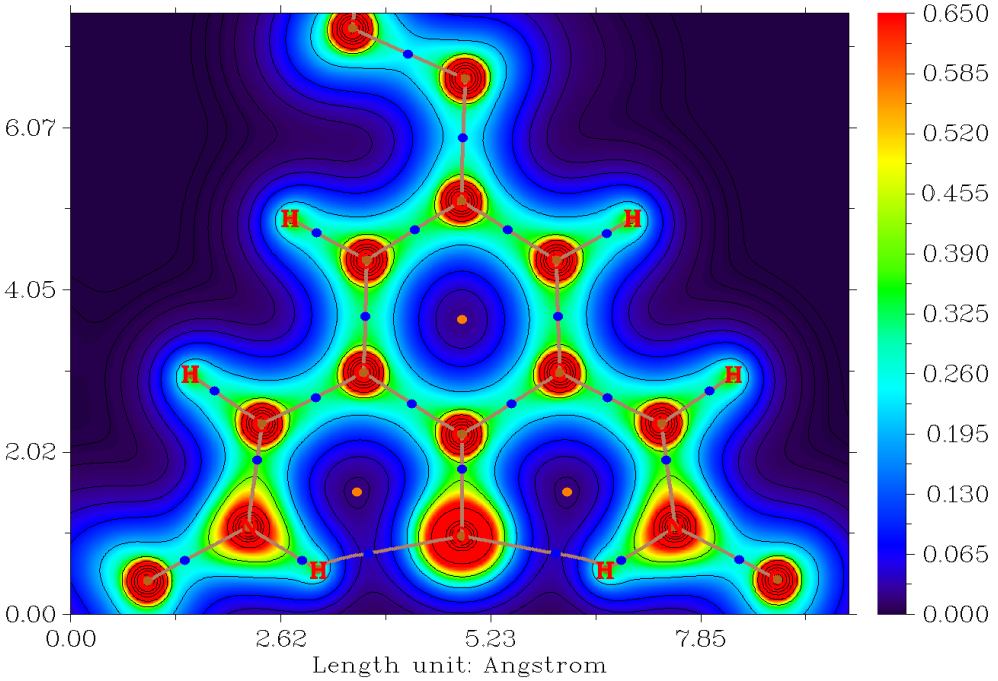

Figure 6.13 Contour map of the electron density of [H$_2$$^{t\text{Bu,Dipp}}$L]$^+$ in its thermodynamically favoured conformation: [HN<O>NH]$^+$ - plotted in the plane of the central aromatic ring. The blue (•) and orange (•) dots mark bonding (3,–1) and ring (3,+1) critical points respectively.

6.3.1.4 p*K*$_a$ studies

As compound **16·thf$_x$** can be classed as a diacid, quantification of the p*K*$_a$ of its acidic N***H*** protons was conducted. The Δp*K*$_a$-values were determined, relative to a reference base, using the NMR titration techniques published by Koppel and co-workers (see

Appendix for further details).[53] These experiments were performed in triplicate with the average result and standard error reported. Pyrazole (pK_a = 3.6 in THF and 9.1 in acetonitrile) was identified as a suitable basic indicator as it only initiated partial deprotonation of the diacids.[54]

The pK_a of **16·thf$_x$**, calculated in THF due to its partial solubility in the typically chosen solvent: acetonitrile, was computed to be 4.2 ± 0.008. This is similar to other borate containing salts such as [HPPh$_3$][BPh$_4$] (pK_a = 3 in THF).[55]

6.3.2 Reactivity of [H$_2$$^{t\text{Bu,Dipp}}$L][BF$_4$] with alkaline-earth amides

After successfully isolating and fully characterising the intermediate organocation, the next step was to investigate its reactivity towards alkaline-earth amide reagents. ^{1}H NMR analysis depicted that, upon addition of 0.5 eq. of [Mg{N(SiMe$_3$)$_2$}$_2$]$_2$, a completely asymmetric product was formed (evidenced by the doubling of the expected number of signals). Although the symmetry indicated was consistent with the formation of a cationic magnesium complex, the actual identity of this compound was confirmed, via solid-state X-ray crystallography (*vide infra*), to be $^{t\text{Bu,Dipp}}$LBF$_2$ (**17**; **Scheme 6.5**). Analogous B-F activation was also observed when Ca{N(SiMe$_3$)$_2$}$_2$(thf)$_2$ was employed as the source of the alkaline-earth metal (**Figure A.61**).

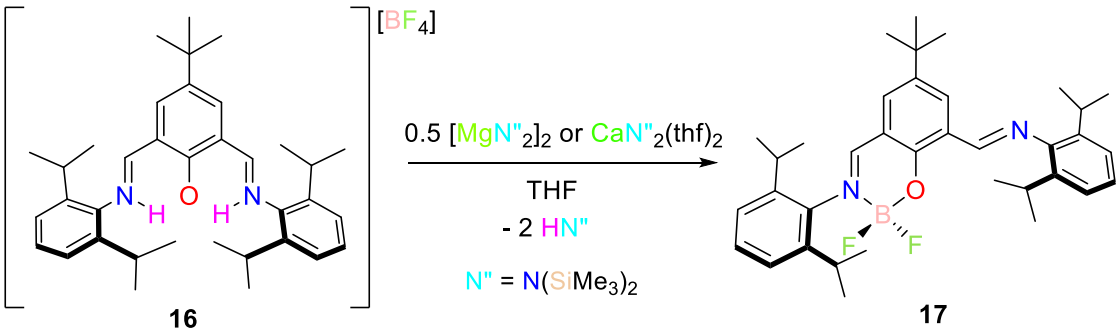

Scheme 6.5 Synthesis of $^{t\text{Bu,Dipp}}$LBF$_2$ (**17**). For clarity, "N(SiMe$_3$)$_2$" has been abbreviated to "N"".

6.3.2.1 Proposed synthetic pathway

Two eq. of HMDS ($HN(SiMe_3)_2$) were identified in the ^1H NMR spectrum of the crude reaction mixture; this is consistent with the initial step being a two-fold (N***H***) protonolysis (**Scheme 6.6**). The remaining, highly Lewis acidic M^{2+} cation is then able to abstract two fluorine atoms from the BF_4^- counterion to form MF_2 as a secondary by-product. This results in the formation of a "BF_2^+" moiety, which is stabilised by the monoanionic "NON" ligand framework to afford the observed, neutral species. The isolated product had the composition $^{t\text{Bu,Dipp}}LBF_2 \cdot thf_{0.9}$ (**17·thf**$_x$).

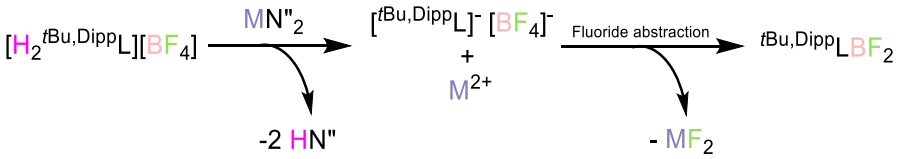

Scheme 6.6 Proposed mechanism for the formation of $^{t\text{Bu,Dipp}}LBF_2$ (**17**).

Monitoring the calcium-mediated reaction by ^{19}F NMR also provided extra evidence for this proposed reaction pathway; it indicated full consumption of the tetrafluoroborate anion (δ –150.7 ppm) and generation of two new fluorine containing species at δ –137.6 ppm and δ –158.3 ppm respectively. The former (a broad unresolved multiplet) was identified as complex **17**, whilst the latter (a sharp singlet) was tentatively assigned to solvated CaF_2 (likely formed as a result of its high lattice enthalpy: 2635 kJ mol^{-1}).[56]

The poor solubility of group 2 fluorides in most organic solvents meant that the solution ^{19}F NMR spectrum of CaF_2 could not be collected and compared to δ –158.3 ppm. Instead, a solid-state ^{19}F-MAS (magic-angle-spinning) experiment was run on a crude mixture sample after the removal of reaction media. In the resultant spectrum, a broad signal is present around δ –108 ppm (**Figure 6.14**); this aligns with previous literature

reports for the resonance of CaF_2.[57] The identification of CaF_2 in the crude mixture is further supporting evidence for the proposed mechanism.

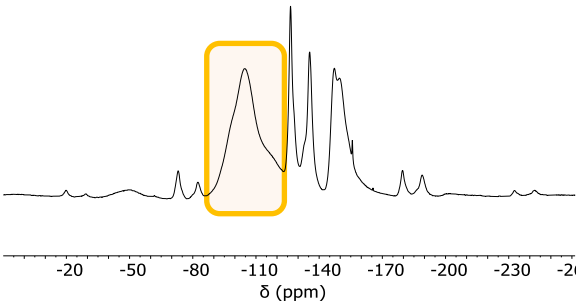

Figure 6.14 ^{19}F-MAS-NMR spectrum of crude calcium-catalysed reaction mixture; broad signal at δ –108 ppm represents CaF_2.[57]

Fluoride abstraction from the tetrafluoroborate anion is very rare as typically such fluorinations employ neutral BF_3 containing reagents.[58-62]

6.3.2.2 NMR spectroscopic analysis

The ^{1}H NMR spectrum of a crystalline sample of **17** (**Figure 6.15**) has 14 signals as a result of the fixed asymmetry of the molecule. The singlet close to δ 8.84 ppm corresponds to the ***H***C=NBF_2 proton; it is broadened as a result of the through-bond proximity to the quadrupolar boron nucleus. The resonance for the imine proton of the freely rotating arm is depicted at δ 8.79 ppm as a sharp singlet. The two central aromatic ring protons, located at δ 8.74 and δ 7.81 ppm, appear as doublets with coupling constants $^4J_{HH}$ = 2.6 Hz. The final four aromatic resonances, which display considerable roofing effects, correspond to the imine-aryl C***H*** protons; the more deshielded pair of signals correlate to the boron-bound half of the molecule as a result of the reduction in electron density on the adjacent nitrogen centre. The *methine* and *methyl* protons of the isopropyl groups are represented by the two septets at δ 3.04 ppm and doublets between δ 1.25–1.13 ppm respectively. The final resonance at δ 1.41 ppm, which integrates to 9 protons, corresponds to the *tert*-butyl protons. The corresponding ^{11}B and ^{19}F NMR spectra exhibit

broad, unresolved multiplets at δ 0.6 ppm (consistent with four-coordinate boron) and δ –137.6 ppm respectively.

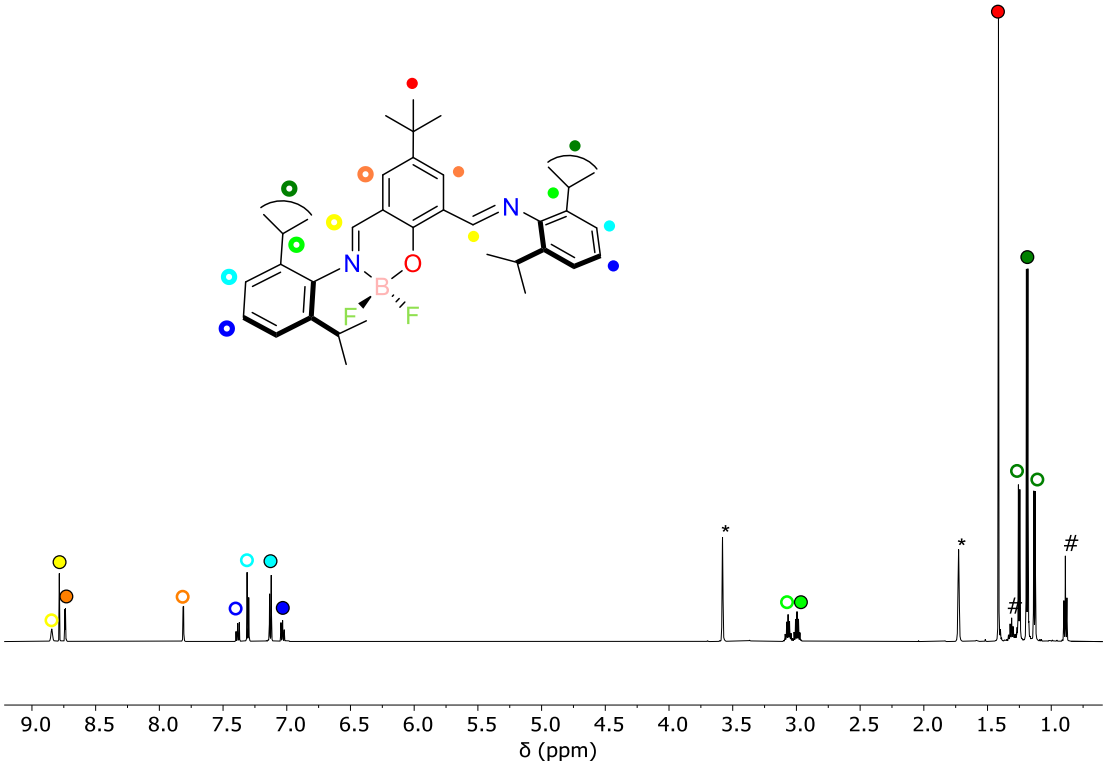

Figure 6.15 ^{1}H NMR spectrum (*THF-d_8, 400 MHz, 298 K) of $^{t\text{Bu,Dipp}}$LBF$_2$ (**17**). # represents residual protio-pentane from work-up.

6.3.2.3 X-ray crystallographic analysis

Single crystals of **17**, suitable for X-ray diffraction analysis, were grown via slow evaporation of a room temperature THF solution and refined in the triclinic space group, $P\bar{1}$. The results are presented in **Figure 6.16** and **Table 6.2**. The asymmetric unit contained two essentially identical molecules of **17** which were found to interact through $\boldsymbol{H}_{\text{imine}}\cdots$F short contacts (~ 2.51 Å). The following discussion relates solely to the B1-containing compound (the experimental metrical parameters of the alternate species can be found in **Table A.11**).

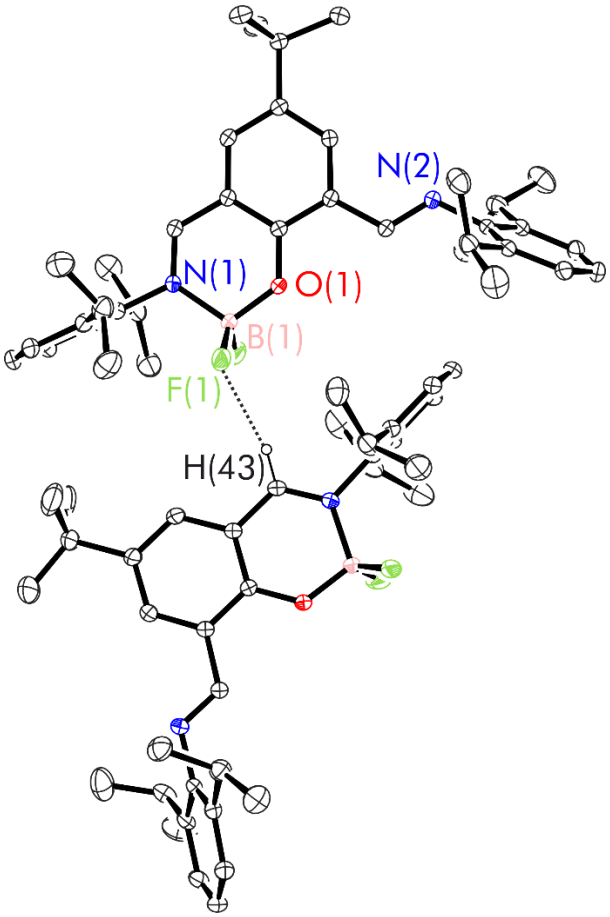

Figure 6.16 Thermal displacement ellipsoid drawings (30% probability) of the asymmetric unit of $^{t\text{Bu,Dipp}}$LBF$_2$ (**17**). All hydrogen atoms, except those bound to C(43) have been omitted for clarity.

The boron centre is in an almost perfect tetrahedral coordination environment as indicated by its tau-parameter: τ_4 = 0.99; this results in the co-planarity of the heterocyclic and phenol rings.[63] The B-F (*av.* 1.375 Å), B-O (1.449(2) Å) and B-N (1.596(2) Å) bond lengths all lie within the ranges reported for comparable BF$_2$-containing Schiff base systems (B-F: 1.357(12)–1.393(2) Å; B-O: 1.408(4)–1.502(3) Å; B-N: 1.545(15)–1.617(4) Å).[58-62] They are also comparable with the B-F/B-O/B-N single bond lengths predicted by Pyykkö (B-F: 1.49 Å; B-O: 1.48 Å; Ca-N: 1.56 Å).[45] As for the heteroleptic calcium iodide complex: **15**, the B-O bond appears shorter than its B-N equivalent as a result of the oxygen atom acting as an X-type donor. In addition, the unbound imine arm

is twisted away from the ligand core for relief of steric strain. The bound C=N distance is much shorter than the freely rotating imine (1.292(2) *vs.* 1.458(2) Å) as a result of increased electron density donation to the boron atom.

Table 6.2 Experimental metrical parameters (bond lengths (Å) and angles (°)) for $^{t\text{Bu,Dipp}}LBF_2$ (**17**). Estimated standard deviations shown in brackets.

B(1)-N(1)	1.596(2)
B(1)-O(1)	1.449(2)
B(1)-F(1)	1.378(3)
B(1)-F(2)	1.372(3)
O(1)-C(1)	1.334(2)
N(1)-C(7)	1.292(2)
O(1)-B(1)-N(1)	109.82(14)
O(1)-B(1)-F(1)	110.21(15)
O(1)-B(1)-F(2)	110.89(17)
N(1)-B(1)-F(1)	108.91(16)
N(1)-B(1)-F(2)	108.22(14)
F(1)-B(1)-F(2)	108.75(16)
τ_4	0.99

Related difluoroboron heterocyclic derivatives, based on Schiff base ligands, are referred to as boranils (**Figure 6.17a**). They are typically synthesised by refluxing the corresponding pro-ligand with $BF_3{\cdot}Et_2O/NEt_3$ in 1,2-dichloroethane and are commonly studied for their impressive fluorescence quantum yields.[58-60] The solid-state structures of these species highlight the same co-planarity of the boranil and phenol cycles as observed with **17**. When the imine nitrogen is part of a secondary pyridine or pyrazine moiety, its electron donation to the boron is reduced; this is evidenced by the elongation of the corresponding B-N bonds (1.57 (*av.*) Å *vs.* 1.61 (*av.*) Å; **Figure 6.17b**).[61]

Comparable intermolecular short contacts have also been observed in *tris*(difluoroboronyl) Schiff base complexes (**Figure 6.17c**). In the solid state, these planar systems form staggered, co-facial stacks as a result of the six $C_{imine}\cdots F$ interactions present between the layers.[62]

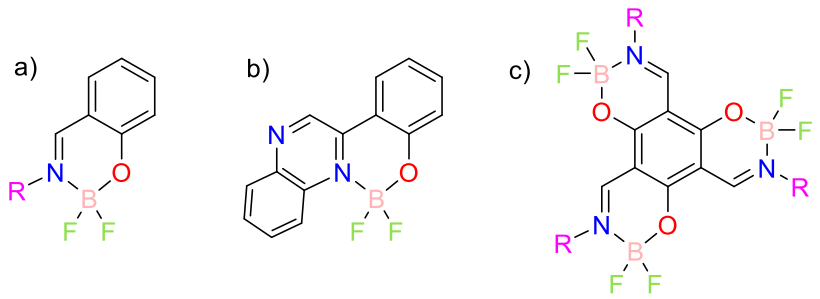

Figure 6.17 Previously reported BF_2-containing Schiff base (and related) complexes.[58-62]

6.3.2.4 Synthesis and characterisation of $[H_2{}^{t\text{Bu,Dipp}}L][H_2N\{B(C_6F_5)_3\}_2]$

Having observed the B-F activation activity upon treatment of **16·thf$_x$** with group 2 amides, it was concluded that the $[BF_4]^-$ anion was unsuitable for the synthesis of cationic, alkaline-earth, bimetallic "NON" species. The $[H_2N\{B(C_6F_5)_3\}_2]^-$ anion, a species derived from Bochmann's acid $[H(OEt_2)_2][H_2N\{B(C_6F_5)_3\}_2]$ (**Scheme 6.7**), was selected as an alternative weakly coordinating anion, due to its proven stability towards highly Lewis acidic alkaline-earth cations.[12-14, 18]

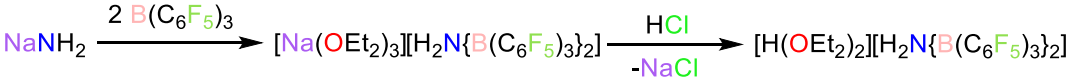

Scheme 6.7 Synthesis of Bochmann's acid.[64]

The synthesis of Bochmann's acid involved a two-step process that started with the reaction of tris(pentafluorophenyl)borane with sodium amide. The intermediate sodium salt was then treated with excess HCl to form the resultant acid as a colourless powder in an overall isolated yield of 45%. The ^{1}H NMR spectrum of $[H(OEt_2)_2][H_2N\{B(C_6F_5)_3\}_2]$ was consistent with those reported in the literature.[64]

Subsequent treatment of $H^{tBuDipp}L$ with an equimolar amount of Bochmann's acid afforded the desired, protonated pro-ligand as its amino diboronate salt, $[H_2{}^{tBu,Dipp}L][H_2N\{B(C_6F_5)_3\}_2]\cdot thf_{0.36}$ (**18·thf$_x$**); a bright orange solid in 87% yield.

The NMR spectral data of compound **18·thf$_x$** is similar to **16·thf$_x$** apart from slight variations in chemical shift and an additional broad singlet at δ 5.77 ppm corresponding to the NH_2 environment of the aminodiboronate anion (**Figure A.62**). New sharp N*H* stretching modes are also observed at 3300 cm^{-1} in the IR spectrum (**Figure A.63**).[64]

Single crystals of **18**, suitable for an X-ray diffraction study, were grown from a –25 °C dichloromethane/pentane mixture and crystallised in the triclinic $P\bar{1}$ space group. The cationic fragment only showed minor differences in bond lengths and angles (**Figure A.64**) when compared to that of **16**.

The use of the alternative weakly coordinating anion allowed **18·thf$_x$** to fully dissolve in acetonitrile (**Figure A.65**). Its pK_a was therefore calculated, in this solvent, to be 11.4 ± 0.09; this is analogous to other nitrogen-based acids like $(C_6F_5\text{-}SO_2)_2NH$ (pK_a = 11.35 in acetonitrile).[65, 66] It also indicates that **18·thf$_x$** is a stronger acid than phenol (pK_a = 29.14 in acetonitrile)[67]; this enhanced acidity can be attributed to the extended electron delocalisation throughout the entire "NON" system.

6.3.3 Reactivity of $[H_2{}^{tBu,Dipp}L][H_2N\{B(C_6F_5)_3\}_2]$ with alkaline-earth metal amides

After successfully isolating and characterising compound **18·thf$_x$**, the next step was to investigate its reactivity with group 2 amides (M = Mg, Ca). Upon addition of 0.5 eq. of $[Mg\{N(SiMe_3)_2\}_2]_2$ or 1 eq. $Ca\{N(SiMe_3)_2\}_2(thf)$, a colour change from bright orange to golden yellow was observed. The crude ^1H NMR spectrum of the calcium reaction revealed that 2 eq. of the protonolysis by-product $HN(SiMe_3)_2$ had been released. The remaining resonances were consistent with a *pseudo*-C_{2v} symmetric "NON" complex;

this was tentatively assigned as the cationic calcium species [^{t}Bu,Dipp LCa(thf)$_4$][H$_2$N{B(C$_6$F$_5$)$_3$}$_2$] (**19**; **Scheme 6.8**). The identity of this compound was confirmed in the solid-state using X-ray crystallographic analysis (*vide infra*). In the case of magnesium, the reaction mixture was contaminated with an amount (ranging between 20–30%) of the neutral homoleptic magnesium complex (**10**), which could not be separated from the reaction mixture. Attempts to introduce 2 eq. of alkaline-earth metal to form a bimetallic complex were unsuccessful; ^{1}H NMR analysis of these crude mixtures indicated the formation of multiple**,** unidentifiable species.

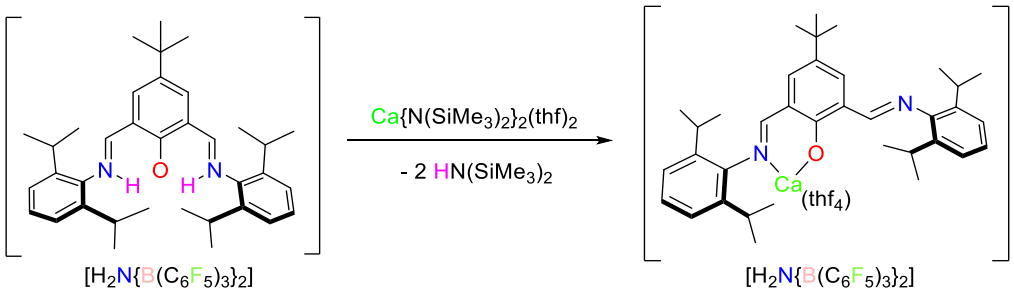

Scheme 6.8 Synthesis of [^{t}Bu,Dipp LCa(thf)$_4$][H$_2$N{B(C$_6$F$_5$)$_3$}$_2$] (**19**).

6.3.3.1 NMR spectroscopic analysis

The ^{1}H NMR spectrum of complex **19** (**Figure 6.18**) is analogous to that of the neutral calcium iodide complex (**15**) previously discussed. It contains the expected resonances for a *pseudo*-C_{2v} symmetric species indicating the fluxional behaviour of the compound in solution (**Figure 6.18**). The resonances corresponding to the imine (***H***C=N) and protons of the central aromatic ring (δ 8.51 and δ 7.96 ppm respectively) are slightly broadened due to dynamic interactions with the freely rotating imine arm(s). The remaining aromatic resonances (δ 7.19–7.11 ppm) represent the imine-*aryl* group C***H*** protons. The broad singlet and multiplets at δ 5.75, δ 2.99 and δ 1.18 ppm correspond to

the anion N***H*** protons and isopropyl *methine*/*methyl* protons respectively. The final resonance, a singlet at δ 1.34 ppm, correlates to the nine *tert*-butyl protons.

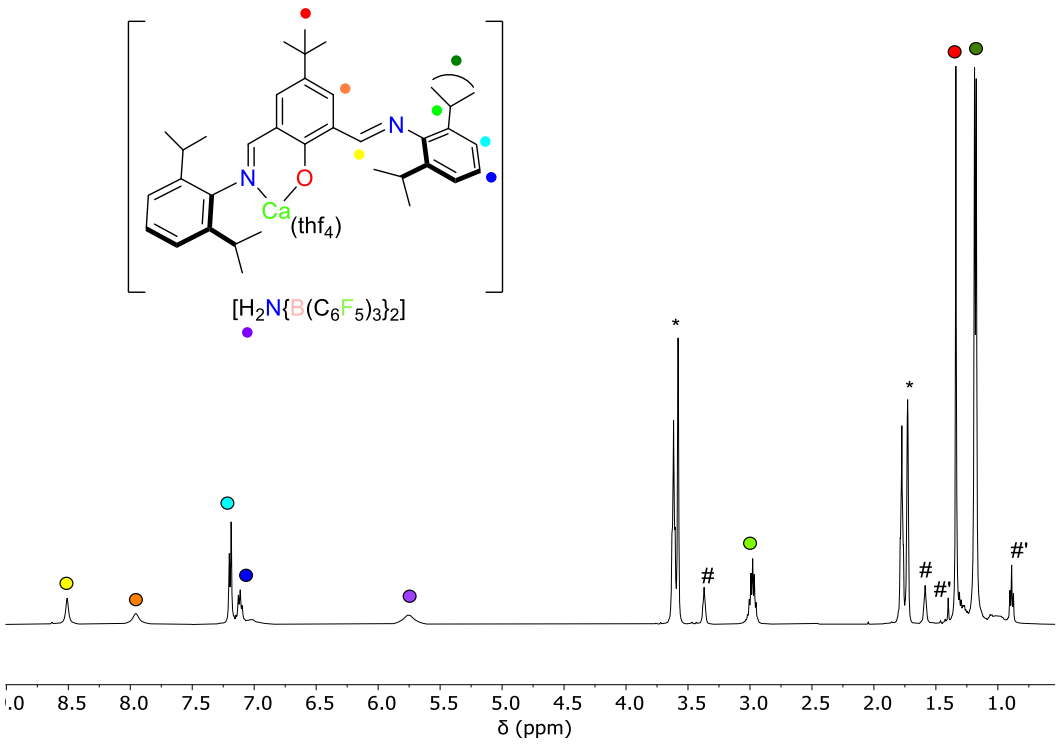

Figure 6.18 ^{1}H NMR spectrum (*THF-d_8, 500 MHz, 298 K) of [$^{t\text{Bu,Dipp}}$LCa(thf)$_4$][H$_2$N{B(C$_6$F$_5$)$_3$}$_2$] (**19**). # and #' denote protio THF and pentane from reaction work up.

The dynamic behaviour of the system, proposed to arise from exchange of the calcium centre between the distinct binding pockets of the ligand unit, was investigated by conducting variable temperature ^{1}H NMR studies (**Figure 6.19**). It is also possible that this fluxionality is the result of ligand aggregation/exchange between metal centres. This however, seems less likely considering such redistribution with this ligand framework has typically resulted in the irreversible formation of homoleptic species.

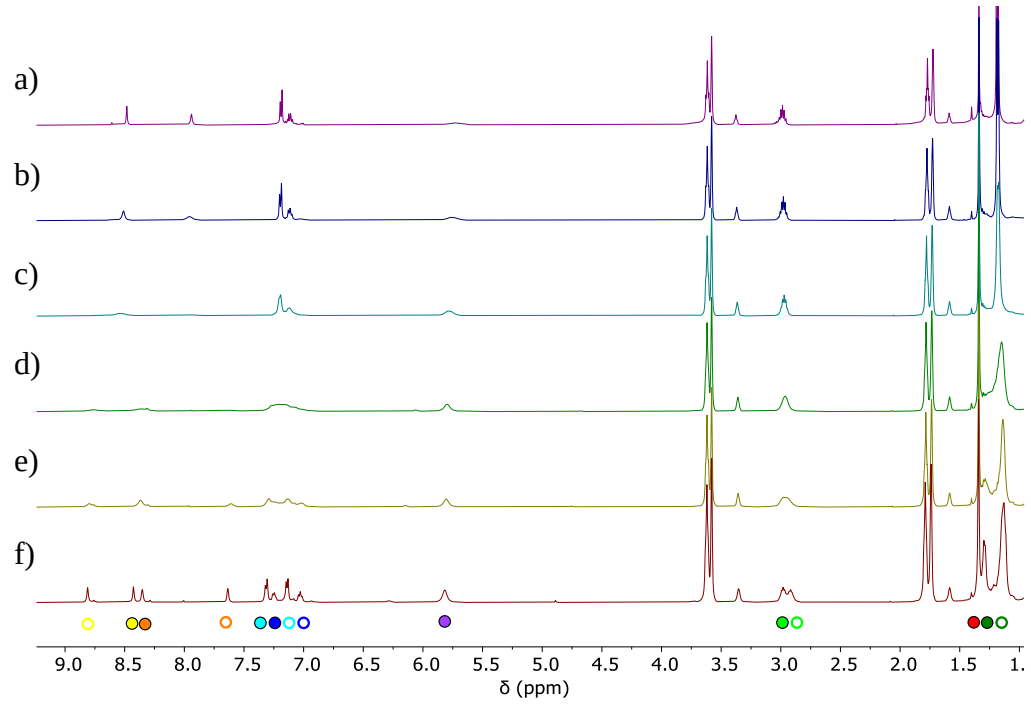

Figure 6.19 ^{1}H NMR spectra (*THF-d_8, 500 MHz) of [$^{t\text{Bu,Dipp}}$LCa(thf)$_4$][H$_2$N{B(C$_6$F$_5$)$_3$}$_2$] (**19**) at a) 333 K, b) 298 K, c) 273 K, d) 243 K, e) 233 K and f) 213 K.

When a THF-d_8 solution of **19** was cooled to 213 K, the asymmetric binding mode of the ligand became distinguishable. This was evidenced by the doubling of the number of resonances observed in the room temperature spectrum. These isolated environments, however, were seen to coalesce as the sample was warmed. Heating the compound to temperatures up to 333 K appeared to have no observable effect on the identity or quality of the sample. The observed coalescence temperature (273 K) and peak to peak separation of the imine (192 Hz) and central aromatic ring (359 Hz) protons were used in the equations reported by Duncalf *et al*. (**Chapter 4**, **Section 4.3.2.1**) to estimate an average activation barrier ($\Delta G^{\ddagger}$) and rate of binding pocket fluctuation of the calcium centre.[68] These values were computed to be 53 kJ mol^{-1} and 433 s^{-1} respectively.

6.3.3.2 X-ray crystallographic analysis

All attempts to grow single crystals of **19** were unsuccessful. However, subsitution of the Bochmann anion for the [BAr$^{F}_4$]$^-$ anion (where Ar^F = 3,5-{CF$_3$}$_2$C$_6$H$_3$) affording

[^{t}Bu,Dipp LCa(thf)$_4$][B(3,5-{CF$_3$}$_2$C$_6$H$_3$)$_4$] (**21**), enabled full characterisation of the cationic fragment in the solid-state, owing to the more crystalline nature of the BAr_4^F salt.

Full spectroscopic analysis of **21**, and its corresponding protonated pro-ligand intermediate [H$_2$ ^{t}Bu,Dipp L][B(3,5-{CF$_3$}$_2$C$_6$H$_3$)$_4$] (**20·thf$_x$**) can be found in **Figures A.66-67** and **Chapter 7**. Complexes **20·thf$_x$** and **21** were made using analogous procedures to **18·thf$_x$** and **19** respectively; their NMR spectral data is almost identical to the Bochmann counterparts aside from the resonances arising from the different anion.

Single crystals of complex **21**, suitable for an X-ray diffraction study, were grown by slow diffusion of pentane into a saturated THF solution at room temperature, and refined in the monoclinic space group, C_2. The results of the analysis are presented in **Figure 6.20** and **Table 6.3**.

The calcium centre in complex **21** resides in one of the [=N,O$^-$] binding pockets; it is additionally ligated by four exogenous thf molecules to give a distorted octahedral metal coordination environment. This is akin to complex **19** and the few examples of crystallographically characterised homoleptic/dimeric Schiff base calcium systems.[69-73] There is only a slight variation between the bond lengths and angles in **21** relative to a comparable, neutral Schiff base calcium system (**Table 6.3**); this implies that the cationic nature of **21** doesn't significantly impact its metrical parameters. The Ca-O$_{phenoxide}$ (2.185(2) Å) and Ca-N$_{imine}$ (2.477(3) Å) bond lengths lie within the range of similar phenoxy-imine systems (Ca-O: 2.203(5)–2.391(4) Å; Ca-N: 2.472(6)–2.752(5) Å)[61-65] and are comparable with the Ca-O/Ca-N single bond lengths predicted by Pyykkö (Ca-O: 2.34 Å; Ca-N: 2.42 Å).[45] The Ca-O bond appears shorter than its Ca-N equivalent as a result of the oxygen atom acting as an X-type donor. Similar to both **15** and an

analogous yttrium "NON" complex, the unbound imine arm is twisted away from the ligand core for relief of steric strain.[42]

Table 6.3 Comparison of the experimental metrical parameters (bond lengths (Å) and angles (°)) of [^{t}Bu,Dipp LCa(thf)$_4$][B(3,5-{CF$_3$}$_2$C$_6$H$_3$)$_4$] (**21**) and the only other reported solid-state structure of a heteroleptic phenoxy-imine based calcium system.[73] Estimated standard deviations shown in brackets.

	[^{t}Bu,Dipp LCa(thf)$_4$][B(3,5-{CF$_3$}$_2$C$_6$H$_3$)$_4$] (**21**)	{ON-NMe$_2$}Ca(thf)(N(SiMe$_3$)$_2$)[73,a]
Ca(1)-N(1)	2.477(3)	2.474(2)
Ca(1)-O(1)	2.185(2)	2.1914(16)
Ca(1)-O(2)	2.395(3)	2.3494(18)
Ca(1)-O(3)	2.370(3)	-
Ca(1)-O(4)	2.391(3)	-
Ca(1)-O(5)	2.403(3)	-
O(1)-C(1)	1.296(4)	1.299(3)
N(1)-C(7)	1.291(4)	1.291(3)
O(1)-Ca(1)-N(1)	75.88(8)	74.50(6)

[a]phenoxy-imine (ON) based initiator with additional pendant amine donor (NMe$_2$)

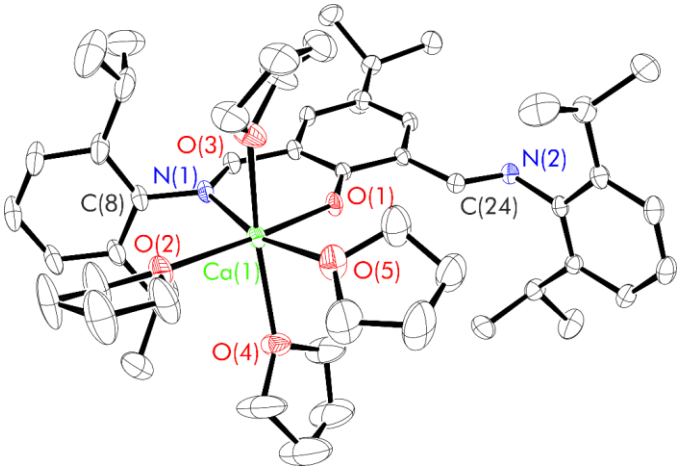

Figure 6.20 Thermal displacement ellipsoid drawing (30% probability) of [^{t}Bu,Dipp LCa(thf)$_4$][B(3,5-{CF$_3$}$_2$C$_6$H$_3$)$_4$] (**21**); cation only displayed.

6.3.3.3 Solid angle calculations

The atomic coordinates of complex **21**, produced from X-ray crystallographic analysis, were used in solid angle calculations; the results are presented in **Figure 6.21** and **Table 6.4**.

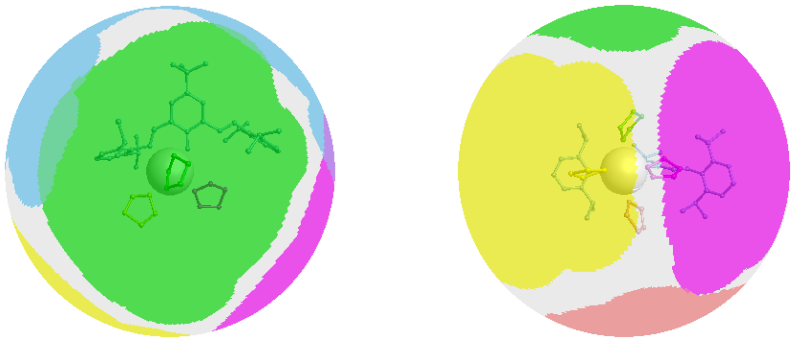

Figure 6.21 Visualisations of *G*(L) values in [$^{t\text{Bu,Dipp}}$LCa(thf)$_4$][B(3,5-{CF$_3$}$_2$C$_6$H$_3$)$_4$] (**21**), showing the percentage of the complex sphere shielded by each ligand. Blue = $^{t\text{Bu,Dipp}}$L, yellow = thf, green = thf, red = thf, pink = thf.

Table 6.4 Summary of ligand solid angles (Ω), the percentage of the sphere shielded by the ligand (*G*), the percent of the metal surface shielded by ligand atoms (*G*(M)) and the percentage of the metal surface "in contact" with ligated atoms (*S*(M)) for [$^{t\text{Bu,Dipp}}$LCa(thf)$_4$][B(3,5-{CF$_3$}$_2$C$_6$H$_3$)$_4$] (**21**).

Ligand	Ω($^{\text{Dipp}}$L) (sr)	*G*($^{\text{Dipp}}$L) (%)	$G_{2.28}$ ($^{\text{Dipp}}$L) (%)	*G*(M) (%)	*S*(M) (%)
$^{t\text{Bu,Dipp}}$L	4.60	36.61	32.64		
thf-1	1.65	13.10	14.15		
thf-2	1.70	13.56	14.42	65.77	65.31
thf-3	1.69	13.44	14.52		
thf-4	1.69	13.44	14.60		

The four exogenous thf ligands all impart comparable shielding on the calcium centre (*G*(%) = *av*. 13.39%). This implies that they all reside at a similar distance from the metal which was confirmed via X-ray analysis (Ca-O_{thf1}: 2.395(3) Å; Ca-O_{thf2}: 2.370(3) Å; Ca-O_{thf3}: 2.391(3) Å and Ca-O_{thf4}: 2.403(3) Å; *av*. = 2.390 Å;). These results also align with the fact that the shielding increases when the ligands are fixed at 2.28 Å from calcium ($G_{2.28}$(%) = *av*. 14.42%).

In contrast, the shielding of the $^{t\text{Bu,Dipp}}$L framework is reduced when fixed 2.28 Å away from the metal (32.64% *vs*. 36.61%). This infers that the Schiff base usually lies closer than this distance which agrees with the reported Ca-O bond length (2.185(2) Å) being shorter than 2.28 Å. The overall shielding of the calcium centre is comparable to that of the neutral heteroleptic calcium iodide complex: **15** (65.77% *vs*. 63.34%); this similarity is most likely due to the adoption of comparable distorted octahedral metal coordination geometries.

6.3.4 Treatment of $[H_2{}^{t\text{Bu,Dipp}}L][H_2N\{B(C_6F_5)_3\}_2]$ with other M^{2+} reagents

6.3.4.1 Reaction with MeMgI

As initial results showed that treatment of $[H_2{}^{t\text{Bu,Dipp}}L][H_2N\{B(C_6F_5)_3\}_2]$ (**18·thf$_x$**) with $[Mg\{N(SiMe_3)_2\}_2]_2$ or $Ca\{N(SiMe_3)_2\}_2(thf)_2$ resulted in the loss of both amide ligands, an alternative method, in which the metallic reagent had only one labile group (and would therefore leave the second binding pocket protonated during the reaction) was considered. The ideal alkaline-earth metallic reagent of this nature is a Grignard; in this case, methyl-magnesium iodide (MeMgI) was chosen for testing (**Scheme 6.9**).

Regardless of the conditions employed (variations in temperature, concentration, rate/direction of addition were tested), the reaction was never observed to produce, or enable the isolation of a single product.

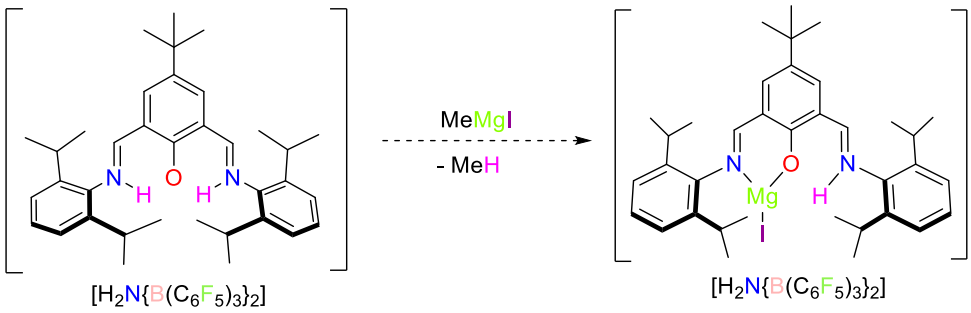

Scheme 6.9 Proposed reaction between $[H_2{}^{t\text{Bu,Dipp}}L][H_2N\{B(C_6F_5)_3\}_2]$ and MeMgI.

6.3.4.1.1 NMR spectroscopic analysis

The ^{1}H NMR spectrum of the homogenous crude reaction mixture showed that: complex **18·thf$_x$** was fully consumed, two new $[{}^{t\text{Bu,Dipp}}L]^-$ containing products had been formed and the $[H_2N\{B(C_6F_5\}_2]^-$ anion was present and intact (**Figure 6.22**).

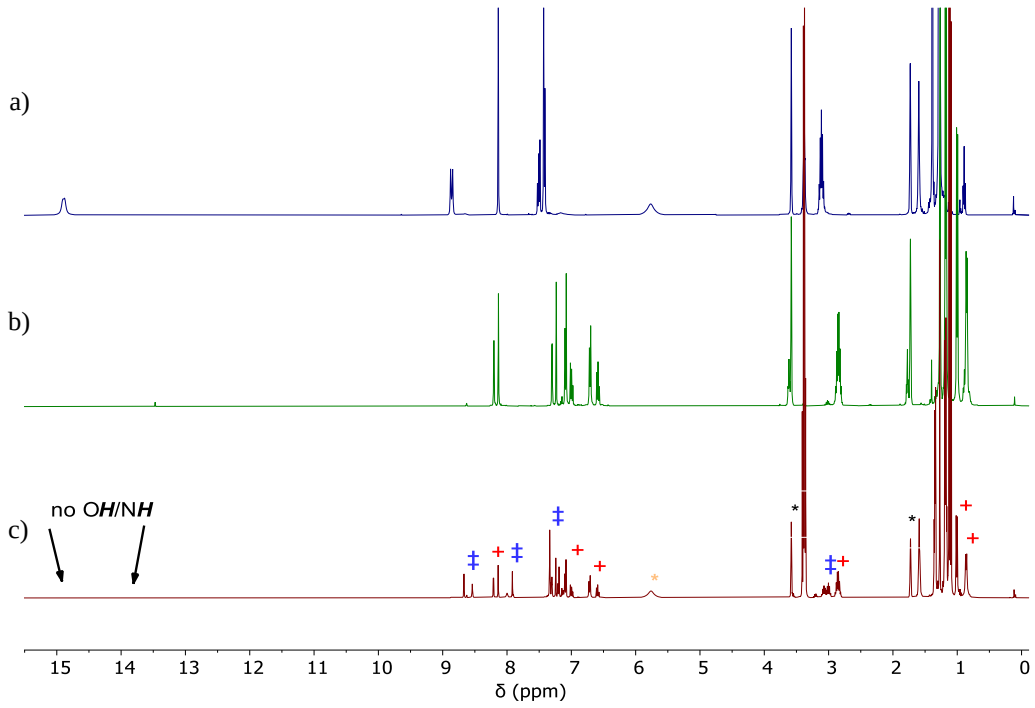

Figure 6.22 ^{1}H NMR spectra (*THF-d_8, 400 MHz, 298 K) of a) $[H_2{}^{t\text{Bu,Dipp}}L][H_2N\{B(C_6F_5)_3\}_2]$ (**18·thf$_x$**), b) *bis*(ligand) homoleptic magnesium complex (**10**, +) and c) an example crude reaction mixture. * and ‡ represent the anion and the unknown asymmetric species respectively.

The first species, typically contributing ~50% of the mixture, was the neutral, *bis*(ligand) magnesium complex **10**. The remaining, and presumably cationic, product was asymmetric (C_s) in nature; this was highlighted by the presence of two septets at δ 3.00 ppm corresponding to the *methine* protons. No N***H*** or O***H*** resonance was observed in this mixture however, suggesting that this was not the desired partially deprotonated magnesium-iodide complex (**Scheme 6.9**). Any attempts to isolate this unknown from the homoleptic species however, resulted in its decomposition and thus it remained unidentifiable.

6.3.4.2 Reaction with EtZnCl followed by alkaline-earth amides

The same reaction was then attempted using an analogous organozinc reagent: ethyl zinc chloride (EtZnCl).[74] It was hoped that the covalent bonding typically observed for zinc compared to group 2 complexes, would render the target product less prone to Schlenk-type redistribution. Stirring **18·thf$_x$** with a slight excess of EtZnCl for 18 h resulted in clean formation of the desired cationic, protonated zinc complex: $[H^{tBu,Dipp}LZnCl(thf)][H_2N\{B(C_6F_5)_3\}_2]$ (**22**). After trituration of the crude oily solid with a 1:1 pentane:ether mixture, the product was isolated as a yellow powder in 94% yield. The corresponding $BAr^F{}_4$ derivative: $[H^{tBu,Dipp}LZnCl][B(3,5\text{-}\{CF_3\}_2C_6H_3)_4]$ (**23**) was also prepared and isolated in 77% yield.

Addition of 2 eq. of ethyl zinc chloride to **18·thf$_x$** resulted in the formation of a completely deprotonated, symmetric species (**Figure A.68**). NMR spectroscopic data is consistent with the formation of a cationic *bis*(zinc chloride) system ($[^{tBu,Dipp}L\{ZnCl(thf)\}_2][H_2N\{B(C_6F_5)_3\}_2]$), however no attempts to isolate or further characterise this compound were made. This result implies that care must be taken to ensure correct reaction stoichiometry in order to obtain **22** cleanly.

6.3.4.2.1 NMR spectroscopic analysis

The ^{1}H NMR spectrum of **22** (**Figure 6.23**) is indicative of an asymmetric (C_s) “NON” system. It contains 15 signals, thus highlighting the inequivalent sides of the compound. A singlet at δ 13.69 ppm, integrating to 1H, represents the remaining N***H*** proton. The broad nature of this signal masks the expected $^{3}J_{HH}$ coupling to the adjacent imine proton. The ***H***C=NH and ***H***C=N protons are represented by the doublet ($^{3}J_{HH}$ = 13.2 Hz) and singlet at δ 9.01 and δ 8.75 ppm, respectively. The mutually coupling doublets ($^{4}J_{HH}$ = 2.8 Hz) at δ 8.22 and δ 8.01 ppm correspond to the two protons of the central aromatic ring. The imine-*aryl* C***H*** protons of the zinc-bound side of the complex appear as distinct triplet and doublet signals close to δ 7.55 and δ 7.45 ppm respectively. In contrast, the imine-*aryl* C***H*** protons of the opposite side of the molecule appear as a broad multiplet between δ 7.38–7.30 ppm. The more deshielded pair of signals correlate to the zinc-bound half of the molecule as a result of the reduction in electron density on the adjacent nitrogen centre. The broad singlet at δ 5.76 ppm represents the amine protons of the aminodiboronate anion. The *methine* and *methyl* protons of the isopropyl groups are represented by the two septets between δ 3.10–3.02 ppm and doublets between δ 1.34–1.22 ppm respectively. The final resonance at δ 1.37 ppm, which integrates to 9H, corresponds to the *tert*-butyl protons.

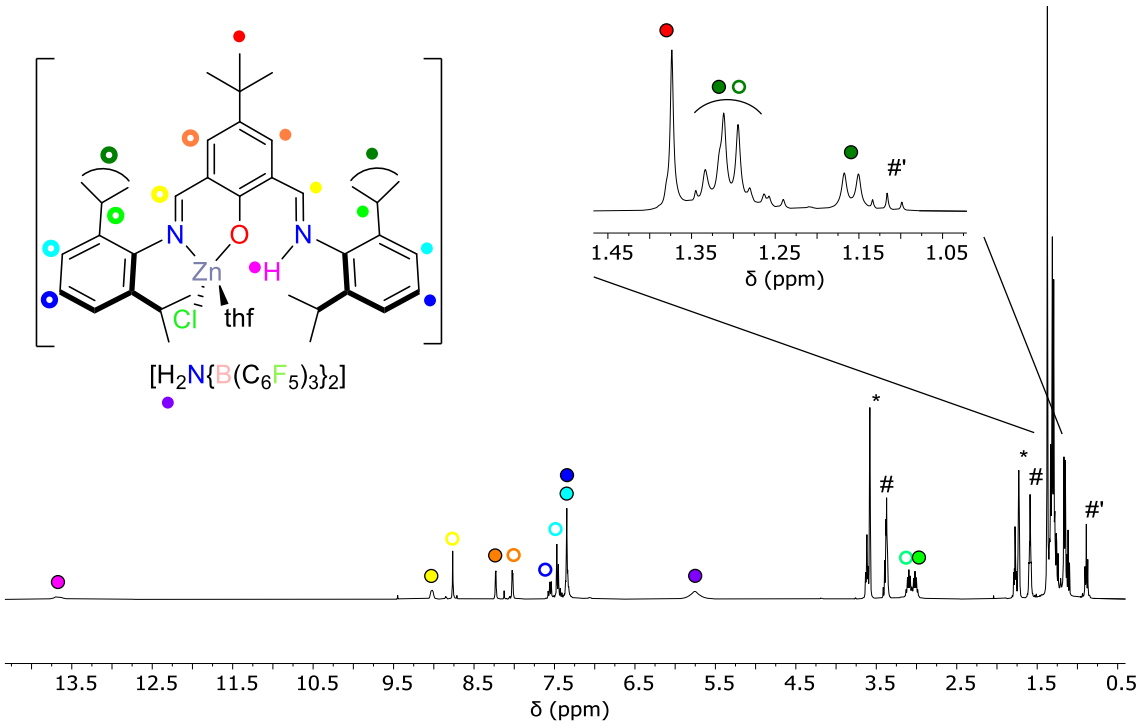

Figure 6.23 ^{1}H NMR spectrum (*THF-d_8, 400 MHz, 298 K) of [H$^{t\text{Bu,Dipp}}$LZnCl(thf)][$H_2N\{B(C_6F_5)_3\}_2$] (**22**). # and #' denote bound-thf and pentane from reaction work up respectively.

The ^{1}H NMR data for the analogous BAr^F_4 system ([H$^{t\text{Bu,Dipp}}$LZnCl][B(3,5-$\{CF_3\}_2C_6H_3)_4$]; **23**) is very similar except for the absence of signals for the exogenous thf ligand (**Figure A.69**). This indicates that the coordinated-thf is more readily lost from **23** under vacuum, probably due to differences in crystal packing or cation-anion interactions in the solid-state.

6.3.4.2.2 X-ray crystallographic analysis

Single crystals of **22**, suitable for an X-ray diffraction study, were grown from a THF/*n*-hexane mixture at –25 ºC and refined in the monoclinic space group, $P2_1/n$. The results are presented in **Figure 6.24** and **Table 6.5**. Some positional disorder in the system, caused by the [ZnCl(thf)] moiety occupying one or the other of the [=N,O$^-$] binding

pockets, was resolved by refinement of a two-component split model (occupancy 90:10). The following discussion therefore relates solely to the major component of the cation, in which the metal centre resides between the O(1) and N(1) atoms.

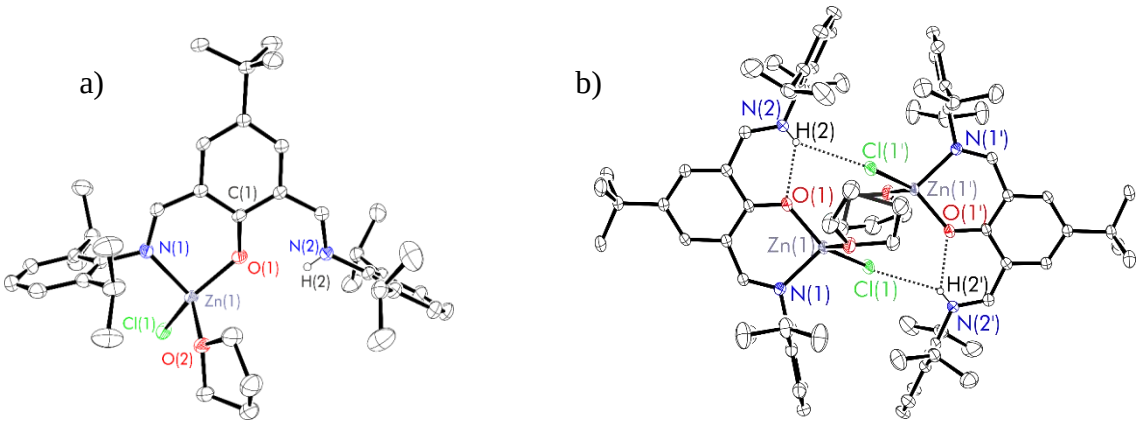

Figure 6.24 Thermal displacement ellipsoid drawings (30% probability) of a) the cation of the asymmetric unit of $[H^{tBu,Dipp}LZnCl(thf)][H_2N\{B(C_6F_5)_3\}_2]$ (**22**) and b) the hydrogen bonded dimer formed between the two cations in the unit cell.

Complex **22** is dimeric in the solid state by virtue of intermolecular N***H***···Cl hydrogen bonding interactions. The zinc centres are coordinated in a distorted tetrahedral geometry (τ_4 = 0.81); this is similar to many other reported 4-coordinate Schiff base zinc systems (τ_4 = 0.71–0.93).[75-78] A centre of inversion between the two thf molecules renders both LZn units equivalent. Furthermore, the Zn-$O_{phenoxide}$ (1.932(2) Å) and Zn-N_{imine} (2.054(3) Å) bond lengths both lie within the range of previously reported neutral phenoxy-imine zinc complexes (Zn-$O_{phenoxide}$: 1.909(3)–2.022(3) Å; Zn-N_{imine}: 1.984(3)–2.14(4) Å)[75-78]; this implies that the cationic nature of **22** doesn't significantly affect the metrical parameters of this type of system. H(2) was located *via* the difference map, and freely refined as being located on N(2). Whilst the uncoordinated imine arm is typically observed to rotate away from the oxygen to relieve steric strain, the hydrogen bonding present between H(2) and the adjacent oxygen (N^+***H***$\cdots O^-$), as confirmed *via* DFT

calculations on similarly protonated systems (see **Section 6.3.1.3**), results in the observed "closed" conformation.

Table 6.5 Experimental metrical parameters (bond lengths in Å and angles in °) of $[H^{tBu,Dipp}LZnCl(thf)][H_2N\{B(C_6F_5)_3\}_2]$ (**22**). Estimated standard deviations shown in brackets.

Zn(1)-N(1)	2.054(3)
Zn(1)-O(1)	1.932(2)
Zn(1)-Cl(1)	2.2031(9)
Zn(1)-O(2)	2.026(3)
O(1)-C(1)	1.330(4)
N(1)-C(7)	1.291(4)
N(2)-H(2)	0.73(4)
O(1)-Zn(1)-N(1)	92.96(10)
O(1)-Zn(1)-O(2)	101.17(10)
N(1)-Zn(1)-O(2)	109.01(11)
O(1)-Zn(1)-Cl(1)	136.85(8)
N(1)-Zn(1)-Cl(1)	107.96(7)
O(2)-Zn(1)-Cl(1)	106.59(8)
τ_4	0.81

A series of similar zinc "NON" systems was previously been reported by Jie and co-workers in 2019 (**Figure 6.25**).[75] These complexes were formed via treatment of the pro-ligands with $ZnCl_2$ in ethanol at room temperature. The overall structure of these compounds is very similar to that of **22**, containing an acidic ligand proton as well as tetrahedrally coordinated zinc centres. However, the second chloride ligand in Jie's systems renders them overall charge-neutral. When tested in the ROP of ε-caprolactone, all of these neutral initiators proved to be inactive, even in the presence of co-initiators such as benzyl alcohol or methyllithium.[75]

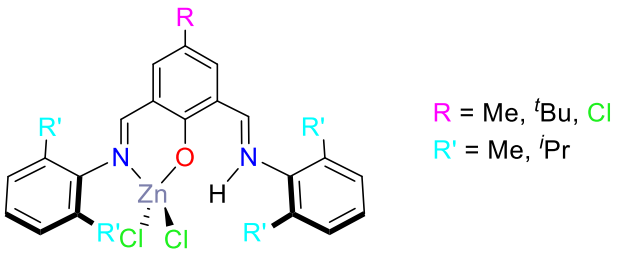

Figure 6.25 The series of neutral zinc dichloride systems reported by Jie *et al.* in 2019.[75]

Single crystals of the $[BAr^{F}{}_{4}]^{-}$ salt (**23**) were obtained from the slow diffusion of pentane into a saturated room temperature THF solution and refined in the triclinic $P\bar{1}$ space group. The cationic part is very similar to that of compound **22**, forming a hydrogen bonded dimer, with the [ZnCl(thf)] moiety disordered across both [=N,O^{-}] binding pockets (modelled in two components with occupancy 65:35). The results are presented in **Figure A.70** and **Table A.12**.

6.3.4.2.3 Solid angle calculations

The atomic coordinates of **22**, produced from X-ray crystallographic analysis, were used in solid angle calculations; the results are presented in **Figure 6.26** and **Table 6.6**.

The chloride ligand imparts less shielding than the bound-thf molecule as it resides further from the metal centre in the solid-state. This was confirmed by X-ray analysis which shows Zn-Cl: 2.2031(9) Å > Zn-O(thf): 2.026(3) (**Table 6.5**). Both of these distances however, are smaller than 2.28 Å; this explains why the shielding effects of both the chloride and thf ligands are observed to decrease when fixed at this distance from the zinc centre. A similar effect is also observed for the $^{t\text{Bu,Dipp}}$L backbone (45.25% *vs*. 35.97%); this again implies that the Schiff base framework is usually positioned much closer to the metal centre. This was confirmed by X-ray crystallographic analysis which shows that the Zn-O (1.932(2) Å) and Zn-N (2.054(3) Å) bonds are much smaller than 2.28 Å. The overall shielding of the metal is comparable to the other monometallic,

heteroleptic "NON" species reported in this thesis (*G*(M)%: 63.34% (**15**), 65.77% (**21**), 64.99 (**22**)) despite the difference in coordination geometry (**22**: distorted tetrahedral (τ_4 = 0.81) *vs.* **15**/**21**: distorted octahedral).

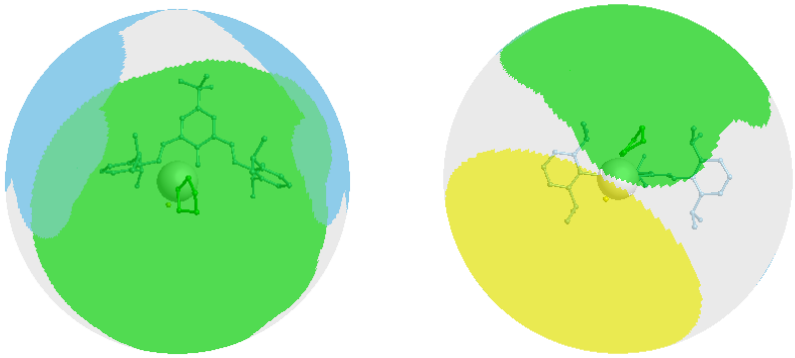

Figure 6.26 Visualisations of *G*(L) values in [H$^{t\text{Bu,Dipp}}$LZnCl(thf)][H$_2$N{B(C$_6$F$_5$)$_3$}$_2$] (**22**), showing the percentage of the complex sphere shielded by each ligand. Blue = $^{t\text{Bu,Dipp}}$L, yellow = chloride, green = thf.

Table 6.6 Summary of ligand solid angles (Ω), the percentage of the sphere shielded by the ligand (*G*), the percent of the metal surface shielded by ligand atoms (*G*(M)) and the percentage of the metal surface "in contact" with ligated atoms (*S*(M)) for [H$^{t\text{Bu,Dipp}}$LZnCl(thf)][H$_2$N{B(C$_6$F$_5$)$_3$}$_2$] (**22**).

Ligand	Ω($^{\text{Dipp}}$L) (sr)	*G*($^{\text{Dipp}}$L) (%)	$G_{2.28}$ ($^{\text{Dipp}}$L) (%)	*G*(M) (%)	*S*(M) (%)
$^{t\text{Bu,Dipp}}$L	5.69	45.25	35.97		
Cl	1.96	15.63	14.38	64.99	64.29
thf	2.30	18.33	15.23		

6.3.4.3 Addition of alkaline-earth amides to complex 22

A solution of **22** in THF-d_8 was prepared *in situ* before 1 eq. of Ca{N(SiMe$_3$)$_2$}$_2$(thf)$_2$ was added. NMR spectroscopic analysis highlighted the release of 1 eq. of the

protonolysis by-product $HN(SiMe_3)_2$, alongside the formation of a new, C_s symmetric species with different line-shapes and chemical shifts to that of the Zn/H intermediate (**22**). It is proposed that the identity of this new species is a cationic Zn/Ca "NON" bimetallic complex with the formula: [$^{t\text{Bu,Dipp}}$L{ZnCl(thf)}CaN(SiMe$_3$)$_2$][H$_2$N{B(C$_6$F$_5$)$_3$}$_2$] (**24**; **Scheme 6.10**).

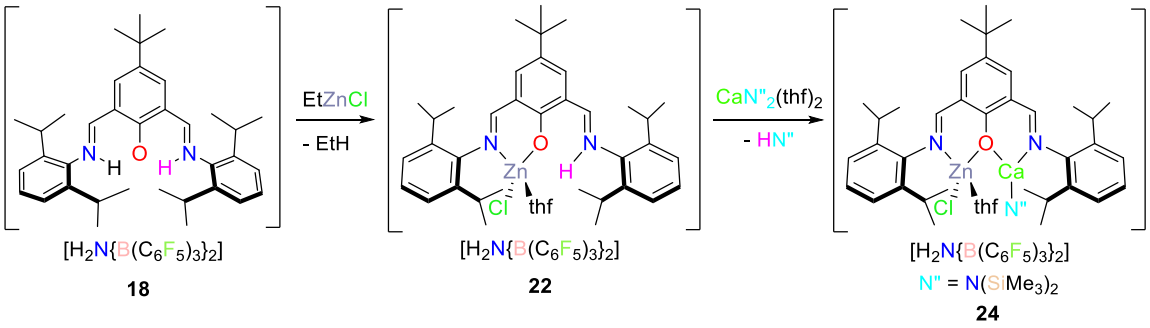

Scheme 6.10 The synthesis of [$^{t\text{Bu,Dipp}}$L{ZnCl(thf)}CaN(SiMe$_3$)$_2$][H$_2$N{B(C$_6$F$_5$)$_3$}$_2$] (**24**).

Although **24** was characterised by NMR spectroscopy *in situ* (**Section 6.3.4.3.1**), all attempts to isolate this compound (wash, extract, sublime) from the HMDS by-product resulted in decomposition. Efforts to synthesise and crystallise the analogous BAr$^F{}_4$ derivative ([$^{t\text{Bu,Dipp}}$L{ZnCl}CaN(SiMe$_3$)$_2$][B(3,5-{CF$_3$}$_2$C$_6$H$_3$)$_4$]; **25**) were also conducted (**Figure A.71**), however only crystalline samples of decomposition products were ever recovered (*vide infra*).

6.3.4.3.1 NMR spectroscopic analysis

The ^{1}H NMR spectrum of **24** is similar to that of **22**. It contains 15 resonances as a result of the asymmetric nature of the complex (**Figure 6.27**). The resonances representing the "Ca-side" of the molecule are typically more deshielded as a result of the greater ionicity/Lewis acidity of the group two metal.

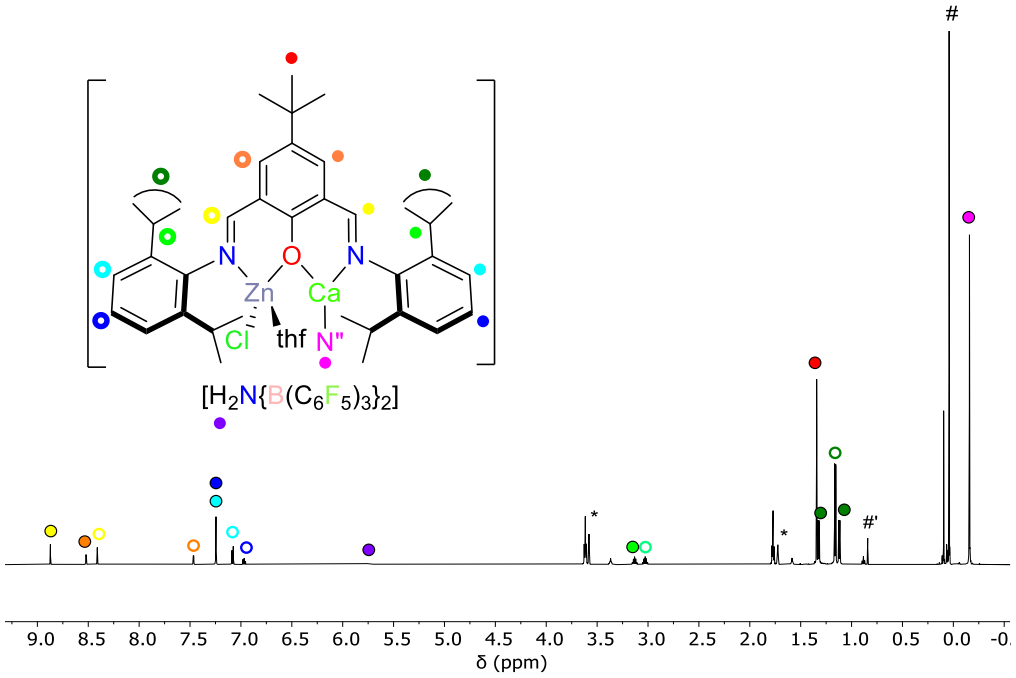

Figure 6.27 ^{1}H NMR spectrum (*THF-d_8, 400 MHz, 298 K) of [$^{t\text{Bu,Dipp}}$L{ZnCl(thf)}CaN(SiMe$_3$)$_2$][H$_2$N{B(C$_6$F$_5$)$_3$}$_2$] (**23**). # and #' denote the HN(SiMe$_3$)$_2$ and ethane synthesis by-products.

In the ^{1}H NMR spectrum of **24**, the imine ***H***C=N protons are represented by the singlets found at δ 8.87 and δ 8.41 ppm. The protons of the central aromatic ring correspond to the mutually coupling doublets ($^{4}J_{HH}$ = 2.9 Hz) at δ 8.52 and δ 7.47 ppm. The imine-*aryl* C***H*** protons of the "Ca-side" side of the molecule appear as a broad singlet at δ 7.24 ppm. In contrast, imine-*aryl* C***H*** protons of the "Zn-side" appear as distinct doublet and multiplet signals close to δ 7.08 and δ 6.97 ppm respectively. The broad singlet at δ 5.76 ppm represents the amine protons of the aminodiboronate anion. Between δ 3.13–3.03 ppm, there are two septets which represent the *methine* protons of the diisopropyl groups. The mutually coupling doublets ($^{3}J_{HH}$ = 6.8 Hz) for the diisopropyl *methyl* protons are located as three separate signals between δ 1.32 and δ 1.12 ppm. The doublet at δ 1.16 ppm integrates to 12H and represents the *methyl* protons of the isopropyl groups on the "Zn-side" of the complex. The remaining two doublets, integrating to 6H each, therefore correspond to the analogous protons on the "Ca-side". The restricted rotation,

and splitting of these *methyl* signals on the alkaline-earth side of the system, is likely due to an increased steric constraint imparted by the bulky $N(SiMe_3)_2$ group. The final two signals are singlets at δ 1.34 and δ –0.16 ppm; these represent the 9 *tert*-butyl and 18 silylamide protons respectively.

The full NMR spectroscopic assignment of this molecule was made possible through NOESY NMR experiments. Irradiation of the signal at δ –0.16 ppm allowed for the identification of the through-space NOE interactions of the $N(Si\boldsymbol{Me}_3)_2$ group and the corresponding Schiff base ligand protons on the same (Ca) side of the molecule (**Figure 6.28**).

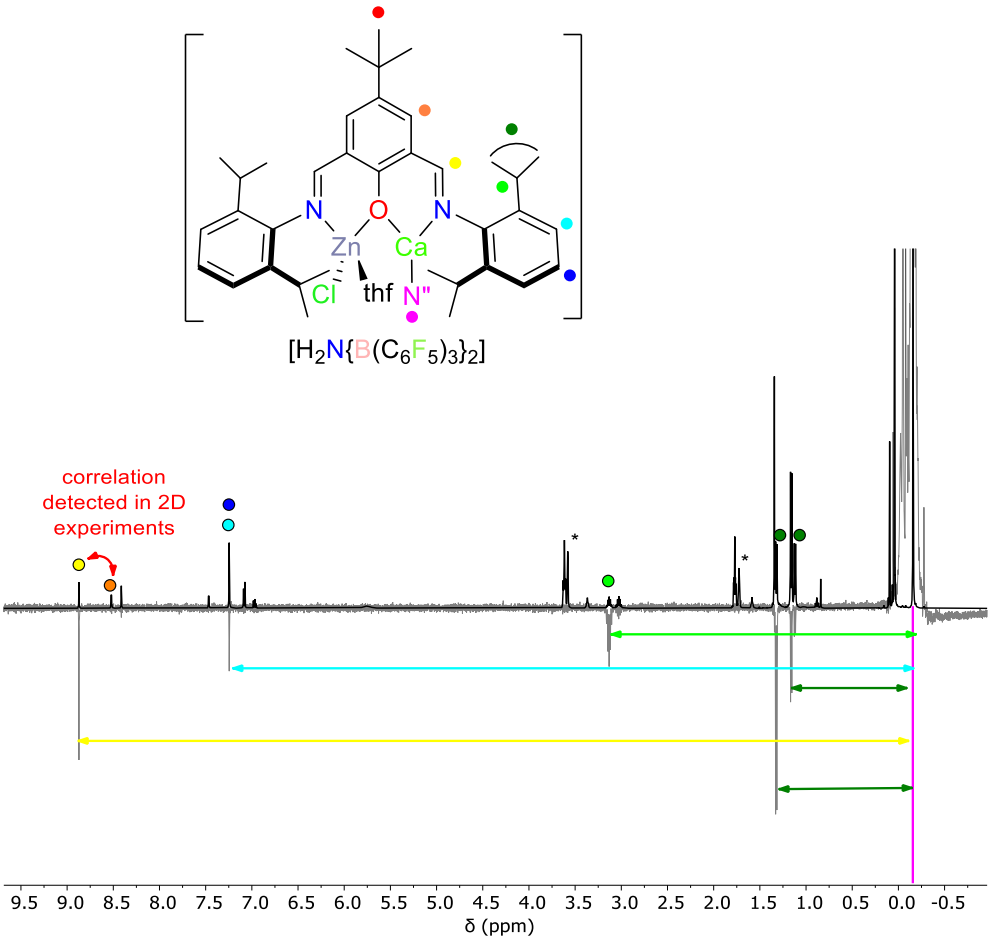

Figure 6.28 NOESY NMR spectrum (*THF-d_8, 500 MHz, 298 K) of **24**. The plot highlights the through space interactions between the $N(SiMe_3)_2$ group and the Schiff base protons of the same side of the molecule.

6.3.4.3.2 X-ray crystallographic analysis

All attempts to crystallise the Zn/Ca "NON" bimetallic systems (**24**, **25**) were unsuccessful. Slow diffusion of pentane into a saturated room temperature THF solution of **25** however, produced crystals of a decomposition product: $[Ca_4Cl_6(thf)_{12}][B(3,5\text{-}\{CF_3\}_2C_6H_3)_4]_2$ (**26**). The results of the X-ray analysis are presented in **Figure 6.29** and **Table 6.7**.

In the solid-state structure of $[Ca_4Cl_6(thf)_{12}][B(3,5\text{-}\{CF_3\}_2C_6H_3)_4]_2$ (**26**), which was refined in the monoclinic $P2_1/c$ space group, the cationic fragment contains two distinct calcium environments. Both adopt distorted octahedral coordination geometries with either two bridging chloride and four terminal thf ligands (Ca_1), or four bridging chloride and two terminal thf ligands (Ca_2). This results in a partial double cubane structure as seen in **Figure 6.29**; the stability of this species is not surprising as it could be considered as a molecular fragment of the notoriously stable $CaCl_2$ lattice. No other such Ca_4Cl_6 motif has yet been reported, to the best of our knowledge.

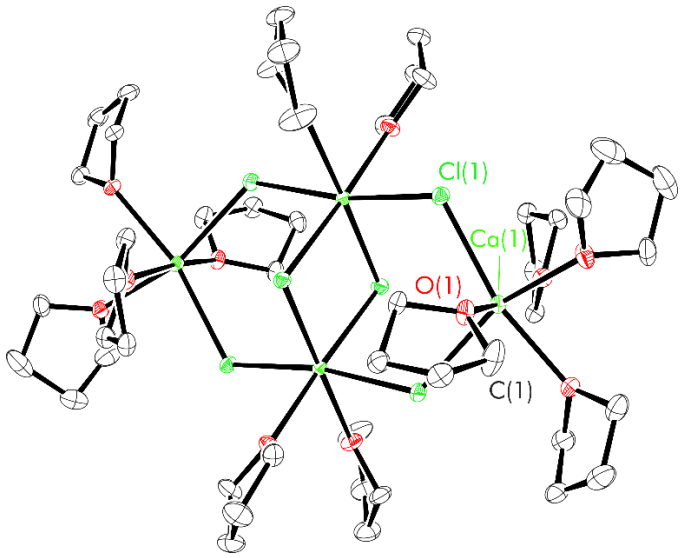

Figure 6.29 Thermal displacement ellipsoid drawings (30% probability) of the decomposition product of **23**: $[Ca_4Cl_6(thf)_{12}][B(3,5\text{-}\{CF_3\}_2C_6H_3)_4]_2$ (**26**). Cation only displayed.

Table 6.7 Experimental metrical parameters (bond lengths (Å) and angles (°)) of $[Ca_4Cl_6(thf)_{12}][B(3,5\text{-}\{CF_3\}_2C_6H_3)_4]_2$ (**26**). Estimated standard deviations shown in brackets.

Ca(1)-Cl(1)	2.6776(10)
Ca(1)-O(1)	2.363(2)
Ca(2)-Cl(1)	2.7114(10)
Ca(2)-O(5)	2.387(2)
Ca(2)-Cl(3)	2.6963(9)
Cl(1)-Ca(1)-O(1)	108.38(7)
Cl(1)-Ca(1)-Cl(2)	109.27(3)
Ca(1)-Cl(1)-Ca(2)	121.03(4)
Ca(2)-Cl(3)-Ca(3)	92.74(3)

The calcium-chloride bond lengths do not vary much depending on the type of metal environment (2.6776(10)-2.7114(10) Å); these values also coincide with those reported for comparable calcium dimers with bridging μ-Cl ligands (2.676(1)–2.7445(17) Å).[73, 79-81] Analogous conclusions can also be drawn regarding the Ca-O bonds (**26**: 2.363(2)–2.387(2) Å; lit.: 2.324(3)–2.489(2) Å).[73, 79-81]

6.4 Preliminary lactide polymerisation studies

6.4.1 General considerations for lactide polymerisation studies

Lactide polymerisations were performed in J. Young's tap NMR tubes with an initial monomer concentration ($[LA]_0$) of 0.5 M. The reactions were halted by submerging the NMR tubes in an ice bath and conversion to polylactide (PLA) was monitored by ^{1}H NMR spectroscopy. Upon completion, the reaction mixture was decanted and the resultant polymer was precipitated by addition of pentane.

Previous control polymerisations using only $H^{tBu,Dipp}L$ (and BnOH) as the catalyst displayed no activity after 24 h, even at the highest temperature studied. As a result, it

can be concluded that any observed polymerisation activity is due solely to the isolated alkaline-earth complexes (and co-catalyst if present).

6.4.2 Comparing the capabilities of neutral / cationic heteroleptic calcium initiators

Preliminary catalytic capability testing of the cationic calcium complex (**19**) was carried out and the results were compared to those of the similar neutral heteroleptic calcium iodide catalyst (**15**). Extra care had to be taken to ensure complete removal of the HMDS by-product from the isolated cationic catalyst as it was found to co-initiate the polymerisations. This was evidenced by the resultant polymers containing –OH/–$N(SiMe_3)_2$ end groups (identified from the mass spectra) – **Figure A.72**.

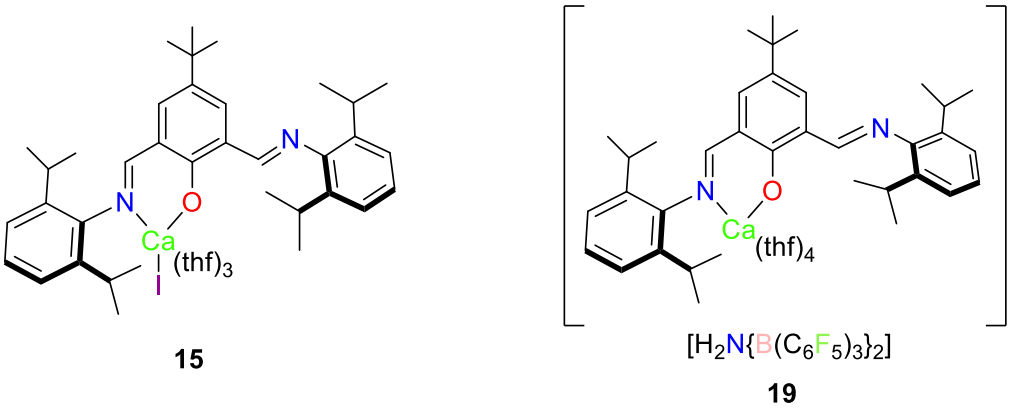

Figure 6.30 The neutral (**15**) and cationic (**19**) calcium catalysts tested as initiators for the ROP of *L*-LA.

The intentional addition of a co-initiator (BnOH) to pure catalyst was tested; the polymerisations were carried out at 60 °C in chloroform-d_1, with $[L\text{-LA}]_0$:$[\mathbf{Ca^+}]_0$:$[\text{BnOH}]_0$ = 50:1:1 and $[L\text{-LA}]_0$ = 0.5 M. The ROP of *L*-LA employing solely **19** as the catalyst proved to be relatively fast, achieving 79% conversion in 0.6 h (**Figure 6.31a**). The experimental rate was fifty times higher than that observed for complex **15** (k_{obs}: 3.01 *vs.* 0.06 h^{-1} for **19** and **15** respectively). This is likely due to the absence of the sterically hindering, non-labile halide ligand as well as, and likely more

importantly, the enhanced Lewis acidity of the cationic metal centre *vs*. its neutral counterpart. Comparable apparent rate constants (k_{obs} = 1.31–3.11 h^{-1}) have been observed for cationic zinc lactate *bis*(phosphinimine) initiators with $[LA]_0$:[**Zn**$^+$] = 200:1 at 60 °C in chloroform-d_1 (**Figure 6.2a**).[8] Furthermore, cationic calcium phenolates (**Figure 6.2b**) are also reported to exhibit experimental rate constants of the same order of magnitude as **19** (k_{obs} = 0.17–2.70 h^{-1}). These catalysts, however, were acting under immortal conditions with [*L*-LA]$_0$:[**Ca**$^+$]:[BnOH]$_0$ = 100–1000:1:100 at 60 °C in chloroform-d_1.[14]

Addition of 1 eq. of benzyl alcohol as a co-initiator saw the observed rate increase a further four-fold (k_{obs}: 3.01 *vs*. 12.27 h^{-1}; **Table 6.8**). This agrees with previous reports that show the ROP of LA is facile and well-controlled in the presence of alcohols.[82-86]

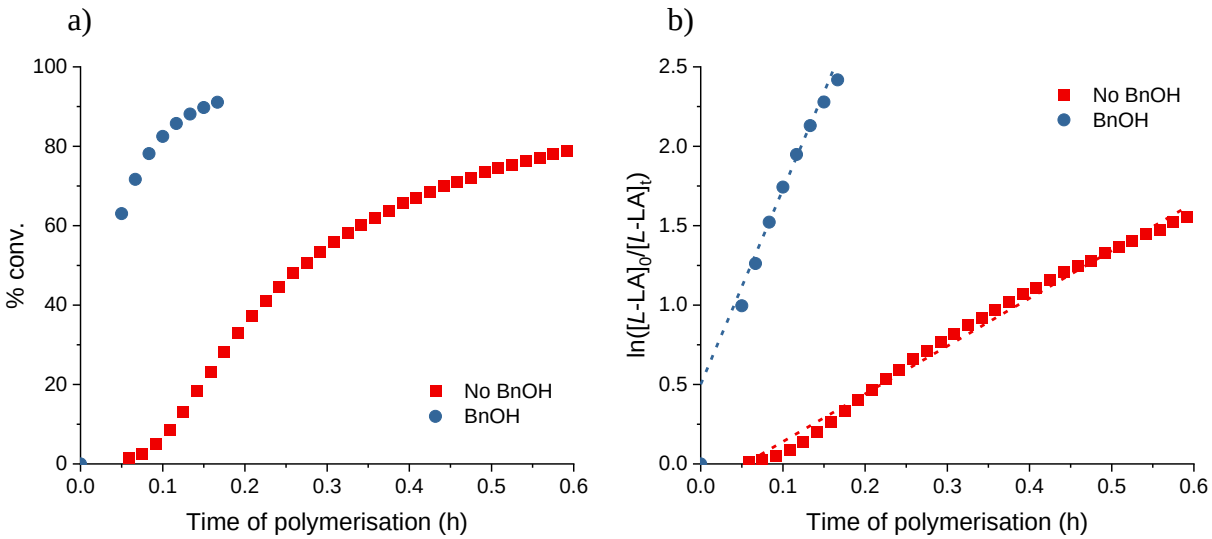

Figure 6.31 a) Plots of percentage conversion *vs.* time. b) Plots of ln([*L*-LA]$_0$/[*L*-LA]$_t$) *vs.* time for *L*-LA polymerisation using **19** with and without BnOH. Red squares: no BnOH (k_{obs} = 3.01 h^{-1}. R^2 = 0.993); blue circles: BnOH (k_{obs} = 12.27 h^{-1}. R^2 = 0.979). Conditions: [*L*-LA]$_0$:[**Ca**$^+$]$_0$(:[BnOH]$_0$) = 50:1(:1), [*L*-LA]$_0$ = 0.5 M in 0.6 mL chloroform-d_1 at 60 °C.

In both cases (i.e. with and without the co-initiator), linear plots of ln([*L*-LA]$_0$/[*L*-LA]$_t$) *vs.* time were observed, implying that the polymerisations are first-order with respect to

L-LA (**Figure 6.31b**). The polymerisation was found to proceed with only moderate control as indicated by the recorded broad polydispersity values (M_w/M_n = 1.63–1.67; **Table 6.8**) which are consistent with transesterification. When **19** is utilised in the absence of BnOH, the recorded experimental molecular weight is much larger than the calculated value (22 966 *vs.* 6430 gmol^{-1}; Δ% = 72) implying that only a fraction of the metal centres are active (**Figure 6.32**). Similar observations were made when studying the use of the neutral heteroleptic calcium complex: **15**.

Table 6.8 ROP of *L*-LA using **19** and BnOH with [*L*-LA]$_0$:[**Ca**$^+$]$_0$(:[BnOH]$_0$) = 50:1(:1) at 60 °C.[a]

BnOH	Time (h)	Conv. (%)[b]	k_{obs} (h^{-1})[c]	R^{2c}	M_n (GPC)[d]	M_n (calcd)[e]	M_w/M_n
No	0.6	79	3.01 ± 0.05	0.993	20 966	6430	1.67
Yes	0.2	91	12.27 ± 0.7	0.979	6719	6975	1.63

[a]Conditions: [*L*-LA]$_0$:[**Ca**$^+$]$_0$(:[BnOH]$_0$) = 50:1(:1), [*L*-LA]$_0$ = 0.5 M in 0.6 mL chloroform-d_1 at 60 °C. [b]Average reported; measured by ^{1}H NMR spectroscopic analyses. [c]First order rate constant and R^2 were obtained from average plots of ln([*L*-LA]$_0$/[*L*-LA]$_t$) *vs.* time. [d]Determined by GPC in THF against PS standards using the appropriate Mark-Houwink corrections.[87] [e]Calculated M_n for PLA synthesised = (conv.(%) × [*L*-LA]$_0$/[**Ca**$^+$]$_0$) × 144.13 + (M_w of end groups).

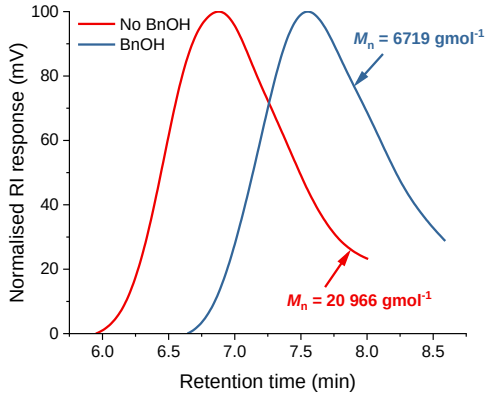

Figure 6.32 GPC traces of PLAs synthesised from the ROP of *L*-LA using **19** with and without BnOH. Red: no BnOH, M_n = 20 966 g mol^{-1}, M_w/M_n = 1.67; blue: BnOH, M_n = 6719 g mol^{-1}, M_w/M_n = 1.63. Conditions: [*L*-LA]$_0$:[**Ca**$^+$]$_0$(:[BnOH]$_0$) = 50:1(:1), [*L*-LA]$_0$ = 0.5 M in 0.6 mL chloroform-d_1 at 60 °C.

Contrastingly, there is a relatively good agreement between the experimental and theoretical molecular weights when BnOH was added as a co-initiator. This implies that benzyl alcohol activates more metal centres, thus leading to the catalyst behaving more like a single-site system. The molecular weight of the PLLA recorded in the presence of BnOH lies within the range reported for similar Ca^{2+}/BnOH systems (2600–110 600 $gmol^{-1}$ for $[LA]_0/[Ca]_0$ = 50-250:1).[69, 71-73, 88-90]

Due to the rapid nature of the *L*-LA polymerisations with the binary **19**/BnOH system, the $[L\text{-LA}]_0/[\mathbf{Ca^+}]_0$ ratio was increased to 500:1 in order to provide a more accurate comparison of the kinetic data to that of **15**/BnOH (**Figure 6.33**). The data for the comparison of the 50:1 ratios can be found in the **Figure A.73** and **Table A.13**.

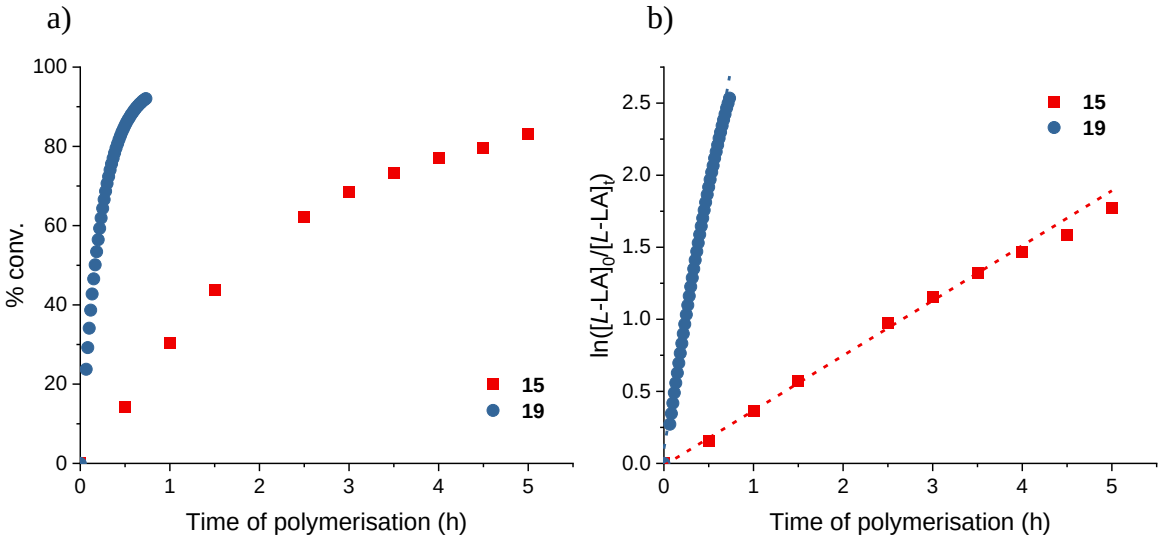

Figure 6.33 a) Plots of percentage conversion *vs.* time. b) Plots of $\ln([L\text{-LA}]_0/[L\text{-LA}]_t)$ *vs.* time for *L*-LA polymerisation. Red squares: cat = **15**/BnOH (k_{obs} = 0.38 h^{-1}. R^2 = 0.999); blue circles: cat = **19**/BnOH (k_{obs} = 3.53 h^{-1}. R^2 = 0.994). Conditions: $[L\text{-LA}]_0$:$[\mathbf{Ca^+}]_0$:$[BnOH]_0$ = 500:1:1, $[L\text{-LA}]_0$ = 0.5 M in 0.6 mL chloroform-d_1 at 60 °C.

Similar conclusions can be drawn at $[L\text{-LA}]$:$[\mathbf{Ca^+}]$ = 500:1, however, the rate of the polymerisation using the cationic calcium system (**19**) at this ratio is only ten times faster than the comparable neutral species (**15**) (k_{obs} = 3.53 *vs.* 0.38 h^{-1}; **Table 6.9**). A similar

disparity between experimental and calculated molecular weights is observed for both systems (31 065 *vs.* 59 519 gmol^{-1} and 27 287 *vs.* 66 105 gmol^{-1} for **15** and **19** respectively). Carpentier and co-workers also rationalised molecular weight discrepancies on the basis of transesterification for their cationic calcium phenolate systems in the presence of excess (5-50 eq.) co-initiator.[14] The disparity in their values (30 000 *vs.* 41 600 gmol^{-1}),[14] however, are not as large as with the **15** or **19**/BnOH systems; this suggests that in the case of **15** and **19**, not only are transesterifications occurring (confirmed by mass spectrometry), but it is also likely that there are multiple propagating polymer chains per metal centre.

Table 6.9 ROP of *L*-LA using **15**/BnOH and **19**/BnOH with [*L*-LA]$_0$:[**Ca**$^+$]$_0$:[BnOH]$_0$ = 500:1:1 at 60 °C.[a]

Catalyst	Time (h)	Conv. (%)[b]	k_{obs} (h^{-1})[c]	R^{2c}	M_n (GPC)[d]	M_n (calcd)[e]	M_w/M_n
15	5.0	83	0.38 ± 0.005	0.999	31 065	59 519	1.57
19	0.7	92	3.53 ± 0.04	0.994	27 287	66 105	1.77

[a]Conditions: [*L*-LA]$_0$:[**Ca**$^+$]$_0$:[BnOH]$_0$ = 500:1:1, [*L*-LA]$_0$ = 0.5 M in 0.6 mL chloroform-d_1 at 60 °C. [b]Average reported; measured by ^{1}H NMR spectroscopic analyses. [c]First order rate constant and R^2 were obtained from average plots of ln([*L*-LA]$_0$/[*L*-LA]$_t$) *vs.* time. [d]Determined by GPC in THF against PS standards using the appropriate Mark-Houwink corrections.[87] [e]Calculated M_n for PLA synthesised = (conv.(%) × [*L*-LA]$_0$/[**Ca**$^+$]$_0$) × 144.13 + (M_w of end groups).

6.4.3 Anion dependency in cationic zinc systems

Preliminary catalytic capability testing of the cationic zinc complexes (**22**/**23**; **Figure 6.34**) was carried out in chloroform-d_1 at 60 °C with [*L*-LA]:[**Zn**$^+$]$_0$:[BnOH]$_0$ = 50:1:1, [*L*-LA]$_0$ = 0.5 M. In the absence of co-initiator, both systems were found to be inactive with 0% conversion recorded after 3 days. Similar observations were made by Comito *et al*. in their study of cationic dizinc *bis*(pyrazolyl) alkane systems.[91]

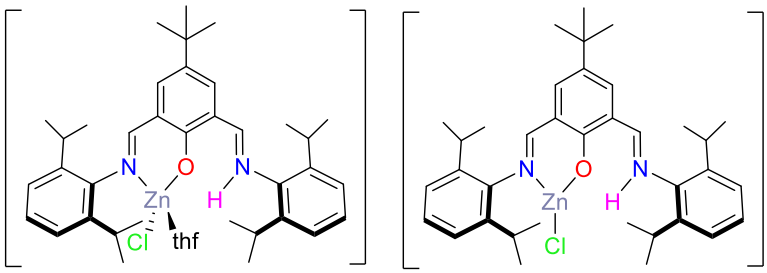

Figure 6.34 The zinc catalysts tested as initiators for the ROP of *L*-LA.

In contrast, when 1 eq. of BnOH was added, both initiators recorded activity within 24 h (**Figure 6.35**). Catalyst **22** was found to be half as active as **23** (k_{obs} = 0.00153 *vs.* 0.00307 h^{-1}; **Table 6.10**) implying that the zinc centre in the $BAr^F{}_4$ analogue is more electrophilic. Since the cationic fragment of both catalysts is near identical, this disparity in electrophilicity (and thus reactivity) is likely to be caused by the varying strength of interactions with the different anions in solution.[92] If this is the case, the $[H_2N\{B(C_6F_5\}_2]^-$ anion can be deemed less weakly coordinating thus rendering **22** less electrophilic/active. The possibility of the bound molecule of thf in **22** also affecting the rate was investigated. However, in the polymerisation mixture the signals associated with this solvent molecule appear at the expected chemical shift for free-THF. This implies that it dissociates from the metal centre during the reaction and therefore does not contribute to the difference in rate between **22** and **23**.

Such poor polymerisation activity with cationic M^{2+} systems has previously been described; it is typically attributed to the reduced nucleophilicity of the initiating group impeding the nucleophilic attack step of a coordination-insertion polymerisation pathway.[6, 14, 91, 92] End-group analysis (*vide infra*) is consistent with such a mechanism being in operation for these cationic Zn-H systems however, no further studies, such as testing co-initiator concentration dependency, were carried out to confirm this.

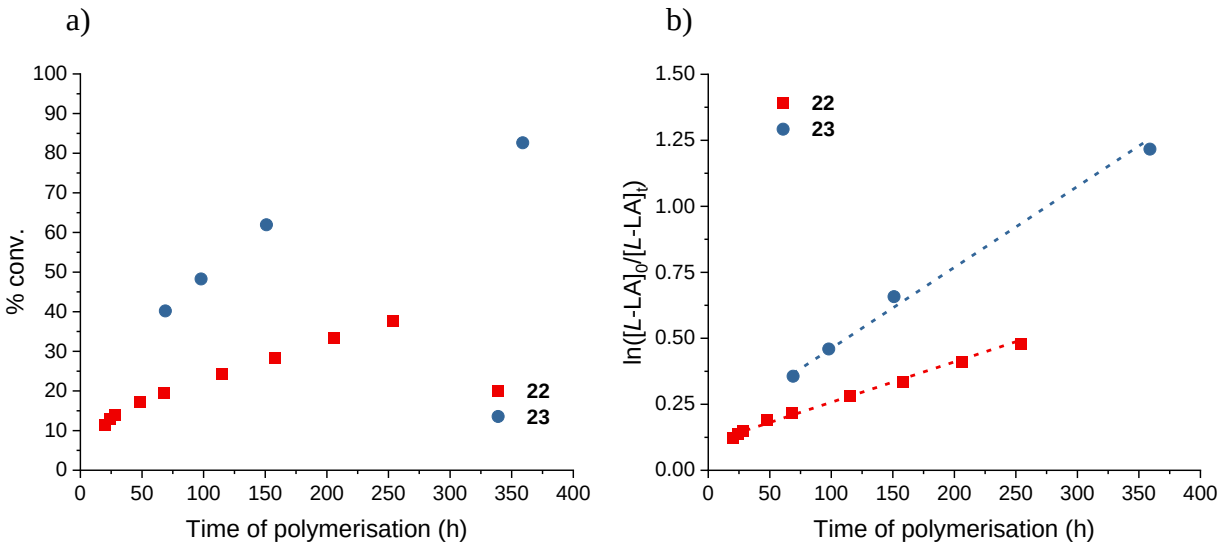

Figure 6.35 a) Plots of percentage conversion *vs.* time. b) Plots of ln([*L*-LA]$_0$/[*L*-LA]$_t$) *vs.* time for *L*-LA polymerisation. Red squares: cat = **22**/BnOH (k_{obs} = 0.00153 h^{-1}. R^2 = 0.981); blue circles: cat = **23**/BnOH (k_{obs} = 0.00307 h^{-1}. R^2 = 0.990). Conditions: [*L*-LA]$_0$:[**Zn**$^+$]$_0$:[BnOH]$_0$ = 50:1:1, [*L*-LA]$_0$ = 0.5 M in 0.6 mL chloroform-d_1 at 60 °C.

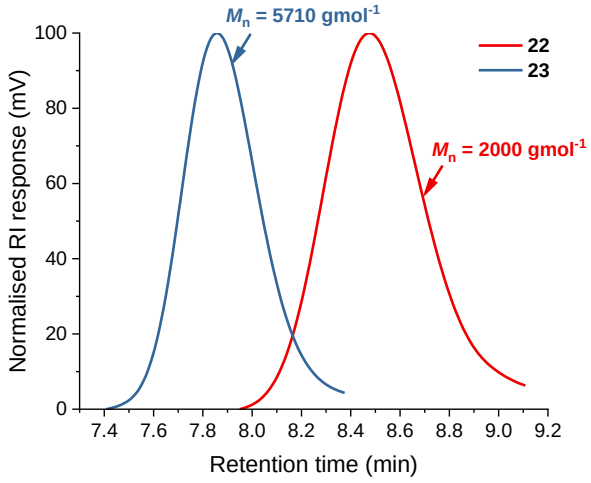

Figure 6.36 GPC traces of PLAs synthesised from the ROP of *L*-LA. Red: **22**/BnOH, M_n = 2000 g mol^{-1}, M_w/M_n = 1.14; blue: **23**/BnOH, M_n = 5710 g mol^{-1}, M_w/M_n = 1.08. Conditions: [*L*-LA]$_0$:[**Zn**$^+$]$_0$:[BnOH]$_0$ = 50:1:1, [*L*-LA]$_0$ = 0.5 M in 0.6 mL chloroform-d_1 at 60 °C.

The polymers produced by both catalysts had a good agreement between experimental and calculated molecular weights and narrow molecular weight distributions (M_w/M_n = 1.08–1.14; **Figure 6.36**).

Table 6.10 ROP of *L*-LA using **22**/BnOH and **23**/BnOH with $[L\text{-LA}]_0:[\mathbf{Zn}^+]_0:[\text{BnOH}]_0 = 50:1:1$ at 60 °C.[a]

Catalyst	Time (h)	Conv. (%)[b]	k_{obs} (h^{-1})[c]	R^{2c}	M_n (GPC)[d]	M_n (calcd)[e]	M_w/M_n
22	254.0	38	0.00153 ± 0.00005	0.981	2000	2321	1.14
23	359.0	66	0.00307 ± 0.0002	0.990	5710	6063	1.08

[a]Conditions: $[L\text{-LA}]_0:[\mathbf{Zn}^+]_0:[\text{BnOH}]_0 = 50:1:1$, $[L\text{-LA}]_0 = 0.5$ M in 0.6 mL chloroform-d_1 at 60 °C. [b]Average reported; measured by ^{1}H NMR spectroscopic analyses. [c]First order rate constant and R^2 were obtained from average plots of $\ln([L\text{-LA}]_0/[L\text{-LA}]_t)$ *vs.* time. [d]Determined by GPC in THF against PS standards using the appropriate Mark-Houwink corrections.[87] [e]Calculated M_n for PLA synthesised = (conv.(%) × $[L\text{-LA}]_0/[\mathbf{Zn}^+]_0$) × 144.13 + ($M_w$ of end groups).

6.4.4 Investigating the catalytic capability of the cationic Zn/Ca bimetallics

Due to the sensitive nature of the Zn/Ca bimetallic cations **24** and **25** (**Section 6.3.4.3**), it was decided that preliminary polymerisation testing would be conducted using the *in situ* prepared initiator. The resultant stock solution would therefore include a quantifiable amount of the $HN(SiMe_3)_2$ synthesis by-product. However, all attempts to prepare solutions of **24** or **25** in the polymerisation solvents used throughout this Thesis (chloroform-d_1 or benzene-d_6) resulted in catalyst degradation. As a result, it was concluded that these bimetallic systems are unsuitable initiators for the solution ROP of LA under the typical polymerisation conditions employed in this Thesis. The use of these systems in the melt ROP of LA was not investigated and therefore should be considered.

6.4.5 Polymer end group analysis

Matrix-assisted laser desorption/ionisation time of flight (MALDI-TOF) mass spectrometry and NMR spectroscopy were used to determine the end groups of the polymers produced using the **19**(/BnOH), **22**/BnOH and **23**/BnOH catalytic systems; representative spectra are presented in **Figures 6.37**-**6.39**.

The mass spectra of the polymers produced using the binary **catalyst**/BnOH systems are consistent with PLA containing the expected –OCH_2Ph and –OH end groups. For example, in the mass spectrum of the polymer produced using **22**/BnOH (**Figure 6.37**), the peak centred at 1588.7 $gmol^{-1}$ is attributed to –OCH_2Ph/–OH terminated PLA, comprising of 10 units of LA with K^+ [144.13(10) + 108.14 + 39.1]. Furthermore, in all cases, a 72 *m*/*z* separation between the peaks was observed thus confirming the occurrence of transesterification reactions during the polymersiations.[83, 85, 86, 93, 94]

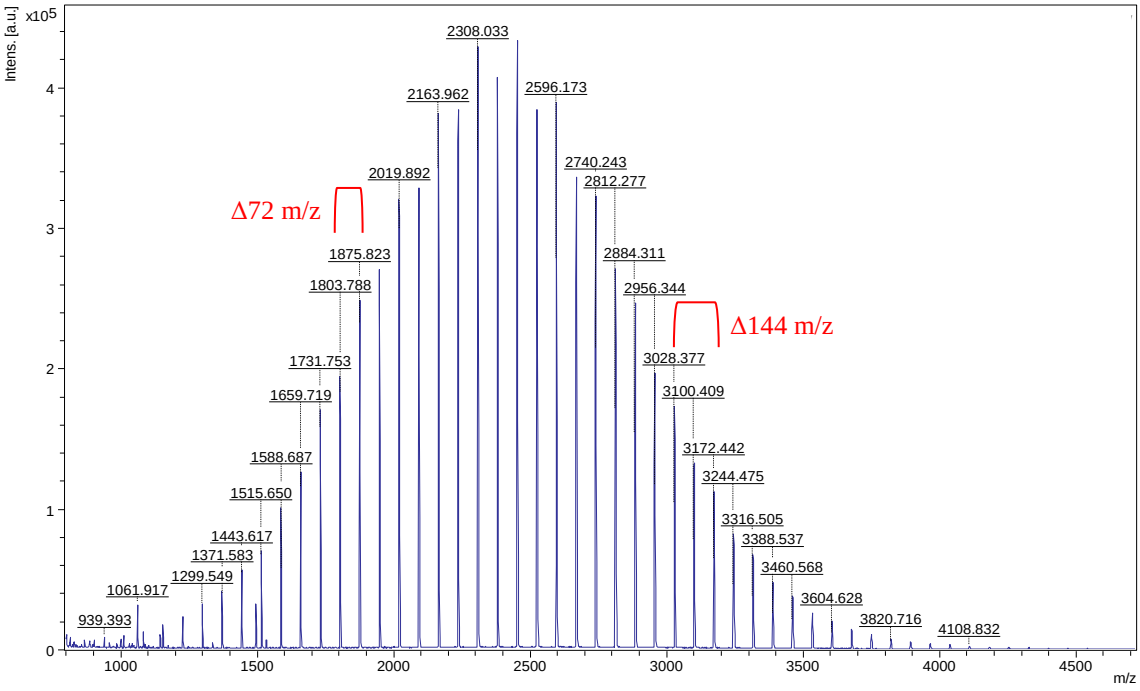

Figure 6.37 MALDI-TOF mass (*m*/*z*) spectrum of PLA produced using **22**/BnOH. Conditions: [*L*-LA]$_0$:[$\mathbf{Zn^+}$]$_0$:[BnOH] = 50:1:1, [*L*-LA]$_0$ = 0.5 M, 0.6 mL chloroform-d_1, 60 °C. M_w/M_n = 1.14.

The benzyl alcohol end group was also detected in the ^1H and $^{13}C\{^1H\}$ NMR spectra (examples shown in **Figure 6.38** and **Figures A.74-76**); for example, in the ^1H NMR spectrum of the PLA produced using **19**/BnOH, a multiplet at δ 4.39 ppm corresponds to the –C***H***(CH_3)OH proton and the aromatic signals of the –OCH_2***Ph*** group appear at δ 7.28–7.40 ppm.

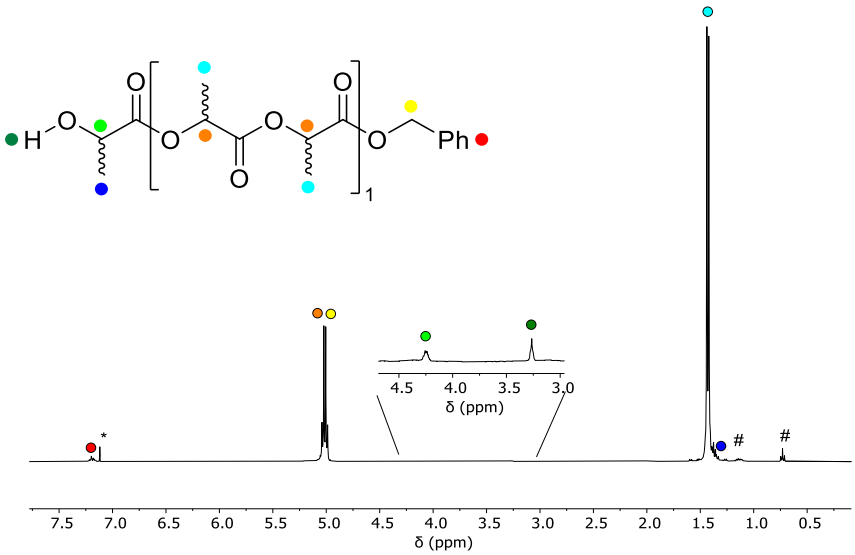

Figure 6.38 ^{1}H NMR spectrum (*choroform-d_1, 400 MHz, 298 K) of PLA isolated from a polymerisation catalysed by complex **19**/BnOH. Conditions: [*L*-LA]$_0$:[**Ca**$^+$]$_0$:[BnOH]$_0$ = 50:1:1, [*L*-LA]$_0$ = 0.5 M, 0.6 mL chloroform-d_1, 60 °C. M_w/M_n = 1.63.

In the case where **19** was used without BnOH, the MALDI-TOF spectrum indicated that the ligand was incorporated as a polymer end group. For example, in the mass spectrum (**Figure 6.39**), the peak centred at 4993.9 gmol^{-1} is attributed to $-^{t\text{Bu,Dipp}}$L/–OH terminated PLA, comprising of 31 units of LA [144.13(31) + 524.79] (no KTFA cationising agent added in this experiment). This is unusual as in the absence of both a dedicated initiating group/co-initiator, PLA could be expected to be cyclic or –OH terminated. This result instead implies that when employing **19** as the catalyst, polymerisation initiation occurs through a Ca-ligand bond. It is proposed that this monomer insertion occurs into the Ca-O$_{\text{phenoxide}}$ bond, as the residual phenolic proton that would be present (upon hydrolysis) if the alternative Ca-N$_{\text{imine}}$ initiation had occurred is not present in the ^{1}H NMR spectrum of the resultant polymer (**Figure 6.40**). Furthermore, the presence of more than one signal in the aromatic region suggests that the imine functionalities remain unchanged. Similar findings have previously been reported for

analogous alkaline-earth phenoxy-imine systems[95]; these observations were not made however, when testing the neutral "NON" complexes prepared in this Thesis (**10**-**15**).

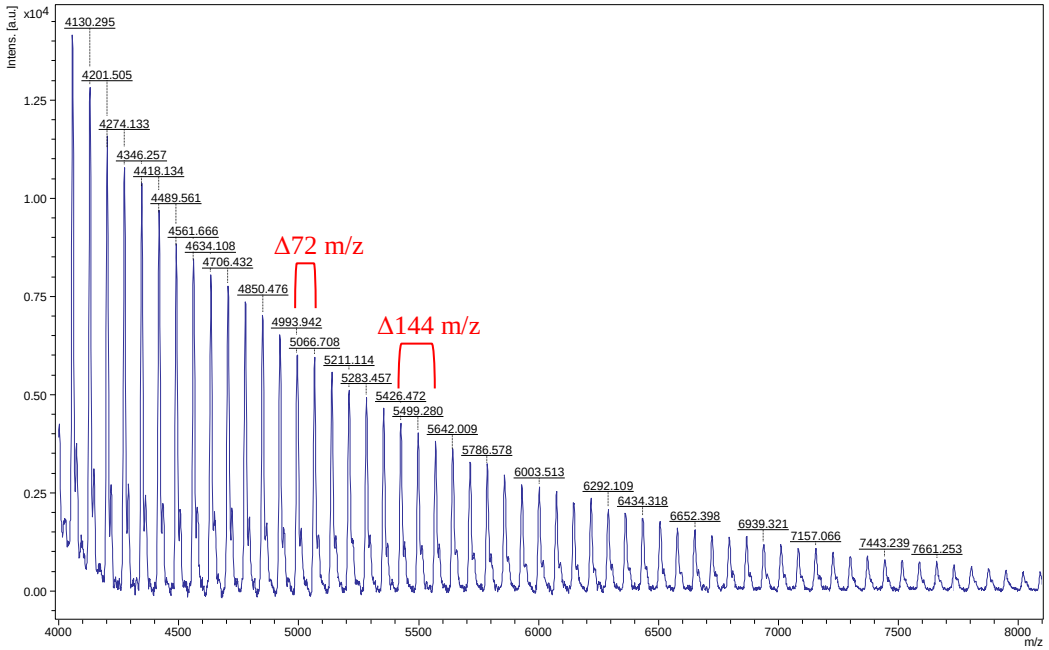

Figure 6.39 MALDI-TOF mass (*m/z*) spectrum of PLA produced using **19**. Conditions: [*L*-LA]$_0$:[**Ca**$^+$]$_0$ = 50:1, [*L*-LA]$_0$ = 0.5 M, 0.6 mL chloroform-d_1, 60 °C. M_w/M_n = 1.67.

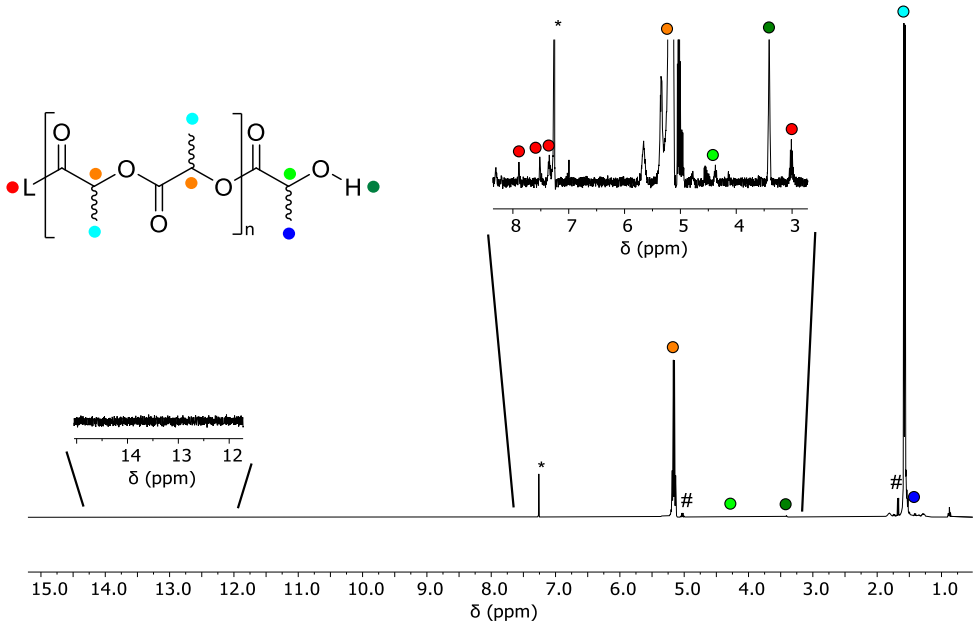

Figure 6.40 ^{1}H NMR spectrum (*choroform-d_1, 400 MHz, 298 K) of PLA isolated from a polymerisation catalysed by complex **19**. Conditions: [*L*-LA]$_0$:[**Ca**$^+$]$_0$ = 50:1, [*L*-LA]$_0$ = 0.5 M, 0.6 mL chloroform-d_1, 60 °C. M_w/M_n = 1.67.

6.5 Conclusions

While the heteroleptic calcium iodide complex **15** did not prove to be a useful intermediate in the synthesis of "NON" bimetallic systems, the observation of pro-ligand protonation opened up a new synthetic pathway via protonolysis using a cationic protonated pro-ligand.

As a result, a study into the synthesis and full characterisation of a *bis*(phenoxy-imine) diacid (**16·thf$_x$**) was conducted. Spectroscopic, X-ray diffraction and DFT analysis showed that the doubly protonated cation adopts an unusual C_{2v} symmetric *bis*(iminium) tautomer: $[HN<O>NH]^+$ (acidic protons have pK_a = 4.2 (THF), 11.4 (acetonitrile)) as a result of increased resonance stabilisation in this conformation. The reactivity of this species with alkaline-earth amides however, resulted in fluoride abstraction from the tetrafluoroborate anion and subsequent formation of a BF_2-containing Schiff base (**17**).

An analogous protonated pro-ligand, incorporating the Bochmann anion $[H_2N\{B(C_6F_5)_3\}_2]^-$, was subsequently synthesised and characterised (**18**). Treatment of this species with $Ca\{N(SiMe_3)_2\}_2(thf)_2$ resulted in the formation of the cationic species: $[^{t\text{Bu,Dipp}}LCa(thf)_4][H_2N\{B(C_6F_5)_3\}_2]$ (**19**). Attempts to remove only a single acidic proton from **18·thf$_x$** with the use of a Grignard reagent were unsuccessful due to favoured formation of the neutral homoleptic magnesium complex **10**. By contrast, the analogous reaction with ethyl zinc chloride, was successful and enabled the isolation of a cationic Zn/H species: $[H^{t\text{Bu,Dipp}}LZnCl(thf)][H_2N\{B(C_6F_5)_3\}_2]$ (**22**).

NMR spectroscopic studies suggest that addition of 1 eq. of $Ca\{N(SiMe_3)_2\}_2(thf)_2$ to **22** results in the formation of the desired, cationic Zn/Ca "NON" bimetallic complex: $[^{t\text{Bu,Dipp}}L\{ZnCl(thf)\}CaN(SiMe_3)_2][H_2N\{B(C_6F_5)_3\}_2]$ (**24**). However, all attempts to isolate/crystallise this compound have resulted in its decomposition.

In some cases, the $[BAr^F_4]^-$ analogues of these systems were synthesised to aid full structural characterisation owing to favourable crystallisation properties compared to the Bochmann anion. Complexes $[H_2{}^{t\text{Bu,Dipp}}L][B(3,5\text{-}\{CF_3\}_2C_6H_3)_4]$ (**20·thf$_x$**), $[{}^{t\text{Bu,Dipp}}LCa(thf)_4][B(3,5\text{-}\{CF_3\}_2C_6H_3)_4]$ (**21**), $[H{}^{t\text{Bu,Dipp}}LZnCl][B(3,5\text{-}\{CF_3\}_2C_6H_3)_4]$ (**23**) and $[{}^{t\text{Bu,Dipp}}L\ \{ZnCl\}CaN(SiMe_3)_2][B(3,5\text{-}\{CF_3\}_2C_6H_3)_4]$ (**25**) were synthesised by analogous procedures to the Bochmann-derivatives and fully characterised.

Complexes **19** and **22–25** were all tested as initiators for the ring-opening polymerisation of lactide. Both with and without the addition of a co-initiator, catalyst **19** was found to be more active than the comparable neutral analogue (**15**; k_{obs} = 3.53 *vs.* 0.38 h^{-1}). This is attributed to the increased Lewis acidity of the cationic calcium centre.

In the absence of BnOH, the zinc chloride complexes (**22** and **23**) were found to be inactive. Upon addition of co-initiator, the ROP was found to proceed but at very slow rates. Use of $[BAr^F_4]^-$ resulted in a doubling of the apparent rate constant (k_{obs} = 0.00153 and 0.00307 h^{-1} for **22** and **23** respectively); this is likely due to the more weakly coordinating nature of this anion making the catalytic centre more electrophilic.

Unfortunately, all attempts to perform polymerisations with the bimetallic Zn/Ca catalysts (**24**/**25**) resulted in complex degradation. As a result, it can be concluded that these species are unsuitable initiators for the ROP of LA under the typical polymerisation conditions employed in this Thesis ($[LA]_0$:$[\mathbf{M}]_0$ = 50:1, $[LA]_0$ = 0.5 M, 0.6 mL chloroform-d_1 or benzene-d_6, 60 °C). It is however promising, that spectroscopic studies suggest that these cationic bimetallic systems can be selectively formed in solution. It would be worthwhile to utilise species such as these under different polymerisation conditions in order to investigate their M-M cooperativity, but further work is required to establish a reliable route to isolate stable cationic bimetallic complexes in bulk purity.

6.6 References

1. V. C. Gibson, D. Nienhuis, C. Redshaw, A. J. P. White and D. J. Williams, *Dalton Trans.*, 2004, 1761-1765.
2. H.-C. Chiu, A. Koley, P. L. Dunn, R. J. Hue and I. A. Tonks, *Dalton Trans.*, 2017, **46**, 5513-5517.
3. S. J. Na, D. J. Joe, S. S, W.-S. Han, S. O. Kang and B. Y. Lee, *J. Organomet. Chem.*, 2006, **691**, 611-620.
4. X.-M. Chen, L.-C. Huang and W. Gao, *Dalton Trans.*, 2021, **50**, 5218-5225.
5. C. A. Wheaton and P. G. Hayes, *Comments Inorg. Chem.*, 2011, **32**, 127-162.
6. C. A. Wheaton, B. J. Ireland and P. G. Hayes, *Organometallics*, 2009, **28**, 1282-1285.
7. H. Sun, J. S. Ritch and P. G. Hayes, *Inorg. Chem.*, 2011, **50**, 8063-8072.
8. C. A. Wheaton and P. G. Hayes, *Catal. Sci. Technol.*, 2012, **2**, 125-138.
9. B. J. Ireland, C. A. Wheaton and P. G. Hayes, *Organometallics*, 2010, **29**, 1079-1084.
10. C. A. Wheaton and P. G. Hayes, *Dalton Trans.*, 2010, **39**, 3861-3869.
11. H. Sun, J. S. Ritch and P. G. Hayes, *Dalton Trans.*, 2012, **41**, 3701-3713.
12. Y. Sarazin, V. Poirier, T. Roisnel and J.-F. Carpentier, *Eur. J. Inorg. Chem.*, 2010, 3423-3428.
13. B. Liu, T. Roisnel and Y. Sarazin, *Inorg. Chim. Acta*, 2012, **380**, 2-13.
14. Y. Sarazin, B. Liu, T. Roisnel, L. Maron and J.-F. Carpentier, *J. Am. Chem. Soc.*, 2011, **133**, 9069-9087.
15. B. Liu, T. Roisnel, L. Maron, J.-F. Carpentier and Y. Sarazin, *Chem. Eur. J.*, 2013, **19**, 3986-3994.
16. C. Goonesinghe, H.-J. Jung, H. Roshandel, C. Diaz, H. A. Baalbaki, K. Nyamayaro, M. Ezhova, K. Hosseini and P. Mehrkhodavandi, *ACS Catal.*, 2022, **12**, 7677-7686.
17. M. G. Cushion and P. Mountford, *Chem. Commun.*, 2011, **47**, 2276-2278.
18. B. Liu, V. Dorcet, L. Maron, J.-F. Carpentier and Y. Sarazin, *Eur. J. Inorg. Chem.*, 2012, **2012**, 3023-3031.
19. Y. Sarazin, M. Schormann and M. Bochmann, *Organometallics*, 2004, **23**, 3296-3302.
20. K. Hiroshi, S. Takaaki, I. Hidetoshi and Y. Masaji, *Chem. Lett.*, 1981, **10**, 579-580.
21. A. J. Martínez-Martínez and A. S. Weller, *Dalton Trans.*, 2019, **48**, 3551-3554.
22. E. Schiebel, M. Voccia, L. Falivene, I. Göttker-Schnetmann, L. Caporaso and S. Mecking, *Angew. Chem. Int. Ed.*, 2021, **60**, 18472-18477.
23. B. Dutta, P. Bag, B. Adhikary, U. Flörke and K. Nag, *J. Org. Chem.*, 2004, **69**, 5419-5427.
24. G. Socrates, *Infrared and Raman characteristic group frequencies: tables and charts*, John Wiley & Sons, 2004.
25. E. Arunan, G. R. Desiraju, R. A. Klein, J. Sadlej, S. Scheiner, I. Alkorta, D. C. Clary, R. H. Crabtree, J. J. Dannenberg, P. Hobza, H. G. Kjaergaard, A. C. Legon, B. Mennucci and D. J. Nesbitt, *Pure Appl. Chem.*, 2011, **83**, 1637-1641.

26. P. E. Hansen, M. Vakili, F. S. Kamounah and J. Spanget-Larsen, *Molecules*, 2021, **26**, 7651.
27. V. Vasylyeva, L. Catalano, C. Nervi, R. Gobetto, P. Metrangolo and G. Resnati, *CrystEngComm*, 2016, **18**, 2247-2250.
28. B. Brzezinski, Z. Rozwadowski, T. Dziembowska and G. Zundel, *J. Mol. Struct.*, 1998, **440**, 73-79.
29. Z. Rozwadowski, T. Dziembowska, G. Schroeder and B. Brzezinski, *J. Mol. Struct.*, 1998, **444**, 221-225.
30. L. Han, J. Du, H. Yang, H. Wang, X. Leng, A. Galstyan, S. Zarić and W.-H. Sun, *Inorg. Chem. Commun.*, 2003, **6**, 5-9.
31. D. Esteban-Gómez, C. Platas-Iglesias, F. Avecilla, A. de Blas and T. Rodríguez-Blas, *Eur. J. Inorg. Chem.*, 2007, 1635-1643.
32. X. Wang, K.-Q. Zhao, M. R. J. Elsegood and C. Redshaw, *Supramol. Chem.*, 2018, **30**, 404-410.
33. S. Majumder, M. Fleck, C. R. Lucas and S. Mohanta, *J. Mol. Struct.*, 2012, **1020**, 127-133.
34. S. Hazra, S. Majumder, M. Fleck, R. Koner and S. Mohanta, *Polyhedron*, 2009, **28**, 2871-2878.
35. J. T. Burke, *J. Chem. Educ.*, 1997, **74**, 1213.
36. L. Sobczyk, M. Obrzud and A. Filarowski, *Molecules*, 2013, **18**, 4467-4476.
37. H. H. Limbach, J. Hennig and J. Stulz, *J. Chem. Phys.*, 1983, **78**, 5432-5436.
38. M. Rozenberg, G. Shoham, I. Reva and R. Fausto, *Spectrochim. Acta, Pt. A: Mol. Biomol. Spectrosc.*, 2004, **60**, 2323-2336.
39. S. Ghosh, R. R. Gowda, R. Jagan and D. Chakraborty, *Dalton Trans.*, 2015, **44**, 10410-10422.
40. W. Yang, K.-Q. Zhao, B.-Q. Wang, C. Redshaw, M. R. J. Elsegood, J.-L. Zhao and T. Yamato, *Dalton Trans.*, 2016, **45**, 226-236.
41. A. Patra, S. Chakraborty, S. Lohar, E. Zangrando and P. Chattopadhyay, *Inorg. Chim. Acta*, 2021, **525**, 120493.
42. L. Qu, T. Roisnel, M. Cordier, D. Yuan, Y. Yao, B. Zhao and E. Kirillov, *Inorg. Chem.*, 2020, **59**, 16976-16987.
43. E. Schiebel, M. Voccia, L. Falivene, L. Caporaso and S. Mecking, *ACS Catal.*, 2021, **11**, 5358-5368.
44. L. Wang, W.-H. Sun, L. Han, Z. Li, Y. Hu, C. He and C. Yan, *J. Organomet. Chem.*, 2002, **650**, 59-64.
45. P. Pyykkö, *J. Phys. Chem. A*, 2015, **119**, 2326-2337.
46. A. Bondi, *J. Phys. Chem.*, 1964, **68**, 441-451.
47. R. S. Rowland and R. Taylor, *J. Phys. Chem.*, 1996, **100**, 7384-7391.
48. J. M. Guevara-Vela, E. Romero-Montalvo, A. Costales, Á. M. Pendás and T. Rocha-Rinza, *Phys. Chem. Chem. Phys.*, 2016, **18**, 26383-26390.
49. R. F. W. Bader and H. Essén, *J. Chem. Phys.*, 1984, **80**, 1943-1960.
50. P. S. V. Kumar, V. Raghavendra and V. Subramanian, *J. Chem. Sci.*, 2016, **128**, 1527-1536.

51. R. Parthasarathi, V. Subramanian and N. Sathyamurthy, *J. Phys. Chem. A*, 2006, **110**, 3349-3351.

52. S. Emamian, T. Lu, H. Kruse and H. Emamian, *J. Comput. Chem.*, 2019, **40**, 2868-2881.

53. T. Rodima, V. Mäemets and I. Koppel, *J. Chem. Soc., Perkin Trans. 1*, 2000, 2637-2644.

54. S. Tshepelevitsh, A. Kütt, M. Lõkov, I. Kaljurand, J. Saame, A. Heering, P. G. Plieger, R. Vianello and I. Leito, *Eur. J. Org. Chem.*, 2019, 6735-6748.

55. K. Abdur-Rashid, T. P. Fong, B. Greaves, D. G. Gusev, J. G. Hinman, S. E. Landau, A. J. Lough and R. H. Morris, *J. Am. Chem. Soc*, 2000, **122**, 9155-9171.

56. J. B. Holbrook, R. Sabry-Grant, B. C. Smith and T. V. Tandel, *J. Chem. Educ.*, 1990, **67**, 304.

57. C. Lorbeer, F. Behrends, J. Cybinska, H. Eckert and A.-V. Mudring, *J. Mater. Chem. C*, 2014.

58. H. H. T. Al-Sharif, R. Ziessel, P. G. Waddell, C. Dixon and A. Harriman, *J. Phys. Chem. A*, 2020, **124**, 2160-2172.

59. S. Guieu, F. Cardona, J. Rocha and A. M. S. Silva, *New J. Chem.*, 2014, **38**, 5411-5414.

60. P. A. A. M. Vaz, J. Rocha, A. M. S. Silva and S. Guieu, *New J. Chem.*, 2018, **42**, 18166-18171.

61. T. N. Moshkina, E. V. Nosova, G. N. Lipunova, M. S. Valova, O. S. Taniya, P. A. Slepukhin and V. N. Charushin, *J. Fluorine Chem.*, 2019, **221**, 17-24.

62. J. A. Riddle, S. P. Lathrop, J. C. Bollinger and D. Lee, *J. Am. Chem. Soc.*, 2006, **128**, 10986-10987.

63. L. Yang, D. R. Powell and R. P. Houser, *Dalton Trans.*, 2007, 955-964.

64. S. J. Lancaster, A. Rodriguez, A. Lara-Sanchez, M. D. Hannant, D. A. Walker, D. H. Hughes and M. Bochmann, *Organometallics*, 2002, **21**, 451-453.

65. A. Kütt, S. Tshepelevitsh, J. Saame, M. Lõkov, I. Kaljurand, S. Selberg and I. Leito, *Eur. J. Org. Chem.*, 2021, **2021**, 1407-1419.

66. A. Kütt, I. Leito, I. Kaljurand, L. Sooväli, V. M. Vlasov, L. M. Yagupolskii and I. A. Koppel, *J. Org. Chem.*, 2006, **71**, 2829-2838.

67. E. Raamat, K. Kaupmees, G. Ovsjannikov, A. Trummal, A. Kütt, J. Saame, I. Koppel, I. Kaljurand, L. Lipping, T. Rodima, V. Pihl, I. A. Koppel and I. Leito, *J. Phys. Org. Chem.*, 2013, **26**, 162-170.

68. D. J. Duncalf, P. B. Hitchcock and G. A. Lawless, *J. Organomet. Chem.*, 1996, **506**, 347-349.

69. H.-Y. Chen, H.-Y. Tang and C.-C. Lin, *Polymer*, 2007, **48**, 2257-2262.

70. Y. Sarazin, R. H. Howard, D. L. Hughes, S. M. Humphrey and M. Bochmann, *Dalton Trans.*, 2006, 340-350.

71. M.-W. Hsiao, G.-S. Wu, B.-H. Huang and C.-C. Lin, *Inorg. Chem. Commun.*, 2013, **36**, 90-95.

72. W. Yi and H. Ma, *Inorg. Chem.*, 2013, **52**, 11821-11835.

73. D. J. Darensbourg, W. Choi, O. Karroonnirun and N. Bhuvanesh, *Macromolecules*, 2008, **41**, 3493-3502.

74. A. Guerrero, D. L. Hughes and M. Bochmann, *Organometallics*, 2006, **25**, 1525-1527.

75. Q. Hu, S. Jie, P. Braunstein and B.-G. Li, *J. Organomet. Chem.*, 2019, **882**, 1-9.

76. I. Nifant'ev, P. Komarov, V. Ovchinnikova, A. Kiselev, M. Minyaev and P. Ivchenko, *Polymers*, 2020, **12**, 2273.

77. D. J. Darensbourg, P. Rainey and J. Yarbrough, *Inorg. Chem.*, 2001, **40**, 986-993.

78. M. H. Chisholm, J. C. Gallucci, H. Zhen and J. C. Huffman, *Inorg. Chem.*, 2001, **40**, 5051-5054.

79. C. Ruspic and S. Harder, *Inorg. Chem.*, 2007, **46**, 10426-10433.

80. B. Blom, G. Klatt, D. Gallego, G. Tan and M. Driess, *Dalton Trans.*, 2015, **44**, 639-644.

81. Y. Liu, Y. Zhao, X.-J. Yang, S. Li, J. Gao, P. Yang, Y. Xia and B. Wu, *Organometallics*, 2011, **30**, 1599-1606.

82. X. Tang, M. Hong, L. Falivene, L. Caporaso, L. Cavallo and E. Y. X. Chen, *J. Am. Chem. Soc.*, 2016, **138**, 14326-14337.

83. J. V. Lamb, J.-C. Buffet, J. E. Matley, C. M. R. Wright, Z. R. Turner and D. O'Hare, *Dalton Trans.*, 2019, **48**, 2510-2520.

84. M. Hu, X. Song, F. Wang, W. Zhang, W. Ma and F. Han, *New J. Chem.*, 2022, **46**, 1175-1181.

85. N. Diteepeng, J.-C. Buffet, Z. R. Turner and D. O'Hare, *Dalton Trans.*, 2019, **48**, 16099-16107.

86. N. Diteepeng, I. A. P. Wilson, J.-C. Buffet, Z. R. Turner and D. O'Hare, *Polym. Chem.*, 2020, **11**, 6308-6318.

87. J. R. Dorgan, J. Janzen, D. M. Knauss, S. B. Hait, B. R. Limoges and M. H. Hutchinson, *J. Polym. Sci., Part B: Polym. Phys.*, 2005, **43**, 3100-3111.

88. V. Poirier, T. Roisnel, J.-F. Carpentier and Y. Sarazin, *Dalton Trans.*, 2009, 9820-9827.

89. D. J. Darensbourg, W. Choi and C. P. Richers, *Macromolecules*, 2007, **40**, 3521-3523.

90. Y. Sarazin, D. Roşca, V. Poirier, T. Roisnel, A. Silvestru, L. Maron and J.-F. Carpentier, *Organometallics*, 2010, **29**, 6569-6577.

91. Z. Gu and R. J. Comito, *Organometallics*, 2022, **41**, 1911-1916.

92. Y. Sarazin and J.-F. Carpentier, *Chem. Rev.*, 2015, **115**, 3564-3614.

93. Z. R. Turner, J. V. Lamb, T. P. Robinson, D. Mandal, J.-C. Buffet and D. O'Hare, *Dalton Trans.*, 2021, **50**, 4805-4818.

94. P. Dubois, O. Coulembier and J. M. Raquez, *Handbook of Ring-Opening Polymerization*, Wiley, 1st edn., 2009.

95. S. Ghosh, D. Chakraborty and V. Ramkumar, *J. Polym. Sci., Part A: Polym. Chem.*, 2015, **53**, 1474-1491.

Chapter 7

Experimental

7.1 General Details

7.1.1 Air- and moisture-sensitive compounds

All air- and moisture-sensitive manipulations were carried out under an inert atmosphere of nitrogen using standard Schlenk line techniques or an MBraun Unilab glove box.[1] Glassware was oven-dried at temperatures greater than 150 °C overnight prior to use.

7.1.2 Commercially supplied reagents

1,8-dihydroxynaphthalene (Fluorochem), sodium hydride (Sigma Aldrich), hydrochloric acid (Fischer Scientific), 2-propanol (Sigma Aldrich), *p*-toluenesulfonic acid (Sigma Aldrich), ^{n}BuLi (2.5 M solution in hexanes; Sigma Aldrich), di-*n*-butyl magnesium (1.0 M in heptane; Sigma Aldrich), magnesium iodide (Sigma Aldrich), calcium iodide (Sigma Aldrich), strontium iodide (Sigma Aldrich), barium iodide (Sigma Aldrich), 18-crown-6 (Sigma Aldrich), 2,6-dimethyl phenol (Sigma Aldrich), 4-methyl phenol (Fluorochem), 4-*tert*-butyl-phenol (Fluorochem), hexamethyltetramine (Sigma Aldrich), trifluoroacetic acid (Fluorochem), acetyl chloride (Sigma Aldrich), pyridine (Sigma Aldrich), N-bromo succinimide (Fluorochem), potassium hydroxide (Sigma Aldrich), sodium amide (Sigma Aldrich) and tris(pentafluorophenyl)borane (Alfa Aesar), 3,5-bis(trifluoromethyl)bromobenzene (Fluorochem), magnesium turnings (Fischer

Scientific) and sodium tetrafluoroborate (Sigma Aldrich) were all used as received. HCl (1.0 M in diethyl ether; VWR) and tetrafluoroboric acid diethyl ether complex (stored only in plastic; Sigma Aldrich) were stored at 4 °C and used as received. Chloromethyl methyl ether (Sigma Aldrich) and benzyl alcohol (Sigma Aldrich) were stored over 3 Å molecular sieves and freeze-pump-thaw degassed three times prior to use. 2,6-diisopropylaniline (Apollo Scientific), hexamethyldisilazane (Sigma Aldrich) and tetramethylethylenediamine (TMEDA; Sigma Aldrich) were dried over calcium hydride, stored over 3 Å molecular sieves and freeze-pump-thaw degassed three times prior to use. Aluminium trichloride (Sigma Aldrich) was dried under reduced pressure and stored under an inert atmosphere prior to use. Potassium hydride (Sigma Aldrich) was purchased as a 30 wt% dispersion in mineral oil. Any excess oil was decanted away before the solid was washed with portions of diethyl ether until a free-flowing powder was obtained; this was dried under reduced pressure before use. Sodium bis(trimethylsilyl)amide (Sigma Aldrich) was washed with portions of pentane and dried under reduced pressure before use. Celite (Sigma Aldrich) was dried at 150 °C under reduced pressure (10^{-3} mbar) for at least 48 h before use.

L- and *rac*-lactide were provided by Corbion Biomaterials and used as received. *D*-lactide was provided by Purac and used as received. *meso*-lactide was provided by Uhde Inventa-Fischer and was recrystallised repeatedly from toluene and dried under reduced pressure prior to use.

7.1.3 Synthesis of literature compounds

1,8-*bis*(methyloxymethoxy)naphthalene,[2] 2,7-diformyl-1,8-*bis*(methyloxymethoxy) naphthalene,[3] 2,7-diformyl-1,8-dihydroxynaphthalene,[3] $Ca(N\{SiMe_3\}_2)_2(thf)_2$,[4] $Sr(N\{SiMe_3\}_2)_2(thf)_2$,[5] $Ba(N\{SiMe_3\}_2)_2(thf)_2$,[5] EtZnCl, [6] $Na[B(3,5\text{-}\{CF_3\}_2C_6H_3)_4]$[7] and

$[H(OEt_2)_2][B(3,5\text{-}\{CF_3\}_2C_6H_3)_4]$[7] were all prepared accorded to reported literature procedures. The preparations of $H_2^{Dipp}L$,[3] 2,6-diformyl-4-methyl phenol,[8, 9] 2,6-diformyl-4-*tert*-butyl phenol,[8, 9] $H^{Dipp}L$,[10] $H^{Me,Dipp}L$,[11] $H^{tBu,Dipp}L$,[11] $[Na(OEt_2)_3][H_2N\{B(C_6F_5)_3\}_2]$[12] and $[H(OEt_2)_2][H_2N\{B(C_6F_5)_3\}_2]$[12] were adapted from literature procedures.

7.1.4 Solvent preparation

Protio solvents (pentane, hexane, toluene, benzene, dichloromethane, chloroform, dimethylformamide) were dried using an MBraun SPS-800 solvent purification system, stored over potassium mirrors or activated 4 Å molecular sieves and degassed under partial pressure prior to use. Tetrahydrofuran was distilled from sodium metal/benzophenone, stored over activated 4 Å molecular sieves and degassed under partial pressure prior to use. Diethyl ether was distilled from sodium metal/benzophenone, stored over a potassium mirror and degassed under partial pressure prior to use.

Deuterated solvents were dried over potassium (benzene-d_6, toluene-d_8) or calcium hydride (tetrahydrofuran-d_8, chloroform-d_1, pyridine-d_5, acetonitrile-d_3), distilled under reduced pressure and freeze-pump-thaw degassed three times prior to use.

7.1.5 Solution NMR spectroscopy

^1H, $^{13}C\{^1H\}$ and $^1H\{^1H\}$ NMR spectra were recorded at 298 K, unless otherwise stated, on Bruker AVIII 400 nanobay, Bruker AVIII 500 or Bruker NEO 600 spectrometers. Two dimensional ^1H-^1H and ^{13}C-^1H correlation experiments were used, when necessary, to confirm ^1H and ^{13}C assignments. ^{19}F and ^{11}B solution NMR spectra were also recorded on the same spectrometers at operating frequencies of 377 or 470 and 128 or 160 MHz respectively. ^1H and ^{13}C NMR spectra were referenced internally to residual protio solvent and are reported relative to tetramethylsilane (δ = 0 ppm). ^{19}F and ^{11}B were

referenced externally to $CFCl_3$ in $CDCl_3$ and $BF_3(OEt_2)$ respectively. Chemical shifts are quoted in δ (ppm) and coupling constants in Hertz. Air-sensitive samples were prepared in a glovebox under an inert atmosphere, using dry deuterated solvents in 5 mm Young's tap NMR tubes. Solid state ^{19}F NMR experiments were performed on a Bruker Avance III HD machine, equipped with a 9.4 T magnet, at 376 MHz.

7.1.6 Fourier transform infrared (FTIR) spectroscopy

Fourier transform infrared (FTIR) spectroscopy samples were prepared in a glove box as pellets using anhydrous potassium bromide (KBr). IR spectra were recorded on a Nicolet iS5 ThermoScientific spectrometer (range = 4000–400 cm^{-1} with resolution = 1 cm^{-1}) in transmission mode. A background spectrum was run prior to the sample and was subtracted from the sample spectra.

7.1.7 Elemental analysis

Samples were prepared in a glove box under a nitrogen atmosphere and sealed in glass vials. CHN analyses were carried out in duplicate by Ms Orla McCullough (London Metropolitan University).

7.1.8 Single crystal X-ray diffraction (XRD)

Single crystal X-ray diffraction data collection and structure determination were performed by Dr Zoë Turner, Dr Louis Morris and Dr Clement Collins-Rice (University of Oxford). Crystals were mounted on MiTeGen MicroMounts using perfluoropolyether oil and rapidly transferred to a goniometer head on a diffractometer fitted with an Oxford Cryostream open-flow nitrogen cooling device.[13] Data collections were carried out at 150 K using an Oxford Diffraction Supernova diffractometer using mirror-monochromated Cu Kα radiation (λ = 1.54178 Å) and the data processed using CrysAlisPro.[14] The structures were solved using direct methods (SIR-92),[15] a charge

flipping algorithm (SUPERFLIP),[16] or intrinsic phasing (SHELXT)[17] and refined by full-matrix least squares procedures using the WinGX software suite,[18] CRYSTALS,[19] or the SHELXL[20] refinement package implemented in Olex2.[21] Where required, interplanar distances and angles were calculated using PLATON[22] and molecular structures were generated using Ortep (with ellipsoids shown at 30% probability).[23]

7.1.9 DFT calculations

All density functional theory (DFT) calculations were performed with the ORCA 5.0.3 software package.[24-26] Geometry optimisations were carried out at the B3LYP[27-29] level of theory using the def2-TZVP basis set.[30, 31] Analytical frequency calculations were carried out to verify all geometries were true minima (NIMAG = 0). Single point energy calculations on all compounds were performed with Grimme's DFT-D3 dispersion corrections.[32] The Resolution of Identity approximation (RIJCOSX) was used to accelerate the calculations.[33, 34] Molecular orbitals maps were generated with the program Chimera[35] and contour plots of the (Laplacian) electron density/delocalisation indices were produced and analysed using Multiwfn 3.8.[36]

7.1.10 General procedure for lactide polymerisation

L-, *D*-, *rac*- or *meso*-lactide (43 mg, 0.298 mmol) was weighed into a Young's tap NMR spectroscopy tube. Stock solutions of complex and benzyl alcohol (when required) in an amount of deuterated solvent corresponding to an initial lactide concentration ($[LA]_0$) of 0.5 M were prepared and the desired quantity added to the NMR tube. Polymerisations were run at various temperatures and were halted at certain time intervals by submerging the NMR tubes in an ice bath. Upon completion, the polymer was precipitated by addition of pentane. The solid PLA was then washed with pentane and dried under vacuum at 30 °C prior to characterisation. All polymerisations were carried out, at least, in duplicate.

The monomer to polymer %conversion was determined using ^{1}H NMR spectroscopy; this involved measuring and comparing the integration of the C***H***Me resonances of unreacted monomer and PLA.

7.1.10.1 Polymer tacticity analysis via ^{1}H{^{1}H} NMR spectroscopy

Polymer tacticity was analysed by ^{1}H{^{1}H} NMR spectroscopy. P_r values were calculated from the integrations obtained from the methine region of ^{1}H{^{1}H} NMR spectra. Alternatively, peak deconvolution, using the Mestrenova software package, was used to improve the accuracy of the determination.[37] The probability of a particular tetrad was then calculated using Bernoullian statistics.[38]

7.1.10.2 Polymer end-group analysis via MALDI-TOF mass spectrometry

Polymer end group analysis was performed using Matrix-assisted laser desorption/ionisation time of flight spectra. Samples were prepared in chloroform at a concentration of 1 mg mL^{-1} and filtered before analysis. MALDI-TOF spectra were collected Dr Victor Mikhailov (University of Oxford) using a Bruker MALDI Autoflex TOF MS. Samples were run using either a DHB or DCTB matrix. The DHB matrix was prepared by mixing the sample with DHB (10 mg mL^{-1} in 70:30 H_2O:CH_3CN) in a 1:1 volume ratio. The DCTB matrix was prepared by mixing 10 µL of sample with 10 µL DCTB (40 mg mL^{-1} in THF) and 2.5 µL KTFA (5 mg mL^{-1} in THF). 1.5 µL of the mixed solutions were spotted on the MALDI plate and dried prior to the run.

7.1.10.3 Polymer molecular weight analysis via gel permeation chromatography (GPC)

Polymer molecular weights and dispersities (M_n, M_w and M_w/M_n) were determined by GPC using a Polymer Laboratories PLGPC50 Plus instrument equipped with a Polymer Laboratories PLgel Mixed-D column (300 mm length, 7.5 mm diameter) and a refractive

index (RI) detector. THF (Sigma Aldrich, HPLC grade) was used as an eluent at 30 °C with a flow rate of 1.0 mL min^{-1}. Samples were dissolved in THF at a concentration of 1.0 mg mL^{-1} and filtered before injection. Linear polystyrenes were used as primary calibration standards and correction factor of 0.58 was applied to calculate the experimental molecular weights.[39]

7.2 Experimental Details for Chapter 2

7.2.1 Naphthalene ring numbering scheme

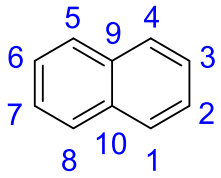

7.2.2 Synthesis of 1,8-*bis*(methyloxymethoxy)naphthalene[2]

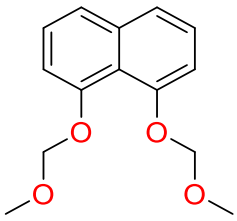

A solution of 1,8-dihydroxynaphthalene (16.1 g, 101 mmol) in DMF (120 mL) was prepared and cooled to 0 °C. NaH (7.28 g, 303 mmol) was slowly added and the reaction mixture left to stir at 0 °C for 2.5 h. A solution of MOMCl (20.0 mL, 263 mmol) in Et_2O (100 mL) was added dropwise to the cooled pale brown reaction mixture which was then stirred at room temperature overnight. Distilled water (200 mL) was added at 0 °C before the reaction mixture was extracted with Et_2O (3 x 200 mL). The organic layer was dried over $MgSO_4$, filtered and concentrated *in vacuo* to yield a pale orange solid. The crude product was washed with pentane (150 mL) to afford 1,8-*bis*(methyloxymethoxy)naphthalene as an off-white solid (18.1 g, 73%). ^{1}H NMR (400 MHz, 298 K, chloroform-d_1): δ 7.50 (dd, $^3J_{HH}$ = 8.4 Hz; $^4J_{HH}$ = 1.1 Hz, 2H,

4,5-$C_{10}\boldsymbol{H}_6$), 7.35 (t, $^3J_{HH}$ = 7.9 Hz, 2H, 3,6-$C_{10}\boldsymbol{H}_6$), 7.09 (dd, $^3J_{HH}$ = 7.9 Hz; $^4J_{HH}$ = 1.0 Hz, 2H, 2,7-$C_{10}\boldsymbol{H}_6$), 5.29 (s, 2H, $C\boldsymbol{H}_2$), 3.60 (s, 3H, $C\boldsymbol{H}_3$) ppm.

7.2.3 Synthesis of 2,7-diformyl-1,8-*bis*(methyloxymethoxy)naphthalene[3]

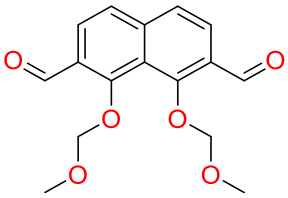

A solution of ^{n}BuLi (38.8 mL, 2.5 M in hexanes, 97.0 mmol) and TMEDA (14.4 mL, 96.0 mmol) in Et_2O (40 mL) was prepared and cooled to 0 °C. Added dropwise to this over a period of 3 h was a solution of 1,8-*bis*(methyloxymethoxy)naphthalene (8.00 g, 32.5 mmol) in Et_2O (360 mL). The reaction mixture was then stirred at 0 °C for 5 h. DMF (15.0 mL, 194 mmol) was added and the resultant pale brown solution was left to stir at room temperature overnight. Distilled water (150 mL) was added at 0 °C and the reaction mixture was then left to stir at room temperature for 1.5 h. Dilute HCl was added to change the pH of the solution to 7 before extracting it with DCM (250 mL). The organic extract was washed with distilled water (3 x 100 mL), dried over $MgSO_4$, and concentrated *in vacuo* affording an oily orange solid. The crude product was washed with ethanol (100 mL) yielding clean 2,7-diformyl-1,8-*bis*(methyloxymethoxy)naphthalene as a golden yellow solid (4.22 g, 43%). ^{1}H NMR (400 MHz, 298 K, chloroform-d_1): δ 10.63 (d, $^4J_{HH}$ = 0.9 Hz, 2H, OC$\boldsymbol{H}$-2,7-$C_{10}H_4$), 8.02 (d, $^3J_{HH}$ = 8.6 Hz, 2H, 4,5-$C_{10}\boldsymbol{H}_4$), 7.72 (dd, $^3J_{HH}$ = 8.7 Hz; $^4J_{HH}$ = 0.8 Hz, 2H, 3,6-$C_{10}\boldsymbol{H}_4$), 5.25 (s, 2H, $C\boldsymbol{H}_2$), 3.60 (s, 3H, $C\boldsymbol{H}_3$).

7.2.4 Synthesis of 2,7-diformyl-1,8-dihydroxynaphthalene[3]

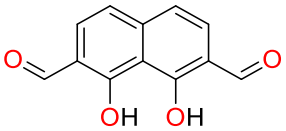

Solutions of 2,7-diformyl-1,8-*bis*(methyloxymethoxy)-naphthalene (2.80 g, 9.20 mmol) in DCM (68 mL) and HCl (12 M, 17.0 mL, 56.0 mmol) in ^{i}PrOH (68 mL) were prepared and degassed for 1 h. The DCM solution was cooled to 0 °C before dropwise addition of the acidic solution. The

reaction mixture was warmed to room temperature and stirred overnight. The yellow solid that precipitated from solution was collected, washed with water (3 x 2 mL), dried *in vacuo* and identified as spectroscopically pure 2,7-diformyl-1,8-dihydroxynaphthalene using NMR spectroscopy. A second crop was obtained via washing the organic phase with distilled water (5 x 100 mL), drying over $MgSO_4$, and concentrating *in vacuo* (combined mass: 1.69 g, combined yield: 85%). ^{1}H NMR (400 MHz, 298 K, chloroform-d_1): 12.70 (s (br), 2H, O***H***), 10.18 (s (br), 2H, OC***H***-2,7-$C_{10}H_4$), 7.73 (d, $^3J_{HH}$ = 8.5 Hz, 2H, 4,5-C_{10}***H***$_4$), 7.30 (d, $^3J_{HH}$ = 8.6 Hz, 2H, 3,6-C_{10}***H***$_4$).

7.2.5 Synthesis of $H_2^{Dipp}L$; adapted from reference 3.

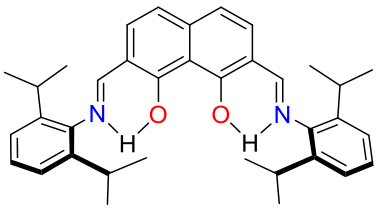

A solution of 2,7-diformyl-1,8-dihydroxynaphthalene (1.61 g, 7.48 mmol) in toluene (60 mL) was prepared. 2,6-diisopropylaniline (2.89 mL, 15.4 mmol) and *p*-toluenesulfonic acid (0.0500 g, 0.290 mmol) were added before the reaction mixture was stirred and heated to 60 °C overnight. The resultant dark red solution was dried *in vacuo* affording an oily red solid which when washed with ice-cold methanol (3 x 10 mL) yielded $H_2^{Dipp}L$ as a pure orange solid (3.14 g, 79%). ^{1}H NMR (500 MHz, 253 K, chloroform-d_1): 14.75 (s, 1H, O***H***), 13.51 (d, $^3J_{HH}$ = 12.7 Hz, 1H, N***H***), 8.80 (s, 1H, ***H***C=N), 8.36 (d, $^3J_{HH}$ = 8.3 Hz, 2H, 3-C_{10}***H***$_4$), 7.73 (d, $^3J_{HH}$ = 12.8 Hz, 1H, ***H***C=NH), 7.40 (t, $^3J_{HH}$ = 7.8 Hz, 1H, HN-4-C_6***H***$_3$), 7.32-7.23 (overlapping m, 3H, 6-C_{10}***H***$_4$ and HN-3,5-C_6***H***$_3$), 7.20 (d, $^3J_{HH}$ = 7.6 Hz, 2H, N-3,5-C_6***H***$_3$), 7.14 (t, $^3J_{HH}$ = 7.5 Hz, 1H, N-4-C_6***H***$_3$), 7.00 (d, $^3J_{HH}$ = 9.0 Hz, 1H, 4-C_{10}***H***$_4$), 6.82 (d, $^3J_{HH}$ = 8.9 Hz, 1H, 5-C_{10}***H***$_4$), 3.12 (sept, $^3J_{HH}$ = 7.0 Hz, 2H, HN-2,6-C_6H_3-C***H***Me_2), 3.04 (sept, $^3J_{HH}$ = 7.0 Hz, 2H, N-2,6-C_6H_3-C***H***Me_2), 1.25 (d, $^3J_{HH}$ = 7.0 Hz, 12H, HN-2,6-C_6H_3-CH***Me***$_2$), 1.19 (d, $^3J_{HH}$ = 6.9 Hz, 12H, N-2,6-C_6H_3-CH***Me***$_2$) ppm. ^{13}C{^{1}H} NMR (100 MHz, 298 K,

chloroform-d_1): δ 184.5 (H***C***=NH), 163.9 (8-***C***$_{10}$H$_4$), 161.0 (1-***C***$_{10}$H$_4$), 157.8 (H***C***=N), 150.5 (N-1-***C***$_6$H$_3$), 144.0 (HN-2,6-***C***$_6$H$_3$), 142.2 (9-***C***$_{10}$H$_4$), 138.2 (N-2,6-***C***$_6$H$_3$), 134.9 (HN-1-***C***$_6$H$_3$), 130.8 (6-***C***$_{10}$H$_4$), 129.9 (5-***C***$_{10}$H$_4$), 129.2 (HN-4-***C***$_6$H$_3$), 124.4 (3-***C***$_{10}$H$_4$), 124.3 (HN-3,5-***C***$_6$H$_3$), 123.8 (7-***C***$_{10}$H$_4$), 123.1 (N-3,5-***C***$_6$H$_3$), 117.6 (N-4-***C***$_6$H$_3$), 117.1 (10-***C***$_{10}$H$_4$), 116.3 (4-***C***$_{10}$H$_4$), 108.7 (2-***C***$_{10}$H$_4$), 28.8, 28.8 (HN-2,6-C$_6$H$_3$-***C***HMe$_2$ and N-2,6-C$_6$H$_3$-***C***HMe$_2$), 23.8, 23.8 (HN-2,6-C$_6$H$_3$-CH***Me***$_2$ and N-2,6-C$_6$H$_3$-CH***Me***$_2$) ppm. IR (KBr): 3445 (br), 2962, 2925, 2868, 2359, 2336, 1621, 1587, 1553, 1529, 1459, 1423, 1343, 1250, 1229, 1138, 1095, 1057, 836, 818, 797, 754 cm^{-1}. Anal. Calcd for C$_{36}$H$_{42}$N$_2$O$_2$: C, 80.86; H, 7.92; N, 5.24. Found: C, 81.88; H, 8.04; N, 5.03.

7.2.6 Synthesis of [^{Dipp}LMg(thf)]$_2$ (1)

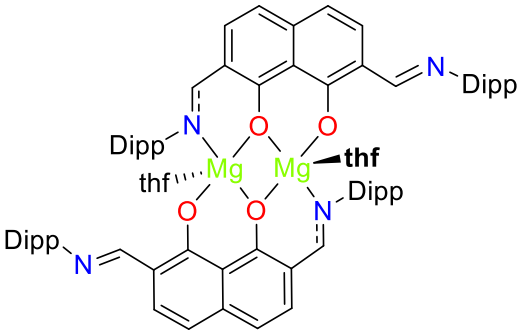

In a Young's tap NMR tube [Mg{N(SiMe$_3$)$_2$}$_2$]$_2$ (0.0099 g, 0.0143 mmol) and H$_2$^{Dipp}L (0.0078 g, 0.0146 mmol) were dissolved in THF-d_8 (0.5 mL). The bright red reaction mixture was then left overnight at room temperature. During this time, X-ray diffraction quality crystals of [^{Dipp}LMg(thf)]$_2$ (**1**) precipitated from solution. ^{1}H NMR (400 MHz, 298 K, THF-d_8): δ 8.20 (s, 2H, ***H***C=NMg), 8.17 (d, $^3J_{HH}$ = 8.3 Hz, 2H, 6-C$_{10}$***H***$_4$), 7.18 (s, 2H, ***H***C=N), 7.11 (overlapping m, 6H, N-3,5-C$_6$***H***$_3$ and 3-C$_{10}$***H***$_4$), 7.02 (t, $^3J_{HH}$ = 7.6 Hz, 2H, N-4-C$_6$***H***$_3$), 6.96 (d, $^3J_{HH}$ = 8.4 Hz, 2H, 4-C$_{10}$***H***$_4$), 6.75 (d, $^3J_{HH}$ = 7.8 Hz, 4H, MgN-3,5-C$_6$***H***$_3$), 6.66 (d, $^3J_{HH}$ = 8.4 Hz, 2H, 5-C$_{10}$***H***$_4$), 6.00 (t, $^3J_{HH}$ = 7.8 Hz, 2H, MgN-4-C$_6$***H***$_3$), 3.58 (s (br), 8H, thf-OC***H***$_2$), 3.02 (sept, $^3J_{HH}$ = 6.9 Hz, 4H, MgN-2,6-C$_6$H$_3$-C***H***Me$_2$), 2.83 (sept, $^3J_{HH}$ = 6.8 Hz, 4H, N-2,6-C$_6$H$_3$-C***H***Me$_2$), 1.73 (s (br), 8H, thf-C***H***$_2$), 1.16 (d, $^3J_{HH}$ = 6.9 Hz, 24H, MgN-2,6-C$_6$H$_3$-CH***Me***$_2$), 1.09 (d, $^3J_{HH}$ = 6.9 Hz, 24H, N-2,6-C$_6$H$_3$-CH***Me***$_2$) ppm. ^{13}C{^{1}H} NMR (126 MHz, 328 K, THF-d_8): δ 174.3 (1-***C***$_{10}$H$_4$), 172.2 (8-***C***$_{10}$H$_4$), 168.8 (MgN=***C***H),

159.8 (N=***C***H), 153.4 (N-1-***C***$_6$H$_3$), 149.5 (MgN-1-***C***$_6$H$_3$), 144.9 (9-***C***$_{10}$H$_4$), 140.6 (MgN-2,6-***C***$_6$H$_3$), 137.9 (N-2,6-***C***$_6$H$_3$), 133.0 (3-***C***$_{10}$H$_4$), 130.6 (6-***C***$_{10}$H$_4$), 126.9 (MgN-4-***C***$_6$H$_3$), 124.1 (MgN-3,5-***C***$_6$H$_3$), 123.5 (10-***C***$_{10}$H$_4$), 122.9 (N-4-***C***$_6$H$_3$), 122.7 (N-3,5-***C***$_6$H$_3$), 121.7 (2-***C***$_{10}$H$_4$), 119.4 (4-***C***$_{10}$H$_4$), 114.6 (7-***C***$_{10}$H$_4$), 113.3 (5-***C***$_{10}$H$_4$), 67.6 (thf-O***C***H$_2$), 29.6 (MgN-2,6-C$_6$H$_3$-***C***HMe$_2$), 28.9 (N-2,6-C$_6$H$_3$-***C***HMe$_2$), 25.5 (thf-***C***H$_2$), 23.8 (N-2,6-C$_6$H$_3$-CH***Me***$_2$), 23.0 (MgN-2,6-C$_6$H$_3$-CH***Me***$_2$) ppm. IR (KBr): 2964, 2935, 2924, 2360, 2344, 1624, 1560, 1551, 1384, 1260, 1228, 1141, 1093, 1020, 800, 669 cm^{-1}. Anal. Calcd for C$_{80}$H$_{94}$N$_4$O$_6$Mg$_2$: C, 76.49; H, 7.54; N, 4.46. Found: C, 74.96; H, 7.67; N, 4.34.

7.2.7 Synthesis of [H^{Dipp}LMgCl]$_2$ (2)

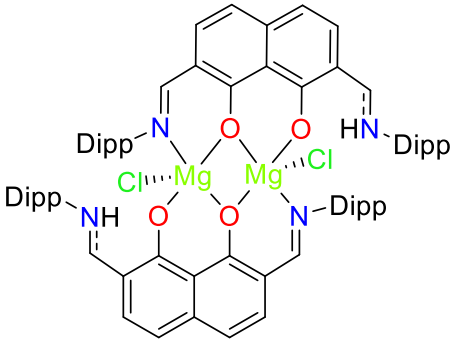

At 0 °C, a solution of [Mg{N(SiMe$_3$)$_2$}$_2$]$_2$ (0.0646 g, 0.0935 mmol) in chloroform (2 mL) was added to a solution of H$_2$^{Dipp}L (0.100 g, 0.187 mmol) in chloroform (2 mL). The dark red reaction mixture was left stirring at 0 °C for 1 h before being warmed to room temperature overnight. Volatiles were removed *in vacuo* and the crude oily red solid was freeze dried in benzene (2 mL) before being washed with –78 °C pentane (4 x 2 mL) to yield [H^{Dipp}LMgCl]$_2$ (**2**) as an orange solid (0.044 g, 40%). Single crystals of [H^{Dipp}LMgCl]$_2$, suitable for an X-ray diffraction study, were obtained by pentane diffusion into a saturated dichloromethane solution at –30 °C. ^{1}H NMR (400 MHz, 298 K, THF-*d*$_8$): δ 13.34 (d, $^3J_{HH}$ = 13.3 Hz, 2H, N***H***), 8.83 (s, 2H, ***H***C=N), 8.20 (d, $^3J_{HH}$ = 8.0 Hz, 2H, 6-C$_{10}$***H***$_4$), 7.76 (d, $^3J_{HH}$ = 13.2 Hz, 2H, ***H***C=NH), 7.32 (t, $^3J_{HH}$ = 6.8 Hz, 2H, HN-4-*C*$_6$***H***$_3$), 7.24 (d, $^3J_{HH}$ = 7.0 Hz, 4H, HN-3,5-*C*$_6$***H***$_3$), 7.04 (d, $^3J_{HH}$ = 7.6 Hz, 4H, N-3,5-*C*$_6$***H***$_3$), 6.91 (t, $^3J_{HH}$ = 7.6 Hz, 2H, N-4-*C*$_6$***H***$_3$), 6.86 (d, $^3J_{HH}$ = 8.8 Hz, 2H, 3-C$_{10}$***H***$_4$), 6.60 (d, $^3J_{HH}$ = 8.9 Hz, 2H, 4-C$_{10}$***H***$_4$), 6.52 (d, $^3J_{HH}$ = 8.1 Hz, 2H, 5-C$_{10}$***H***$_4$), 3.31 (sept, $^3J_{HH}$ = 7.0 Hz, 4H, HN-2,6-C$_6$H$_3$-C***H***Me$_2$), 3.09 (sept, $^3J_{HH}$ = 6.8 Hz, 4H, N-

2,6-C_6H_3-C***H***Me_2), 1.29 (d, $^3J_{HH}$ = 6.9 Hz, 24H, HN-2,6-C_6H_3-CH***Me***$_2$), 1.13 (d, $^3J_{HH}$ = 6.9 Hz, 24H, N-2,6-C_6H_3-CH***Me***$_2$) ppm. $^{13}C\{^1H\}$ NMR (125 MHz, 298 K, THF-d_8): δ 182.4 (H***C***=NH), 174.4 (H***C***=N), 162.0 (1-***C***$_{10}H_4$), 161.4 (8-***C***$_{10}H_4$), 153.3 (N-1-***C***$_6H_3$), 146.0 (9-***C***$_{10}H_4$), 145.7 (HN-2,6-***C***$_6H_3$), 138.7 (N-2,6-***C***$_6H_3$), 137.8 (HN-1-***C***$_6H_3$), 132.7 (6-***C***$_{10}H_4$), 130.4 (3-***C***$_{10}H_4$), 129.4 (HN-4-***C***$_6H_3$), 124.6 (HN-3,5-***C***$_6H_3$), 123.5 (N-4-***C***$_6H_3$), 123.4 (7-***C***$_{10}H_4$), 123.3 (N-3,5-***C***$_6H_3$), 122.3 (2-***C***$_{10}H_4$), 118.0 (4-***C***$_{10}H_4$), 111.9 (5-***C***$_{10}H_4$), 110.8 (10-***C***$_{10}H_4$), 29.5 (HN-2,6-C_6H_3-***C***HMe_2), 28.8 (N-2,6-C_6H_3-***C***HMe_2), 24.0, 24.0 (HN-2,6-C_6H_3-CH***Me***$_2$, N-2,6-C_6H_3-CH***Me***$_2$) ppm. IR (KBr): 2962, 2917, 2360, 2344, 1628, 1555, 1385, 1260, 1142, 1078, 1021, 799, 668 cm^{-1}. Anal. Calcd for $C_{72}H_{82}N_4O_4Mg_2Cl_2$: C, 72.86; H, 6.96; N, 4.72. Found: C, 71.19; H, 7.00; N, 4.49.

7.2.8 Synthesis of ^{Dipp}LM(thf)$_x$ (M = Ca (3(thf)$_x$), Sr (4(thf)$_x$) and Ba (5(thf)$_x$))

General procedure:

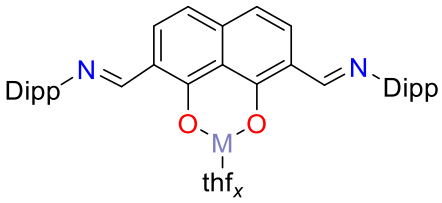

A solution of $H_2{}^{Dipp}L$ (1.00 g, 1.87 mmol, 1.0 eq.) in THF (5 mL) was added dropwise to a solution of M{N(SiMe$_3$)$_2$}$_2$(thf)$_2$ (1.0 eq) in THF (5 mL). The reaction mixture was left to stir at room temperature for 3 h before volatiles were removed *in vacuo*. The crude oily solid was then freeze-dried in benzene (3 x 5 mL) to yield ^{Dipp}LM(thf)$_x$ (M = Ca (**3(thf)$_x$**), Sr (**4(thf)$_x$**) and Ba (**5(thf)$_x$**)) as dark orange solids. No, or extremely poor, $^{13}C\{^1H\}$ NMR data was obtained for these compounds (even at high/low temperatures) due to broadening of the signals into the baseline.

M = Ca (*x* = 2, 1.11 g, 69%)

^1H NMR (400 MHz, 298 K, THF-d_8): δ 8.58 (s (br), 2H, ***H***C=N), 7.84 (s (br), 2H, 3,6-$C_{10}H_4$), 7.03 (d, $^3J_{HH}$ = 7.6 Hz, 4H, N-3,5-C_6H_3), 6.93 (t, $^3J_{HH}$ = 7.6 Hz, 2H, N-4-C_6H_3), 6.72 (d, $^3J_{HH}$ = 8.6 Hz, 2H, 4,5-$C_{10}H_4$), 3.62 (m, 8H, thf-OCH_2), 3.01 (sept, $^3J_{HH}$ = 6.9 Hz,

2H, N-2,6-C_6H_3-C***H***Me_2), 1.77 (m, 8H, thf-C***H***$_2$), 1.05 (d, $^3J_{HH}$ = 6.9 Hz, 24H, N-2,6-C_6H_3-CH***Me***$_2$) ppm. IR (KBr): 3055, 3025, 2959, 2929, 2871, 1607, 1561, 1544, 1516, 1438, 1407, 1361, 1224, 1159, 1139, 1096, 1064, 1035, 888, 831, 755, 741, 710, 664 cm^{-1}. Anal. Calcd for $C_{44}H_{54}N_2O_4Ca$: C, 73.91; H, 7.61; N, 3.92. Found: C, 73.84; H, 7.51; N, 4.07.

M = Sr (*x* = 1, 1.08 g, 84%)

^{1}H NMR (400 MHz, 298 K, THF-d_8): δ 8.55 (s (br), 2H, ***H***C=N), 7.76 (s (br), 2H, 3,6-C_{10}***H***$_4$), 7.03 (d, $^3J_{HH}$ = 7.1 Hz, 4H, N-3,5-C_6***H***$_3$), 6.94 (t, $^3J_{HH}$ = 7.1 Hz, 2H, N-4-C_6***H***$_3$), 6.63 (d, $^3J_{HH}$ = 8.4 Hz, 2H, 4,5-C_{10}***H***$_4$), 3.62 (m, 4H, thf-OC***H***$_2$), 2.98 (sept, $^3J_{HH}$ = 6.8 Hz, 2H, N-2,6-C_6H_3-C***H***Me_2), 1.77 (m, 4H, thf-C***H***$_2$), 1.05 (d, $^3J_{HH}$ = 6.8 Hz, 24H, N-2,6-C_6H_3-CH***Me***$_2$) ppm. IR (KBr): 3057, 3024, 2960, 2927, 2868, 1612, 1572, 1515, 1437, 1383, 1361, 1260, 1223, 1140, 1059, 889, 831, 799, 754, 707, 662 cm^{-1}. Anal. Calcd for $C_{40}H_{47}N_2O_3Sr$: C, 69.48; H, 6.85; N, 4.05. Found: C, 67.49; H, 6.88; N, 3.96.

M = Ba (*x* = 1, 1.05 g, 75%)

^{1}H NMR (400 MHz, 298 K, THF-d_8): δ 8.55 (s (br), 2H, ***H***C=N), 7.75 (s (br), 2H, 3,6-C_{10}***H***$_4$), 7.03 (d, $^3J_{HH}$ = 7.5 Hz, 4H, N-3,5-C_6***H***$_3$), 6.96 (t, $^3J_{HH}$ = 7.4 Hz, 2H, N-4-C_6***H***$_3$), 6.58 (d, $^3J_{HH}$ = 8.4 Hz, 2H, 4,5-C_{10}***H***$_4$), 3.62 (m, 4H, thf-OC***H***$_2$), 3.00 (sept, $^3J_{HH}$ = 6.7 Hz, 2H, N-2,6-C_6H_3-C***H***Me_2), 1.77 (m, 4H, thf-C***H***$_2$), 1.06 (d, $^3J_{HH}$ = 7.0 Hz, 24H, N-2,6-C_6H_3-CH***Me***$_2$) ppm. IR (KBr): 3057, 3023, 2959, 2926, 2868, 1606, 1567, 1514, 1436, 1385, 1359, 1254, 1223, 1158, 1138, 1096, 1058, 886, 831, 754, 661 cm^{-1}. Anal. Calcd for $C_{40}H_{47}N_2O_3Ba$: C, 64.82; H, 6.39; N, 3.78. Found: C, 62.76; H, 6.31; N, 3.79.

7.2.9 Synthesis of potassium 2,6-di-tert-butyl-4-methyl phenoxide

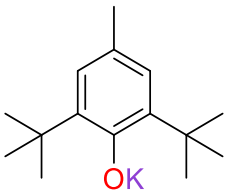

At 0 °C, a solution of 2,6-di-tert-butyl-4-methyl phenol (5.00 g, 22.7 mmol) in THF (30 mL) was added dropwise to a slurry of potassium hydride (0.827 g, 20.6 mmol) in THF (20 mL). The resultant reaction mixture was warmed to room temperature and stirred for 3 h. Volatiles were then removed *in vacuo* and the crude solid was washed with pentane (3 x 20 mL) to afford potassium 2,6-di-tert-butyl-4-methyl phenoxide as a colourless powder (4.80 g, 90%). ^{1}H NMR (400 MHz, 298 K, THF-d_8) δ 6.59 (s, 2H, O-2,6-^{t}Bu-4-Me-C$_6$***H***$_2$), 2.06 (s, 3H, O-2,6-^{t}Bu-4-***Me***-C$_6$H$_2$), 1.40 (s, 18H, O-2,6-^{t}***Bu***-4-Me-C$_6$H$_2$) ppm.

7.2.10 Synthesis of alkaline-earth aryloxide reagents: M{O-2,6-^{t}Bu-4-Me-C$_6$H$_2$}$_2$(thf)$_3$ (M = Ca, Sr and Ba)

General procedure:

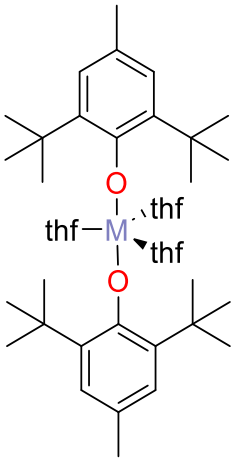

A solution of potassium 2,6-di-tert-butyl-4-methyl phenoxide (1.00 g, 2.0 eq.) in THF (10 mL) was added dropwise to a slurry of metal-iodide (1.0 eq.) in THF (10 mL). The resultant reaction mixture was left stirring overnight prior to filtration. Volatiles were removed *in vacuo* to afford the desired products as off-white powders.

M = Ca (1.00 g, 83%)

^{1}H NMR (400 MHz, 298 K, benzene-d_6) δ 7.31 (s, 4H, O-2,6-^{t}Bu-4-Me-C$_6$***H***$_2$), 3.65 (m (br), 12H, thf-OC***H***$_2$), 2.47 (s, 6H, O-2,6-^{t}Bu-4-***Me***-C$_6$H$_2$), 1.65 (s, 36H, O-2,6-^{t}***Bu***-4-Me-C$_6$H$_2$), 1.29 (m (br), 12H, thf-C***H***$_2$) ppm.

M = Sr (1.12 g, 86%)

^{1}H NMR (400 MHz, 298 K, benzene-d_6) δ 7.32 (s, 4H, O-2,6-^{t}Bu-4-Me-C$_6$***H***$_2$), 3.58 (m, 12H, thf-OC***H***$_2$), 2.49 (s, 6H, O-2,6-^{t}Bu-4-***Me***-C$_6$H$_2$), 1.67 (s, 36H, O-2,6-^{t}***Bu***-4-Me-C$_6$H$_2$), 1.28 (m (br), 12H, thf-C***H***$_2$) ppm.

M = Ba (1.16 g, 83%)

^{1}H NMR (400 MHz, 298 K, benzene-d_6) δ 7.21 (s, 4H, O-2,6-^{t}Bu-4-Me-C$_6$***H***$_2$), 3.49 (m, 12H, thf-OC***H***$_2$), 2.39 (s, 6H, O-2,6-^{t}Bu-4-***Me***-C$_6$H$_2$), 1.59 (s, 36H, O-2,6-^{t}***Bu***-4-Me-C$_6$H$_2$), 1.28 (m (br), 16H, thf-C***H***$_2$) ppm.

7.2.11 Synthesis of ^{Dipp}LM(18-c-6) (M = Ca (3(18-c-6)), Sr (4(18-c-6)) and Ba (5(18-c-6))

General procedure:

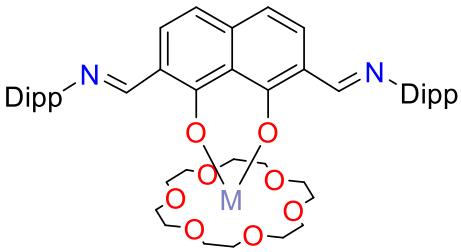

In a Young's tap NMR tube ^{Dipp}LM(thf)$_x$ (0.0500 g, 1.0 eq.) and 18-crown-6 (1.0 eq.) were dissolved in THF-d_8 (0.5 mL). The dark brown reaction mixture was then left overnight at room temperature. ^{1}H NMR spectroscopic studies revealed quantitative formation of the Sr and Ba crown ether complexes ^{Dipp}LM(18-c-6) (**4(18-c-6)** and **5(18-c-6)**) during this time. In the case of Ca, a mixture of ^{Dipp}LCa(thf)$_x$ and ^{Dipp}LCa(18-c-6) (**3(thf)$_x$**:**3(18-c-6)** ~ 45:55) was exclusively formed regardless of reaction time or temperature. None of these systems were isolated in bulk, the following characterisation was recorded on the results of the NMR scale reactions.

M = Ca

Analysis of the ^{1}H, ^{13}C{^{1}H} and 2D NMR spectra of the resultant mixture revealed signals that can be associated with the supported complex (**3(18-c-6)**; *vide infra*). Slow evaporation of this THF mixture allowed for the formation of a small crystalline sample of ^{Dipp}LCa(18-c-6), suitable for an X-ray diffraction study and elemental analysis only. In this instance, the solid-state data is not representative of the bulk in solution. ^{1}H NMR (500 MHz, 298 K, THF-d_8): δ 8.84 (s, 2H, ***H***C=N), 7.88 (d, $^{3}J_{HH}$ = 8.3 Hz, 2H, 3,6-C_{10}***H***$_4$), 6.99 (d, $^{3}J_{HH}$ = 7.6 Hz, 4H, N-3,5-C_6***H***$_3$), 6.83 (t, $^{3}J_{HH}$ = 7.5 Hz, 2H, N-4-C_6***H***$_3$), 6.34 (d, $^{3}J_{HH}$ = 8.4 Hz, 2H, 4,5-C_{10}***H***$_4$), 3.54 (s (br), 24H, **18-c-6**), 3.20 (m (br), 4H, N-2,6-C_6H_3-C***H***Me_2), 1.12 (d, *J* = 7.0 Hz, 24H, N-2,6-C_6H_3-CH***Me***$_2$) ppm. ^{13}C{^{1}H} NMR (125 MHz, 298 K, THF-d_8) δ 175.4 (1,8-***C***$_{10}H_4$), 161.9 (H***C***=N), 154.8 (N-1-***C***$_6H_3$), 139.1 (N-2,6-***C***$_6H_3$), 127.4 (3,6-***C***$_{10}H_4$), 124.9 (9-***C***$_{10}H_4$), 123.5 (10-***C***$_{10}H_4$), 123.0 (N-3,5-***C***$_6H_3$), 122.3 (N-4-***C***$_6H_3$), 117.6 (2,7-***C***$_{10}H_4$), 112.1 (4,5-***C***$_{10}H_4$), 71.4 (**18-c-6**), 28.9 (N-2,6-C_6H_3-***C***HMe_2), 24.0 (N-2,6-C_6H_3-CH***Me***$_2$) ppm. Anal. Calcd for $C_{48}H_{64}N_2O_8Ca$: C, 68.87; H, 7.71; N, 3.35. Found: C, 71.38; H, 7.73; N, 3.15.

M = Sr

Single crystals with the composition ^{Dipp}LSr(18-c-6)(thf), suitable for X-ray diffraction studies, were formed cleanly from the saturated THF solution at room temperature. ^{1}H NMR (600 MHz, 298 K, THF-d_8) δ 8.83 (s, 2H, ***H***C=N), 7.83 (d, $^{3}J_{HH}$ = 8.3 Hz, 2H, 3,6-C_{10}***H***$_4$), 6.97 (d, $^{3}J_{HH}$ = 7.6 Hz, 4H, N-3,5-C_6***H***$_3$), 6.81 (t, $^{3}J_{HH}$ = 7.7 Hz, 2H, N-4-C_6***H***$_3$), 6.30 (d, $^{3}J_{HH}$ = 8.3 Hz, 2H, 4,5-C_{10}***H***$_4$), 3.94 (m (br), 12H, **18-c-6**), 3.45 (m (br), 12H, **18-c-6**), 3.20 (sept, $^{3}J_{HH}$ = 6.9 Hz, 4H, N-2,6-C_6H_3-C***H***Me_2), 1.12 (d, $^{3}J_{HH}$ = 6.9 Hz, 24H, N-2,6-C_6H_3-CH***Me***$_2$) ppm. ^{13}C{^{1}H} NMR (151 MHz, 298 K, THF-d_8) δ 176.0 (1,8-***C***$_{10}H_4$), 162.4 (H***C***=N), 155.3 (N-1-***C***$_6H_3$), 146.3 (9-***C***$_{10}H_4$), 139.2 (N-2,6-***C***$_6H_3$), 127.2 (10-***C***$_{10}H_4$), 127.0 (3,6-***C***$_{10}H_4$), 122.9 (N-3,5-***C***$_6H_3$), 122.1 (N-4-***C***$_6H_3$), 117.7 (2,7-***C***$_{10}H_4$), 111.6 (4,5-***C***$_{10}H_4$), 70.9 (**18-c-6**), 28.7 (N-2,6-C_6H_3-***C***HMe_2), 24.0 (N-2,6-C_6H_3-

CH***Me***$_2$) ppm. IR (KBr): 2959, 2929, 2866, 2360, 2346, 1601, 1559, 1523, 1509, 1437, 1389, 1327, 1261, 1164, 1133, 1100, 1063, 974, 827, 753, 668 cm^{-1}. Anal. Calcd for $C_{48}H_{64}N_2O_8Sr$: C, 65.17; H, 7.29; N, 3.17. Found: C, 63.62; H, 7.44; N, 2.80.

M = Ba

The bulk material precipitated from THF and was therefore crystallised, with the composition ^{Dipp}LBa(18-c-6)(pyr), from a saturated pyridine solution. ^{1}H NMR (600 MHz, 298 K, pyridine-d_5) δ 9.40 (s, 2H, ***H***C=N), 8.61 (d, $^3J_{HH}$ = 8.4 Hz, 2H, 3,6-C$_{10}$***H***$_4$), 7.28 (d, $^3J_{HH}$ = 7.6 Hz, 4H, N-3,5-C$_6$***H***$_3$), 7.17 (t, $^3J_{HH}$ = 7.8 Hz, 2H, N-4-C$_6$***H***$_3$), 6.85 (d, $^3J_{HH}$ = 8.3 Hz, 2H, 4,5-C$_{10}$***H***$_4$), 3.77 (m (br), 12H, **18-c-6**), 3.66 (m, 2.9H, thf-OC***H***$_2$), 3.58 (sept, $^3J_{HH}$ = 6.6 Hz, 4H, N-2,6-C$_6$H$_3$-C***H***Me$_2$), 3.35 (m (br), 12H, **18-c-6**), 1.62 (m, 2.9H, thf-C***H***$_2$), 1.27 (d, $^3J_{HH}$ = 6.4 Hz, 24H, N-2,6-C$_6$H$_3$-CH***Me***$_2$) ppm. ^{13}C{^{1}H} NMR (151 MHz, 298 K, pyridine-d_5) δ 176.0 (1,8-***C***$_{10}$H$_4$), 163.1 (H***C***=N), 155.1 (N-1-***C***$_6$H$_3$), 146.3 (9-***C***$_{10}$H$_4$), 139.6 (N-2,6-***C***$_6$H$_3$), 127.4 (3,6-***C***$_{10}$H$_4$), 127.2 (10-***C***$_{10}$H$_4$), 123.4 (N-3,5-***C***$_6$H$_3$), 122.9 (N-4-***C***$_6$H$_3$), 117.9 (2,7-***C***$_{10}$H$_4$), 111.6 (4,5-***C***$_{10}$H$_4$), 70.6 (**18-c-6**), 68.3 (thf-O***C***H$_2$), 28.5 (N-2,6-C$_6$H$_3$-***C***HMe$_2$), 26.3 (thf-***C***H$_2$), 24.2 (N-2,6-C$_6$H$_3$-CH***Me***$_2$) ppm. IR (KBr): 3042, 2958, 2920, 2867, 2361, 2343, 1597, 1560, 1511, 1437, 1352, 1328, 1261, 1229, 1163, 1126, 1098, 1062, 965, 829, 816, 752, 709, 668 cm^{-1}. Anal. Calcd for $C_{50.92}H_{69.84}N_2O_{8.73}Ba$: C, 61.96; H, 7.13; N, 2.84. Found: C, 62.35; H, 7.20; N, 2.81.

7.2.12 Synthesis of ^{Dipp}LK$_2$ (6)

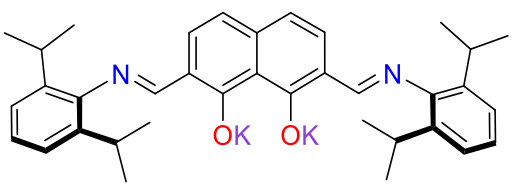

At 0 °C, a solution of H$_2$^{Dipp}L (0.100 g, 0.187 mmol) in THF (2 mL) was added dropwise to a slurry of potassium hydride (0.0188 g, 0.468 mmol, 2.5 eq.) in THF (2 mL). The resultant reaction mixture was left

stirring overnight prior to filtration. Volatiles were removed *in vacuo* and the crude oily red solid was triturated with pentane (5 mL) to afford $^{Dipp}LK_2$ (**6**) as a pale orange powder (0.0470 g, 41%). ^{1}H NMR (400 MHz, 298 K, THF-d_8): δ 8.45 (s (br), 2H, ***H***C=N), 7.56 (s (br), 2H, 3,6-C_{10}***H***$_4$), 6.95 (d, $^3J_{HH}$ = 7.6 Hz, 4H, N-3,5-C_6***H***$_3$), 6.81 (t, $^3J_{HH}$ = 7.6 Hz, 2H, N-4-C_6***H***$_3$), 6.15 (d, $^3J_{HH}$ = 8.3 Hz, 2H, 4,5-C_{10}***H***$_4$), 3.14 (sept, $^3J_{HH}$ = 6.9 Hz, 4H, N-2,6-C_6H_3-C***H***Me_2), 1.08 (d, $^3J_{HH}$ = 6.9 Hz, 24H, N-2,6-C_6H_3-CH***Me***$_2$) ppm. ^{13}C{^{1}H} NMR (125 MHz, 298 K, THF-d_8): δ 178.3 (***C***=N), 163.5 (1,8-***C***$_{10}H_4$), 155.1 (N-1-***C***$_6H_3$), 146.8 (9-***C***$_{10}H_4$), 139.4 (N-2,6-***C***$_6H_3$), 129.0 (2,7-***C***$_{10}H_4$), 127.3 (3,6-***C***$_{10}H_4$), 123.0 (N-3,5-***C***$_6H_3$), 122.2 (N-4-***C***$_6H_3$), 118.6 (10-***C***$_{10}H_4$), 110.0 (4,5-***C***$_{10}H_4$), 28.6 (N-2,6-C_6H_3-***C***HMe_2), 24.3 (N-2,6-C_6H_3-CH***Me***$_2$) ppm. IR (KBr): 3059, 2959, 2926, 2868, 1610, 1584, 1527, 1436, 1384, 1361, 1258, 1222, 1138, 1096, 1062, 906, 831, 756 cm^{-1}. Anal. Calcd for $C_{36}H_{40}N_2O_2K_2$: C, 70.78; H, 6.60; N, 4.59. Found: C, 69.84; H, 6.62; N, 4.42.

7.2.13 Targeting bimetallic heavier alkaline-earth complexes through salt-metathesis

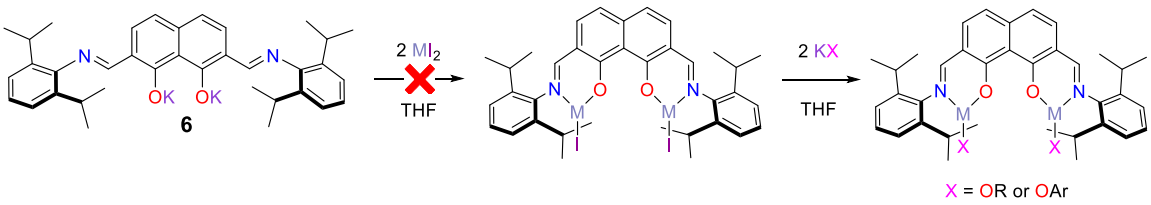

In a Young's tap NMR tube, $H_2{}^{Dipp}L$ (0.0200 g, 0.0374 mmol) and KH (0.00300 g, 0.0749 mmol) were dissolved in THF-d_8 (0.5 mL). The reaction mixture was sonicated until NMR spectroscopic analyses confirmed quantitative conversion of compound **6** (typically about 1 h). One equivalent of alkaline-earth diiodide (0.0374 mmol, M = Ca, Sr, Ba) was then added before further sonication for 0.5 h. Analysis of the resultant solution indicated that in all cases a mixture of two different, yet inseparable, products had been formed.

7.3 Experimental Details for Chapter 4

7.3.1 Synthesis of 2,6-dimethyl phenyl acetate[40]

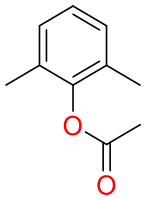

At 0 °C, pyridine (6.59 mL, 81.0 mmol) was added to a solution of 2,6-dimethyl phenol (5.00 g, 40.9 mmol) in DCM (100 mL). A solution of acetyl chloride (4.37 mL, 61.4 mmol) in DCM (50 mL) was then added dropwise before the reaction mixture was left to stir for 4 h at 0 °C. Addition of 0.1 N HCl (100 mL) quenched the reaction before the product was extracted with DCM (50 mL). The combined organic extracts were then washed with HCl (3 x 50 mL), distilled water (3 x 50 mL) and 0.1 M NaOH (3 x 50 mL), dried over $MgSO_4$ and concentrated *in vacuo* affording of 2,6-dimethyl phenyl acetate as a golden oil (5.77 g, 86%). ^{1}H NMR (400 MHz, 298 K, chloroform-d_1): δ 7.09 (m, 3H, 3,4,5-$C_6\boldsymbol{H}_3$), 2.35 (s, 3H, O(CO)C$\boldsymbol{H}_3$), 2.20 (s, 6H, 2,6-C$\boldsymbol{H}_3$-C_6H_3) ppm.

7.3.2 Synthesis of 2,6-*bis*(dibromomethyl)phenyl acetate[41]

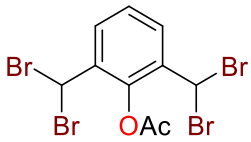

At –78 °C, $AlCl_3$ (0.447 g, 3.35 mmol) was added to a solution of NBS (10.25 g, 57.6 mmol) in DCM (80 mL). 2,6-dimethyl phenyl acetate (2.20 g, 13.4 mmol) was then added and the reaction mixture was left to stir for 5 days at room temperature. The reaction was quenched by the addition of sat. $NaHCO_3$ solution (50 mL) before the product was extracted with DCM (50 mL). The organic extracts were then washed with brine (3 x 50 mL), dried over $MgSO_4$ and concentrated *in vacuo* affording 2,6-*bis*(dibromomethyl)phenyl acetate as a pale-yellow solid (4.11 g, 62%). ^{1}H NMR (400 MHz, 298 K, chloroform-d_1): δ 7.93 (d, $^3J_{HH}$ = 7.9 Hz, 2H, 3,5-$C_6\boldsymbol{H}_3$), 7.44 (t, $^3J_{HH}$ = 7.9 Hz, 1H, 4-$C_6\boldsymbol{H}_3$), 6.64 (s, 2H, 2,6-$Br_2\boldsymbol{H}$-C_6H_3), 2.50 (s, 3H, -O(CO)C$\boldsymbol{H}_3$) ppm.

7.3.3 Synthesis of 2,6-diformyl phenol[42]

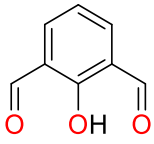

A slurry of 2,6-bis(dibromomethyl) phenyl acetate (4.70 g, 9.80 mmol) and KOH (4.58 g, 81.3 mmol) in distilled water (40 mL) was heated to reflux for 3 h. The resultant dark red solution was cooled and filtered into 20% aqueous HCl (60 mL). 2,6-diformyl phenol precipitated and was collected via filtration as a pale brown solid (0.509 g, 35%). ^{1}H NMR (400 MHz, 298 K, chloroform-d_1): δ 11.66 (s, 1H, O***H***), 10.25 (s, 2H, ***H***CO), 7.97 (d, $^{3}J_{HH}$ = 7.6 Hz, 2H, 3,5-C$_6$***H***$_3$), 7.14 (t, $^{3}J_{HH}$ = 7.6 Hz, 1H, 4-C$_6$***H***$_3$) ppm.

7.3.4 Synthesis of 2,6-diformyl-*para*-substituted phenols (R = Me, ^{t}Bu)[8, 9]

General procedure:

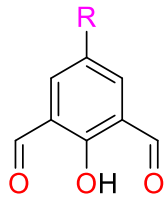

R = Me, ^{t}Bu

A mixture of phenol (5.00 g, 1.0 eq.) and hexamethyltetramine (2.0 eq) in trifluoroacetic acid (15.0 eq.) was heated to 145 °C for 18 h. The resultant hot dark brown solution was poured into 4 N HCl (115 mL) and stirred at room temperature for 2 h. The reaction mixture was then stored overnight at 5 °C before the precipitate was isolated via filtration. The crude product was washed with ice-cold distilled water (3 x 50 mL) and –78 °C methanol (3 x 20 mL) affording the appropriate 2,6-diformyl-*para*-substituted phenol as a bright yellow solid. A second crop of pure material crystallised overnight from the room temperature washings.

R = Me (combined mass: 5.47 g, combined yield: 72%)

^{1}H NMR (400 MHz, 298 K, chloroform-d_1): δ 11.45 (s, 1H, O***H***), 10.21 (s, 2H, ***H***CO), 7.77 (s, 2H, 3,5-C$_6$***H***$_3$), 2.39 (s, 3H, C***H***$_3$) ppm.

R = ^{t}Bu (combined mass: 6.77 g, combined yield: 99%)

^{1}H NMR (400 MHz, 298 K, chloroform-d_1): δ 11.47 (s, 1H, O***H***), 10.24 (s, 2H, ***H***CO), 7.98 (s, 2H, 3,5-C$_6$***H***$_3$), 1.35 (s, 9H, C(C***H***$_3$)$_3$) ppm.

7.3.5 Synthesis of H^{R,Dipp}L (R = H, Me, ^{t}Bu); adapted from reference 10.

General procedure:

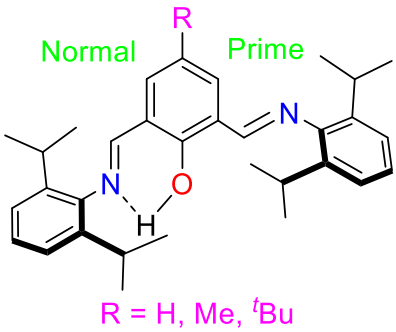

A solution of phenol (0.500 g, 1.0 eq.) and 2,6-diisopropylaniline (2.0 eq.) in methanol (10 mL) was prepared. *p*-toluenesulfonic acid (0.0500 g, 0.263 mmol) was added to the solution and the resultant mixture was stirred at room temperature overnight. The precipitate that had formed during this time was isolated via filtration and washed with ice-cold methanol (2 x 5 mL) to yield the desired pro-ligand as a pale-yellow powder.

R = H (0.905 g, 58%)

^{1}H NMR (500 MHz, 223 K, chloroform-d_1): δ 13.79 (s, 1H, O***H***), 8.79 (s, 1H, ***H***C=N'), 8.40 (s, 1H, ***H***C=N), 8.37 (d, $^{4}J_{HH}$ = 7.8 Hz, 1H, 3'-C$_6$***H***$_3$), 7.57 (dd, $^{4}J_{HH}$ = 1.8 Hz; $^{3}J_{HH}$ = 7.6 Hz, 1H, 3-C$_6$***H***$_3$), 7.28–7.11 (m, 7H, 4-C$_6$***H***$_3$ and N$^{(')}$-3,4,5-C$_6$***H***$_3$), 3.00 (overlapping septets, $^{3}J_{HH}$ = 7.6, 7.7 Hz, 4H, N$^{(')}$-2,6-C$_6$H$_3$-C***H***Me$_2$), 1.16 (dd, $^{3}J_{HH}$ = 7.7, 7.8 Hz, 24H, N$^{(')}$-2,6-C$_6$H$_3$-CH***Me***$_2$) ppm. ^{13}C{^{1}H} NMR (125 MHz, 223 K, chloroform-d_1): δ 166.4 (H***C***=N), 161.49 (1-***C***$_6$H$_3$), 157.6 (H***C***=N'), 149.4 (N'-1-***C***$_6$H$_3$), 145.5 (N-1-***C***$_6$H$_3$), 138.6 (N-2-***C***$_6$H$_3$), 137.7 (N'-2-***C***$_6$H$_3$), 135.7 (3-***C***$_6$H$_3$), 130.7 (3'-***C***$_6$H$_3$), 125.7 (4-***C***$_6$H$_3$), 124.0 (N-4-***C***$_6$H$_3$), 123.7 (N'-4-***C***$_6$H$_3$), 123.3 (N-3,5-***C***$_6$H$_3$), 123.0 (N'-3,5-***C***$_6$H$_3$), 119.1 (2$^{(')}$-***C***$_6$H$_3$), 28.0 (N-2,6-C$_6$H$_3$-***C***HMe$_2$), 27.8 (N'-2,6-C$_6$H$_3$-***C***HMe$_2$), 23.7 (N$^{(')}$-2,6-C$_6$H$_3$-CH***Me***$_2$) ppm. IR (KBr): 3062, 2962, 2926, 2868, 1625, 1582, 1460, 1384, 1362, 1301, 1255, 1181, 990, 840, 798, 760, 703 cm^{-1}. Anal. Calcd for C$_{32}$H$_{40}$N$_2$O: C, 82.01; H, 8.60; N, 5.98. Found: C, 82.66; H, 8.39; N, 5.54.

R = Me (0.615 g, 42%)

^{1}H NMR (500 MHz, 223 K, chloroform-d_1): δ 13.50 (s, 1H, O***H***), 8.77 (s, 1H, ***H***C=N'), 8.34 (s, 1H, ***H***C=N), 8.16 (d, $^{4}J_{HH}$ = 2.3 Hz, 1H, 3'-C_6***H***$_2$), 7.36 (d, $^{4}J_{HH}$ = 2.3 Hz, 1H, 3-C_6***H***$_2$), 7.25–7.13 (m, 6H, N$^{(')}$-3,4,5-C_6***H***$_3$), 2.99 (overlapping sept, $^{3}J_{HH}$ = 6.8, 6.9 Hz, 4H, N$^{(')}$-2,6-C_6H_3-C***H***Me_2), 2.43 (s, 3H, C(C***H***$_3$)), 1.19 (dd, $^{3}J_{HH}$ = 6.7, 6.8 Hz, 24H, N$^{(')}$-2,6-C_6H_3-CH***Me***$_2$) ppm. ^{13}C{^{1}H} NMR (125 MHz, 223 K, chloroform-d_1): δ 166.5 (H***C***=N), 159.6 (1-***C***$_6H_2$), 158.0 (H***C***=N'), 149.5 (N'-1-***C***$_6H_3$), 145.8 (N-1-***C***$_6H_3$), 138.8 (N-2-***C***$_6H_3$), 138.0 (N'-2-***C***$_6H_3$), 136.3 (3-***C***$_6H_2$), 131.0 (3'-***C***$_6H_2$), 128.6 (4-***C***$_6H_2$), 125.8 (N-4-***C***$_6H_3$), 124.2 (N'-4-***C***$_6H_3$), 123.5 (N-3,5-***C***$_6H_3$), 123.4 (2'-***C***$_6H_2$), 123.1 (N'-3,5-***C***$_6H_3$), 119.1 (2-***C***$_6H_2$), 28.2 (N-2,6-C_6H_3-***C***HMe_2) 28.0 (N'-2,6-C_6H_3-***C***HMe_2), 23.9 (N$^{(')}$-2,6-C_6H_3-CH***Me***$_2$), 20.7 (C(***C***H_3)) ppm. IR (KBr): 3067, 2963, 2865, 1625, 1590, 1460, 1362, 1310, 1258, 1182, 1157, 1035, 979, 932, 789, 758, 698 cm^{-1}. Anal. Calcd for $C_{33}H_{42}N_2O$: C, 82.11; H, 8.77; N, 5.80. Found: C, 83.76; H, 8.86; N, 5.75.

R = ^{t}Bu (1.13 g, 89%)

^{1}H NMR (500 MHz, 223 K, chloroform-d_1): δ 13.64 (s, 1H, O***H***), 8.80 (s, 1H, ***H***C=N'), 8.42 (d, $^{4}J_{HH}$ = 2.5 Hz, 1H, 3'-C_6***H***$_2$), 8.39 (s, 1H, ***H***C=N), 7.53 (d, $^{4}J_{HH}$ = 2.6 Hz, 1H, 3-C_6***H***$_2$), 7.25-7.14 (overlapping m, 6H, N$^{(')}$-3,4,5-C_6***H***$_3$), 2.99 (overlapping sept, $^{3}J_{HH}$ = 6.8, 7.0 Hz, 4H, N$^{(')}$-2,6-C_6H_3-C***H***Me_2), 1.42 (s, 9H, C(C***H***$_3$)$_3$), 1.19 (dd, $^{3}J_{HH}$ = 6.9, 6.9 Hz, 24H, N$^{(')}$-2,6-C_6H_3-CH***Me***$_2$) ppm. ^{13}C{^{1}H} NMR (125 MHz, 223 K, chloroform-d_1): δ 166.5 (H***C***=N), 159.5 (1-***C***$_6H_2$), 157.6 (H***C***=N'), 149.4 (N'-1-***C***$_6H_3$), 145.5 (N-1-***C***$_6H_3$), 141.7 (4-***C***$_6H_2$), 138.5-137.8 (N-3,5-***C***$_6H_3$ and N'-3,5-***C***$_6H_3$), 132.5 (3-***C***$_6H_2$), 127.5 (3'-***C***$_6H_2$), 125.5 (N-4-***C***$_6H_3$ and N'-4-***C***$_6H_3$), 124.0 (2'-***C***$_6H_2$), 123.2-123.0 (N-2-***C***$_6H_3$ and N'-2-***C***$_6H_3$), 118.5 (2-***C***$_6H_2$), 34.4 (***C***$(CH_3)_3$), 31.4 (C(***C***H_3)$_3$), 28.0-27.8 (N-2,6-C_6H_3-***C***HMe_2 and N'-2,6-C_6H_3-***C***HMe_2), 23.8 (N-2,6-C_6H_3-CH***Me***$_2$ and N'-2,6-C_6H_3-

CH***Me***$_2$) ppm. IR (KBr): 3064, 3018, 2962, 2924, 2868, 1628, 1585, 1459, 1362, 1311, 1178, 1108, 1031, 1007, 932, 869, 856, 786, 756 cm^{-1}. Anal. Calcd for $C_{36}H_{48}N_2O$: C, 82.39; H, 9.22; N, 5.34. Found: C, 83.92; H, 9.31; N, 5.33.

7.3.6 Synthesis of ^{R,Dipp}LK·thf$_x$ (R = H (**7·thf$_x$**), Me (**8·thf$_x$**), ^{t}Bu (**9·thf$_x$**))

General procedure:

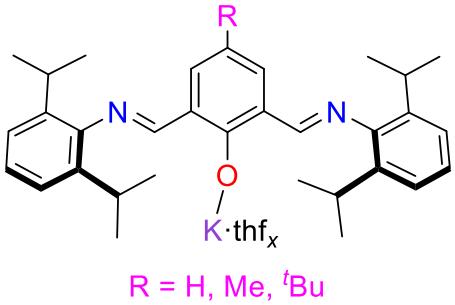

At 0 °C, a solution of pro-ligand (1.00 g, 1.0 eq.) in THF (5 mL) was added dropwise to a slurry of potassium hydride (1.5 eq.) in THF (5 mL). The resultant reaction mixture was left stirring overnight prior to filtration. Volatiles were removed *in vacuo* and the crude oily solid was triturated with pentane (5 mL) to afford ^{R,Dipp}LK·thf$_x$ (R = H (**7·thf$_x$**), Me (**8·thf$_x$**) and ^{t}Bu (**9·thf$_x$**)) as yellow powders. Single crystals of ^{R,Dipp}LK(18-c-6) (R = H, **[7(18-c-6)]$_n$**; R = Me , **[8(18-c-6)]$_n$**) suitable for an X-ray diffraction studies, were obtained by the slow evaporation of a saturated THF solutions containing 1 eq. 18-crown-6 at room temperature. The ^{t}Bu analogue crystallised as a thf-adduct **[9(18-c-6)(thf)]**.

R = H The bulk material had the composition ^{Dipp}LK·thf$_{1.4}$ (0.762 g, 71%)

^{1}H NMR (400 MHz, 298 K, THF-d_8): δ 8.54 (s, 2H, ***H***C=N), 7.80 (d, $^3J_{HH}$ = 7.4 Hz, 2H, 3-C$_6$***H***$_3$), 7.03 (d, $^3J_{HH}$ = 7.6 Hz, 4H, N-3,5-C$_6$***H***$_3$), 6.90 (t, $^3J_{HH}$ = 7.6 Hz, 2H, N-4-C$_6$***H***$_3$), 6.10 (t, $^3J_{HH}$ = 7.4 Hz, 1H, 4-C$_6$***H***$_3$), 3.62 (m, 6H, thf-OC***H***$_2$), 3.11 (sept, $^3J_{HH}$ = 6.9 Hz, 4H, N-2,6-C$_6$H$_3$-C***H***Me$_2$), 1.77 (m, 6H, thf-C***H***$_2$), 1.13 (d, $^3J_{HH}$ = 6.9 Hz, 24H, N-2,6-C$_6$H$_3$-CH***Me***$_2$) ppm. ^{13}C{^{1}H} NMR (151 MHz, 298 K, THF-d_8): δ 175.9 (1-***C***$_6$H$_3$), 163.4 (H***C***=N), 153.8 (N-1-***C***$_6$H$_3$), 139.0 (N-2-***C***$_6$H$_3$), 133.6 (3-***C***$_6$H$_3$), 127.4 (2-***C***$_6$H$_3$), 123.3 (N-3,5-***C***$_6$H$_3$), 123.2 (N-4-***C***$_6$H$_3$), 108.6 (4-***C***$_6$H$_3$), 67.3 (thf-O***C***H$_2$), 28.7 (N-2,6-C$_6$H$_3$-

CHMe$_2$), 25.4 (thf-***C***H$_2$), 24.1 (N-2,6-C$_6$H$_3$-CH***Me***$_2$) ppm. IR (KBr): 3060, 2960, 2925, 2866, 1642, 1615, 1520, 1437, 1314, 1222, 1180, 1098, 1054, 999, 838, 801, 771, 762, 744 cm^{-1}. Anal. Calcd for $C_{37.6}H_{48.8}N_2O_{2.4}K$: C, 74.49; H, 8.11; N, 4.62. Found: C, 72.92; H, 7.35; N, 4.10.

R = Me The bulk material had the composition ^{Me,Dipp}LK·thf$_{0.7}$ (0.982 g, 91%)

^{1}H NMR (600 MHz, 298 K, THF-d_8): δ 8.52 (s, 2H, ***H***C=N), 7.67 (s, 2H, 3-C$_6$***H***$_2$), 7.02 (d, $^3J_{HH}$ = 7.6 Hz, 4H, N-3,5-C$_6$***H***$_3$), 6.89 (t, $^3J_{HH}$ = 7.6 Hz, 2H, N-4-C$_6$***H***$_3$), 3.62 (m, 3H, thf-OC***H***$_2$), 3.11 (sept, $^3J_{HH}$ = 6.8 Hz, 4H, N-2,6-C$_6$H$_3$-C***H***Me$_2$), 2.18 (s, 3H, C(C***H***$_3$)), 1.77 (m, 3H, thf-C***H***$_2$), 1.13 (d, J = 6.9 Hz, 24H, N-2,6-C$_6$H$_3$-CH***Me***$_2$) ppm. ^{13}C{^{1}H} NMR (151 MHz, 298 K, THF-d_8): δ 174.5 (1-***C***$_6$H$_2$), 163.4 (H***C***=N), 154.0 (N-1-***C***$_6$H$_3$), 139.0 (N-2-***C***$_6$H$_3$), 134.0 (3-***C***$_6$H$_2$), 126.8 (2-***C***$_6$H$_2$), 123.2 (N-3,5-***C***$_6$H$_3$), 123.1 (N-4-***C***$_6$H$_3$), 116.1 (***C***(CH$_3$)), 67.3 (thf-O***C***H$_2$), 28.7 (N-2,6-C$_6$H$_3$-***C***HMe$_2$), 25.4 (thf-***C***H$_2$), 24.1 (N-2,6-C$_6$H$_3$-CH***Me***$_2$), 21.0 (C(***C***H$_3$)) ppm. IR (KBr): 3059, 2960, 2927, 2858, 1636, 1612, 1588, 1511, 1463, 1438, 1321, 1305, 1222, 1177, 1106, 1056, 1025, 980, 842, 794, 768, 714 cm^{-1}. Anal. Calcd for $C_{35.8}H_{45.9}N_2O_{1.7}K$: C, 75.36; H, 8.11; N, 4.91. Found: C, 75.55; H, 7.93; N, 5.02.

R = ^{t}Bu The bulk material had the composition ^{tBu,Dipp}LK·thf$_{0.3}$ (0.800 g, 75%)

^{1}H NMR (600 MHz, 298 K, THF-d_8): δ 8.53 (s, 2H, ***H***C=N), 7.93 (s, 2H, 3-C$_6$***H***$_2$), 7.03 (d, $^3J_{HH}$ = 7.7 Hz, 4H, N-3,5-C$_6$***H***$_3$), 6.90 (t, $^3J_{HH}$ = 7.7 Hz, 2H, N-4-C$_6$***H***$_3$), 3.62 (m, 2H, thf-OC***H***$_2$), 3.11 (sept, $^3J_{HH}$ = 6.9 Hz, 4H, N-2,6-C$_6$H$_3$-C***H***Me$_2$), 1.77 (m, 2H, thf-C***H***$_2$), 1.32 (s, 9H, C(C***H***$_3$)$_3$), 1.14 (d, $^3J_{HH}$ = 6.9 Hz, 24H, N-2,6-C$_6$H$_3$-CH***Me***$_2$) ppm. ^{13}C{^{1}H} NMR (151 MHz, 298 K, THF-d_8): δ 173.2 (1-***C***$_6$H$_2$), 162.6 (H***C***=N), 152.8 (N-1-***C***$_6$H$_3$), 137.9 (N-2-***C***$_6$H$_3$), 129.3 (3-***C***$_6$H$_2$), 128.9 (4-***C***$_6$H$_2$), 125.22 (2-***C***$_6$H$_2$), 122.1 (N-3,5-***C***$_6$H$_3$), 122.0 (N-4-***C***$_6$H$_3$), 67.3 (thf-O***C***H$_2$), 33.3 (***C***(CH$_3$)$_3$), 31.3 (C(***C***H$_3$)$_3$), 27.6 (N-2,6-C$_6$H$_3$-

CHMe$_2$), 25.4 (thf-***C***H$_2$), 22.9 (N-2,6-C$_6$H$_3$-CH***Me***$_2$) ppm. IR (KBr): 3061, 2960, 2927, 2867, 2237, 1628, 1616, 1509, 1459, 1440, 1361, 1320, 1231, 1177, 1099, 1034, 1004, 844, 774, 760, 717 cm^{-1}. Anal. Calcd for $C_{37.2}H_{49.1}N_2O_{1.3}K$: C, 76.48; H, 8.47; N, 4.80. Found: C, 74.10; H, 8.48; N, 4.90.

7.3.7 Synthesis of ($^{t\text{Bu,Dipp}}$L)$_2$Mg(thf) (10)

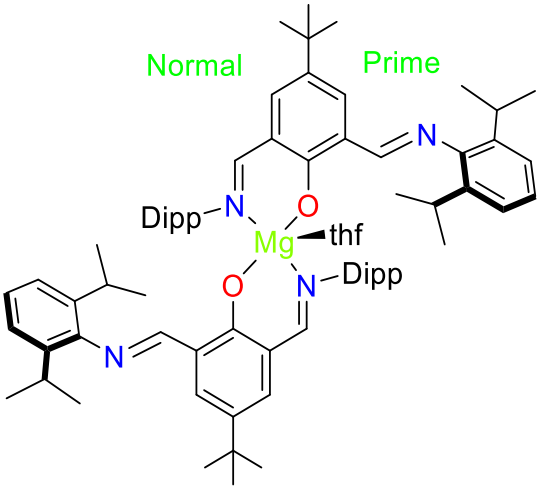

A solution of $^{t\text{Bu,Dipp}}$LK·thf$_{0.3}$ (0.500 g, 0.860 mmol) in THF (2 mL) was added to a slurry of MgI$_2$ (0.120 g, 0.430 mmol) in THF (2 mL). The mixture was sonicated for 0.5 h and then left to stir at room temperature for a further 3 h prior to filtration. Volatiles were removed *in vacuo* from the filtrate and the resultant oily solid was triturated with pentane (2 x 5 mL) to afford ($^{t\text{Bu,Dipp}}$L)$_2$Mg(thf) (**10**) as a bright yellow powder (0.361 g, 81%). Single crystals of ($^{t\text{Bu,Dipp}}$L)$_2$Mg(thf) (**10**), suitable for an X-ray diffraction study, were obtained by slow evaporation of a THF/pentane mixture. ^{1}H NMR (600 MHz, 298 K, THF-d_8) δ 8.21 (d, $^3J_{HH}$ = 2.8 Hz, 2H, 3'-C$_6$***H***$_2$), 8.13 (s, 2H, ***H***C=N), 7.30 (d, $^3J_{HH}$ = 2.9 Hz, 2H, 3-C$_6$***H***$_2$), 7.24 (s, 2H, ***H***C=N'), 7.09 (d, $^3J_{HH}$ = 7.7 Hz, 4H, N'-3,5-C$_6$***H***$_3$), 7.00 (t, $^3J_{HH}$ = 7.7 Hz, 2H, N'-4-C$_6$***H***$_3$), 6.71 (d, $^3J_{HH}$ = 7.7 Hz, 4H, N-3,5-C$_6$***H***$_3$), 6.59 (t, $^3J_{HH}$ = 7.7 Hz, 2H, N-4-C$_6$***H***$_3$), 3.62 (m, 4H, thf-OC***H***$_2$), 2.85 (overlapping sept, 8H, N$^{(')}$-2,6-C$_6$H$_3$-C***H***Me$_2$), 1.77 (m, 4H, thf-C***H***$_2$), 1.27 (s, 18H, C(C***H***$_3$)$_3$), 1.18 (d, $^3J_{HH}$ = 6.9 Hz, 24H, N'-2,6-C$_6$H$_3$-CH***Me***$_2$), 1.00 (d, $^3J_{HH}$ = 6.8 Hz, 12H, N-2,6-C$_6$H$_3$-CH***Me***$_2$), 0.85 (d, $^3J_{HH}$ = 6.9 Hz, 12H, N-2,6-C$_6$H$_3$-CH***Me***$_2$). ^{13}C{^{1}H} NMR (151 MHz, 298 K, THF-d_8) δ 175.0 (H***C***=N), 169.5 (1-***C***$_6$H$_2$), 160.1 (H***C***=N'), 152.5 (N'-1-***C***$_6$H$_3$), 150.7 (N-1-***C***$_6$H$_3$), 140.8 (N'-2,6-C$_6$H$_3$-

CH***Me***$_2$), 137.6 (N-2,6-C$_6$H$_3$-CH***Me***$_2$), 136.7 (3-***C***$_6$H$_2$), 136.0 (4-***C***$_6$H$_2$), 131.2 (3'-***C***$_6$H$_2$), 128.5 (2'-***C***$_6$H$_2$), 126.4 (N'-4-***C***$_6$H$_3$), 123.5 (N-4-***C***$_6$H$_3$), 123.5 (N'-3,5-***C***$_6$H$_3$), 122.8 (N-3,5-***C***$_6$H$_3$), 122.3 (2-***C***$_6$H$_2$), 68.1 (thf-O***C***H$_2$), 34.5 (***C***(CH$_3$)$_3$), 32.0 (C(***C***H$_3$)$_3$), 29.0 (N$^{(')}$-2,6-C$_6$H$_3$-***C***HMe$_2$), 26.6 (thf-***C***H$_2$), 25.7 (N-2,6-C$_6$H$_3$-CH***Me***$_2$), 23.1 (N-2,6-C$_6$H$_3$-CH***Me***$_2$), 22.9 (N'-2,6-C$_6$H$_3$-CH***Me***$_2$) ppm. IR (KBr): 3064, 2959, 2860, 2361, 2337, 1613, 1585, 1528, 1465, 1436, 1387, 1362, 1268, 1237, 1173, 1034, 1012, 885, 835, 791, 760, 729, 530 cm^{-1}. Anal. Calcd for C$_{76}$H$_{101}$N$_4$O$_3$Mg: C, 79.86; H, 8.91; N, 4.90. Found: C, 78.58; H, 8.88; N, 4.65.

7.3.8 Synthesis of ($^{t\text{Bu,Dipp}}$L)$_2$M(thf)$_2$ (M = Sr (11) and Ba (12))

General procedure:

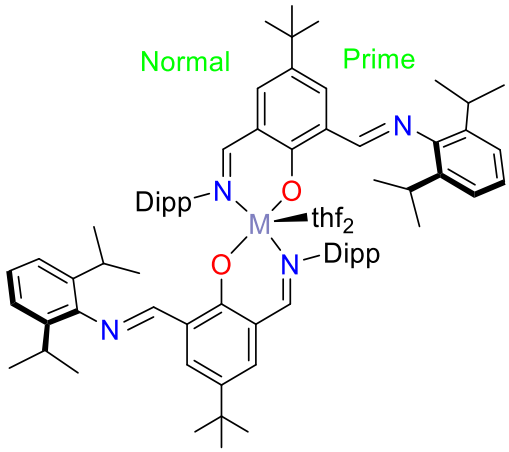

A solution of $^{t\text{Bu,Dipp}}$LK·thf$_{0.3}$ (0.360 g, 0.622 mmol, 2.0 eq.) in THF (2 mL) was added to a slurry of MI$_2$ (1.0 eq.) in THF (2 mL). The mixture was left to stir at room temperature for 1 h prior to filtration. Volatiles were removed *in vacuo* from the filtrate and the resultant oily solid was washed with –78 °C pentane (3 x 2 mL) to afford the homoleptic complexes, ($^{t\text{Bu,Dipp}}$L)$_2$M(thf)$_2$ (M = Sr (**11**) and Ba (**12**)), as bright yellow powders.

M = Sr (0.236 g, 59%)

Single crystals of ($^{t\text{Bu,Dipp}}$L)$_2$Sr(thf)$_2$, suitable for an X-ray diffraction study, were obtained by slow evaporation of a HMDSO mixture. ^{1}H NMR (500 MHz, 233 K, THF-d_8) δ 8.73 (s, 2H, ***H***C=N'), 8.29 (d, $^4J_{HH}$ = 2.9 Hz, 2H, 3'-C$_6$***H***$_2$), 7.98 (s, 2H, ***H***C=N), 7.30 (d, $^4J_{HH}$ = 3.0 Hz, 2H, 3-C$_6$***H***$_2$), 7.05 (m (br), 6H, N-3,4,5-C$_6$***H***$_3$), 7.02 (d, $^3J_{HH}$ = 7.7 Hz, 4H, N'-

3,5-$C_6\boldsymbol{H}_3$), 6.94 (t, $^3J_{HH}$ = 7.6 Hz, 2H, N'-4-$C_6\boldsymbol{H}_3$), 3.64 (m, 4H, thf-OC$\boldsymbol{H}_2$), 2.93 (overlapping sept, 8H, N$^{(')}$-2,6-C_6H_3-C$\boldsymbol{H}$Me$_2$), 1.78 (m, 4H, thf-C$\boldsymbol{H}_2$), 1.33 (s, 18H, C(C$\boldsymbol{H}_3$)$_3$), 1.10–1.03 (m (br), 12H, N-2,6-C_6H_3-CH$\boldsymbol{Me}_2$), 1.00 (d, $^3J_{HH}$ = 6.9 Hz, 24H, N'-2,6-C_6H_3-CH$\boldsymbol{Me}_2$), 0.76 (d, $^3J_{HH}$ = 6.7 Hz, 12H, N-2,6-C_6H_3-CH$\boldsymbol{Me}_2$) ppm. $^{13}C\{^1H\}$ NMR (126 MHz, 193 K, THF-d_8) δ 172.8 (1-$\boldsymbol{C}_6H_2$), 170.3, (H$\boldsymbol{C}$=N), 160.9 (H$\boldsymbol{C}$=N'), 152.8 (N'-1-$\boldsymbol{C}_6H_3$), 152.1 (N-1-$\boldsymbol{C}_6H_3$), 140.2 (N-2,6-$\boldsymbol{C}_6H_3$), 139.1 (3-$\boldsymbol{C}_6H_2$), 138.1 (N'-2,6-$\boldsymbol{C}_6H_3$), 133.0 (4-$\boldsymbol{C}_6H_2$), 129.5 (3'-$\boldsymbol{C}_6H_2$), 126.4 (2'-$\boldsymbol{C}_6H_2$), 125.9 (N-4-$\boldsymbol{C}_6H_3$), 124.4 (2-$\boldsymbol{C}_6H_2$), 124.0 (N-3,5-$\boldsymbol{C}_6H_3$), 123.7 (N'-4-$\boldsymbol{C}_6H_3$), 123.1 (N'-3,5-$\boldsymbol{C}_6H_3$), 68.4 (thf-O$\boldsymbol{C}H_2$), 34.4 ($\boldsymbol{C}$(CH$_3$)$_3$), 32.1 (C($\boldsymbol{C}$H$_3$)$_3$), 28.7 (N$^{(')}$-2,6-C6H3-$\boldsymbol{C}$HMe$_2$), 26.6 (thf-$\boldsymbol{C}H_2$), 26.4 (N-2,6-C_6H_3-CH$\boldsymbol{Me}_2$), 24.0–22.4 (N-2,6-C_6H_3-CH$\boldsymbol{Me}_2$ and N'-2,6-C_6H_3-CH$\boldsymbol{Me}_2$) ppm. IR (KBr): 3060, 2961, 2927, 2868, 2367, 2342, 1617, 1584, 1527, 1457, 1362, 1328, 1264, 1235, 1171, 1034, 1005, 796, 755 cm^{-1}. Anal. Calcd for $C_{76}H_{101}N_4O_3Sr$: C, 75.67; H, 8.44; N, 4.64. Found: C, 75.23; H, 8.81; N, 4.18.

M = Ba (0.240 g, 58%)

Single crystals of ($^{t\text{Bu,Dipp}}$L)$_2$Ba(thf)$_2$, suitable for an X-ray diffraction study, were obtained by slow evaporation of a pentane solution. ^{1}H NMR (500 MHz, 233 K, THF-d_8) δ 8.67 (s, 2H, $\boldsymbol{H}$C=N'), 8.25 (d, $^4J_{HH}$ = 2.9 Hz, 2H, 3'-$C_6\boldsymbol{H}_2$), 7.99 (s, 2H, $\boldsymbol{H}$C=N), 7.28 (d, $^4J_{HH}$ = 3.1 Hz, 2H, 3-$C_6\boldsymbol{H}_2$), 7.14 (d, $^3J_{HH}$ = 7.6 Hz, 4H, N'-3,5-$C_6\boldsymbol{H}_3$), 7.06 (t, $^3J_{HH}$ = 7.9 Hz, 2H, N-4-$C_6\boldsymbol{H}_3$), 6.97 (d, $^3J_{HH}$ = 7.6 Hz, 2H, N'-4-$C_6\boldsymbol{H}_3$), 6.90 (d, $^3J_{HH}$ = 7.6 Hz, 4H, N-3,5-$C_6\boldsymbol{H}_3$), 3.62 (m, 4H, thf-OC$\boldsymbol{H}_2$), 2.90 (overlapping sept, 8H, N$^{(')}$-2,6-C_6H_3-C$\boldsymbol{H}$Me$_2$), 1.77 (m, 4H, thf-C$\boldsymbol{H}_2$), 1.27 (s, 18H, C(C$\boldsymbol{H}_3$)$_3$), 1.09 (d, $^3J_{HH}$ = 6.9 Hz, 24H, N'-2,6-C_6H_3-CH$\boldsymbol{Me}_2$), 0.96 (dd, $^3J_{HH}$ = 6.7, 6.9 Hz, 24H, N-2,6-C_6H_3-CH$\boldsymbol{Me}_2$) ppm. $^{13}C\{^1H\}$ NMR (126 MHz, 193 K, THF-d_8) δ 170.9 (1-$\boldsymbol{C}_6H_2$), 170.1 (H$\boldsymbol{C}$=N), 161.0 (H$\boldsymbol{C}$=N'), 152.9 (N'-1-$\boldsymbol{C}_6H_3$), 151.4 (N-1-$\boldsymbol{C}_6H_3$), 139.9 (N-2,6-$\boldsymbol{C}_6H_3$), 139.3 (3-$\boldsymbol{C}_6H_2$), 138.1 (N'-2,6-$\boldsymbol{C}_6H_3$), 137.6 (2'-$\boldsymbol{C}_6H_2$), 132.4 (4-$\boldsymbol{C}_6H_2$), 129.0 (3'-$\boldsymbol{C}_6H_2$), 125.9 (N-3,5-

C$_6$H$_3$), 125.6 (N'-4-***C***$_6$H$_3$), 124.8 (2-***C***$_6$H$_2$), 123.7 (N-4-***C***$_6$H$_3$), 123.0 (N'-3,5-***C***$_6$H$_3$), 68.1 (thf-O***C***H$_2$), 34.4, ***C***(CH$_3$)$_3$, 32.1, C(***C***H$_3$)$_3$, 28.8-28.6, N$^{(')}$-2,6-C$_6$H$_3$-***C***HMe$_2$, 26.0 (thf-***C***H$_2$), 26.5 (N-2,6-C$_6$H$_3$-CH***Me***$_2$), 23.1 (N'-2,6-C$_6$H$_3$-CH***Me***$_2$), ppm. IR (KBr): 3061, 2961, 2928, 2867, 2360, 2339, 1618, 1586, 1525, 1450, 1385, 1363, 1326, 1262, 1234, 1170, 1097, 1042, 1004, 829, 796, 758 cm^{-1}. Anal. Calcd for C$_{76}$H$_{101}$N$_4$O$_3$Ba: C, 72.68; H, 8.11; N, 4.46. Found: C, 72.36; H, 8.47; N, 4.24.

7.3.9 Synthesis of ^{R,Dipp}LCaI(thf)$_3$ (R = H (13), Me (14) and ^{t}Bu (15))

General procedure:

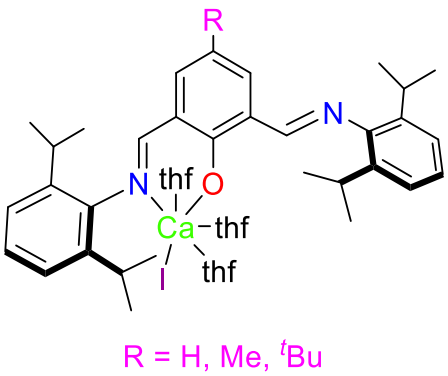

At room temperature, a solution of potassium salt ^{R,Dipp}LK·thf$_x$ (0.500 g, 1.0 eq.) in THF (5 mL) was added dropwise to a solution of calcium iodide (1.0 eq.) in THF (5 mL). The resultant cloudy solution was left stirring at room temperature for 30 minutes prior to filtration. Volatiles were removed *in vacuo* and the crude oily solid was triturated with pentane (5 mL) to afford ^{R,Dipp}LCaI(thf)$_3$ (R = H (**13**), Me (**14**) and ^{t}Bu (**15**)) as yellow powders. Single crystals of ^{tBu,Dipp}LCaI(thf)$_3$ (**15**), suitable for an X-ray diffraction studies, were obtained by the slow evaporation of a saturated THF solution at room temperature.

R = H (0.353 g, 42%)

^{1}H NMR (600 MHz, 298 K, THF-d_8) δ 8.45 (s, 2H, ***H***C=N), 7.76 (s, 2H, 3-C$_6$***H***$_3$), 7.09 (d, $^3J_{HH}$ = 7.6 Hz, 4H, N-3,5-C$_6$***H***$_3$), 7.02 (t, $^3J_{HH}$ = 7.7 Hz, 2H, N-4-C$_6$***H***$_3$), 6.52 (t, $^3J_{HH}$ = 7.5 Hz, 1H, 4-C$_6$***H***$_3$), 3.62 (m, 12H, thf-OC***H***$_2$), 3.00 (sept, $^3J_{HH}$ = 6.8 Hz, 4H, N-2,6-C$_6$H$_3$-C***H***Me$_2$), 1.77 (m, 12H, thf-C***H***$_2$), 1.16 (d, $^3J_{HH}$ = 6.9 Hz, 24H, N-2,6-C$_6$H$_3$-CH***Me***$_2$). ^{13}C{^{1}H} NMR (151 MHz, THF-d_8) δ 172.0 (1-***C***$_6$H$_3$), 171.0 (H***C***=N), 152.2 (N-

1-***C***$_6$H$_3$), 139.6 (N-2-***C***$_6$H$_3$), 126.4 (3-***C***$_6$H$_3$), 125.0 (N-3,5-***C***$_6$H$_3$), 123.7 (N-4-***C***$_6$H$_3$), 113.5 (4-***C***$_6$H$_3$), 112.7 (2-***C***$_6$H$_3$), 67.3 (thf-O***C***H$_2$), 29.0 (N-2,6-C$_6$H$_3$-***C***HMe$_2$), 25.4 (thf-***C***H$_2$), 24.3 (N-2,6-C$_6$H$_3$-CH***Me***$_2$). IR (KBr): 3061, 2961, 2926, 2868, 1617, 1614, 1543, 1459, 1449, 1399, 1383, 1327, 1181, 1100, 1027, 989, 877, 842, 800, 757 cm^{-1}. Anal. Calcd for $C_{44}H_{60}N_2O_4CaI$: C, 62.32; H, 7.13; N, 3.30. Found: C, 58.27; H, 6.43; N, 3.56.

R = Me (0.678 g, 82%)

^{1}H NMR (600 MHz, 298 K, THF-d_8) δ 8.41 (s, 1H, ***H***C=N), 7.59 (s, 1H, 3-C$_6$***H***$_2$), 7.09 (d, $^3J_{HH}$ = 7.6 Hz, 4H, N-3,5-C$_6$***H***$_3$), 7.01 (t, $^3J_{HH}$ = 7.7 Hz, 2H, N-4-C$_6$***H***$_3$), 3.62 (m, 12H, thf-OC***H***$_2$), 3.00 (sept, $^3J_{HH}$ = 6.9 Hz, 4H, N-2,6-C$_6$H$_3$-C***H***Me$_2$), 2.24 (s, 3H, C(C***H***$_3$)), 1.77 (m, 12H, thf-C***H***$_2$), 1.16 (d, $^3J_{HH}$ = 6.98 Hz, 24H, N-2,6-C$_6$H$_3$-CH***Me***$_2$) ppm. ^{13}C{^{1}H} NMR (151 MHz, THF-d_8) δ 170.4 (1-***C***$_6$H$_2$), 169.3 (H***C***=N), 152.3 (N-1-***C***$_6$H$_3$), 139.6 (N-2-***C***$_6$H$_3$), 125.8 (3-***C***$_6$H$_2$), 125.0 (N-4-***C***$_6$H$_3$), 121.8 (N-3,5-***C***$_6$H$_3$), 120.8 (4-***C***$_6$H$_2$), 121.8 (2-***C***$_6$H$_2$), 67.3 (thf-O***C***H$_2$), 28.9 (N-2,6-C$_6$H$_3$-***C***HMe$_2$), 25.4 (thf-***C***H$_2$), 24.3 (N-2,6-C$_6$H$_3$-CH***Me***$_2$), 20.5 (C(***C***H$_3$)) ppm. IR (KBr): 3074, 3063, 2983, 2964, 2867, 1620, 1587, 1536, 1462, 1392, 1383, 1326, 1255, 1226, 1176, 1034, 976, 910, 879, 798, 760 cm^{-1}. Anal. Calcd for $C_{45}H_{62}N_2O_4CaI$: C, 62.70; H, 7.25; N, 3.25. Found: C, 58.84; H, 6.59; N, 3.06.

R = ^{t}Bu (0.645 g, 75%)

^{1}H NMR (400 MHz, 298 K, THF-d_8): δ 8.46 (s, 2H, ***H***C=N), 7.87 (s, 2H, 3-C$_6$***H***$_2$), 7.09 (m, 4H, N-3,5-C$_6$***H***$_3$), 7.01 (dd, $^3J_{HH}$ = 8.6, 8.7 Hz, 2H, N-4-C$_6$***H***$_3$), 3.62 (m, 12H, thf-OC***H***$_2$), 3.00 (sept, $^3J_{HH}$ = 6.9 Hz, 4H, N-2,6-C$_6$H$_3$-C***H***Me$_2$), 1.77 (m, 12H, thf-C***H***$_2$), 1.32 (s, 9H, C(C***H***$_3$)$_3$), 1.16 (d, $^3J_{HH}$ = 6.9 Hz, 24H, N-2,6-C$_6$H$_3$-CH***Me***$_2$) ppm. ^{13}C{^{1}H} NMR (151 MHz, 298 K, THF-d_8): δ 170.4 (1-***C***$_6$H$_2$), 169.3 (H***C***=N), 152.3 (N-1-***C***$_6$H$_3$), 139.6 (N-2-***C***$_6$H$_3$), 135.39 (3-***C***$_6$H$_2$), 125.56(2-***C***$_6$H$_2$), 124.95 (N-4-***C***$_6$H$_3$), 123.7 (N-3,5-

C$_6$H$_3$), 122.4 (4-***C***$_6$H$_2$), 67.3 (thf-O***C***H$_2$), 34.55 (***C***(CH$_3$))), 32.1 (C(***C***H$_3$)), 29.0 (N-2,6-C$_6$H$_3$-***C***HMe$_2$), 25.4 (thf-***C***H$_2$), 24.3 (N-2,6-C$_6$H$_3$-CH***Me***$_2$) ppm. IR (KBr): 3061, 2961, 2928, 2868, 1626, 1615, 1584, 1531, 1461, 1397, 1362, 1329, 1237, 1170, 1034, 877, 832, 783, 760 cm^{-1}. Anal. Calcd for C$_{48}$H$_{68}$N$_2$O$_4$CaI: C, 63.77; H, 7.58; N, 3.10. Found: C, 60.69; H, 6.93; N, 3.25.

7.3.10 Alternative attempts to synthesise a heteroleptic $^{t\text{Bu,Dipp}}$LMgI(thf)$_3$ initiator

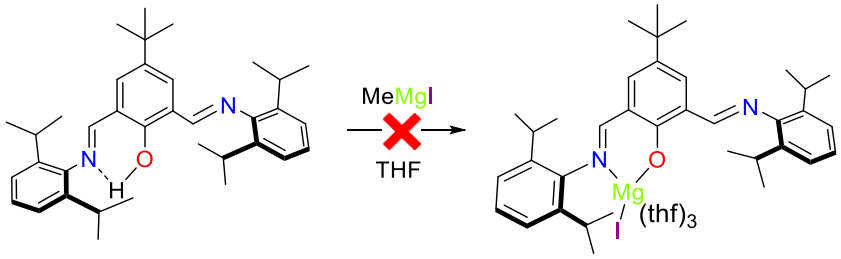

A solution of H$^{t\text{Bu,Dipp}}$L (0.100 g, 0.191 mmol) in diethyl ether (2 mL) was prepared and cooled to –78 °C. To this was added a solution of MeMgI (0.5 M in diethyl ether, 0.381 mL, 0.191 mmol). The reaction mixture was then manipulated in different ways (warmed to room temperature and left stirring overnight or kept at –78 °C for 0.25–1 h) prior to the removal of volatiles *in vacuo*. ^{1}H NMR spectroscopic analysis of the crude mixture revealed that multiple species were present: the *bis*(ligand) homoleptic magnesium complex (**10**), residual pro-ligand and an unknown compound. The unknown was tentatively assigned as the desired heteroleptic complex.

7.4 Experimental Details for Chapter 6

7.4.1 Treatment of ^{tBu,Dipp}LCaI(thf)$_3$ (15) with NaBAr$^F_4$

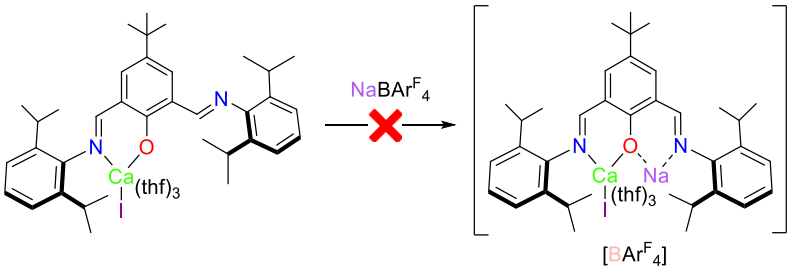

In a Young's tap NMR tube, complex **15** (0.0200 g, 0.0250 mmol) and NaBAr$^F_4$ (Ar^F = 3,5-{CF$_3$}$_2$C$_6$H$_3$) (0.0223 g, 0.0250 mmol) were dissolved in THF-d_8 (0.5 mL). No reaction was observed over the course of several days at room or elevated temperatures.

7.4.2 Treatment of ^{tBu,Dipp}LCaI(thf)$_3$ (15) with cationic alkaline-earth reagents

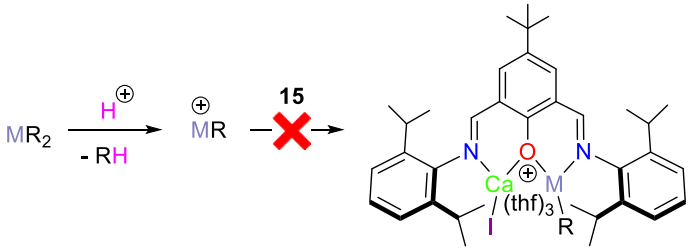

when M = Mg, R = Et, N(SiMe$_3$)$_2$, O-2,6-Me-C$_6$H$_3$ when M = Ca, R = N(SiMe$_3$)$_2$, O-2,6-Me-C$_6$H$_3$

In a Young's tap NMR tube, a disubstituted group two reagent (0.0200 g, 1.0 eq.) was treated with [H(OEt$_2$)$_2$][H$_2$N{B(C$_6$F$_5$)$_3$}$_2$] (1.0 eq.) in THF-d_8. Addition of complex **15** (1.0 eq.) to these solutions however, resulted in mixtures of inseparable species.

7.4.3 Treatment of ^{tBu,Dipp}LCaI(thf)$_3$ (15) with [HOEt$_2$][BF$_4$]

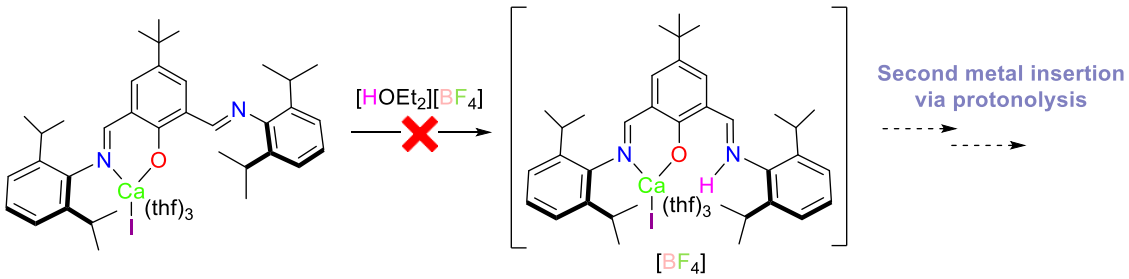

In a Young's tap NMR tube, complex **15** (0.0200 g, 0.0250 mmol) and $[HOEt_2][BF_4]$ (0.00394 mL, 0.0290 mmol) were dissolved in THF-d_8 (0.5 mL). NMR spectroscopic analysis seemed promising and so the reaction was scaled up using the literature protocol reported by Mecking and co-workers[43]: A solution of complex **15** (0.0200 g, 0.0250 mmol) in benzene (2 mL) was prepared and cooled to –30 °C. The benzene solution was then allowed to warm and upon thawing, dilute $[HOEt_2][BF_4]$ (0.0685 M in diethyl ether, 0.433 mL, 0.290 mmol) was added under rapid stirring. After 20 minutes, volatiles were removed by freeze-drying and the resultant orange solid was crystallised at room temperature from a saturated benzene solution. The identity of the reaction product was determined to be: $[H_2{}^{t\text{Bu,Dipp}}L][I]$.

7.4.4 Synthesis of $[H_2{}^{t\text{Bu,Dipp}}L][BF_4]\cdot thf_x$ (**16**$\cdot thf_x$)

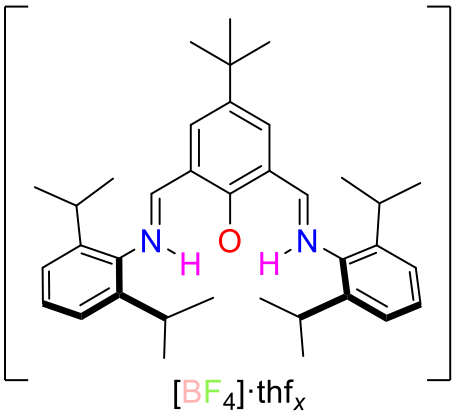

$[HOEt_2][BF_4]$ (130 µL, 0.953 mmol) was added to a solution of $H^{t\text{Bu,Dipp}}L$ (0.500 g, 0.953 mmol) in THF (5 mL). The bright orange reaction mixture was then left stirring for 3 h at room temperature before volatiles were removed *in vacuo*. The crude oily solid was washed by sonication in pentane (3 x 15 mL) and filtered to afford $[H_2{}^{t\text{Bu,Dipp}}L][BF_4]\cdot thf_x$ (**16**$\cdot thf_x$) as a bright orange solid. The bulk material had the composition $[H_2{}^{t\text{Bu,Dipp}}L][BF_4]\cdot thf_4$ (0.694 g, 81%). Single crystals of $[H_2{}^{t\text{Bu,Dipp}}L][BF_4]$ (**16**), suitable for an X-ray diffraction study, were obtained by the slow evaporation of a saturated benzene solution at room temperature. ^{1}H NMR (500 MHz, 298 K, THF-d_8): δ 15.05 (d, $^3J_{HH}$ = 13.5 Hz, 2H, N***H***), 9.04 (d, $^3J_{HH}$ = 13.3 Hz, 2H, ***H***C=N), 8.42 (s, 2H, 3-C$_6$***H***$_2$), 7.44 (dd, $^3J_{HH}$ = 8.5, 7.0 Hz, 2H, N-4-C$_6$***H***$_3$), 7.35 (d, $^3J_{HH}$ = 7.8 Hz, 4H, N-3,5-C$_6$***H***$_3$), 3.37 (m, 16H, thf-OC***H***$_2$), 3.14 (sept, $^3J_{HH}$ = 6.7 Hz, 4H,

N-2,6-C_6H_3-C***H***Me_2), 1.59 (m, 16H, thf-C***H***$_2$), 1.36 (s, 9H, C(C***H***$_3$)$_3$), 1.25 (d, $^3J_{HH}$ = 6.8 Hz, 24H, N-2,6-C_6H_3-CH***Me***$_2$) ppm. $^{13}C\{^1H\}$ NMR (151 MHz, 298 K, THF-d_8): δ 178.1 (1-***C***$_6H_2$), 171.0 (H***C***=N), 145.5 (3-***C***$_6H_2$), 143.3 (N-2,6-***C***$_6H_3$), 139.3 (4-***C***$_6H_2$), 134.4 (N-1-***C***$_6H_3$), 129.8 (N-4-***C***$_6H_3$), 124.0 (N-3,5-***C***$_6H_3$), 117.4 (2-***C***$_6H_2$), 69.3 (thf-O***C***H_2), 34.0 (***C***$(CH_3)_3$), 30.3 (C(***C***$H_3)_3$), 28.6 (N-2,6-C_6H_3-***C***HMe_2), 25.5 (thf-***C***H_2), 22.8 (N-2,6-C_6H_3-CH***Me***$_2$) ppm. ^{19}F NMR (377 MHz, 298 K, THF-d_8): δ –150.7 ppm. ^{11}B NMR (128 MHz, 298 K, THF-d_8): δ –1.0 ppm. IR (KBr): 3061, 3045, 2966, 2931, 2869, 2856, 1659, 1623, 1586, 1530, 1464, 1389, 1368, 1329, 1292, 1237, 1186, 1108, 1058, 1020, 937, 901, 801, 768, 756 cm^{-1}. Anal. Calcd for $C_{36}H_{49}N_2OBF_4$: C, 70.58; H, 8.06; N, 4.57. Found: C, 70.91; H, 8.52; N, 4.31.

7.4.5 Synthesis of $^{t\text{Bu,Dipp}}$LBF$_2$·thf$_x$ (17·thf$_x$)

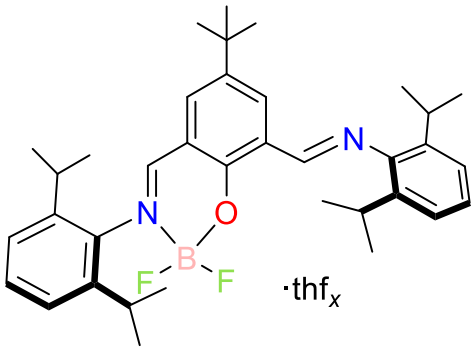

A solution of [H$_2$$^{t\text{Bu,Dipp}}$L][BF$_4$]·thf$_4$ (0.100 g, 0.146 mmol) in THF (1 mL) was added to a solution of Ca{N(SiMe$_3$)$_2$}$_2$(thf)$_2$ (0.0782 g, 0.146 mmol) in THF (1 mL). The reaction mixture was left overnight before volatiles were removed *in vacuo*.* $^{t\text{Bu,Dipp}}$LBF$_2$·thf$_x$ (**17·thf$_x$**) was extracted with pentane (3 x 2 mL) and crystallised by evaporation of the solvent at room temperature. The bulk material had the composition $^{t\text{Bu,Dipp}}$LBF$_2$·thf$_{0.9}$ (0.0615 g, 66%). Single crystals of $^{t\text{Bu,Dipp}}$LBF$_2$ (**17**), suitable for an X-ray diffraction study, were obtained at 0 °C from a saturated pentane solution. ^1H NMR (600 MHz, 298 K, THF-d_8): δ 8.84 (s (br), 1H, ***H***C=N), 8.79 (s, 1H, ***H***C=N'), 8.74 (d, $^4J_{HH}$ = 2.6 Hz, 1H, 3'-C$_6$***H***$_2$), 7.81 (d, $^4J_{HH}$ = 2.6 Hz, 1H, 3-C$_6$***H***$_2$), 7.39 (m, $^3J_{HH}$ = 7.6 Hz, 1H, N-4-C$_6$***H***$_3$), 7.30 (d, $^3J_{HH}$ = 7.6 Hz, 2H, N-3,5-C$_6$***H***$_3$), 7.13 (d, $^3J_{HH}$ = 7.7 Hz, 2H, N'-3,5-C$_6$***H***$_3$), 7.03 (m, $^3J_{HH}$ = 7.7 Hz, 1H, N'-4-C$_6$***H***$_3$), 3.37 (m, 4H, thf-

OC***H***$_2$), 3.07 (sept, $^3J_{HH}$ = 6.9 Hz, 1H, N-2,6-C$_6$H$_3$-C***H***Me$_2$), 3.00 (sept, $^3J_{HH}$ = 6.9 Hz, 1H, N'-2,6-C$_6$H$_3$-C***H***Me$_2$), 1.59 (m, 4H, thf-C***H***$_2$), 1.41 (s, 9H, C(C***H***$_3$)$_3$), 1.25 (d, $^3J_{HH}$ = 6.7 Hz, 6H, N-2,6-C$_6$H$_3$-CH***Me***$_2$), 1.19 (d, $^3J_{HH}$ = 6.9 Hz, 12H, N'-2,6-C$_6$H$_3$-CH***Me***$_2$), 1.13 (d, $^3J_{HH}$ = 6.9 Hz, 6H, N-2,6-C$_6$H$_3$-CH***Me***$_2$) ppm. ^{13}C{^{1}H} NMR (151 MHz, 298 K, THF-d_8): δ 169.7 (H***C***=N), 158.9 (1-***C***$_6$H$_2$), 157.8 (H***C***=N'), 151.1 (N'-1-***C***$_6$H$_3$), 145.1 (N-2,6-***C***$_6$H$_3$), 144.2 (4-***C***$_6$H$_3$), 139.4 (N-1-***C***$_6$H$_3$), 138.3 (N'-2,6-***C***$_6$H$_3$), 134.4 (3'-***C***$_6$H$_2$), 132.8 (3-***C***$_6$H$_2$), 130.1 (N-4-***C***$_6$H$_3$), 126.5 (2'-***C***$_6$H$_2$), 125.1 (N-3,5-***C***$_6$H$_3$), 125.0 (N'-4-***C***$_6$H$_3$), 123.8 (N'-3,5-***C***$_6$H$_3$), 117.7 (2-***C***$_6$H$_2$), 71.5 (thf-O***C***H$_2$), 35.2 (***C***(CH$_3$)$_3$), 31.6 (C(***C***H$_3$)$_3$), 29.5 (N-2,6-C$_6$H$_3$-***C***HMe$_2$), 29.1 (N'-2,6-C$_6$H$_3$-***C***HMe$_2$), 27.8 (thf-***C***H$_2$), 25.6 (N-2,6-C$_6$H$_3$-CH***Me***$_2$), 23.9 (N'-2,6-C$_6$H$_3$-CH***Me***$_2$), 23.8 (N-2,6-C$_6$H$_3$-CH***Me***$_2$) ppm. ^{19}F NMR (377 MHz, 298 K, THF-d_8): δ –137.6 ppm. ^{11}B NMR (128 MHz, 298 K, THF-d_8): δ 0.6 ppm. IR (KBr): 3065, 2958, 2934, 2863, 2795, 2358, 1634, 1574, 1465, 1364, 1327, 1286, 1250, 1229, 1184, 1107, 1050, 935, 842, 829, 798, 759, 636, 541 cm^{-1}. Anal. Calcd for $C_{40}H_{55}N_2O_2BF_2$: C, 74.52; H, 8.60; N, 4.35. Found: C, 72.82; H, 8.76; N, 4.49.

*The solid-state NMR experiments were performed on a sample of the crude reaction mixture.

7.4.6 Synthesis of [Na(OEt$_2$)$_3$][H$_2$N{B(C$_6$F$_5$)$_3$}$_2$]; adapted from reference 12.

At 0 °C, a slurry of B(C$_6$F$_5$)$_3$ (2.10 g, 4.10 mmol) in diethyl ether (25 mL) was added to a slurry of NaNH$_2$ (0.0800 g, 2.05 mmol) in diethyl ether (5 mL). The reaction mixture was then warmed to room temperature and stirred for 2 h. The solution was concentrated until crystallisation was initiated and the resultant glassy solid was washed with –78 °C diethyl ether (3 x 5 mL) to afford [Na(OEt$_2$)$_3$][H$_2$N{B(C$_6$F$_5$)$_3$}$_2$] as a colourless powder (1.32 g, 50%). ^{1}H NMR (400 MHz, 298 K, chloroform-d_1) δ 5.64 (s (br), 2H, [***H***$_2$N{B(C$_6$F$_5$)$_3$}$_2$]$^-$), 3.57 (q, $^3J_{HH}$ = 7.1 Hz, 12H, OC***H***$_2$CH$_3$), 1.20 (t, $^3J_{HH}$ = 7.1 Hz,

18H, OCH_2CH_3) ppm. ^{19}F NMR (377 MHz, 298 K, chloroform-d_1) δ –132.8 (d, $^3J_{FF}$ = 20.7 Hz, 12F, *o*-F:C_6F_5), –159.1 (t, $^3J_{FF}$ = 20.6 Hz, 6F, *p*-F:C_6F_5), –165.2 (t, $^3J_{FF}$ = 21.2 Hz, 12F, *m*-F:C_6F_5) ppm. ^{11}B NMR (128 MHz, 298 K, chloroform-d_1) δ –8.3 ppm; all of these spectroscopic values are consistent with previous literature reports.[12]

7.4.7 Synthesis of $[H(OEt_2)_2][H_2N\{B(C_6F_5)_3\}_2]$; adapted from reference 12.

A solution of $[Na(OEt_2)_3][H_2N\{B(C_6F_5)_3\}_2]$ (2.20 g, 1.71 mmol) in diethyl ether (10 mL) was prepared. To this was added an excess of HCl (1.0 M in diethyl ether, 3.42 mL, 2.0 eq). The reaction mixture was stirred at room temperature for 18 h prior to filtration. Removal of volatiles *in vacuo* afforded a crude oily solid which, when washed under rapid stirring with pentane (15 mL), yielded $[H(OEt_2)_2][H_2N\{B(C_6F_5)_3\}_2]$ as a colourless solid (1.84 g, 90%). ^{1}H NMR (400 MHz, 298 K, chloroform-d_1) δ 5.65 (s (br), 2H, $[H_2N\{B(C_6F_5)_3\}_2]^-$), 4.10 (q, $^3J_{HH}$ = 7.3 Hz, 8H, OCH_2CH_3), 1.46 (t, $^3J_{HH}$ = 7.2 Hz, 12H, OCH_2CH_3) ppm. ^{19}F NMR (377 MHz, 298 K, chloroform-d_1) δ –132.5 (d, $^3J_{FF}$ = 20.8 Hz, 12F, *o*-F:C_6F_5), –159.5 (t, $^3J_{FF}$ = 20.4 Hz, 6F, *p*-F:C_6F_5), –165.1 (t, $^3J_{FF}$ = 21.3 Hz, 12F, *m*-F:C_6F_5) ppm. ^{11}B NMR (128 MHz, 298 K, chloroform-d_1) δ –8.3 ppm; all of these spectroscopic values are consistent with previous literature reports.[12]

7.4.8 Synthesis of $[H_2{}^{t\text{Bu,Dipp}}L][H_2N\{B(C_6F_5)_3\}_2]\cdot thf_x$ ($18\cdot thf_x$)

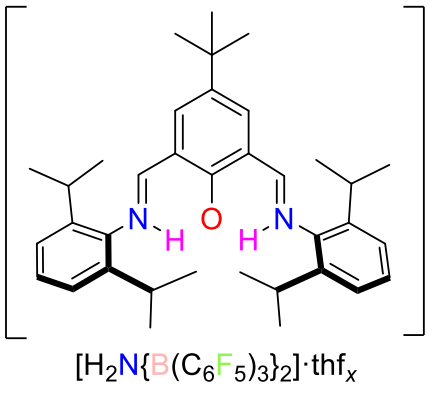

$[H_2N\{B(C_6F_5)_3\}_2]\cdot thf_x$

A solution of $[H(OEt_2)_2][H_2N\{B(C_6F_5)_3\}_2]$ (0.456 g, 0.381 mmol) in THF (3 mL) was added dropwise to a solution of $H^{t\text{Bu,Dipp}}L$ (0.200 g, 0.381 mmol) in THF (2 mL). The bright orange reaction mixture was then left to stir for 3 h at room temperature before volatiles were removed *in vacuo*. The crude oily solid was triturated with a 1:1 mixture of pentane:diethyl ether (4 x 5 mL) to afford

$[H_2{}^{t\text{Bu,Dipp}}L][H_2N\{B(C_6F_5)_3\}_2]\cdot thf_x$ (**18·thf$_x$**) as a bright orange solid. The bulk material had the composition $[H_2{}^{t\text{Bu,Dipp}}L][H_2N\{B(C_6F_5)_3\}_2]\cdot thf_{0.36}$ (0.528 g, 87%). Single crystals of $[H_2{}^{t\text{Bu,Dipp}}L][H_2N\{B(C_6F_5)_3\}_2]$ (**18**), suitable for an X-ray diffraction study, were obtained from a dichloromethane/pentane mixture at –25 ºC. ^{1}H NMR (600 MHz, THF-d_8) δ 14.90 (s (br), 2H, HC=N***H***), 8.86 (s (br), 2H, ***H***C=NH), 8.14 (s, 2H, 3-C_6***H***$_2$), 7.51 (t, $^3J_{HH}$ = 7.8 Hz, 2H, N-4-C_6***H***$_3$), 7.42 (d, $^3J_{HH}$ = 7.8 Hz, 4H, N-3,5-C_6***H***$_3$), 5.77 (s (br), 2H, [***H***$_2$N{B(C_6F_5)$_3$}$_2$]$^-$), 3.37 (m, 1H, thf-OC***H***$_2$), 3.11 (sept, $^3J_{HH}$ = 6.6 Hz, 4H, N-2,6-C_6H_3-C***H***Me$_2$), 1.60 (m, 1H, thf-C***H***$_2$), 1.39 (s, 9H, C(C***H***$_3$)$_3$), 1.28 (d, $^3J_{HH}$ = 6.8 Hz, 24H, N-2,6-C_6H_3-CH***Me***$_2$) ppm. ^{13}C{^{1}H} NMR (151 MHz, 298 K, THF-d_8) δ 179.2 (1-***C***$_6H_2$), 171.2 (H***C***=N), 149.9-148.2 (*o*-F:***C***$_6F_5$), 145.7 (3-***C***$_6H_2$), 144.4 (N-2,6-***C***$_6H_3$), 141.1-139.8 (*p*-F:***C***$_6F_5$), 139.8 (4-***C***$_6H_2$), 138.6-136.9 (*m*-F:***C***$_6F_5$), 135.7 (N-1-***C***$_6H_3$), 131.5 (N-4-***C***$_6H_3$), 125.5 (N-3,5-***C***$_6H_3$), 118.9 (2-***C***$_6H_2$), 69.3 (thf-O***C***H$_2$), 34.9 (***C***(CH$_3$)$_3$), 31.2 (C(***C***H$_3$)$_3$), 29.9 (N-2,6-C_6H_3-***C***HMe$_2$), 25.5 (thf-***C***H$_2$), 23.8 (N-2,6-C_6H_3-CH***Me***$_2$) ppm. ^{19}F NMR (377 MHz, 298 K, THF-d_8) δ –133.1 (d, $^3J_{FF}$ = 20.8 Hz, 12F, *o*-F:C_6***F***$_5$), –161.0 (t, $^3J_{FF}$ = 20.2 Hz, 6F, *p*-F:C_6***F***$_5$), –166.3 (t, $^3J_{FF}$ = 20.0 Hz, 12F, *m*-F:C_6***F***$_5$) ppm. ^{11}B NMR (128 MHz, 298 K, THF-d_8) δ –8.2 ppm. IR (KBr): 3383, 3344, 3073, 2974, 2933, 2875, 2362, 2334, 1647, 1622, 1519, 1461, 1369, 1329, 1275, 1228, 1103, 1085, 986, 953, 885, 800, 779, 764, 715, 692, 652, 619, 517 cm^{-1}. Anal. Calcd for $C_{74.27}H_{54.15}N_3O_{1.41}B_2F_{30}$ (sample contained residual protio-solvent: 0.4 eq THF and 0.1 eq. pentane): C, 55.66; H, 3.41; N, 2.62. Found: C, 55.81; H, 3.59; N, 2.63.

7.4.9 Synthesis of [pyrazole-H][H$_2$N{B(C_6F_5)$_3$}$_2$]·(OEt$_2$)$_x$

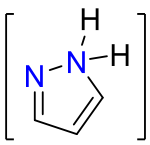

$[H_2N\{B(C_6F_5)_3\}_2].(OEt_2)_x$

A solution of $[H(OEt_2)_2][H_2N\{B(C_6F_5)_3\}_2]$ (0.176 g, 0.147 mmol) in THF (3 mL) was added dropwise to a solution of pyrazole (0.0100 g, 0.147 mmol) in THF (2 mL).

The pale-yellow reaction mixture was then left to stir for 1 h at room temperature before volatiles were removed *in vacuo*. The crude oily solid was washed with cold pentane (3 x 5 mL) to afford an off-white powder. The bulk material had the composition [pyrazole-H(OEt_2)$_{0.75}$][$H_2N\{B(C_6F_5)_3\}_2$] (0.139 g, 81%). ^{1}H NMR (400 MHz, 298 K, acetonitrile-d_3) δ 12.52 (s, 2H, N***H***$_2$), 8.09 (d, $^3J_{HH}$ = 2.8 Hz, 2H, C1,C3-***H***), 6.76 (t, $^3J_{HH}$ = 2.7 Hz, 1H, C2-***H***), 5.77 (s (br), 2H, [***H***$_2$N{B(C_6F_5)$_3$}$_2$]$^-$) ppm. ^{13}C{^{1}H} NMR (151 MHz, 298 K, acetonitrile-d_3) δ 149.6 (***C***1,***C***3), 148.0 (***C***2), 141.0-139.3 (*o*-F:***C***$_6F_5$), 138.5-136.8 (*p*-F:***C***$_6F_5$), 135.7 (*m*-F:***C***$_6F_5$), 66.3 (diethyl ether-***C***H_2), 15.6 (diethyl ether-***C***H_3) ppm. ^{19}F NMR (377 MHz, 298 K, acetonitrile-d_3) δ –133.7 (d, $^3J_{FF}$ = 20.3 Hz, 12F, *o*-F:C_6***F***$_5$), –160.6 (t, $^3J_{FF}$ = 19.7 Hz, 6F, *p*-F:C_6***F***$_5$), –166.6 (t, $^3J_{FF}$ = 19.4 Hz, 12F, *m*-F:C_6***F***$_5$) ppm. ^{11}B NMR (128 MHz, 298 K, acetonitrile-d_3) δ –8.3 ppm. IR (KBr): 3431, 3384, 3347, 3176, 3161, 2990, 1648, 1520, 1466, 1304, 1276, 1098, 1095, 955, 800, 780, 764, 715, 693 cm^{-1}. Anal. Calcd for $C_{42}H_{14.5}N_3B_2O_{0.75}F_{30}$: C, 43.31; H, 1.25; N, 3.61. Found: C, 43.70; H, 1.20; N, 3.60.

7.4.10 Synthesis of [$^{t\text{Bu,Dipp}}$LCa(thf)$_4$][$H_2N\{B(C_6F_5)_3\}_2$] (19)

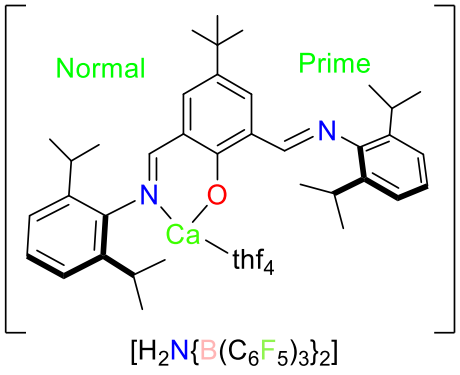

A solution of [$H_2$$^{t\text{Bu,Dipp}}$L][$H_2N\{B(C_6F_5)_3\}_2$]·thf$_{0.36}$ (0.186 g, 0.116 mmol) in THF (2 mL) was added dropwise to a solution of Ca{$N(SiMe_3)_2$}$_2$(thf)$_2$ (0.0620 g, 0.116 mmol) in THF (2 mL). The yellow reaction mixture was then left to stir for 3 h at room temperature before volatiles were removed *in vacuo*. The crude oily solid was then triturated with a 1:1 mixture of diethyl ether/pentane (3 x 5 mL). The resultant powder was washed with pentane (3 x 2 mL) to afford [$^{t\text{Bu,Dipp}}$LCa(thf)$_4$][$H_2N\{B(C_6F_5)_3\}_2$] (**19**) as a yellow solid (0.132 g, 60%). ^{1}H NMR

(600 MHz, 298 K, THF-d_8) δ 8.52 (s, 2H, ***H***C=N), 7.96 (s, 2H, 3-C$_6$***H***$_2$), 7.19 (d, $^3J_{HH}$ = 7.7 Hz, 4H, N-3,5-C$_6$***H***$_3$), 7.11 (t, $^3J_{HH}$ = 7.8 Hz, 2H, N-4-C$_6$***H***$_3$), 5.75 (s (br), 2H, [***H***$_2$N{B(C$_6$F$_5$)$_3$}$_2$]$^-$), 3.37 (m, 16H, thf-OC***H***$_2$), 2.98 (sept, $^3J_{HH}$ = 6.6 Hz, 4H, N-2,6-C$_6$H$_3$-C***H***Me$_2$), 1.59 (m, 16H, thf-C***H***$_2$), 1.34 (s, 9H, C(C***H***$_3$)$_3$), 1.18 (d, $^3J_{HH}$ = 6.7 Hz, 24H, N-2,6-C$_6$H$_3$-CH***Me***$_2$) ppm. ^{13}C NMR (126 MHz, 203 K, THF-d_8) δ 174.5 (1-***C***$_6$H$_2$), 168.8, (H***C***=N'), 160.8 (H***C***=N), 152.5 (N'-1-***C***$_6$H$_3$), 150.1 (N-1-***C***$_6$H$_3$), 149.8-147.4 (*o*-F:***C***$_6$F$_5$), 144.1-139.0 (*p*-F:***C***$_6$F$_5$), 140.9 (N-2,6-***C***$_6$H$_3$), 139.3 (3'-***C***$_6$H$_2$), 138.7-136.3 (*m*-F:***C***$_6$F$_5$), 138.2 (N'-2,6-***C***$_6$H$_3$), 136.1 (4-***C***$_6$H$_2$), 130.4 (3-***C***$_6$H$_2$), 127.0 (N-4-***C***$_6$H$_3$), 126.3 (2'-***C***$_6$H$_2$), 124.8 (N-3,5-***C***$_6$H$_3$), 124.3 (2-***C***$_6$H$_2$), 124.2 (N'-4-***C***$_6$H$_3$), 123.5 (N'-3,5-***C***$_6$H$_3$), 71.5 (thf-O***C***H$_2$), 34.7 (***C***(CH$_3$)$_3$), 32.0 (C(***C***H$_3$)$_3$), 29.1 (N'-2,6-C$_6$H$_3$-***C***HMe$_2$), 28.6 (N-2,6-C$_6$H$_3$-***C***HMe$_2$), 27.8 (thf-***C***H$_2$), 25.9 (N'-2,6-C$_6$H$_3$-CH***Me***$_2$), 23.9 (N-2,6-C$_6$H$_3$-CH***Me***$_2$), 22.9 (N-2,6-C$_6$H$_3$-CH***Me***$_2$) ppm. ^{19}F NMR (565 MHz, 298 K, THF-d_8) δ –133.1 (d, $^3J_{FF}$ = 20.6 Hz, 12F, *o*-F:C$_6$***F***$_5$), –161.1 (t, $^3J_{FF}$ = 20.3 Hz, 6F, *p*-F:C$_6$***F***$_5$), –166.4 (t, $^3J_{FF}$ = 20.6 Hz, 12F, *m*-F:C$_6$***F***$_5$). ^{11}B NMR (193 MHz, 298 K, THF-d_8) δ –8.2 ppm. IR (KBr): 3385, 3359, 3344, 3068, 2969, 2872, 2360, 2340, 1646, 1519, 1464, 1365, 1278, 1172, 1104, 1085, 987, 976, 872, 800, 781, 764, 711, 692, 513 cm^{-1}. Anal. Calcd for C$_{88}$H$_{77}$N$_3$O$_5$CaB$_2$F$_{30}$: C, 55.98; H, 4.11; N, 2.23. Found: C, 54.95; H, 4.17; N, 2.36.

7.4.11 Synthesis of [H$_2$$^{t\text{Bu,Dipp}}$L][B(3,5-{CF$_3$}$_2C_6H_3$)$_4$]·thf$_x$ (20·thf$_x$)

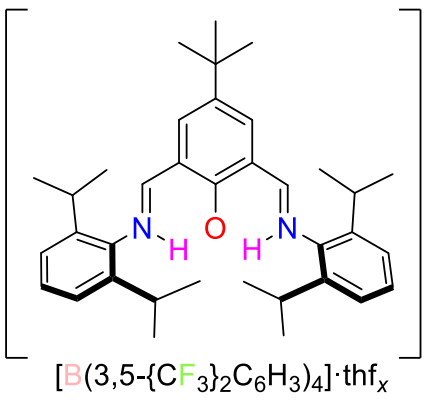

A solution of [H(OEt$_2$)$_2$][B(3,5-{CF$_3$}$_2$C$_6$H$_3$)$_4$] (0.465 g, 0.459 mmol) in THF (2 mL) was added dropwise to a solution of H$^{t\text{Bu,Dipp}}$L (0.241 g, 0.459 mmol) in THF (2 mL). The bright orange reaction mixture was then left to stir for 4 h at room temperature before volatiles were removed *in vacuo*. The crude oily solid was triturated with pentane (3 x 5 mL) to afford [H$_2$$^{t\text{Bu,Dipp}}$L][B(3,5-

{CF$_3$}$_2$C$_6$H$_3$)$_4$]·thf$_{0.13}$ (**20·thf$_x$**) as a bright pale orange solid (0.578 g, 88%). ^{1}H NMR (400 MHz, 298 K, THF-d_8): δ 14.87 (d, $^3J_{HH}$ = 13.8 Hz, 2H, N***H***), 9.04 (d, $^3J_{HH}$ = 13.8 Hz, 2H, ***H***C=N), 8.42 (s, 2H, 3-C$_6$***H***$_2$), 7.79 (m, 8H, [2,6-**Ar**]$^-$), 7.57 (m, 4H, [4-**Ar**]$^-$), 7.50 (dd, $^3J_{HH}$ = 8.6, 6.9 Hz, 2H, N-4-C$_6$***H***$_3$), 7.41 (d, $^3J_{HH}$ = 7.1 Hz, 4H, N-3,5-C$_6$***H***$_3$), 3.10 (sept, $^3J_{HH}$ = 6.8 Hz, 4H, N-2,6-C$_6$H$_3$-C***H***Me$_2$), 1.37 (s, 9H, C(C***H***$_3$)$_3$), 1.27 (d, $^3J_{HH}$ = 6.8 Hz, 24H, N-2,6-C$_6$H$_3$-CH***Me***$_2$) ppm. ^{13}C{^{1}H} NMR (101 MHz, 298 K, THF-d_8): δ 179.2 (1-***C***$_6$H$_2$), 171.2 (H***C***=N), 163.7–162.3 (q, $^1J_{CB}$ = 50.4 Hz, [1-**Ar**]$^-$), 145.7 (3-***C***$_6$H$_2$), 144.3 (N-1-***C***$_6$H$_3$), 139.8 (4-***C***$_6$H$_2$), 135.8 ([2,6-**Ar**]$^-$), 135.7 (N-2,6-***C***$_6$H$_3$), 131.5 (N-4-***C***$_6$H$_3$), 130.4–129.7 ([3,5-**Ar**]$^-$), 129.7-121.6 (q, $^1J_{CF}$ = 272.0 Hz, [Ar-***C***F$_3$]$^-$), 125.5 (N-3,5-***C***$_6$H$_3$), 118.9 (2-***C***$_6$H$_2$), 118.3 (m, [4-**Ar**]$^-$), 35.2 (***C***(CH$_3$)$_3$), 31.2 (C(***C***H$_3$)$_3$), 29.9 (N-2,6-C$_6$H$_3$-***C***HMe$_2$), 23.8 (N-2,6-C$_6$H$_3$-CH***Me***$_2$) ppm. ^{19}F NMR (377 MHz, 298 K, THF-d_8): δ –63.4 ppm. ^{11}B NMR (128 MHz, 298 K, THF-d_8): δ –6.5 ppm. IR (KBr): 3074, 2970, 2936, 2909, 2876, 2360, 2340, 2329, 1639, 1625, 1530, 1355, 1278, 1159, 1125, 1020, 887, 838, 80, 714, 682, 670 cm^{-1}. Anal. Calcd for C$_{68.5}$H$_{62}$N$_2$O$_{1.13}$BF$_{24}$: C, 58.85; H, 4.47; N, 2.00. Found: C, 61.38; H, 4.69; N, 2.06.

7.4.12 Synthesis of [$^{t\text{Bu,Dipp}}$LCa(thf)$_4$][B(3,5-{CF$_3$}$_2$C$_6$H$_3$)$_4$] (21)

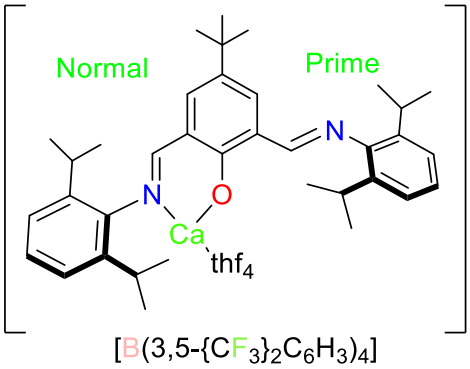

In a Young's tap NMR tube, [H$_2$$^{t\text{Bu,Dipp}}$L][B(3,5-{CF$_3$}$_2C_6H_3$)$_4$]·thf$_{0.13}$ (0.0200 g, 0.0143 mmol) and Ca{N(SiMe$_3$)$_2$}$_2$(thf)$_2$ (0.0076 g, 0.0143 mmol) were dissolved in THF-d_8 (0.5 mL). The bright yellow reaction mixture was left overnight and then concentrated *in vacuo*. Single crystals of [$^{t\text{Bu,Dipp}}$LCa(thf)$_4$][B(3,5-{CF$_3$}$_2$C$_6$H$_3$)$_4$] (**21**), suitable for an X-ray diffraction study, were afforded by slow diffusion of pentane into this solution at room temperature. ^{1}H NMR (400 MHz, 298 K,

THF-d_8) δ 8.52 (s, 2H, ***H***C=N), 7.96 (s, 2H, 3-C$_6$***H***$_2$), 7.79 (m, 8H, [2,6-**Ar**]$^-$), 7.57 (m, 4H, [4-**Ar**]$^-$), 7.20 (d, $^3J_{HH}$ = 7.5 Hz, 4H, N-3,5-C$_6$***H***$_3$), 7.11 (m, 2H, N-4-C$_6$***H***$_3$), 2.98 (sept, $^3J_{HH}$ = 6.9 Hz, 4H, N-2,6-C$_6$H$_3$-C***H***Me$_2$), 1.34 (s, 9H, C(C***H***$_3$)$_3$), 1.18 (d, $^3J_{HH}$ = 7.0 Hz, 24H, N-2,6-C$_6$H$_3$-CH***Me***$_2$) ppm. ^{13}C{^{1}H} NMR (101 MHz, 298 K, THF-d_8): δ 168.7 (H***C***=N), 163.5-162.5 (q, $^1J_{CB}$ = 50.3 Hz, [1-**Ar**]$^-$), 151.6 (N-1-***C***$_6$H$_3$), 139.7 (N-2,6-***C***$_6$H$_3$), 137.0 (4-***C***$_6$H$_2$), 135.8 ([2,6-**Ar**]$^-$), 130.5-129.8 ([3,5-**Ar**]$^-$), 128.4-123.0 (q, $^1J_{CF}$ = 272.2 Hz, [Ar-***C***F$_3$]$^-$), 125.8 (N-4-***C***$_6$H$_3$), 125.4 (3-***C***$_6$H$_2$), 124.3 (N-3,5-***C***$_6$H$_3$), 118.4 (m, [4-**Ar**]$^-$), 34.7 (***C***(CH$_3$)$_3$), 32.0 (C(***C***H$_3$)$_3$), 29.0 (N-2,6-C$_6$H$_3$-***C***HMe$_2$), 23.3 (N-2,6-C$_6$H$_3$-CH***Me***$_2$) ppm. Quaternary carbons representing 1-***C***$_6$H$_2$ and 2-***C***$_6$H$_2$ not observed. ^{19}F NMR (377 MHz, 298 K, THF-d_8) δ –63.4 ppm. ^{11}B NMR (128 MHz, 298 K, THF-d_8) δ –6.5 ppm. IR (KBr): 2966, 2937, 2871, 2368, 2333, 2252, 2096, 1621, 1534, 1462, 1356, 1283, 1165, 1133, 1037, 1006, 887, 839, 714, 682, 671 cm^{-1}. Anal. Calcd for C$_{84}$H$_{87}$N$_2$O$_5$BF$_{24}$Ca: C, 58.95; H, 5.12; N, 1.64. Found: C, 57.97; H, 3.99; N, 1.62.

7.4.13 Synthesis of [H$^{t\text{Bu,Dipp}}$LZnCl(thf)][H$_2$N{B(C$_6$F$_5$)$_3$}$_2$] (22)

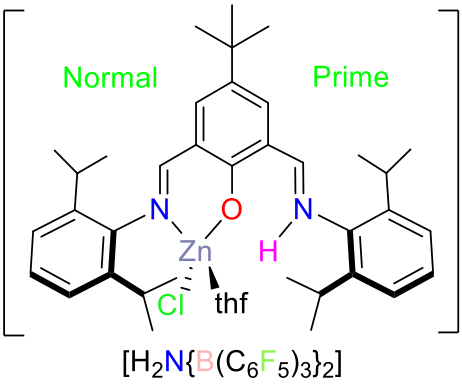

A solution of [H$_2$$^{t\text{Bu,Dipp}}$L][H$_2$N{B(C$_6F_5$)$_3$}$_2$]·thf$_{0.36}$ (0.466 g, 0.283 mmol) in THF (2 mL) was added dropwise to a solution of EtZnCl (0.0406 g, 0.283 mmol) in THF (2 mL). The reaction mixture was then left to stir overnight at room temperature before volatiles were removed *in vacuo*. The crude oily solid was triturated with a 1:1 mixture of pentane:diethyl ether (3 x 5 mL) to afford [H$^{t\text{Bu,Dipp}}$LZnCl(thf)][H$_2$N{B(C$_6$F$_5$)$_3$}$_2$] (**22**) as a pale orange solid (0.474 g, 94%). Single crystals of [H$^{t\text{Bu,Dipp}}$LZnCl(thf)][H$_2$N{B(C$_6$F$_5$)$_3$}$_2$] (**22**), suitable for an X-ray diffraction study, were

obtained from a THF/hexane solution at –25 °C. ^{1}H NMR (600 MHz, 298 K, THF-d_8) δ 13.69 (s (br), 1H, N'***H***), 9.01 (d, $^{3}J_{HH}$ = 13.2 Hz, 1H, ***H***C=N'), 8.75 (s, 1H, ***H***C=N), 8.22 (d, $^{3}J_{HH}$ = 2.8 Hz, 1H, 3'-C$_6$***H***$_2$), 8.02 (d, $^{3}J_{HH}$ = 2.8 Hz, 1H, 3-C$_6$***H***$_2$), 7.55 (t, $^{3}J_{HH}$ = 7.8 Hz, 1H, N-3,5-C$_6$***H***$_3$), 7.45 (d, $^{3}J_{HH}$ = 7.8 Hz, 2H, N-4-C$_6$***H***$_3$), 7.38-7.30 (m, 3H, N'-3,5-C$_6$***H***$_3$ and N'-4-C$_6$***H***$_3$), 5.76 (s, 2H, [***H***$_2$N{B(C$_6$F$_5$)$_3$}$_2$]$^-$), 3.38 (m, 4H, thf-OC***H***$_2$), 3.10 (sept, $^{3}J_{HH}$ = 6.8 Hz, 2H, N-2,6-C$_6$H$_3$-C***H***Me$_2$), 3.02 (sept, $^{3}J_{HH}$ = 6.8 Hz, 2H, N'-2,6-C$_6$H$_3$-C***H***Me$_2$), 1.59 (m, 4H, thf-C***H***$_2$), 1.37 (s, 9H, C(C***H***$_3$)$_3$), 1.34–1.22 (m, 18H, N-2,6-C$_6$H$_3$-CH***Me***$_2$ and N'-2,6-C$_6$H$_3$-CH***Me***$_2$), 1.16 (d, $^{3}J_{HH}$ = 6.8 Hz, 6H, N'-2,6-C$_6$H$_3$-CH***Me***$_2$) ppm. ^{13}C NMR (151 MHz, 298 K, THF-d_8) δ 175.9 (H***C***=N), 173.2 (1-***C***$_6$H$_2$), 173.0 (H***C***=N'), 150.1-148.0 (*o*-F:***C***$_6$F$_5$), 147.8 (3-***C***$_6$H$_2$), 145.4 (N-1-***C***$_6$H$_3$), 144.5 (N'-2,6-***C***$_6$H$_3$), 142.3 (2'-***C***$_6$H$_2$), 141.8 (N-2,6-***C***$_6$H$_3$), 141.7 (3'-***C***$_6$H$_2$), 141.4-139.2 (*p*-F:***C***$_6$F$_5$), 139.0-136.6 (*m*-F:***C***$_6$F$_5$), 135.3 (N'-1-***C***$_6$H$_3$), 132.0 (N'-4-***C***$_6$H$_3$), 129.2 (N-4-***C***$_6$H$_3$), 125.7 (N'-3,5-***C***$_6$H$_3$), 125.3 (N-3,5-***C***$_6$H$_3$), 122.6 (2-***C***$_6$H$_2$), 118.8 (4-***C***$_6$H$_2$), 71.5 (thf-O***C***H$_2$), 35.0 (***C***(CH$_3$)$_3$), 31.2 (C(***C***H$_3$)$_3$), 30.0 (N'-2,6-C$_6$H$_3$-***C***HMe$_2$), 29.5 (N-2,6-C$_6$H$_3$-***C***HMe$_2$), 27.8 (thf-***C***H$_2$), 25.7 (2C, N-2,6-C$_6$H$_3$-CH***Me***$_2$), 23.9-23.4 (6C, N-2,6-C$_6$H$_3$-CH***Me***$_2$ and N'-2,6-C$_6$H$_3$-CH***Me***$_2$) ppm. ^{19}F NMR (565 MHz, 298 K, THF-d_8) δ –133.1 (d, $^{3}J_{FF}$ = 20.8 Hz, 12F, *o*-F:C$_6$***F***$_5$), –161.1 (t, $^{3}J_{FF}$ = 20.2 Hz, 6F, *p*-F:C$_6$***F***$_5$), –166.4 (t, $^{3}J_{FF}$ = 20.1 Hz, 12F, *m*-F:C$_6$***F***$_5$) ppm. ^{11}B NMR (160 MHz, 298 K, THF-d_8) δ –8.3 ppm. IR (KBr): 3384, 3346, 3072, 2968, 2934, 2873, 2359, 2343, 1643, 1621, 1541, 1519, 1467, 1367, 1303, 1277, 1231, 1101, 1094, 1059, 987, 986, 958, 802, 781, 765 cm^{-1}. Anal. Calcd for $C_{80.91}H_{68.02}N_3O_{2.59}B_2F_{30}ZnCl$: C, 53.48; H, 3.83; N, 2.31. Found: C, 54.28; H, 3.82; N, 2.33.

7.4.14 Synthesis of [H$^{t\text{Bu,Dipp}}$LZnCl][B(3,5-{CF$_3$}$_2$C$_6$H$_3$)$_4$] (23)

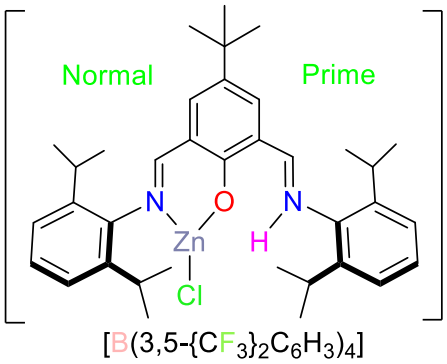

A solution of [H$_2$$^{t\text{Bu,Dipp}}$L][B(3,5-{CF$_3$}$_2C_6H_3$)$_4$]·thf$_{0.13}$ (0.300 g, 0.209 mmol) in THF (2 mL) was added dropwise to a solution of EtZnCl (0.0374 g, 0.288 mmol) in THF (2 mL). The bright orange reaction mixture was then left to stir overnight before volatiles were removed *in vacuo*. The crude oily solid was triturated with pentane (3 x 5 mL) to afford the [H$^{t\text{Bu,Dipp}}$LZnCl][B(3,5-{CF$_3$}$_2$C$_6$H$_3$)$_4$] (**23**) as a bright orange solid (0.252 g, 77%). Single crystals of complex **23(thf)**, suitable for an X-ray diffraction study, were obtained from layering a saturated THF solution with pentane at room temperature. ^{1}H NMR (400 MHz, 298 K, THF-d_8) δ 13.67 (d, $^3J_{HH}$ = 14.6 Hz, 1H, N'***H***), 9.02 (d, $^3J_{HH}$ = 14.4 Hz, 1H, ***H***C=N'), 8.76 (s, 1H, ***H***C=N), 8.22 (d, $^3J_{HH}$ = 2.8 Hz, 1H, 3'-C$_6$***H***$_2$), 8.02 (d, $^3J_{HH}$ = 2.8 Hz, 1H, 3-C$_6$***H***$_2$), 7.79 (m, 8H, [2,6-**Ar**]$^-$), 7.61–7.52 (overlapping m, 5H, [4-**Ar**]$^-$ and N-4-C$_6$***H***$_3$), 7.45 (d, $^3J_{HH}$ = 7.7 Hz, 2H, N-3,5-C$_6$***H***$_3$), 7.38–7.30 (m, 3H, N'-3,5-C$_6$***H***$_3$ and N'-4-C$_6$***H***$_3$), 3.05 (overlapping sept, 4H, N$^{(')}$-2,6-C$_6$H$_3$-C***H***Me$_2$), 1.37 (s, 9H, C(C***H***$_3$)$_3$), 1.34–1.26 (m, 18H, N-2,6-C$_6$H$_3$-CH***Me***$_2$ and N'-2,6-C$_6$H$_3$-CH***Me***$_2$), 1.16 (d, $^3J_{HH}$ = 6.8 Hz, 6H, N'-2,6-C$_6$H$_3$-CH***Me***$_2$) ppm. ^{13}C{^{1}H} NMR (101 MHz, 298 K, THF-d_8): δ 176.0 (1-***C***$_6$H$_2$), 173.2 (H***C***=N'), 173.1 (H***C***=NH), 163.5–162.5 (q, $^1J_{CB}$ = 49.7 Hz, [1-**Ar**]$^-$), 147.8 (3-***C***$_6$H$_2$), 145.3 (N-1-***C***$_6$H$_3$), 144.5 (N'-2,6-***C***$_6$H$_3$), 142.4 (4-***C***$_6$H$_2$), 141.8 (N-2,6-***C***$_6$H$_3$), 141.7 (3'-***C***$_6$H$_2$), 135.8 ([2,6-**Ar**]$^-$), 135.3 (N'-1-***C***$_6$H$_3$), 132.0 (N'-4-***C***$_6$H$_3$), 130.5–129.9 ([3,5-**Ar**]$^-$), 129.2 (N-4-***C***$_6$H$_3$), 128.4–123.0 (q, $^1J_{CF}$ = 271.9 Hz, [Ar-***C***F$_3$]$^-$), 125.7 (N'-3,5-***C***$_6$H$_3$), 125.3 (N-3,5-***C***$_6$H$_3$), 122.6 (2-***C***$_6$H$_2$), 118.8 (2'-***C***$_6$H$_2$), 118.4–118.3 (m, [4-**Ar**]$^-$), 35.0 (***C***(CH$_3$)$_3$), 31.2 (C(***C***H$_3$)$_3$), 30.0–29.6 (N$^{(')}$-2,6-C$_6$H$_3$-***C***HMe$_2$), 24.0–23.4 (N$^{(')}$-2,6-C$_6$H$_3$-CH***Me***$_2$) ppm. ^{19}F NMR (377 MHz, 298 K, THF-d_8) δ –63.4 ppm. ^{11}B NMR (128 MHz, 298 K, THF-

d_8) δ –6.5 ppm. IR (KBr): 3454, 2964, 2930, 2868, 2365, 2360, 2343, 1623, 1541, 1385, 1357, 1281, 1262, 1126, 1108, 1027, 883, 801, 710, 682, 669 cm^{-1}. Anal. Calcd for $C_{72}H_{67}N_2O_2BF_{24}ZnCl$: C, 55.44; H, 4.33; N, 1.80. Found: C, 56.40; H, 4.74; N, 1.69.

7.4.15 Synthesis of [$^{t\text{Bu,Dipp}}$L{ZnCl(thf)}CaN(SiMe$_3$)$_2$][H$_2$N{B(C$_6$F$_5$)$_3$}$_2$] (24)

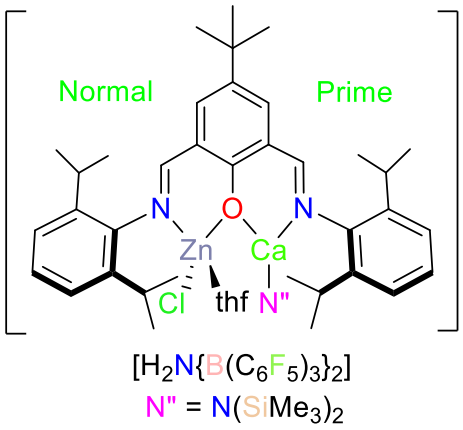

In a Young's tap NMR tube, [H$_2$$^{t\text{Bu,Dipp}}$L][H$_2$N{B(C$_6F_5$)$_3$}$_2$]·thf$_{0.36}$ (0.0400 g, 0.0250 mmol) and EtZnCl (0.0032 g, 0.0250 mmol) were dissolved in THF-d_8 (0.5 mL). The bright orange reaction mixture was left overnight before Ca{N(SiMe$_3$)$_2$}$_2$(thf)$_2$ (0.0133 g, 0.0250 mmol) was added. The resultant yellow reaction mixture was judged to be >95% [$^{t\text{Bu,Dipp}}$L{ZnCl(thf)}CaN(SiMe$_3$)$_2$][H$_2$N{B(C$_6$F$_5$)$_3$}$_2$] (**24**) by NMR spectroscopy. ^{1}H NMR (600 MHz, 298 K, THF-d_8) δ 8.87 (s, 1H, ***H***C=N'), 8.52 (d, $^4J_{HH}$ = 2.9 Hz, 1H, 3'-C$_6$***H***$_2$), 8.41 (s, 1H, ***H***C=N), 7.47 (d, $^4J_{HH}$ = 2.9 Hz, 1H, 3-C$_6$***H***$_2$), 7.24 (s, 3H, N'-3,5-C$_6$***H***$_3$ and N'-4-C$_6$***H***$_3$), 7.08 (d, $^3J_{HH}$ = 7.7 Hz, 2H, N-3,5-C$_6$***H***$_3$), 6.97 (m, 1H, N-4-C$_6$***H***$_3$), 5.75 (s (br), 2H, [***H***$_2$N{B(C$_6$F$_5$)$_3$}$_2$]$^-$), 3.37 (m, 4H, thf-OC***H***$_2$), 3.13 (sept, $^3J_{HH}$ = 6.9 Hz, 2H, N'-2,6-C$_6$H$_3$-C***H***Me$_2$), 3.03 (sept, $^3J_{HH}$ = 6.9 Hz, 2H, N-2,6-C$_6$H$_3$-C***H***Me$_2$), 1.59 (m, 4H, thf-C***H***$_2$), 1.34 (s, 9H, C(C***H***$_3$)$_3$), 1.32 (d, $^3J_{HH}$ = 6.8 Hz, 6H, N'-2,6-C$_6$H$_3$-CH***Me***$_2$), 1.16 (d, $^3J_{HH}$ = 6.9 Hz, 12H, N-2,6-C$_6$H$_3$-CH***Me***$_2$), 1.12 (d, $^3J_{HH}$ = 6.9 Hz, 6H, N'-2,6-C$_6$H$_3$-CH***Me***$_2$), -0.16 (s, 18H, N(Si***Me***$_3$)$_2$) ppm. ^{13}C NMR (151 MHz, 298 K, THF-d_8) δ 176.4 (H***C***=N), 170.3 (1-***C***$_6$H$_2$), 159.9 (H***C***=N'), 151.8 (N'-1-***C***$_6$H$_3$), 149.9-148.1 (*o*-F:***C***$_6$F$_5$), 148.2 (N-1-***C***$_6$H$_3$), 142.0 (N'-2,6-***C***$_6$H$_3$), 141.3-139.3 (*p*-F:***C***$_6$F$_5$), 138.7-136.7 (*m*-F:***C***$_6$F$_5$), 138.2 (N-2,6-***C***$_6$H$_3$), 137.8 (3-***C***$_6$H$_2$), 137.7 (4-***C***$_6$H$_2$), 132.7 (3'-***C***$_6$H$_2$), 128.5 (2'-***C***$_6$H$_2$), 127.9 (N'-4-***C***$_6$H$_3$), 124.7 (N'-3,5-***C***$_6$H$_3$), 124.2 (N-4-***C***$_6$H$_3$),

123.5 (N-3,5-***C***$_6$H$_3$), 119.9 (2-***C***$_6$H$_2$), 71.5 (thf-O***C***H$_2$), 34.7 (***C***(CH$_3$)$_3$), 31.9 (C(***C***H$_3$)$_3$), 29.1 (N'-2,6-C$_6$H$_3$-***C***HMe$_2$), 28.9 (N-2,6-C$_6$H$_3$-***C***HMe$_2$), 27.8 (thf-***C***H$_2$), 25.7 (N-2,6-C$_6$H$_3$-CH***Me***$_2$), 24.0 (N-2,6-C$_6$H$_3$-CH***Me***$_2$), 23.1 (N'-2,6-C$_6$H$_3$-CH***Me***$_2$), 5.7 (N(Si***Me***$_3$)$_2$) ppm. ^{19}F NMR (565 MHz, 298 K, THF-d_8) δ –133.1 (d, $^3J_{FF}$ = 21.0 Hz, 12F, *o*-F:C$_6$***F***$_5$), –161.1 (t, $^3J_{FF}$ = 20.2 Hz, 6F, *p*-F:C$_6$***F***$_5$), –166.4 (t, $^3J_{FF}$ = 20.1 Hz, 12F, *m*-F:C$_6$***F***$_5$) ppm. ^{11}B NMR (160 MHz, 298 K, THF-d_8) δ –8.3 ppm.

7.4.16 Synthesis of [$^{t\text{Bu,Dipp}}$L{ZnCl}CaN(SiMe$_3$)$_2$][B(3,5-{CF$_3$}$_2$C$_6$H$_3$)$_4$] (25)

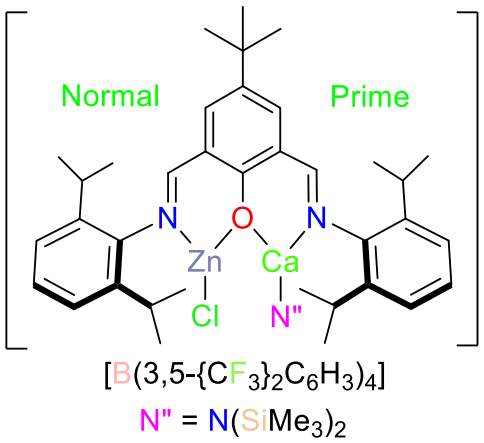

In a Young's tap NMR tube, [H$_2$$^{t\text{Bu,Dipp}}$L][B(3,5-{CF$_3$}$_2C_6H_3$)$_4$]·thf$_{0.13}$ (0.0200 g, 0.0143 mmol) and EtZnCl (0.0019 g, 0.0143 mmol) were dissolved in THF-d_8 (0.5 mL). The bright orange reaction mixture was left overnight before Ca{N(SiMe$_3$)$_2$}$_2$(thf)$_2$ (0.0076 g, 0.0143 mmol) was added. The resultant yellow reaction mixture was judged to be >95% [$^{t\text{Bu,Dipp}}$L{ZnCl(thf)}CaN(SiMe$_3$)$_2$][B(3,5-{CF$_3$}$_2$C$_6$H$_3$)$_4$] (**25**) by NMR spectroscopy. ^{1}H NMR (400 MHz, 298 K, THF-d_8) δ 8.87 (s, 1H, ***H***C=N'), 8.52 (d, $^4J_{HH}$ = 2.9 Hz, 1H, 3'-C$_6$***H***$_2$), 8.42 (s, 1H, ***H***C=N), 7.78 (m, 8H, [2,6-**Ar**]$^-$), 7.58 (m, 4H, [4-**Ar**]$^-$), 7.47 (d, $^4J_{HH}$ = 2.9 Hz, 1H, 3-C$_6$***H***$_2$), 7.25 (s, 3H, N'-3,5-C$_6$***H***$_3$ and N'-4-C$_6$***H***$_3$), 7.09 (d, $^3J_{HH}$ = 7.6 Hz, 2H, N-3,5-C$_6$***H***$_3$), 6.97 (m, 1H, N-4-C$_6$***H***$_3$), 3.13 (sept, $^3J_{HH}$ = 7.0 Hz, 2H, N'-2,6-C$_6$H$_3$-C***H***Me$_2$), 3.02 (sept, $^3J_{HH}$ = 6.9 Hz, 2H, N-2,6-C$_6$H$_3$-C***H***Me$_2$), 1.34 (s, 9H, C(C*H*$_3$)$_3$), 1.32 (d, $^3J_{HH}$ = 6.8 Hz, 6H, N'-2,6-C$_6$H$_3$-CH***Me***$_2$), 1.16 (d, $^3J_{HH}$ = 6.9 Hz, 12H, N-2,6-C$_6$H$_3$-CH***Me***$_2$), 1.12 (d, $^3J_{HH}$ = 6.8 Hz, 6H, N'-2,6-C$_6$H$_3$-CH***Me***$_2$), -0.16 (s, 18H, N(Si***Me***$_3$)$_2$) ppm. ^{13}C NMR (151 MHz, 298 K, THF-d_8) δ 176.4 (H***C***=N), 169.9 (1-***C***$_6$H$_2$), 163.5–162.5 (q, $^1J_{CB}$ = 49.7 Hz, [1-**Ar**]$^-$), 159.9 (H***C***=N'), 151.8 (N'-1-***C***$_6$H$_3$), 148.3 (N-

1-***C***$_6$H$_3$), 142.0 (N'-2,6-***C***$_6$H$_3$), 138.2 (N-2,6-***C***$_6$H$_3$), 137.8 (3-***C***$_6$H$_2$), 137.7 (4-***C***$_6$H$_2$), 135.8 ([2,6-**Ar**]$^-$), 132.7 (3'-***C***$_6$H$_2$), 130.5-129.8 ([3,5-**Ar**]$^-$), 128.5 (2'-***C***$_6$H$_2$), 128.4-123.0 (q, $^1J_{CF}$ = 271.7 Hz, [Ar-***C***F$_3$]$^-$), 127.9 (N'-4-***C***$_6$H$_3$), 124.7 (N'-3,5-***C***$_6$H$_3$), 124.2 (N-4-***C***$_6$H$_3$), 123.5 (N-3,5-***C***$_6$H$_3$), 119.9 (2-***C***$_6$H$_2$), 118.3 (m, [4-**Ar**]$^-$), 34.7 (***C***(CH$_3$)$_3$), 31.9 (C(***C***H$_3$)$_3$), 29.1 (N'-2,6-C$_6$H$_3$-***C***HMe$_2$), 28.9 (N-2,6-C$_6$H$_3$-***C***HMe$_2$), 25.7 (N-2,6-C$_6$H$_3$-CH***Me***$_2$), 24.0 (N-2,6-C$_6$H$_3$-CH***Me***$_2$), 23.1 (N'-2,6-C$_6$H$_3$-CH***Me***$_2$), 5.7 (N(Si***Me***$_3$)$_2$) ppm. ^{19}F NMR (377 MHz, 298 K, THF-d_8) δ –63.4 ppm. ^{11}B NMR (128 MHz, 298 K, THF-d_8) δ –6.5 ppm.

7.5 References

1. D. F. Shriver, *The Manipulations of Air-Sensitive Compounds*, 2nd edn., 1986.
2. C.-Y. Peng, J.-Y. Shen, Y.-T. Chen, P.-J. Wu, W.-Y. Hung, W.-P. Hu and P.-T. Chou, *J. Am. Chem. Soc*, 2015, **137**, 14349-14357.
3. M. R. Salata and T. J. Marks, *Macromolecules*, 2009, **42**, 1920-1933.
4. Y. Sarazin, R. H. Howard, D. L. Hughes, S. M. Humphrey and M. Bochmann, *Dalton Trans.*, 2006, 340-350.
5. T. M. Cameron, C. Xu, A. G. Dipasquale and A. L. Rheingold, *Organometallics*, 2008, **27**, 1596-1604.
6. A. Guerrero, D. L. Hughes and M. Bochmann, *Organometallics*, 2006, **25**, 1525-1527.
7. M. Brookhart, B. Grant and A. F. Volpe, Jr., *Organometallics*, 1992, **11**, 3920-3922.
8. L. F. Lindoy, G. V. Meehan and N. Svenstrup, *Synthesis*, 1998, 1029-1032.
9. P. D. Knight, A. J. P. White and C. K. Williams, *Inorg. Chem.*, 2008, **47**, 11711-11719.
10. H.-C. Chiu, A. Koley, P. L. Dunn, R. J. Hue and I. A. Tonks, *Dalton Trans.*, 2017, **46**, 5513-5517.
11. L. Wang, W.-H. Sun, L. Han, Z. Li, Y. Hu, C. He and C. Yan, *J. Organomet. Chem.*, 2002, **650**, 59-64.
12. S. J. Lancaster, A. Rodriguez, A. Lara-Sanchez, M. D. Hannant, D. A. Walker, D. H. Hughes and M. Bochmann, *Organometallics*, 2002, **21**, 451-453.
13. J. Cosier and A. M. Glazer, *J. Appl. Crystallogr.*, 1986, **19**, 105-107.
14. CrysAlisPRO, *Journal*, Oxford Diffraction / Agilent Technologies UK Ltd.
15. A. Altomare, G. Cascarano, C. Giacovazzo and A. Guagliardi, *J. Appl. Crystallogr.*, 1993, **26**, 343-350.
16. L. Palatinus and G. Chapuis, *J. Appl. Crystallogr.*, 2007, **40**, 786-790.
17. G. Sheldrick, *Acta Crystallogr. A*, 2015, **71**, 3-8.

18. L. Farrugia, *J. Appl. Crystallogr.*, 2012, **45**, 849-854.

19. P. W. Betteridge, J. R. Carruthers, R. I. Cooper, K. Prout and D. J. Watkin, *J. Appl. Crystallogr.*, 2003, **36**, 1487.

20. G. Sheldrick, *Acta Crystallogr. C*, 2015, **71**, 3-8.

21. O. V. Dolomanov, L. J. Bourhis, R. J. Gildea, J. A. K. Howard and H. Puschmann, *J. Appl. Crystallogr.*, 2009, **42**, 339-341.

22. A. Spek, *J. Appl. Crystallogr.*, 2003, **36**, 7-13.

23. L. Farrugia, *J. Appl. Crystallogr.*, 1997, **30**, 565.

24. F. Neese, F. Wennmohs, U. Becker and C. Riplinger, *Chem. Phys.*, 2020, **152**, 224108.

25. F. Neese, *WIREs Computational Molecular Science*, 2012, **2**, 73-78.

26. F. Neese, *WIREs Computational Molecular Science*, 2022, **12**, e1606.

27. A. D. Becke, *Chem. Phys.*, 1986, **84**, 4524-4529.

28. C. Lee, W. Yang and R. G. Parr, *Phys. Rev. B*, 1988, **37**, 785-789.

29. A. D. Becke, *Chem. Phys.*, 1993, **98**, 5648-5652.

30. D. A. Pantazis, X.-Y. Chen, C. R. Landis and F. Neese, *J. Chem. Theory Comput.*, 2008, **4**, 908-919.

31. D. A. Pantazis and F. Neese, *J. Chem. Theory Comput.*, 2009, **5**, 2229-2238.

32. S. Grimme, J. Antony, S. Ehrlich and H. Krieg, *Chem. Phys.*, 2010, **132**, 154104.

33. F. Neese, F. Wennmohs, A. Hansen and U. Becker, *Chem. Phys.*, 2009, **356**, 98-109.

34. R. Izsák and F. Neese, *Chem. Phys.*, 2011, **135**, 144105.

35. E. F. Pettersen, T. D. Goddard, C. C. Huang, G. S. Couch, D. M. Greenblatt, E. C. Meng and T. E. Ferrin, *J. Comput. Chem.*, 2004, **25**, 1605-1612.

36. T. Lu and F. Chen, *J. Comput. Chem.*, 2012, **33**, 580-592.

37. P. McKeown, M. G. Davidson, G. Kociok-Köhn and M. D. Jones, *Chem. Commun.*, 2016, **52**, 10431-10434.

38. J. Coudane, C. Ustariz-Peyret, G. Schwach and M. Vert, *J. Polym. Sci., Part A: Polym. Chem.*, 1997, **35**, 1651-1658.

39. J. R. Dorgan, J. Janzen, D. M. Knauss, S. B. Hait, B. R. Limoges and M. H. Hutchinson, *J. Polym. Sci., Part B: Polym. Phys.*, 2005, **43**, 3100-3111.

40. X. Wang, T. Zhao, B. Yang, Z. Li, J. Cui, Y. Dai, Q. Qiu, H. Qiang, W. Huang and H. Qian, *Biorg. Med. Chem.*, 2015, **23**, 132-140.

41. Y. Zhang, K. Shibatomi and H. Yamamoto, *Synlett*, 2005, 2837-2842.

42. M. T. Rispens, O. J. Gelling, A. M. de Vries, A. Meetsma, F. van Bolhuis and B. L. Feringa, *Tetrahedron*, 1996, **52**, 3521-3546.

43. E. Schiebel, M. Voccia, L. Falivene, I. Göttker-Schnetmann, L. Caporaso and S. Mecking, *Angew. Chem. Int. Ed.*, 2021, **60**, 18472-18477.

Concluding Remarks

The results discussed within this Thesis have covered two main topics: (i) the synthesis and characterisation of new alkaline-earth *bis*(phenoxy-imine) complexes, and (ii) the application of these systems as initiators in the ring-opening polymerisation of lactide monomers. The key highlights and conclusions are detailed below.

(i) New alkaline-earth *bis*(phenoxy-imine) compounds

The synthesis of fifteen new group 2 containing *bis*(phenoxy-imine) systems, based on either "NOON" or "NON" frameworks, were reported and fully characterised (including ten solid-state structures). The corresponding data for the potassium- or zinc-based intermediates is also detailed.

In the case of the "NOON" systems, the preferential binding of the oxophilic M^{2+} centres into the $[O^{-},O^{-}]$ binding pocket resulted in dimerisation (Mg) or the formation of a solution monomer ⇌ dimer equilibrium (Ca, Sr, Ba).

When utilising the "NON" backbone, homoleptic *bis*(ligand) systems were afforded for Mg, Sr and Ba. Curiously, heteroleptic analogues were isolated in the case of Ca; this was attributed to favourable kinetic stabilisation as a result of sufficient steric shielding of the metal centre and increased Ca-I bond strength (*vs.* Mg-I).

The deliberate protonation of "NON" pro-ligands generated a cationic scaffold that enabled the insertion of multiple metals. This pathway to Zn/Ca bimetallics was found to be successful only if the first metal to be added was zinc (in the form of EtZnCl). These initial results suggest this is a promising route to a wide range of Zn/X *bis*(metal) systems.

(i) Active initiators for the ROP of *L*-, *D*- and *rac*-lactide

"NOON" initiators

In the presence of benzyl alcohol co-initiator, $[H^{Dipp}LMgCl]_2$ (**2**) was found to be active towards the ROP of LA. The experimental rate constants (k_{obs} = 0.0046–0.091 h^{-1}) were much lower than previously reported dimeric magnesium species with pre-formed highly active initiating groups but were similar to an aggregating $[LMgCl]_n$ species. All polymerisations were shown to have narrow molecular weight distributions (M_w/M_n <1.32) indicating good polymerisation control. Analysis of the polymers revealed that the initiator produced isotactic PLA for the ROP of *L*-/*D*-lactide, and atatic/heterotactic-enriched PLA for the ROP of *rac*-lactide (P_m ~ 0.53) and *meso*-lactide (P_m ~ 0.70) respectively. The complex displayed first order dependency on both monomer and catalyst concentration thus allowing the propagation rate constant to be determined (3.19 $M^{-1}\,h^{-1}$) from the overall rate law:

$$-\frac{d[\mathrm{LA}]}{dt} = k_p[\mathrm{LA}][\mathbf{Mg}]$$

The analogous, but less well-defined, $^{Dipp}LM(thf)_x/[^{Dipp}LM(thf)_x]_2$ systems (M = Ca (**3**), Sr (**4**) and Ba (**5**)) displayed much higher reactivity both with and without co-initiator. The dependency on monomer concentration was found to vary depending on the alkaline-earth metal used (Ca = first-order; Sr and presumably Ba = second-order). Further studies with **4** suggested that, in the absence of BnOH, the monometallic "NOON" systems operate via an anionic mechanism. This results in poor polymerisation control as evidenced by the broad, bimodal molecular weight distributions ($1.23<M_w/M_n<1.73$). The bimodality was rationalised as the result of multiple initiating species (caused by the solution monomer ⇌ dimer equilibria associated with these complexes) and/or the formation of different polymeric structures.

"NON" initiators

All of the isolated monometallic "NON" complexes (**10**–**15**) were found to be active for lactide polymerisation, with compounds **11** and **12** being the first recorded examples of phenoxy-imine strontium/barium LA ROP initiators. The homoleptic magnesium catalyst (**10**) was observed to have an initiation period (3.5 h) and second-order dependency on monomer concentration in the absence of co-initiator. The analogous strontium and barium systems showed no initiation period and first- (k_{obs} = 0.84 h^{-1})/second-order (k_{obs} = 19.53 M^{-1} h^{-1}) dependencies on $[LA]_0$ respectively. These heavier alkaline-earth systems however, were found to be unstable in the presence of benzyl alcohol.

All polymerisations with **10**/BnOH proceeded with good control ($1.11<M_n/M_w<1.75$). The experimental molecular weights, however, were always found to be lower than the calculated values ($56<\Delta\%<92$); this may result from excess co-initiator acting as a chain transfer agent or from multiple propagating polymer chains growing per metal centre. (Co)-initiator concentration studies revealed a first and second-order dependency on **10** and BnOH concentrations respectively. The overall rate law for the ROPs of LA catalysed by **10**/BnOH, consistent with the proposed activated monomer mechanism, can therefore be described by the following equation in which the propagation rate constant was computed to be 966 ± 26 M^{-1} h^{-1}:

$$\frac{d[\mathrm{LA}]}{dt} = k_p[\mathrm{LA}][\mathbf{Mg}][\mathrm{BnOH}]^2$$

All three heteroleptic calcium initiators (**13**–**15**) also proved active towards the ROP of LA. The addition of co-initiator was seen to dramatically increase the rate e.g. ~12 fold difference for **15** (0.70 *vs*. 0.06 h^{-1}). The experimental rate constants are comparable to those reported by Darensbourg *et al*. in their investigation of heteroleptic tridentate N,N,O phenoxy-imine calcium catalysts (k_{obs} = 0.0955–0.8083 h^{-1}).[9]

Variation of the *para*-substituent proved to have little effect on the microstructure of the resultant PLA as heterotactic- and syndiotactically-enriched polymers were formed in all cases from *rac*- (P_r = 0.55–0.62) and *meso*-LA respectively (P_r = 0.51–0.67).

Co-initiator dependency studies revealed only a fractional dependence on $[BnOH]_0$; this agrees with the other experimental observations, which suggest the heteroleptic catalysts work via an unusual "ligand-assisted, activated monomer" mechanism.

Under immortal conditions, the recorded polydispersity values of **13**–**15** are intermediate in nature ($1.52<M_w/M_n<1.73$). This implies that the rate of transfer does not vastly exceeds that of propagation ($k_{tr} >> k_p$).

Cationic initiators

The cationic heteroleptic calcium system (**19**) was found to be more active than the comparable neutral analogue (**15**; k_{obs} = 3.53 *vs.* 0.38 h^{-1}). This is attributed to the increased Lewis acidity of the cationic calcium centre.

In the absence of BnOH, the zinc chloride complexes (**22**/**23**) were found to be inactive. Upon addition of co-initiator, the ROP was found to proceed but at very slow rates. Use of the BAr^F_4 anion resulted in a doubling of the apparent rate constant (k_{obs} = 0.00153 and 0.00307 h^{-1} for **22** and **23** respectively); this was attributed to the more weakly coordinating nature of this anion.

Unfortunately, all attempts to perform polymerisations with the bimetallic Zn/Ca catalysts (**24**/**25**) resulted in complex degradation. As a result, it can be concluded that these species are unsuitable initiators for the ROP of LA under the typical polymerisation conditions employed in this Thesis ($[LA]_0:[M]_0$ = 50:1, $[LA]_0$ = 0.5 M, 0.6 mL chloroform-d_1 or benzene-d_6, 60 °C). However, with a route now established to this class

of complex; it is anticipated that future studies will yield active initiators that can be used to probe metal-metal cooperativity.

Appendix

Supplementary Data for Chapters 2-6

Chapter 2

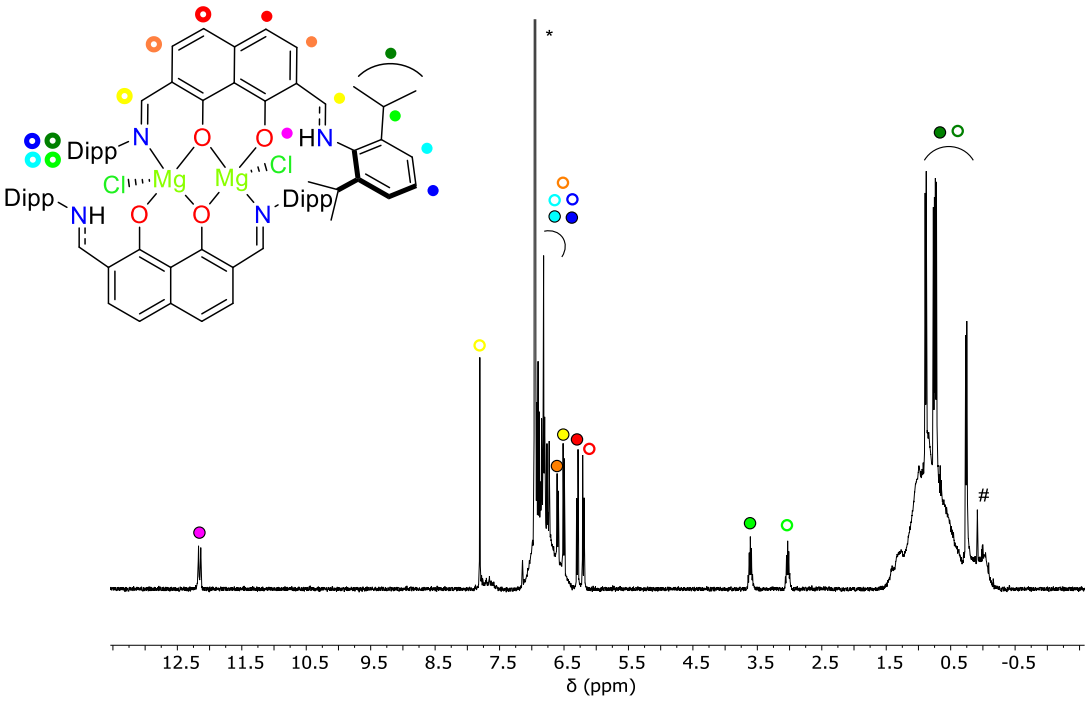

Figure A.1 ^{1}H NMR spectrum (*benzene-d_6, 400 MHz, 298 K) of $[H^{Dipp}LMgCl]_2$ (**2**). # represents residual hexamethyldisilazane (HMDS).

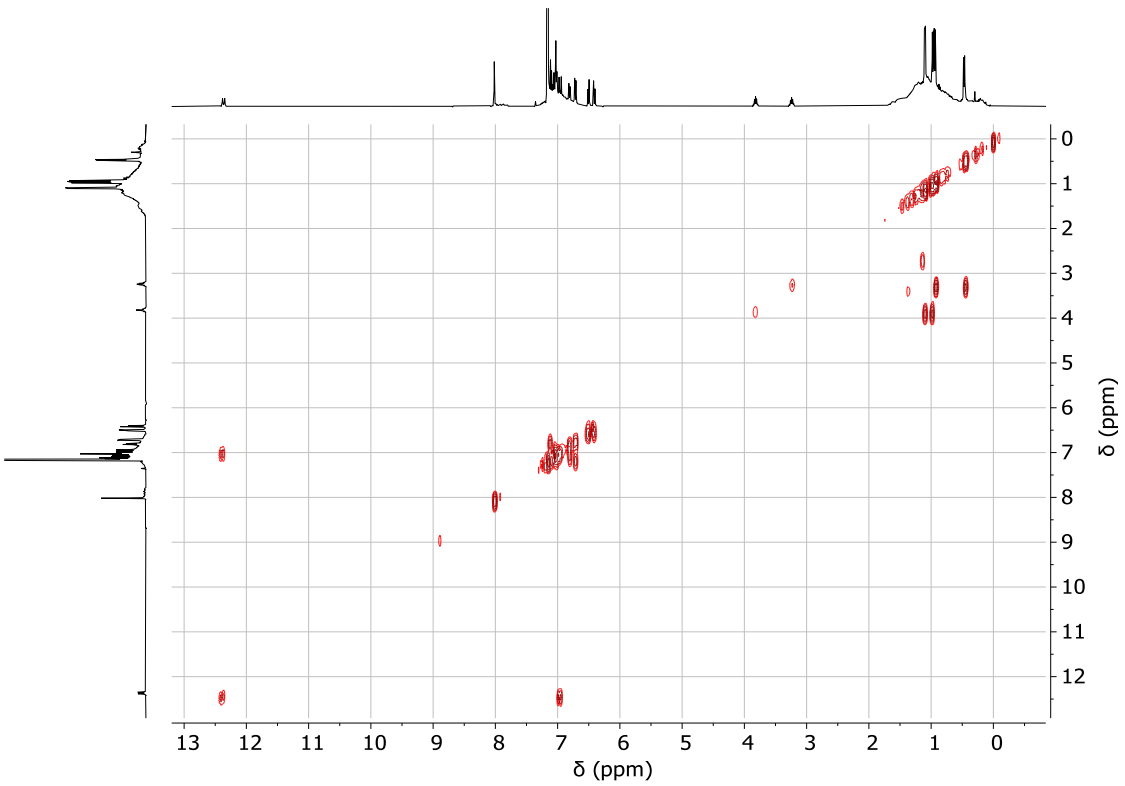

Figure A.2 ^{1}H-^{1}H COSY NMR spectrum (*benzene-d_6, 400 MHz, 298 K) of $[H^{Dipp}LMgCl]_2$ (**2**).

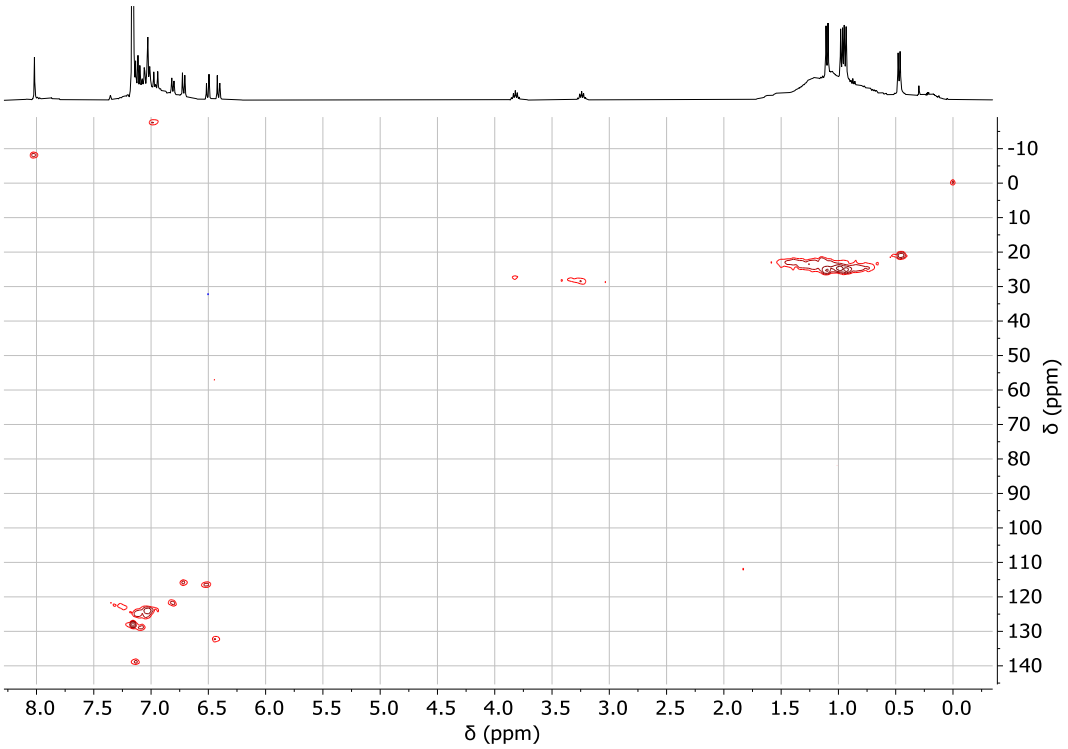

Figure A.3 ^{1}H-^{13}C HSQC NMR spectrum (*benzene-d_6, 400 MHz, 298 K) of $[H^{Dipp}LMgCl]_2$ (**2**).

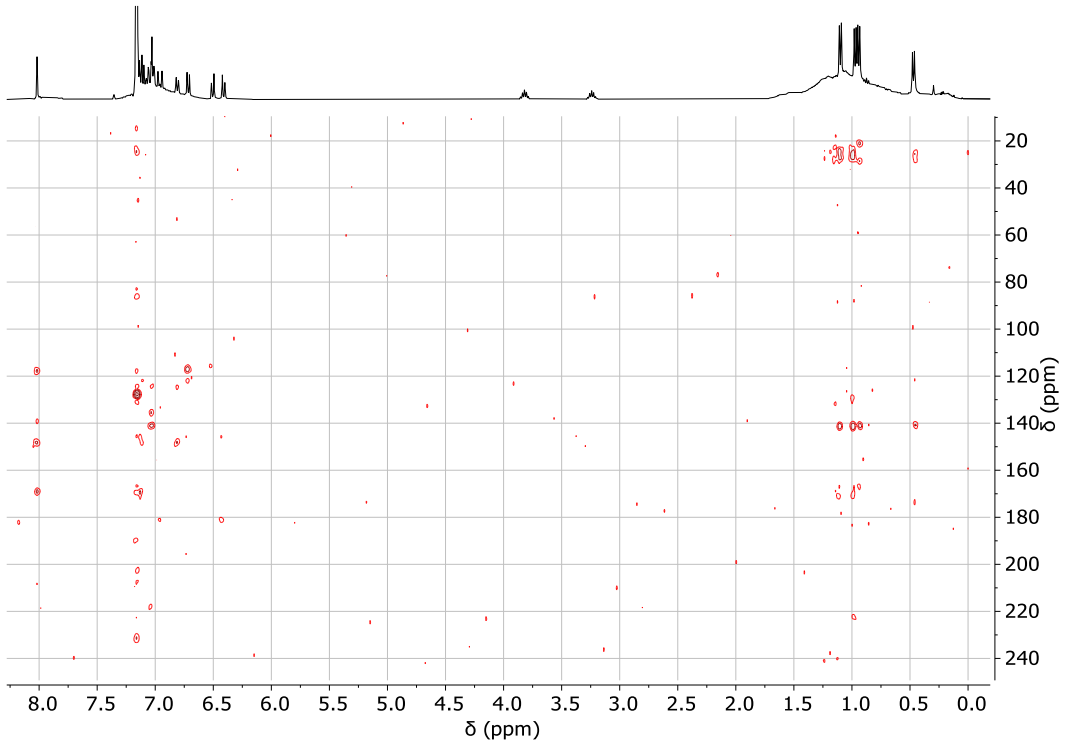

Figure A.4 ^{1}H-^{13}C HMBC NMR spectrum (*benzene-d_6, 400 MHz, 298 K) of $[H^{Dipp}LMgCl]_2$ (**2**).

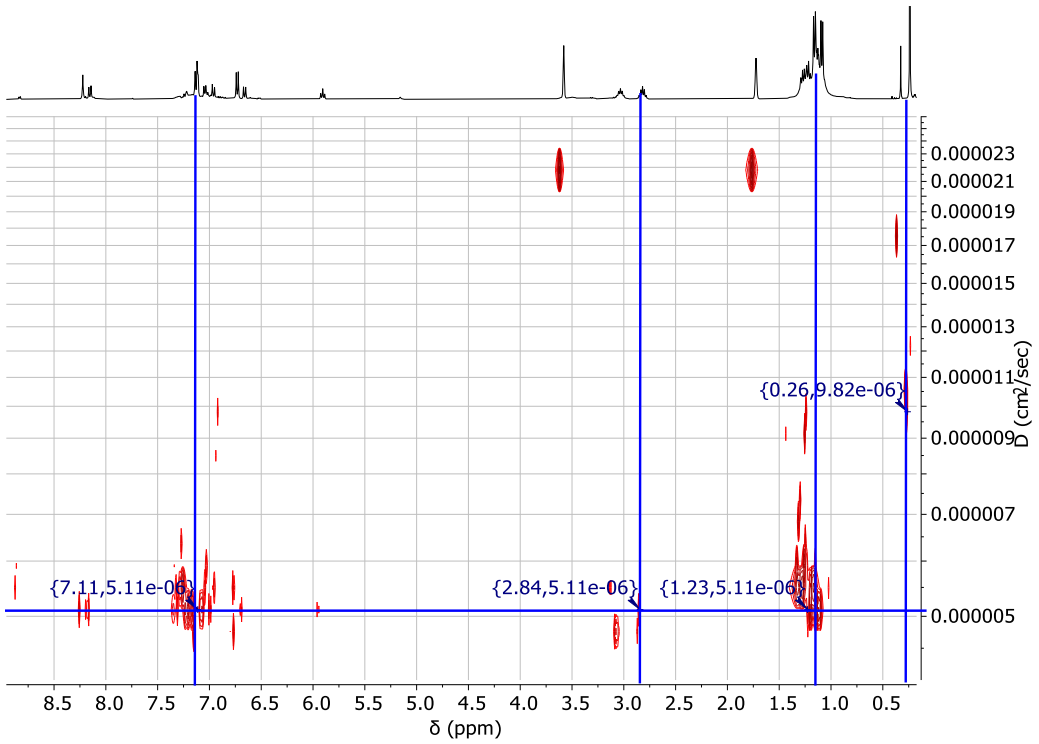

Figure A.5 DOSY NMR spectrum (THF-d_8, 500 MHz, 298 K) of [^{Dipp}LMg(thf)]$_2$ (**1**).

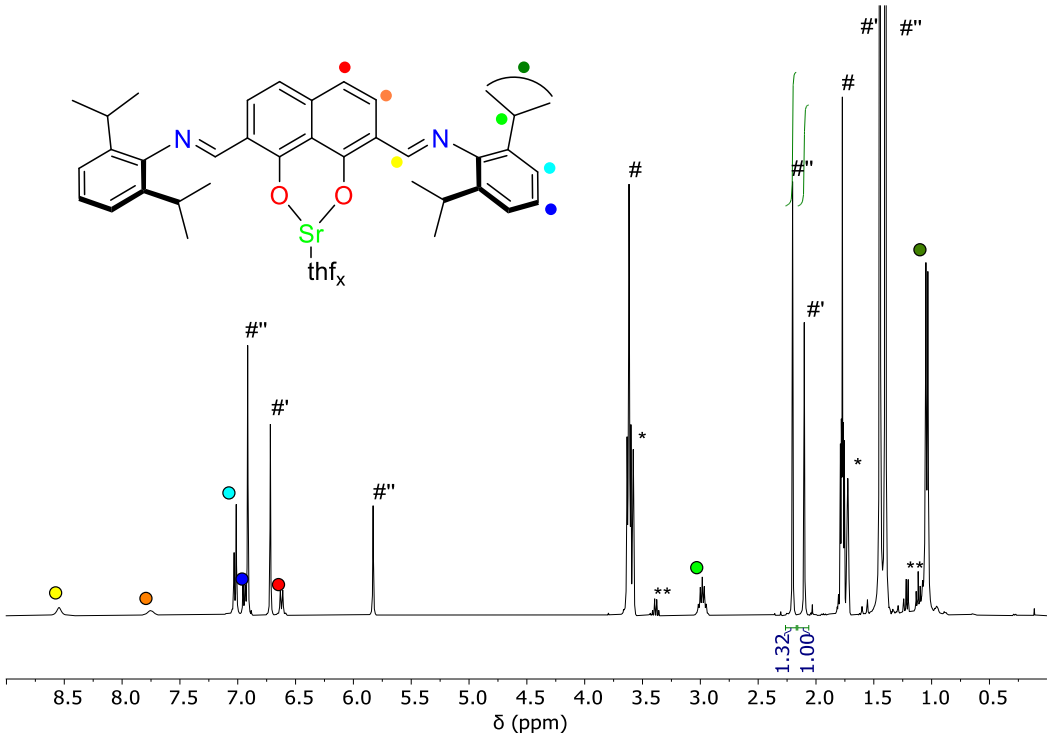

Figure A.6 ^{1}H NMR spectrum (*THF-d_8, 400 MHz, 298 K) of the crude reaction mixture between $H_2{}^{Dipp}L$ and Sr(O-2,6-^{t}Bu-4-Me-C_6H_2)$_2$(thf)$_2$. #, #' and #'' represent protio THF, unreacted eq. of Sr starting material and equimolar amount of 2,6-di-*tert*-butyl-4-methyl phenol by-product respectively. ** represents residual protio diethyl ether contamination of the deuterated solvent.

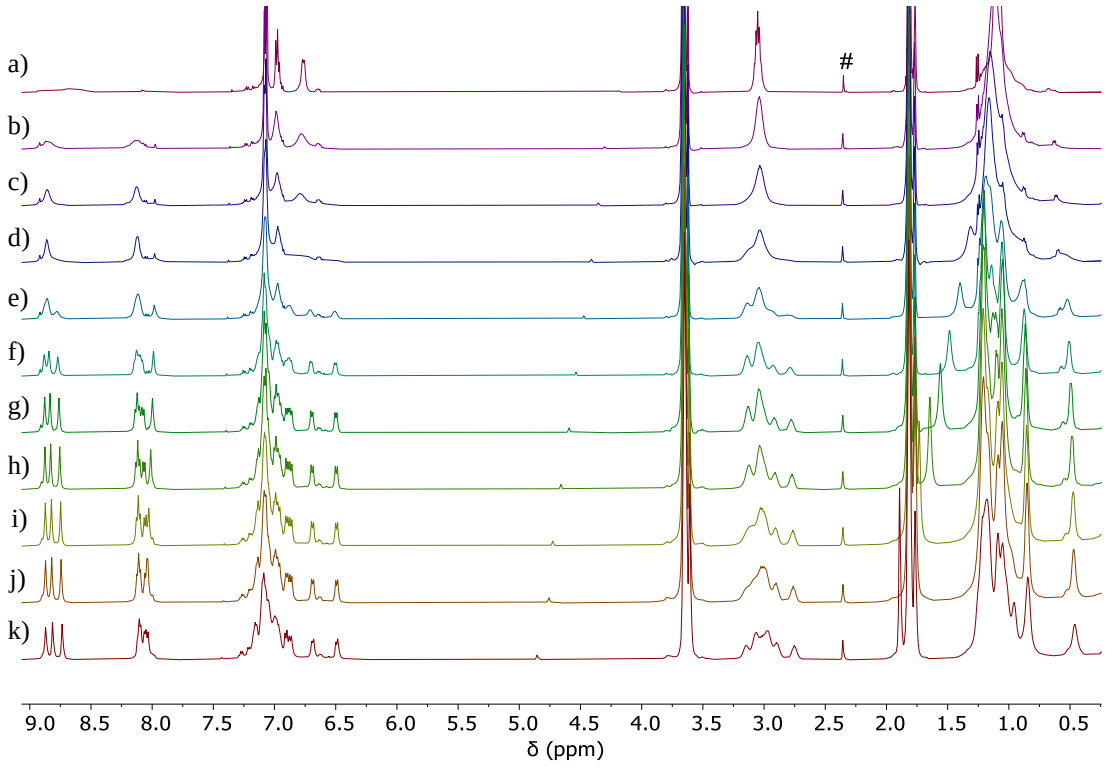

Figure A.7 ^{1}H NMR spectra (*THF-d_8, 500 MHz) of ^{Dipp}LCa(thf)$_2$ (**3(thf)$_2$**) at a) 298 K, b) 273 K, c) 263 K, d) 253 K, e) 243 K, f) 233 K, g) 223 K, h) 213 K, i) 203 K, j) 193 K and k) 183 K. # represents acetone contamination of deuterated solvent.

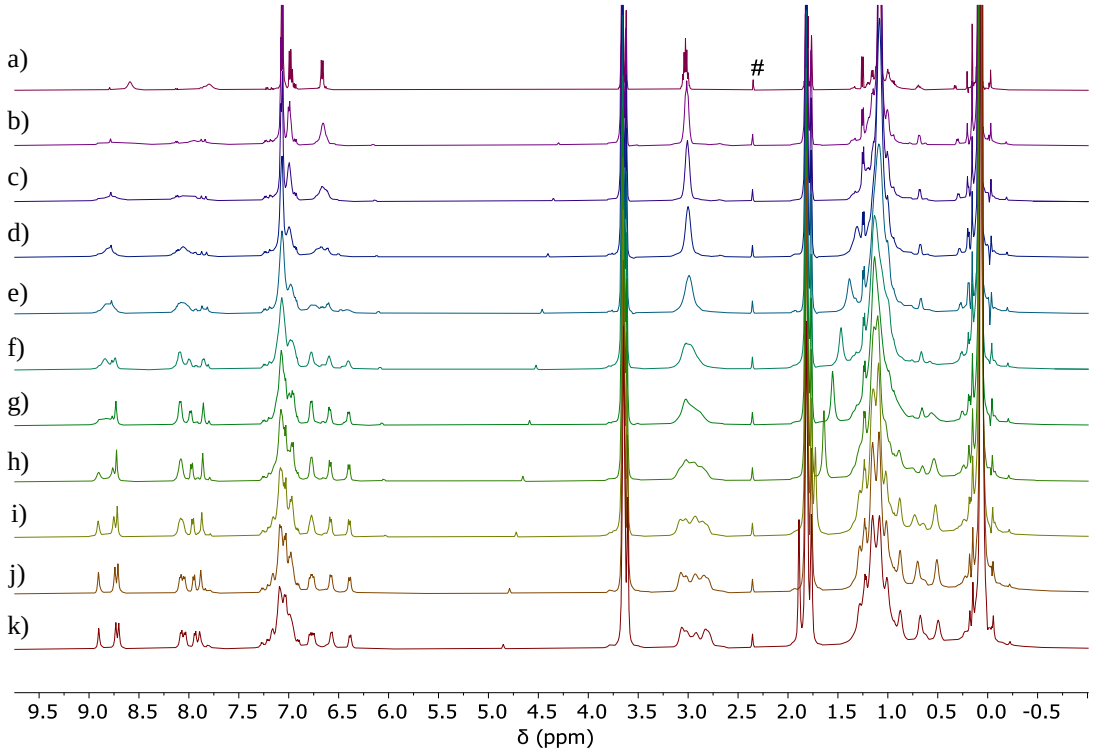

Figure A.8 ^{1}H NMR spectra (*THF-d_8, 500 MHz) of ^{Dipp}LSr(thf) (**4(thf)**) at a) 298 K, b) 273 K, c) 263 K, d) 253 K, e) 243 K, f) 233 K, g) 223 K, h) 213 K, i) 203 K, j) 193 K and k) 183 K. # represents acetone contamination of deuterated solvent.

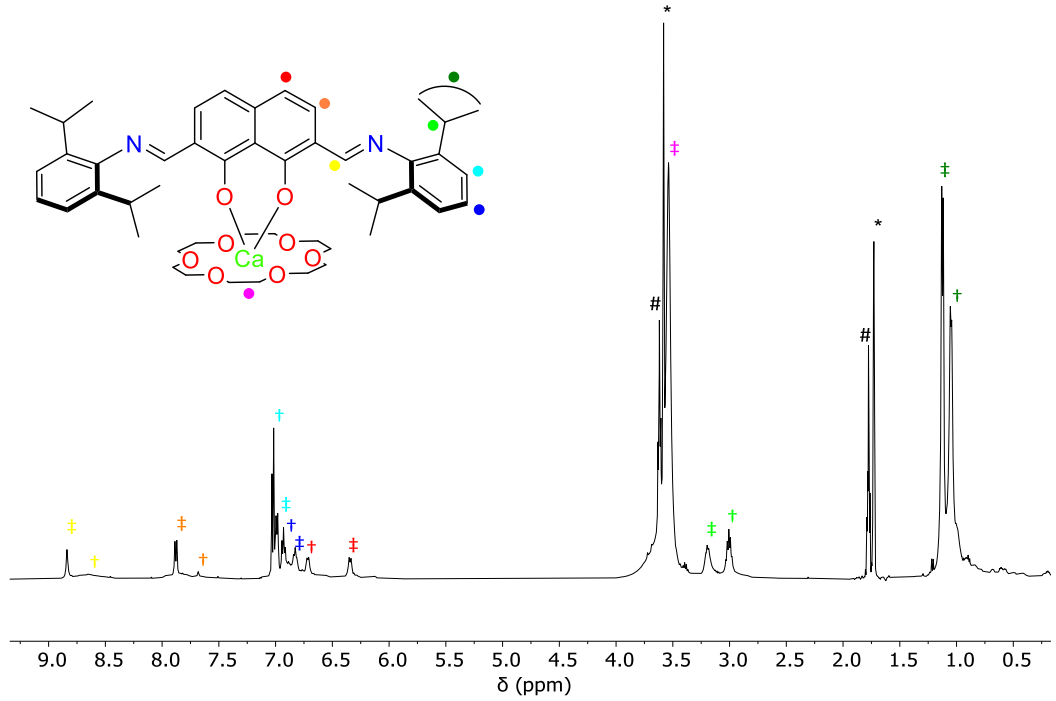

Figure A.9 ^{1}H NMR spectrum (*THF-d_8, 500 MHz, 298 K) of reaction mixture between **3(thf)$_2$** and 18-crown-6. #, † and ‡ denote residual protio THF, **3(thf)$_2$** and **3(18c6)** respectively.

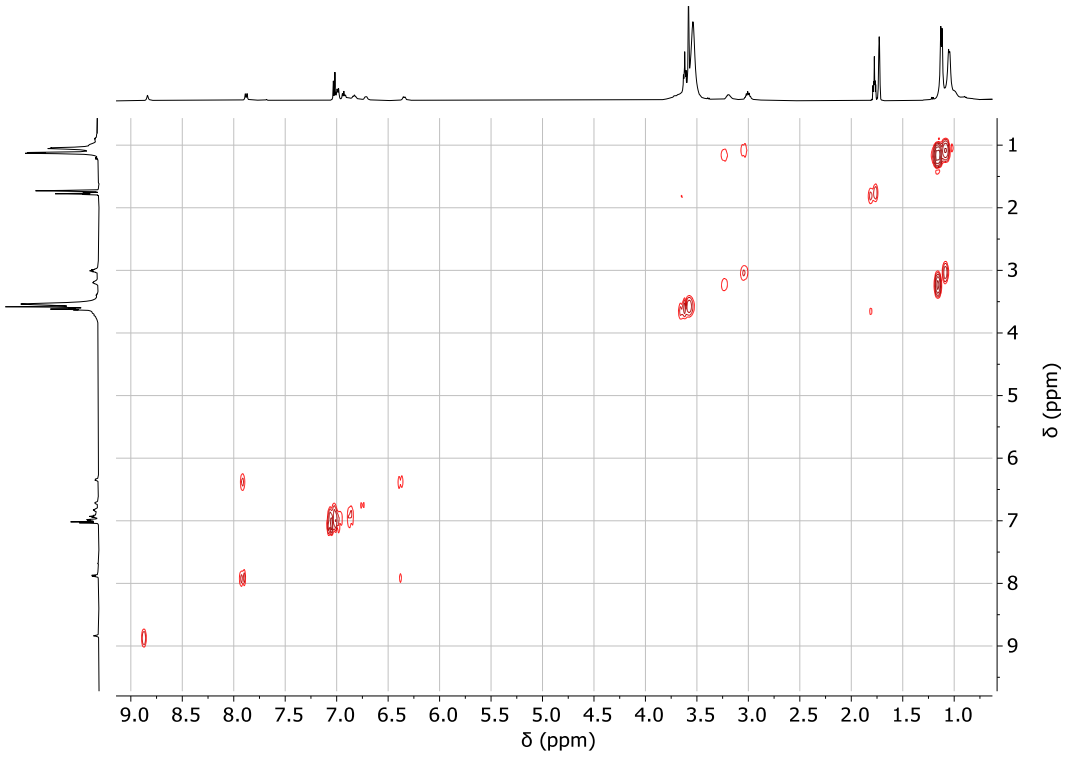

Figure A.10 ^{1}H-^{1}H COSY NMR spectrum (THF-d_8, 500 MHz, 298 K) of reaction mixture between **3(thf)$_2$** and 18-crown-6.

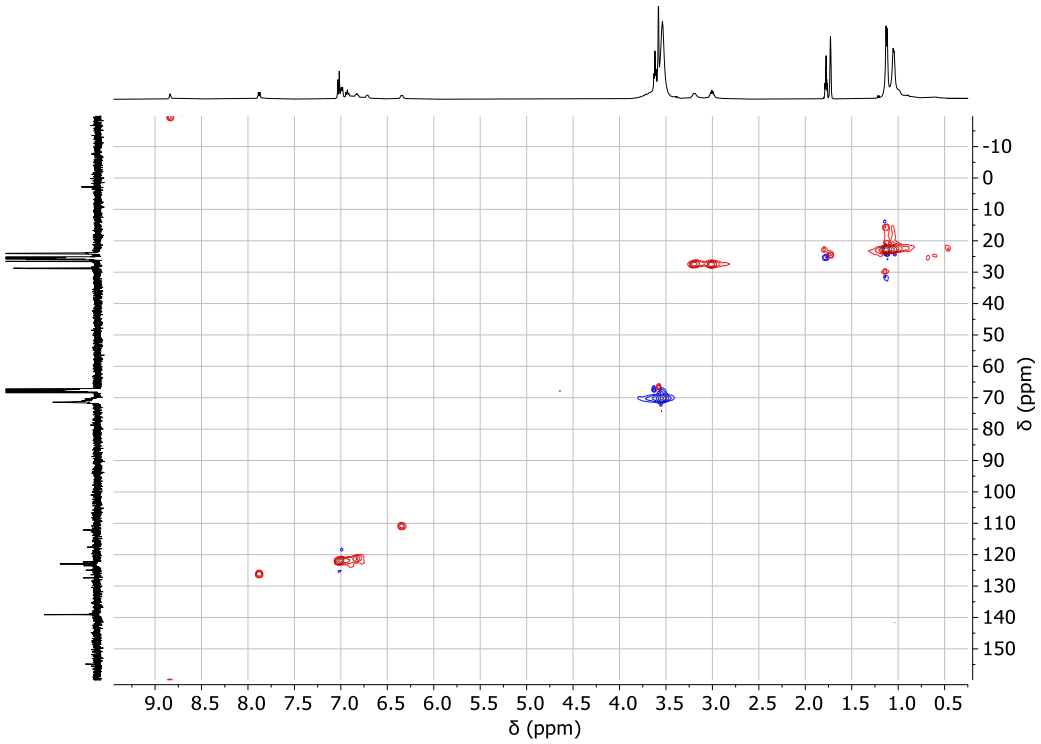

Figure A.11 ^{1}H-^{13}C HSQC NMR spectrum (THF-d_8, 500 MHz, 298 K) of reaction mixture between **3(thf)$_2$** and 18-crown-6.

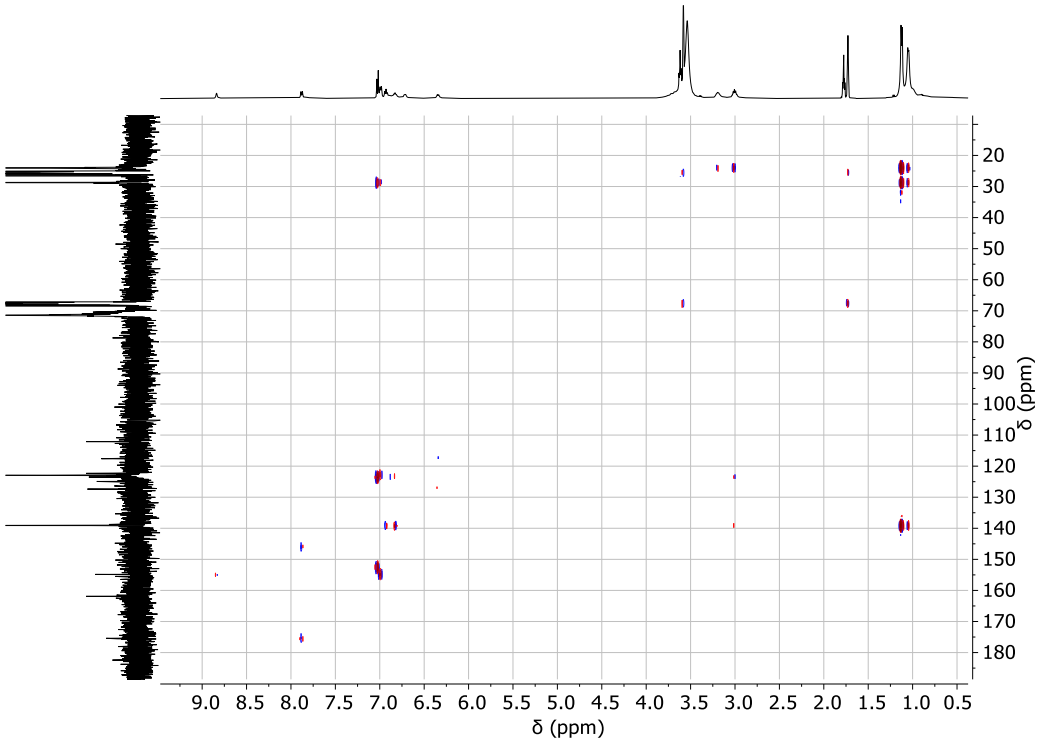

Figure A.12 ^{1}H-^{13}C HMBC NMR spectrum (THF-d_8, 500 MHz, 298 K) of reaction mixture between **3(thf)$_2$** and 18-crown-6.

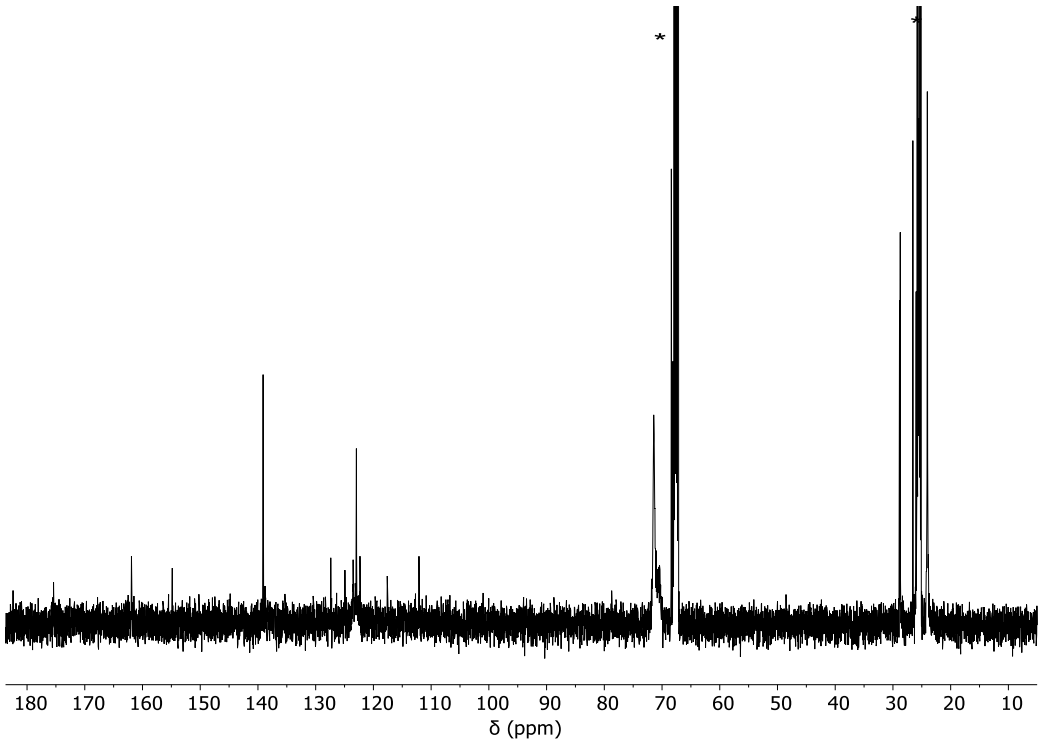

Figure A.13 $^{13}C\{^{1}H\}$ NMR spectrum (*THF-d_8, 125 MHz, 298 K) of reaction mixture between **3(thf)$_2$** and 18-crown-6.

Chapter 3

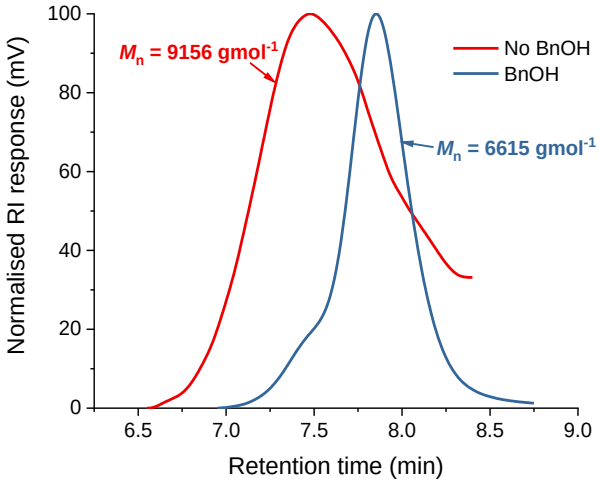

Figure A.14 GPC traces of PLA synthesised from the ROP of *L*-LA using **2** with and without BnOH. Red: No BnOH, M_n = 9156 gmol^{-1}, M_w/M_n = 1.55; blue: BnOH, M_n = 6615 gmol^{-1}, M_w/M_n = 1.14. Conditions: [*L*-LA]$_0$:[**Mg**]$_0$(:[BnOH]$_0$) = 50:1(:1), [*L*-LA]$_0$ = 0.5 M in 0.6 mL benzene-d_6 at 80 °C.

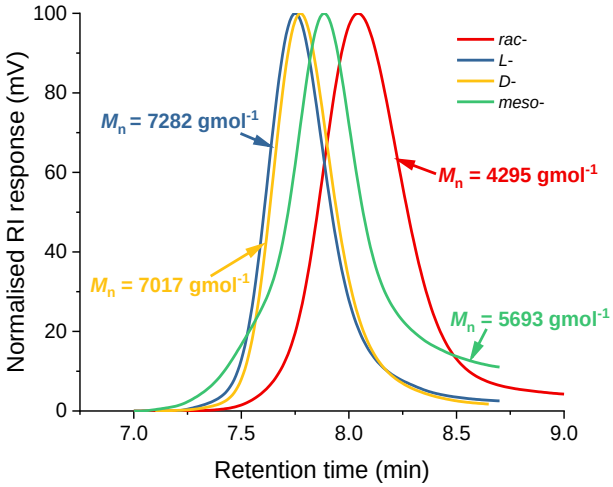

Figure A.15 GPC traces of PLA synthesised from the ROP of LA using **2**/BnOH. Red: *rac*-LA, M_n = 4295 gmol^{-1}, M_w/M_n = 1.15; blue: *L*-LA, M_n = 7282 gmol^{-1}, M_w/M_n = 1.09; yellow: *D*-LA, M_n = 7017 gmol^{-1}, M_w/M_n = 1.09; green: *meso*-LA, M_n = 5693 gmol^{-1}, M_w/M_n = 1.20. Conditions: [LA]$_0$:[**Mg**]$_0$:[BnOH] = 50:1:1, [LA]$_0$ = 0.5 M in 0.6 mL benzene-d_6 at 60 °C.

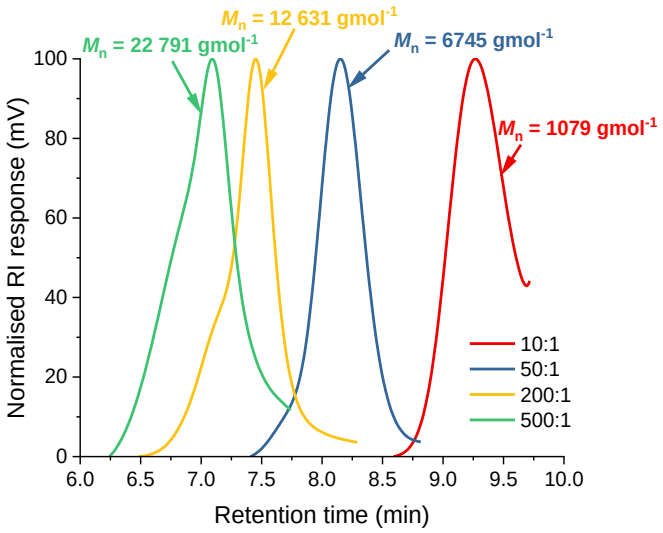

Figure A.16 GPC traces of PLAs synthesised from the ROP of *L*-LA using **2**/BnOH. Red: 10:1, M_n = 1079 gmol^{-1}, M_w/M_n = 1.29; blue: 50:1, M_n = 6615 gmol^{-1}, M_w/M_n = 1.14; yellow: 200:1, M_n = 12 631 gmol^{-1}, M_w/M_n = 1.32; green: 500:1, M_n = 22 791 gmol^{-1}, M_w/M_n = 1.29. Conditions: [*L*-LA]$_0$:[**Mg**]$_0$ as stated, [*L*-LA]$_0$ = 0.5 M in 0.6 mL benzene-d_6 at 80 °C.

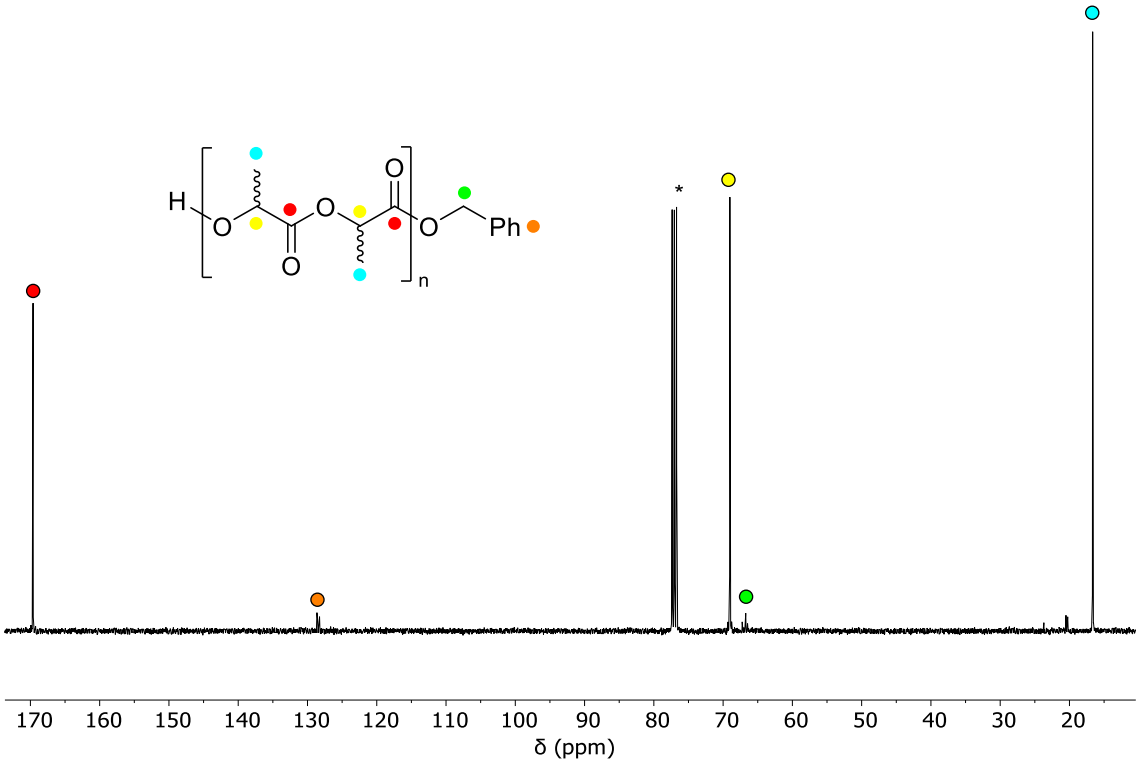

Figure A.17 ^{13}C{^{1}H} NMR spectrum (*chloroform-d_1, 101 MHz, 298 K) of PLA produced using **2**/BnOH. Conditions: [*L*-LA]$_0$:[**Mg**]$_0$:[BnOH]$_0$ = 50:1:1, [*L*-LA]$_0$ = 0.5 M, 0.6 mL benzene-d_6, 60 °C. M_w/M_n = 1.09.

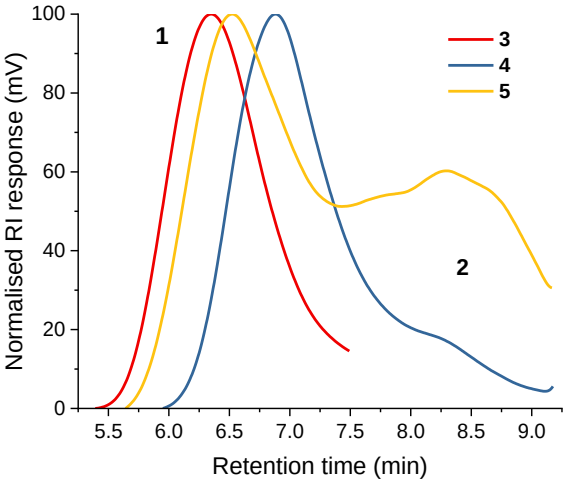

Figure A.18 GPC traces of PLAs synthesised from the ROP of *L*-LA. Red: cat = **3**, M_n = 55 276 gmol^{-1}, M_w/M_n = 1.59; blue: cat = **4**, M_n = 34 403 gmol^{-1}, M_w/M_n = 1.69; yellow: cat = **5**, M_n = 40 556 gmol^{-1}, M_w/M_n = 1.55. Conditions: [*L*-LA]$_0$:[**M**]$_0$ = 500:1, [*L*-LA]$_0$ = 0.5 M in 0.6 mL benzene-d_6 at 40 °C. Analysis reported is of major peak **1**.

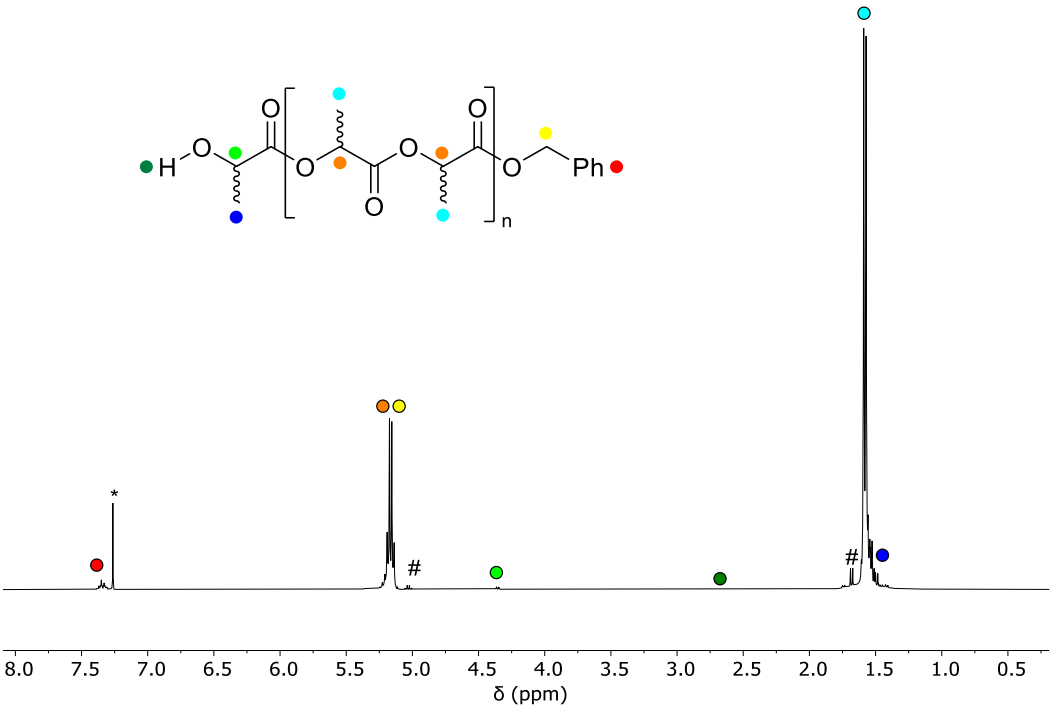

Figure A.19 ^{1}H NMR spectrum (*chloroform-d_1, 400 MHz, 298 K) of PLA produced using the **4**/BnOH system. Polymerisation conditions: [*L*-LA]$_0$:[**Sr**]$_0$:[BnOH]$_0$ = 500:1:1, [*L*-LA]$_0$ = 0.5 M, 0.6 mL benzene-d_6, 70 °C. M_w/M_n = 1.69.

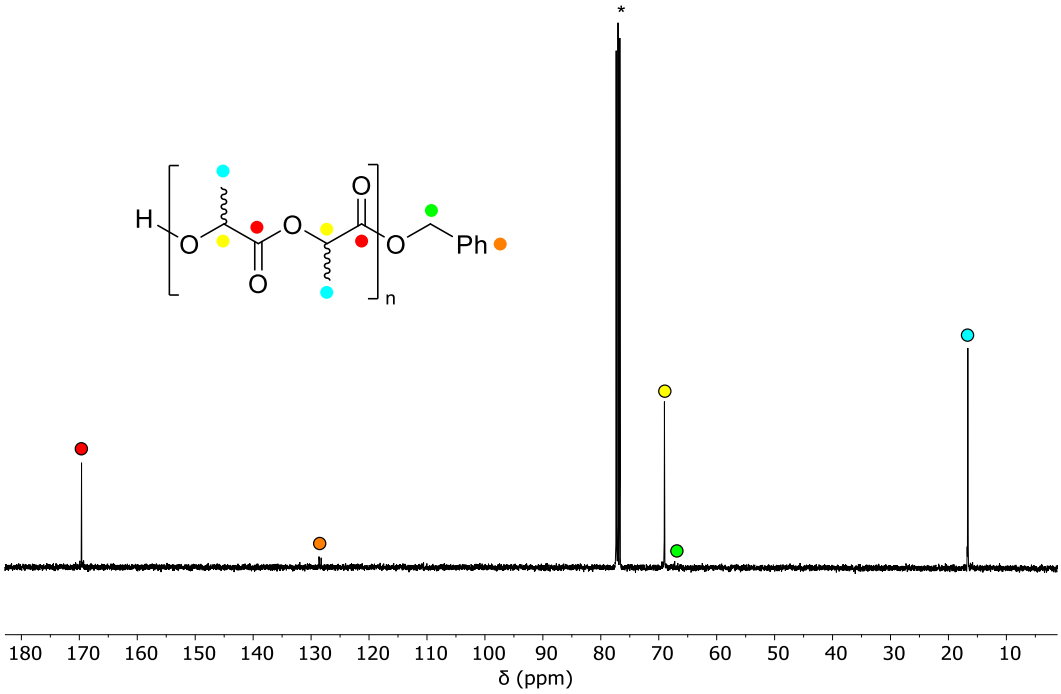

Figure A.20 $^{13}C\{^{1}H\}$ NMR spectrum (*chloroform-d_1, 101 MHz, 298 K) of PLA produced using the **4**/BnOH system. Conditions: [*L*-LA]$_0$:[**Sr**]$_0$:[BnOH]$_0$ = 500:1:1, [*L*-LA]$_0$ = 0.5 M, 0.6 mL benzene-d_6, 70 °C. M_w/M_n = 1.69.

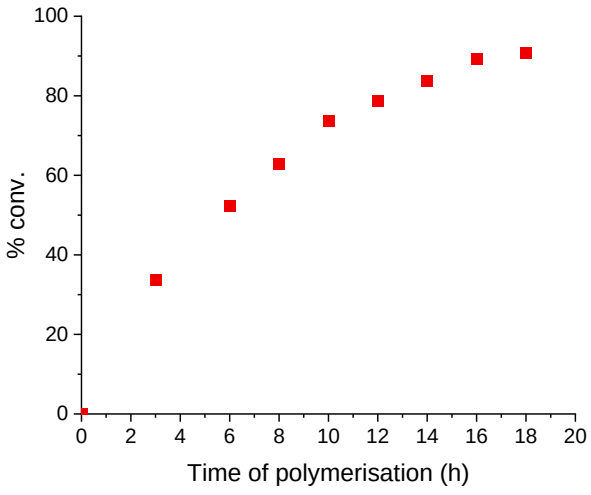

Figure A.21 Plot of percentage conversion to PLA as a function of time; reaction catalysed by the **3**/BnOH system. Conditions: [*L*-LA]$_0$:[**Ca**]$_0$:[BnOH]$_0$ = 500:1:1, [*L*-LA]$_0$ = 0.5 M in 0.6 mL benzene-d_6 at 40 °C.

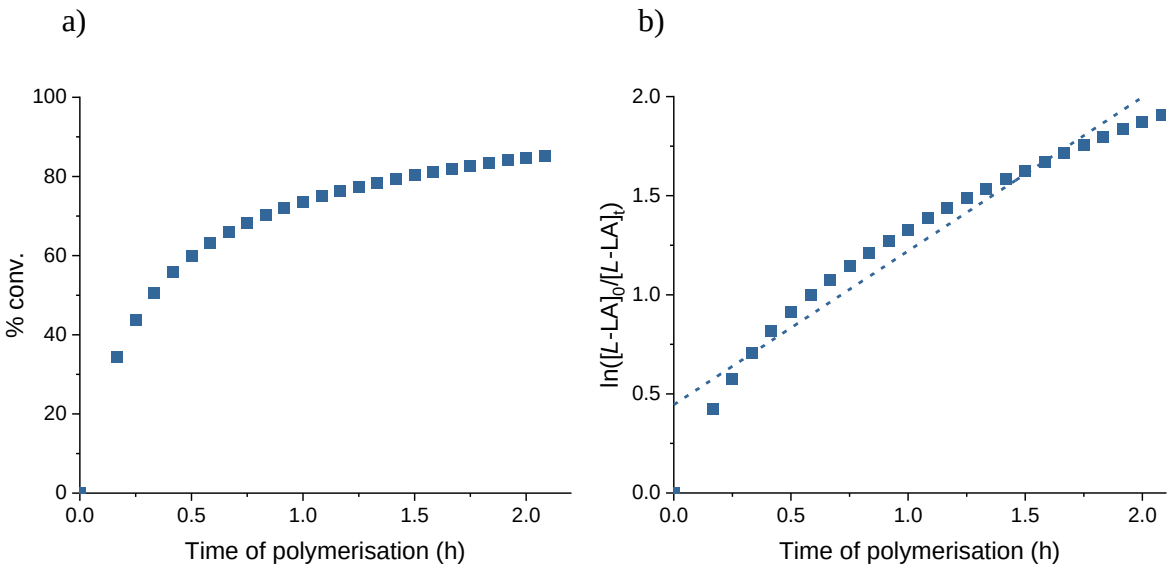

Figure A.22 a) Plot of percentage conversion to PLA as a function of time. b) Non-linear plot of $\ln([L\text{-LA}]_0/[L\text{-LA}]_t)$ *vs.* time for *L*-LA polymerisation using **4**/BnOH. Conditions: $[L\text{-LA}]_0$:$[\mathbf{Sr}]_0$:$[\text{BnOH}]_0$ = 500:1:1, $[L\text{-LA}]_0$ = 0.5 M in 0.6 mL benzene-d_6 at 40 °C.

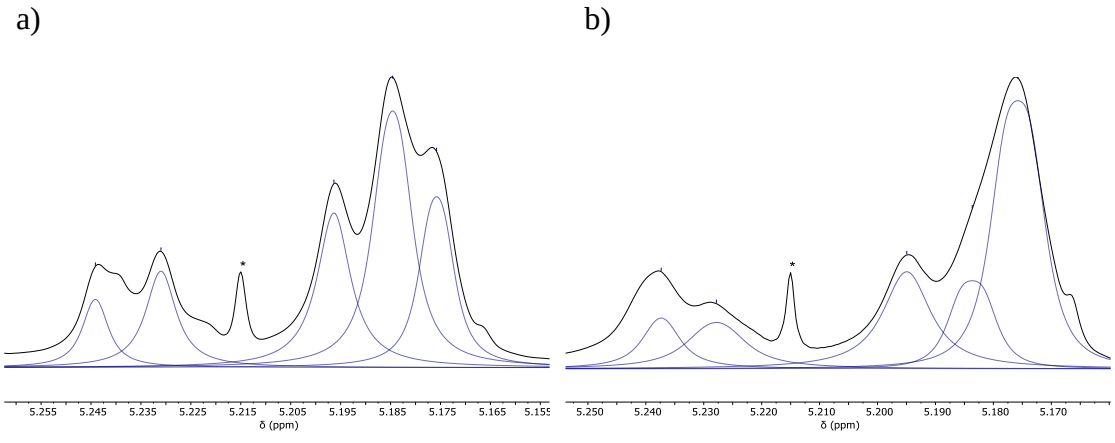

Figure A.23 ^{1}H{^{1}H} NMR spectra (chloroform-d_1, 500 MHz, 298 K) of the methine protons in the PLA produced from the **4** system and a) *rac*-lactide (P_m = 0.52) and b) *meso*-lactide (P_r = 0.74). Conditions: $[\text{LA}]_0$:$[\mathbf{Sr}]_0$ = 500:1, $[\text{LA}]_0$ = 0.5 M in 0.6 mL benzene-d_6 at 70 °C. * denotes an artefact from NMR "BASH" experiment set-up.

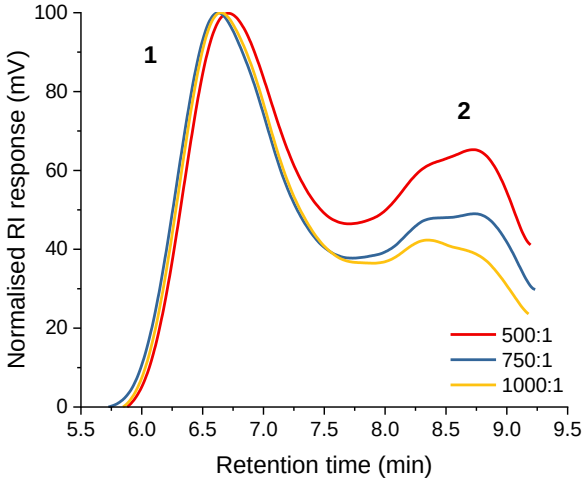

Figure A.24 Bimodal GPC traces of PLAs synthesised from the ROP of *L*-LA using **4**. Red: 500:1, M_n = 31 845 (**1**), 1945 (**2**) gmol^{-1}, M_w/M_n = 1.52 (**1**), 1.70 (**2**); blue: 750:1, M_n = 32 806 (**1**), 1902 (**2**) gmol^{-1}, M_w/M_n = 1.60 (**1**), 1.65 (**2**); yellow: 1000:1, M_n = 32 782 (**1**), 1828 (**2**) gmol^{-1}, M_w/M_n = 1.73 (**1**), 1.53 (**2**). Conditions: [*L*-LA]$_0$:[**Sr**]$_0$ as stated, [*L*-LA]$_0$ = 0.5 M in 0.6 mL benzene-d_6 at 70 °C.

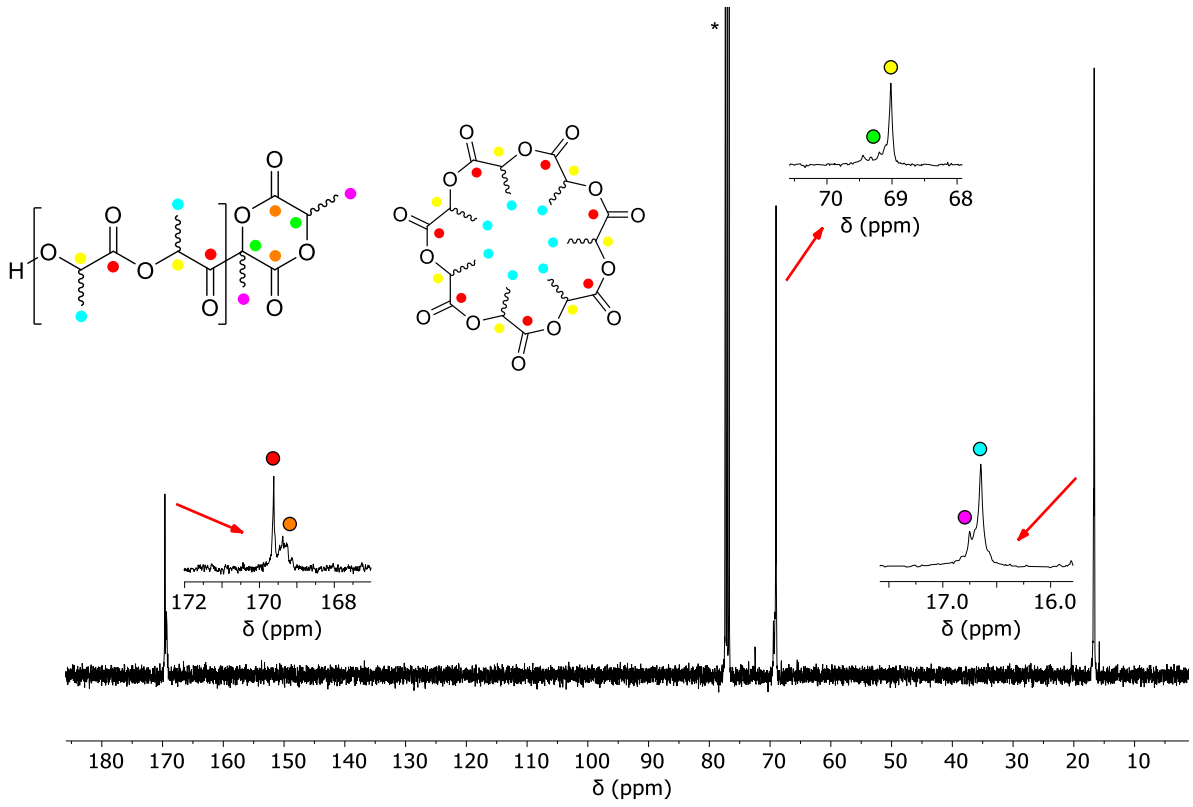

Figure A.25 $^{13}C\{^1H\}$ NMR spectrum (*choroform-d_1, 101 MHz, 298 K) of PLA isolated from a polymerisation catalysed by complex **4**. Conditions: [*L*-LA]$_0$:[**Sr**]$_0$ = 500:1:1, [*L*-LA]$_0$ = 0.5 M, 0.6 mL benzene-d_6, 40 ºC. M_w/M_n = 1.52, 1.39.

Chapter 4

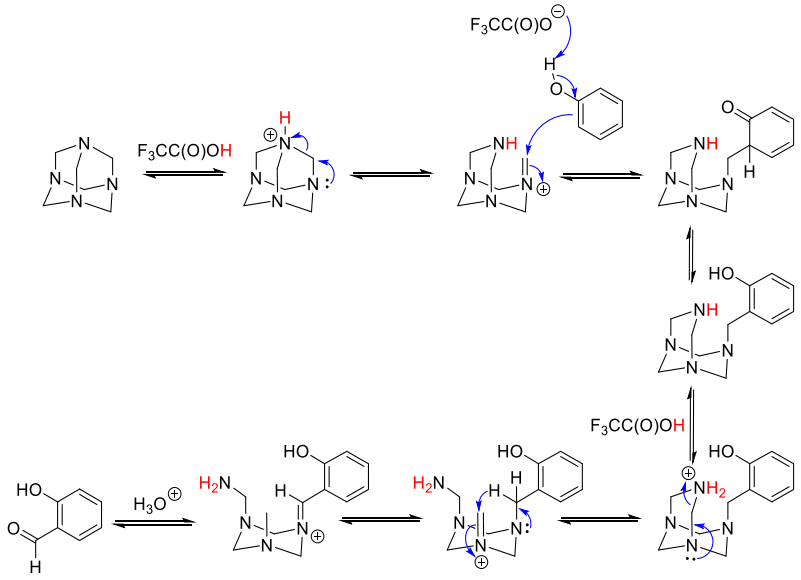

Scheme A.1 Mechanism of the "Duff" reaction by which *para*–substituted phenols are formylated using hexamethylenetetramine and trifluoroacetic acid ($CF_3C(O)OH$).[1]

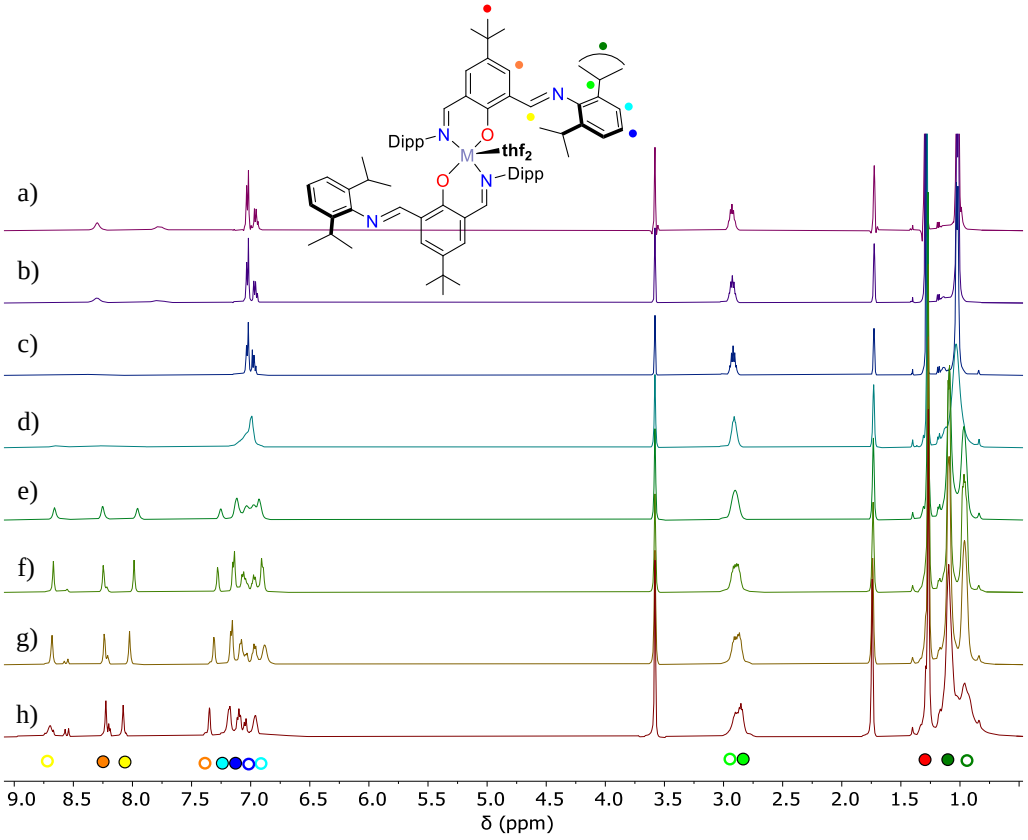

Figure A.26 ^{1}H NMR spectra (*THF-d_8, 500 MHz) of ($^{t\text{Bu,Dipp}}$L)$_2$Ba(thf)$_2$ (**12**) at a) 323 K, b) 313 K, c) 298 K, d) 273 K, e) 253 K, f) 233 K, g) 213 K and h) 193 K.

Chapter 5

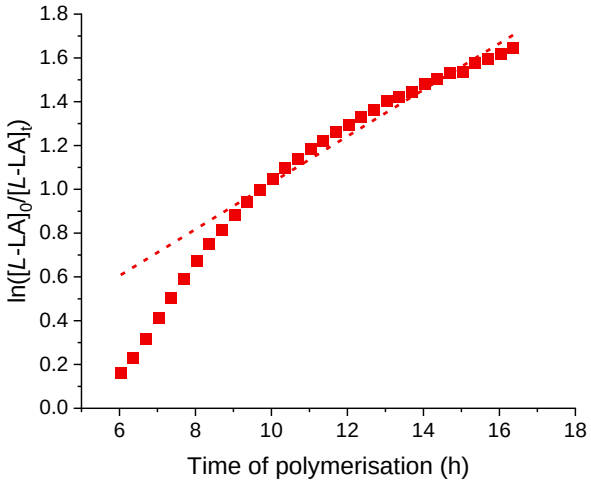

Figure A.27 Non-linear plot of ln([*L*-LA]$_0$/[*L*-LA]$_t$) *vs.* time for *L*-LA polymerisation using **10**. Conditions: [*L*-LA]$_0$:[**Mg**]$_0$ = 50:1, [*L*-LA]$_0$ = 0.5 M in 0.6 mL chloroform-d_1 at 60 °C.

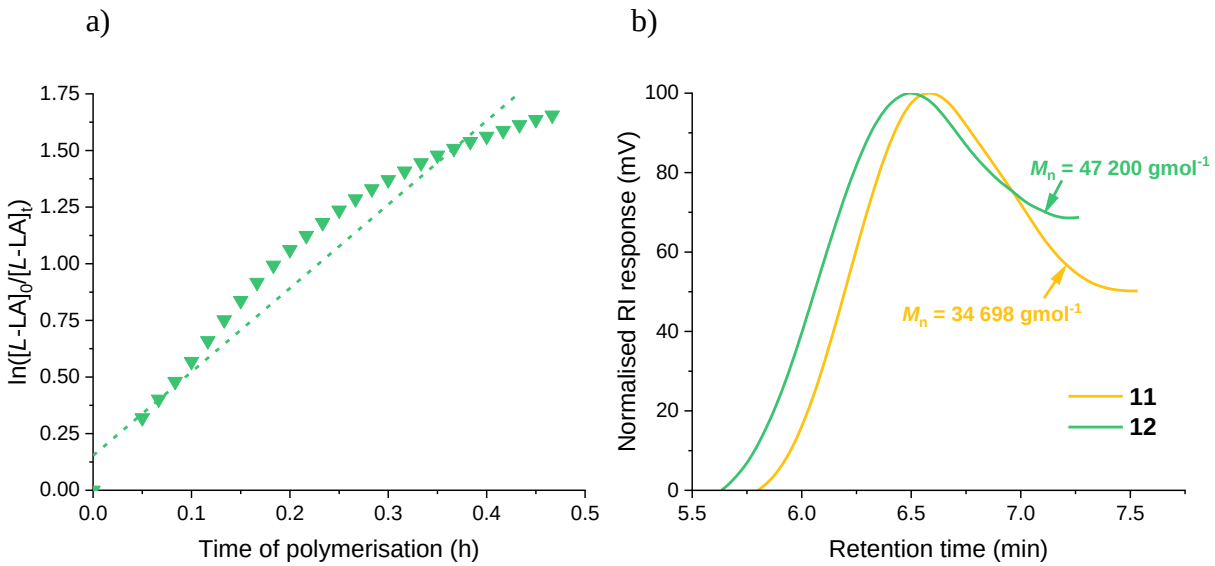

Figure A.28 a) Non-linear plot of ln([*L*-LA]$_0$/[*L*-LA]$_t$) *vs.* time for *L*-LA polymerisation using **12**. b) GPC traces of PLAs synthesised from the ROP of *L*-LA using **11** and **12**. Yellow: cat = **11**, M_n = 34 698 gmol^{-1}, M_w/M_n = 1.56; green: cat = **12**, M_n = 47 200 gmol^{-1}, M_w/M_n = 1.51. Conditions: [*L*-LA]$_0$:[**M**]$_0$ = 500:1, [*L*-LA]$_0$ = 0.5 M in 0.6 mL benzene-d_6 at 60 °C.

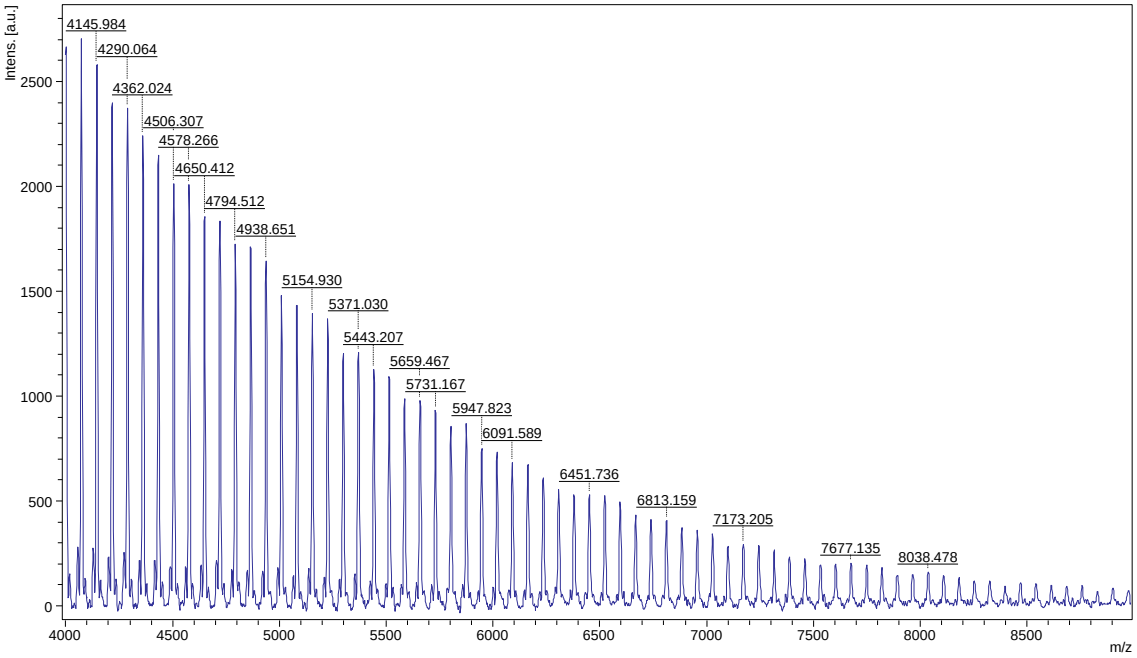

Figure A.29 MALDI-TOF mass (*m/z*) spectrum of PLA produced using **11**. Conditions: [*L*-LA]$_0$:[**Sr**]$_0$ = 50:1, [*L*-LA]$_0$ = 0.5 M, 0.6 mL benzene-d_6, 60 ºC. M_w/M_n = 1.56. E.g. the peak centred at 5371.0 gmol^{-1} is attributed to cyclic PLA, comprising of 37 units of LA with K^+ [144.13(37) + 39.1].

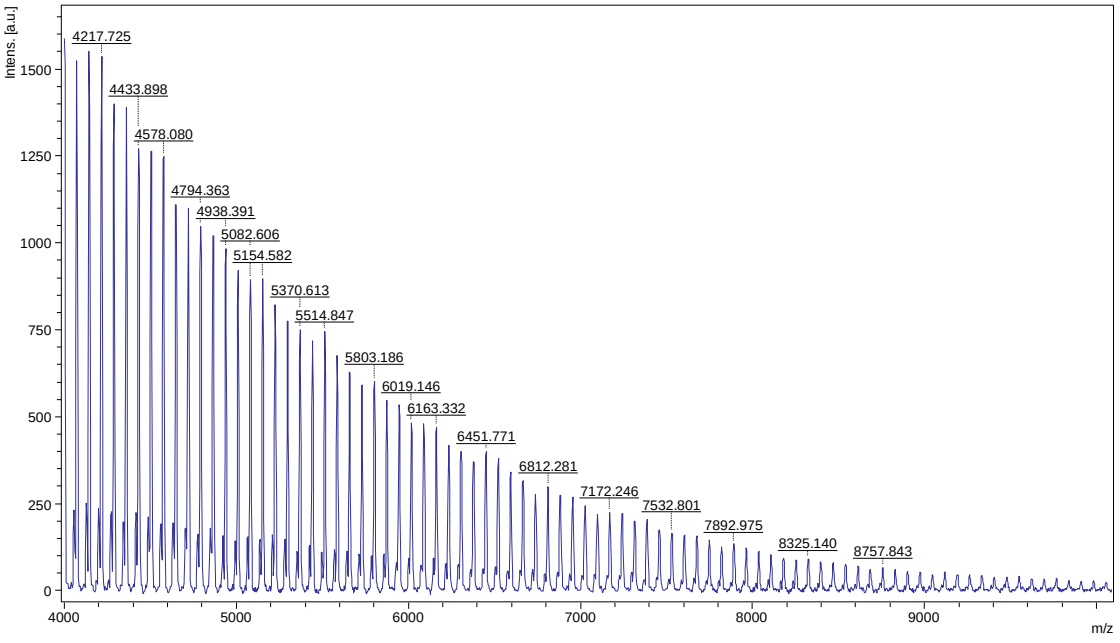

Figure A.30 MALDI-TOF mass (*m/z*) spectrum of PLA produced using **12**. Conditions: [*L*-LA]$_0$:[**Ba**]$_0$ = 50:1, [*L*-LA]$_0$ = 0.5 M, 0.6 mL benzene-d_6, 60 ºC. M_w/M_n = 1.51. E.g. the peak centred at 5514.8 gmol^{-1} is attributed to cyclic PLA, comprising of 38 units of LA with K^+ [144.13(38) + 39.1].

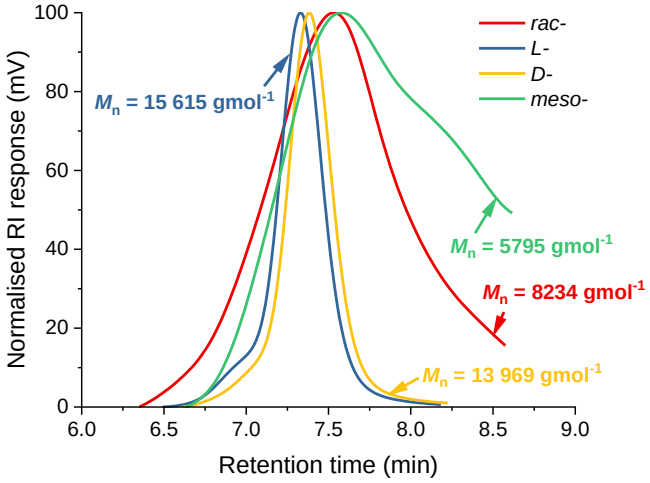

Figure A.31 GPC traces of PLAs synthesised from the ROP of LA using **10**/BnOH. Red: *rac*-LA, M_n = 8234 gmol^{-1}, M_w/M_n = 1.75; blue: *L*-LA, M_n = 15 615 gmol^{-1}, M_w/M_n = 1.13; yellow: *D*-LA, M_n = 13 969 gmol^{-1}, M_w/M_n = 1.12; green: *meso*-LA, M_n = 5795 gmol^{-1}, M_w/M_n = 1.72. Conditions: $[LA]_0$:[**Mg**]$_0$:$[BnOH]_0$ = 500:1:1, $[LA]_0$ = 0.5 M in 0.6 mL chloroform-d_1 at 40 °C.

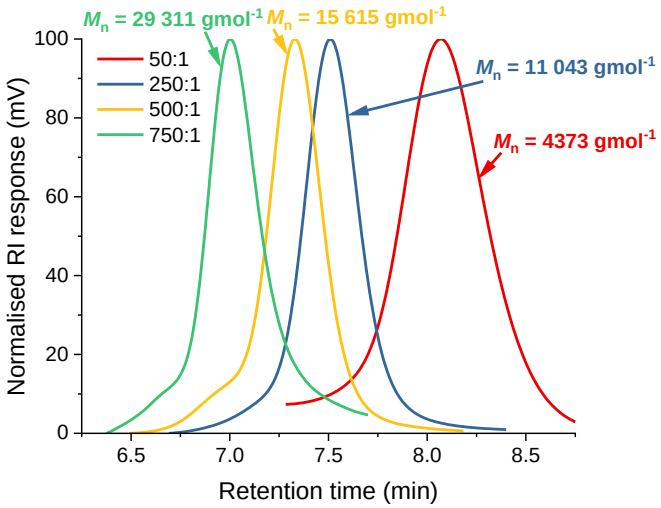

Figure A.32 GPC traces of PLAs synthesised from the ROP of *L*-LA using **10**/BnOH. Red: 50:1, M_n = 4373 gmol^{-1}, M_w/M_n = 1.51; blue: 250:1, M_n = 11 043 gmol^{-1}, M_w/M_n = 1.14; yellow: 500:1, M_n = 15 615 gmol^{-1}, M_w/M_n = 1.13; green: 750:1, M_n = 29 311 gmol^{-1}, M_w/M_n = 1.13. Conditions: $[L\text{-LA}]_0$:[**Mg**]$_0$ as stated, $[L\text{-LA}]_0$ = 0.5 M in 0.6 mL chloroform-d_1 at 40 °C.

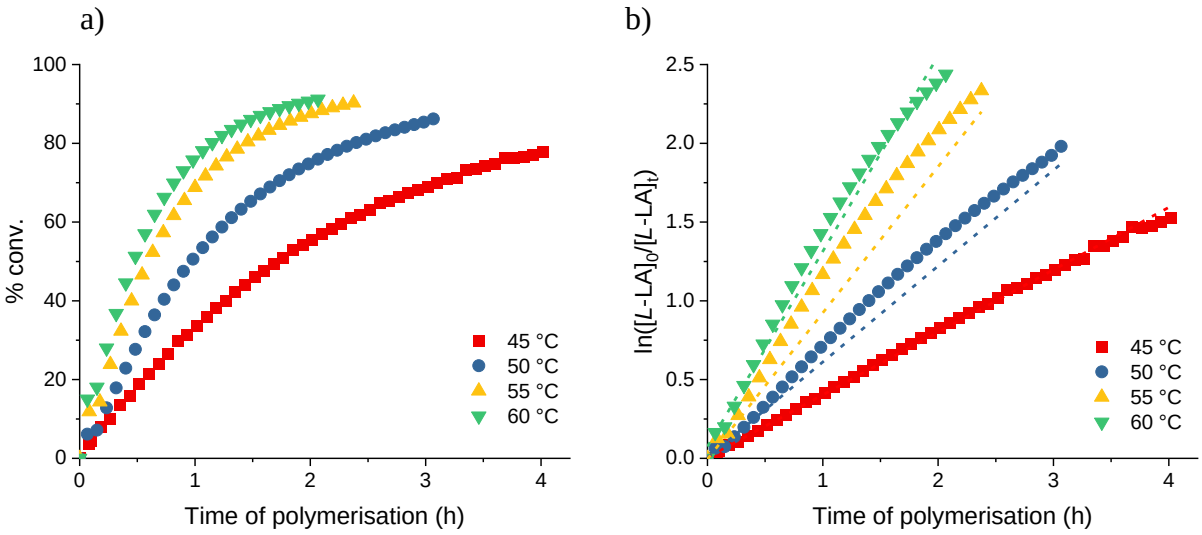

Figure A.33 a) Plot of percentage conversion *vs.* time. b) Plot of $\ln([L\text{-LA}]_0/[L\text{-LA}]_t)$ *vs.* time for *L*-LA polymerisation using **13**/BnOH. Red squares: 45 °C (k_{obs} = 0.40 h^{-1}. R^2 = 0.999); blue circles: 50 °C (k_{obs} = 0.61 h^{-1}. R^2 = 0.912); yellow up triangles: 55 °C (k_{obs} = 0.93 h^{-1}. R^2 = 0.887); green down triangles: 60 °C (k_{obs} = 1.24 h^{-1}. R^2 = 0.993). Conditions: $[L\text{-LA}]_0$:$[\mathbf{Ca}]_0$:$[\text{BnOH}]_0$ = 50:1:1, $[L\text{-LA}]_0$ = 0.5 M in 0.6 mL chloroform-d_1 at stated temperature.

Table A.1 ROP of *L*-LA using **13**/BnOH with $[L\text{-LA}]_0$:$[\mathbf{Ca}]_0$:$[\text{BnOH}]_0$ = 50:1:1 in chloroform-d_1 at stated temperature.[a]

Temp. (°C)	Time (h)	Conv. (%)[b]	k_{obs} (h^{-1})[c]	R^{2c}	M_n (GPC)[d]	M_n (calcd)[e]	M_w/M_n
45	4.0	78	0.40 ± 0.002	0.999	3887	5348	1.44
50	3.1	86	0.61 ± 0.03	0.912	3771	6305	1.51
55	2.4	90	0.93 ± 0.07	0.887	4054	6698	1.67
60	2.1	91	1.24 ± 0.02	0.993	4150	6861	1.79

[a]Conditions: $[L\text{-LA}]_0$:$[\mathbf{Ca}]_0$:$[\text{BnOH}]_0$ = 50:1:1, $[L\text{-LA}]_0$ = 0.5 M in 0.6 mL chloroform-d_1 at stated temperature. [b]Average reported; measured by ^{1}H NMR spectroscopic analyses. [c]First order rate constant (k_{obs}) and R^2 were obtained from average plots of $\ln([L\text{-LA}]_0/[L\text{-LA}]_t)$ *vs.* time. [d]Determined by GPC in THF against PS standards using the appropriate Mark-Houwink corrections.[2] [e]Calculated M_n for PLA synthesised = (conv.(%) × $[L\text{-LA}]_0/[\mathbf{Ca}]_0$) × 144.13 + ($M_w$ of end groups).

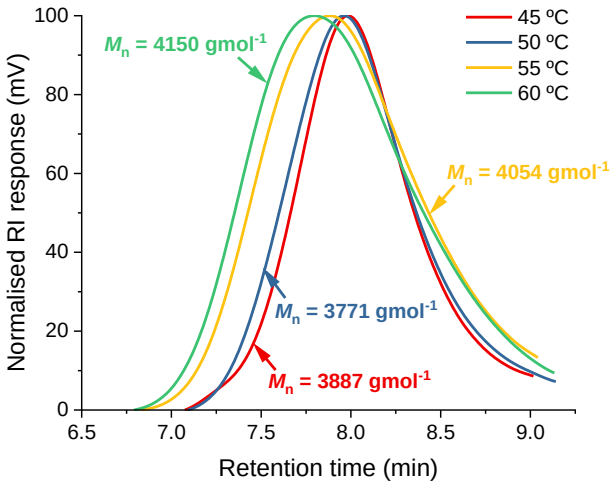

Figure A.34 GPC traces of PLAs synthesised from the ROP of *L*-LA using **13**/BnOH. Red: 45 ºC, M_n = 3887 gmol^{-1}, M_w/M_n = 1.44; blue: 50 ºC, M_n = 3771 gmol^{-1}, M_w/M_n = 1.51; yellow: 55 ºC, M_n = 4054 gmol^{-1}, M_w/M_n = 1.67; green: 60 ºC, M_n = 4150 gmol^{-1}, M_w/M_n = 1.79. Conditions: [*L*-LA]$_0$:[**Ca**]$_0$:[BnOH]$_0$ = 50:1:1, [*L*-LA]$_0$ = 0.5 M in 0.6 mL chloroform-d_1 at stated temperature.

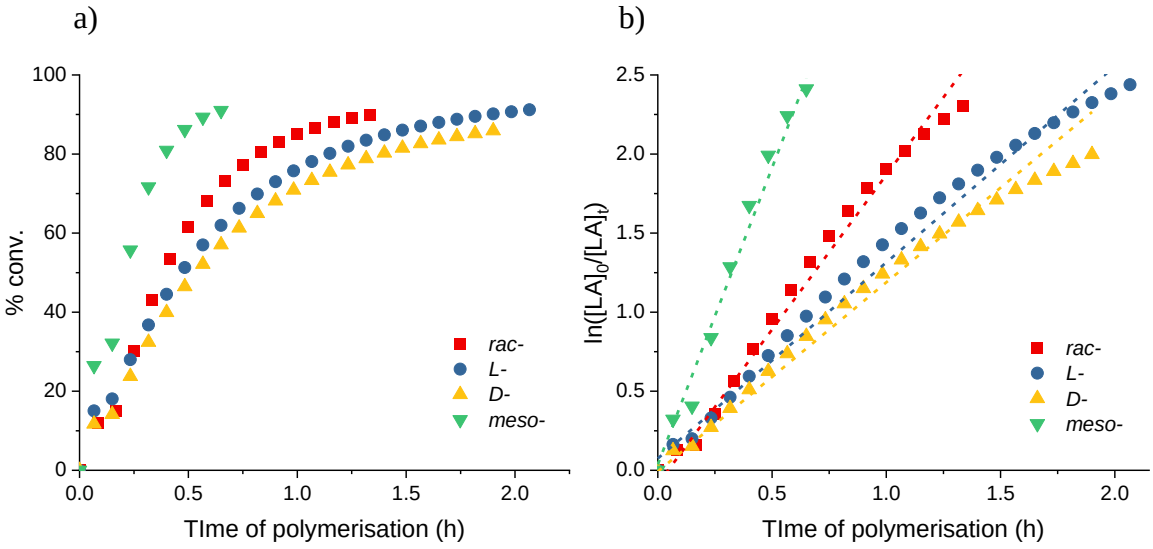

Figure A.35 a) Plot of percentage conversion *vs*. time. b) Plot of ln([LA]$_0$/[LA]$_t$) *vs*. time for LA polymerisation using **13**/BnOH. Red squares: *rac*-LA (k_{obs} = 1.96 h^{-1}. R^2 = 0.988); blue circles: *L*-LA (k_{obs} = 1.24 h^{-1}. R^2 = 0.993); yellow up triangles: *D*-LA (k_{obs} = 1.20 h^{-1}. R^2 = 0.971); green down triangles: *meso*-LA (k_{obs} = 3.75 h^{-1}. R^2 = 0.984). Conditions: [LA]$_0$:[**Ca**]$_0$:[BnOH]$_0$= 50:1:1, [LA]$_0$ = 0.5 M in 0.6 mL chloroform-d_1 at 60 ºC.

Table A.2 ROP of *L*-LA using **13**/BnOH with $[LA]_0$:$[\mathbf{Ca}]_0$:$[BnOH]_0$ = 50:1:1 in chloroform-d_1 at 60 °C.[a]

LA	Time (h)	Conv. (%)[b]	k_{obs} (h^{-1})[c]	R^{2c}	M_n (GPC)[d]	M_n (calcd)[e]	M_w/M_n
rac-	1.3	90	1.96 ± 0.06	0.988	1995	6836	1.66
L-	2.1	91	1.24 ± 0.02	0.993	4150	6861	1.79
D-	1.9	86	1.20 ± 0.05	0.971	3453	6203	1.72
meso-	0.7	91	3.75 ± 0.2	0.984	2134	6843	1.79

[a]Conditions: $[LA]_0$:$[\mathbf{Ca}]_0$:$[BnOH]_0$ = 50:1:1, $[LA]_0$ = 0.5 M in 0.6 mL chloroform-d_1 at 60 °C. [b]Average reported; measured by ^{1}H NMR spectroscopic analyses. [c]First order rate constant (k_{obs}) and R^2 were obtained from average plots of $\ln([LA]_0/[LA]_t)$ *vs.* time. [d]Determined by GPC in THF against PS standards using the appropriate Mark-Houwink corrections.[2] [e]Calculated M_n for PLA synthesised = (conv.(%) × $[LA]_0/[\mathbf{Ca}]_0$) × 144.13 + (M_w of end groups).

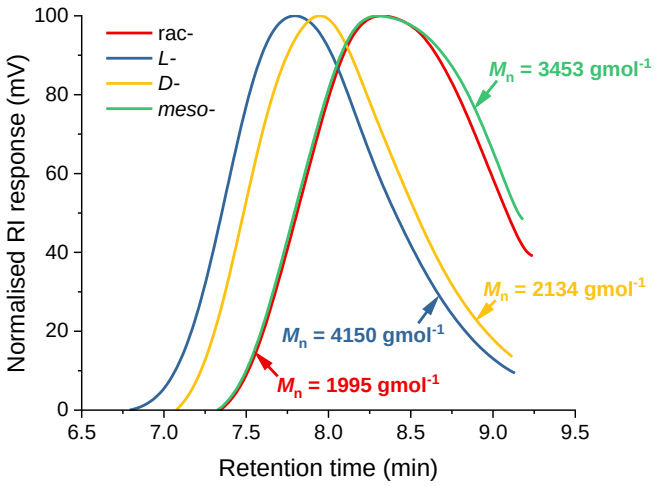

Figure A.36 GPC traces of PLAs synthesised from the ROP of LA using **13**/BnOH. Red: *rac*-LA, M_n = 1995 $gmol^{-1}$, M_w/M_n = 1.66; blue: *L*-LA, M_n = 4150 $gmol^{-1}$, M_w/M_n = 1.79; yellow: *D*-LA, M_n = 3453 $gmol^{-1}$, M_w/M_n = 1.72; green: *meso*-LA, M_n = 2134 $gmol^{-1}$, M_w/M_n = 1.79. Conditions: $[LA]_0$:$[\mathbf{Ca}]_0$:$[BnOH]_0$ = 50:1:1, $[LA]_0$ = 0.5 M in 0.6 mL chloroform-d_1 at 60 °C.

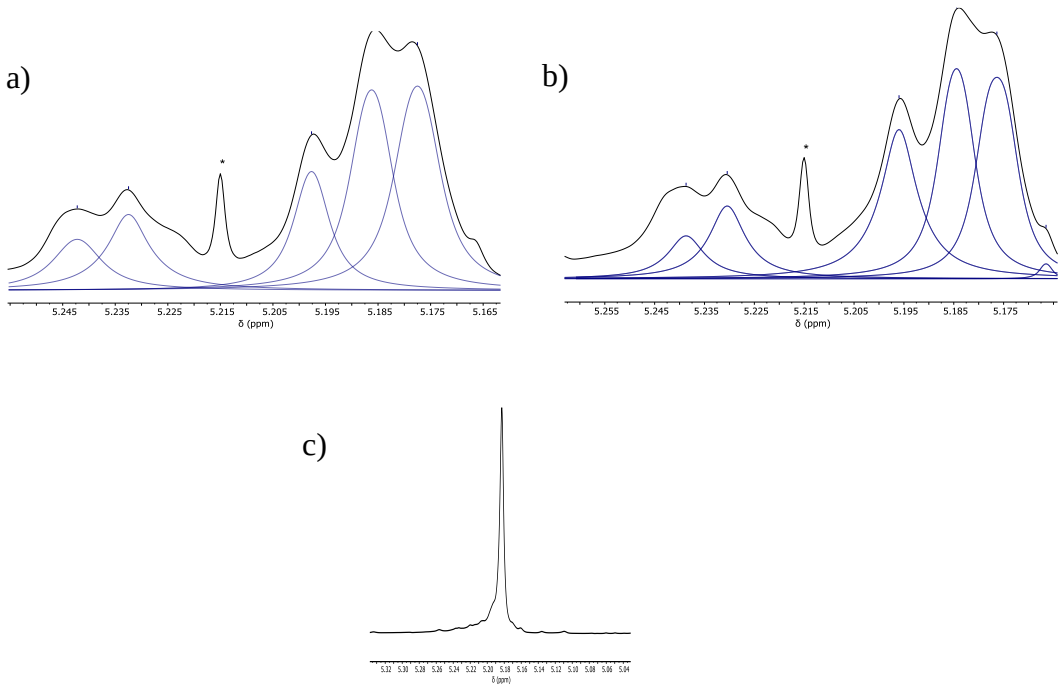

Figure A.37 $^{1}H\{^{1}H\}$ NMR spectra (chloroform-d_1, 500 MHz, 298 K) of the methine protons in the PLA produced from the **13**/BnOH system and a) *rac*-lactide (P_m = 0.55), b) *meso*-lactide (P_r = 0.59) and c) *L*/*D*-lactide (P_m = 1.00). Conditions: $[LA]_0$:[**Ca**]$_0$:$[BnOH]_0$ = 50:1:1, $[LA]_0$ = 0.5 M in 0.6 mL chloroform-d_1 at 60 °C. * denotes an artefact from NMR "BASH" experiment set-up.

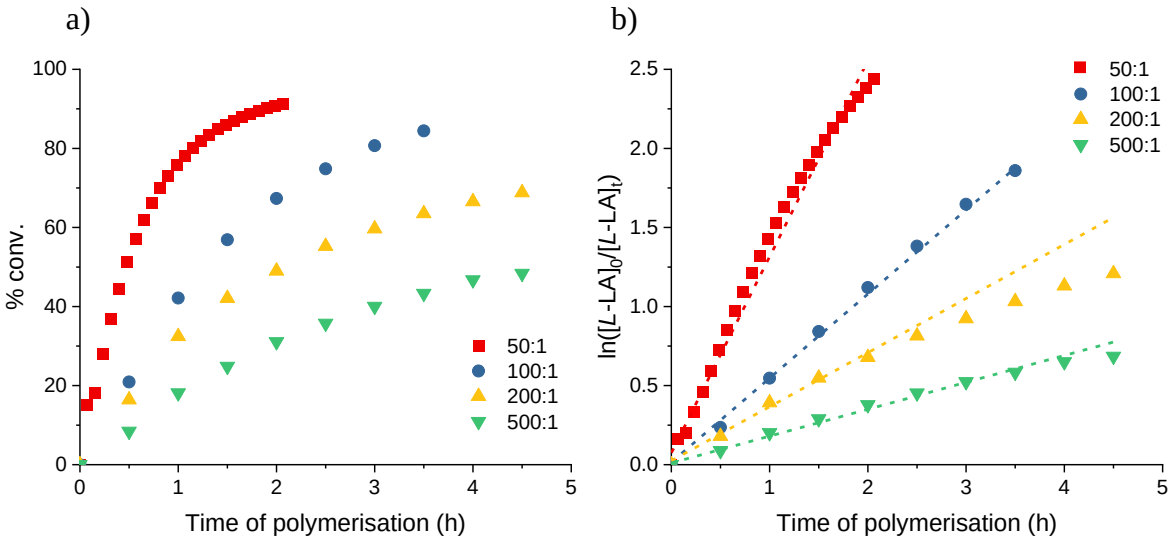

Figure A.38 a) Plot of percentage conversion *vs.* time. b) Plot of $\ln([L\text{-LA}]_0/[L\text{-LA}]_t)$ *vs.* time for *L*-LA polymerisation using **13**/BnOH. Red squares: 50:1 (k_{obs} = 1.24 h^{-1}. R^2 = 0.993); blue circles: 100:1 (k_{obs} = 0.53 h^{-1}. R^2 = 0.999); yellow up triangles: 200:1 (k_{obs} = 0.34 h^{-1}. R^2 = 0.960); green down triangles: 500:1 (k_{obs} = 0.17 h^{-1}. R^2 = 0.985). Conditions: $[L\text{-LA}]_0$:[**Ca**]$_0$ as stated, $[L\text{-LA}]_0$ = 0.5 M in 0.6 mL chloroform-d_1 at 60 °C.

Table A.3 ROP of *L*-LA using **13** with [*L*-LA]$_0$:[**Ca**]$_0$ as stated in chloroform-d_1 at 60 °C.[a]

[*L*-LA]$_0$: [**Ca**]$_0$	Time (h)	Conv. (%)[b]	k_{obs} (h^{-1})[c]	R^{2c}	M_n (GPC)[d]	M_n (calcd)[e]	M_w/M_n
50:1	2.1	91	1.24 ± 0.02	0.993	4150	6861	1.79
100:1	3.5	84	0.53 ± 0.008	0.999	13 936	12 323	1.63
200:1	4.5	69	0.34 ± 0.02	0.960	22 849	22 546	1.62
500:1	4.5	48	0.17 ± 0.008	0.985	30 538	27 017	1.37

[a]Conditions: [*L*-LA]$_0$:[**Ca**]$_0$: as stated, [*L*-LA]$_0$ = 0.5 M in 0.6 mL chloroform-d_1 at 60 °C. [b]Average reported; measured by ^{1}H NMR spectroscopic analyses. [c]First order rate constant (k_{obs}) and R^2 were obtained from average plots of ln([*L*-LA]$_0$/[*L*-LA]$_t$) *vs.* time. [d]Determined by GPC in THF against PS standards using the appropriate Mark-Houwink corrections.[2] [e]Calculated M_n for PLA synthesised = (conv.(%) × [*L*-LA]$_0$/[**Ca**]$_0$) × 144.13 + (M_w of end groups).

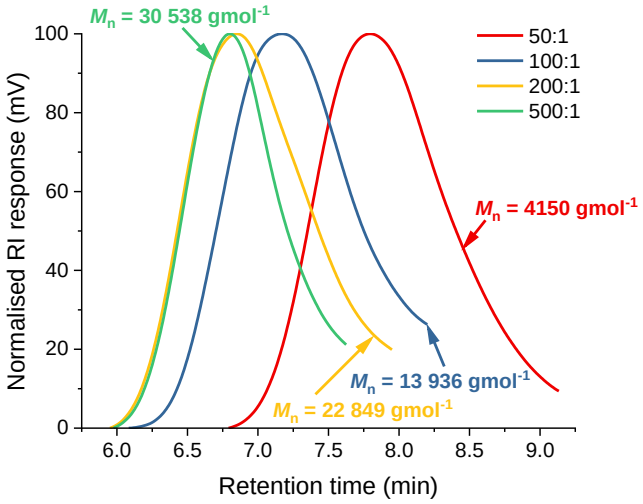

Figure A.39 GPC traces of PLAs synthesised from the ROP of *L*-LA using **13**/BnOH. Red: 50:1, M_n = 4150 $gmol^{-1}$, M_w/M_n = 1.79; blue: 100:1, M_n = 13 936 $gmol^{-1}$, M_w/M_n = 1.63; yellow: 200:1, M_n = 22 849 $gmol^{-1}$, M_w/M_n = 1.62; green: 500:1, M_n = 30 538 $gmol^{-1}$, M_w/M_n = 1.37. Conditions: [*L*-LA]$_0$:[**Ca**]$_0$ as stated, [*L*-LA]$_0$ = 0.5 M in 0.6 mL chloroform-d_1 at 60 °C.

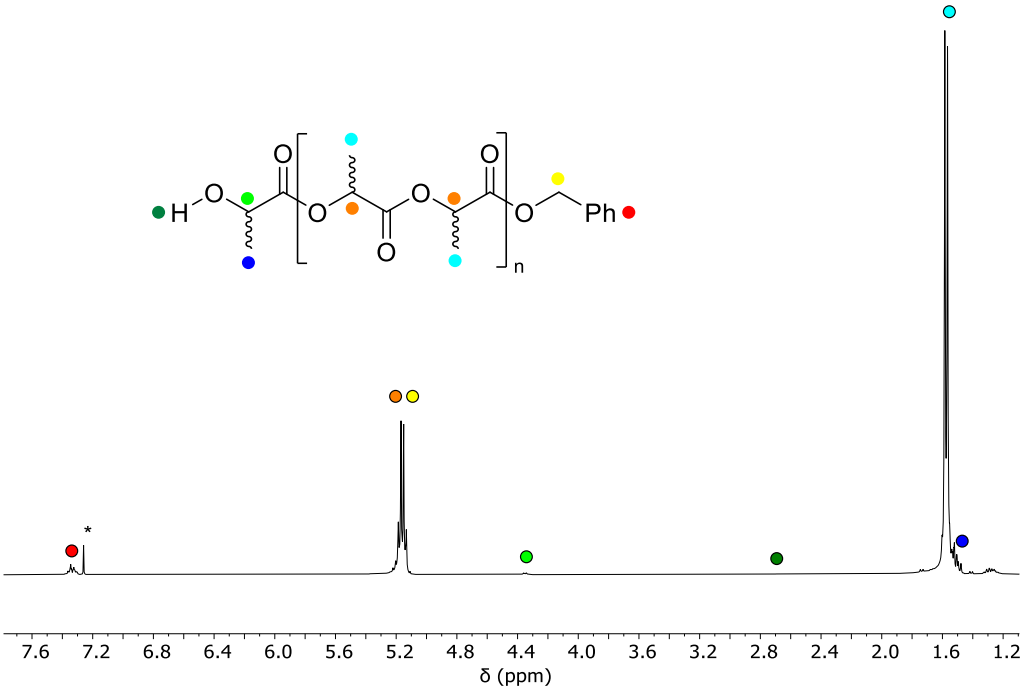

Figure A.40 ^{1}H NMR spectrum (*chloroform-d_1, 400 MHz, 298 K) of PLA produced using the **13**/BnOH system. Conditions: [*L*-LA]$_0$:[**Ca**]$_0$:[BnOH]$_0$ = 50:1:1, [*L*-LA]$_0$ = 0.5 M, 0.6 mL chloroform-d_1, 60 ºC. M_w/M_n = 1.79.

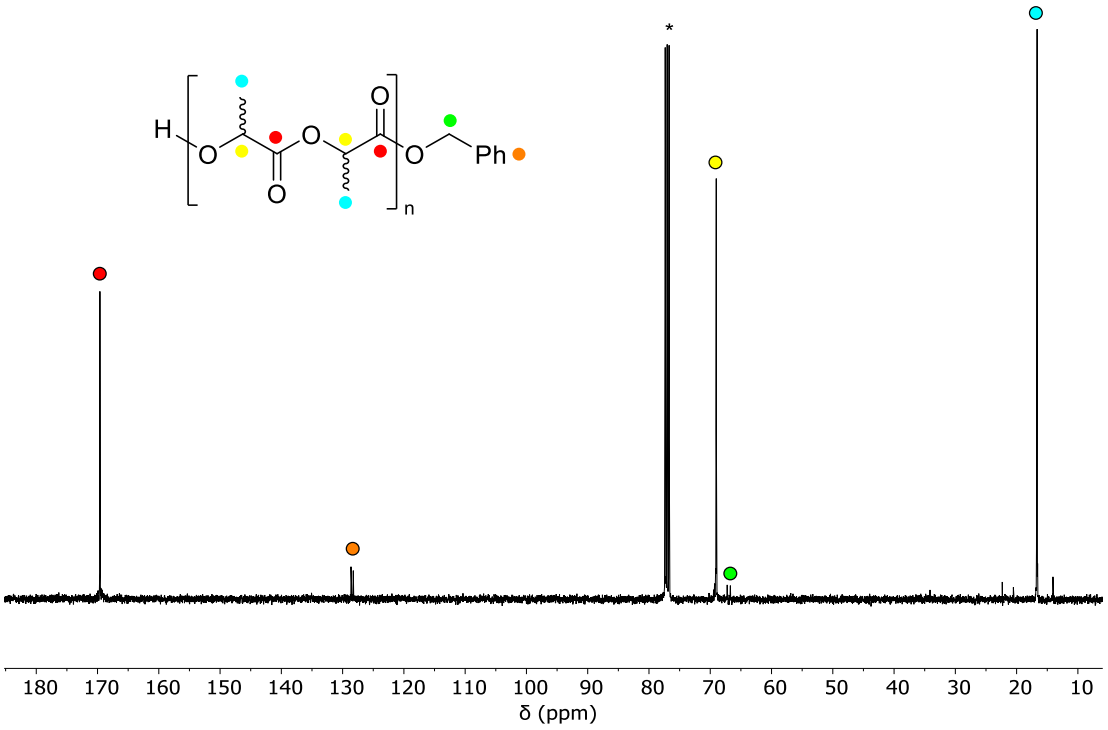

Figure A.41 ^{13}C{^{1}H} NMR spectrum (*chloroform-d_1, 101 MHz, 298 K) of PLA produced using the **13**/BnOH system. Conditions: [*L*-LA]$_0$:[**Ca**]$_0$:[BnOH]$_0$ = 50:1:1, [*L*-LA]$_0$ = 0.5 M, 0.6 mL chloroform-d_1, 60 ºC. M_w/M_n = 1.79.

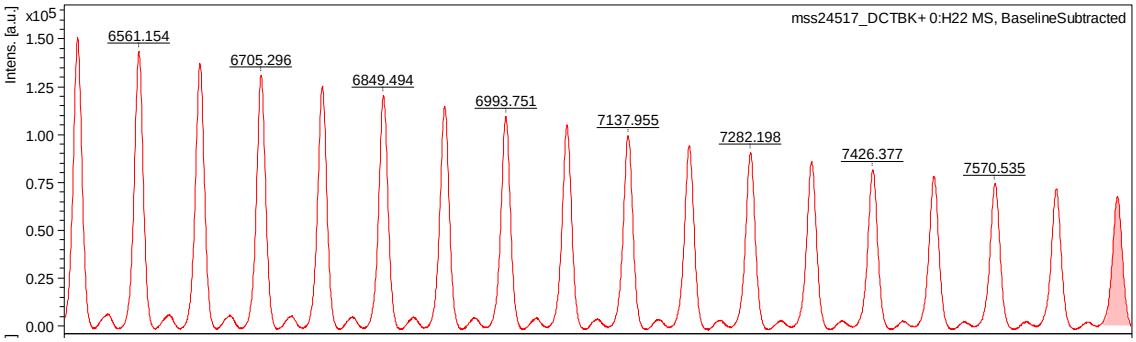

Figure A.42 MALDI-TOF mass (*m/z*) spectrum of PLA produced using **13**/BnOH. Conditions: [*L*-LA]$_0$:[**Ca**]$_0$:[BnOH] = 50:1:1, [*L*-LA]$_0$ = 0.5 M, 0.6 mL chloroform-d_1, 60 ºC. M_w/M_n = 1.79. E.g. the peak centred at 6705.3 gmol^{-1} is attributed to –OCH$_2$Ph/–OH terminated PLA, comprising of 45.5 units of LA with K$^+$ [144.13(45.4) + 108.14 + 39.1].

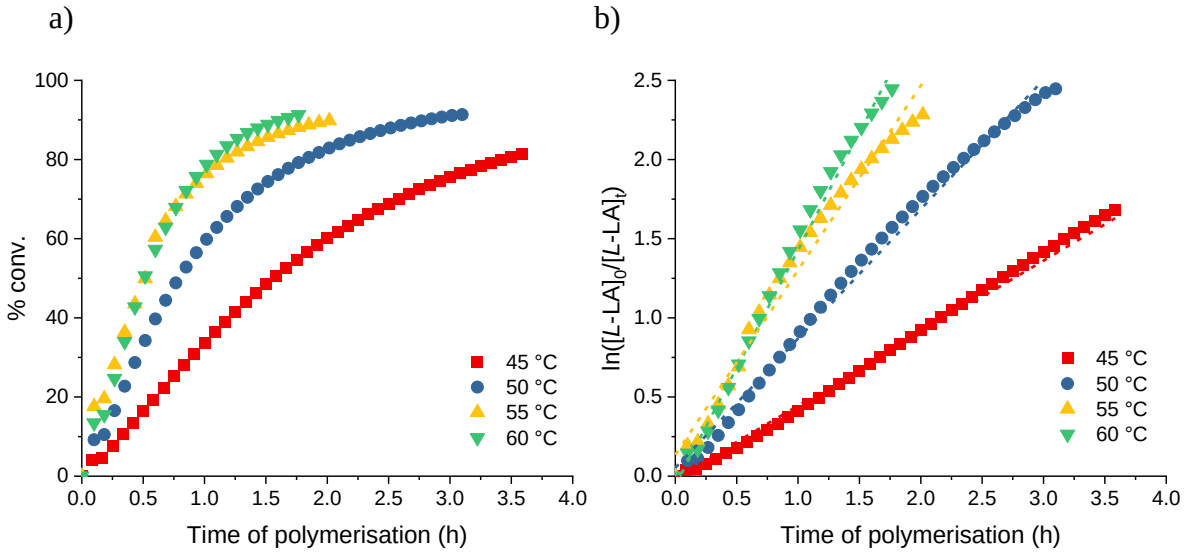

Figure A.43 a) Plot of percentage conversion *vs.* time. b) Plot of ln([*L*-LA]$_0$/[*L*-LA]$_t$) *vs.* time for *L*-LA polymerisation using **14**/BnOH. Red squares: 45 °C (k_{obs} = 0.46 h^{-1}. R^2 = 0.990); blue circles: 50 °C (k_{obs} = 0.82 h^{-1}. R^2 = 0.991); yellow up triangles: 55 °C (k_{obs} = 1.17 h^{-1}. R^2 = 0.978); green down triangles: 60 °C (k_{obs} = 1.49 h^{-1}. R^2 = 0.994). Conditions: [*L*-LA]$_0$:[**Ca**]$_0$:[BnOH]$_0$ = 50:1:1, [*L*-LA]$_0$ = 0.5 M in 0.6 mL chloroform-d_1 at stated temperature.

Table A.4 ROP of *L*-LA using **14**/BnOH with [*L*-LA]$_0$:[**Ca**]$_0$:[BnOH]$_0$ = 50:1:1 in chloroform-d_1 at stated temperature.[a]

Temp. (°C)	Time (h)	Conv. (%)[b]	k_{obs} (h^{-1})[c]	R^{2c}	M_n (GPC)[d]	M_n (calcd)[e]	M_w/M_n
45	3.6	81	0.46 ± 0.007	0.990	5418	6123	1.48
50	3.1	91	0.82 ± 0.01	0.991	4293	6683	1.59
55	2.0	90	1.17 ± 0.04	0.978	3911	6666	1.84
60	1.8	91	1.49 ± 0.03	0.994	4209	6848	1.94

[a]Conditions: [*L*-LA]$_0$:[**Ca**]$_0$:[BnOH]$_0$ = 50:1:1, [*L*-LA]$_0$ = 0.5 M in 0.6 mL chloroform-d_1 at stated temperature. [b]Average reported; measured by ^{1}H NMR spectroscopic analyses. [c]First order rate constant (k_{obs}) and R^2 were obtained from average plots of ln([*L*-LA]$_0$/[*L*-LA]$_t$) *vs.* time. [d]Determined by GPC in THF against PS standards using the appropriate Mark-Houwink corrections.[2] [e]Calculated M_n for PLA synthesised = (conv.(%) × [*L*-LA]$_0$/[**Ca**]$_0$) × 144.13 + (M_w of end groups).

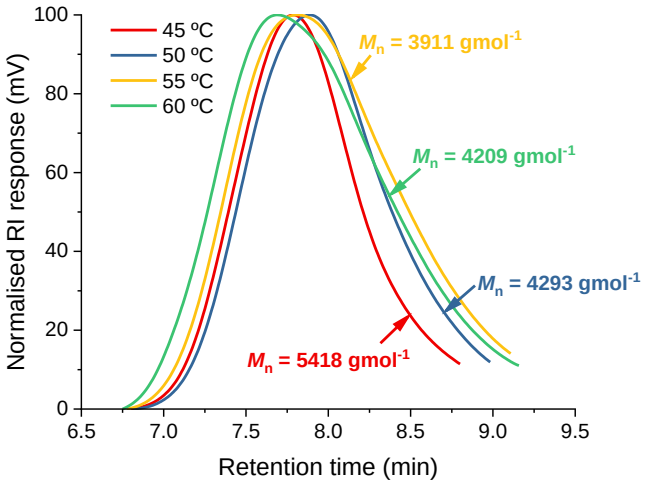

Figure A.44 GPC traces of PLAs synthesised from the ROP of *L*-LA using **14**/BnOH. Red: 45 °C, M_n = 5418 gmol^{-1}, M_w/M_n = 1.48; blue: 50 °C, M_n = 4293 gmol^{-1}, M_w/M_n = 1.59; yellow: 55 °C, M_n = 3911 gmol^{-1}, M_w/M_n = 1.84; green: 60 °C, M_n = 4209 gmol^{-1}, M_w/M_n = 1.94. Conditions: [*L*-LA]$_0$:[**Ca**]$_0$:[BnOH]$_0$ = 50:1:1, [*L*-LA]$_0$ = 50:1, 0.5 M in 0.6 mL chloroform-d_1 at stated temperature.

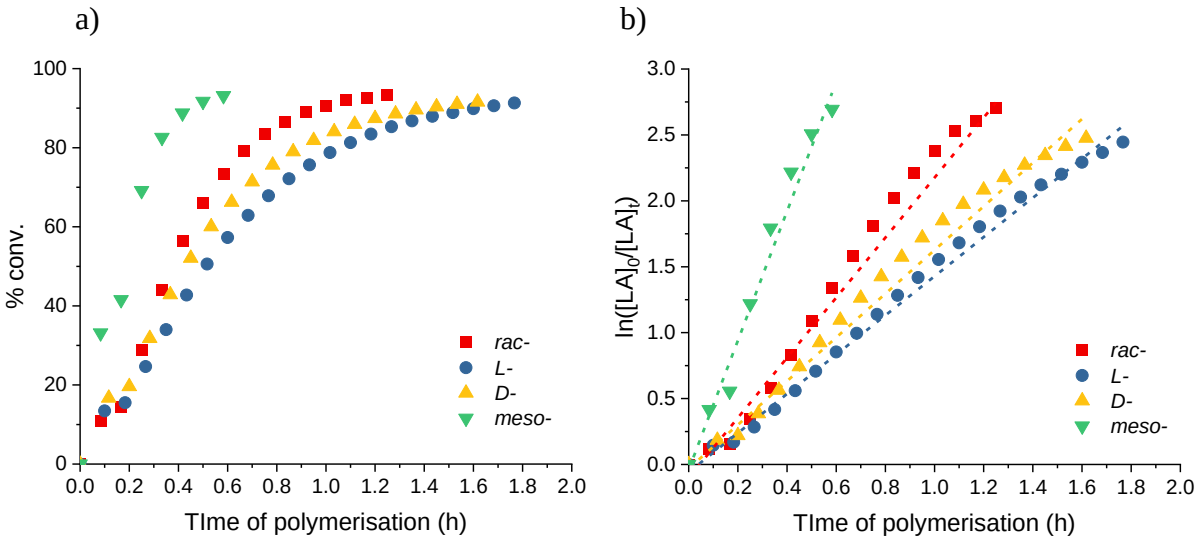

Figure A.45 a) Plot of percentage conversion *vs.* time. b) Plot of ln([LA]$_0$/[LA]$_t$) *vs.* time for LA polymerisation using **14**/BnOH. Red squares: *rac*-LA (k_{obs} = 2.28 h^{-1}. R^2 = 0.996); blue circles: *L*-LA (k_{obs} = 1.49 h^{-1}. R^2 = 0.994); yellow up triangles: *D*-LA (k_{obs} = 1.66 h^{-1}. R^2 = 0.990); green down triangles: *meso*-LA (k_{obs} = 4.90 h^{-1}. R^2 = 0.979). Conditions: [LA]$_0$:[**Ca**]$_0$:[BnOH]$_0$= 50:1:1, [LA]$_0$ = 0.5 M in 0.6 mL chloroform-d_1 at 60 ºC.

Table A.5 ROP of LA using **14**/BnOH with [LA]$_0$:[**Ca**]$_0$:[BnOH]$_0$ = 50:1:1 in chloroform-d_1 at 60 ºC.[a]

LA	Time (h)	Conv. (%)[b]	k_{obs} (h^{-1})[c]	R^{2c}	M_n (GPC)[d]	M_n (calcd)[e]	M_w/M_n
***rac*-**	1.3	93	2.28 ± 0.04	0.996	2417	6928	1.69
***L*-**	1.8	91	1.49 ± 0.03	0.994	4209	6848	1.94
***D*-**	1.6	92	1.66 ± 0.04	0.990	3878	6857	1.78
***meso*-**	0.6	93	4.90 ± 0.3	0.979	2275	6850	1.67

[a]Conditions: [LA]$_0$:[**Ca**]$_0$:[BnOH]$_0$ = 50:1:1, [LA]$_0$ = 0.5 M in 0.6 mL chloroform-d_1 at 60 ºC. [b]Average reported; measured by ^{1}H NMR spectroscopic analyses. [c]First order rate constant (k_{obs}) and R^2 were obtained from average plots of ln([LA]$_0$/[LA]$_t$) *vs.* time. [d]Determined by GPC in THF against PS standards using the appropriate Mark-Houwink corrections.[2] [e]Calculated M_n for PLA synthesised = (conv.(%) × [LA]$_0$/[**Ca**]$_0$) × 144.13 + (M_w of end groups).

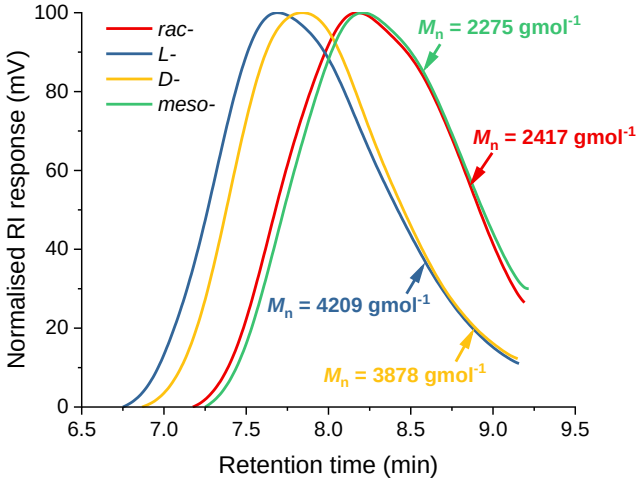

Figure A.46 GPC traces of PLAs synthesised from the ROP of LA using **14**/BnOH. Red: *rac*-LA, M_n = 2417 gmol^{-1}, M_w/M_n = 1.69; blue: *L*-LA, M_n = 4209 gmol^{-1}, M_w/M_n = 1.94; yellow: *D*-LA, M_n = 3878 gmol^{-1}, M_w/M_n = 1.78; green: *meso*-LA, M_n = 2275 gmol^{-1}, M_w/M_n = 1.67. Conditions: $[LA]_0$:[**Ca**]$_0$:$[BnOH]_0$ = 50:1:1, $[LA]_0$ = 0.5 M in 0.6 mL chloroform-d_1 at 60 °C.

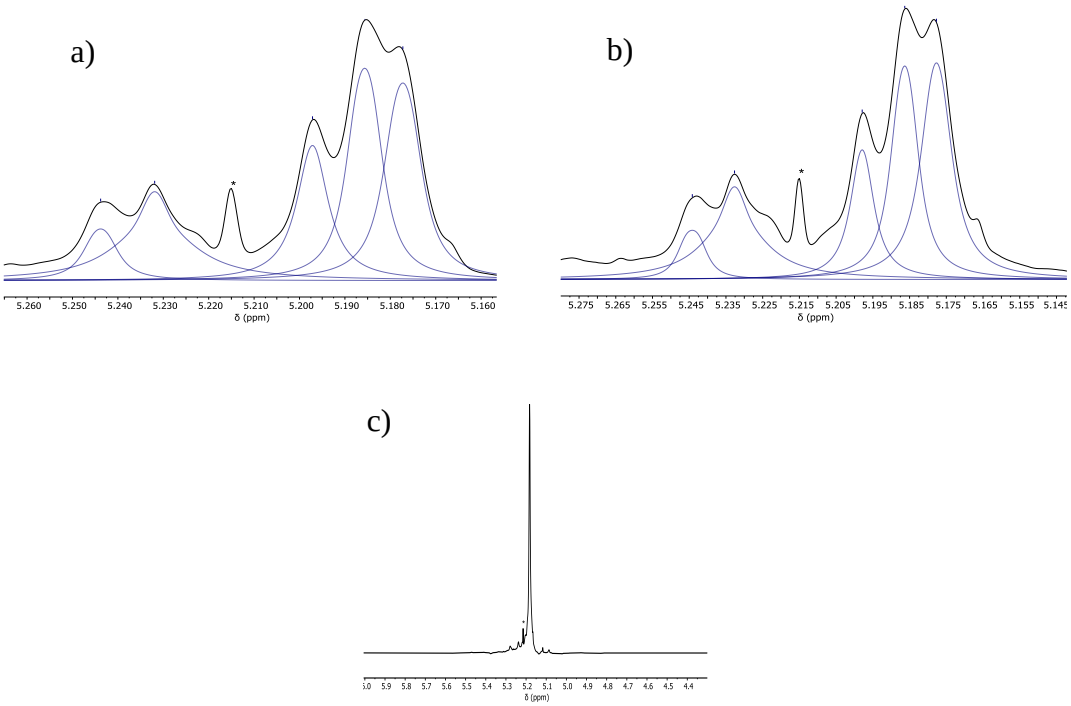

Figure A.47 ^{1}H{^{1}H} NMR spectra (chloroform-d_1, 500 MHz, 298 K) of the methine protons in the PLA produced from the **14**/BnOH system and a) *rac*-lactide (P_m = 0.51), b) *meso*-lactide (P_r = 0.53) and c) *L*/*D*-lactide (P_m = 1.00). Conditions: $[LA]_0$:[**Ca**]$_0$:$[BnOH]_0$ = 50:1:1, $[LA]_0$ = 0.5 M in 0.6 mL chloroform-d_1 at 60 °C. * denotes an artefact from NMR "BASH" experiment set-up.

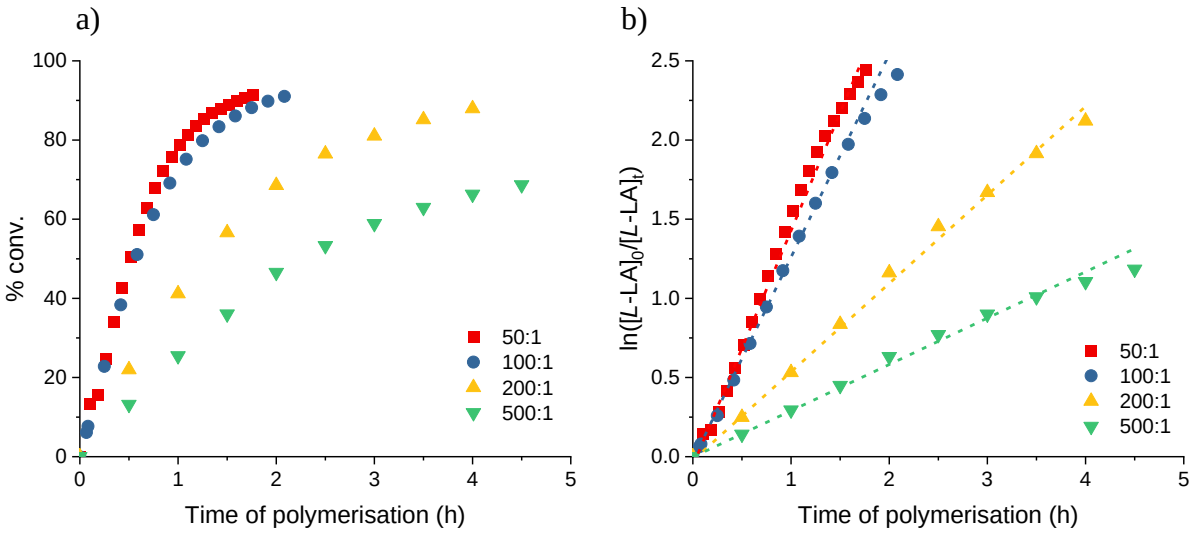

Figure A.48 a) Plot of percentage conversion *vs.* time. b) Plot of ln([*L*-LA]$_0$/[*L*-LA]$_t$) *vs.* time for *L*-LA polymerisation using **14**/BnOH. Red squares: 50:1 (k_{obs} = 1.49 h^{-1}. R^2 = 0.994); blue circles: 100:1 (k_{obs} = 1.29 h^{-1}. R^2 = 0.999); yellow up triangles: 200:1 (k_{obs} = 0.56 h^{-1}. R^2 = 0.997); green down triangles: 500:1 (k_{obs} = 0.29 h^{-1}. R^2 = 0.994). Conditions: [*L*-LA]$_0$:[**Ca**]$_0$ as stated, [*L*-LA]$_0$ = 0.5 M in 0.6 mL chloroform-d_1 at 60 °C.

Table A.6 ROP of *L*-LA using **14**/BnOH with [*L*-LA]$_0$:[**Ca**]$_0$ as stated in chloroform-d_1 at 60 °C.[a]

[*L*-LA]$_0$: [**Ca**]$_0$	Time (h)	Conv. (%)[b]	k_{obs} (h^{-1})[c]	R^{2c}	M_n (GPC)[d]	M_n (calcd)[e]	M_w/M_n
50:1	1.8	91	1.49 ± 0.03	0.994	4209	6848	1.94
100:1	2.1	91	1.29 ± 0.008	0.999	13 711	8179	1.56
200:1	4.0	88	0.56 ± 0.01	0.997	25 872	25 821	1.64
500:1	4.5	69	0.29 ± 0.008	0.994	36 780	44 709	1.59

[a]Conditions: [*L*-LA]$_0$:[**Ca**]$_0$ as stated, [*L*-LA]$_0$ = 0.5 M in 0.6 mL chloroform-d_1 at 60 °C. [b]Average reported; measured by ^{1}H NMR spectroscopic analyses. [c]First order rate constant (k_{obs}) and R^2 were obtained from average plots of ln([*L*-LA]$_0$/[*L*-LA]$_t$) *vs.* time. [d]Determined by GPC in THF against PS standards using the appropriate Mark-Houwink corrections.[2] [e]Calculated M_n for PLA synthesised = (conv.(%) × [*L*-LA]$_0$/[**Ca**]$_0$) × 144.13 + (M_w of end groups).

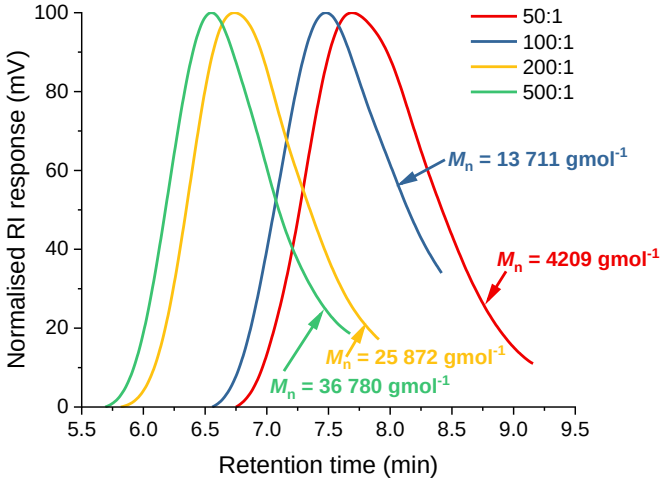

Figure A.49 GPC traces of PLAs synthesised from the ROP of *L*-LA using **14**/BnOH. Red: 50:1, M_n = 4209 gmol^{-1}, M_w/M_n = 1.94; blue: 100:1, M_n = 13 711 gmol^{-1}, M_w/M_n = 1.56; yellow: 200:1, M_n = 25 872 gmol^{-1}, M_w/M_n = 1.64; green: 500:1, M_n = 36 780 gmol^{-1}, M_w/M_n = 1.59. Conditions: [*L*-LA]$_0$:[**Ca**]$_0$ as stated, [*L*-LA]$_0$ = 0.5 M in 0.6 mL chloroform-d_1 at 60 °C.

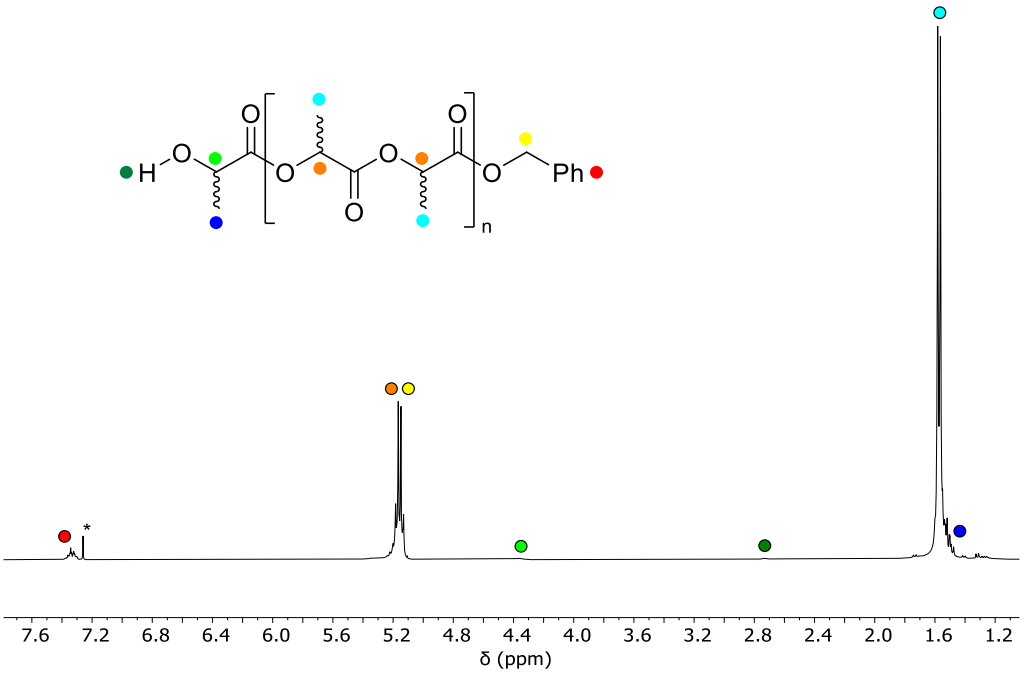

Figure A.50 ^{1}H NMR spectrum (*chloroform-d_1, 400 MHz, 298 K) of PLA produced using the **14**/BnOH system. Conditions: [*L*-LA]$_0$:[**Ca**]$_0$:[BnOH]$_0$ = 50:1:1, [*L*-LA]$_0$ = 0.5 M, 0.6 mL chloroform-d_1, 60 °C. M_w/M_n = 1.94.

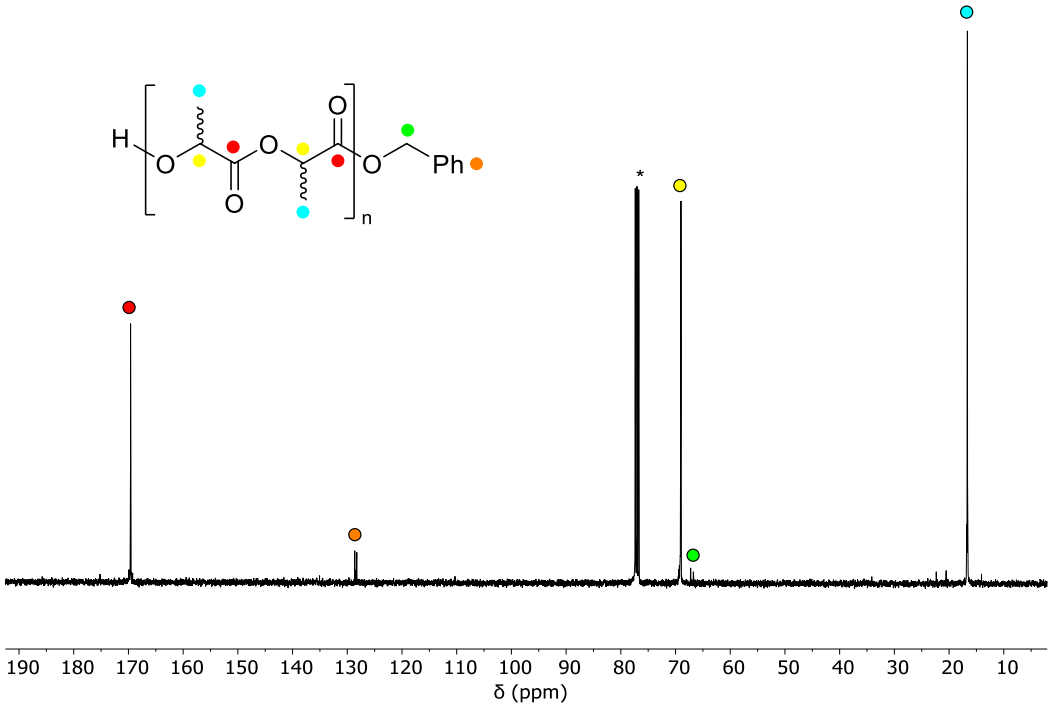

Figure A.51 $^{13}C\{^{1}H\}$ NMR spectrum (*chloroform-d_1, 101 MHz, 298 K) of PLA produced using the **14**/BnOH system. Conditions: [*L*-LA]$_0$:[**Ca**]$_0$:[BnOH]$_0$ = 50:1:1, [*L*-LA]$_0$ = 0.5 M, 0.6 mL chloroform-d_1, 60 °C. M_w/M_n = 1.94.

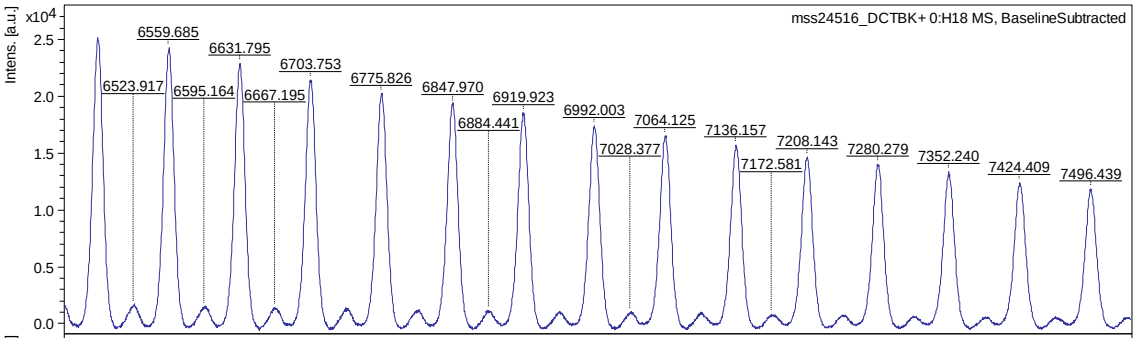

Figure A.52 MALDI-TOF mass (*m/z*) spectrum of PLA produced using **14**/BnOH. Conditions: [*L*-LA]$_0$:[**Ca**]$_0$:[BnOH]$_0$ = 50:1:1, [*L*-LA]$_0$ = 0.5 M, 0.6 mL chloroform-d_1, 60 °C. M_w/M_n = 1.94. E.g. the peak centred at 7064.1 gmol^{-1} is attributed to –OCH$_2$Ph/–OH terminated PLA, comprising of 48 units of LA with K$^+$ [144.13(48) + 108.14 + 39.1].

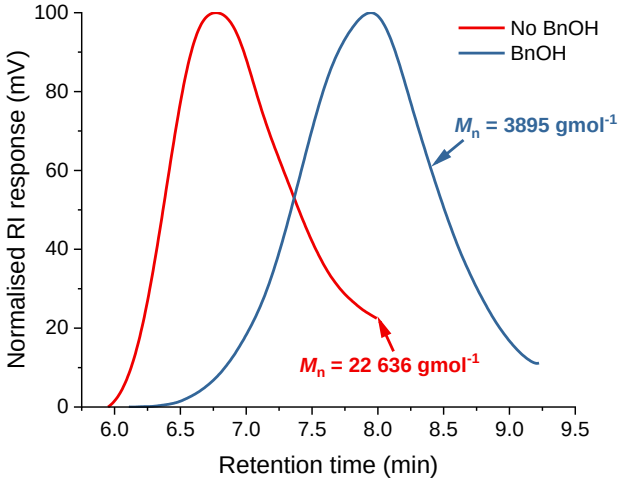

Figure A.53 GPC traces of PLAs synthesised from the ROP of *L*-LA using **15** with and without BnOH. Red: No BnOH, M_n = 22 636 gmol^{-1}, M_w/M_n = 1.72; blue: BnOH, M_n = 3895 gmol^{-1}, M_w/M_n = 2.08. Conditions: [*L*-LA]$_0$:[**Ca**]$_0$:([BnOH]$_0$) = 50:1(:1), [*L*-LA]$_0$ = 0.5 M in 0.6 mL benzene-d_6 at 60 °C.

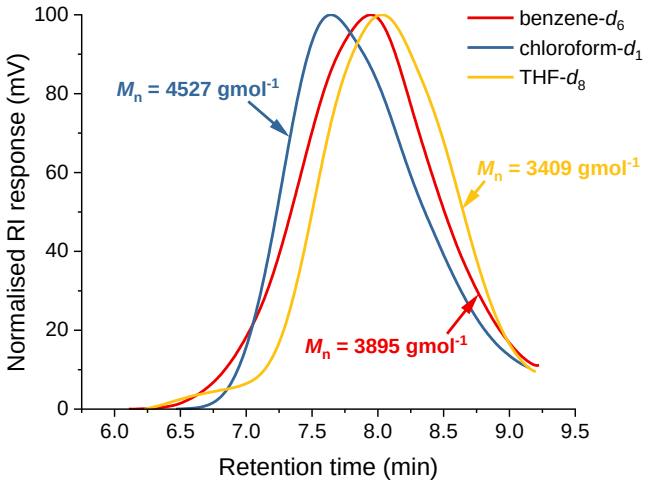

Figure A.54 GPC traces of PLAs synthesised from the ROP of *L*-LA using **15**/BnOH. Red: benzene-d_6, M_n = 3895 gmol^{-1}, M_w/M_n = 2.08; blue: chloroform-d_1, M_n = 4527 gmol^{-1}, M_w/M_n = 1.92; yellow: THF-d_8, M_n = 3409 gmol^{-1}, M_w/M_n = 1.99. Conditions: [*L*-LA]$_0$:[**Ca**]$_0$:[BnOH]$_0$ = 50:1:1, [*L*-LA]$_0$ = 0.5 M in 0.6 mL of stated solvent at 60 °C.

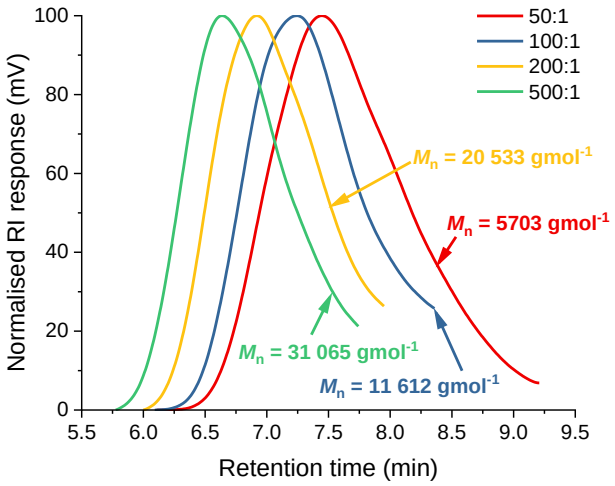

Figure A.55 GPC traces of PLAs synthesised from the ROP of *L*-LA using **15**/BnOH. Red: 50:1, M_n = 5703 gmol^{-1}, M_w/M_n = 2.33; blue: 100:1, M_n = 11 612 gmol^{-1}, M_w/M_n = 1.73; yellow: 200:1, M_n = 20 533 gmol^{-1}, M_w/M_n = 1.59; green: 500:1, M_n = 31 065 gmol^{-1}, M_w/M_n = 1.57. Conditions: [*L*-LA]$_0$:[**Ca**]$_0$ as stated, [*L*-LA]$_0$ = 0.5 M in 0.6 mL chloroform-d_1 at 60 °C.

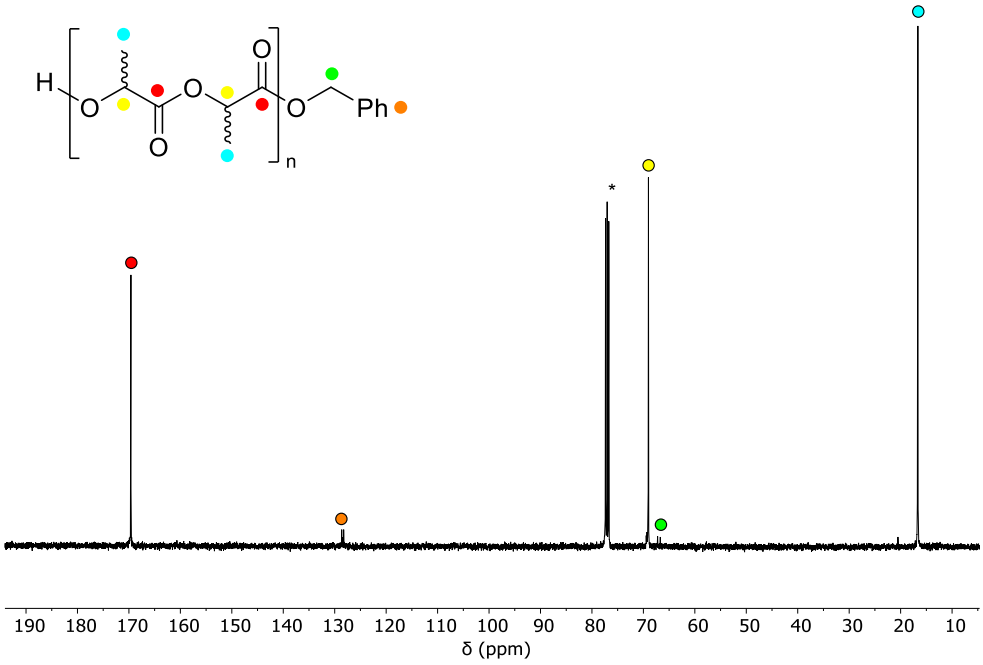

Figure A.56 $^{13}C\{^1H\}$ NMR spectrum (*chloroform-d_1, 101 MHz, 298 K) of PLA produced using the **15**/BnOH system. Conditions: [*L*-LA]$_0$:[**Ca**]$_0$:[BnOH]$_0$ = 50:1:1, [*L*-LA]$_0$ = 0.5 M, 0.6 mL chloroform-d_1, 60 °C. M_w/M_n = 2.33.

Chapter 6

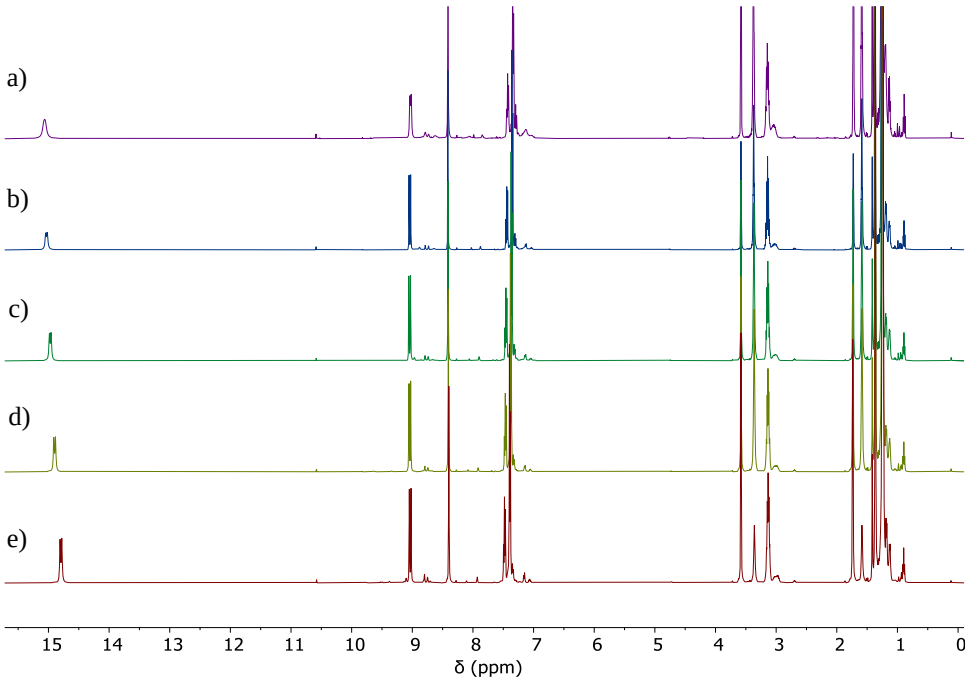

Figure A.57 ^{1}H NMR spectra (*THF-d_8, 500 MHz) of [$H_2$$^{t\text{Bu,Dipp}}$L][$BF_4$] (**16·thf$_x$**) at a) 323 K, b) 298 K, c) 273 K, d) 253 K and e) 233 K.

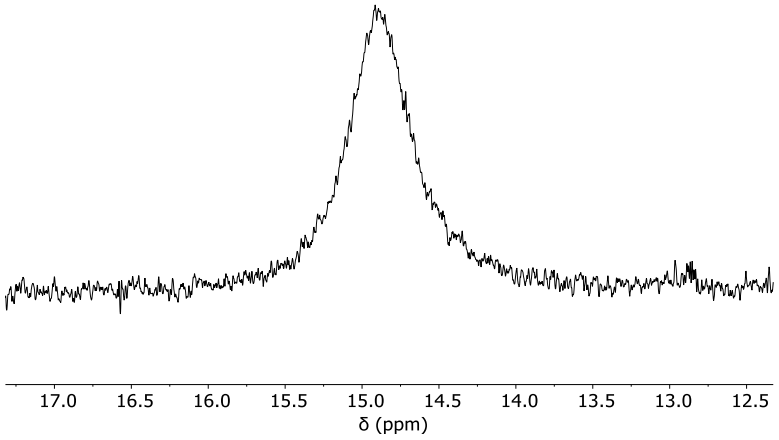

Figure A.58 Expanded ^{2}H NMR spectrum (77 MHz, THF-d_8, 298 K) of [$D_2$$^{t\text{Bu,Dipp}}$L][$BF_4$] from deuteration of [$H_2$$^{t\text{Bu,Dipp}}$L][$BF_4$] with methanol-$d_1$.

Table A.7 Experimental metrical parameters (bond lengths (Å)) for the O2-containing cationic fragment present in the asymmetric unit of compound **16**. Estimated standard deviations shown in brackets.

C(37)-O(2)	1.276(3)
C(37)-C(38)	1.441(3)
C(37)-C(42)	1.431(3)
C(38)-C(43)	1.422(3)
C(42)-C(56)	1.418(3)
N(3)-C(43)	1.299(3)
N(4)-C(56)	1.301(3)
N(3)-H(3A)	0.90(4)
N(4)-H(4)	0.91(4)

Table A.8 Final single point energies of dispersion corrected, optimised structures

Structure	Single point energy (with DFT-D3; kJ mol^{-1})	Dispersion correction (kJ mol^{-1})
$H^{tBu,Dipp}L$	-4161753.1	-263.0
$[HN<O>NH]^+$	-4163011.8	-271.2
$[HN<OH>N]^+$	-4162985.1	-270.1
$[N<OH_2>N]^+$	-4162736.5	-274.1

Table A.9 Thermodynamic parameters of dispersion corrected, optimised structures

Structure	ΔG (kJ mol^{-1})	ΔH (kJ mol^{-1})	ΔS (kJ mol^{-1})
$H^{tBu,Dipp}L$	-4159940.4	-4159657.2	-283.3
$[HN<O>NH]^+$	-4161155.8	-4160872.7	-283.0
$[HN<OH>N]^+$	-4161133.2	-4160849.6	-283.6
$[N<OH_2>N]^+$	-4160892.7	-4160603.2	-289.4

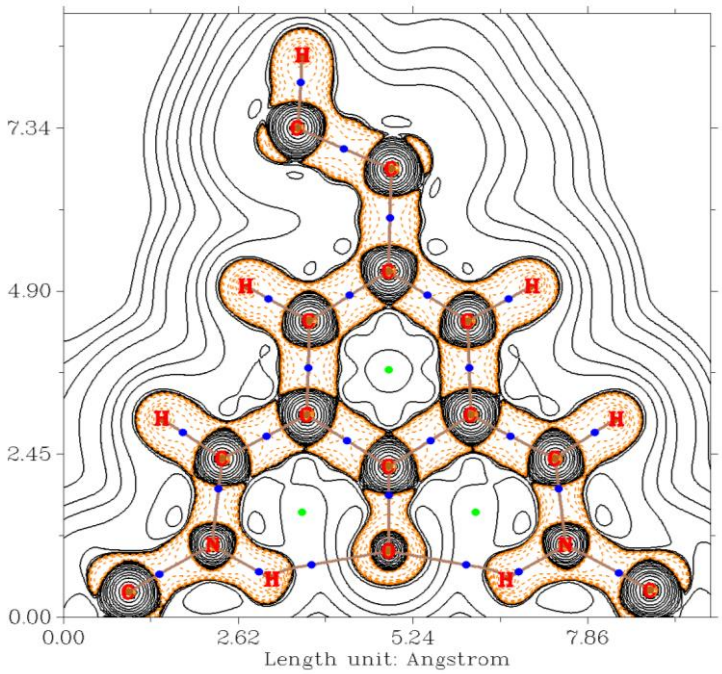

Figure A.59 Contour map of the Laplacian ($\nabla^2\rho(\mathbf{r})$) of electron density of $[H_2{}^{t\text{Bu,Dipp}}L]^+$ (**16**) – plotted in the plane of the central benzene ring. The solid (black) and dashed (orange) lines correspond to positive and negative Laplacian values respectively. The blue (•) and green (•) dots mark bonding (3,–1) and ring (3,+1) critical points respectively.

Calculating hydrogen bond energies:

The energy associated with the hydrogen bonding interactions within these systems was estimated using the methods reported by Lu *et al.*[3] These take into account the electron density at the bonding critical point of the hydrogen bonds:

- For a neutral hydrogen bond: $\Delta E \approx -223.08 \times \rho(\boldsymbol{r}_{BCP}) + 0.7423$
- For a charged hydrogen bond: $\Delta E \approx -332.34 \times \rho(\boldsymbol{r}_{BCP}) - 1.0661$

These equations were determined to be more accurate than the original energy predictor proposed by Espinosa in 1998 which instead utilised the potential energy at the bonding critical points: $\Delta E \approx \frac{V(\boldsymbol{r}_{BCP})}{2}$.[4]

Table A.10 Calculated delocalisation indices – δ(A,B) – reported in atomic units

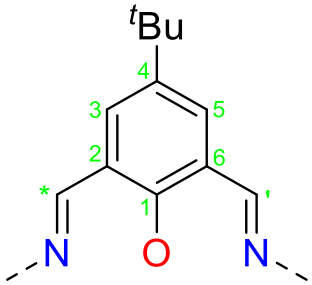

	$H^{tBu,Dipp}L$	[HN<O>NH]$^+$	[N<OH>NH]$^+$	[N<OH$_2$>N]$^+$
(L)N-H	-	0.63	0.66	-
N=C*	1.53	1.28	1.31	1.54
C*-C2	1.05	1.21	1.17	1.03
C2-C1	1.28	1.11	1.20	1.32
C2-C3	1.31	1.29	1.28	1.31
C3-C4	1.38	1.37	1.37	1.36
C4-C5	1.38	1.34	1.34	1.34
C5-C6	1.34	1.31	1.33	1.32
C6-C1	1.25	1.10	1.23	1.31
C-O	0.95	1.19	1.00	0.75
O-H	0.59	-	0.42	0.47
				0.48
C6-C’	1.05	1.19	1.08	1.02
C’=N	1.52	1.30	1.47	1.54
N-H (R)	-	0.63	-	-
$\frac{1}{2}\sum_{A\neq B}\delta(A,B)$	7.32	7.48	7.43	7.40
Difference	-	+0.16	+0.11	+0.08

Conducting pK_a titrations:

1:1 mixtures of protonated pro-ligand and base were prepared and analysed by ^{1}H NMR spectroscopy.[5] When separate signals were observed for conjugate acid and base, the relative integrals of the resonances were used to determine the concentration of these species in the mixture. When time-averaged signals were observed for the conjugate acid/base or conjugate base/acid couples, the chemical shifts of the individual components were then used to determine relative concentrations:

$$\frac{[base]}{[conjugate\ acid]} = \frac{|\delta_{mix} - \delta_{base}|}{|\delta_{conjugate\ acid} - \delta_{mix}|} \ \boldsymbol{OR}\ \frac{[conjugate\ base]}{[acid]} = \frac{|\delta_{mix} - \delta_{acid}|}{|\delta_{conjugate\ base} - \delta_{mix}|}$$

The ΔpK_a values, relative to the base used, were then computed using the following equation:

$$\Delta pK_a = \log\left(\frac{[acid][base]}{[conjugate\ acid][conjugate\ base]}\right)$$

Poor solubility of **16·thf$_x$** in acetonitrile, the typical solvent for non-aqueous acid-base chemistry, led to its acid dissociation constant being determined instead in THF.[6] On the NMR time-scale, well-defined and identifiable resonances for both pyrazole and its protonated form were observable (at δ 6.3 and δ 6.6 ppm respectively – see **Figure A.60**). Conversely, fast exchange between **16·thf$_x$** and its original pro-ligand form resulted in the detection of a time-averaged signal (see **Figure A.60**). In contrast to **16·thf$_x$**, the alternative protonated pro-ligand **18·thf$_x$**, was fully soluble in acetonitrile. In this titration, time-averaged signals were observed for both couples (see **Figure A.65**).

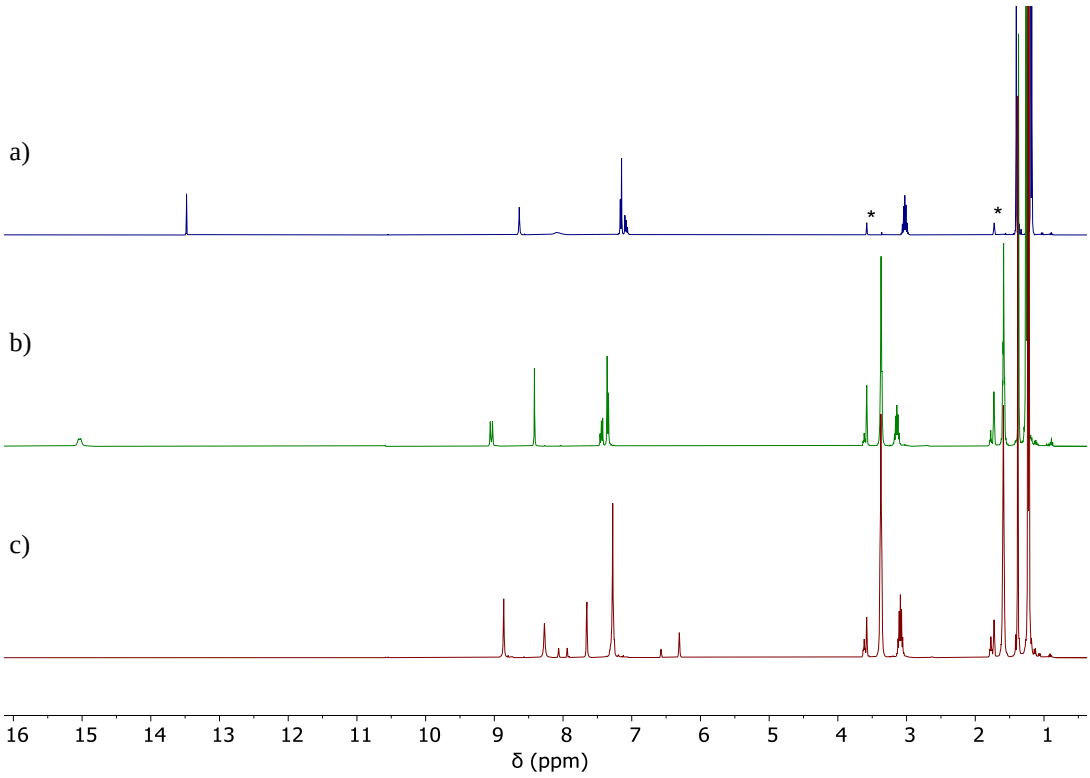

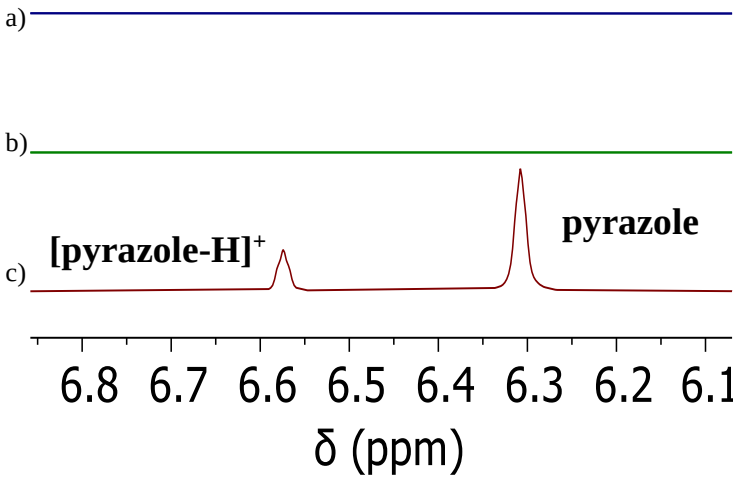

Figure A.60 ^{1}H NMR spectra (*THF-d_8, 400 MHz, 298 K) of a) H$^{t\text{Bu,Dipp}}$L, b) [H$_2$$^{t\text{Bu,Dipp}}$L][BF$_4$] (**16·thf$_x$**) and c) 1:1 reaction mixture of [H$_2$$^{t\text{Bu,Dipp}}$L][BF$_4$] (**16·thf$_x$**) and pyrazole. Expansion highlights signals used in pK_a calculations.

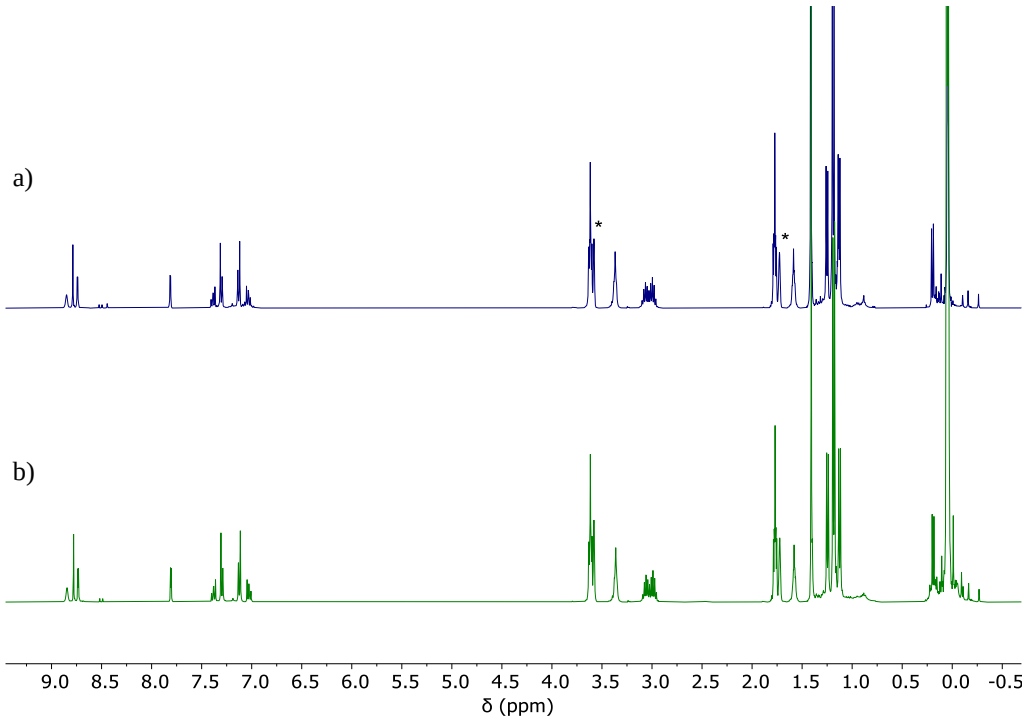

Figure A.61 ^{1}H NMR spectra (*THF-d_8, 400 MHz, 298 K) of a) reaction mixture between $[H_2{}^{t\text{Bu,Dipp}}L][BF_4]$ (**16·thf**$_x$) and $Mg\{N(SiMe_3)_2\}_2$ and b) reaction mixture between $[H_2{}^{t\text{Bu,Dipp}}L][BF_4]$ (**16·thf**$_x$) and $Ca\{N(SiMe_3)_2\}_2$.

Table A.11 Experimental metrical parameters (bond lengths (Å)) for the B2-containing molecule present in the asymmetric unit of compound **17**. Estimated standard deviations shown in brackets.

B(1)-N(1)	1.596(2)
B(1)-O(1)	1.449(2)
B(1)-F(1)	1.377(3)
B(1)-F(2)	1.370(3)
O(1)-C(1)	1.334(2)
N(1)-C(7)	1.294(2)
O(1)-B(1)-N(1)	109.61(13)
O(1)-B(1)-F(1)	111.13(17)
O(1)-B(1)-F(2)	110.11(17)
N(1)-B(1)-F(1)	107.89(16)
N(1)-B(1)-F(2)	109.21(16)
F(1)-B(1)-F(2)	108.84(16)
τ_4	0.98

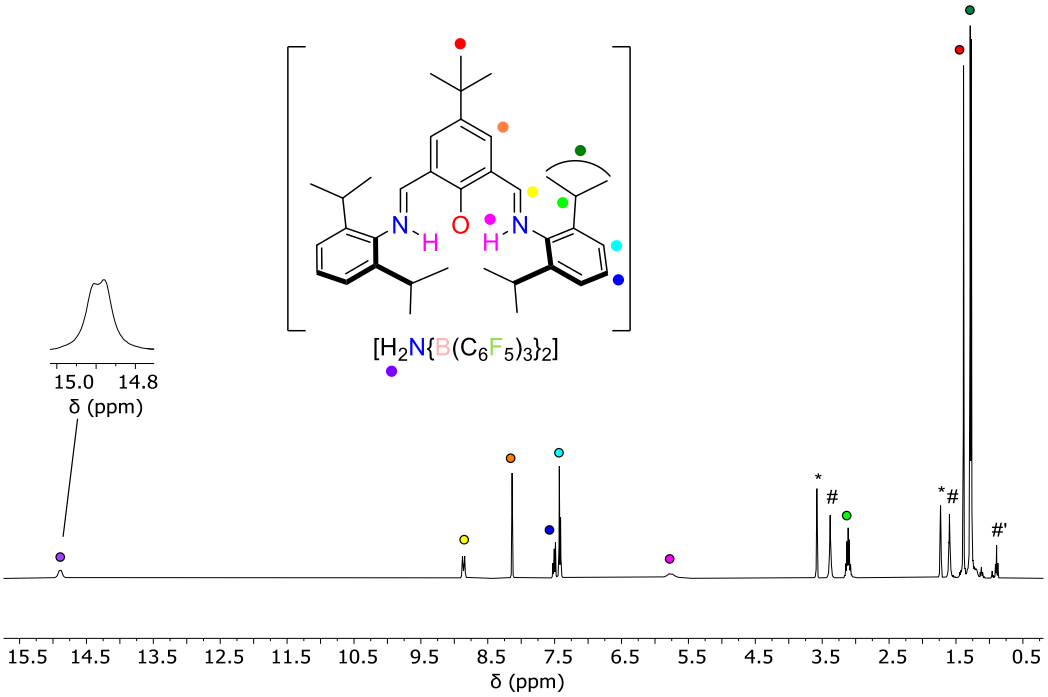

Figure A.62 ^{1}H NMR spectrum (*THF-d_8, 400 MHz, 298 K) of $[H_2{}^{tBu,Dipp}L][H_2N\{B(C_6F_5)_3\}_2]$ (**18·thf$_x$**). # and #' denote residual protio THF and pentane from reaction work-up.

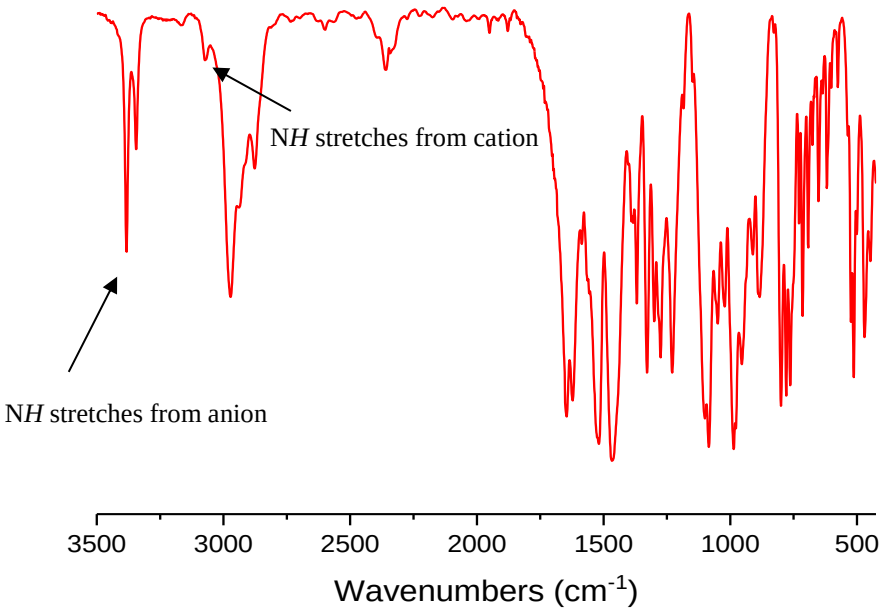

Figure A.63 IR (KBr) spectrum of $[H_2{}^{tBu,Dipp}L][H_2N\{B(C_6F_5)_3\}_2]$ (**18·thf$_x$**).

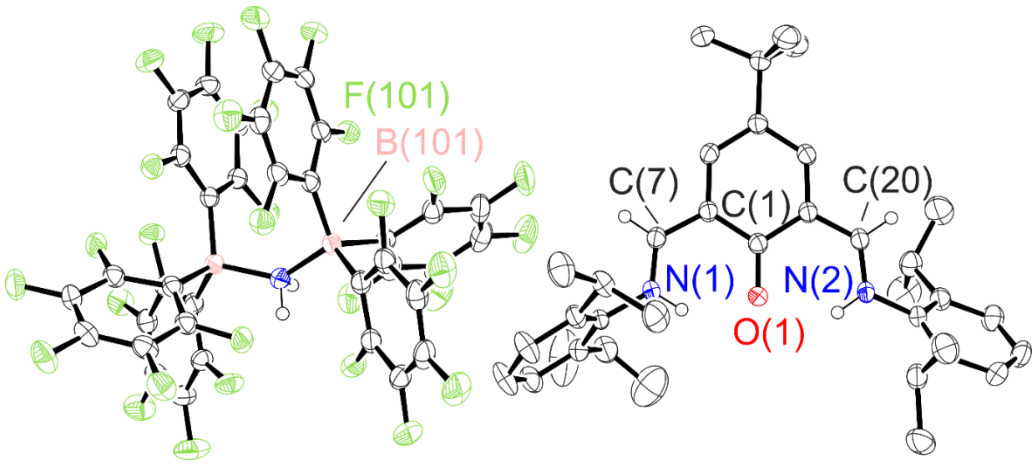

Figure A.64 Thermal displacement ellipsoid drawings (30% probability) of $[H_2{}^{tBu,Dipp}L][H_2N\{B(C_6F_5)_3\}_2]$ (**18**). All hydrogen atoms apart from those on N1, N2, N3, C7 and C20 have been omitted for clarity.

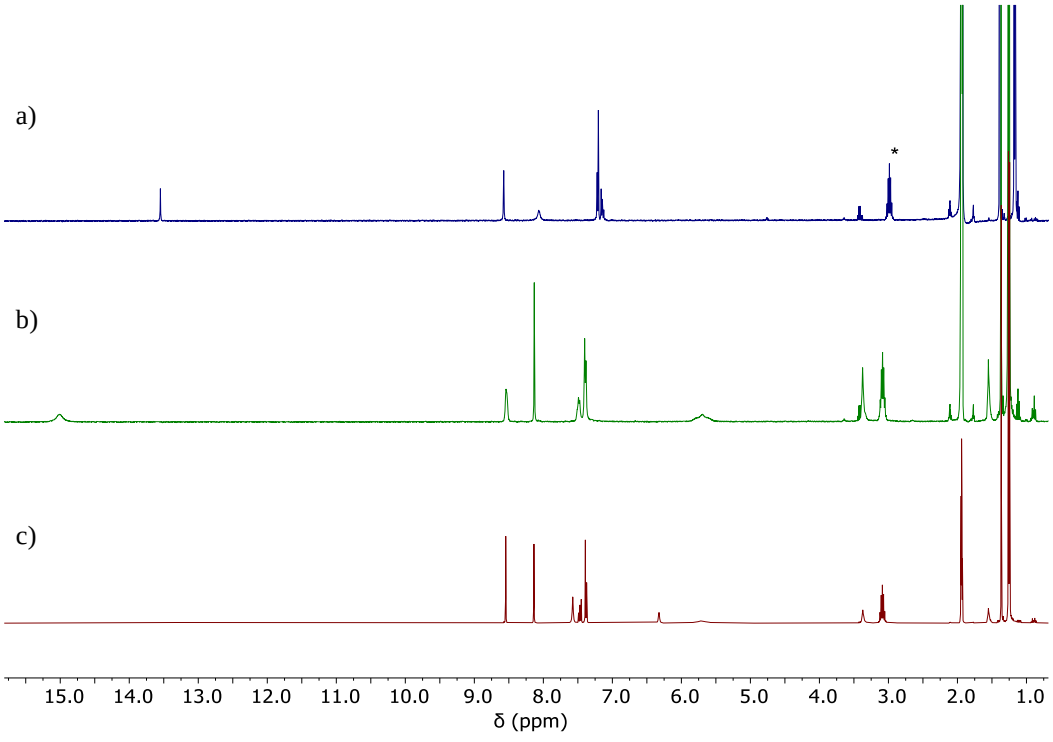

Figure A.65 ^{1}H NMR spectra (*acetonitrile-d_3, 400 MHz, 298 K) of a) $H^{tBu,Dipp}L$, b) $[H_2{}^{tBu,Dipp}L][H_2N\{B(C_6F_5)_3\}_2]$ (**18·thf$_x$**) and c) 1:1 reaction mixture of $[H_2{}^{tBu,Dipp}L][H_2N\{B(C_6F_5)_3\}_2]$ (**18·thf$_x$**) and pyrazole.

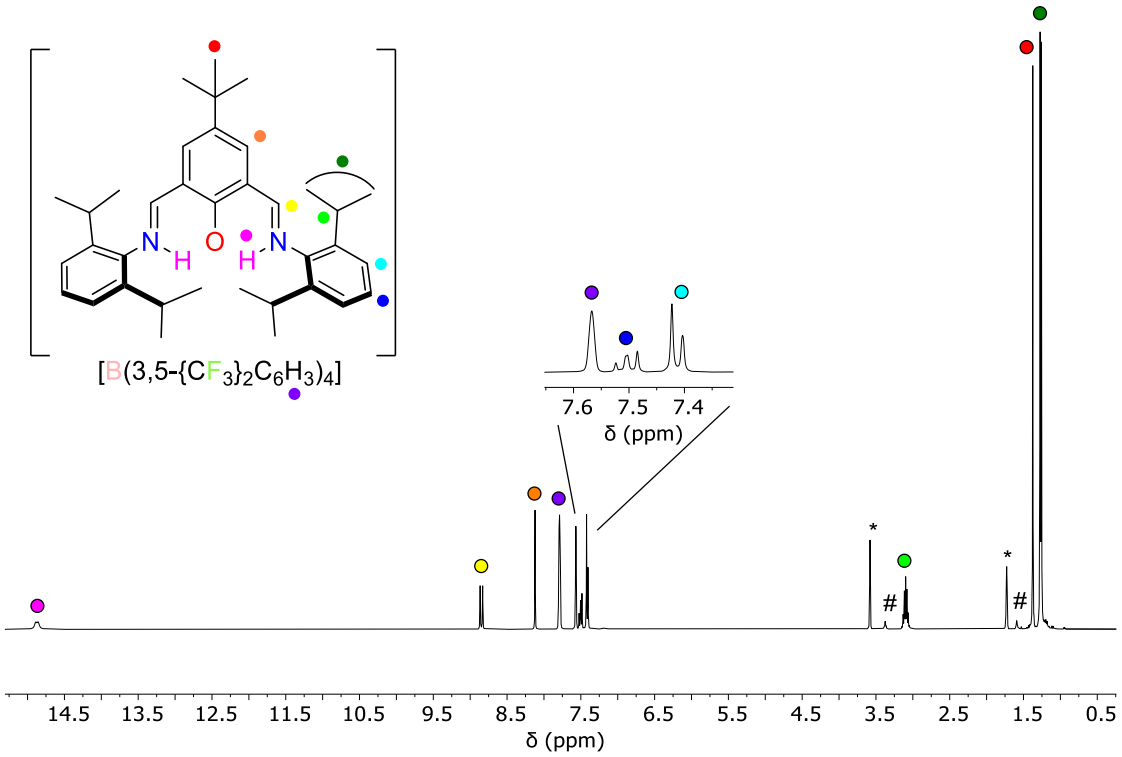

Figure A.66 ^{1}H NMR spectrum (*THF-d_8, 400 MHz, 298 K) of [$H_2{}^{t\text{Bu,Dipp}}$L][B(3,5-{CF_3}$_2$$C_6H_3$)$_4$] (**20·thf$_x$**). # denotes residual protio THF.

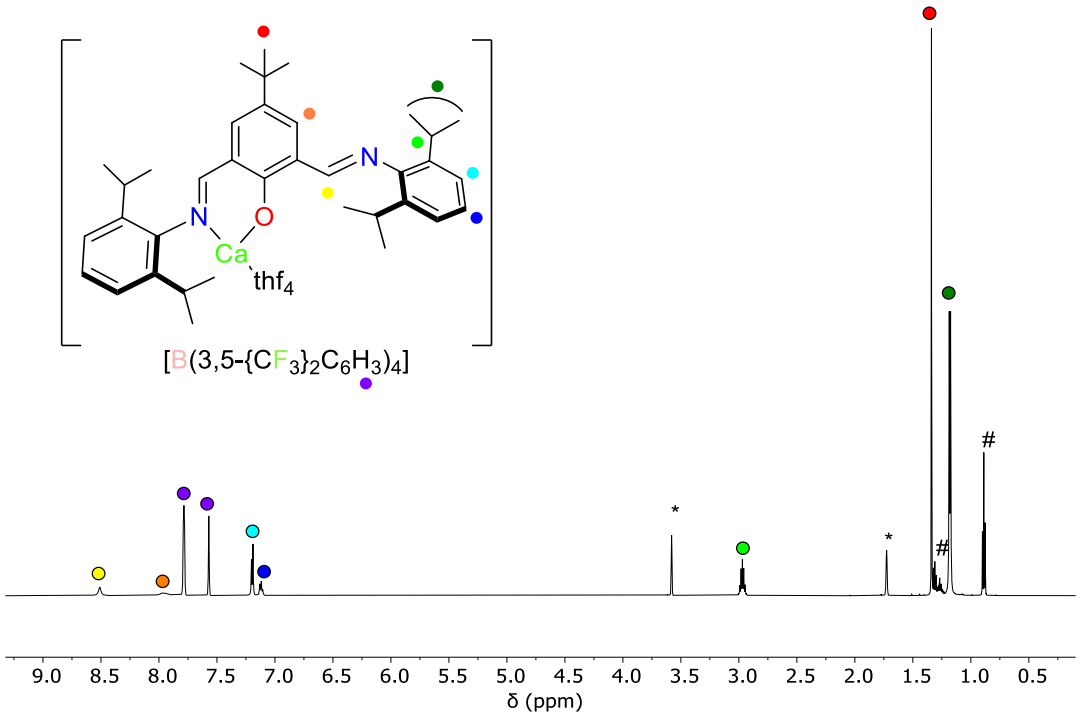

Figure A.67 ^{1}H NMR spectrum (*THF-d_8, 600 MHz, 298 K) of [$^{t\text{Bu,Dipp}}$LCa(thf)$_4$][B(3,5-{CF_3}$_2$$C_6H_3$)$_4$] (**21**). # denotes residual protio pentane from crystallisation.

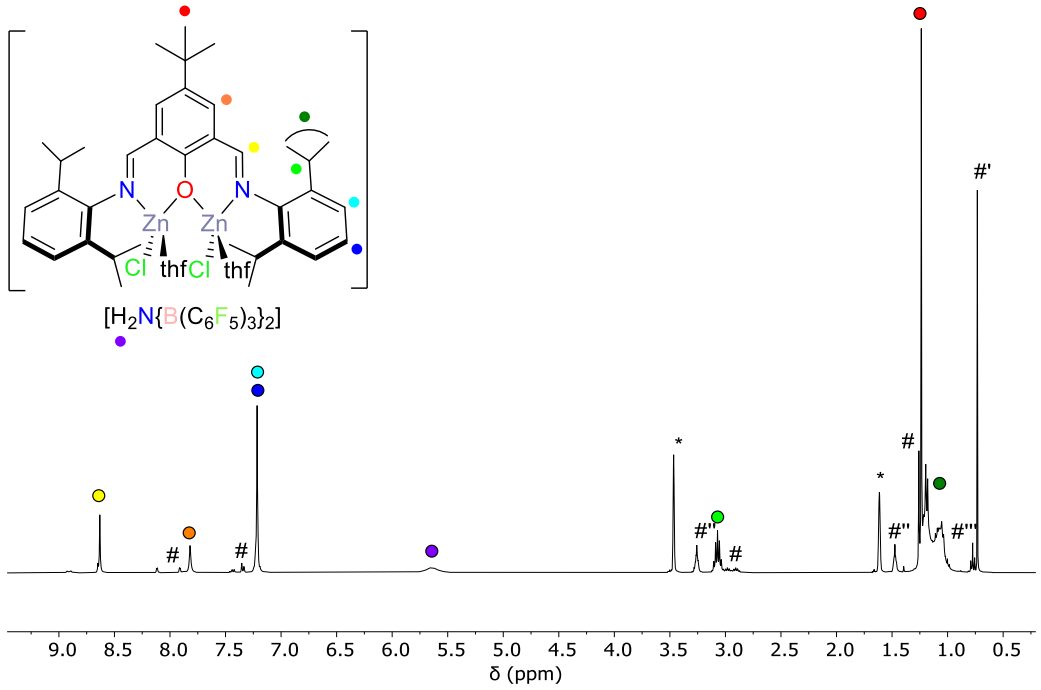

Figure A.68 ^{1}H NMR spectrum (*THF-d_8, 400 MHz, 298 K) of the reaction mixture between **18·thf**$_x$ and 2 eq. EtZnCl; the proposed product is [$^{t\text{Bu,Dipp}}$L{ZnCl(thf)}$_2$][H$_2$N{B(C$_6$F$_5$)$_3$}$_2$]. # and #' represent residual **22** and ethane whilst #'' and #''' represent protio THF and pentane respectively.

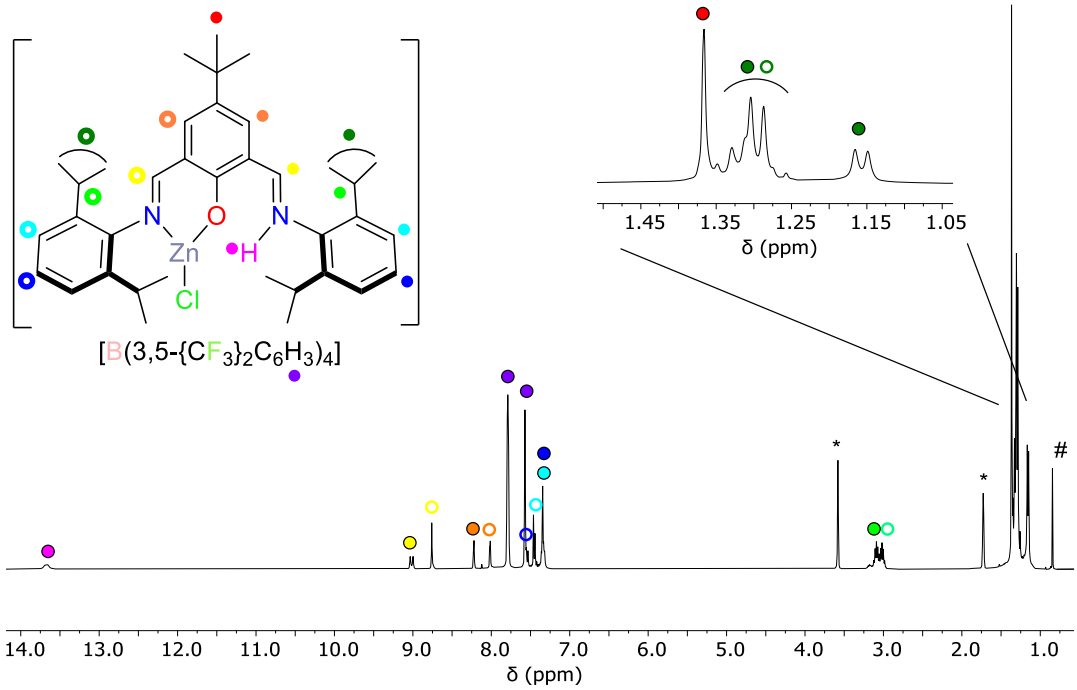

Figure A.69 ^{1}H NMR spectrum (*THF-d_8, 400 MHz, 298 K) of [H$^{t\text{Bu,Dipp}}$LZnCl][B(3,5-{CF$_3$}$_2$C$_6$H$_3$)$_4$] (**23**). # represents ethane by-product.

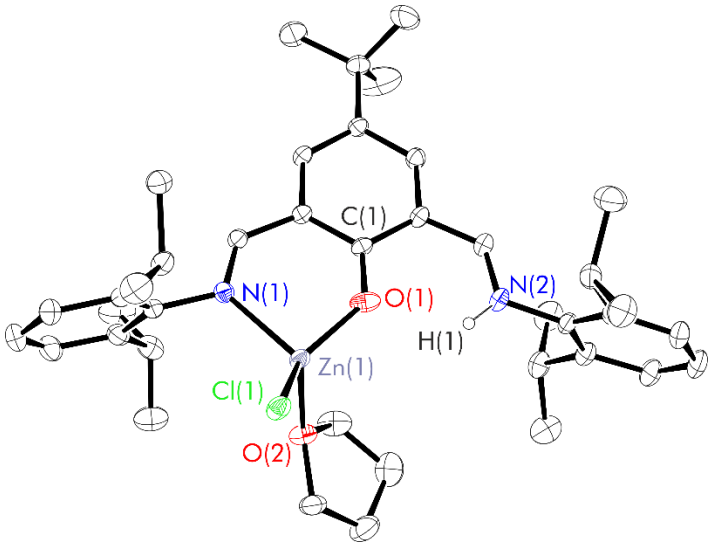

Figure A.70 Thermal displacement ellipsoid drawings (30% probability) of [H$^{t\text{Bu,Dipp}}$LZnCl(thf)][B(3,5-{CF_3}$_2$$C_6H_3$)$_4$] (**23(thf)**). All hydrogen atoms apart from those on N2 have been omitted for clarity; cation only displayed with major component of modelled disorder shown.

Table A.12 Experimental metrical parameters (bond lengths (Å)) for [H$^{t\text{Bu,Dipp}}$LZnCl(thf)][B(3,5-{CF_3}$_2$$C_6H_3$)$_4$] (**23(thf)**). Estimated standard deviations shown in brackets.

Zn(1)-N(1)	2.0982(14)
Zn(1)-O(1)	1.8496(15)
Zn(1)-Cl(1)	2.1972(8)
Zn(1)-O(2)	2.027(2)
O(1)-C(1)	1.295(2)
N(1)-C(7)	1.284(2)
N(2)-H(2)	0.8800
O(1)-Zn(1)-N(1)	91.05(6)
O(1)-Zn(1)-O(2)	102.14(8)
N(1)-Zn(1)-O(2)	108.36(7)
O(1)-Zn(1)-Cl(1)	134.30(5)
N(1)-Zn(1)-Cl(1)	112.85(4)
O(2)-Zn(1)-Cl(1)	105.84(6)
τ_4	0.80

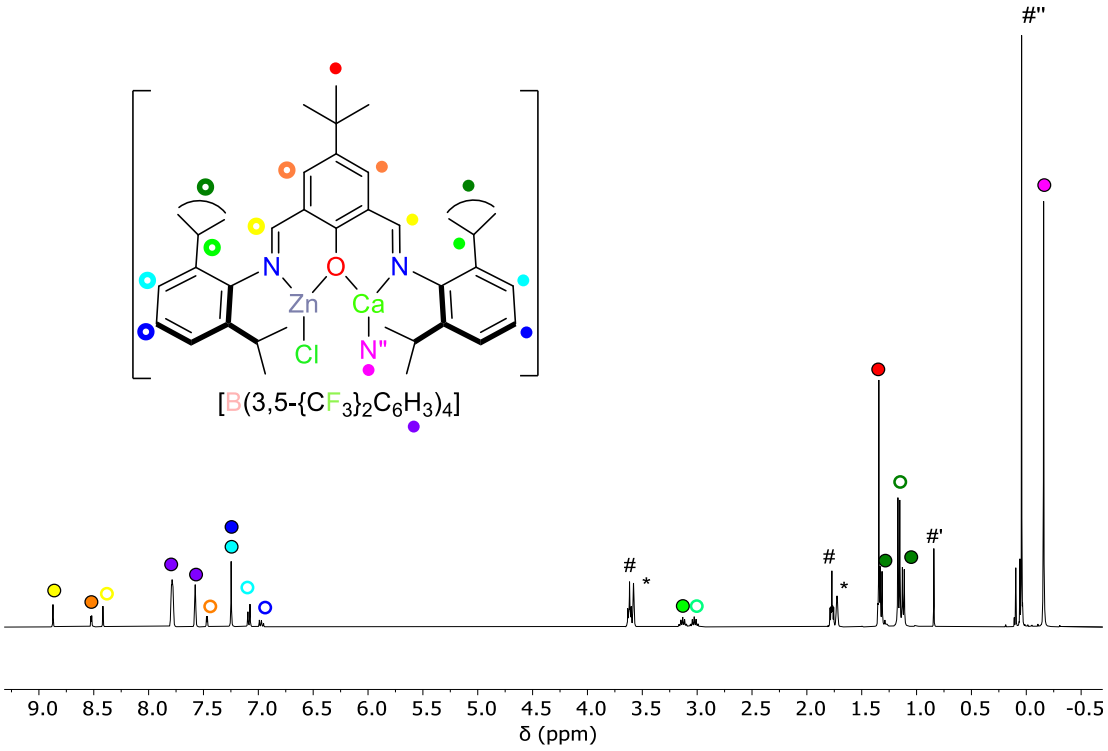

Figure A.71 ^{1}H NMR spectrum (*THF-d_8, 400 MHz, 298 K) of [$^{t\text{Bu,Dipp}}$L{ZnCl}CaN(SiMe$_3$)$_2$][B(3,5-{CF$_3$}$_2$C$_6$H$_3$)$_4$] (**25**). # denotes residual protio THF whilst #' and #" represent ethane and HMDS by-products.

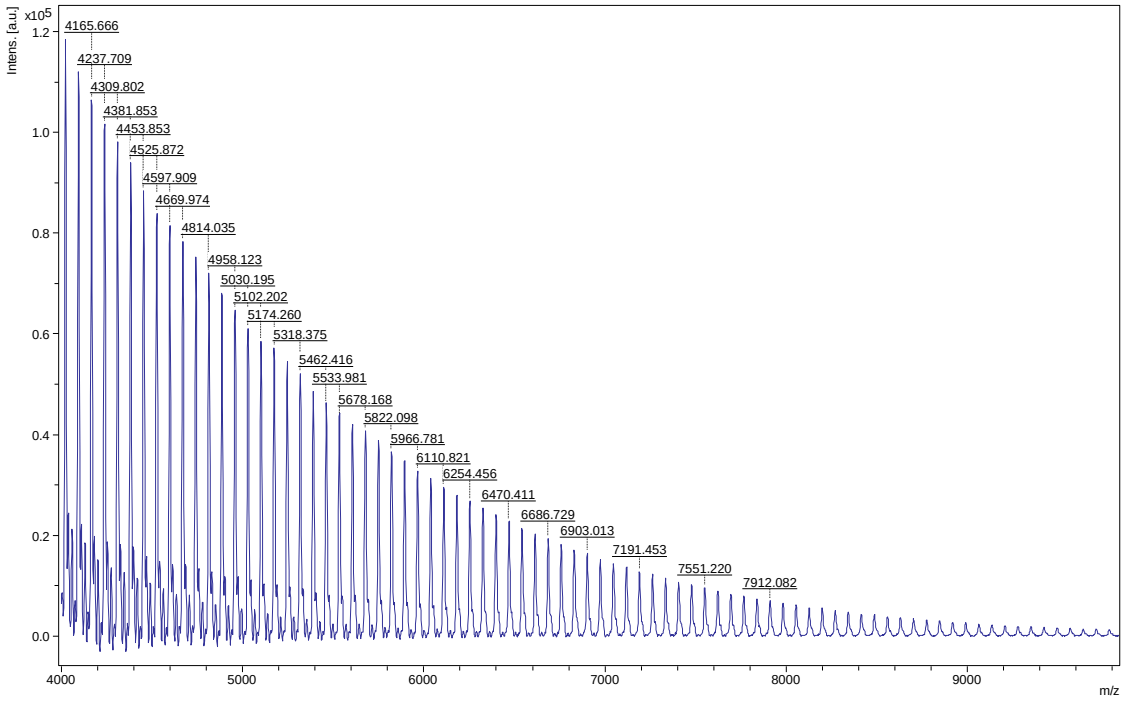

Figure A.72 MALDI-TOF mass (*m/z*) spectrum of PLA produced using **19** contaminated with residual HMDS. Conditions: [*L*-LA]$_0$:[**Ca**$^+$]$_0$:[BnOH]$_0$ = 50:1:1, [*L*-LA]$_0$ = 0.5 M, 0.6 mL chloroform-d_1, 60 ºC. E.g. the peak centred at 6110.8 gmol^{-1} is attributed to –N(SiMe$_3$)$_2$/–OH terminated PLA, comprising of 41 units of LA with K$^+$ [144.13(41) + 161.39 + 39.1].

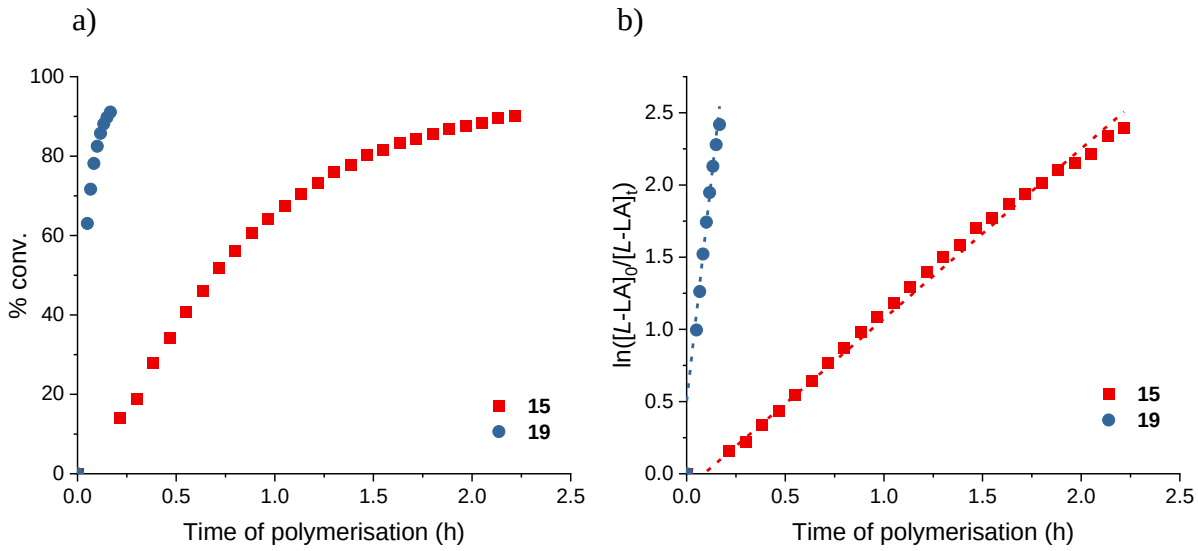

Figure A.73 a) Plots of percentage conversion *vs.* time. b) Plots of ln([*L*-LA]$_0$/[*L*-LA]$_t$) *vs.* time for *L*-LA polymerisation. Red squares: cat = **15**/BnOH (k_{obs} = 1.18 h^{-1}. R^2 = 0.997); blue circles: cat = **19**/BnOH (k_{obs} = 12.27 h^{-1}. R^2 = 0.979). Conditions: [*L*-LA]$_0$:[**Ca**$^+$]$_0$:[BnOH]$_0$ = 50:1:1, [*L*-LA]$_0$ = 0.5 M in 0.6 mL chloroform-d_1 at 60 °C.

Table A.13 ROP of *L*-LA using **15**/BnOH and **19**/BnOH with [*L*-LA]$_0$:[**Ca**$^+$]$_0$:[BnOH]$_0$ = 50:1:1 at 60 °C.[a]

Catalyst	Time (h)	Conv. (%)[b]	k_{obs} (h^{-1})[c]	R^{2c}	M_n (GPC)[d]	M_n (calcd)[e]	M_w/M_n
15	2.2	90	1.18 ± 0.01	0.997	5703	6206	2.33
19	0.2	91	12.27 ± 0.7	0.979	6719	6975	1.63

[a]Conditions: [*L*-LA]$_0$:[**Ca**$^+$]$_0$:[BnOH]$_0$ = 50:1:1, [*L*-LA]$_0$ = 0.5 M in 0.6 mL chloroform-d_1 at 60 °C. [b]Average reported; measured by ^{1}H NMR spectroscopic analyses. [c]First order rate constant and R^2 were obtained from average plots of ln([*L*-LA]$_0$/[*L*-LA]$_t$) *vs.* time. [d]Determined by GPC in THF against PS standards using the appropriate Mark-Houwink corrections.[80] [e]Calculated M_n for PLA synthesised = (conv.(%) × [*L*-LA]$_0$/[**Ca**$^+$]$_0$) × 144.13 + (M_w of end groups).

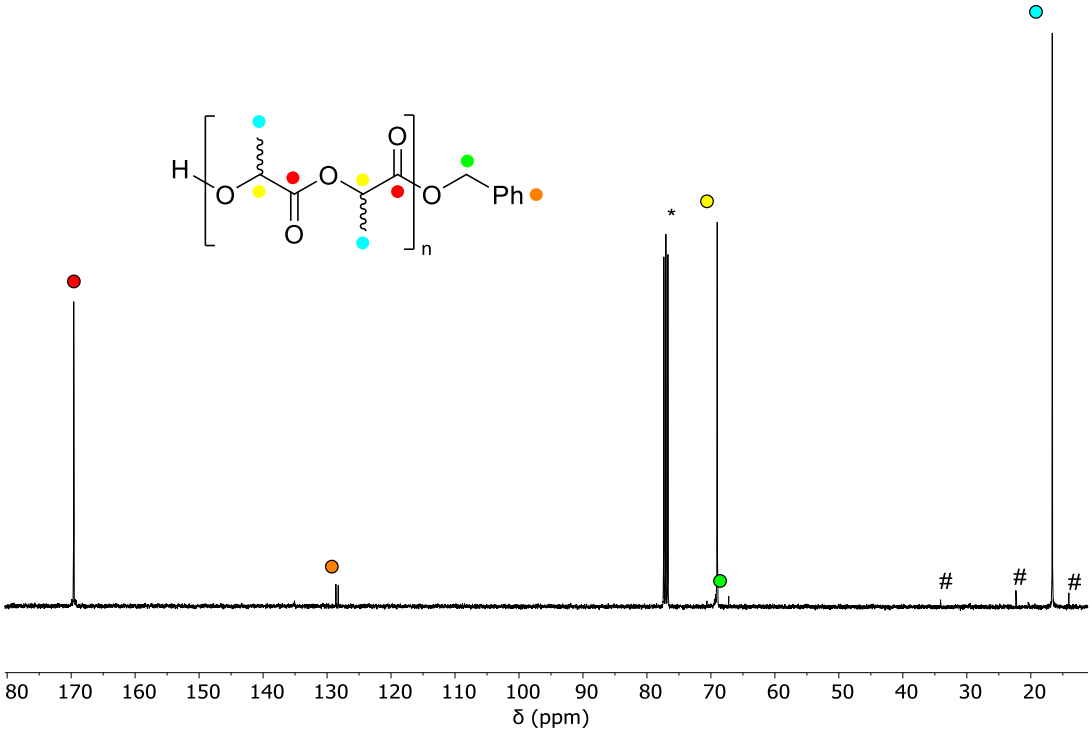

Figure A.74 $^{13}C\{^{1}H\}$ NMR spectrum (*choroform-d_1, 101 MHz, 298 K) of PLA isolated from a polymerisation catalysed by complex **19**/BnOH. Conditions: [*L*-LA]$_0$:[**Ca**$^+$]$_0$:[BnOH]$_0$ = 50:1:1, [*L*-LA]$_0$ = 0.5 M, 0.6 mL chloroform-d_1, 60 °C. M_w/M_n = 1.63.

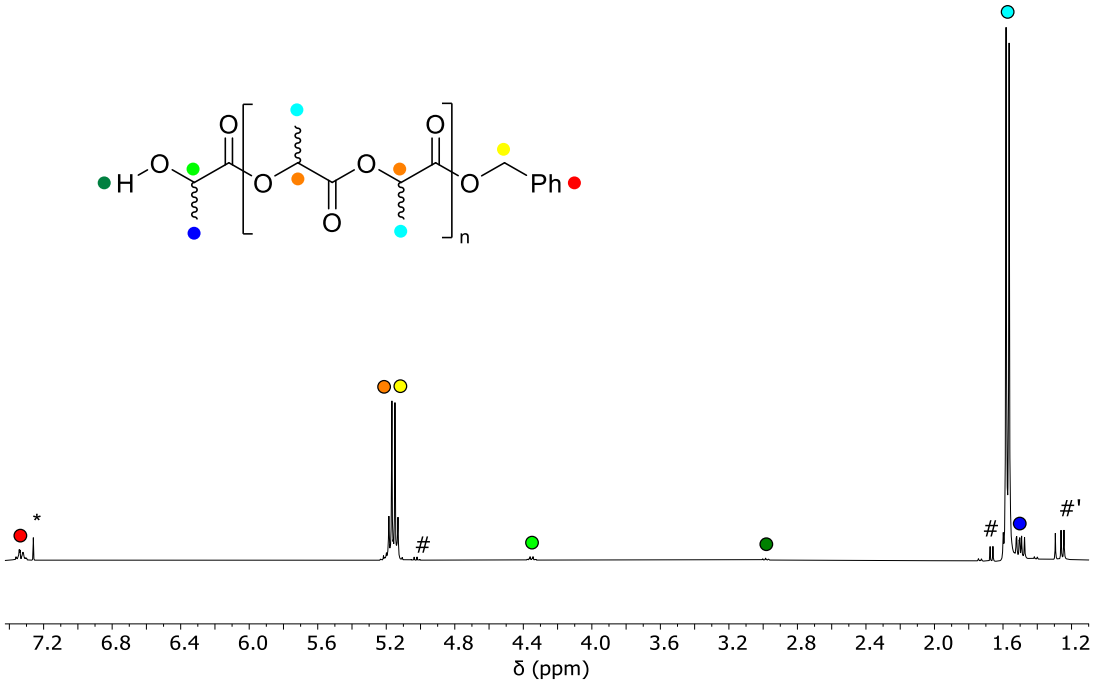

Figure A.75 ^{1}H NMR spectrum (*choroform-d_1, 400 MHz, 298 K) of PLA isolated from a polymerisation catalysed by complex **24**/BnOH. Conditions: [*L*-LA]$_0$:[**Zn**$^+$]$_0$:[BnOH]$_0$ = 50:1:1, [*L*-LA]$_0$ = 0.5 M, 0.6 mL chloroform-d_1, 60 °C. M_w/M_n = 1.08. # and #' represent residual monomer and catalyst respectively.

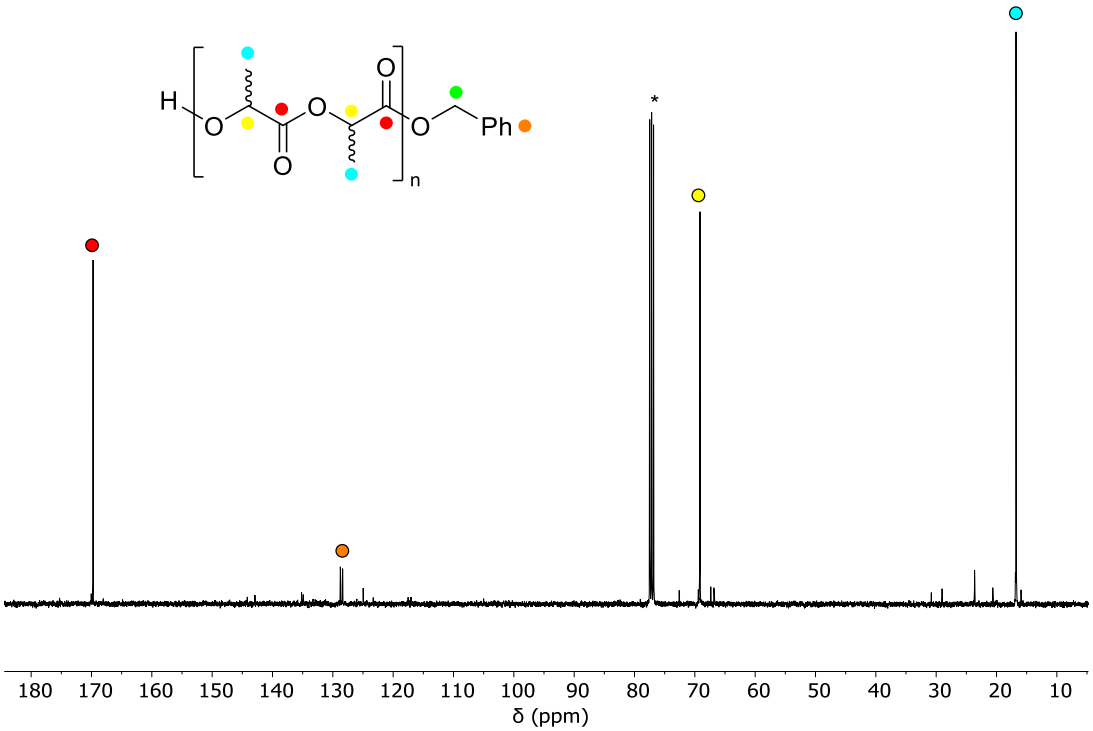

Figure A.76 $^{13}C\{^{1}H\}$ NMR spectrum (*choroform-d_1, 101 MHz, 298 K) of PLA isolated from a polymerisation catalysed by complex **24**/BnOH. Conditions: $[L\text{-LA}]_0$:$[\mathbf{Zn^+}]_0$:$[BnOH]_0$ = 50:1:1, $[L\text{-LA}]_0$ = 0.5 M, 0.6 mL chloroform-d_1, 60 °C. M_w/M_n = 1.08.

References

1. J. March, *Advanced Organic Chemistry: Reactions, Mechanisms, and Structure*, Wiley, New York, 3rd edn., 1985.
2. J. R. Dorgan, J. Janzen, D. M. Knauss, S. B. Hait, B. R. Limoges and M. H. Hutchinson, *J. Polym. Sci., Part B: Polym. Phys.*, 2005, **43**, 3100-3111.
3. S. Emamian, T. Lu, H. Kruse and H. Emamian, *J. Comput. Chem.*, 2019, **40**, 2868-2881.
4. E. Espinosa, E. Molins and C. Lecomte, *Chem. Phys. Lett.*, 1998, **285**, 170-173.
5. T. Rodima, V. Mäemets and I. Koppel, *J. Chem. Soc., Perkin Trans. 1*, 2000, 2637-2644.
6. A. Kütt, S. Tshepelevitsh, J. Saame, M. Lõkov, I. Kaljurand, S. Selberg and I. Leito, *Eur. J. Org. Chem.*, 2021, **2021**, 1407-1419.